

11/24/3797

W. J. M. ...

MONASH UNIVERSITY
THESIS ACCEPTED IN SATISFACTION OF THE
REQUIREMENTS FOR THE DEGREE OF
DOCTOR OF PHILOSOPHY

ON..... 29 June 2004.....

Sec. Research Graduate School Committee

Under the Copyright Act 1968, this thesis must be used only under the normal conditions of scholarly fair dealing for the purposes of research, criticism or review. In particular no results or conclusions should be extracted from it, nor should it be copied or closely paraphrased in whole or in part without the written consent of the author. Proper written acknowledgement should be made for any assistance obtained from this thesis.

Room Temperature Ionic Liquids as Electrolytes for use with the Lithium Metal Electrode

By

Patrick C. Howlett

B. Sc. (Hons.)

A thesis submitted to the Faculty of Science, Monash University, in fulfilment
of the requirements for the degree of *Doctor of Philosophy*.

Department of Chemistry

Monash University

Australia

February 2004

Table of Contents

Abstract.....	vi
Declaration.....	ix
Acknowledgements.....	x
List of Figures & Tables.....	xi
Glossary of Terms.....	xxiii
Introduction.....	1
1.1 Lithium:.....	6
1.2 Lithium batteries:.....	7
1.2.1 Lithium ion batteries:.....	7
1.2.2 Lithium metal rechargeable batteries:.....	9
1.2.3 Lithium metal rechargeable vs. lithium-ion systems:.....	10
1.3 Electrolytes:.....	13
1.3.1 Mass transfer in solution:.....	13
1.3.2 Electrochemical stability:.....	20
1.3.3 Important properties:.....	21
1.3.4 Characterisation:	23

1.4 Lithium battery electrolytes:	26
1.4.1 Salts:	26
1.4.2 Aprotic liquids:	28
1.4.3 Polymer electrolytes:	32
1.4.4 Ceramics and glasses:	38
1.4.5 Room temperature ionic liquids (RTILs):	39
1.5 The solid electrolyte interphase (SEI):	56
1.5.1 Properties:	56
1.5.2 Structure:	57
1.5.3 Relationship to battery operation – dendrite formation:	61
1.5.4 Characterisation:	74
1.6 Summary:	78
1.7 Aims:	79
Experimental	88
2.1 Materials and preparation:	88
2.1.1 Glovebox:	88
2.1.2 Lithium metal:	88
2.1.3 Positive electrode materials:	89
2.1.4 Separators:	89
2.1.5 Electrolytes:	89
2.1.6 Room temperature ionic liquids (RTILs):	90
2.1.7 Additives:	91

2.2 Cells:	93
2.2.1 Resealable stainless steel 'cup' cells:	93
2.2.2 Optical cells:	94
2.2.3 3-electrode cells:	99
2.2.4 Conductivity cell:	101
2.3 Apparatus:	102
2.3.1 Electrochemical measurements:	102
2.3.2 Cycling experiments:	103
2.4 Characterisation techniques:	106
2.4.1 Raman spectroscopy:	106
2.4.2 Fourier transform infrared spectroscopy:	107
2.4.3 X-ray diffractometry (XRD):	108
2.4.4 X-ray photoelectron spectroscopy (XPS):	109
2.4.5 Electrochemical impedance spectroscopy (EIS):	110
2.4.6 Nuclear magnetic resonance spectroscopy:	111
2.5 Cycling Experiments:	112
2.5.1 Optical cell:	112
2.5.2 3-electrode cell:	113
2.5.3 Resealable stainless steel cup cells:	114
2.6 Methodology:	115
2.6.1 Electrochemical impedance spectroscopy:	115
2.6.2 Voltammetry:	117
2.6.3 Cycling Efficiency:	117

Results & Discussion	119
3.1 Optical cell:	119
3.1.1 Initial studies in 2-electrode configuration:.....	119
3.1.2 3-electrode optical cell experiments:.....	137
3.1.3 Conclusions:.....	196
3.2 3-electrode cell:	207
3.2.1 $P_{14}(Tf)_2N$ – Cycling efficiency:.....	220
3.2.2 $P_{13}(Tf)_2N$ – Cycling efficiency:.....	227
3.2.3 $P_{12}(Tf)_2N$ – Cycling efficiency:.....	228
3.2.4 Conclusions:.....	229
3.3 Diffusion & transport in $Li(Tf)_2N / P_{1x}(Tf)_2N$:	233
3.3.1 Diffusion by 3-electrode cell (Randles-Sevcik):.....	233
3.3.2 Conductivity:.....	235
3.3.3 Multinuclear PFGSE-NMR diffusion:.....	242
3.3.4 Nernst-Einstein calculations:.....	249
3.3.5 Transport number:.....	254
3.3.6 Conclusions:.....	258
3.4 Surface Characterisation:	263
3.4.1 X-ray photoelectron spectroscopy (XPS):.....	264
3.4.2 Grazing angle X-ray diffraction (GAXRD):.....	279
3.4.3 Diffuse reflectance FTIR - (DRFTIR) and Raman spectroscopy:.....	282
3.4.4 Electrochemical impedance spectroscopy (EIS):.....	299
3.4.5 Conclusions:.....	309
3.5 Additives:	315

3.6 Cell studies:	325
3.6.1 Asymmetrical (Li/Cu) cells:.....	328
3.6.2 Lithium metal ionic liquid (LMIL) rechargeable cells:.....	330
3.6.3 Comparison with $PP_{13}(Tf)_2N$:.....	333
3.6.4 Conclusions:.....	338

Conclusions & Future Work	341
--	-----

Publications	351
---------------------------	-----

Abstract

Lithium metal is an attractive material for use in rechargeable cells because of its high electrochemical energy density. However, its use results in cells that exhibit a short cycle-life and have a tendency to short circuit, a serious safety concern. Room temperature ionic liquids (RTILs) are attractive electrolyte materials because of their high ionic conductivity, wide electrochemical window, non-flammability, high thermal stability and negligible vapour pressure. This work describes the investigation of these materials as a possible solution to the problems associated with cycling the lithium metal electrode.

An optical cell was developed to allow in-situ observation of the lithium electrode | electrolyte interface during the deposition and dissolution of lithium. The cell incorporated a borosilicate window to allow in-situ Raman spectra to be acquired. The cell was used to survey, and rank, in terms of their cycling efficiency on a copper substrate, a matrix of RTILs for use with the lithium metal electrode. The experiments were conducted at 50 °C to facilitate lithium transport in the electrolyte and through the SEI. The pyrrolidinium cation was found to be superior to the imidazolium cation, presumably because of its reduced tendency for reduction. Of the anions surveyed, bis(trifluoromethanesulfonyl)amide ((Tf)₂N⁻) exhibited a tendency to passivate the lithium surface, resulting in relatively high cycling efficiencies. The RTIL, alkylmethylpyrrolidinium bis(trifluoromethanesulfonyl)amide (P_{1X}(Tf)₂N) was found to be a potential electrolyte solvent for lithium metal rechargeable cells.

The optical cell experiments indicated that the lithium deposit morphology in P_{1X}(Tf)₂N electrolytes (with 0.5 mol/kg of Li(Tf)₂N added) was highly sensitive to the applied current density. At low current density (< ~1.0 – 1.5 mAcm⁻²) the deposit was uniform and hemispherical; above ~1.5 – 2.0 mAcm⁻² the lithium deposit became dendritic. When the deposit morphology was non-dendritic, the cycling efficiency in the optical cell was high, around 90 %. Dendritic deposit morphology resulted in significantly reduced cycling efficiency. The formation of dead (disconnected) lithium was observed on these occasions. A marked difference in the behaviour (particularly the deposit morphology) was noted between the native lithium surface (with its glovebox surface film) and that of lithium

deposited on a copper substrate. The native lithium surface was associated with a much-reduced tendency to form dendrites.

Experiments were conducted in a conventional 3-electrode cell to allow a more accurate determination of the influence of current density. Platinum, nickel and copper substrates were also compared in these experiments. Very high cycling efficiencies (> 99 %) were obtained on a platinum substrate at appreciable current densities (1.0 mAcm⁻²). The improved behaviour was related to the underpotential deposition and alloy formation that occurs when lithium is deposited on platinum, indicating that the slightly less negative potentials involved made a significant difference to the cycling behaviour of the deposit. The cycling efficiency rapidly decayed at rates above 1.75 mAcm⁻². The cycling behaviour of lithium on copper and nickel substrates was very similar. Cycling efficiencies were reduced compared to those obtained on platinum, typically around 90 %. At low current density (0.1 mAcm⁻²), high cycling efficiency (>99 %) on copper was obtained. Initial cycling at low rates (0.1 mAcm⁻²) on copper allowed improved cycling efficiencies to be obtained at higher rates (0.25 & 0.5 mAcm⁻²).

Conductivity (Electrochemical impedance spectroscopy) and diffusion (Pulsed field gradient spin echo nuclear magnetic resonance spectroscopy) measurements were used to investigate the transport properties of the P_{1X}(Tf)₂N electrolytes. The electrolyte conductivity was found to decrease with increasing lithium salt concentration and to increase with temperature. At all concentrations the diffusivity of all three species (i.e., P_{1X}⁺, Li⁺ and (Tf)₂N⁻) was found to be similar, and all three species exhibited similar activation energies. The calculated Nernst-Einstein conductivity was greater than the measured conductivity and the disparity increased with temperature. Such behaviour indicated the presence of 'currentless' modes of diffusion within the RTIL, and that their influence increased with temperature. A cross coefficient was determined to account for the currentless modes and was used to determine transport numbers for each ion in the RTIL. The lithium transport number was found to be low and increasing with temperature (e.g., 0.05 – 0.2 in 0.5 mol/kg P₁₄(Tf)₂N for temperatures 25 – 70 °C).

Spectroscopic analysis of the lithium surface cycled in a P_{1X}(Tf)₂N electrolyte indicated that reduced electrolyte species were present. The majority of compounds were reduction

products of the $(\text{Tf})_2\text{N}^-$ anion. A clear difference in the composition of the native lithium surface (i.e., that prepared in the glovebox and then exposed to the electrolyte) and that of the surface of lithium deposited 'in-situ' on a copper substrate was evidenced. The native surface retained species such as Li_2O and Li_2CO_3 in significant quantities. These species were absent from the lithium on copper substrate samples. XPS and DRFTIR spectra indicated the presence of materials related to the pyrrolidinium cation within the $(\text{Tf})_2\text{N}^-$ dominated SEI for the lithium deposited on copper sample. The difference in surface composition was related to the observation that the cycling behaviour and deposit morphology differed depending on the substrate. EIS analysis at varied temperatures indicated phases exhibiting distinctly different activation energies for lithium conduction. Coupled with results from XPS etching experiments, this information indicated a layered structure for the SEI formed in $\text{P}_{1X}(\text{Tf})_2\text{N}$ electrolytes. It was concluded that the RTIL anion was responsible for the formation of the SEI. Replacing the lithium salt, $\text{Li}(\text{Tf})_2\text{N}$, with LiAsF_6 resulted in a more viscous liquid, with reduced rate capability but improved cycling efficiency. In light of the spectroscopic evidence for SEI formation, it is proposed that the variation of the RTIL anion and/or the lithium salt anion represents a powerful tool for improving lithium cycling behaviour in an RTIL (where the cation is stable versus reduction).

Rechargeable lithium cells incorporating transition metal cathode materials were investigated. All of the cells exhibited a pronounced capacity fade with cycling. The rate of capacity fade was reduced when a LiCoO_2 cathode with a platinum current collector was employed. The cells were capable of cycling at elevated temperatures ($> 50^\circ\text{C}$), offering a possible niche application for devices employing these electrolytes. Symmetrical lithium cells cycled under identical conditions did not exhibit any modes that would have contributed to the capacity fade. Thus, it was concluded that the capacity fade was associated with the cathode, and this was suggested as the principle avenue for further investigation to enable the application of these materials in rechargeable lithium cells.

Declaration

This thesis contains no material which has been accepted for the award of any degree or diploma in any university and, to the best of the author's knowledge and belief, contains no material previously published or written by another person, except where due reference has been made in the text.



Patrick C. Howlett

Acknowledgements

I would like to express my sincere thanks to my supervisors, Prof. Doug MacFarlane and Dr. Tony Hollenkamp. Together, they have provided me with just the right balance of guidance and support to allow me to advance my skills and abilities, while also advancing science.

I have had the good fortune to be part of two research groups during my candidature.

I would like to thank all of the members of the Monash electrolytes group for their assistance. Particularly Prof. Maria Forsyth, who with Doug, has established a strong, supportive and diverse research group. I would also like to thank Maria for her help with the transport and characterisation sections of this thesis. Dr. Peter Newman, the cornerstone of our group, thanks for your almost daily assistance with just about everything, and for your excellent proof reading. Thanks also to the other members of the group who have become my friends as well as collaborators. Jim Efthimiadis, Dr. Stewart Forsyth, Dr. Kate Naim, Dr. Jenny Pringle, Tim Wooster (thanks for keeping an eye on those squiggly lines), Dr. Adam Best, Nolene Byrne, Churat Tiyaiboonchaiya, Sharyn Long, Dr. Qing Dai and Steve Pas. Thanks also to Rod Hall for his help with the infrared spectroscopy. Also, thanks to Alan Holland and the guys in the workshop for their patience and practical suggestions.

My other workplace, the CSIRO energy storage group, was another invaluable resource. I would like to thank all of the members of the group. Particularly Dr. Russell Newnham, who was instrumental in establishing my candidature. Thanks also to Andrew Urban, Warren Baldsing, Dr. David Rand and Chris Phyland for their help along the way.

Special thanks to Dr. Jonian Nikolov for his technical expertise and sense of humour. Dr. Narelle Brack for performing the XPS measurements and for her expert assistance in interpreting the results.

I would like to thank my family and friends for their support and for providing valuable distractions along the way. Particularly David Monk, for his proof reading efforts.

I would like to recognise the financial support of the Monash University Department of Chemistry and CSIRO Energy Technology, which has made this work possible. I also acknowledge the support of the Monash Research Graduate School for providing travel grants to present my research in the United States.

Finally, and most importantly, thanks to Ashley for making the sandwiches.

List of Figures & Tables

Introduction

- | | |
|-----------|---|
| Fig. 1.1 | World energy demand by fuel, 1971-2020. |
| Fig. 1.2 | Percentage of publications per year for 'batteries' and 'lithium AND batteries'. |
| Fig. 1.3 | Market forecast for portable batteries to 2010. |
| Fig. 1.4 | Schematic representation of the lithium metal rechargeable cell and the lithium ion cell. |
| Fig. 1.5 | Volumetric and gravimetric energy content of various rechargeable batteries |
| Fig. 1.6 | Scheme for laboratory scale synthesis of RTILs. |
| Fig. 1.7 | General preparative route for halide free synthesis of alkylimidazolium RTILs. |
| Fig. 1.8 | Graph showing RTIL publications. |
| Fig. 1.9 | Schematic representation of a section of the polyheteromicrophase SEI. |
| Fig. 1.10 | Schematic representation of the deposition/dissolution process. |
| Fig. 1.11 | Schematic representation of an optical cell. |
| Table 1.1 | Some common and experimental intercalation materials used as cathodes for lithium metal rechargeable and lithium ion batteries. |
| Table 1.2 | Properties of various non-aqueous electrolytes. |
| Table 1.3 | Table of forms of the Laplacian operator (∇^2) for different geometries. |
| Table 1.4 | Table of names, structures and properties of solvents used in nonaqueous electrochemistry. |
| Table 1.5 | Table of examples of RTILs (highlighting the cation or anion). |
| Table 1.6 | Summary of key developments pertaining to chloroaluminate RTILs since 1982. |
| Table 1.7 | Lithium battery research pertaining to air and moisture stable RTILs. |
| Table 1.8 | Bimolecular rate constants (k_e) for the reaction of hydrated electrons with Li battery related materials. |

Experiment 1

- Fig. 2.1 Cup cell schematic.
- Fig. 2.2 Tools used in the fabrication of the optical cell.
- Fig. 2.3 Schematic of the fabrication of the optical cell.
- Fig. 2.4 3-Electrode cell apparatus.
- Fig. 2.5 Nickel and copper working electrodes.
- Fig. 2.6 2-electrode conductivity dip cell.
- Fig. 2.7 Schematic of optical cell cycling equipment.
- Fig. 2.8 Schematic of the 'Bolt cell' used for ex-situ Raman spectra acquisition.
- Fig. 2.9 Schematic of the DRFTIR chamber.
- Fig. 2.10 Schematic of the XRD environmental chamber.
- Fig. 2.11 Schematic of the XRD geometry.
- Fig. 2.12 Example of the plots used to determine macroelectrode surface area.
- Table 2.1 Details of the synthesis and typical analysis results for each of the RTILs used in this work.

Results & Discussion

3.1 Optical cell:

- Fig. 3.1.1 Voltage profile of a PC/LiPF₆ optical cell cycled at 2 mAcm⁻², 1 Ccm⁻² and ambient temperature.
- Fig. 3.1.2 Images obtained from a PC/LiPF₆ optical cell cycled at 2 mAcm⁻², 1 Ccm⁻² and ambient temperature.
- Fig. 3.1.3 Voltage profile of a PC/LiPF₆ optical cell cycled at 6 mAcm⁻², 20 Ccm⁻² and ambient temperature.
- Fig. 3.1.4 Images obtained from a PC/LiPF₆ optical cell cycled at 6 mAcm⁻² and 20 Ccm⁻² at ambient temperature.
- Fig. 3.1.5 Representative plot of the voltage profile for a 0.5 molkg⁻¹ EMI(Tf)₂N optical cell cycled at 1 mAcm⁻², 1 Ccm⁻² and 75 °C.

- Fig. 3.1.6 Images obtained from a 0.5 molkg⁻¹ EMI(Tf)₂N optical cell cycled at 1 mAcm⁻², 1 Ccm⁻² and 75 °C.
- Fig. 3.1.7 0.25 molkg⁻¹ P₁₃BF₄ optical cell, a) initial cycles at 0.1 mAcm⁻² and 0.1 Ccm⁻² at 80 °C, b) representative cycles at 0.05 mAcm⁻² and 0.1 Ccm⁻² at 80 °C.
- Fig. 3.1.8 Images acquired from a 0.25 molkg⁻¹ P₁₃BF₄ optical cell cycled at 0.05 mAcm⁻², 0.1 Ccm⁻² at 80 °C,
- Fig. 3.1.9 Voltage profile of a 0.4 molkg⁻¹ P₁₃(Tf)₂N optical cell, 1500 cycles at 1 mAcm⁻², 1 Ccm⁻² and 75 °C.
- Fig. 3.1.10 Images acquired from a 0.4 molkg⁻¹ P₁₃(Tf)₂N optical cell, cycled at 1 mAcm⁻², 1 Ccm⁻² and 75 °C.
- Fig. 3.1.11 Voltage profile of a 0.4 molkg⁻¹ P₁₃(Tf)₂N optical cell at 75 °C at varied rates.
- Fig. 3.1.12 Colour micrographs obtained from a 0.4 molkg⁻¹ P₁₃(Tf)₂N optical cell after 1500 charge-discharge cycles.
- Fig. 3.1.13 0.5 molkg⁻¹ EMIDCA cycling efficiency potential profile.
- Fig. 3.1.14 0.5 molkg⁻¹ EMIDCA cycling efficiency images.
- Fig. 3.1.15 0.5 molkg⁻¹ EMIDCA post cycling efficiency images.
- Fig. 3.1.16 0.5 molkg⁻¹ EMIBF₄ images, uncycled.
- Fig. 3.1.17 0.5 molkg⁻¹ EMIBF₄ cycling efficiency potential profile
- Fig. 3.1.18 0.5 molkg⁻¹ EMIBF₄ cycling efficiency images.
- Fig. 3.1.19 0.5 molkg⁻¹ EMI(Tf)₂N cycling efficiency potential profile (1st experiment).
- Fig. 3.1.20 0.5 molkg⁻¹ EMI(Tf)₂N post deposition images (1st experiment).
- Fig. 3.1.21 0.5 molkg⁻¹ EMI(Tf)₂N post cycling images (1st experiment).
- Fig. 3.1.22 0.5 molkg⁻¹ EMI(Tf)₂N cycling efficiency potential profile (2nd experiment).
- Fig. 3.1.23 0.5 molkg⁻¹ EMI(Tf)₂N post deposition images (2nd experiment).
- Fig. 3.1.24 0.5 molkg⁻¹ EMI(Tf)₂N cycling efficiency potential profile (3rd experiment).
- Fig. 3.1.25 0.5 molkg⁻¹ EMI(Tf)₂N cycling efficiency potential profile (4th experiment).
- Fig. 3.1.26 0.5 molkg⁻¹ EMI(Tf)₂N post deposition images (4th experiment).
- Fig. 3.1.27 0.5 molkg⁻¹ EMI(Tf)₂N post cycling images (4th experiment).
- Fig. 3.1.28 0.5 molkg⁻¹ EMI(Tf)₂N cycling efficiency potential profile (5th experiment).
- Fig. 3.1.29 0.5 molkg⁻¹ EMI(Tf)₂N post deposition images (5th experiment).
- Fig. 3.1.30 0.5 molkg⁻¹ EMI(Tf)₂N cycling efficiency potential profile (6th experiment).

- Fig. 3.1.31 0.5 molkg⁻¹ EMI(Tf)₂N post cycling images (6th experiment).
- Fig. 3.1.32 0.5 molkg⁻¹ P₁₃BF₄ cycling efficiency potential profile.
- Fig. 3.1.33 0.5 molkg⁻¹ P₁₃BF₄ post deposition images.
- Fig. 3.1.34 0.5 molkg⁻¹ P₁₃BF₄ post cycling images.
- Fig. 3.1.35 0.5 molkg⁻¹ P₁₄DCA cycling efficiency potential profile.
- Fig. 3.1.36 0.5 molkg⁻¹ P₁₄DCA post deposition images.
- Fig. 3.1.37 0.5 molkg⁻¹ P₁₄DCA post cycling images.
- Fig. 3.1.38 0.5 molkg⁻¹ BMII cycling efficiency potential profile.
- Fig. 3.1.39 0.5 molkg⁻¹ BMII post deposition images.
- Fig. 3.1.40 0.5 molkg⁻¹ BMII post cycling images.
- Fig. 3.1.41 0.5 molkg⁻¹ P₁₄(Tf)₂N cycling efficiency potential profile (1st experiment).
- Fig. 3.1.42 0.5 molkg⁻¹ P₁₄(Tf)₂N post deposition images (1st experiment).
- Fig. 3.1.43 0.5 molkg⁻¹ P₁₄(Tf)₂N post cycling images (1st experiment).
- Fig. 3.1.44 0.5 molkg⁻¹ P₁₄(Tf)₂N cycling efficiency potential profile, (2nd experiment).
- Fig. 3.1.45 0.5 molkg⁻¹ P₁₄(Tf)₂N post deposition images (2nd experiment).
- Fig. 3.1.46 0.5 molkg⁻¹ P₁₄(Tf)₂N post cycling images (2nd experiment).
- Fig. 3.1.47 0.5 molkg⁻¹ P₁₄(Tf)₂N cycling efficiency potential profile (3rd experiment).
- Fig. 3.1.48 0.5 molkg⁻¹ P₁₄(Tf)₂N cycling efficiency potential profile (4th experiment).
- Fig. 3.1.49 0.5 molkg⁻¹ P₁₄(Tf)₂N post deposition images (4th experiment).
- Fig. 3.1.50 0.5 molkg⁻¹ P₁₄(Tf)₂N post cycling images (4th experiment).
- Fig. 3.1.51 0.5 molkg⁻¹ P₁₃(Tf)₂N cycling efficiency potential profile (1st experiment).
- Fig. 3.1.52 0.5 molkg⁻¹ P₁₃(Tf)₂N post deposition image (1st experiment).
- Fig. 3.1.53 0.5 molkg⁻¹ P₁₃(Tf)₂N post cycling images (1st experiment).
- Fig. 3.1.54 0.5 molkg⁻¹ P₁₃(Tf)₂N cycling efficiency potential profile (2nd experiment).
- Fig. 3.1.55 0.5 molkg⁻¹ P₁₃(Tf)₂N post deposition and post cycling images (2nd experiment).
- Fig. 3.1.56 0.5 molkg⁻¹ P₁₃(Tf)₂N cycling efficiency potential profile (3rd experiment).
- Fig. 3.1.57 0.5 molkg⁻¹ P₁₃(Tf)₂N post cycling images (3rd experiment).
- Fig. 3.1.58 0.5 molkg⁻¹ P₁₃(Tf)₂N cycling efficiency potential profile – High rate (1st experiment).
- Fig. 3.1.59 0.5 molkg⁻¹ P₁₃(Tf)₂N in-situ deposition images – High rate (1st experiment).
- Fig. 3.1.60 0.5 molkg⁻¹ P₁₃(Tf)₂N post deposition images – High rate (1st experiment).
- Fig. 3.1.61 0.5 molkg⁻¹ P₁₃(Tf)₂N in-situ cycling images – High rate (1st experiment).

- Fig. 3.1.62 0.5 molkg⁻¹ P₁₃(Tf)₂N post cycling images – High rate (1st experiment).
- Fig. 3.1.63 0.5 molkg⁻¹ P₁₃(Tf)₂N cycling efficiency potential profile – High rate (2nd experiment).
- Fig. 3.1.64 0.5 molkg⁻¹ P₁₃(Tf)₂N in-situ deposition images – High rate (2nd experiment).
- Fig. 3.1.65 0.5 molkg⁻¹ P₁₃(Tf)₂N post deposition images – High rate (2nd experiment).
- Fig. 3.1.66 0.5 molkg⁻¹ P₁₃(Tf)₂N post cycling images – High rate (2nd experiment).
- Fig. 3.1.67 0.5 molkg⁻¹ P₁₃(Tf)₂N in-situ deposition images - Very high rate experiment.
- Fig. 3.1.68 0.5 molkg⁻¹ P₁₃(Tf)₂N post deposition image – Very high rate experiment.
- Fig. 3.1.69 Schematic of the cell for deposition on an insulating substrate.
- Fig. 3.1.70 0.5 molkg⁻¹ P₁₃(Tf)₂N, lithium deposited on a gold sputtered substrate.
- Fig. 3.1.71 0.5 molkg⁻¹ P₁₃(Tf)₂N / 0.30 wt% PVP cycling efficiency potential profile (1st experiment).
- Fig. 3.1.72 0.5 molkg⁻¹ P₁₃(Tf)₂N / 0.3 wt% PVP, representative images (4 experiments).
- Fig. 3.1.73 0.5 molkg⁻¹ P₁₃(Tf)₂N / 0.3 wt% PVP post cycling counter electrode images.

Table 3.1.1 Parameters used in the optical cell cycling efficiency measurements.

Table 3.1.2 Summary of EMI(Tf)₂N optical cell experiments.

Table 3.1.3 Summary of P₁₄(Tf)₂N optical cell experiments.

Table 3.1.4 Summary of P₁₃(Tf)₂N/PVP optical cell experiments.

Table 3.1.5 Summary of optical cell measurements.

3.2 3-electrode cell:

- Fig. 3.2.1 Electrochemical window of P₁₄(Tf)₂N on a Pt substrate, 100 mVs⁻¹ at 25 °C.
- Fig. 3.2.2 Cyclic voltammogram of 0.5 molkg⁻¹ P₁₄(Tf)₂N at 25 °C, 100 mVs⁻¹ on a platinum substrate.
- Fig. 3.2.3 CVs showing the influence of Li(Tf)₂N concentration in P₁₄(Tf)₂N.
- Fig. 3.2.4 Steady state current (a) and low frequency impedance touchdown (b) for equivalent P₁₃(Tf)₂N cells at varying Li(Tf)₂N concentrations.

- Fig. 3.2.5 CVs for a) $0.25 \text{ mol kg}^{-1} \text{ P}_{12}(\text{Tf})_2\text{N}$, b) $0.5 \text{ mol kg}^{-1} \text{ P}_{13}(\text{Tf})_2\text{N}$ & c) $0.5 \text{ mol kg}^{-1} \text{ P}_{14}(\text{Tf})_2\text{N}$. Pt substrate, 100 mVs^{-1} at 25°C .
- Fig. 3.2.6 Multiple cyclic voltammogram of $0.25 \text{ mol kg}^{-1} \text{ P}_{12}(\text{Tf})_2\text{N}$, Pt substrate, 100 mVs^{-1} at 25°C .
- Fig. 3.2.7 Multiple cyclic voltammogram of $0.5 \text{ mol kg}^{-1} \text{ P}_{13}(\text{Tf})_2\text{N}$, Pt substrate, 100 mVs^{-1} at 25°C .
- Fig. 3.2.8 Multiple cyclic voltammogram of $0.5 \text{ mol kg}^{-1} \text{ P}_{14}(\text{Tf})_2\text{N}$, Pt substrate, 100 mVs^{-1} at 25°C .
- Fig. 3.2.9 Multiple cyclic voltammogram of $0.5 \text{ mol kg}^{-1} \text{ P}_{14}(\text{Tf})_2\text{N}$, Ni substrate, 100 mVs^{-1} at 25°C .
- Fig. 3.2.10 Multiple cyclic voltammogram of $0.5 \text{ mol kg}^{-1} \text{ P}_{14}(\text{Tf})_2\text{N}$, Cu substrate, 100 mVs^{-1} at 25°C .
- Fig. 3.2.11 Multiple CVs for a) $0.25 \text{ mol kg}^{-1} \text{ P}_{12}(\text{Tf})_2\text{N}$, b) $0.5 \text{ mol kg}^{-1} \text{ P}_{13}(\text{Tf})_2\text{N}$ & c) $0.5 \text{ mol kg}^{-1} \text{ P}_{14}(\text{Tf})_2\text{N}$.
- Fig. 3.2.12 Multiple CVs for $0.5 \text{ mol kg}^{-1} \text{ P}_{14}(\text{Tf})_2\text{N}$, a) Ni substrate, b) Cu substrate.
- Fig. 3.2.13 Potential profile obtained from a $0.5 \text{ mol kg}^{-1} \text{ P}_{14}(\text{Tf})_2\text{N}$ cycling efficiency experiment, 0.25 mAcm^{-2} , 1 Ccm^{-2} excess & 0.25 Ccm^{-2} cycling capacity at 50°C on a Pt electrode.
- Fig. 3.2.14 Potential profile obtained from a $0.5 \text{ mol kg}^{-1} \text{ P}_{14}(\text{Tf})_2\text{N}$ cycling efficiency experiment, 1.0 mAcm^{-2} , 1 Ccm^{-2} excess & 0.25 Ccm^{-2} cycling capacity at 50°C on a Pt electrode.
- Fig. 3.2.15 Potential profile obtained from a $0.5 \text{ mol kg}^{-1} \text{ P}_{14}(\text{Tf})_2\text{N}$ cycling efficiency experiment, 1.75 mAcm^{-2} , 1 Ccm^{-2} excess & 0.25 Ccm^{-2} cycling capacity at 50°C on a Pt electrode.
- Fig. 3.2.16 Average cycling efficiency (%) at various current densities on a Pt electrode. 1 Ccm^{-2} excess charge & 0.25 Ccm^{-2} cycling charge at 50°C .
- Fig. 3.2.17 Potential profile obtained from a $0.5 \text{ mol kg}^{-1} \text{ P}_{14}(\text{Tf})_2\text{N}$ cycling efficiency experiment, 0.25 mAcm^{-2} , 1 Ccm^{-2} excess & 0.25 Ccm^{-2} cycling capacity at 50°C on a Cu electrode.
- Fig. 3.2.18 Potential profile obtained from a $0.5 \text{ mol kg}^{-1} \text{ P}_{14}(\text{Tf})_2\text{N}$ cycling efficiency experiment, 0.1 mAcm^{-2} , 1 Ccm^{-2} excess & 0.25 Ccm^{-2} cycling capacity at 50°C on a Cu electrode.

- Fig. 3.2.19 Potential profile obtained from a $0.5 \text{ mol kg}^{-1} \text{ P}_{14}(\text{Tf})_2\text{N}$ cycling efficiency experiment, 1 Ccm^{-2} excess & 0.25 Ccm^{-2} cycling capacity at 50°C on a Cu electrode, a) Cycles 330-402 at 0.25 mAcm^{-2} , b) cycles 402-465 at 0.5 mAcm^{-2} .
- Fig. 3.2.20 Cycling efficiency (%) for $0.5 \text{ mol kg}^{-1} \text{ P}_{14}(\text{Tf})_2\text{N}$ at various current densities on a Cu electrode, two experiments. 1 Ccm^{-2} excess charge & 0.25 Ccm^{-2} cycling charge at 50°C .
- Fig. 3.2.21 Potential profile obtained from a $0.5 \text{ mol kg}^{-1} \text{ P}_{13}(\text{Tf})_2\text{N}$ cycling efficiency experiment, 1.0 mAcm^{-2} , 1 Ccm^{-2} excess & 0.25 Ccm^{-2} cycling capacity at 50°C on a Cu electrode.
- Fig. 3.2.22 Cycling efficiency (%) for $0.5 \text{ mol kg}^{-1} \text{ P}_{13}(\text{Tf})_2\text{N}$ at various current densities on a Cu electrode, two experiments. 1 Ccm^{-2} excess charge & 0.25 Ccm^{-2} cycling charge at 50°C .
- Fig. 3.2.23 Potential profile obtained from the excess deposition phase of a $0.5 \text{ mol kg}^{-1} \text{ P}_{12}(\text{Tf})_2\text{N}$ cycling efficiency experiment, 0.1 mAcm^{-2} , 1 Ccm^{-2} excess 60°C on a Cu electrode.

3.3 Diffusion & transport in $\text{Li}(\text{Tf})_2\text{N} / \text{P}_{1x}(\text{Tf})_2\text{N}$:

- Fig. 3.3.1 Cyclic voltammograms obtained at 300K in $0.5 \text{ mol kg}^{-1} \text{ P}_{14}(\text{Tf})_2\text{N}$ at varying scan rates.
- Fig. 3.3.2 Plot of current versus $\sqrt{\text{Scan-rate}}$ for determination of the diffusion coefficient of lithium in $0.5 \text{ mol kg}^{-1} \text{ P}_{14}(\text{Tf})_2\text{N}$.
- Fig. 3.3.3 $0.25 \text{ mol kg}^{-1} \text{ P}_{12}(\text{Tf})_2\text{N}$ EIS complex plane plot, real axis touchdown used to determine the specific conductivity.
- Fig. 3.3.4 0.25 and $0.5 \text{ mol kg}^{-1} \text{ P}_{12}(\text{Tf})_2\text{N}$ specific conductivity.
- Fig. 3.3.5 Neat and $0.5 \text{ mol kg}^{-1} \text{ P}_{13}(\text{Tf})_2\text{N}$ specific conductivity.
- Fig. 3.3.6 Neat, 0.005 , 0.05 & $0.5 \text{ mol kg}^{-1} \text{ P}_{14}(\text{Tf})_2\text{N}$ specific conductivity.
- Fig. 3.3.7 Comparison of the specific conductivity of neat $\text{P}_{13}(\text{Tf})_2\text{N}$ and neat $\text{P}_{14}(\text{Tf})_2\text{N}$.
- Fig. 3.3.8 $0.5 \text{ mol kg}^{-1} \text{ P}_{12}(\text{Tf})_2\text{N}$, $\text{P}_{13}(\text{Tf})_2\text{N}$ & $\text{P}_{14}(\text{Tf})_2\text{N}$ specific conductivity comparison.

- Fig. 3.3.9 Representative 1D Spectra and fits for $\text{Li}(\text{Tf})_2\text{N} / \text{P}_{1\text{x}}(\text{Tf})_2\text{N}$ PFGSE-NMR experiments.
- Fig. 3.3.10 $0.25 \text{ \& } 0.5 \text{ mol kg}^{-1} \text{ P}_{12}(\text{Tf})_2\text{N}$ Arrhenius plot of multinuclear PFGSE-NMR diffusion coefficients.
- Fig. 3.3.11 Neat & $0.5 \text{ mol kg}^{-1} \text{ P}_{13}(\text{Tf})_2\text{N}$ Arrhenius plot of multinuclear PFGSE-NMR diffusion coefficients.
- Fig. 3.3.12 $0.005 \text{ mol kg}^{-1} \text{ P}_{14}(\text{Tf})_2\text{N}$ Arrhenius plot of multinuclear PFGSE-NMR diffusion coefficients.
- Fig. 3.3.13 $0.05 \text{ mol kg}^{-1} \text{ P}_{14}(\text{Tf})_2\text{N}$ Arrhenius plot of multinuclear PFGSE-NMR diffusion coefficients.
- Fig. 3.3.14 $0.5 \text{ mol kg}^{-1} \text{ P}_{14}(\text{Tf})_2\text{N}$ Arrhenius plot of multinuclear PFGSE-NMR diffusion coefficients.
- Fig. 3.3.15 Data from Figs 3.3.11, 3.3.12 & 3.3.13 replotted to compare nuclei at different $\text{Li}(\text{Tf})_2\text{N}$ concentrations.
- Fig. 3.3.16 Comparison of observed and calculated molar conductivities for $\text{P}_{12}(\text{Tf})_2\text{N}$ samples.
- Fig. 3.3.17 Comparison of observed and calculated molar conductivities for $\text{P}_{13}(\text{Tf})_2\text{N}$ samples.
- Fig. 3.3.18 Comparison of observed and calculated molar conductivities for $\text{P}_{14}(\text{Tf})_2\text{N}$ samples.
- Fig. 3.3.19 Plots showing transport number versus temperature, a) Neat $\text{P}_{13}(\text{Tf})_2\text{N}$, b) $0.5 \text{ mol kg}^{-1} \text{ P}_{13}(\text{Tf})_2\text{N}$ and c) $0.5 \text{ mol kg}^{-1} \text{ P}_{14}(\text{Tf})_2\text{N}$.
- Table 3.3.1 Specific conductivity (mS cm^{-1}) of all samples at 25°C and 50°C .
- Table 3.3.2 Apparent Arrhenius activation energies for all samples (300-340K).
- Table 3.3.3 VTF equation parameters for conductivity data for liquid samples (i.e., excludes $\text{P}_{12}(\text{Tf})_2\text{N}$ samples).

3.4 Surface characterisation:

- Fig. 3.4.1 Examples of the voltage profile obtained from galvanostatic cycling of $\text{P}_{1\text{x}}(\text{Tf})_2\text{N}$ cells at 50°C .
- Fig. 3.4.2 Representative XPS scans; a) Survey scan b) Region scans F 1s, N 1s, S 2p, O 1s, C 1s and Li 1s.
- Fig. 3.4.3 Region scan summary for atmosphere and argon transferred Li and Li-Cu samples.
- Fig. 3.4.4 Atomic concentration for each photoelectron line versus etching time for Li (black) and Li-Cu (red) samples.
- Fig. 3.4.5 F 1s high-resolution region spectra with etching for Li and Li-Cu samples.
- Fig. 3.4.6 O 1s high-resolution region spectra with etching for Li and Li-Cu samples.
- Fig. 3.4.7 N 1s high-resolution region spectra with etching for Li and Li-Cu samples.
- Fig. 3.4.8 C 1s high-resolution region spectra with etching for Li and Li-Cu samples.
- Fig. 3.4.9 S 2p high-resolution region spectra with etching for Li and Li-Cu samples.
- Fig. 3.4.10 Li 1s high-resolution region spectra with etching for Li and Li-Cu samples.
- Fig. 3.4.11 Cu 2p high-resolution region spectra with etching for Li-Cu sample.
- Fig. 3.4.12 Phase transformations on the lithium surface within several hours of exposure to air (ageing process).
- Fig. 3.4.13 Phase transformations and phase dependence information at different incident angles immediately and 24 hours after exposure.
- Fig. 3.4.14 Representative diffraction patterns obtained from lithium surfaces cycled in $\text{P}_{1\text{x}}(\text{Tf})_2\text{N}$ electrolytes at 7° incident angle.
- Fig. 3.4.15 Comparison of $\text{P}_{14}(\text{Tf})_2\text{N}$ (red) and the cycled Li-Cu surface (blue) IR spectra (baseline corrected).
- Fig. 3.4.16 Difference spectra obtained for the cycled Li-Cu surface, peaks used to normalise the spectra are indicated.
- Fig. 3.4.17 Comparison of $\text{P}_{14}(\text{Tf})_2\text{N}$ (red) and the cycled Li surface (blue) IR spectra (baseline corrected).
- Fig. 3.4.18 Difference spectra obtained for the cycled Li surface ($0.5 \text{ mol kg}^{-1} \text{ P}_{13}(\text{Tf})_2\text{N}$), peaks used to normalise the spectra are indicated.
- Fig. 3.4.19 Spectra obtained from a separator surface wipe (blue) and uncycled $0.5\text{M} \text{ P}_{13}(\text{Tf})_2\text{N}$ (red).

- Fig. 3.4.20 Difference spectrum obtained from a separator from a cycled $P_{13}(Tf)_2N$ cell and uncycled $P_{13}(Tf)_2N$.
- Fig. 3.4.21 Normalised Raman spectra obtained from a 1M $LiPF_6/PC$ optical cell showing the spectra obtained from the bulk electrolyte, a deposit surface and the lithium surface.
- Fig. 3.4.22 Raman difference spectrum obtained for the Li surface, in-situ optical cell measurement.
- Fig. 3.4.23 Raman spectra of the lithium surface 'native glovebox film', (acquired using the bolt cell) before and after exposure to the atmosphere.
- Fig. 3.4.24 Normalised Raman spectra obtained from a $0.5 \text{ mol kg}^{-1} P_{13}(Tf)_2N$ optical cell showing the spectra obtained from the uncycled bulk electrolyte, after cycling at low rate (potentiostatic) and after cycling at high rates ($\sim 2 \text{ mA cm}^{-2}$).
- Fig. 3.4.25 Normalised Raman spectra obtained from a $0.5 \text{ mol kg}^{-1} P_{13}(Tf)_2N$ optical cell showing the spectra obtained from the uncycled bulk electrolyte, from the surface of a dendrite (Li-Cu) and from the Li surface.
- Fig. 3.4.26 $0.5 \text{ mol kg}^{-1} P_{13}(Tf)_2N$ optical cell Li surface difference spectrum.
- Fig. 3.4.27 $0.5 \text{ mol kg}^{-1} P_{13}(Tf)_2N$ optical cell dendrite (Li-Cu) surface difference spectrum.
- Fig. 3.4.28 Fitted impedance data for a cycled $Li/0.5 \text{ mol kg}^{-1} P_{13}(Tf)_2N/Li$ cell a) simple model b) PEI model A c) PEI model B.
- Fig. 3.4.29 Fitted impedance data for a cycled $Li/0.5 \text{ mol kg}^{-1} P_{13}(Tf)_2N/Li$ cell a) 5 element layer model b) 4 element layer model c) 4 element layer model (locked).
- Fig. 3.4.30 Fitted impedance data for a cycled $Li/0.5 \text{ mol kg}^{-1} P_{13}(Tf)_2N/Li$ cell, 3 element layer model.
- Fig. 3.4.31 Arrhenius plot of the low frequency arc resistance versus temperature for a cycled $Li/0.5 \text{ mol kg}^{-1} P_{13}(Tf)_2N/Li$ cell a) temperature increasing b) temperature decreasing.
- Fig. 3.4.32 Arrhenius plot of the high frequency arc resistance versus temperature for a cycled $Li/0.5 \text{ mol kg}^{-1} P_{13}(Tf)_2N/Li$ cell a) temperature increasing b) temperature decreasing.

- Fig. 3.4.33 Plot of the low frequency touchdown resistance versus time for a cycled $Li/0.5 \text{ mol kg}^{-1} P_{13}(Tf)_2N/Li$ cell.
- Fig. 3.4.34 Simple models of the SEI structure on the Li (a) and Li-Cu (b) surfaces.
- Table 3.4.1 Peak position and assignment for Raman and FTIR spectra of $P_{13}(Tf)_2N$ electrolytes.
- Table 3.4.2 Position and assignment for the most consistently prominent positive peaks in the difference spectrum for the cycled Li-Cu surface.
- Table 3.4.3 Position and assignment for the most consistently prominent negative peaks in the difference spectrum for the cycled Li-Cu surface.
- Table 3.4.4 Position and assignment for the most consistently prominent positive peaks in the difference spectrum for the cycled Li surface.
- Table 3.4.5 Position and assignment for the most consistently prominent negative peaks in the difference spectrum for the cycled Li surface.
- Table 3.4.6 Position and assignment for peaks in the difference spectrum for the separator sample.
- Table 3.4.7 Prominent peaks and tentative assignments for the Li surface Raman difference spectrum.
- Table 3.4.8 Prominent peaks and tentative assignments for the Li-Cu surface Raman difference spectrum.

3.5 Additives:

- Table 3.5.1 Literature survey of additives demonstrated to have improved the cycling behaviour of the lithium metal electrode.
- Table 3.5.2 Additive $P_{13}(Tf)_2N$ electrolyte systems and their cycling efficiencies at various temperatures and rates.
- Table 3.5.3 Typical Li cycling efficiency values obtained for various molecular solvent based electrolytes. Applied current density = 1 mA cm^{-2} , excess charge = 5 C cm^{-2} and cycling charge = 1.25 C cm^{-2} .

3.6 Cell studies:

- Fig. 3.6.1 Coulombic efficiency for 0.5 molkg⁻¹ P₁₄(Tf)₂N cells deposition and dissolution at 1 mAcm⁻² and 1 Ccm⁻² charge at 50 °C.
- Fig. 3.6.2 Cycling behaviour of a Li / P₁₄(Tf)₂N - Celgard™ / LiMn₂O₄(Al) cell cycled at C/10 at 50 °C.
- Fig. 3.6.3 Cycling behaviour of a Li / P₁₃(Tf)₂N - GFFP / LiMn₂O₄(Pt) cell cycled at C/10 at 80 °C.
- Fig. 3.6.4 Cycling behaviour of a Li / P₁₃(Tf)₂N - GFFP / LiCoO₂(Pt) cell cycled at C/10 at 80 °C.
- Fig. 3.6.5 Arrhenius plot showing a comparison of neat and 0.5 molkg⁻¹ samples of P₁₃(Tf)₂N and PP₁₃(Tf)₂N.
- Fig. 3.6.6 Cycling behaviour of a Li / PP₁₃(Tf)₂N - GFFP / LiCoO₂(Pt) cell cycled at C/10 at 80 °C.
- Fig. 3.6.7 Galvanostatic cycling of symmetrical lithium cells at the 'C/10' rate (0.0625 mAcm⁻², 2.25 Ccm⁻²) at 80 °C.

Table 3.6.1 Summary of 'Battery' cells incorporating P_{1X}(Tf)₂N electrolytes studied in this work.

Conclusions

- Fig. 4.1 Energy minimised 3D structures for a) methyl propyl pyrrolidinium b) methyl propyl piperidinium c) methyl propyl phospholanium d) methyl propyl phosphorinanium.

Glossary of terms

2-Me-THF	2-methyl-tetrahydrofuran
AES	Auger electron microscopy
AFM	Atomic force microscopy
ACN	Acrylonitrile
CSL	Compact stratified layer
CV	Cyclic voltammogram
DC	Direct current
DEC	Diethyl carbonate
DEP	Diethyl phthalate
DMC	Dimethyl carbonate
DME	Dimethoxyethane
DMF	Dimethylformamide
DMS	Dimethyl sulphoxide
DN	Dioxolane
DRFTIR	Diffuse reflectance fourier transform infrared reflectance
EC	Ethyl carbonate
EDAX	Energy dispersive analysis of X-rays
Eff.	Cycling efficiency
EGDMA	Ethylene glycol dimethacrylate
EIS	Electrochemical impedance spectroscopy
FOM	Figure of merit
FTIR	Fourier transform infrared reflectance
γ-BL	Gamma butyrolactone
GAXRD	Grazing angle X-ray diffraction

GITT	Galvanostatic intermittent titration technique
GS	Glycol sulfite
HMPA	Hexamethylphosphoramide
K(Tf) ₂ N	Potassium bis(trifluoromethanesulfonyl)amide
LIPON	Lithium phosphorous oxynitride
Li(Tf) ₂ N	Lithium bis(trifluoromethanesulfonyl)amide
LiTriTFSM	Lithium tris(trifluoromethanesulfonyl)methide
MC ₃	2-Keto-4-(2,5,8,11-tetra oxadecyl) 1,3-dioxalane (Modified Carbonate)
MDSC	Modulated differential scanning calorimetry
MEC	Methyl ethyl carbonate
MEEP	Methoxy ethoxy ethoxide phosphazene
NMP	1-methyl-2- pyrrolidinone
NMR	Nuclear magnetic resonance
PAN	Poly(acrylonitrile)
PC	Propylene carbonate
PEGA	Poly(ethylene glycol acrylate)
PEGDME	Poly(ethylene glycol dimethylether)
PEI ~	Polymer electrolyte Interface
PEO	Poly(ethylene oxide)
PGSE-NMR	Pulsed field gradient spin echo nuclear magnetic resonance
PGPS	PEO-grafted polysiloxane
PISE	Polymer in salt electrolyte
PITT	Potentiometric intermittant titration technique
PMMA	Poly(methyl methacrylate)
POO	Poly(oxymethylene-oligo-oxyethylene)
POM	Poly(oxymethylene)

PPO	Poly(propylene oxide)
PPTA	Poly(p-phenylene terephthalamide)
PVC	Poly(vinyl chloride)
PVdC	Poly(vinylidene carbonate)
PVdF	Poly(vinylidne fluoride)
PVP	Poly(vinyl pyrrolidone)
PVS	Poly(vinyl sulfone)
QCMB	Quartz crystal microbalance
Qex	Amount of current to plate an excess of lithium
Qp	Amount of current to plate lithium
Qps	Constant capacity cycling (charge)
Qs	Amount of current to strip plated lithium
RTIL	Room temperature ionic liquid
SAM	Scanning auger electron microscopy
SC	Siloxane crosslinked
SEI	Solid electrolyte interphase
SEM	Scanning electron microscopy
SHE	Standard hydrogen electrode
SPL	Solid polymer layer
STM	Scanning tunnelling microscopy
TDF	Perdeuterated tetrahydrofuran
TEG	Tetra ethylene glycol
TEM	Transmission electron microscopy
Tg	Glass transition temperature
THF	Tetrahydrofuran
TMEDA	N,N,N',N'-tetramethylethylenediamine

TPD	Temperature programmed desorption
XPS	X-ray photoelectron spectroscopy
XRD	X-ray diffraction

Introduction

The population of the world is expected to double by 2050.^{1,2} As a result, our demand for energy is increasing, as are our CO₂ emissions which are predicted to increase 70% by 2030.^{1,3} Figure 1.1 shows the projected world energy usage to the year 2020. Our consumption is predicted to increase by 50 to 100% by 2020. At present 85% of our energy consumption is derived from fossil fuels and is predicted to rise to 90% by the year 2020.^{1,4} The use of renewable resources such as wind, solar and tidal energy is expected to grow but is not expected to impact significantly as a fraction of the total amount of energy consumed (Fig. 1.1).

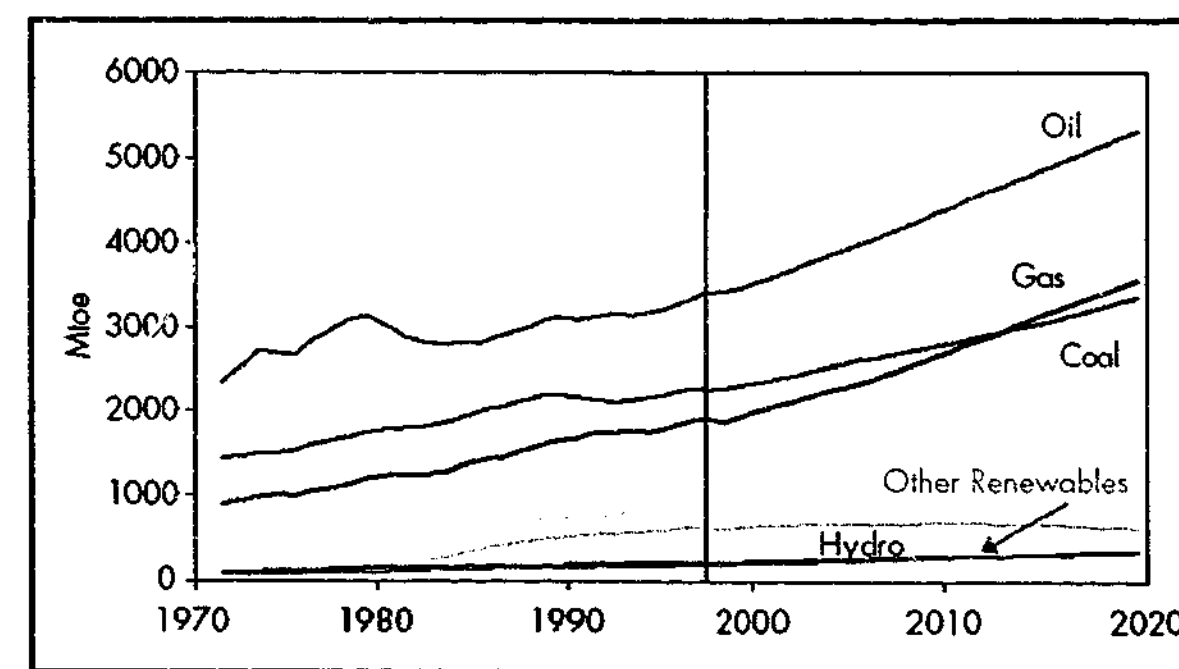


Fig. 1.1 World energy demand by fuel, 1971-2020 (Mtoe – Million tonnes of oil equivalent).¹

All of these trends point towards a global society which will be placing increasing demands on the environment in order to maintain its standard of living. Depletion of the reserves of fossil fuels is not predicted to impact on global energy consumption until after 2050. The development of energy resources derived from nuclear fusion, photovoltaics, biomass, hydropower and wind power are expected to begin to meet the shortfall as fossil fuel reserves become depleted.^{5,6}

Better use of renewable energy sources requires the development of enabling technologies to allow competition on a cost basis with conventional energy sources. One of the key developments required is a safe, efficient means to store the energy produced for later use, and to smooth out variability in supply for some energy sources (e.g., wind and solar energy).^{4,6} This is true for large-scale production, linked to a grid, and for small-to-medium applications (personal devices to electric vehicles) where the energy is generated on a distributed basis. The increasing efficiency of electronic devices (reduced demand for energy) could conceivably herald the onset of personal technology that is easily powered by small-scale distributed supplies.

Numerous devices exist that allow energy to be stored for later use, the most common of which is a battery. A variety of battery chemistries exists in the marketplace and many more exist that have not yet found application. Batteries work by storing chemical energy that is released by the progression of a chemical reaction. In some cases, the reaction is irreversible (a primary battery) and in others, it is reversible (a secondary battery). For secondary batteries, the chemical storage of energy can be a very efficient process, often approaching 100%. This is an attractive feature, particularly for storing renewable energy where the conversion efficiency is often quite low (e.g. solar energy). However, for secondary batteries to begin to have an impact on the way in which we use our available energy resources, significant improvements are required of the present technology.

The requirements for a device that would allow the maximum benefit to be obtained from the chemical storage of energy are quite simple. The device needs to be versatile (i.e., capable of operating under a wide range of conditions and duties), reliable, safe, lightweight, compact, robust, have high power and a long cycle life (i.e., many charge-discharge cycles). These requirements are extremely difficult to achieve and present technology falls well short of the ideal. However, developments over the past few decades have made rapid progress towards a device that could fulfil many of these requirements.

Progress has been made because of a massive worldwide research effort that has been devoted to the development of small, lightweight rechargeable devices for use in personal electronic applications. These applications have been dubbed the 3C's, specifically, cell

phones, camcorders and laptop computers. The rapid growth of the portable electronics market has meant that an economic driver supplying considerable resources for research and development of rechargeable batteries has produced continual improvement of the technology. This research activity is now well established, with many active groups worldwide, and looks set to continue in the same manner. Figure 1.2 displays the results of an ISI Web of Science database search for 'batteries' and 'lithium and batteries' in the title, keyword or abstract. The results are displayed as a percentage of the total number of publications in the database since 1986. It can be seen that the number of 'non-lithium' battery publications has remained relatively static while the number pertaining to lithium has grown steadily.

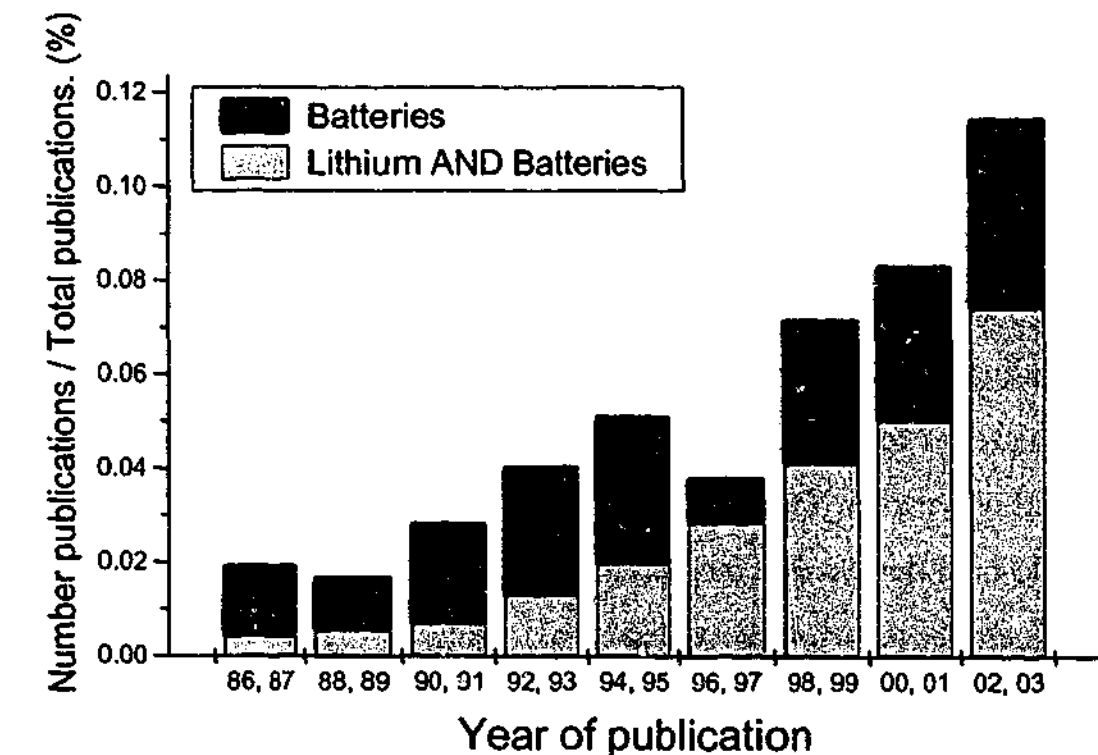


Fig. 1.2 Percentage of publications per year for 'batteries' and 'lithium AND batteries' (Source: ISI Web of Science database).

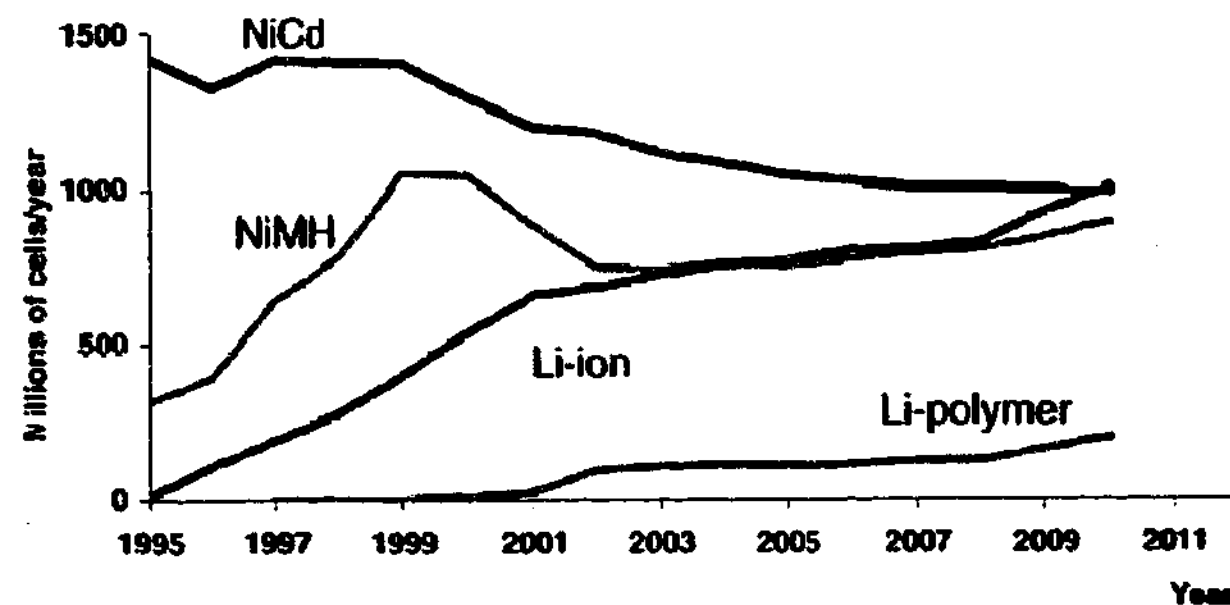


Fig. 1.3 Market forecast for portable batteries to 2010.⁷

Commercially available rechargeable battery chemistries have progressed from lead-acid, through nickel-cadmium, nickel-metal hydride and lithium-ion. Presently these battery chemistries dominate the market with lithium-based devices beginning to become pre-eminent for portable applications (see Fig.1.3).⁷

The focus of this thesis has been an investigation of novel materials that might enable rechargeable batteries to take another step along the path towards a device that will meet the criteria outlined earlier. One advance that would constitute a significant step towards this goal would be a device that incorporates a lithium metal electrode. This has been the underlying precept for the work presented here.

The lithium metal electrode offers several advantages over any other electrode material. Lithium is the lightest metal and in addition, it has the highest anodic potential of any metal, making it an ideal battery anode material. However, due to its very nature lithium metal presents many challenges. Lithium is a reactive metal and will reduce virtually any material it contacts, often reacting vigorously.⁸ Another problem is the fire hazard represented by elemental lithium, the relatively low melting point (180 °C) of the metal carries the risk of generating a pool of molten lithium in the event of accidental overheating.⁹ Furthermore, lithium has a tendency to develop a high surface area with cycling thus producing an even more reactive and potentially dangerous material. As a

result, lithium is diminished to an unsafe material, which exhibits a poor cycle-life and is difficult to handle.^{10,11}

An extensive amount of work has been devoted to the study of the surface of the lithium metal electrode. The poor cycle-life and poor safety characteristics of the lithium metal rechargeable battery are a direct result of the complex processes that occur at the lithium | electrolyte interface, specifically the imperfect reversibility of the charge transfer deposition/dissolution process.

The aim of this work was to develop the means to allow the lithium metal electrode to be used in a secondary cell. Specifically, this involved obtaining an understanding of the behaviour of the electrode | electrolyte interface and the reversibility of the deposition/dissolution process during cycling. The approach used in this work involved the discovery and application of a new electrolyte system, composed of a room temperature ionic liquid (RTIL).

The introductory chapter of this thesis will provide an introduction to rechargeable lithium batteries, an introduction to electrolytes and their properties, and will focus on studies of the charge transfer deposition/dissolution process, the factors affecting it and strategies to enhance its reversibility.

1.1 Lithium:

The dominant raw material for lithium carbonate production, the raw feedstock for the majority of lithium compound production, is from subsurface brines. Production has shifted from hard rock ores (predominantly spodumene) due to lower costs for the brine operations. Chile is the world's largest producer of lithium ores and has reserve of 3×10^6 t (of Lithium content). South American production produced an oversupply of lithium in 1999 resulting in reduced prices. The situation is predicted to continue with benefits for industry through increased competitiveness. Recycling of lithium has been insignificant but has been growing through the recycling of batteries.^{12,13}

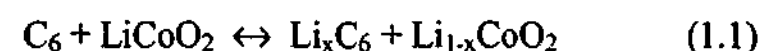
1.2 Lithium batteries:

Rechargeable lithium batteries can be divided into two types.

1.2.1 Lithium ion batteries:

Lithium ion batteries are widely available and have found great commercial success in the marketplace. Market predictions indicate that they will hold the premiere position, in terms of market share, within the portable rechargeable battery market by the end of the present decade, as shown in Fig. 1.3.^{7,14,15}

Lithium ion batteries are also known as 'swing' or 'rocking chair' batteries. These names refer to the principle by which they operate. Figure 1.4 shows the operation of a lithium ion cell during charge (a lithium metal cell is also shown, which will be discussed later). The electrodes are host structures that can reversibly accommodate, by intercalation, guest ions and electrons into their structure without destruction of the lattice.¹¹ A variety of electrode materials can be used (see Table 1.1). The most common combination at present is a graphitic carbon negative electrode and a LiCoO_2 positive electrode.¹⁶ The battery operates under the following stoichiometry;



During charge and discharge the lithium ions flow, via an electrolyte, between the intercalation electrodes. The flow of ions induces a corresponding flow of electrons in an external circuit to maintain charge balance within the electrodes (see Fig. 1.4). Apart from the intercalation materials that form the electrodes, the other major component of the battery is the electrolyte. The electrolyte must conduct lithium ions and be an electrical insulator. A variety of solid and liquid electrolytes have been investigated (see Table 1.2).

By comparison with other competing secondary battery technologies, the lithium ion cell exhibits higher gravimetric and volumetric capacities as well as higher specific energy (see

Fig. 1.5). In addition the cells possess high operating voltage, high cycle-life, low rate of self discharge, no memory effect and a flat discharge curve.^{11,16,17}

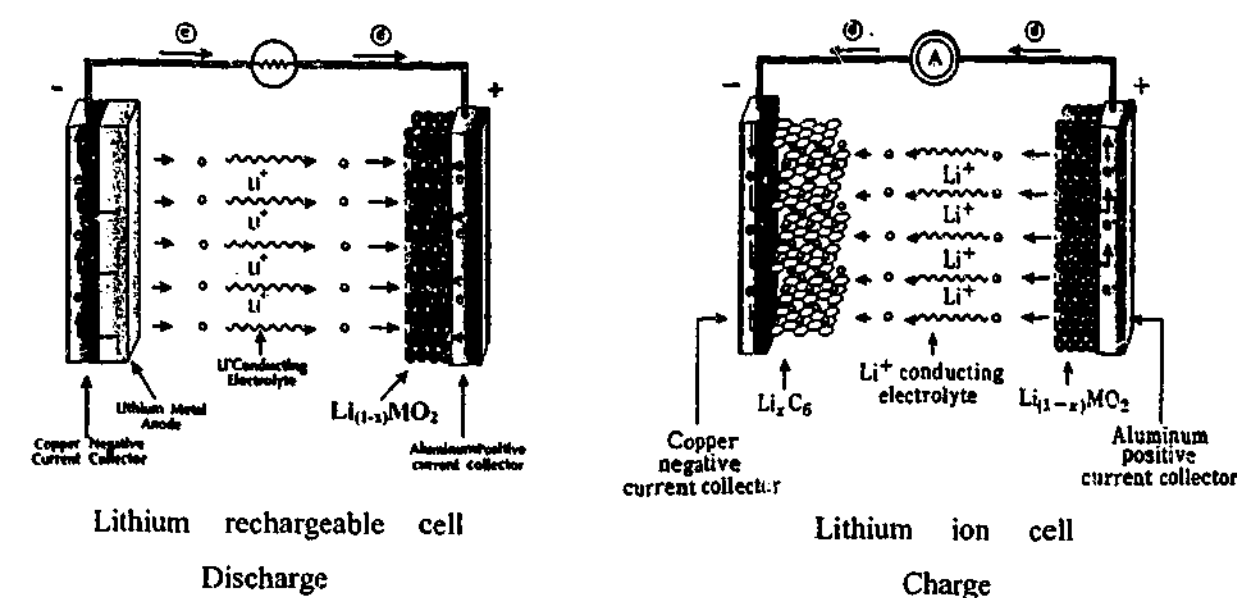


Fig. 1.4 Schematic representation of the lithium metal rechargeable cell and the lithium ion cell.^{16,18}

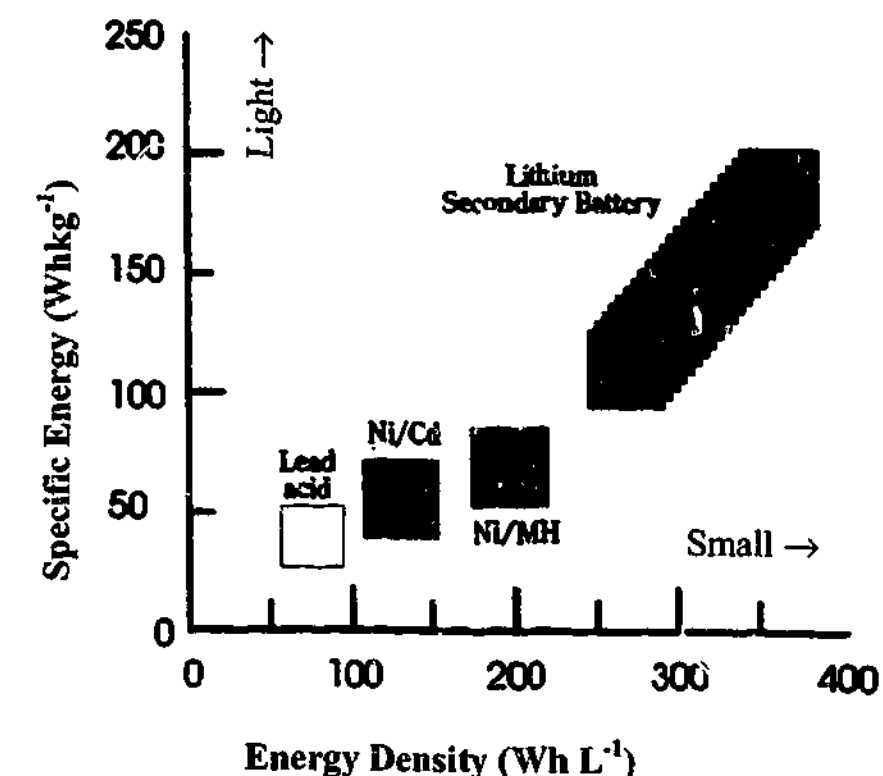


Fig. 1.5 Volumetric and gravimetric energy content of various rechargeable batteries.¹⁶

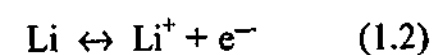
Table 1.1 Some common and experimental intercalation materials used as cathodes for lithium metal rechargeable and lithium ion batteries.

Intercalation Material	Theoretical Specific Capacity (mAhg ⁻¹)	Operating Voltage (V)	Comment	Reference
LiCoO ₂	274	3.0 – 4.3	Expensive and toxic	15
LiNiO ₂	274	2.8 – 4.1	Moderately expensive, difficult to synthesise	15
LiMn ₂ O ₄	148	3.5 – 4.3	Difficult to synthesise, green, low cost	15
LiMnO ₂	270	1.8 – 2.4	Converts to spinel with cycling	19,20
LiCo _x Mn _(1-y) O ₂	200 (demonstrated)	2.6 – 4.8	No conversion to spinel with cycling	19

1.2.2 Lithium metal rechargeable batteries:

Lithium metal rechargeable batteries are presently only commercially available, in a limited range, from a small number of suppliers.^{16,21-23} This is due to issues with their safety and reliability that, despite extensive research effort, have not been overcome.²⁴

The rechargeable lithium battery is comprised of a lithium metal electrode, an electrolyte and a lithium ion intercalation electrode (see Table 1.1). The principle by which they operate is similar to the lithium ion cell except that during cycling the lithium metal electrode undergoes deposition/dissolution via the charge transfer reaction (see Scheme 1.2);



The lithium metal rechargeable cell is shown schematically alongside the lithium ion cell in Figure 1.4.

A great variety of electrolytes, liquid and solid, have been studied in the lithium metal rechargeable battery system. Table 1.2 presents a summary of electrolytes and their properties.

In their present form, lithium metal rechargeable batteries exhibit poor cycle lives and are prone to short circuits, due to dendritic growth on recharge (discussed further in section 1.5.3).^{14-17,21-24} A short circuit in a lithium battery has the potential to result in an explosion and presents serious safety concerns.^{16,25,26}

1.2.3 Lithium metal rechargeable vs. lithium-ion systems:

The success of the lithium ion battery has grown out of the necessity of finding a solution to the shortcomings of the lithium metal rechargeable battery. The advent of the use of a graphitic carbon negative electrode is a direct result of research aimed at finding ways to circumvent the problems inherent in the use of a lithium metal negative electrode.^{9,22,27} In this respect the lithium ion battery has been immensely successful.

However, extensive research is still being undertaken to find ways to improve the safety and cycle-ability of lithium metal rechargeable batteries. The driving force behind this research is the potential that exists for significant improvements in energy density that the use of a lithium metal electrode represents. The graphitic carbon anode offers a theoretical specific capacity of 372 mAhg⁻¹, the theoretical specific capacity of metallic lithium is 3860 mAhg⁻¹.^{21,28} The technological impetus in this area comes from three main sources, consumer electronics, electric vehicles and implantable medical devices. All three applications would benefit from the reduction in size and weight that the use of a lithium metal electrode would provide.^{10,16}

Table 1.2 Properties of various non-aqueous electrolytes.

Electrolyte	Salt	Salt Conc. (O/Li)	System studied	Conductivity (S ^{cm} ⁻¹)	Reference	Remarks
Liquid Electrolytes						
PC-DMC (30-70vol%)	LiPF ₆ (1M)			1×10 ⁻² @ 20 °C	27	
EC-DMC (30-70vol%)	LiPF ₆ (1M)			1.1×10 ⁻² @ 20 °C	27	
ACN	LiClO ₄ (1M)			3.6×10 ⁻² @ 25 °C	29	
ACN	LiCl (2.2M)			4.3×10 ⁻⁴ @ 25 °C	29	
PC	LiAlCl ₄ (0.6M)			6.6×10 ⁻³ @ 25 °C	29	
PC	LiClO ₄ (0.66)			5.4×10 ⁻³ @ 25 °C	29	
PC	LiPF ₆ (0.86)			5.41×10 ⁻³ @ 25 °C	29	
PC	LiCl (1M)			3.4×10 ⁻⁴ @ 25 °C	29	
PC	LiBF ₄ (1M)			4.0×10 ⁻³ @ 25 °C	29	
PC-DME (42-58wt%)	LiClO ₄ (1.39M)			1.46×10 ⁻² @ 25 °C	29	
EC	LiClO ₄ (1M)			7.9×10 ⁻³ @ 25 °C	29	
γ-BL	LiClO ₄ (1.1M)			7.6×10 ⁻³ @ 25 °C	29	
γ-BL-1,1 DME (1:1)	LiClO ₄ (0.75M)			4.5×10 ⁻³ @ 25 °C	29	
γ-BL-1,2 DME (1:1)	LiClO ₄ (1.1M)			1.3×10 ⁻² @ 25 °C	29	
THF	LiClO ₄ (1.5M)			4.3×10 ⁻³ @ 25 °C	29	
THF	LiBF ₄ (2.6M)			4×10 ⁻³ @ 25 °C	29	
DMS	LiClO ₄ (1.5M)			1×10 ⁻² @ 25 °C	29	
DMF	LiClO ₄ (1.16M)			2.2×10 ⁻² @ 25 °C	29	
2-Me-THF	LiAsF ₆ (1.5M)			4×10 ⁻³ @ 25 °C	29	
Solid Polymer Electrolytes						
MEEP	(LiClO ₄) 0.04		Pt/Pt	1.7×10 ⁻⁵ @ 20 °C	30,31	T _g = -58 °C, electrochemical window 0 → 4V, poor mechanical properties
MEEP	(LiCF ₃ SO ₃) 0.02		Pt/Pt	1.5×10 ⁻⁵ @ 20 °C	30,31	T _g = -67 °C, electrochemical window 0 → 4V, poor mechanical properties
MEEP	(LiCF ₃ SO ₃) 0.04		Pt/Pt	1.5×10 ⁻⁵ @ 20 °C	30,31	T _g = -62 °C, electrochemical window 0 → 4V, poor mechanical properties
PEO-MC ₃	LiCF ₃ SO ₃	9		5×10 ⁻⁵ @ 30 °C	32	
PEO-TEG	LiCF ₃ SO ₃	9		6.5×10 ⁻⁵ @ 30 °C	32	
PEO	LiN(CF ₃ SO ₂) ₂	8	Li/V ₆ O ₁₃	5×10 ⁻⁵ @ 25 °C	30,32	poor interfacial stability
PEO	LiCH(SO ₂ CF ₃) ₂	10		3×10 ⁻⁵ @ 25 °C	32	
PEO	LiSO ₃ CF ₃ SO ₃	4		1×10 ⁻⁵ @ 30 °C	32	
PEO	LiCH(SO ₂ CF ₃) ₂	16		1×10 ⁻⁴ @ 30 °C	32	
MEEP-PEO (Blend)	LiN(CF ₃ SO ₂) ₂	28.85:0.13	Pt/Pt	6.7×10 ⁻³ @ 25 °C	30,32	electrochemical window 0 → 4V
(PEO) ₄	LiClO ₄			1×10 ⁻⁸ @ 20 °C	30	
(POM)	LiClO ₄			1×10 ⁻⁸ @ 20 °C	30	
(PPO) ₈	LiClO ₄			1×10 ⁻⁸ @ 20 °C	30	
(POO) ₂₅	LiCF ₃ SO ₃			3×10 ⁻⁵ @ 20 °C	30	
DMS	LiClO ₄			1×10 ⁻⁵ @ 20 °C	30	
(PEO-PPO-PEO)SC	LiClO ₄ (4:1 molar)			1.5×10 ⁻⁵ @ 20 °C	30	

Table 1.2 (cont.) Properties of various non-aqueous electrolytes.

Electrolyte	Salt	Salt Conc. (O/Li)	System studied	Conductivity (S ^{cm} ⁻¹)	Reference	Remarks
(MEEP) ₄	LiBF ₄		Pt/Pt	2×10 ⁻⁵ @ 20 °C	30	electrochemical window 0 → 4V
(MEEP) ₄	LiC(CF ₃ SO ₂) ₂		Pt/Pt	1×10 ⁻⁴ @ 20 °C	30	electrochemical window 0 → 4V
PEO	C ₄ F ₉ SO ₃ Li			1×10 ⁻⁶ @ 20 °C	30	
PEO	C ₈ F ₁₇ SO ₃ Li			1×10 ⁻⁵ @ 20 °C	30	
PEO	C ₁₀ F ₂₁ SO ₃ Li			1×10 ⁻⁶ @ 20 °C	30	
PEO	((C ₄ F ₉ SO ₂ N) ₂ Li ₂)			3-4×10 ⁻⁷ @ 20 °C	30	
PEO	(C ₄ F ₉ SO ₂ NLiSO ₂ C ₄ F ₉)			2-5×10 ⁻⁶ @ 20 °C	30	
PEO-MEEP (55-45wt%)	LiN(CF ₃ SO ₂) ₂		Pt/Pt	6.7×10 ⁻³ @ 25 °C	30	electrochemical window 0 → 4V, good mechanical properties
Polymer Gel Electrolytes						
EC-PC-PMMA (46.5-19-30mol%)	LiClO ₄ (4.5mol%)			7×10 ⁻⁴ @ 20 °C	33	electrochemical window 0 → 4.9V, t ₀ = 0.4
EC-DMC-PMMA (50-20-25mol%)	LiN(CF ₃ SO ₂) ₂ (5mol%)			7×10 ⁻⁴ @ 20 °C	33	electrochemical window 0 → 4.9V, t ₀ = 0.4
PEGDME-PEO (10wt%γ-LiAlO ₂) (80.9-14.3mol%)	LiN(CF ₃ SO ₂) ₂ (4.8mol%)		Li/LiMn ₂ O ₄	1×10 ⁻⁴ @ 20 °C	33,34	good interfacial stability, electrochemical window 0 → 5V, good mechanical properties, good lithium deposition efficiency, t ₀ = 0.3
PEGDME-PC-PEO (10wt%γ-LiAlO ₂) (56-18.7-18.7mol%)	LiN(CF ₃ SO ₂) ₂ (6.6mol%)			1.9×10 ⁻³ @ 20 °C	33	poor interfacial stability, electrochemical window 0 → 4.9V, good mechanical properties, t ₀ = 0.3
PVdF:HFP (88:12)-EC-PC-(28-29.1-29.1wt%)	LiN(SO ₂ CF ₃) ₂ (13.8wt%)			1.74×10 ⁻³ @ 20 °C	35	good interfacial stability, electrochemical window 0 → 4.5V, good mechanical properties, good lithium deposition efficiency
EC-PC-PVP (35-31-24-10mol%)	LiCF ₃ SO ₃ (10mol%)			5×10 ⁻⁴ @ 20 °C	32	
(PEO)-salt/PC (50-50wt%)	LiClO ₄	8		8×10 ⁻⁴ @ 20 °C	30	poor mechanical properties
PVdF-salt/EC/PC (25-75wt%)	LiN(CF ₃ SO ₂) ₂		Al/Al	1.5×10 ⁻³ @ 20 °C	30	poor interfacial stability, electrochemical window 0 → 4V
PEGA	PO, 1M LiClO ₄			1×10 ⁻³ @ 20 °C	30	
PEI	LiClO ₄			1×10 ⁻³ @ 20 °C	30	
PPTA	PC/EC/LiBF ₄ , 25:25:0.08 mol%			2.2×10 ⁻³ @ 20 °C	30	
EGDMA	PC, 1M LiClO ₄			2×10 ⁻³ @ 20 °C	30	
PAN 38mol%	(EC/PC/LiClO ₄) (33/21/8 mol%)		Li/LiCr-Mn ₂ O ₄	1×10 ⁻³ @ 20 °C	30	poor interfacial stability, electrochemical window 0 → 4.3V, t ₀ = >0.5
Polymer Composite Electrolytes						
PAN-zeolite	PC/EC/LiAsF ₆			1×10 ⁻² @ 20 °C	30	good interfacial stability, good mechanical properties
(PEO) ₃ -alumina (10wt%)	LiBF ₄			1×10 ⁻⁴ @ 20 °C	30	
PEG ₂₀₀ -silica (20wt%)	LiCF ₃ SO ₃			1.5×10 ⁻² @ 20 °C	30	
P(EO) ₆ (0.56Li ₂ -0.19B ₂ S ₃ -0.25Li) (87-13 vol%)	LiC(CF ₃ SO ₂) ₂			1×10 ⁻⁴ @ 20 °C	30	
MEEP-silica	LiCF ₃ SO ₃			3×10 ⁻⁵ @ 20 °C	30	good mechanical properties
(Si(OCH ₃) ₄)-EC-PC-(MeOH(H ₂ O))	LiBF ₄			1×10 ⁻² @ 20 °C	30	good mechanical properties

Research relevant to the improvement of the lithium metal rechargeable battery can be broadly classified into two regions. The remainder of this introduction will deal firstly with non-aqueous electrolytes and their development, the most obvious avenue to overcome problems with the lithium | electrolyte interface. The latter part of the introduction will focus mainly on the properties of the lithium electrode | electrolyte interface and its relationship to the lithium deposition/dissolution process.

1.3 Electrolytes:

A general introduction to electrolytes and the way in which mass transfer occurs in a liquid is appropriate before describing the electrolytes used in rechargeable cells.

An electrolyte is a phase through which charge is carried by the movement of ions. Electrolytes may be liquid solutions, fused salts or ionically conducting solids.³⁶

1.3.1 Mass transfer in solution:

Mass transfer, the movement of material from one location in solution to another, arises from differences in electrical or chemical potential at the two locations, or from movement of a volume element of solution.³⁶

One-dimensional mass transfer to an electrode along the x-axis is governed by the Nernst-Planck equation;

$$J_i(x) = -D_i \frac{\partial C_i(x)}{\partial x} - \frac{z_i F}{RT} D_i C_i \frac{\partial \phi(x)}{\partial x} + C_i v(x) \quad (1.3)$$

where $J_i(x)$ is the flux of species i ($\text{mol s}^{-1}\text{cm}^{-2}$) at distance x from the surface, D_i is the diffusion coefficient (cm^2s^{-1}), $\partial C_i(x)/\partial x$ is the concentration gradient at distance x , $\partial \phi(x)/\partial x$ is the potential gradient, z_i and C_i are the charge and concentration of species i ,

respectively, and $v(x)$ is the velocity (cm s^{-1}) with which a volume element moves along the axis. The three terms on the right represent the contributions of diffusion, migration, and convection, respectively, to the flux.³⁶

Diffusion:

Diffusion is defined as the movement of a species under the influence of a gradient of chemical potential (i.e., a concentration gradient).³⁶ Diffusion occurs in all solutions and arises from local uneven concentrations of reagents. Entropic forces act to smooth out these uneven distributions of concentration and are therefore the main driving force for this process. Diffusion is particularly significant in an electrolysis experiment since the conversion reaction only occurs at the electrode surface. Consequently there will be a lower reactant concentration at the electrode than in the bulk solution.

Fick's Laws:

Fick's laws are differential equations describing the flux of a substance and its concentration as a function of time and position. $J_i(x, t)$ – net mass transfer rate of i in units of amount per unit time per unit area (e.g., $\text{mol s}^{-1}\text{cm}^{-2}$).

Fick's first law:

Flux is proportional to the concentration gradient, $\partial C_o/\partial x$:

$$-J_i(x, t) = D_i \frac{\partial C_i(x, t)}{\partial x} \quad (1.4)$$

The negative sign signifies that material moves down a concentration gradient i.e., from regions of high to low concentration.

Fick's second law:

The change in the concentration of i with time:

$$\frac{\partial C_i(x,t)}{\partial t} = D_i \left(\frac{\partial^2 C_i(x,t)}{\partial x^2} \right) \quad (1.5)$$

In this case, diffusion normal to an electrode surface (in the x direction) is considered (i.e., linear diffusion). The rate of change of the concentration ($[i]$) as a function of time (t) is related to the change in the concentration gradient. Thus, the steeper the concentration change, the greater the rate of diffusion. In practice, for many electrolysis reactions, diffusion is often found to be the most significant transport process.

Fick's second law is an important relationship since it permits the prediction of the variation of concentration of different species as a function of time within an electrochemical cell. In order to solve these expressions, analytical or computational models are usually employed. Solutions of the equation for Fick's second law yield concentration profiles, $C_i(x,t)$, while the flux at the electrode surface will give the current.

For any geometry, the general formulation of Fick's second law is:

$$\frac{\partial C_i}{\partial t} = D_i \nabla^2 C_i \quad (1.6)$$

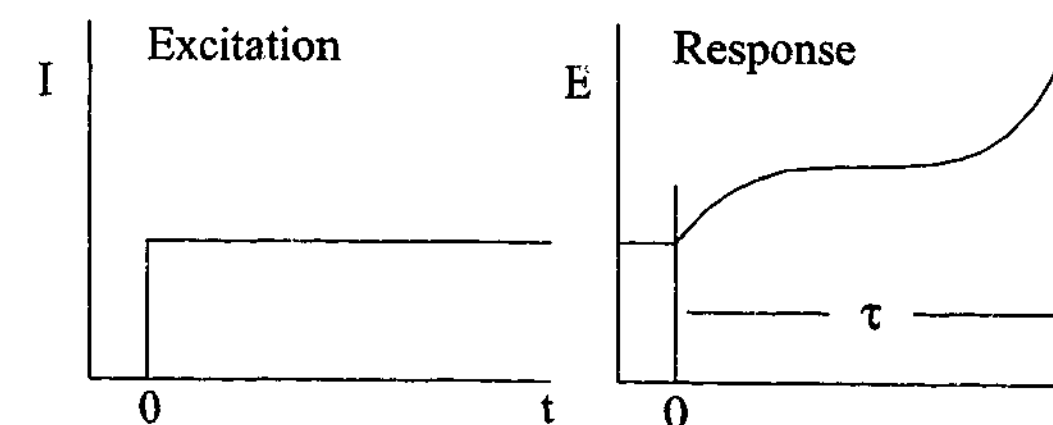
where ∇^2 is the Laplacian operator. Table 1.3 gives forms of ∇^2 for different geometries.³⁶

Table 1.3 Forms of the Laplacian operator (∇^2) for different diffusion geometries.

Type	Variables	∇^2	Example
Linear	x	$\partial^2/\partial x^2$	Planar disk electrode
Rectangular	x, y, z	$\partial^2/\partial x^2 + \partial^2/\partial y^2 + \partial^2/\partial z^2$	Cube-shaped electrode
Spherical	r	$\partial^2/\partial r^2 + (2/r)(\partial/\partial r)$	Hanging drop electrode
Cylindrical	r	$\partial^2/\partial r^2 + (1/r)(\partial/\partial r)$	Wire electrode

The majority of battery cycling experiments are conducted under a galvanostatic regime (as is the case in this work). Under these conditions, the current at the electrode surface can be described in terms of the electrode area, the diffusion coefficient and the concentration by the application of the Sand equation.

The Sand equation - The application of a constant current i applied to the electrode causes an electroactive species to be oxidised/reduced at a constant rate. The potential of the electrode moves to values characteristic of the couple and varies with time as the [reactants]:[products] concentration ratio changes at the electrode surface. Eventually as the concentration of the reactant drops to zero at the electrode surface, the flux to the surface is insufficient to accept all of the electrons being forced across the electrode-solution interface. The potential then jumps to a value where another electrode process can occur, as shown below.³⁶



The time after application of a constant current for the potential transition to occur is called τ , the transition or Sands' time.

The transition time at a given applied current and bulk concentration of oxidant is related to the diffusion coefficient and the electrode area. The relationship is known as the Sand equation;

$$\frac{i\tau^{1/2}}{C_i^*} = \frac{nFAD_i^{1/2}\pi^{1/2}}{2} = 85.5nD_i^{1/2}A \text{ (mAs}^{1/2}\text{/cm}^2\text{mM)} \quad (1.7)$$

The measured value of τ at known i can be used to determine C_i^* or D_i . A lack of constancy of the transition time constant ($i\tau^{1/2}$) with i or C_i^* indicates complications to the electrode reaction from coupled homogeneous chemical reactions, adsorption, or measurement artefacts (double-layer charging or convection).³⁶

Migration (t_L):

Migration is defined as the movement of a charged body under the influence of an electric field (a gradient of electrical potential).³⁶

This is essentially an electrostatic effect which arises due to the application of a voltage on the electrodes. This effectively creates a charged interface (the electrodes). Any charged species near that interface will either be attracted or repelled from it by electrostatic forces. The Nernst-Planck equation contains an expression for the flux due to migration:

$$\frac{\partial C_i(x,t)}{\partial t} = -\frac{u_i}{z_i F} C_i \left(\frac{\partial \phi}{\partial x} \right) \quad (1.8)$$

The term u_i refers to the electrochemical mobility of the ion, defined as the limiting velocity of the ion in an electric field of unit strength (usually $\text{cm}^2\text{V}^{-1}\text{s}^{-1}$).³⁶ The electrochemical mobility is derived from the absolute mobility, u_{abs} , which is a measure of the drift velocity, v_d , acquired by an ionic species when it is subjected to a force \vec{F} ; ³⁷

$$u_{abs} = \frac{v_d}{F} \quad (1.9)$$

The Einstein relation relates the absolute mobility to the diffusion coefficient;

$$D = u_{abs} kT \quad (1.10)$$

In turn, by likening a particle in solution to a macroscopic sphere moving through an incompressible medium, the Stokes-Einstein relation can be obtained;

$$D = -\frac{kT}{6\pi\eta r} \quad (1.11)$$

where η is the solvent viscosity and r is the solvated radius of the ion. The Einstein relation also allows the equivalent conductivity of a solution to be calculated from the diffusion coefficients of individual ions, the Nernst-Einstein relation;

$$\Lambda = \frac{zF^2}{RT} (D_+ + D_-) \quad (1.12)$$

The presence of ion-ion interactions in solutions (for instance, ion pairing) causes both of the above relations to deviate from ideality. The deviations occur due to the varying influences of the interactions (as a function of concentration) on D , η and Λ . The difference between experimentally determined parameters (D , Λ) and the predicted values provides insight into the nature of ion-ion interactions in solution.

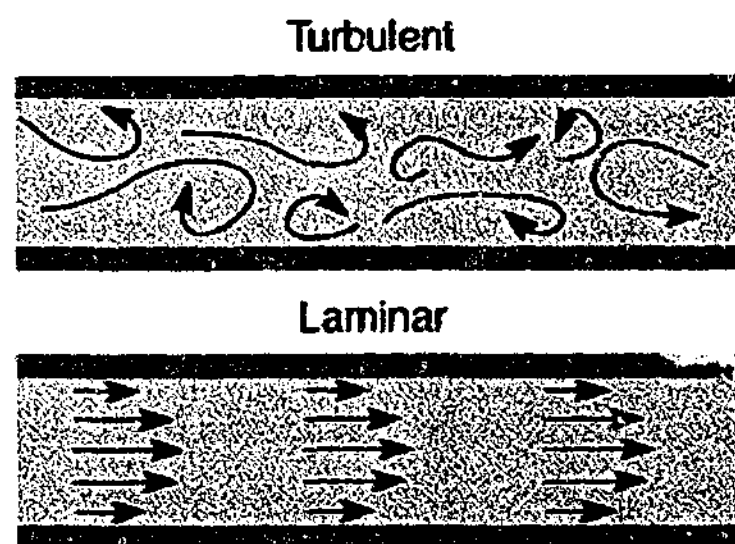
As a consequence of unequal mobilities of ions in solution, the fraction of total current carried by each ionic species can differ. This fraction is known as the transport (or transference) number of the ion, t_i ;

$$t_i = \frac{i_i}{i_T} = \frac{|z_i|u_i C_i}{\sum_j |z_j|u_j C_j} \quad (1.13)$$

The transport number only pertains to migration flux (i.e., the flux produced by an electric field), any flux of an ionic species arising from a chemical potential gradient (i.e., diffusion flux) is not counted in its transport number. Thus the transport number of an ionic species can tend toward zero but the species can still exhibit a finite diffusion flux. This property is frequently exploited in electroanalytical chemistry where an excess of a non-electroactive 'supporting electrolyte' is added, the added electrolyte does not participate in the reaction taking place at the electrode interface but carries the majority of the conduction current. In this manner the flux of the analyte to the electrode interface is produced by diffusion only. Then, under defined conditions, Fick's second law can be solved and an expression for the bulk concentration of the analyte can be obtained.

Convection:

Generally fluid flow occurs because of natural convection (convection caused by density gradients) and forced convection, and may be characterised by stagnant regions, laminar flow, and turbulent flow.



Convection results from the action of a force on the solution. This can be a pump, a flow of gas or even gravity. There are two forms of convection, the first is termed natural convection and is present in any solution. This natural convection is generated by small thermal or density differences and acts to mix the solution in a random and therefore unpredictable manner.

It is possible to drown out the natural convection effects from an electrochemical experiment by deliberately introducing convection into the cell. This form of convection is termed forced convection. It is typically several orders of magnitude greater than any natural convection effects and therefore effectively removes the random aspect from the experimental measurements. This is only true if the convection is introduced in a well-defined and quantitative manner.

Temperature dependence:

The temperature dependence of diffusion can, in many cases, be described by the Arrhenius equation;

$$D = D_0 \exp\left(\frac{-E_a}{RT}\right) \quad (1.14)$$

However in some circumstances the temperature dependence can depart from 'ideal' Arrhenius behaviour. This is the case in some liquids and solid polymer electrolytes where the Vogel-Tamann-Fulcher (VTF) relationship can be used;

$$\sigma(T) = AT^{-0.5} e^{-(B/(T-T_0))} \quad (1.15)$$

where T_0 is a parameter to be determined (but in many cases is very close to T_g), A is proportional to the charge carrier concentration and B is a constant called the pseudo activation energy.³² The application is limited to simple monophasic amorphous polymer systems where the salts are almost fully dissociated.³⁸ Successful fitting of these types of relationships indicates that ionic transport in polymers and liquid phases is similar.³⁹

1.3.2 Electrochemical stability:

An electrochemical stability window is defined as the potential range in which an electrode can be polarised in a solution without the passage of substantial Faradaic currents. In general, the electrochemical stability window for a solution-electrode system is limited by the electrochemical stability of the electrolyte or the solvent or by the dissolution or degradation of the electrode.⁴⁰ The processes that occur at extreme potentials define the window, usually reduction at low (negative) potentials and oxidation at high (positive) potentials.

The electrochemical window of a system is usually quoted as a potential range, bounded by an upper and lower potential between which the system is said to be stable. The electrochemical window reported for any system is unique to its specific components, including solvents, salts, electrode materials, the purity of the system, and its preparation procedure.

1.3.3 Important properties:

For an electrolyte to find application in an electrochemical device, (in this case a rechargeable lithium cell) it must meet a number of requirements before the device will function with any degree of utility or lifetime.

Electrochemical stability:

One of the most important requirements for an electrolyte in a battery is chemical stability to both of the electrodes in the charged state, it is also one of the most difficult to meet. In the case of the lithium electrode this is a difficult problem. A lithium metal cell with a high voltage cathode requires an electrolyte with a window that is stable below -3.0 V (vs. SHE) and above +1.0 V (vs. SHE). This represents an electrochemical window of greater than 4 V. The majority of solvents and salts do not possess an electrochemical window anywhere

near this value, which limits the number of potential electrolytes available for application to a relatively small number.

Conductivity:

The general rule of thumb for a lithium battery electrolyte requires a minimum conductivity between 10^{-4} and $10^{-3} \text{ S cm}^{-1}$ at the temperature of application.⁴¹ Some latitude is available depending on the required rates and design geometry of the cell. For example, thin film cells with high surface area electrodes maximise the ability of the electrolyte to transport lithium to the electrode surface in sufficient quantities. A high transport number for lithium (t_{Li}^+) also reduces the electrolyte requirements for high conductivity.⁴¹

Transport number (t_{Li}^+):

A high transport (or transference) number for lithium in the electrolyte indicates a high degree of mobility relative to the other ions in the system. A high transport number is desirable because it reduces concentration polarisation in the cell and increases lithium flux to (and from) the electrode surface. In many cases the transport number of lithium is quite low (0.1 to 0.3) because of its tendency to coordinate to other ions (anions), this formation of ion pairs (and triplets) reduces the influence of an applied potential on lithium transport.⁴⁰

Thermal stability:

The operating environments for a rechargeable lithium cell are likely to require the electrolyte to remain stable over a range of temperatures. In many cases electrolytes will not function effectively over a wide temperature range for a number of reasons:

- Poor lithium transport at low temperatures.
- Poor electrochemical stability at elevated temperatures.
- Solvent volatility or lack of stability at elevated temperatures.

Flammability:

The flammability of an electrolyte is important for a number of reasons. A flammable electrolyte presents problems for manufacturers during fabrication, incurring considerable costs with respect to occupational health and safety issues. More importantly a flammable electrolyte presents safety concerns during transport and operation of the device. In the event of overcharge, short circuit or other abuse a large amount of heat is generated in the cell. In this respect the flammability and the nature of the decomposition products of the electrolyte are an important consideration.

Interfacial stability:

The interfacial stability of the electrolyte is a measure of its tendency to react at the electrode surface(s) over time and is closely related to its electrochemical stability. Processes occurring at the surface can lead to self-discharge of the charged cell during storage. In addition a lack of interfacial stability can lead to an increase in the impedance of the cell, thus reducing its capacity and power.

1.3.4 Characterisation:**Ionic conductivity:**

The measurement of the ionic conductivity of an electrolyte is made difficult by the resistance to ion flow at the electrolyte | electrode interface. In order to overcome this problem conductivity measurements are carried out by the AC impedance method, which minimizes the effects of cell polarization. Measurements are usually made with the electrolyte between a pair of electrochemically inert electrodes made of platinum or stainless steel. In this technique the impedance is directly measured in the frequency domain by applying a single frequency voltage to the interface and measuring the phase shift and amplitude of the real and imaginary parts of current at that frequency. In the impedance spectrum, also known as the Nyquist plot, the real part of impedance is plotted against the imaginary part for the data collected at various frequencies. From this plot the

resistance of the electrolyte (R_s) is obtained. The conductivity, σ (Scm^{-1}), may be calculated from;

$$\sigma = g/R_s \quad (1.16)$$

where g is the geometric factor of the electrolyte sample, thickness and area, in cm^{-1} .³²

Interfacial stability:

The interfacial stability of candidate electrolytes is also determined by impedance spectroscopy. The interface is evaluated over storage time using Li/electrolyte/Li cells. Borghini *et al.*⁴², for example, followed a profile which they considered would reproduce conditions of use for an EV propulsion battery. The method involved heating the sample to 70°C for impedance tests and returning the sample to room temperature for storage. The tests were conducted for up to 5000 hours of storage. Fitting of the data to equivalent circuits provides a measure of the interface resistance in the cell and enables a plot of its evolution with time. Jiang *et al.*³⁵ and Appetecchi *et al.*³⁴ also make use of this method.

Electrochemical window:

The most common method of determining the electrochemical stability range is running a sweep voltammetry cycle on an inert electrode (i.e., different from the electrode to be used in the battery) in the selected electrolyte. As already mentioned (section 1.3.2), a stable electrolyte will exhibit minimal current response and the commencement of a significant current response at the anodic and cathodic limits describes the electrochemical window. This method gives only approximate values since it may be affected by the kinetics of the probing electrode.

Cycling efficiency

Deposited lithium frequently has a high surface area and is chemically active. In many cases the deposited lithium will react with the organic electrolyte or impurities (e.g., water) after deposition. Often the reaction product is electrochemically inactive and will take no further part in the cycling process. As a result the amount of charge required to deposit lithium is more than that required to strip the deposit. This leads to a cycling efficiency of less than 100% for lithium.

Cycling efficiency (Eff) may be defined as:

$$\text{Eff} = 100 \times Q_s / Q_p \quad (1.17)$$

Where Eff is a percentage, Q_s is the amount of charge required to strip all of the lithium and Q_p is the amount of charge required to plate lithium.^{21,43}

The figure of merit (FOM) for lithium cycling efficiency is also often used to evaluate the cycle-ability of a lithium cell.²¹ The FOM is defined as the number of cycles completed by one atom of lithium before it becomes electrochemically inactive;

$$\text{FOM} = \frac{\text{Sum of each discharge capacity to the end of cycle - life}}{\text{Capacity of the lithium cell}}$$

$$= 1/[1 - (\text{Eff}/100)] \quad (1.18)$$

An alternative method to determine the FOM for a lithium cell is to plate an excess of lithium (Q_{ex}) on a lithium substrate and then cycle at constant capacity (Q_{ps}) until all of the excess lithium is consumed. $Q_{ps} < Q_{ex}$.

$$\text{FOM} = \frac{(\text{cycle-life}) \times Q_{ps}}{Q_{ex}} \quad (1.19)$$

The cycling efficiency may be affected by many factors other than the electrode and electrolyte materials. These factors include the cell configuration, electrode orientation, electrode surface area, working electrode substrate, charge-discharge currents, charge quantity, and the amount of electrolyte.²¹

1.4 Lithium battery electrolytes:

The conception of the use of non-aqueous electrolytes can be viewed as a significant advance in battery science. The use of these electrolytes brought previously unusable electrode materials, for example the alkali metals, into the realms of possibility.¹¹

The majority of rechargeable lithium cells utilise solutions of lithium salts in organic solvents that are liquid at room temperature. The solvents must be aprotic, as reactive protons react with lithium to evolve hydrogen gas. No organic solvents are reported to be thermodynamically stable against lithium metal but varying degrees of kinetic stability have been found in aprotic solvents.¹¹

1.4.1 Salts:

A range of lithium salts have found use as the solute for non-aqueous electrolytes;¹⁵

- Halides - LiCl, LiBr, LiI
- Complex Fluorides - LiBF₄, LiPF₆, LiAsF₆, LiSbF₆
- Complex Chlorides - LiAlCl₄, LiGaCl₄
- Oxo Ions - LiClO₄, LiCF₃SO₃, LiN(CF₃SO₂)₂, LiC(CF₃SO₂)₃, LiCF₃CO₂

Ionic conduction is found to decrease with increasing lattice energy of the salt. Ogata⁴⁴ provides the following series showing increasing lattice energy with demonstrated decreased ionic conductivity;



Efforts have been made to increase the ionic conductivity of solid polymer electrolytes through the use of plasticising salts. Plasticising salts are non-volatile ionic compounds with bulky anions such as:

$\text{LiN}(\text{SO}_2\text{CF}_3)_2$ – Lithium bis(trifluoromethanesulfonyl)amide – $\text{Li}(\text{Tf})_2\text{N}$.

$\text{LiC}(\text{SO}_2\text{CF}_3)_3$ – Lithium tris(trifluoromethanesulfonyl)methide – Li Tri TFSM.

$\text{LiSO}_3\text{CF}_2\text{SF}_5$ – Lithium pentafluoro sulfur difluoro methylene sulphonate.

$\text{LiCH}(\text{SO}_2\text{CF}_3)_2$ – Lithium bis(trifluoro methane sulfonyl) methane.

Complexes of the above salts with PEO have been shown to exhibit higher conductivities than 'normal' salt complexes. The higher conductivities are attributed to the presence of large stable anions with strong electron withdrawing substituents that are thought to be responsible for a reduction of the crystalline phase due to their structural flexibility and the possibility of a disordered arrangement. In addition, bulky anions, by not favouring ion pair formation, might also aid in the increased dissociation of the salt thereby increasing the Li^+ ion concentration.³²

The most commonly used salt in Li-ion rechargeable batteries is LiPF_6 .⁴¹ With the increasing use of these batteries, limitations have become apparent in terms of their ability to operate at elevated temperatures ($>50^\circ\text{C}$).⁴⁵ The unavoidable presence of HF in all LiPF_6 solutions⁴⁶ is thought to induce dissolution of cations of the transition metal in the cathode, leading to capacity fade.⁴⁷ In addition, the most promising plasticising salt, $\text{Li}(\text{Tf})_2\text{N}$, is expensive to synthesise and suffers from a tendency for corrosion of the aluminium current collector.⁴⁸⁻⁵⁰ Thus, recently, there has been a concerted effort by several groups to develop an alternative lithium salt for use in Li-ion batteries, some examples are shown below:

$\text{LiPF}_3(\text{C}_x\text{F}_y\text{CF}_3)$ – Lithium fluoroalkylphosphate – LiFAP.^{47,51}

$\text{Li}_3\text{PW}_{12}\text{O}_{40}$ – Lithium heteropolyacid – LiHPA.⁵²

$\text{LiIm}(\text{BF}_3)_2$ – Lithium bis(trifluoroborane)imidazolid.⁵³

$\text{Li}[\text{B}(\text{OCOCF}_3)_4]$ – Lithium tetrakis(trifluoroacetoxy)borate – LiTFAB.⁵⁴

$\text{LiAl}(\text{HFIP})_4$ – Lithium tetra(1,1,1,3,3,3-hexafluoro-2 propyl)aluminate.⁵⁵

$\text{Li}[\text{B}(\text{OCO})_2]_2$ – Lithium bis(oxolatoborate) – LiBOB.⁵⁶

The bis(oxolatoborate) salt, LiBOB, in particular, has received attention in the literature because of its high conductivity,⁵⁶ ability to operate in a Li-ion cell at elevated temperature,⁵⁷ and because of the unique properties of the surface film formed on the graphite anode.⁵⁸

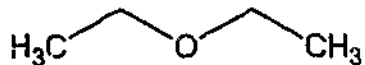
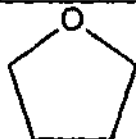
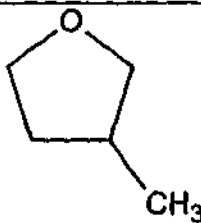
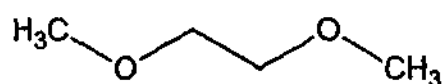
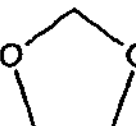
1.4.2 Aprotic liquids:

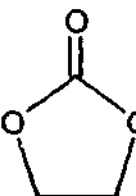
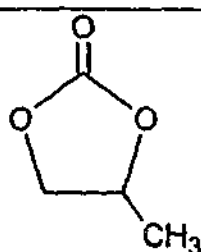
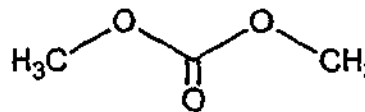
The most important and widely used class of nonaqueous electrolyte solvents are the polar aprotic solvents.⁴⁰ Aprotic solvents are characterised by their inability to donate or accept protons. Polar aprotic solvents can be further classified according to the division between organic and inorganic systems. For lithium battery applications the most important solvent groups are the alkyl carbonates, ethers and esters.⁴⁰ Table 1.4 provides the names, structures and some physical properties of the most important solvents used in nonaqueous electrochemistry.^{29,40,41,59} Aprotic solvents find application because they are able to overcome several of the limitations imposed when water is used as an electrolyte solvent:

- many important substances with electrochemical reactivity are insoluble in water.
- water, as a protic solvent, is highly reactive with a variety of materials of interest (e.g., alkali metals).
- the liquid range of water is about 100°C .
- water has a narrow electrochemical window ($\sim 1.3\text{ V}$).

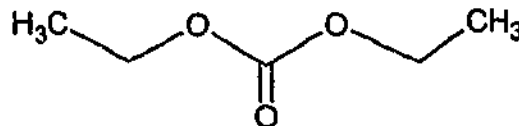
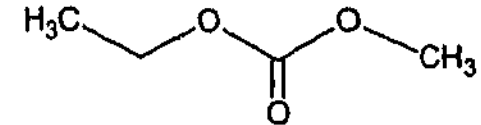
Introduction

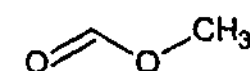
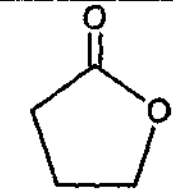
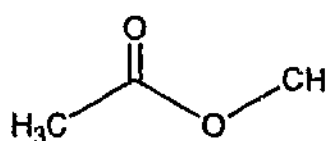
Table 1.4 Table of names, structures and properties of important non-aqueous solvents.^{29,40,41,59}

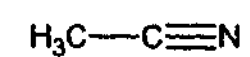
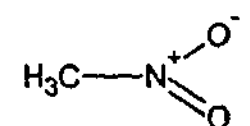
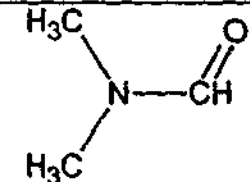
Ethers	Structure	MP (°C)	BP (°C)	ϵ	η (cP)
Diethyl ether (DEE)		-116.3	34.6	4.23	0.24
Tetrahydrofuran (THF)		-108.5	66.0	7.43	0.46
2-Methyl- Tetrahydrofuran (2Me-THF)		-137.2	80.0	6.24	0.46
Dimethoxyethane (DME)		-58.0	85.0	7.07	0.41
1-3 Dioxolane		-97.2	76.5	6.97	0.60

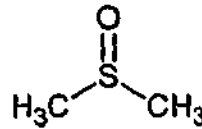

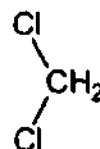
Alkyl Carbonates	Structure	MP (°C)	BP (°C)	ϵ	η (cP)
Ethylene carbonate (EC)		36.5	238	90.36	1.90
Propylene carbonate		-54.5	242	64.95	2.51
Dimethyl carbonate		4.6	90.0	3.10	0.59

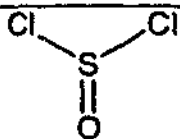
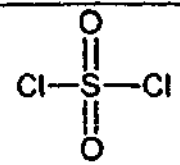
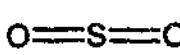
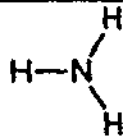
Introduction

Alkyl Carbonates	Structure	MP (°C)	BP (°C)	ϵ	η (cP)
Diethyl carbonate		-43.0	126.8	2.81	0.75
Ethyl methyl carbonate				2.40	0.65

Esters	Structure	MP (°C)	BP (°C)	ϵ	η (cP)
Methyl formate (MF)		-99.0	31.7	8.50	0.33
γ -Butyrolactone		-43.5	204.0	39.10	1.73
Methyl acetate		-98.0	56.9	6.68	0.36

Others	Structure	MP (°C)	BP (°C)	ϵ	η (cP)
Acetonitrile		-48.8	81.6	35.95	0.34
Nitromethane		-28.6	101.2	35.94	0.69
N-N dimethyl formamide		-61.0	158.0	36.71	0.80

Others	Structure	MP (°C)	BP (°C)	ϵ	η (cP)
Dimethyl sulfoxide		18.6	189.0	46.45	1.99
Sulfolane		28.9	287.3	43.26	10.28
Methylene chloride		-95.1	39.7	8.93	0.41

Inorganics	Structure	MP (°C)	BP (°C)	ϵ	η (cP)
Thionyl chloride		-104.5	75.8	9.25	0.60
Sulfuryl chloride		-54.1	69.4	9.15	0.67
Sulfur dioxide		-75.5	-10.0	1.41	0.29
Ammonia		-77.7	-33.3	23.90	0.17

Solvent mixtures are commonly used for battery applications because of improved conductivity of the mixture and to manipulate interfacial properties. Many of the important aprotic solvents are highly polar, possessing strong intermolecular interactions, and thus high viscosity. These solvents, due to their high polarity, possess the ability to dissociate salts to a high concentration and hence generate a large number of charge carriers. In this situation the advantage of high salt dissociation is offset by the high viscosity, which

reduces the solution conductivity. However, combining these solvents with a solvent of low polarity and low viscosity can produce a system that exhibits enhanced conductivity compared to the single solvent system. Some examples of aprotic liquid electrolyte systems and their conductivities were presented in Table 1.2.

1.4.3 Polymer electrolytes:

Wright discovered ionic conduction in a polymer in 1975 when he demonstrated $1 \times 10^{-7} \text{ S cm}^{-1}$ at room temperature in a PEO/ Na^+ complex.⁶⁰ In 1978 Armand proposed the application of a solid polymer electrolyte to lithium batteries.^{38,60} The events sparked a continuing worldwide research effort aimed at the development of a practical solid lithium battery. Avastor commissioned the first commercial lithium-metal-polymer (LMP) battery manufacturing plant in September 2002.^{61,62} The company produces 48 V, 70 Ah batteries capable of delivering a maximum continuous discharge of 18 A (C/4), which will operate between -40°C and 75°C , and are supplied with a 10 year warranty. The product is aimed at telecommunications and industrial stationary applications (utility power distribution, signaling, power peak shaving/load leveling, emergency lighting and security, uninterruptible power supply (UPS) Systems). Research activity directed towards the development of a product suitable for electric vehicle (EV) and hybrid electric vehicle (HEV) applications is also being pursued.

Arguments for polymer electrolytes:

The use of a polymer electrolyte instead of a liquid electrolyte provides several perceived advantages:¹¹

- A liquid electrolyte must be contained in a porous solid or elastomeric separator that prevents direct contact between the electrodes. Problems arise because separators containing liquid electrolytes tend to dry out, particularly with gas evolution during the first cycle.

- The volatility of solvent-based liquid electrolytes is also seen as a safety concern, particularly with the use of a lithium metal electrode.^{63,64}
- Thin film, offering high rate processes of manufacture.
- Thin film, offering flexibility in design.
- Thin film, allowing fabrication of low volume - high energy density batteries.
- Lightweight packaging and improved safety.

Mechanism of conduction:

The dissolution of ionic salts in a solid polymer matrix requires that the solvation energy of the ions in the polymer overcome the lattice energy of the salt.³¹ Solvation is dictated by the presence of electron donating atoms to solvate the cation, the presence of electron withdrawing groups to solvate the anion and by the spatial disposition of the solvating groups within the polymer structure.

The archetypal polymer electrolyte system, PEO, has been extensively investigated. Lithium ions coordinate to the ether oxygen atoms which wrap around to form a helical structure. The mechanism can be described as the hopping of cations between equilibrium sites via a sequence of association and disassociation steps accompanied by thermal motion of the polymer chains.³⁹ The cation mobility is regulated by ion-polymer interactions, primarily between the ether oxygen and the cation, a strong interaction reduces the ionic mobility. As a consequence the ionic mobility is strongly influenced by the polymer chain flexibility and ability to undergo rearrangements (micro-Brownian motion). The segmental motion of the polymer chain appears to be the rate-determining step for ionic conduction.⁴⁴ These conditions are best obtained above the glass transition point of the polymer in the amorphous phase.¹⁸

With varying salt concentrations ionic conductivity in polymers is seen to exhibit a maximum. It is believed that conductivity increases with salt concentration owing to the increase in the number of charge carriers, but there is also a simultaneous increase in T_g and a corresponding decrease in ionic mobility. Thus the maximum is a result of the two opposing effects on ionic conductivity.⁴⁴

Practical polymer electrolytes for the lithium metal electrode:

The polymer electrolyte has two functions, that of a solid organic solvent and that of a separator. In addition to the normal requirements for lithium battery electrolytes, ideally, the polymer electrolyte must:^{65,66}

- Have high thermal stability to temperatures above 200 °C.
- Have high mechanical stability in order to allow lower electrolyte film thickness, thus minimizing ohmic drop in the electrolyte, while avoiding the risk of a short circuit.
- Have a high transference number of the lithium ion.
- Have good mechanical strength and an environment friendly manufacturing process.

Polymer electrolyte development:

The development of a practical solid polymer electrolyte has progressed steadily. The primary goal of researchers has been the improvement of the room temperature conductivity from the original values of around 10^{-7} Scm^{-1} . The work has led to the development of three classes of solid polymer electrolyte:

- Dry solid polymers
- Polymer gels
- Polymer composites

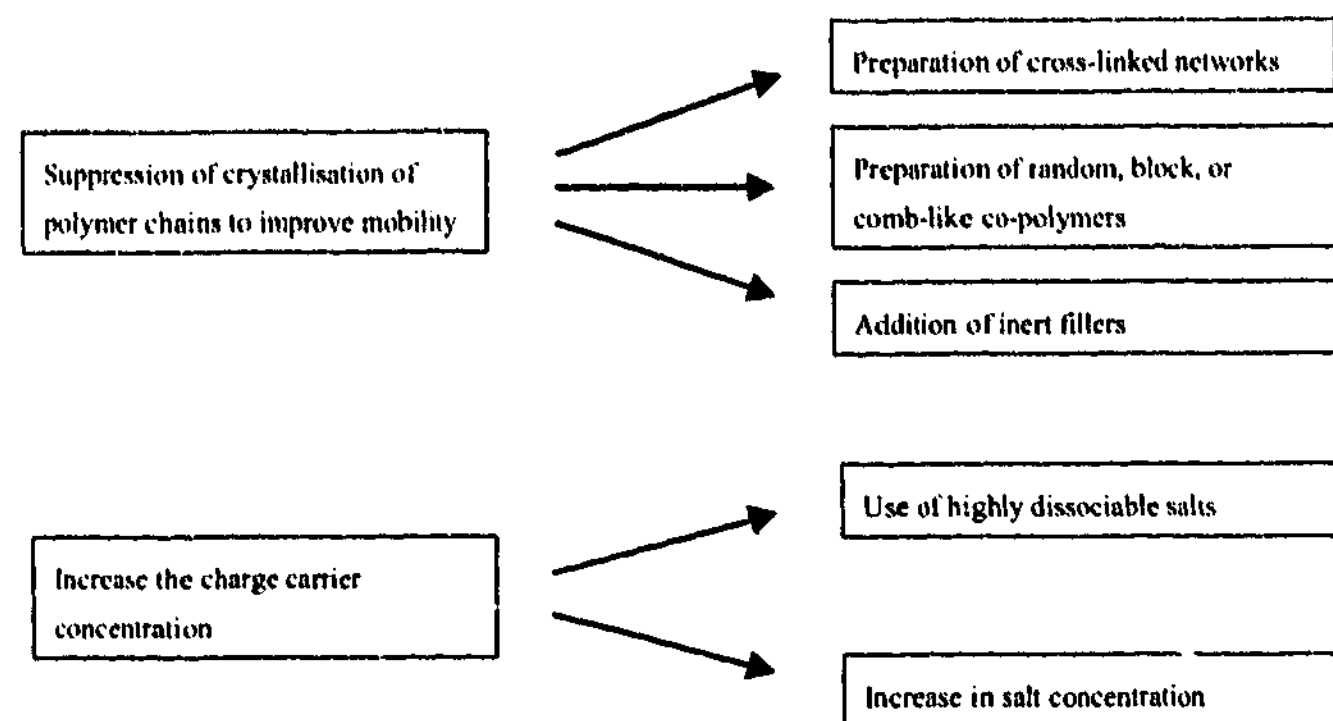
The development of different classes of solid polymer electrolyte has proceeded in parallel with the study and development of new salts.

Dry solid polymers:

The dry solid polymer systems consist of host polymers capable of solvating lithium salts. It has been found that polymers containing sequential polar groups such as O-, -NH- and -

C-N- are capable of dissolving lithium salts.³⁰ The high donor number (i.e., presence of electron donating atoms) of these groups allow a strong Li⁺/electron pair interaction.

Two main avenues to increase the conductivity of the dry solid polymers have been pursued, the approaches are shown schematically below:^{60,67}



Because of the inherent limitations of the segmental mobility of the PEO backbone, flexible inorganic backbones to which PEO units are attached have been designed and synthesised. An example of this is MEEP (methoxy ethoxy ethoxide phosphazene). Another example of a flexible inorganic backbone which has been extensively studied is the silicone based poly(dialkyl siloxanes) (Si-O)_n. MEEP and siloxane based electrolytes exhibit lower *T_g* than PEO and room temperature conductivity is improved. However the room temperature conductivities are still not high enough for battery applications and the electrolytes exhibit poor mechanical strength.³¹

In 1993 Angell *et al.*⁶⁸ introduced the concept of 'Polymer in Salt electrolytes' (PISE) in which lithium salts were mixed with small quantities of the polymers polypropylene oxide and polyethylene oxide. The materials exhibited glass transitions low enough to remain rubbery at room temperature while preserving good lithium ion conductivities and high electrochemical stability. However, progress towards realising practical (i.e., chemically, electrochemically and physically stable) versions of this type of electrolyte has been slow.⁶⁹

Some examples of PISE systems studied are; LiI:LiOAc:LiClO₄ (50:30:20)-PPO, PAN/LiCF₃SO₃ (70 wt.%), PVP/LiCF₃SO₃ (40 wt.%).^{32,70,71}

Polymer gels:

A polymer gel consists of a polymer that is plasticised with an aprotic solution containing an alkali metal salt. The salt solution remains trapped within the matrix of the polymer. Plasticiser solvents that have been investigated include ethylene carbonate (EC), propylene carbonate (PC), dimethyl formamide (DMF), diethyl phthalate (DEP), diethyl carbonate (DEC), methyl ethyl carbonate (MEC), dimethyl carbonate (DMC), γ -butyrolactone (γ -BL) and glycol sulfite (GS). The solvents have been used separately or as a mixture.³⁰ Some polymer gels are also shown in Table 1.2.

Mustarelli *et al.*⁷² have studied PVdF based polymer gels by means of modulated differential scanning calorimetry (MDSC) and nuclear magnetic resonance (NMR). The study indicated that the polymer behaved as an inert cage for the cations and that ionic conduction occurred in a liquid phase which is continuously interconnected through a system of cavities.

The gels have demonstrated high conductivity, high mechanical strength and a high lithium ion transference number (due to greater dissociation of the lithium salt than in the dry solid polymers). The majority of the plasticisers investigated have been highly polar solvents with low vapour pressure, which allow a greater plasticising effect to the polymer host.³⁰ Unfortunately plasticisers of this nature are easily decomposed at the lithium metal electrode. As a result the gels have been found to exhibit poor interfacial stability versus the lithium metal electrode.²²

Tatsuma *et al.*⁷³ discussed the possible disadvantages of using a gel electrolyte with a lithium metal electrode:

- High viscosity, which may lead to diffusion controlled deposition and hence increased surface roughness.

- Uneven polymer concentration promoting surface roughness.
- Poor contact between the rigid gel and the metal surface leading to uneven current density at the interface.
- The polymer chain or its cross-linking points may promote nucleation of depositing lithium.

Possible approaches for improving the stability of the lithium | gel interface may be:

- Selection of low reactivity solvents and/or polymer components.
- The addition of ceramic powders.

The effectiveness of these approaches has been demonstrated, however the improvements are seen as not being satisfactory for use with a lithium metal electrode. Instead the gel electrolytes are suggested for use in plastic like lithium ion batteries.^{33,74}

Polymer composite electrolytes:

The incorporation of electrochemically inert particulate fillers was initially used as a means to increase the mechanical stability of the polymer. Fillers such as SiO_2 , $\gamma\text{-LiAlO}_2$, ZrO_2 , TiO_2 , Al_2O_3 , hydrophobic fumed silica and fibreglass have been investigated.^{42,75} Composite polymer electrolytes have also been shown to possess higher ionic conductivity.⁷⁴

The phenomenon of conductivity enhancement by the addition of electrochemically inert fillers is not clearly understood, but low inter-particle resistance between inorganic particles has been observed.³⁰ A possible explanation for the low inter-particle resistance is the promotion of a high degree of disorder around the ceramic particles.⁷⁴

The presence of inorganic fillers has been found to increase the stability of the electrolyte and the interfacial stability towards the lithium metal electrode.^{30,42} The reason for the increase in interfacial stability is not clearly understood. It is postulated that the affinity of the powders for water and other liquid impurities would result in the reduction of the level of impurities at the interface and the subsequent promotion of a compact and uniform

passivating film.⁷⁴ In the absence of liquids, the lithium passivation process may only be due to the reaction with the lithium salt, thus promoting the formation of a thin, compact inorganic film.

Polyelectrolytes and polyelectrolyte composites:

A polyelectrolyte can be formed by incorporating a lithium salt into the backbone of the polymer, by fixing the anion to the backbone, dissociation of the lithium ion results in a lithium ion conductor. These electrolytes have the advantage of being a single ion conductor, and thus have a unity lithium transference number. However, the presence of regularly spaced anionic charges on the polymer backbone leads to poor ion dissociation due to the strong coulombic repulsion between the anionic groups, leading to low ionic conductivity. The use of uncharged comonomer 'spacers'⁷⁶ has been demonstrated to enhance dissociation and improve conductivity, particularly for polyelectrolyte gels. However, although exhibiting significant conductivity ($\sim 10^{-3} \text{ Scm}^{-1}$), these materials typically incorporate a volatile solvent and exhibit poor mechanical properties. Recently, the addition of either boroxine ring compounds or ionic liquids have been demonstrated to enhance dissociation.⁷⁷ In addition, the use of fillers and zwitterions as additives has been shown to enhance dissociation, used together the additives exhibit a combined effect.⁷⁸ These materials still require an increase in charge carrier concentration while maintaining ion dissociation, good mechanical properties and electrochemical stability.

1.4.4 Ceramics and glasses:

In some cases thermodynamic stability in contact with metallic lithium is possible, e.g., the lithium halides. Cells incorporating solid electrolytes of this nature have been manufactured, e.g., the lithium-iodine pacemaker cells.¹¹ Kudo³⁹ provides a survey of Li conducting solid electrolytes (excluding polymer electrolytes), examples presented include; Ceramics - LiI , $\text{LiI}/1\text{mol}\%\text{CaI}_2$, $\text{LiI-Al}_2\text{O}_3$, Li_3N , $\text{Li}_3\text{N-LiCl}$, $\text{Li}_3\text{N-LiI-LiOH}$, Li_2CdCl_4 , Li_3PO_4 , Li_4SiO_4 , $\text{LiZr}_2(\text{PO}_4)_3$, $\text{LiTi}_2(\text{PO}_4)_3$ and Glasses - $\text{Li}_2\text{O-SiO}_2$, $\text{Li}_2\text{O-Bi}_2\text{O}_3$, $\text{Li}_4\text{SiO}_4\text{-Li}_3\text{BO}_3$, $\text{LiCl-Li}_2\text{O-B}_2\text{O}_3$, $\text{Li}_2\text{S-B}_2\text{S}_3$, $\text{Li}_2\text{S-SiS}_2$. It is not within the scope of this survey to detail the properties of these types of lithium ion conductors. A problem with brittle solid

electrolytes is that on cycling large strains occur at the electrode | electrolyte interface, which cause disintegration of the structure if the film thickness exceeds a few μm .¹¹

1.4.5 Room temperature ionic liquids (RTILs):

Definition:

Room temperature ionic liquids are organic ionic salts that are liquid over a wide temperature range, typically from below room temperature to above 200°C. Current convention specifies that an ionic liquid is any salt that melts below the boiling point of water (100 °C). These materials are known by numerous other synonyms including; low/ambient/room temperature molten salt, ionic fluid, liquid organic salt, fused salt and neoteric solvent.

History and development:

The first recorded evidence for the observation of a room temperature ionic liquid occurred in 1927 when NMR was used to identify a 'red-oil' that had previously been observed, a century before, by chemists performing an aluminium trichloride catalysed Friedel-Crafts alkylation.^{79,80} The 'red-oil' was determined to be a stable ionic intermediate comprised of an aromatic carbocation and a heptachlorodialuminate anion. In the 1920's low melting alkylammonium nitrates were discovered and later investigated for use as liquid gun propellents.⁸¹ In 1951 Hurley and Wier described the first haloaluminate ionic liquids that melted at room temperature.⁸² These materials, often dubbed the first RTILs, were binary mixtures of 1-alkyl pyridinium halide salts and AlCl_3 or AlBr_3 . Later 1,3-dialkyl imidazolium binaries were discovered, the imidazolium cation being less easily reduced, extended the electrochemical working range of the melt.⁸³ The chloroaluminate dialkyl imidazolium systems have been extensively investigated for application as electrolytes in batteries and for the electroplating of metals.⁸⁴⁻⁸⁹ NMR studies have established that little or no AlCl_3 exists in the binary mixture and that the predominant anions are Al_2Cl_7^- and AlCl_4^- (Lewis acidic melt), and AlCl_4^- and Cl^- (Lewis basic melt).^{90,91} The widest

electrochemical window was determined for the Lewis neutral melt, -1.9 V to +2.5 V.^{91,92} Later it was demonstrated that the melts could be buffered in the neutral region by the addition of metal chlorides, particularly LiCl and NaCl .^{92,93} Reversible lithium cycling has been demonstrated in buffered (LiCl) 1-ethyl-methyl imidazolium chloride: AlCl_3 with the addition of SOCl_2 ⁸⁴ and triethanolamine-hydrogen chloride.⁸⁵

The application of the chloroaluminate ionic liquids has been hampered by the fact that both the starting materials and the ionic liquid are moisture sensitive. When exposed to moisture the AlCl_3 hydrolyses to form corrosive HCl . Thus a significant breakthrough in the utility of RTILs occurred in 1992, when the first air and moisture stable ionic liquids were reported.⁹⁴ Since that time the number of reported cation-anion combinations that form RTILs, including some that display hydrophobic character,⁹⁵ has expanded rapidly.

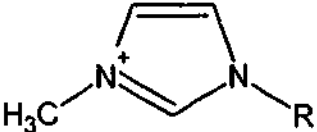
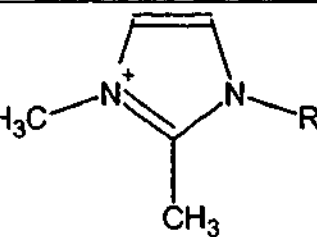
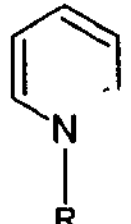
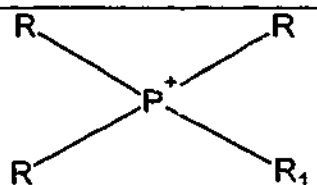
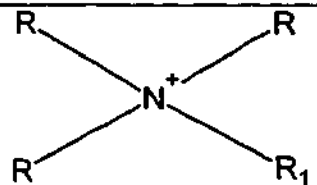
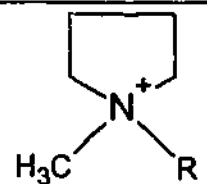
Cations and anions:

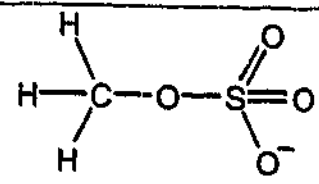
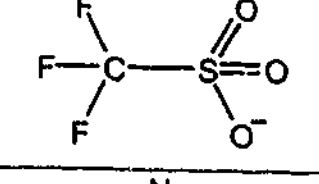
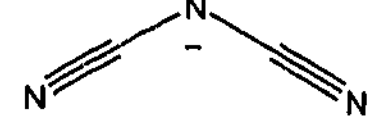
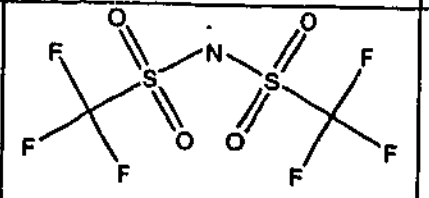
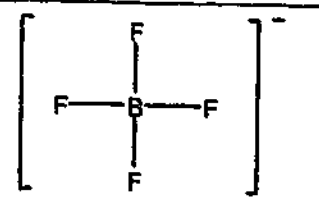
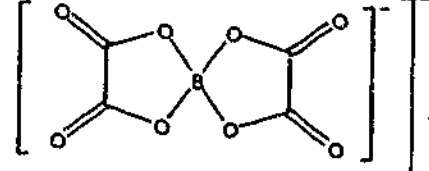
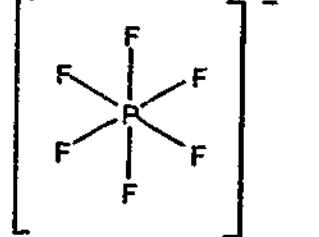
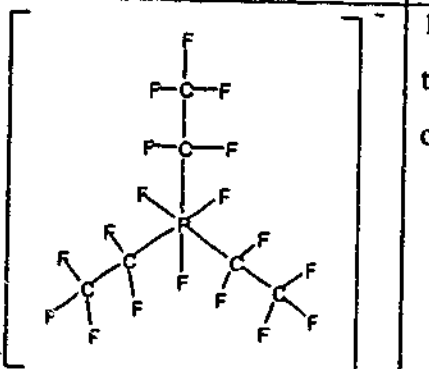
RTILs obtain their liquid character from the properties of the anions and cations of which they are comprised. Typically, the charge on both ions is diffuse (i.e., able to occupy more than one site on the ion at different times) and is 'spread' across the molecule. In addition, the charge on the anion is often shielded by electron withdrawing substituents such as fluoride. The other common property that ionic liquids possess is a high degree of flexibility (rotational and longitudinal) of both the cation and anion. In addition, the cation is usually asymmetrical, the asymmetry typically being imparted by a (relatively) large alkyl group. The asymmetry of the cation serves to disrupt the crystal lattice structure, thus reducing the lattice energy of the salt. The combined effects of these properties produce a material that has weak short-range intermolecular forces but strong long-range intramolecular forces resulting in a non-volatile liquid.

The range of available anions and cations that form room temperature ionic liquids has expanded rapidly. It has been estimated that there are approximately one trillion (10^{18}) candidate room temperature ionic liquids.⁹⁶ Many ionic liquids are already commercially available (from Acros, Aldrich, Covalent Associates, Cytec Industries, Merck, Sachem, Solvent Innovation and Strem). The Merck website lists a range of cations and anions

which are claimed to be available in any combination.⁹⁷ Table 1.5 reproduces some of the information available at the website and provides an example of a RTIL incorporating the cation or anion.

Table 1.5 Table showing structures of RTIL cations and anions, an example RTIL and its melting point are also provided.

Cations	Structure	Example IL	Mp (°C) ^(ref)
Disubstituted Imidazolium		1-ethyl-3-methyl imidazolium bis(trifluoromethanesulfonyl)amide	-15 ⁽⁹⁸⁾
Trisubstituted Imidazolium		1-Hexyl-2,3-dimethyl-imidazolium tetrafluoroborate	15 ⁽⁹⁷⁾
Pyridinium		N-Butyl-pyridinium hexafluorophosphate	76 ⁽⁹⁷⁾
Phosphonium		Trihexyl(tetradecyl)phosphonium tris(pentafluoroethyl)trifluorophosphate	-50 ⁽⁹⁷⁾
Ammonium		Trimethylpropylammonium bis(trifluoromethanesulfonyl)amide	17 ⁽⁹⁹⁾
Pyrrolidinium		N-butyl-N-methylpyrrolidinium bis(trifluoromethanesulfonyl)amide	-18 ⁽¹⁰⁰⁾

Anions	Structure	Example IL	Mp (°C) ^(ref)
Halogenides	Cl ⁻ , Br ⁻	1-ethyl-3-methyl imidazolium chloride	89 ⁽⁹⁸⁾
Sulphates		1-butyl-3-methyl imidazolium methyl sulfate	-5 ⁽¹⁰¹⁾
Sulphonate		1-ethyl-3-methyl imidazolium triflate	-9 ⁽⁹⁵⁾
Amides		N-butyl-N-methylpyrrolidinium dicyanamide	-105 ⁽¹⁰²⁾
Sulfonylamides		1,3-diethyl-4-methylimidazolium bis(trifluoromethanesulfonyl)amide	-22 ⁽⁹⁵⁾
Borates (tetrafluoroborate)		Tetrabutylammonium tetrafluoroborate	90 ⁽⁹⁸⁾
Borates (bis(oxolato)borate)		1-ethyl-3-methyl imidazolium chloride bis(oxolato)borate	62 ⁽⁹⁷⁾
Phosphates (hexafluorophosphate)		1-butyl-3-methyl imidazolium hexafluorophosphate	40 ⁽⁹⁸⁾
Phosphates (tris(pentafluoroethyl)trifluorophosphate)		1,1-dimethyl-pyrrolidinium tris(pentafluoroethyl)trifluorophosphate	95 ⁽⁹⁷⁾

Anions	Structure	Example II.	Mp (°C) ^(ref)
Antimonates (hexafluoroantimonate)		1-ethyl-3-methyl imidazolium hexafluoroantimonate	53 ⁽⁹⁸⁾

Synthesis:

A scheme outlining the routes commonly used to synthesise RTILs is shown in Fig. 1.6.⁹⁵ The pyrrolidinium cation is shown in the example; by replacing the pyrrole with imidazole, an imidazolium RTIL could be produced and so on. The halide precursor (often commercially available) can be prepared from the corresponding amine by alkylation, as shown in Fig. 1.6. The RTIL is obtained from the halide precursor by metathesis, the route being dictated by the relative solubility of the product and byproduct. For example, *N*-methyl-*N*-propylpyrrolidinium bis(trifluorosulfonyl)amide is obtained by metathesis of *N*-methyl-*N*-propylpyrrolidinium iodide with lithium bis(trifluorosulfonyl)amide in aqueous solution, the product is insoluble in water.¹⁰³ Alternatively *N*-methyl-*N*-propylpyrrolidinium dicyanamide is obtained by metathesis of *N*-methyl-*N*-propylpyrrolidinium iodide with silver dicyanamide in aqueous solution. The insoluble byproduct, silver iodide, is removed by filtration and the product is obtained by the evaporation of water at reduced pressure.^{102,104}

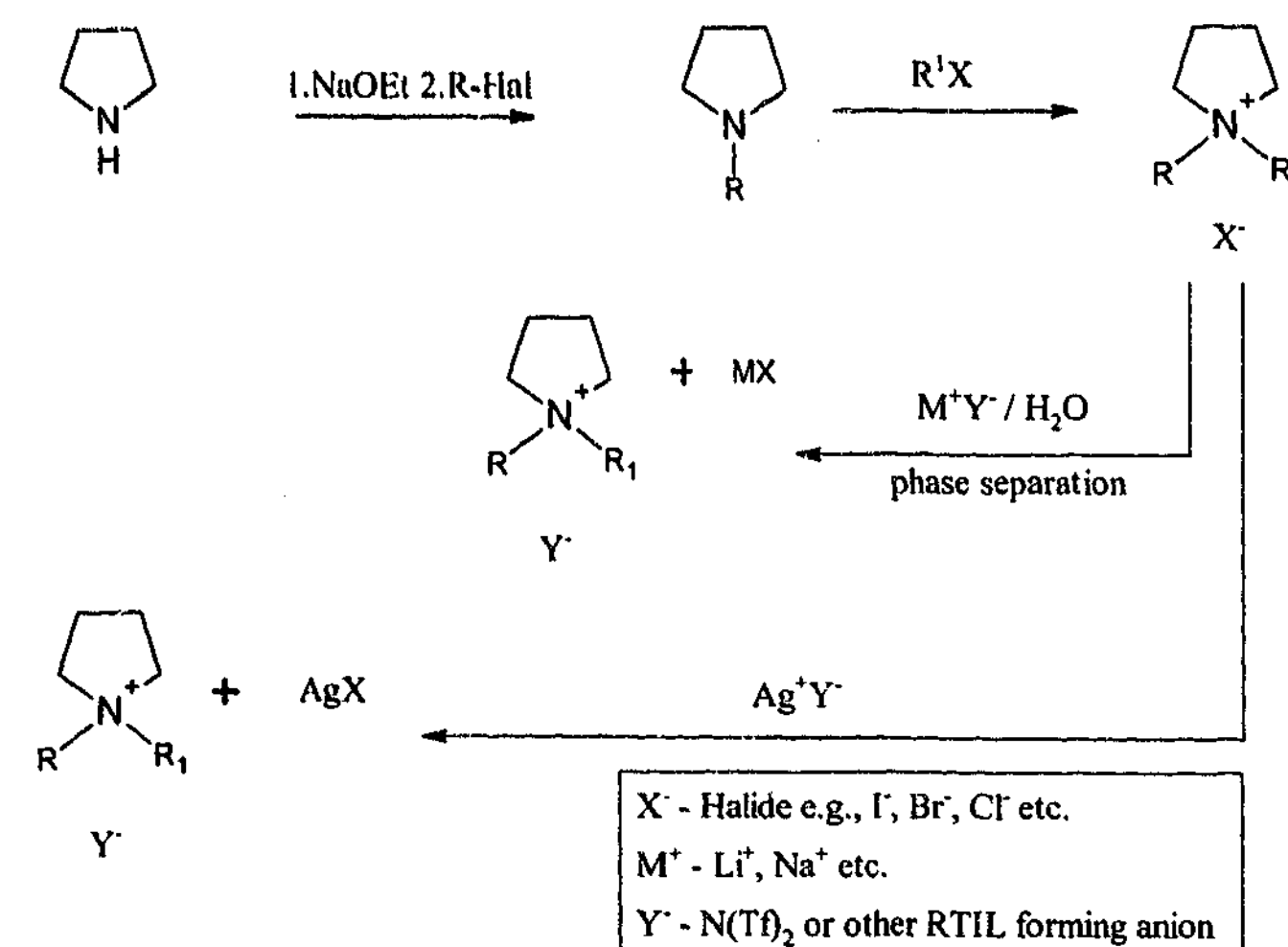


Fig 1.6 Scheme for laboratory scale synthesis of RTILs.

A methodology suitable for large-scale, silver-free, synthesis has been demonstrated for mesylate and tosylate anions using ion exchange resins.¹⁰⁵ Recently a 'one-pot' synthesis involving direct alkylation of a 1,3-dialkylimidazolium cation with an alkyl sulfate has been reported.¹⁰¹ Fig. 1.7 outlines the general reaction scheme;

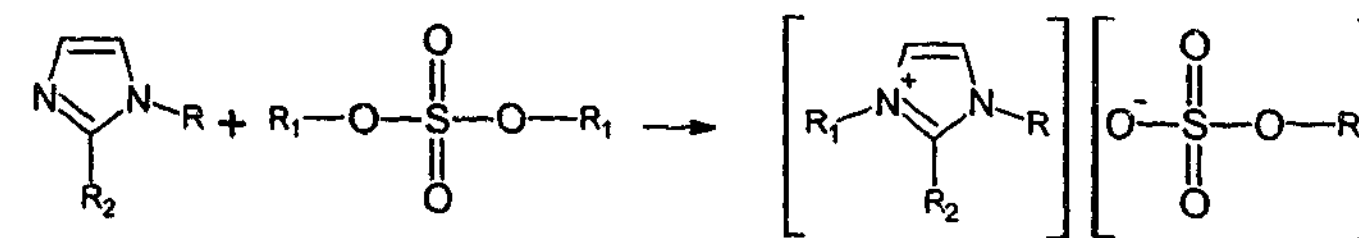


Fig 1.7 General preparative route for halide free synthesis of alkylimidazolium RTILs.

Properties:

RTILs are receiving a great deal of attention as new environmentally benign solvents for a variety of processes, primarily as replacements for conventional media in chemical processes. This is because ionic liquids possess a number of desirable features, namely:

- A wide liquid range (room temperature to above 300 °C).
- Outstandingly good solvent properties, able to dissolve a wide range of organic and inorganic compounds to high concentration.
- They offer advantages with respect to catalyst recovery and product separation;
- Negligible vapour pressure and hence minimal harmful effects of solvent evaporation on human health and the environment.
- They are re-useable, relatively cheap, and easy to prepare.

Ultimately the use of ionic liquids to replace conventional volatile organic solvents could provide a 'greener' process with less waste per unit yield.^{96,106} In recent years RTILs have been the focus of a great deal of research effort for use as solvents for synthesis where improved yields and reaction rates have been demonstrated, presumably through the stabilisation of ionic intermediates in the reaction scheme.¹⁰⁷⁻¹¹⁸ In addition, enhanced catalyst recovery, better regioselectivity and simplified product separation have been reported.¹¹⁸⁻¹²⁴

In addition to the features detailed above, RTILs also possess a number of important attributes that make them very attractive for use as solvents in electrochemical applications:¹²⁵

- A wide electrochemical window.
- High conductivity.
- High thermal stability.
- Low safety hazards (non-flammable, non-volatile).
- Low toxicity.
- Due to their inert properties, RTILs are re-usable.

As a result of the combination of the advantageous properties listed above and the previously mentioned design flexibility (i.e., adjusting solvent properties by varying anion – cation combinations), RTILs have attracted an increasing amount of research activity focussing on electrochemical applications.¹²⁶⁻¹⁶⁰

Lithium battery studies:

Compared to 'traditional' solvent systems (i.e., aprotic liquids and polymers), published research pertaining to the use of RTILs in lithium secondary batteries is relatively sparse.

The largest body of published work focuses on the chloroaluminate dialkyl imidazolium system, described earlier. The timeline presented in Table 1.6 highlights the key developments that have occurred since they were first reported in 1982.

Table 1.6 Summary of key developments pertaining to chloroaluminate RTILs since 1982.

Date	Description of work
1982	1,3-dialkyl imidazolium binaries discovered, imidazolium cation less easily reduced, extended electrochemical working range of the melt. ⁸³
1990	Use of metal chlorides as Lewis acid-base buffer reported. ^{92,93}
1992	Addition of protons (methyl ethyl imidazolium chloride:HCl) to buffered melt extends negative voltage limit. Reversible plating and stripping of Na. ¹⁶¹
1994	Triethanolamine-hydrogen chloride added to buffered melt extends negative voltage limit. Reversible plating and stripping of Li. ⁸⁶
1995	Thionyl chloride (SOCl ₂) added to buffered melt promotes reversible plating and stripping of Li. Cycling efficiencies ~90%. ⁸⁴
1996	Optical study of Li deposit in buffered melt with SOCl ₂ indicates dendritic deposit which becomes disconnected upon discharge. ⁸⁷
1999	LiAl / EMI·AlCl ₃ ·LiCl / LiCoO ₂ cell demonstrated with C ₆ H ₅ SO ₂ Cl additive demonstrates 90% coulombic efficiency and 112 mAhg ⁻¹ discharge capacity for 20 cycles at 1 mAcm ⁻² . ⁸⁸
1999	EMI·AlCl ₃ ·LiCl melt treated with SOCl ₂ or Li metal to remove Al ₂ Cl ₇ ⁻ . Demonstrated reversible plating and stripping of lithium. ¹⁶²

The remaining work of significance to lithium battery applications can be classified as that pertaining to the 'new' RTILs, often referred to as air and moisture stable ionic liquids (Table 1.7).

Table 1.7 Lithium battery research pertaining to air and moisture stable RTILs.

1992	Wilkes <i>et al.</i> report the first air and moisture stable RTILs, 1-ethyl-3-methylimidazolium tetrafluoroborate (EMIBF ₄). ⁹⁴
1995	Koch <i>et al.</i> publish the results of a study indicating that 1,2-dimethyl-3-propylimidazolium bis(trifluoromethanesulfonyl)amide (DMPI(Tf) ₂ N) forms a stable interface with lithium. ¹⁶³
1996	Bonhote <i>et al.</i> publish a comprehensive study of the properties of a group of hydrophobic RTILs based on 1,3-dialkyl imidazolium cations and six different hydrophobic anions. Structure property relationships were investigated and related to melting point, thermal stability, viscosity, conductivity and electrochemical stability. ⁹⁵
1996	US Patent #5589291 (1996) claims the use of EMIBF ₄ as an electrolyte for use in a secondary lithium metal cell. The addition of H ₂ O (eg. 40mM) provides a stabilizing film for the lithium electrode. ¹⁶⁴
1997	Fuller <i>et al.</i> publish an electrochemical study of EMIBF ₄ as a solvent. Lithium ions were reduced to lithium metal at a Pt electrode following the addition of water. Lithium ion reduction at an Al wire produced the beta-LiAl alloy. ¹⁶⁵
1999	MacFarlane <i>et al.</i> published details of the synthesis and some physical properties of a family of ionic liquids and plastic crystal phases, the <i>N</i> -methyl- <i>N</i> -alkyl pyrrolidinium bis(trifluoromethanesulfonyl)amides (P _{1x} (Tf) ₂ N). ¹⁰³
2000	Caja and Dunstan publish two papers describing the application of 1,2-dimethyl-4-fluoropyrazolium tetrafluoroborate (DMFPBF ₄ – air and moisture stable) to lithium batteries. A Li / LiAsF ₆ -(DMFPBF ₄) / LiMn ₂ O ₄ cell operated at 96% coulombic efficiency and 27% of theoretical capacity. ^{166,167}
2000	Matsumoto <i>et al.</i> report the synthesis of electrochemically stable and relatively highly conductive RTILs based on small ammonium cations such as methoxymethyltrimethylammonium and the bis(trifluoromethanesulfonyl)imide anion. ⁹⁹
2001	US Patent #6326104-B1 claims an electrochemical cell using the compound 1,2-dimethyl-4-fluoropyrazolium tetrafluoroborate (DMFPBF ₄ or other anion) as electrolyte. ¹⁶⁸
2001	Matsumoto and Miyazaki report reversible lithium cycling in trimethylpropylammonium bis(trifluoromethanesulfonyl)amide (TMPA(Tf) ₂ N), 81% coulombic efficiency was obtained for a 0.87 M Li(Tf) ₂ N solution. ¹⁶⁹

2002	Bhatt <i>et al.</i> report some electrochemical properties of Group 15 quaternary alkyl [(Me) ₄ N] ⁺ , (Me) ₄ P ⁺ and (Me) ₄ As ⁺ bis(trifluoromethanesulfonyl)amide salts. Melting points were similar for each IL (140-150°C). All three ILs were found to have extremely large electrochemical windows (~6V). Cathodic stability was found to decrease in order - As ⁺ > P ⁺ > N ⁺ . Deposition of electropositive metals (including lithium in (Me) ₄ P ⁺) was demonstrated. ¹⁷⁰
2002	Egashira <i>et al.</i> suggest the possibility of manipulating the electrochemical stability of RTILs in binary mixtures by choice of anion combinations. A mixture of 1-ethyl-3-methyl imidazolium with tetrafluoroborate and bis(trifluoromethanesulfonyl)imide anions was found to exhibit improved anodic stability over either of the 'single anion' RTILs. ¹⁷¹
2002	Quinn <i>et al.</i> compare methyltributylammonium bis(trifluoromethanesulfonyl)amide (N ₁₄₄₄ (Tf) ₂ N) and 1-butyl-3-methylimidazolium hexafluorophosphate (BMIPF ₆) and report that the cathodic limit at a Pt electrode is enhanced for the tetraalkylammonium-based IL. ¹⁷²
2002	Patent # WO200276924-A1 claims an ionic liquid for electrolytic solution for storage devices, electric double layer capacitors and secondary batteries. The RTIL comprises quaternary ammonium or phosphonium compound and a monovalent anion. ¹⁷³
2003	Sutto <i>et al.</i> provide XRD evidence for the reversible intercalation and deintercalation of the 1,2-dimethyl-3- <i>n</i> -butylimidazolium cation (from the tetrafluoroborate RTIL) in graphite. ¹⁷⁴
2003	Katayama <i>et al.</i> demonstrate reversible intercalation and deintercalation of lithium in graphite from trimethyl- <i>n</i> -hexylammonium bis(trifluoromethanesulfonyl)amide when ethylene carbonate was used as an additive. The ethylene carbonate was proposed to prevent co-intercalation of the organic cation by the formation of a solid electrolyte interphase. ¹⁷⁵
2003	Nakagawa <i>et al.</i> report the results of a study of 1M LiBF ₄ / EMIBF ₄ electrolytes as a liquid and as a gel (GLiEMIBF ₄ – 15wt% poly(ethylene glycol) diacrylate). Li[Li _{1/3} Ti _{5/3}]O ₄ / EMIBF ₄ / LiCoO ₂ cells were prepared and cycled at 25 °C. The liquid electrolyte cell displayed an average voltage of 2.0 V and delivered 93.8% of the initial capacity after 50 cycles (C/5). The gel electrolyte cell displayed an average voltage of 1.9 V and delivered 73.1% of the initial capacity after 50 cycles (C/5). Concentration polarisation was identified as a factor limiting rate capability in the cells. ¹⁷⁶
2003	Sakaebe and Matsumoto publish a comparison of 1-ethyl-3-methylimidazolium (EMI), trimethylpropylammonium (N ₁₁₁₃), <i>N</i> -methyl- <i>N</i> -propylpyrrolidinium (P ₁₃) and <i>N</i> -methyl- <i>N</i> -propylpiperidinium (PP ₁₃) bis(trifluoromethanesulfonyl)amide RTILs. The cathodic stability increased in the order of EMI < TMHA < P ₁₃ = PP ₁₃ . The PP ₁₃ cation was reported to display the best cycling properties in a Li / PP ₁₃ / LiCoO ₂ 4 V cell – consistent capacity (>50 cycles), 97% coulombic efficiency at C/10 and 85% at C/2. ¹⁷⁷

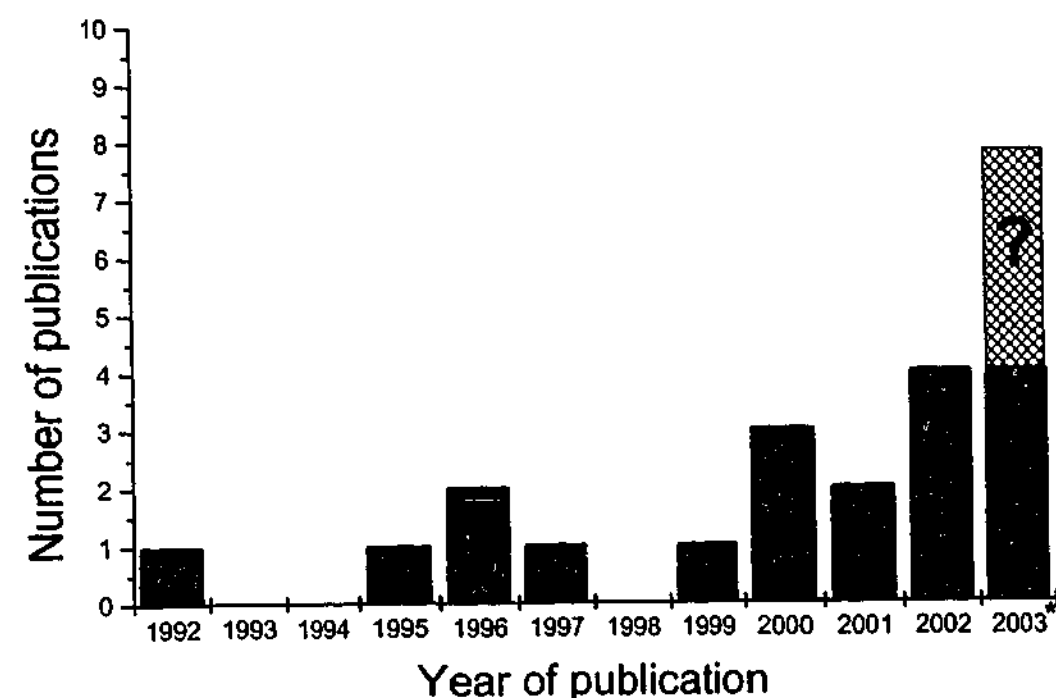


Fig. 1.8 Graph showing RTIL publications relevant to lithium battery research since the discovery of air and moisture stable RTILs in 1992 (* up to June 2003).

The graph shown in Figure 1.8 clearly shows an increasing trend in RTIL based lithium battery research, particularly in the past few years. The data are current until June 2003, the hatched area indicating the potential for more publications in the latter part of the year. The papers consistently cite the need to replace flammable organic liquid electrolytes to improve the safety of lithium-based cells, particularly for larger scale batteries. Recent literature shows a significant amount of interest from several Japanese groups.

The liquid state:

The majority of information available pertaining to models of the liquid state and to mass transport in RTILs must be derived from work performed on molten or 'fused' salts e.g., molten NaCl.¹⁷⁸⁻¹⁸⁰ The main difference between the structure of an ionic liquid and a molecular liquid arises from the need to arrange oppositely charged particles with their nearest neighbours, which causes an ordered arrangement in the ionic liquid that is not present in the molecular liquid.¹⁷⁸ Various models have been proposed to describe the liquid state for a 'pure' electrolyte (i.e., a fused salt) based on experimental evidence

obtained for these materials. These models describe the liquid state either from the perspective of a molten solid or from the perspective of a condensed gas. Each model endeavours to describe the structure of the molten salt in light of the fact that there is a volume increase upon fusion,¹⁷⁸ which is usually observed along with retention or even diminution of the mean interionic distances (as determined from X-ray and neutron diffraction data)^{179,181} This suggests that empty space is produced in the liquid during the process of fusion.

Vacancy model

The vacancy (or quasi-lattice) model was originated by Frenkel (1935) and developed by Bressler (1939).¹⁷⁸ Some elements of the crystalline lattice are maintained resulting in a liquid that (in places) resembles an ionic crystal with Schottky defects arising from lattice ions moving out of position to the surface. The vacancies are the same size and occur in lattice positions.

Hole model

This model originated with Altar (1937) and was developed by Fürth (1941).¹⁷⁸ Empty space arises from thermally generated fluctuations in local density. Holes are random in size and location (Swiss cheese). Holes are constantly changing in size, new holes appearing and old holes disappearing. Holes move by a mechanism whereby an ion jumps into a hole thus creating a new hole in its wake.⁴⁰ The theory has been successfully applied to calculate the expansion coefficients and compressibilities of alkali halides and nitrates.¹⁸²

Cell / free-volume models

The models consider the territory available for the motion of a particle. Transition from gaseous state to liquid state reduces the territory from the entire vessel (gaseous) to a cell (liquid). Within the cell the particle has free volume, the cell free volume is described as the difference between the total volume available for movement (of the particle within its

cage) and the volume of the particle.¹⁷⁸ The model prohibits multiple occupancy of cells and cannot explain volume increase upon fusion.

Liquid free-volume

This model was originated by Zernicke and Prins (1927) and developed by Eyring and Hirschfelder (1937).¹⁷⁸ Free-volume cells differ in size. The liquid as a whole contains a certain free-volume, and a statistical distribution of cell free-volumes. Free volume may be distributed throughout the system with no energy change.¹⁷⁹ Cells can expand and contract; interionic distance need not increase to explain the increase in free volume to account for the volume increase upon fusion.

Significant structures

Due to Eyring, Ree and Hirai (1958).¹⁷⁸ This model derives from the vacancy model, fusion occurs with the creation of two types of defects, holes (Schottky and Frenkel) and dislocations. The significant structures are essentially solids that have their properties modified by the presence of strain centres. The holes exist, gas-like, in the passageways associated with dislocations. The properties of the liquid are presumed to be expressible as a suitably weighted combination of the properties of solid-like molecules and gas-like molecules, the weighting factor being related to the difference between the liquid volume and the volume of the solid.^{40,179} The significant structure theory has been successful in describing the thermodynamics of melting and in calculating the specific heats and compressibilities of the alkali halides.¹⁸²

The hole model yields more qualitative and quantitative agreement with experiment than do the other models.¹⁷⁸

Transport in ionic liquids:

The conductivity of a pure fused salt (i.e., containing only one cation and one anion) is described by;

$$\sigma = F(c_i z_i u_i + c_j z_j u_j) \quad (1.21)$$

Fused salts have been found to exhibit a surprising degree of applicability to the Stokes-Einstein equation (Equation 1.11).¹⁸⁰ Stokes law (on which the Stokes-Einstein relation is based) relates the viscous force experienced by a large sphere moving through an incompressible continuum to its radius, velocity and the viscosity of the medium. The situation in a fused salt is obviously very different, instead of a continuum, ions are moving amongst other ions of approximately the same size in a structured medium. A more accurate form of the Stokes-Einstein relation has been presented and has been found to be applicable to fused salts;⁹⁵

$$D_i = RT/(6\pi N_A \zeta_i r_i \eta) \quad (1.22)$$

where ζ_i is a micro-viscosity factor of the ion, a 'correction' factor which accounts for interactions between the ions in the melt. Specific conductivity can in turn be related to viscosity;⁹⁵

$$\sigma = \gamma F^2 d / (6\pi N_A F W \eta) [(\zeta_a r_a)^{-1} + (\zeta_c r_c)^{-1}] \quad (1.23)$$

Where $0 < \gamma < 1$ is the degree of dissociation of the ions, d is the density, FW the formula weight, ζ is a microviscosity factor and the subscripts a and c refer to the anion and cation respectively. The equation highlights the importance of low viscosity, low formula weight and low ionic radius as contributors to high ionic conductivity.

The Nernst-Einstein equation relates the transport processes of diffusion and conduction;

$$\Lambda = \frac{F^2}{RT} \sum_i z_i D_i \quad (1.24)$$

Fused salts have been found to deviate from the Nernst-Einstein equation, typically;

$$\Lambda_{obs} < \Lambda_{calc} \quad (1.25)$$

Conductive transport depends only on the movement of charged particles (and only charged particles) under the influence of an electric field. Therefore, if two oppositely charged particles unite, permanently or temporarily, giving rise to an uncharged entity, then they will not contribute to the conduction flux. Current-less diffusion will occur and the conductivity calculated from the diffusion coefficients will always exceed the observed value.

It is assumed that the predominant cause of the deviation between experiment and theory in the Nernst-Einstein equation is due to the simultaneous movement of cations and anions in the same direction[†]. By considering the hole model, a mode whereby the movement of a cation and anion together into a vacancy pair hole of abnormally large size can be envisaged.¹⁷⁸ The influence of the diffusion of paired species on the observed conductivity can be calculated;

$$\Lambda_{obs} = \Lambda_{calc} - \frac{2zF^2}{RT} D_{+-} \quad (1.26)$$

where D_{+-} represents a diffusion coefficient for current-less modes of diffusion, often termed the cross coefficient. And;

[†] As opposed to attributing the deviation to 'drag effects' imposed by the movement of ions under an applied electric field. The frictional force produced by a large number of ions moving in opposite directions causes the electrical mobilities to fall below the diffusional mobilities.^{178,179}

$$D_{+,ind} = D_{+,obs} - D_{+-} \quad (1.27)$$

$$D_{-,ind} = D_{-,obs} - D_{+-} \quad (1.28)$$

where $D_{+,ind}$ and $D_{-,ind}$ are the diffusion coefficients of the cation and anion, respectively resulting solely from diffusion due to independent jumps of the individual ion. By application of the Einstein relation;

$$u_+ = \frac{z_+ F}{RT} D_{+,ind} \quad \text{and} \quad u_- = \frac{z_- F}{RT} D_{-,ind} \quad (1.29a \& b)$$

The transport or transference number of an ion in an ionic liquid is defined as the fraction of current carried by that ion when an electric current is passed through the system.¹⁷⁹ In a pure ionic liquid there is no frame of reference analogous to that of the solvent when dealing with molecular solvents. Generally some external reference is invoked such as a porous disk or the wall of the container.¹⁷⁸ The external transport number can be defined as:

$$t_i = z_i J_i / \sum_j z_j J_j = z_i c_i v_i / \sum_j z_j c_j v_j = z_i c_i u_i / \sum_j z_j c_j u_j \quad (1.30)$$

For a pure fused salt, i.e., containing one cation and one anion, the equation (for the cation) reduces to:

$$t_+ = z_+ c_+ u_+ / (z_+ c_+ u_+ + z_- c_- u_-) \quad (1.31)$$

Similarly, where the diffusion coefficients for the independent motion of the ions can be determined:

$$t_+ = \frac{D_{+,ind}}{D_{+,ind} + D_{-,ind}} \quad \text{and} \quad t_- = \frac{D_{-,ind}}{D_{+,ind} + D_{-,ind}} \quad (1.32)$$

Choosing one of the ions (e.g., the anion) as an internal reference for ionic motion is equivalent to setting $u_- = 0$, which would give $t_+ = 1$ and $t_- = 0$, a meaningless result. However, if the ionic liquid contains at least three species (e.g., two cations and a common anion), one species may be chosen as the velocity reference for the others and both internal and external transference numbers can be determined. The conductivity in the case of three ions is described by;

$$\sigma = F(c_1 z_1 u_1 + c_2 z_2 u_2 + c_3 z_3 u_3) = F(c_1 z_1 u_{13} + c_2 z_2 u_{23}) \quad (1.33)$$

where 1 and 2 are like-charged ions and 3 is a counter-ion. u_1 , u_2 and u_3 are external mobilities, while u_{13} and u_{23} are the internal mobilities of the ions 1 and 2 with respect to 3;

$$u_{13} = u_1 - u_3 \quad \text{and} \quad u_{23} = u_2 - u_3 \quad (1.34)$$

Then with reference to equation 1.31, the external transport number can be calculated;

$$t_1 = \frac{z_1 c_1 u_1}{z_1 c_1 u_1 + z_2 c_2 u_2 + z_3 c_3 u_3} \quad (1.35)$$

and similarly for ions 2 and 3. The internal transport number for ions 1 and 2 is given by;

$$t_{13} = \frac{z_1 c_1 u_{13}}{z_1 c_1 u_{13} + z_2 c_2 u_{23}} \quad (1.36)$$

$$t_{23} = \frac{z_2 c_2 u_{23}}{z_1 c_1 u_{13} + z_2 c_2 u_{23}} \quad (1.37)$$

where t_{13} and t_{23} are the fractions of current carried, respectively, by ions 1 and 2 relative to ion 3.⁴⁰

By determining the diffusivity and conductivity of a RTIL using independent techniques (i.e., diffusivity from PFGSE-NMR, and conductivity from AC impedance), it is possible to use the preceding treatment to assess an electrolyte in terms of its adherence to the Nernst-Einstein equation. In addition, the cross coefficient (D_{+-}) can be calculated, which allows the determination of the transport number for each of the mobile species.

1.5 The solid electrolyte interphase (SEI):

It is now well established that in lithium batteries containing liquid or polymer electrolytes, the anode is always covered by a passivating layer called the solid electrolyte interphase (SEI) which was suggested by Peled in 1979.^{183,184} The properties of the SEI are recognised as playing a determining role in the batteries' operating characteristics. Peled¹⁸⁴ states that the SEI properties affect the safety, self discharge, power capability, low temperature performance, faradaic efficiency, cycle-life, and the morphology of the lithium deposits.

1.5.1 Properties:

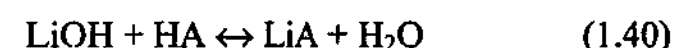
The passivity of metals and alloys is an essential and significant phenomenon responsible for their stability and utility in almost all applications. In this respect, lithium metal, with its passivating layer, is no different from the rest of the metals. However, in aqueous and oxygen containing/rich environments, which are highly reactive, the thin passivating layer on the lithium surface does not protect the metal. Instead, a rapid reaction takes place resulting in the complete oxidation of the metal. In the case of organic aprotic media the passivating surface film protects the lithium metal.²⁸

A native film covers the surface of commercially available, uncycled lithium foil. The film consists of various compounds – LiOH, Li₂O, Li₃N, (Li₂O-CO₂) adduct or Li₂CO₃. These compounds are produced by the reaction of lithium with O₂, H₂O, CO₂ or N₂.^{21,185}

Morigaki *et al.*¹⁸⁶ studied the surface of lithium in an organic electrolyte using AFM, FTIR and SEM techniques. The authors found that the lithium surface consisted of grain

boundaries, ridgelines and flat areas. The native surface was covered in a non-uniform film with Li_2O , Li_2CO_3 and LiOH localised at the ridgelines and grain boundaries. Further, when immersed in a 1M LiClO_4/PC solution for 24 hours, the surface is entirely covered with a film of lithium alkylcarbonate ROCO_2Li , a reduction product of PC. The lithium alkylcarbonate morphology differs at the ridgelines and grain boundaries where it forms large particles. The presence of LiCl , a reduction product of the perchlorate anion, at the ridgelines and grain boundaries is assumed to account for the expansion of the particles at these lines.

Kanamura *et al.*¹⁸⁷ studied the lithium surface using XPS. The lithium electrode was immersed in LiClO_4 , LiAsF_6 , LiPF_6 or $\text{LiBF}_4/\gamma\text{-BL}$ solutions. After immersion, a lithium halide was detected on the surface in addition to the native surface compounds (LiOH , Li_2CO_3 and Li_2O). The rate of reaction of the native film was much faster for LiBF_4 and LiPF_6 than for LiClO_4 and LiAsF_6 . The film formed in the presence of LiPF_6 was more compact and thinner than that formed in the other electrolytes. The morphology of lithium deposited in the LiPF_6 electrolyte was hemi-spherical while that deposited in the other electrolytes was dendritic. Similar studies were performed in other solvents¹⁸⁸ and the authors concluded the following reactions to be occurring on the native lithium surface,



where HA is an acid present as an impurity in a non-aqueous electrolyte. The amounts of HA present and hence the extent of surface film modification is a function of the stability of the salt in the non-aqueous electrolyte.

1.5.2 Structure:

Initially it was suggested that the passivating layer consisted of one or two layers.¹⁸³ The first being a thin, compact SEI made up of crystals that are thermodynamically stable with respect to lithium. The second layer on top of the SEI is a more porous, open structure that suppresses ion transport in the electrolyte filling its pores. Later, other models were proposed¹⁸⁹ that were modifications of the original SEI model:

- Polymer electrolyte interphase model (PEI): the surface layer in PC/LiClO_4 electrolyte consists of Li_2CO_3 , LiClO_4 and polypropylene oxide (PPO). PPO is formed by the reduction-induced polymerisation of PC.
- Solid polymer layer (SPL) model, where the surface layer is assumed to consist of solid compounds dispersed in a polymer electrolyte.
- Compact stratified layer (CSL) model, where the surface layer consists of two sublayers, the first being the SEI and the second being either a SEI or PEI.

Peled¹⁸⁴ refutes the PEI and SPL models as being irrelevant to lithium systems because the PEIs are not thermodynamically stable towards lithium. Recently, Peled^{184,190} has introduced the concept of a SEI which consists of 'polyheteromicrophases' (see Fig. 1.9). The model is based on evidence that indicates that grain boundary resistance, associated with the crossover of ions from particle to particle through grain boundaries perpendicular to the current flow, is a dominant impedance component.¹⁹⁰

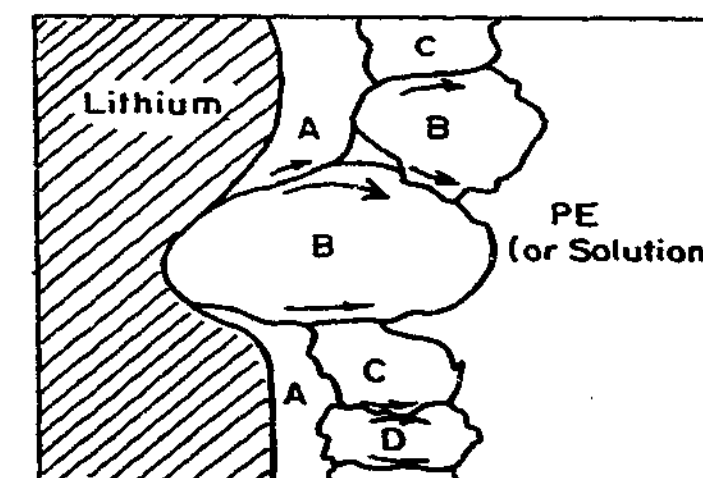


Fig. 1.9 Schematic representation of a section of the polyheteromicrophase SEI.

Peled *et al.*¹⁸⁵ listed the required properties of a good SEI:

- Must be an electronic resistor.
- Cation transfer number $t^+ = 1$ to eliminate concentration polarisation and to ease the deposition/dissolution process.
- High ionic conductivity to reduce overvoltage.
- Uniform morphology and chemical composition for homogeneous current distribution.
- Good adhesion to the anode.
- Mechanical strength and flexibility.

Peled states that the occurrence of the SEI is necessary and that SEI free batteries are not practical.¹⁹⁰

Peled *et al.*¹⁸⁵ suggest the use of bimolecular rate constants (k_e) for the reaction of hydrated electrons with electrolyte components as a useful method to predict reactivity towards lithium. It is suggested that SEI forming reactants should be chosen from materials that react very quickly (i.e., rate constants higher than $\sim 10^9$ Lmol⁻¹s⁻¹), and inert electrolyte components should be chosen which are likely to react very slowly with lithium (i.e., rate constants lower than $\sim 10^7$ Lmol⁻¹s⁻¹). Table 1.7 shows rate-constant values for some materials relevant to film formation in lithium cells.

More recently, other authors have stated their belief that a passivated lithium electrode could only offer a limited cycle-life and that in order to obtain a deep discharge and long cycle-life the lithium negative electrode must be free of a passivating film and be kinetically stable towards the electrolyte.²⁸

Table 1.7 Bimolecular rate constants (k_e) for the reaction of hydrated electrons with Li battery related materials.¹⁸⁵

Reactant	pH	Rate constant k_e at 15–25 °C (Lmol ⁻¹ s ⁻¹)
AsF ₆ ⁻	7	9×10^9
BF ₄ ⁻	5.8	$< 2.3 \times 10^5$
CO ₂	7	7.7×10^9
CO ₃ ²⁻		$< 3.9 \times 10^8$
ClO ₄		$< 10^6$
CrO ₄ ²⁻	13	5.4×10^{10}
H ⁺		2.5×10^{10}
HF		6×10^7
MnO ₄ ⁻	7	4.4×10^{10}
NO ₃ ⁻		8.2×10^9
O ₂	7	1.9×10^9
H ₂ PO ₄ ⁻	6.7	7.7×10^6
SO ₄ ²⁻	7	$< 10^6$
S ₂ O ₈ ²⁻	7	1×10^{10}
SF ₆	7	1.6×10^{10}
Acetone	7	6×10^9
Acetonitrile		4×10^7
Acetophenone		2.4×10^{10}
Acrylamide		2.2×10^{10}
Acrylate ion	9.2	5.3×10^9
Acrylonitrile		1.3×10^{10}
Carbon Disulfide		3.1×10^{10}
Cyclopentanone		7.4×10^9
Ethyl Acrylate	11	8.7×10^9
Cyclohexane	11	$< 10^6$
Diethyl ether		$< 10^7$
Dimethyl fumarate	9.2	3.3×10^{10}
Dimethyl oxalate		2×10^{10}
Ethyl acetate	6.5	5.9×10^7
Furane	8	3×10^6
Propylene glycol carbonate		7.2×10^7
Naphthalene	11	5.4×10^9
Styrene	12.7	1.1×10^{10}
Trifluorotoluene	11	1.8×10^9

1.5.3 Relationship to battery operation – dendrite formation:

The poor performance of lithium metal rechargeable batteries is mainly explained by lithium dendrite growth.^{21,191,192}

Early researchers believed that lithium was kinetically stable in many organic solvents. A passivating film was assumed to cover at least part of the surface but it was generally accepted that the rate-determining step of the deposition/dissolution process was the electron transfer process between the lithium electrode and the lithium ion in solution. Investigations of the lithium thionyl chloride system led to the discovery that lithium was covered by a lithium carbonate film when in contact with propylene carbonate. It was concluded, for this system, that the rate-determining step for the deposition/dissolution process was the migration of lithium cations through the passivating film.²⁸

Munichandraiah *et al.*²⁸ reviewed electrochemical studies of the lithium | electrolyte interface. The authors highlighted the ambiguity in much of the published literature with respect to the importance of the charge transfer reaction rate and the rate of diffusion through the surface film. When assessing the kinetics of the deposition/dissolution process at the surface of the lithium electrode the authors believe that both processes are important factors that must be taken into account.

Peled¹⁸³ considered the deposition/dissolution process in terms of the solid electrolyte interphase (SEI) electrode. In simple terms, the kinetics of the deposition/dissolution process could be viewed as a function of the thickness and conductivity of the SEI. For a thin and/or conductive SEI the rate determining step would be the charge transfer reaction. For a thick and/or less conductive SEI the rate determining step would be the rate of ionic migration through the SEI.

In the study discussed earlier (1.5.1 Properties) Morigaki *et al.*¹⁸⁶ also studied the deposition of lithium at high current density. Electrodeposition resulted in the observation of many particles of lithium at the grain boundaries and ridgelines. AFM measurements indicated that some of the surface morphology remained unchanged after deposition. The authors propose that, during deposition, the migration of lithium ions occurs through the

ridgelines and grain boundaries. They then suggest that, because the rate of diffusion from the bulk electrolyte is slower than the rate of migration along the ridgelines and grain boundaries, the deposition occurs at a small number of energetically favoured sites.

Yamaki *et al.*²¹ have presented a possible mechanism for the formation of lithium dendrites and the accumulation of dead lithium (see Fig. 1.10):

- (i) Lithium is deposited under the film without any serious damage to the surface film.
- (ii) Lithium is deposited at points where the surface film has higher lithium ion conductivity.
- (iii) Due to the non-uniform deposition of lithium, mechanical stress is created in the lithium electrode under the surface film.
- (iv) Stress causes lithium atom transport, which allows the release of the stress in the lithium surface. The transport is conditioned by the lithium surface tension, and also possibly by crystalline defects and grain boundaries.

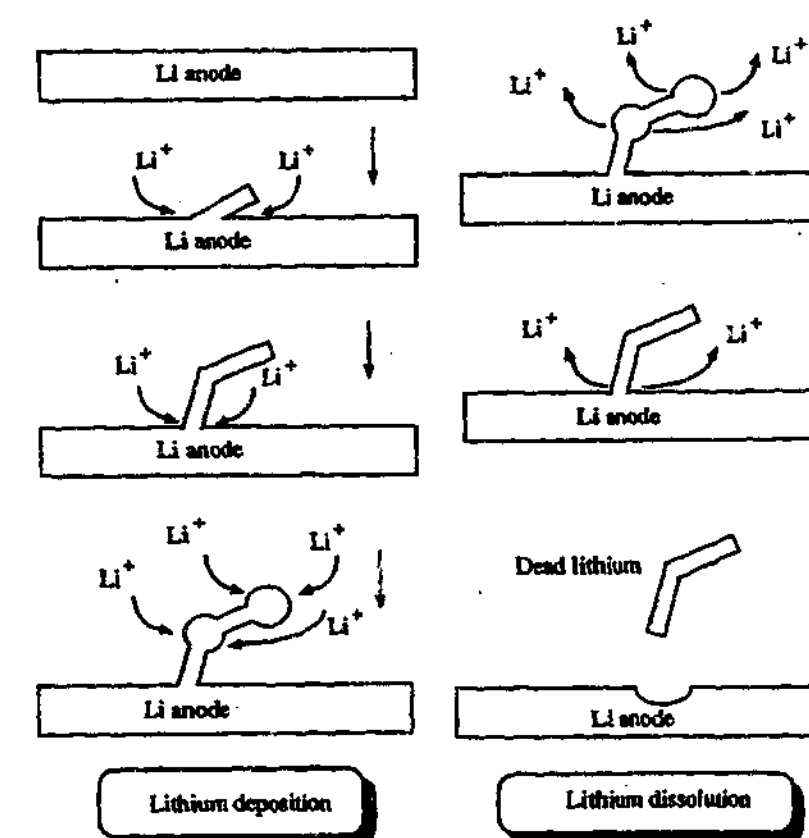


Fig. 1.10 A schematic representation of the deposition/dissolution process presented by Yamaki *et al.*²¹

- (v) The surface film is broken by the stress at certain points. Lithium grows as an extrusion through the holes. At low current densities the stress may not be great enough to break the film and lithium deposition will be uniform.
- (vi) The dendrites continue to grow from the base. Eventually the surface will be covered with lithium dendrites and diffusion to the lithium surface will be hindered. Deposition will begin to occur at the kinks and tips of the dendrites where there are crystalline defects. Current density will be reduced by the increase in the number of effective deposition sites leading to particle like deposition morphology. The morphology as a whole takes on the appearance of mushroom like growths.
- (vii) Dissolution is likely to follow a reverse process. Initially the particle-like lithium on the kinks will be dissolved. Then the dendrites will begin to be dissolved from the base. This can result in the dendrite being cut from the substrate forming 'dead lithium'. Under high rate and/or low temperature deposition the dendrites have a small diameter which will result in a large amount of dead lithium because the dendrites are easily cut.

Brissot *et al.*^{193,194} studied the evolution of dendrites under a constant current regime. A symmetrical Li/PEO-Li(Tf)₂N/Li cell was constructed and observed using optical techniques. The study was based on a model that predicts dendrite growth will occur at the Sand's time (Section 1.3.1), when the ionic concentrations in the vicinity of the negative electrode drop to zero. Different behaviour of the cations and anions lead to a build up of positive charges at the negative electrode. This results in a local space charge with a large electric field. This situation creates instabilities such as dendritic growth. The model also predicts that the velocity of dendrite growth (modelled as a set of rectilinear, equally spaced, parallel filaments) will match the velocity of anionic drift in order to avoid the increase of the space charge.¹⁹⁵ The authors made numerous observations:

- The cell potential exhibits reproducible Sand behaviour at current densities below 2 mAcm⁻².
- The individual dendrites can grow at different velocities, however the overall velocity is close to that of the anionic drift velocity ($v = -\mu_a E$) and is proportional to the current density.

- There is a global motion of the solid electrolyte toward the negative electrode during polarisation. The motion is due to variations in the salt concentration near the electrode which induces changes in the shape of the polymer electrolyte. Large anions accumulate in the vicinity of the positive electrode, causing the polymer to 'inflate'. There is a corresponding decrease in the volume of the polymer at the negative electrode. In the confined space of the experimental cell the volume changes result in a 'push' and 'pull' effect on the bulk electrolyte which induces the observed motion. The motion is (in the experimental cell configuration) sufficient to break the delicate dendrites.
- At low current densities, the concentration does not approach zero at the negative electrode. Needle-like dendrites are observed. The time to the onset of growth increases with decreasing current density. During growth, the potential decreases due to the decrease in inter-electrode distance.
- At high current densities, dendrites are not usually observed in the first polarisation. After a few cycles, dendrite growth is observed to occur close to the Sand's time. The dendrites exhibit arborescent morphologies and are unable to grow beyond certain maximum distance from the electrode. Further cycling enhances dendritic growth, the onset of growth begins to occur immediately when the cell is polarised and large fluctuations in growth velocity occur. The enhancement is attributed to current density inhomogeneities due to local surface features which become more pronounced with cycling.

Dead lithium and cycle-life:

When a lithium metal rechargeable cell is charged, deposition occurs on the substrate of the lithium negative electrode. The plated lithium does not necessarily plate uniformly but frequently deposits as a fibre-like growth or dendrite. During discharge the negative electrode is dissolved, and sometimes, the fibre-like lithium is cut and isolated from the substrate. Known as 'dead lithium', the deposit is electrochemically inactive but chemically active. The dead lithium accumulated during cycling reduces the cell cycle-life, has a high surface area and makes the cell more susceptible to thermal runaway.^{191,192}

There are considered to be two secondary reasons for loss of capacity of the lithium negative electrode during cycling:²¹

- (i) During deposition/dissolution the shape of the surface changes and a fresh surface is formed. Lithium is consumed by its reaction with the electrolyte to form a new surface film.¹⁸⁵
- (ii) Local heating of the surface film may occur during deposition. The heating may cause part of the film to become an electrical conductor causing the deposition of electrochemically inactive lithium within the film. It is unlikely that these deposits would take any further part in cycling as they would be electrically isolated from the lithium substrate.

Current density:

Yamaki *et al.*¹⁹² demonstrated that the surface area of the lithium electrode increases with a decrease in discharge current and with an increase in the number of cycles.

Orsini *et al.*¹⁰ observed dendrite growth and loss of interfacial contact, and hence rapid capacity loss, in laminated Li/PVdF-EC-DMC-LiPF₆/LiMn₂O₄ cells. The occurrence of dendritic deposits was observed (SEM) to increase at high charging currents. The cells were configured to purposely favour dendrite growth.

It has been shown that the morphology of the lithium deposit depends on both the current density during charge and discharge and on the native state of the metallic surface.¹⁰ Arakawa *et al.*¹⁹⁶ studied the dependence of lithium electrode cycle-ability and morphology on current density using SEM and optical microscopy, observing that:

- Low current density during dissolution results in the formation of a small number of localised pits and a reduced cycle-life. The authors believe that the low overpotential applied by low current density focuses the current on regions of the surface film that have relatively low impedance.

- High current density during dissolution results in the formation of a large number of delocalised pits and an increased cycle-life. High current density results in a more uniform dissolution because of sufficient overpotential to dissolve lithium across the entire surface.
- Low current density during deposition leads to an increase in cycle-life and particle like morphology.
- High current density during deposition leads to a decrease in cycle-life and needle-like morphology.

Aurbach *et al.*¹⁹⁷ studied the effect of varying charge and discharge current densities and found similar effects. The authors explained the effect of varying current densities in the following terms:

- At high discharge rates ($>1 \text{ mAcm}^{-2}$) the native films which cover the active material are rapidly and completely replaced by surface films which originate from solvent reduction processes. These films induce uniform dendrite free Li deposition.
- At low discharge rates ($<1 \text{ mAcm}^{-2}$) part of the native film remains. The surface film is heterogeneous and leads to non-uniform deposition and the formation of dendrites.
- At high charging rates ($>1 \text{ mAcm}^{-2}$) fresh lithium is exposed to the solution. The fresh lithium reacts predominantly with the salt anion (in this case, LiAsF₆). The surface film produced leads to non-uniform deposition.
- At low charging rates ($<0.5 \text{ mAcm}^{-2}$) Li deposition is sufficiently slow to occur beneath the existing surface film. The surface will be covered with a uniform solvent reduction film and uniform deposition is promoted.

Arakawa *et al.*¹⁹⁶ demonstrated the recombination of isolated lithium with the bulk negative electrode at high discharge rates. A cell was constructed and a small piece of lithium was set isolated from the electrode at a small distance, simulating a piece of dead lithium. Observation of the isolated lithium during cycling showed that deposition occurred on the surface facing the bulk electrode. The deposition caused the eventual

'recombination' of the isolated piece by bridging the space between the isolated lithium and the bulk negative electrode. The authors propose that at sufficiently high current densities, there will be a large potential gradient and the isolated lithium will be at sufficiently cathodic potentials for lithium deposition to occur on its surface.

Yamaki *et al.*²¹ provide four possible explanations for the reduction of dead lithium formation at high discharge current densities:

- (i) At high discharge currents large numbers of small delocalised pits are formed on the lithium surface. The pits become deposition sites during charging and result in a low charge current density. Hence the dendrites formed are thick and not easily cut to form dead lithium.
- (ii) The delocalised pits formed are shallow and emerging lithium dendrites are amenable to the application of stack pressure.
- (iii) Isolated lithium near the lithium surface becomes a local cell because of stray current. The stray current is high at high discharge currents allowing the dissolution of dead lithium.
- (iv) At high discharge current dissolution of the lithium from the tips and kinks of the dendrites is promoted resulting in the formation of less dead lithium.

Methods of Dendrite Suppression:

Research on the lithium metal electrode is being pursued in many laboratories. The majority of research is geared toward suppression of dendrite formation and the improvement of lithium metal rechargeable battery cycle-ability. Owen lists the following approaches:¹¹

- The use of more inert solvent systems and salts
- Increasing stack pressure on the electrode
- The addition to the electrolyte of compounds which improve plating morphology
- The use of polymer electrolytes

Additives

Additives that improve plating morphology may be classified into three types:²¹

- (i) Stable additives that cover the surface and limit reaction between the lithium and the electrolyte e.g., *Cis* or *trans*-decalin, benzene, toluene, PEGDME, 4,4-dipyridyl.
- (ii) Additives which modify the state of solvation of lithium ions e.g., N,N,N',N'-tetramethylethylenediamine (TMEDA).
- (iii) Reactive additives used to make a better surface film e.g., Hexamethylphosphoric triamide (HMPA), CO₂, HF, 2-methylfuran (2MeF), AlCl₃.

Additives reported to reduce the formation of lithium dendrites:

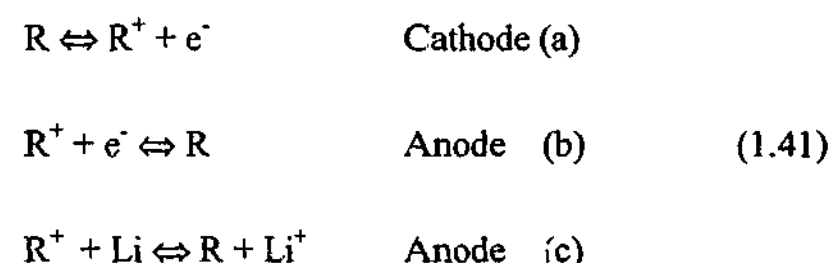
- *Cis*- or *trans*-decalin in LiClO₄/PC electrolyte.
- HF in LiClO₄/PC electrolyte.
- CO₂ protects against reaction with H₂O in LiClO₄/PC electrolyte.

The additive effects are reported to be a result of modification of the lithium surface film.¹⁹²

Orsini *et al.*¹⁰ demonstrated the effectiveness of NMP (1-methyl-2-pyrrolidinone) in enhancing polymer adhesion to metallic lithium. The laminate cells exhibited a longer cycle-life, at moderate current densities, than the cells without NMP pretreatment. In the same paper, the authors demonstrated that lithium dendrites did not grow as easily on a copper substrate as they did on a lithium substrate.

In their 1996 patent, Alamgir *et al.*¹⁹⁸ claimed the use of metallocenes to provide overcharge protection and suppress dendrite growth. The authors cite the use of acetylferrocene or ferrocene carboxaldehyde as chemical redox shuttles. The materials have an oxidation potential slightly higher than the normal charge cut-off voltage. The shuttle is unreactive until the cell is fully charged. Then, the shuttle is electrochemically oxidised and the products diffuse to the anode where they are regenerated either by reduction or

chemical reaction. The cycle continues which effectively locks the cell potential at the oxidation potential of the shuttle. The redox shuttle should possess good solubility in the electrolyte, an oxidation potential slightly higher than the normal charge limit of the cell but lower than the oxidation potential of the electrolyte, the ability to reduce the oxidised form of the reagent at the anode without any side reactions, and chemical stability of both the oxidised and reduced forms of the reagent in the cell. The reactions occur according to the following equations:



Reaction 1.41(a-c) involves reaction with the lithium anode. The lithium dendrites, having higher surface area than the underlying lithium foil, react preferentially with the shuttle. Hence, the shuttle also acts as a scavenger which reduces the amount of dendrites in the cell and extends the cycle-life.

Choquette *et al.*¹⁹⁹ claim the use of potassium salts to increase the rate capability of lithium metal rechargeable batteries and also claim that the addition of potassium stabilises the lithium anode and extends cycle-life. Various examples of potassium salts are provided e.g., $\text{KN}(\text{RFSO}_2)_2$, $\text{KN}(\text{FSO}_2)\text{RSO}_2$, KPF_6 , KRFSO_3 or $\text{K}(\text{Tf})_2\text{N}$ – where F is a perhalogenoalkyl or a perhalogenoaryl and R is an organic radical. EDAX and TEM evidence indicates that K^+ is present throughout the intercalation cathode and polymer electrolyte. TEM evidence indicates that K^+ is not reduced at the anode but is present very close to the lithium surface. The invention produces depolarising effects during recharge, which extends the number of cycles before the appearance of dendrites.

Kanamura *et al.*²⁰⁰ compared the deposition of lithium on a nickel substrate in PC/ LiClO_4 with and without the addition of 5×10^{-3} M HF. In the absence of HF, the lithium morphology was dendritic whereas in the presence of HF the deposited lithium had a hemispherical form for up to five deposition/dissolution cycles. XPS analysis of the surface

film indicated a uniform LiF layer overlaying a layer of Li_2O . The favourable deposition characteristics in the presence of HF are attributed to the uniformity of the LiF layer. The HF is not likely to represent a significant safety concern given the low concentrations used and the fact that a considerable fraction is expected to form LiF on the lithium surface.

Electrolytes

Tatsuma *et al.*⁷³ demonstrated the effectiveness of polyacrylonitrile (PAN) gel electrolytes in suppressing dendrite formation. The gel ((1-17 wt.%) PAN in PC-EC- LiClO_4) was shown, using an optical technique, to suppress dendrite formation with increasing PAN concentration. The mechanical strength decreased and the interfacial resistance increased with increasing PAN concentration. Taking these factors into account the authors suggested an optimum concentration of 5-10 wt.% PAN. The authors also noted that prolonging the pre-cooling time, a step in the preparation method, led to a further increase in the ability of the electrolyte to suppress dendrite formation.

Using the QCM technique, Koike *et al.*²⁰¹ investigated surface reactions during the electrodeposition of lithium. The authors concluded that the electrodeposited lithium reacts immediately with electrolyte and/or residual impurities to form surface films. The authors studied the deposition process in two solutions, LiClO_4/PC and $\text{LiPF}_6/\gamma\text{-BL}$. The surface film formed in LiClO_4/PC did not protect the surface from further reaction with the electrolyte whereas the film formed in $\text{LiPF}_6/\gamma\text{-BL}$ was close and protective.

Aurbach²⁰² discusses the use of 1,3 dioxolane (DN) with LiAsF_6 as an electrolyte. Lithium cycling efficiency in these solutions is very high, and deposition morphology in them is very smooth. The improved reversibility of the lithium electrode is explained by the nature of the surface film formed in the DN solution. The surface film contains, in addition to the reduction products of the salt and solvent (HCOOLi , $\text{CH}_3\text{CH}_2\text{OCH}_2\text{OLi}$ – DN reduction products, LiF and Li_xAsF_y – salt reduction products), oligomers of polydioxolane. The polyDN oligomers adhere to the lithium surface by the alkoxy (OLi) edge groups providing a flexible surface film that is better able to accommodate the volume changes which occur during deposition. A similar situation is thought to occur in PEO electrolytes where

elastomeric fragments of PEO with alkoxy edge groups are formed, giving rise to surprisingly high cycling efficiencies (here the author cites a private communication). The author concludes that a necessary condition for the stabilisation of lithium anodes in rechargeable battery systems is the formation of elastic, flexible surface films which can accommodate volume changes during cycling, thus providing the surface with good passivation.

Stack pressure

Stack pressure perpendicular to the lithium metal electrode suppresses the creation of dead lithium and improves thermal stability. The dependence of the cell FOM on stack pressure varies significantly with electrolyte composition.²⁰³ However, the cell is unsafe if the stack pressure is not uniform due to a manufacturing defect. Non-uniform stack pressure results in uneven current density that can lead to dendrite growth and gas generation. Lithium is a soft metal and stack pressure causes dendrites to deform and achieve a flat surface.²⁰⁴

Current density and the cycling regime

Arakawa *et al.*²⁰⁵ cycled Li/LiAsF₆-(EC)-(2-MeTHF)/ α -V₂O₅ cells between 1.8 V and 3.3 V and between 1.8 V and 3.5 V. The cells were found to have vanadium deposited on the lithium anode with oxidation number ranging from V(III) to V(V). The cell cycled to 3.5 V had higher vanadium content in the anode. The thermal stability of the cells was assessed using calorimetry and the cells cycled to 3.5 V were found to be more stable and SEM showed that they displayed increased surface roughness of the lithium anode. The increased thermal stability was attributed to changes in the features of the passivation film.

Aurbach *et al.*¹⁹⁷ noted that it is possible to improve the cycling performance of the Li anode cycled at high charging rates and/or low discharging rates by cycling them initially at low charging and high discharging rates. Pretreating the anode in such a way creates a favourable surface film and extends cycle-life for high charge and/or low discharge current density applications. A patent held by Yoon²⁰⁶ claims the use of a 5–10 mAcm⁻² discharge pulse of the cell of less than 2% of the cell capacity followed by charging at less than

2 mAcm⁻² to form a lithiated film at the anode. The pretreatment yields increased battery life, suppression of gas generation and flat voltage discharge.

In a 1988 patent, Wagner²⁰⁷ claims the use of an interrupted current charging mode to prolong the useful life of lithium metal rechargeable batteries. A similar Japanese patent is held by Sony Corp²⁰⁸ published in 1995. The invention utilises a charging current interrupted at intervals of 1 millisecond to 9 seconds, in a frequency range of 0.1 to 10 Hz. The method is shown to extend battery cycling life. Cycle-life is extended 'via a lithium ion transport process and uniform lithium replating at the anode'. The interrupted current charging mode may be superimposed over a constant potential charging mode. The combination of anodic pulses with cathodic charging pulses is shown to be advantageous in breaking down and preventing possible lithium penetration fronts. Published work investigating the use of pulsed charging currents in lithium metal rechargeable batteries is not available. However the use of pulsed currents to modify the morphology of electrodeposited metal particles has been known for some time.²⁰⁹ It has been shown for Ag, Sn and Cu deposition that the shape of a pulsating overpotential wave has a strong effect on the morphology of metal powder particles. Generally the higher the pause-to-pulse ratio, the less dendritic powder particles are obtained. Dendrites with very low tip radii can be dissolved during the pause and the branching of dendrites can be prevented.²⁰⁹

Surface treatment

Neudecker *et al.*²¹⁰ demonstrated the fabrication of a 'lithium free' thin film battery. The battery consists of a LiCoO₂ cathode, a LIPON solid electrolyte and a copper anode current collector. Plating metallic lithium onto the anode on the initial charge activates the cell. The battery operates as a lithium metal rechargeable battery which contains only the amount of lithium that is supplied by the positive electrode. The authors demonstrated that by coating the exterior of the anode current collector with a gas tight seal of LIPON or Parylene C the cycle-life of the cell could be significantly improved. The improvement was attributed to the prevention of the formation of Li₂O and/or LiOH by exposure to O₂ and H₂O from the atmosphere.

Skotheim *et al.*^{211,212} claim the use of a vacuum evaporated thin film of a lithium conducting polymer interposed between the lithium electrode and the electrolyte to suppress dendrite formation. Due to the high electrical conductivity of the film there is a constant potential across the lithium surface. This results in uniform deposition and dissolution of lithium and a suppression of dendrite formation. The authors state that the film also has the ability to dissolve 'micro-dendrites' as they are formed. The films are prepared by vacuum evaporation of a starting polymer that is thermally decomposed on the lithium surface. The decomposition leads to highly reactive fragments of low molecular weight. Polymerisation of the fragments to form a highly branched and crosslinked electroconductive film occurs on the lithium surface. The patent presents an illustrative list of starting polymers – poly(p-phenylene), polyacetylene, poly(phenyl vinylene), polyazulene, poly(perinaphthalene), polyacenes, and poly(naphthalene-2,6-diyl). Poly(p-phenylene) is preferred.

Hong and Takeuchi²¹³ studied the effect of pretreating the lithium electrode by exposing the fresh lithium surface to CO₂. Linear polarisation measurements demonstrated an increased exchange current density for the pretreated surface compared with the native surface film. The surface film was found to be relatively strong and able to withstand high current pulses without significant damage. The authors propose a fast ion exchange mechanism for the Li₂CO₃ film which involves charge delocalisation of the carbonate anion. Improvement in lithium battery performance in the presence of CO₂ is attributed to the formation of the Li₂CO₃ film and its ability to maintain a low ionic resistance in the SEI. The authors demonstrated the necessity of brushing the lithium surface as a step in the surface pretreatment prior to exposure to CO₂.

Takehara *et al.*²¹⁴ utilised plasma polymerisation of 1,1-difluoroethane to prepare an ultra-thin and uniform solid polymer electrolyte layer on the lithium surface. The electrolyte showed room temperature conductivity of $3 \times 10^{-8} \text{ Scm}^{-1}$. SEM observation of the electrode surface revealed that deposition was uniform and dendrite growth was suppressed. The authors propose that the uniformity of the film and its low surface energy contributed to the suppression of dendritic growth.

1.5.4 Characterisation:

There are a variety of methods applicable to the study of the lithium surface. The major difficulty encountered by researchers is related to the reactivity of lithium. Obtaining a representative sample requires avoiding exposure of the sample to air and moisture, and ensuring that the lithium surface is not physically disturbed.¹⁰ There have been two approaches to overcoming these difficulties:

- In-situ study of the interface within an operating cell requiring specially designed cells.^{193,194,196,215}
- Ex-situ study of dismantled cell components requiring hermetic transference techniques.^{10,191}

Both of the above techniques have shortcomings:

- (i) The specially designed in-situ cells do not necessarily represent conditions in a practical battery;
- (ii) Ex-situ studies run the risk of altering the lithium surface during transfer.²¹⁶

Each method also has its advantages:

- (i) In-situ study allows continuous observation of surface changes with time and cycling;
- (ii) Ex-situ study provides versatility for analysis once a representative sample is obtained.

Several researchers have combined both techniques in one study.^{186,197,216}

Researchers have generally followed two approaches in the preparation of the lithium surface prior to the assembly of a cell. One approach is to assemble the cell with the lithium surface as received, to duplicate conditions that are most likely to exist in

industry.^{187,188,204} The other approach has been to prepare a fresh lithium surface, usually by cutting, which is then exposed to the electrolyte under an argon atmosphere.^{168,215,217}

Orsini *et al.*¹⁰ used a cell transfer system to introduce a cell into a SEM without exposure to air. The transfer system comprised a moveable air lock and a Peltier plate. The sample was cooled ($\sim -20^\circ\text{C}$) to prevent damage and evaporation of the electrolyte due to vacuum in the antechamber during observation. The SEM images obtained were of high quality. The authors claimed the ability to observe dendrites with a higher degree of resolution, sharpness and integrity than previously reported elsewhere.

Kanamura *et al.*^{187,188} characterised the lithium surface in various solvents and salts using XPS. Argon sputtering provided depth profile information for the surface film. Samples were immersed in the electrolyte for three days and then washed in pure solvent, dried under vacuum for 1 hour and attached to a XPS sample holder. These treatments were performed in an argon dry box. Transfer to the XPS instrument was accomplished using a desiccator (P_2O_5), the sample being exposed to the atmosphere for only a limited time.

Optically transparent cells are frequently used to monitor changes to the electrode, electrolyte and lithium | electrolyte interface during cycling.⁷³ Various cell designs are reported in the literature, which comprise the same basic features.^{193-196,218} An example is given in Fig. 1.11. Brissot *et al.*^{193,194} utilised National Institute of Health (NIH) image processing software, the study allowed the observation of concentration profiles in the electrolyte near the electrode due to variations in the optical index.

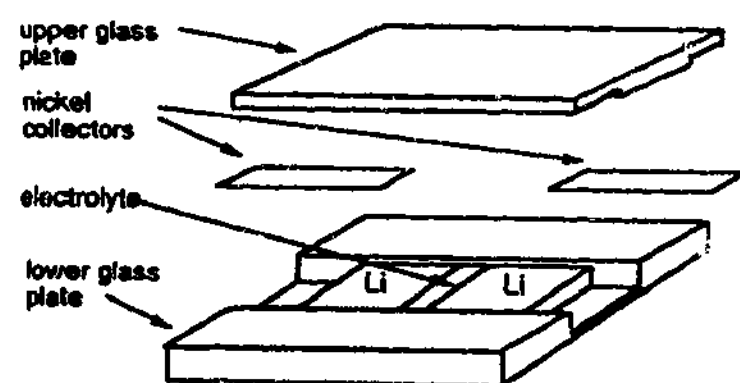


Fig. 1.11 Schematic representation of an optical cell.¹⁹³

Instrumental Techniques:

Aurbach has intensively studied the surface of the lithium electrode.^{168,197,217,219} In a recent review, Aurbach²⁰² discusses the characterisation of the lithium surface with respect to the stabilisation and failure modes of lithium anodes. Information on the surface chemistry can be obtained from FTIR spectroscopy, XPS, EDAX and morphological aspects from SEM, AFM, and STM. Characterisation of the electrochemical behaviour can be performed using a variety of techniques such as EIS, GITT, PITT, variable scan rates, cyclic voltammetry, chronoamperometry, chronopotentiometry and QCMB. The most common source of information for lithium surface characterisation has been a combination of FTIR spectroscopy and XPS,²⁰² which enables identification of the surface compounds and the determination of their depth profile.

Munichandraiah *et al.*²⁸ reviewed DC polarisation studies on lithium electrodes. DC polarization studies make use of the Butler-Volmer equation to obtain values for the charge transfer resistance (R_{ct}) and the exchange current density (i^0);

$$i = i^0 \left(e^{-\alpha F \eta / RT} - e^{(1-\alpha) F \eta / RT} \right) \quad (1.42)$$

where η is electrode overpotential corresponding to current density i and α is the charge transfer coefficient. At low overpotentials, the equation is reduced to:

$$i = i^0 F \eta / RT \quad (1.43)$$

or

$$i^0 = RT / FR_{ct} \quad (1.44)$$

Koike *et al.*²⁰¹ demonstrated the use of a QCMB in studying the electrodeposition of lithium in a non-aqueous solution. The authors demonstrated that by monitoring the changes in the frequency response of the crystal it was possible to estimate the identity of compounds formed on the lithium surface during electrodeposition from the value of the mass accumulated per mole of electrons (mpe), where;

$$mpe = (d\Delta m/dQ)F(d\Delta f/dQ)(F/C_f) \quad (1.45)$$

F is the Faraday number, Δf is change in the quartz resonance frequency, Δm is the mass accumulation per unit area, Q is the charge per unit area and C_f is the correlation coefficient between Δf and Δm . The value of mpe is related to possible surface compounds by comparison with the average molecular weight per electron transferred of each compound.

Morigaki and Ohta¹⁸⁶ obtained information on the nanostructure of the lithium surface using in-situ AFM. Details of the surface chemistry were obtained using in-situ FTIR, ex-situ XPS and ex-situ scanning auger electron microscopy (SAM). All sample transfer was conducted under a dry air atmosphere.

Aurbach^{168,217} used FTIR and nuclear magnetic resonance spectroscopy (NMR) to study the surface films on lithium and lithium amalgam in uncontaminated and contaminated γ -Butyrolactone solutions. FTIR measurements required the use of a modified measurement chamber to prevent exposure of the sample to air.

Wang *et al.*²²⁰ utilised XPS, Auger electron scanning microscopy (AES) and temperature programmed desorption (TPD) to investigate the interactions between perdeuterated tetrahydrofuran (TDF) and metallic lithium in ultra-high vacuum.

Wilkinson *et al.*²⁰⁴ demonstrated the use of a specially designed apparatus to monitor and control stack pressure and electrode growth in lithium cells during cycling. Electrode growth, due to growth of a porous lithium layer between the separator and the lithium substrate, was related to electrolyte, stack pressure, charge and discharge current density, and thermal stability. The authors promote the use of the apparatus as a powerful technique to optimise cell design and chemistry.

Odziemkowski *et al.*²¹⁶ utilised in-situ and ex-situ Raman microspectroscopy to study the lithium | electrolyte interface. A specially designed cell was used to allow in-situ cutting of

the lithium electrode. The surface film formed, in the THF and 2Me-THF solutions of LiAsF_6 , was found to be Raman laser, moisture and air sensitive. An electrochemical study using potentiodynamic polarisation measurements in the same cell permitted ranking of electrolyte reactivity by corrosion potential-time transients.²²¹

1.6 Summary:

Li metal has been extensively studied for application as a rechargeable battery electrode. Recent research has focussed mainly on polymer electrolytes and large-scale commercial lithium metal polymer (LMP) batteries have been developed. Polymer electrolytes have been studied for use with a lithium metal electrode because of perceived advantages over aprotic liquid electrolytes, particularly with respect to safety, and because of an observed tendency for dendrite suppression.

The development of air and moisture stable RTILs has led to renewed interest in their behaviour as lithium battery electrolytes. RTILs are perceived to offer similar safety advantages to polymers, and research into their application as plasticisers for gelled electrolytes has been reported.^{138,222} However, by comparison with 'traditional' lithium battery electrolyte solvents (i.e., aprotic liquids and polymers), there is a distinct lack of information relating to the behaviour of the lithium | electrolyte interface, particularly SEI formation and deposit morphology, and their cycling behaviour in general.

1.7 Aims:

This thesis will detail the development of techniques to study the morphological evolution of the cycled lithium surface in RTILs. Specifically through the development of an optical cell, its use to survey a number of RTILs and the identification of a candidate RTIL for use as an electrolyte solvent in lithium metal batteries.

The development of techniques to characterise the lithium surface in contact with the candidate electrolyte and the results thereof will be reported. Similarly, important properties of the electrolyte will be characterised and presented.

Finally, the results of a study to characterise lithium cycling behaviour of the candidate electrolyte will be presented, along with the cycling behaviour of some prototype rechargeable lithium metal ionic liquid (LMIL) cells.

References

1. F. Birol, Web Page, *World energy outlook 2000* (Available: <http://www.worldenergyoutlook.org/weo/pubs/weo2000/weo2000.pdf>) Accessed 13 June 2003.
2. N. Lior, *Energy Conversion and Management*, **42**, 1769 (2001).
3. F. Birol, Web Page, *World energy outlook 2002* (Available: <http://www.worldenergyoutlook.org/weo/papers/Weoc02.pdf>) Accessed 13 June 2003.
4. S. Yoda and K. Ishihara, *J. Power Sources*, **81-82**, 162 (1999).
5. G. T. T. Molitor, *Technological Forecasting and Social Change*, **70**, 473 (2003).
6. R. M. Dell and D. A. J. Rand, *J. Power Sources*, **100**, 2 (2001).
7. B. Scrosati, *J. Power Sources*, **116**, 4 (2003).
8. P. R. Birkin, E. Eweka and J. R. Owen, *J. Power Sources*, **81**, 833 (1999).
9. S. Basu, *J. Power Sources*, **81**, 200 (1999).
10. F. Orsini, A. Du Pasquier, B. Beaudoin, J. M. Tarascon, M. Trentin, N. Langenhuisen, E. De Beer and P. Notten, *J. Power Sources*, **76**, 19 (1998).
11. J. R. Owen, *Chem. Soc. Rev.*, **26**, 259 (1997).
12. J. A. Ober, *Lithium, mineral commodity survey. U.S. Geological survey 2003*, U.S. Geological Survey Publications, 2003.
13. J. A. Ober, *U.S. Geological Survey Minerals Yearbook, Lithium*, U.S. Geological Survey Publications, 2001.
14. J.-Y. Sanchez, F. Alloin and C. Poinsignon, *Mol. Cryst. Liq. Cryst. Sci. Technol., Sect. A*, **324**, 257 (1998).
15. D. H. Doughty, *SAMPE J.*, **32**, 75 (1996).
16. B. Scrosati, *Chim. Ind. (Milan)*, **79**, 463 (1997).
17. G. Campet, *Bull. Korean Chem. Soc.*, **20**, 885 (1999).
18. B. Scrosati, in *Lithium Ion Batteries*, Eds M. Wakihara and O. Yamamoto (Wiley-VCH, Tokyo, Japan., 1998), p. 218.
19. P. G. Bruce, *Chem. Commun. (Cambridge)*, (19) 1817 (1997).
20. B. Scrosati, *Electrochim. Acta*, **45**, 2461 (2000).
21. J.-I. Yamaki and S.-I. Tobishima, *Handb. Battery Mater.* J. O. Besenhard, Editor p. 339, Wiley-VCH, Weinheim (1999).
22. V. S. Bagotzky and A. M. Skundin, *Russ. J. Electrochem.*, **34**, 654 (1998).
23. B. B. Owens and T. Osaka, *J. Power Sources*, **68**, 173 (1997).
24. Y. S. Fung, *Trends Inorg. Chem.*, **5**, 117 (1998).
25. S. C. Levy, *J. Power Sources*, **68**, 75 (1997).
26. J. A. Banner and C. S. Winchester, *J. Power Sources*, **65**, 271 (1997).
27. G. E. Blomgren, *J. Power Sources*, **81**, 112 (1999).
28. N. Munichandraiah, L. G. Scanlon and R. A. Marsh, *J. Power Sources*, **72**, 203 (1998).
29. A. Cisak and L. Werblan, *High-Energy Non-Aqueous Batteries*, Ellis Horwood Limited, West Sussex,

- England (1993).
30. F. B. Dias, L. Plomp and J. B. J. Veldhuis, *J. Power Sources*, **88**, 169 (2000).
 31. G. Nagasubramanian and D. Boone, *Int. SAMPE Tech. Conf.*, **27**, 795 (1995).
 32. V. Chandrasekhar, *Adv. Polym. Sci.*, **135**, 139 (1998).
 33. G. B. Appetecchi, F. Croce and B. Scrosati, *J. Power Sources*, **66**, 77 (1997).
 34. G. B. Appetecchi, G. Dautzenberg and B. Scrosati, *J. Electrochem. Soc.*, **143**, 6 (1996).
 35. Z. Jiang, B. Carroll and K. M. Abraham, *Electrochim. Acta*, **42**, 2667 (1997).
 36. A. J. Bard and L. R. Faulkner, *Electrochemical Methods, Fundamentals and Applications*, John Wiley and Sons, New York (1980).
 37. J. O. Bockris and A. K. N. Reddy, *Modern Electrochemistry, Vol. 1 & 2*, Plenum Publishing corporation, New York (1973).
 38. E. Quartarone, P. Mustarelli and A. Magistris, *Solid State Ionics*, **110**, 1 (1998).
 39. T. Kudo, in *CRC Handb. Solid State Electrochem.*, Eds. P. J. Gellings and H. J. M. Bouwmeester (CRC Press, Inc., Boca Raton, Fla., 1997), p. 195.
 40. D. Aurbach (ed.), *Nonaqueous Electrochemistry*, Marcel Dekker, New York (1999).
 41. J. O. Besenhard (ed.), *Handbook of Battery Materials*, Wiley-VCH, Weinheim (1999).
 42. M. C. Borghini, M. Mastragostino, S. Passerini and B. Scrosati, *J. Electrochem. Soc.*, **142**, 2118 (1995).
 43. S. V. Sazhin, M. Yu. Khimchenko, Y. N. Trittenchenko, W. Roh and H. Y. Kang, *J. Power Sources*, **66**, 141 (1997).
 44. N. Ogata, in *Funct. Monomers Polym. (2nd Ed.)*, Eds K. Takemoto, R. M. Ottenbrite, and M. Kamachi (Dekker, New York, N. Y., 1997), p. 387.
 45. M. Broussely, S. Herreyre, P. Biensan, P. Kaszlejna, K. Nechev and R. J. Staniewicz, *J. Power Sources*, **97-98**, 13 (2001).
 46. A. M. Andersson and K. Edstrom, *J. Electrochem. Soc.*, **148**, A1100-A1109 (2001).
 47. J. S. Gnanaraj, M. D. Levi, Y. Gofei, D. Aurbach and M. Schmidt, *J. Electrochem. Soc.*, **150**, A445-A454 (2003).
 48. L. J. Krause, W. Lamanna, J. Summerfield, M. Engle, G. Korba, R. Loch and R. Atanasoski, *J. Power Sources*, **68**, 320 (1997).
 49. H. Yang, K. Kwon, T. M. Devine and J. W. Evans, *J. Electrochem. Soc.*, **147**, 4399 (2000).
 50. M. Morita, T. Shibata, N. Yoshimoto and M. Ishikawa, *J. Power Sources*, **119-121**, 784 (2003).
 51. M. Schmidt, U. Heider, A. Kuehner, R. Oesten, M. Jungnitz, N. Ignat'ev and P. Sartori, *J. Power Sources*, **97-98**, 557 (2001).
 52. Y.-G. Chen, C.-G. Wang, X.-Y. Zhang, D.-M. Xie and R.-S. Wang, *Synth. Met.*, **135-136**, 225 (2003).
 53. T. J. Barbarich and P. F. Driscoll, *Electrochemical and Solid State Letters*, **6**, A113-A116 (2003).
 54. H. Yamaguchi, H. Takahashi, M. Kato and J. Arai, *J. Electrochem. Soc.*, **150**, p A312-A315 (2003).
 55. H. Tokuda and M. Watanabe, *Electrochim. Acta*, **48**, 2085 (2003).
 56. W. Xu and C. A. Angell, *Electrochemical and Solid-State Letters*, **4**, p E1-E4 (2001).
 57. K. Xu, S. S. Zhang, T. R. Jow, W. Xu and C. A. Angell, *Electrochemical and Solid State Letters*, **5**, A26-A29 (2002).
 58. K. Xu, S. Zhang, B. A. Poese and T. R. Jow, *Electrochemical and Solid-State Letters*, **5**, p A259-A262 (2002).
 59. J. Barthel and H. J. Clores, *Chem. Nonaqueous Solutions, 1-148*. Edited by: Mumantov, Gileh; Popov, Alexander I. VCH: New York, N. Y. (English) 1994.
 60. K. Murata, S. Izuchi and Y. Yoshikisa, *Electrochim. Acta*, **45**, 1501 (2000).
 61. W. A. Henderson and S. Passerini, *Electrochemistry Communications*, **3**, 575 (2003).
 62. Marie de Loppinot, Web Page, *Avestor: World leader in lithium-metal-polymer batteries* (Available: <http://www.avestor.com/home.ch2>, 2002) Accessed 16 July 2003.
 63. M. Gauthier, A. Bélanger, P. Bouchard, B. Kapfer, S. Ricard, G. Vassort, M. Armand, J. Y. Sanchez and L. Krause, *J. Power Sources*, **54**, 163 (1995).
 64. P. Haudry, S. Lascaud, H. Majastre and D. Bloch, *J. Power Sources*, **68**, 412 (1997).
 65. J. Y. Sanchez, F. Alloin, D. Benrabah and C. Roux, *Macromol. Symp.*, **114**, 85 (1997).
 66. M. C. Borghini, M. Mastragostino and A. Zanelli, *J. Power Sources*, **68**, 52 (1997).
 67. M. C. Borghini, M. Mastragostino and A. Zanelli, *Electrochim. Acta*, **41**, 2369 (1996).
 68. C. A. Angell, C. Liu and E. Sanchez, *Nature (London)*, **362**, 137 (1993).
 69. C. A. Angell, *Molten Salt Forum*, **5-6**, 39 (1998).
 70. A. Ferry, L. Edman, M. Forsyth, D. R. MacFarlane and J. Sun, *Electrochim. Acta*, **45**, 1237 (2000).
 71. M. Forsyth, S. Jiazeng and D. R. MacFarlane, *Electrochim. Acta*, **45**, 1249 (2000).
 72. P. Mustarelli, E. Quartarone, C. Capiglia, C. Tomasi and A. Magistris, *Solid State Ionics*, **122**, 285 (1999).
 73. T. Tatsuma, M. Taguchi, M. Iwaku, T. Sotomura and N. Oyama, *J. Electroanal. Chem.*, **472**, 142 (1999).
 74. B. Scrosati, *Polym. Int.*, **47**, 50 (1998).
 75. C. Capiglia, P. Mustarelli, E. Quartarone, C. Tomasi and A. Magistris, *Solid State Ionics*, **118**, 73 (1999).
 76. J. Travas-Sejdic, R. Steiner, J. Deslvestro and P. Pickering, *Electrochim. Acta*, **46**, 1461 (2001).
 77. C. Tiyaiboonchaiya, J. M. Pringle, D. R. MacFarlane, M. Forsyth and J. Sun, *Macromolecular Chemistry and Physics*, **204**, 2147 (2003).
 78. C. Tiyaiboonchaiya, J. M. Pringle, J. Sun, N. Byrne, P. C. Howlett, D. R. MacFarlane and M. Forsyth, *Nature Materials*, **3**, 29 (2004).
 79. J. V. Braun and M. Kuhn, *Ber.*, **60B**, 2557 (1927).
 80. N. O. Calloway, *Chem. Rev.*, **17**, 327 (1935).
 81. K. P. Rao, A. S. Bartakke and R. G. K. Nair, *Defence Science Journal*, **37**, 45 (1987).
 82. F. H. Hurley and T. P. Wier, *J. Electrochem. Soc.*, **98**, 203 (1951).
 83. J. S. Wilkes, J. A. Levisky, R. A. Wilson and C. L. Huey, *Performer: Frank J. Seiler Research Lab., United States Air Force Academy, CO. Mar 1982. 2p. Report: FJSRL-JR 82 0008* (1982).
 84. J. Fuller, R. A. Ostryoung and R. T. Carlin, *J. Electrochem. Soc.*, **142**, 3632 (1995).
 85. B. J. Pierana, D. M. Ryan, E. R. Schumacher and T. L. Riechel, *J. Electrochem. Soc.*, **143**, 908

- (1996).
86. B. J. Piersma, *Proc. - Electrochem. Soc.*, **94-13**, 415 (1994).
 87. J. Fuller, R. T. Carlin and R. A. Osteryoung, *J. Electrochem. Soc.*, **143**, L145-L147 (1996).
 88. Y. S. Fung and R. Q. Zhou, *J. Power Sources*, **81-82**, 891 (1999).
 89. Y. S. Fung and S. M. Chau, *Proc. - Electrochem. Soc.*, **94-13**, 475 (1994).
 90. A. A. Fannin, L. A. King, J. A. Levisky and J. S. Wilkes, *Performer: Frank J. Seiler Research Lab., United States Air Force Academy, CO. 7 Jun 1984, 7p. Report: FJSRL-JR-84-0003*.
 91. A. M. Elias and J. S. Wilkes, *J. Chem. Eng. Data*, **39**, 79 (1994).
 92. M. A. M. Noel and R. A. Osteryoung, *Journal of Electroanalytical Chemistry*, **293**, 139 (1990).
 93. T. J. Melton, J. Joyce, J. T. Maloy, J. A. Boon and J. S. Wilkes, *J. Electrochem. Soc.*, **137**, 3865 (1990).
 94. J. S. Wilkes and M. J. Zaworotko, *Chem. Comm.*, **13**, 965 (1992).
 95. P. Bonhote, A. P. Dias, N. Papageorgiou, M. Armand, K. Kalyanasundaram and M. Gratzel, *Inorg. Chem.*, **35**, 1168 (1996).
 96. J. D. Holbrey and K. R. Seddon, *Clean Products and Processes*, **1**, 0223 (1999).
 97. Web Page, *Ionic Liquids* (Available: http://www.ionicliquids-merck.de/servlet/PB/menu/1014040_index.html, May 2003) Accessed 23 June 2003.
 98. H. L. Ngo, K. LeCompte, L. Hargens and A. B. McEwen, *Thermochim. Acta*, **357-358**, 97 (2000).
 99. H. Matsumoto, M. Yanagida, K. Tanimoto, M. Nomura, Y. Kitagawa and Y. Miyazaki, *Chem. Lett.*, **(8)** 922 (2000).
 100. D. R. MacFarlane, J. Sun, J. Golding, P. Meakin and M. Forsyth, *Electrochim. Acta*, **45**, 1271 (2000).
 101. J. D. Holbrey, W. M. Reichert, R. P. Swatoski, G. A. Broker, W. R. Pitner, K. R. Seddon and R. D. Rogers, *Green Chemistry*, **4**, 407 (2002).
 102. D. R. MacFarlane, J. Golding, S. Forsyth, M. Forsyth and G. B. Deacon, *Chem. Comm.*, 1430 (2001).
 103. D. R. MacFarlane, P. Meakin, J. Sun, N. Amini and M. Forsyth, *J. Phys. Chem. B*, **103**, 4164 (1999).
 104. D. R. MacFarlane, S. A. Forsyth, J. Golding and G. B. Deacon, *Green Chemistry*, **4**, 444 (2002).
 105. J. Golding, S. Forsyth, D. R. MacFarlane, M. Forsyth and G. B. Deacon, *Green Chemistry*, **4**, 223 (2002).
 106. K. R. Seddon, *J. Chem. Tech. & Biotech.*, **68**, 351 (1997).
 107. C. W. Lee, *Tetrahedron Lett.*, **40**, 2461 (1999).
 108. F. Zulfikar and T. Kitazume, *Green Chemistry*, **2**, 137 (2000).
 109. M. J. Earle, P. H. McCormac and K. R. Seddon, *Green Chemistry*, **1**, 23 (1999).
 110. A. Aggarwal, N. L. Lancaster, A. R. Sethi and T. Welton, *Green Chemistry*, **4**, 517 (2002).
 111. J. S. Yadav, B. V. S. Reddy, J. S. S. Reddy and R. S. Rao, *Tetrahedron*, **59**, 1599 (2003).
 112. J. S. Yadav, B. V. S. Reddy, K. U. Gayathri and A. R. Prasad, *Synthesis* 2537 (2002).
 113. E. Van der Eycken, P. Appukkuttan, W. De Brugghe, W. Dehaen, D. Dallinger and C. O. Kappe, *J. Org. Chem.*, **67**, 7904 (2002).
 114. J. H. Jr. Davis and K. J. Forrester, *Tetrahedron Lett.*, **40**, 1621 (1999).
 115. J. F. Dubreuil and J. P. Barreau, *Tetrahedron Lett.*, **41**, 7351 (2000).

116. M. J. Earle, K. R. Seddon, C. J. Adams and G. Roberts, *Chem. Comm.*, 2097 (1998).
117. A. Stark, B. L. MacLean and R. D. Singer, *J. Chem. Soc., Dalton Trans.*, 63 (1999).
118. W. Keim, D. Vogt, H. Waffenschmidt and P. Wasserscheid, *J. Catal.*, **186**, 481 (1999).
119. P. Wasserscheid, H. Waffenschmidt, P. Machnitzki, K. W. Kottsieper and O. Stelzer, *Chem. Comm.*, 451 (2001).
120. F. Favre, H. Olivier-Bourbigou, D. Commereuc and L. Saussine, *Chem. Comm.*, 1360 (2001).
121. Y. Chauvin and H. Olivier-Bourbigou, *Chemtech*, **25**, 26 (1995).
122. C. J. Mathews, P. J. Smith and T. Welton, *Chem. Comm.*, 1249 (2000).
123. S. M. Silva, P. A. Z. Suarez, R. F. De Souza and J. Dupont, *Polymer Bulletin*, **40**, 401 (1998).
124. S. H. Schofer, N. Kaftzik, U. Kragl and P. Wasserscheid, *Chem. Comm.*, 425 (2001).
125. S. Forsyth, J. Golding, D. R. MacFarlane and M. Forsyth, *Electrochim. Acta*, **46**, 1753 (2001).
126. C. A. Angell, *Molten Salt Forum*, **5-6**, 39 (1998).
127. Y. S. Fung and R. Q. Zhou, *J. Power Sources*, **81-82**, 891 (1999).
128. J. Caja, T. D. J. Dunstan, V. Katovic and D. M. Ryan, *Proc. Power Sources Conf.*, **39th**, 124 (2000).
129. D. R. MacFarlane, J. Sun, J. Golding, P. Meakin and M. Forsyth, *Electrochim. Acta*, **45**, 1271 (2000).
130. S. Forsyth, J. Golding, D. R. MacFarlane and M. Forsyth, *Electrochim. Acta*, **46**, 1753 (2001).
131. J. Golding, N. Hamid, D. R. MacFarlane, M. Forsyth, C. Forsyth, C. Collins and J. Huang, *Chem. Mater.*, **13**, 558 (2001).
132. H. Every, A. G. Bishop, M. Forsyth and D. R. MacFarlane, *Electrochim. Acta*, **45**, 1279 (2000).
133. Y. Katayama, S. Dan, T. Miura and T. Kishi, *J. Electrochem. Soc.*, **148**, C102-C105 (2001).
134. D. R. MacFarlane, J. H. Huang and M. Forsyth, *Nature*, **402**, 792 (1999).
135. J. Caja, T. Don, J. Dunstan, D. Ryan and V. Katovic, *Molten Salts XII, Proceedings*, **99**, 150 (2000).
136. J. Sun, D. R. MacFarlane and M. Forsyth, *Solid State Ionics*, **147**, 333 (2002).
137. M. Egashira, S. Okada and J. Yamaki, *Solid State Ionics*, **148**, 457 (2002).
138. C. Tiyyapiboonchaiya, D. R. MacFarlane, J. Sun and M. Forsyth, *Macromolecular Chemistry and Physics*, **203**, 1906 (2002).
139. U. Schroder, J. D. Wadhawan, R. G. Compton, F. Marken, P. A. Z. Suarez, C. S. Consorti, R. F. De Souza and J. Dupont, *New J. Chem.*, **24**, 1009 (2000).
140. J. Caja and T. Dunstan D J, US6326104-B1 (2001).
141. A. I. Bhatt, I. May, V. A. Volkovich, M. E. Hetherington, B. Lewin, R. C. Thied and N. Ertok, *J. Chem. Soc.*, 4532 (2002).
142. K. Murase, K. Nitta, T. Hirato and Y. Awakura, *J. App. Electrochem.*, **31**, 1089 (2001).
143. D. L. Boxall and R. A. Osteryoung, *J. Electrochem. Soc.*, **149**, E185-E188 (2002).
144. D. R. MacFarlane, P. Meakin, J. Sun, N. Amini and M. Forsyth, *J. Phys. Chem. B*, **103**, 4164 (1999).
145. P. C. Howlett, D. R. MacFarlane and A. F. Hollenkamp, *J. Power Sources*, **114**, 277 (2003).
146. T. Nishida, Y. Tashiro and M. Yamamoto, *J. Fluorine Chem.*, **120**, 135 (2003).
147. J. Huang, M. Forsyth and D. R. MacFarlane, *Solid State Ionics*, **136**, 447 (2000).
148. T. E. Sutto, P. C. Trulove and H. C. De Long, *Electrochemical and Solid-State Letters*, **6**, A50-A52

- (2003).
149. F. Endres, *ChemPhysChem*, **3**, 144 (2002).
 150. N. Nanbu, Y. Sasaki and F. Kitamura, *Electrochemistry Communications*, **5**, 383 (2003).
 151. B. M. Quinn, Z. Ding, R. Moulton and A. J. Bard, *Langmuir*, **18**, 1734 (2002).
 152. D. Zhou, G. M. Spinks, G. G. Wallace, C. Tiyaipoonchaiya, D. R. MacFarlane, M. Forsyth and J. Sun, *Electrochim. Acta*, **48**, 2355 (2003).
 153. H. Matsumoto, M. Yanagida, K. Tanimoto, M. Nomura, Y. Kitagawa and Y. Miyazaki, *Chem. Lett.*, (8) 922 (2000).
 154. H. Sakaebe and H. Matsumoto, *Electrochemistry Communications*, **5**, 594 (2003).
 155. Y. S. Fung, *Trends Inorg. Chem.*, **5**, 117 (1998).
 156. H. Matsumoto and Y. Miyazaki, *Yoyuen Oyobi Koon Kagaku*, **44**, 7 (2001).
 157. T. Sato, G. Masuda, R. Nodu and T. Maruo, WO200276924-A; WO200276924-A1 (03 Oct 2002) (2002).
 158. V. Koch R, C. Nanjundiah and R. Carlin T, WO9702252-A; EP839139-A; WO9702252-A1 (23 Jan 1997); EP839139-A1 (06 May 1998); JP2001517205-W (02 Oct 2001) (2001).
 159. A. McEwen, WO200103211-A; FR2795725-A1 (05 Jan 2001); WO200103211-A1 (11 Jan 2001) (2001).
 160. A. McEwen B, Y. Ein-Eli and E. Yair, WO9908299-A; EP1027713-A; WO9908299-A1 (18 Feb 1999); US5965054-A (12 Oct 1999); EP1027713-A1 (16 Aug 2000); JP2001512903-W (28 Aug 2001) (2001).
 161. T. L. Riechel and J. S. Wilkes, *J. Electrochem. Soc.*, **139**, 977 (1992).
 162. N. Koura, K. Iizuka, Y. Idemoto and K. Ui, *Electrochemistry (Tokyo)*, **67**, 706 (1999).
 163. V. R. Koch, C. Nanjundiah, G. B. Appetecchi and B. Scrosati, *J. Electrochem. Soc.*, **142**, L116-L118 (1995).
 164. F. Alloin, B. Baradie, D. Benrabah, C. Roux, and J-Y. Sanchez, in *Solid State Ionics*, [Proc. Asian Conf.], Eds B. V. R. Chowdari, M. A. K. L. Dissanayake, and M. A. Careem (World Scientific, Singapore, Singapore), **5**, 189 (1996).
 165. J. Fuller, R. T. Carlin and R. A. Osteryoung, *J. Electrochem. Soc.*, **144**, 3881 (1997).
 166. , Molten Salts XII, Proceedings, (2000).
 167. J. Caja, T. D. J. Dunstan, V. Katovic and D. M. Ryan, *Proc. Power Sources Conf.*, **39th**, 124 (2000).
 168. D. Aurbach, *J. Electrochem. Soc.*, **136**, 1611 (1989).
 169. H. Matsumoto and Y. Miyazaki, *Yoyuen Oyobi Koon Kagaku*, **44**, 7 (2001).
 170. A. I. Bhatt, I. May, V. A. Volkovich, M. E. Hetherington, B. Lewin, R. C. Thied and N. Ertok, *J. Chem. Soc.*, 4532 (2002).
 171. M. Egashira, S. Okada and J. Yamaki, *Solid State Ionics*, **148**, 457 (2002).
 172. B. M. Quinn, Z. Ding, R. Moulton and A. J. Bard, *Langmuir*, **18**, 1734 (2002).
 173. T. Sato, G. Masuda, R. Nodu and T. Maruo, WO200276924-A; WO200276924-A1 (03 Oct 2002) (2002).
 174. T. E. Sutto, P. C. Trulove and H. C. De Long, *Electrochemical and Solid-State Letters*, **6**, p A50-A52

- (2003).
175. Y. Katayama, M. Yukumoto and T. Miura, *Electrochemical and Solid State Letters*, **6**, A96-A97 (2003).
 176. H. Nakagawa, S. Izucni, K. Kuwana, T. Nukuda and Y. Aihara, *J. Electrochem. Soc.*, **150**, A695-A700 (2003).
 177. H. Sakaebe and H. Matsumoto, *Electrochemistry Communications*, **5**, 594 (2003).
 178. B. R. ed. Sundheim, *Fused Salts*, McGraw-Hill Book Company, New York (1964).
 179. S. ed. Petrucci, *Ionic Interactions: From Dilute Solutions to Fused Salts*, Academic Press, New York and London (1971).
 180. J. O. Bockris and Reddy Amulya K. N., *Modern Electrochemistry I: Ionics*, Plenum Press, New York (1998).
 181. H. A. Levy, P. A. Agron, M. A. Bredig and M. D. Danford, *Ann. N. Y. Acad. Sci.*, **79**, 762 (1960).
 182. B. E. Conway, J. O. Bockris and E. Yeager, *Comprehensive Treatise of Electrochemistry: Volume 5 Thermodynamic and Transport Properties of Aqueous and Molten Electrolytes*, Plenum Press, New York (1983).
 183. E. Peled, *J. Electrochem. Soc.*, **126**, 2047 (1979).
 184. E. Peled, D. Golodnitsky and G. Ardel, *J. Electrochem. Soc.*, **144**, L208-L210 (1997).
 185. E. Peled, D. Golodnitsky, and J. Penciner, in *Handb. Battery Mater.* Ed J. O. Besenhard (Wiley-VCH, Weinheim, Germany, 1999), p. 419.
 186. K. Morigaki and A. Ohta, *J. Power Sources*, **76**, 159 (1998).
 187. K. Kanamura, H. Tamura, S. Shiraishi and Z.-I. Takehara, *Electrochim. Acta*, **40**, 913 (1995).
 188. K. Kanamura, H. Tamura and Z. Takehara, *J. Electroanal. Chem.*, **333**, 127 (1992).
 189. J. G. Thevenin and R. H. Muller, *J. Electrochem. Soc.*, **134**, 273 (1987).
 190. E. Peled, D. Golodnitsky, G. Ardel and V. Eshkenazy, *Electrochim. Acta*, **40**, 2197 (1995).
 191. I. Yoshimatsu, T. Hirai and J. Yamaki, *J. Electrochem. Soc.*, **135**, 2422 (1988).
 192. J. Yamaki, S. Tobishima, K. Hayashi, S. Keiichi, Y. Nemoto and M. Arakawa, *J. Power Sources*, **74**, 219 (1998).
 193. C. Brissot, M. Rosso, J.-N. Chazalviel, P. Baudry and S. Lascaud, *Electrochim. Acta*, **43**, 1569 (1998).
 194. C. Brissot, M. Rosso, J.-N. Chazalviel and S. Lascaud, *J. Power Sources*, **81**, 925 (1999).
 195. M. Rosso, J. N. Chazalviel, V. Fleury and E. Chassaing, *Electrochim. Acta*, **39**, 507 (1994).
 196. M. Arakawa, S. Tobishima, Y. Nemoto, M. Ichimura and J. Yamaki, *J. Power Sources*, **43**, 27 (1993).
 197. D. Aurbach, I. Weissman, H. Yamin and E. Elster, *J. Electrochem. Soc.*, **145**, 1421 (1998).
 198. M. Alamgir and K. M. Abraham, US 5536599 (1996).
 199. Y. Choquette, M. Armand, M. Simoneau, R. Gagnon and A. Belanger, US 5798191 (1998).
 200. K. Kanamura, S. Shiraishi and Z. Takehara, *J. Electrochem. Soc.*, **141**, L108-L110 (1994).
 201. S. Koike, T. Fujieda, N. Wakabayashi and S. Higuchi, *J. Power Sources*, **68**, 480 (1997).
 202. D. Aurbach, *J. Power Sources*, **89**, 206 (2000).
 203. T. Hirai, I. Yoshimatsu and J. Yamaki, *J. Electrochem. Soc.*, **141**, 611 (1994).
 204. D. P. Wilkinson and D. Wainwright, *J. Electroanal. Chem.*, **355**, 193 (1993).

205. M. Arakawa, Y. Nemoto, S. Tobishima, M. Ichimura and J. Yamaki, *J. Power Sources*, **44**, 517 (1993).
206. J. Yoon, IL119031-A; US5632784-A (27 May 1997); EP824278-A1 (18 Feb 1998); JP10079255-A (24 Mar 1998) (1999).
207. O. C. Wagner, US 4736150 (1988).
208. H. Koichiro, N. Kazuhiro and T. Koichi, JP07263031-A (1995).
209. K. I. Popov, M. G. Pavlovic and G. Z. Removic, *J. Appl. Electrochem.*, **21**, 743 (1991).
210. B. J. Neudecker, N. J. Dudney and J. B. Bates, *J. Electrochem. Soc.*, **147**, 517 (2000).
211. T. A. Skotheim, US 5648187 (1997).
212. T. A. Skotheim, G. L. Soloveichik and A. B. Gavrilov, US 5961672 (1999).
213. G. Hong and E. S. Takeuchi, *J. Power Sources*, **62**, 45 (1996).
214. Z. Takehara, O. Zempachi, Y. Uchimoto, K. Yasuda and H. Yoshida, *J. Power Sources*, **43-44**, 377 (1993).
215. F. Kong and F. McLarnon, *J. Power Sources*, **89**, 180 (2000).
216. M. Odziemkowski, M. Krell and D. E. Irish, *J. Electrochem. Soc.*, **139**, 3052 (1992).
217. D. Aurbach, *J. Electrochem. Soc.*, **136**, 1606 (1989).
218. G. L. M. K. S. Kahanda and M. Tomkiewicz, *J. Electrochem. Soc.*, **136**, 1497 (1989).
219. D. Aurbach, M. L. Daroux, P. W. Faguy and E. Yeager, *J. Electrochem. Soc.*, **134**, 1611 (1987).
220. K. Wang, G. S. Chottiner and D. A. Scherson, *J. Phys. Chem.*, **97**, 11075 (1993).
221. M. Odziemkowski and D. E. Irish, *J. Electrochem. Soc.*, **139**, 3063 (1992).
222. J. Sun, D. R. MacFarlane and M. Forsyth, *Solid State Ionics*, **147**, 333 (2002).

Experimental

2.1 Materials and preparation:

2.1.1 Glovebox:

The majority of the work presented here was carried out in an argon filled glovebox. The glovebox was manufactured in the Monash University Department of Chemistry workshop. All material was admitted through an antechamber, which was evacuated and refilled three times with high purity Argon (BOC gases). The glovebox atmosphere was maintained by pumping the atmosphere through a series of columns containing A4 molecular sieves and BASF copper catalyst R3 - 11G. Finally, the exhaust from the columns was passed over brushed lithium. In this manner contaminant CO₂, O₂ and N₂ were sequestered. Atmosphere purity was monitored by observing the condition of a freshly brushed piece of lithium metal. A change in appearance of the metal surface prompted action to search for leaks, and to reactivate the sieves and/or catalyst. The molecular sieves were reactivated monthly by passing dry nitrogen through the column at ~250 °C. The copper catalyst was reactivated by passing hydrogen gas through the column at ~300 °C. The completion of both procedures was indicated by the cessation of water condensation at the base of the column.

2.1.2 Lithium metal:

Lithium metal foil (Aldrich 99.9 %) of thickness 180 µm was used throughout the course of the project. At all times the foil was prepared as follows. In the glovebox, a piece of foil of appropriate dimensions was cut using scissors. The foil was blotted dry with a tissue (Kimwipe) to remove excess paraffin and then washed, twice, in hexane (dried over A4 molecular sieves). Using a polyethylene brush, the surface was roughened to remove the native surface film and washed again in hexane to form a 'glovebox' surface film.

2.1.3 Positive electrode materials:

The positive electrode foils, supplied by Pacific Lithium (NZ) Limited and by the Technical University of Delft (Netherlands) were dried at 50 °C under dynamic vacuum for greater than 24 hours.

Foils were also prepared in-house. The active material (AM), either LiCoO_2 (Pacific Lithium – NZ) or LiMn_2O_4 (TU Delft) was used as received. The electrode coating was prepared by weighing the components in the following ratios;– AM – 80%, Graphite (KS_4) – 7%, Carbon Black – 3%, PVdF – 10%. The solid components were mixed in a mortar and pestle and a quantity of dimethylacetamide (DMAc ~130%) was added slowly with mixing to form a slurry. The slurry was transferred to a beaker and heated (low heat) with constant stirring until the mixture had reached the correct consistency. The correct consistency was indicated when the mixture was thick enough to cling to the stirrer in large droplets, but not separate into liquid and solid phases. The consistency could be likened to 'wet mud'. The slurry was then applied to the current collector (aluminium or platinum) using the doctor blade technique. The resulting coated foil was then dried at 60 °C for several hours prior to drying under vacuum at 60 °C for greater than 24 hours.

2.1.4 Separators:

All separator materials used in the project were dried at 50 - 70 °C under dynamic vacuum for greater than 24 hours. In the case of glass-fibre mats and micro-porous polyethylene the separators were cut using a 20 mm hole punch and washed sequentially in boiling water, acetone and cyclohexane prior to drying.

2.1.5 Electrolytes:

Propylene Carbonate / LiPF_6 – The propylene carbonate was distilled at reduced pressure over sodium wire and stored in the glovebox. LiPF_6 (dried under vacuum at 90 °C for greater than 24 hours) was made up to 1 M concentration and allowed to dissolve at 50 °C.

2.1.6 Room temperature ionic liquids (RTILs):

The room temperature ionic liquids used in this study were prepared in our laboratories according to the scheme described previously (Section 1.4.5). Following synthesis, the RTILs were characterised by IR spectroscopy, ^1H and ^{13}C NMR spectroscopy and electrospray mass spectroscopy. Thermal properties and purity were also determined by DSC and TGA. Details of the synthesis and typical analysis results for each of the RTILs used in this work are provided in the references listed in Table 2.1.

Nomenclature

Typically, the RTIL names are abbreviated for convenience. At present, no IUPAC convention for the abbreviations exists. However, a general convention for naming the most common RTILs has developed in the literature. The abbreviations used in this work are listed below;

Cations:

- 1-ethyl-3-methylimidazolium – EMI^+
- 1-butyl-3-methylimidazolium – BMI^+
- *N*-methyl-*N*-alkylpyrrolidinium – $\text{P}_{1\text{X}}^+$ (X refers to different alkyl substituents, i.e., ethyl, propyl, butyl)
- *N*-methyl-*N*-alkylpiperidinium – $\text{PP}_{1\text{X}}^+$ (X refers to different alkyl substituents, i.e., ethyl, propyl, butyl)

Anions:

- iodide – I^-
- tetrafluoroborate – BF_4^-
- dicyanamide – DCA^-
- bis(trifluorosulfonyl)amide – $(\text{TF})_2\text{N}^-$

Electrolytes

The neat RTILs were dried in a vacuum oven at 90 °C for over 24 hours. The liquid was then degassed overnight with a stream of dried argon to remove additional water and dissolved gases. Electrolytes were prepared by adding the required amount of the dried lithium salt of the anion (e.g., $\text{Li}(\text{TF})_2\text{N}$ to $\text{P}_{13}(\text{TF})_2\text{N}$) to give a concentration (molality) in mol (lithium salt) per kg (solution). The salt was allowed to dissolve at 50 °C overnight. For simplicity, the solutions are referred to in terms of the concentration of salt in the RTIL solvent, e.g., $0.5 \text{ mol kg}^{-1} \text{ P}_{13}(\text{TF})_2\text{N}$ refers to 0.5 mol of $\text{Li}(\text{TF})_2\text{N}$ per kg of $\text{Li}(\text{TF})_2\text{N}/\text{P}_{13}(\text{TF})_2\text{N}$ solution. This convention is followed unless a salt other than that of the RTIL anion is added, in which case the type of salt is stated.

Table 2.1 References synthesis and analysis of RTILs used in this work.

RTIL	Reference
EMIBF ₄	1
EMI(TF) ₂ N	2
EMIDCA	3,4
BMII	2
P ₁₄ DCA	3,4
P ₁₃ BF ₄	5
P ₁₂ , P ₁₃ , and P ₁₄ (TF) ₂ N	6,7

2.1.7 Additives:

Generally, a limited amount of ionic liquid was available, making it necessary in most cases to first dissolve (or form a suspension of) the additive in another solvent at low concentration prior to addition to the ionic liquid. The solvent was then evaporated at low temperature and finally removed under vacuum at 90 °C.

Polyvinylpyrrolidone (PVP) – A solution of 0.30 wt% PVP in acetonitrile (ACN) was prepared in a volumetric flask. Sufficient PVP/ACN solution was then added to the ionic liquid electrolyte (i.e., IL plus added salt) to form a 0.2 wt% solution of PVP. The

acetonitrile was removed by evaporation. Finally, the solution was dried at 50 °C under dynamic vacuum.

Polyethyleneoxide (PEO) – A solution of 0.31 wt% PEO in acetonitrile (ACN) was prepared in a volumetric flask. Sufficient PEO/ACN solution was then added to the ionic liquid electrolyte to form a 0.2 wt% solution of PEO. The acetonitrile was removed by evaporation. Finally, the solution was dried at 50 °C under dynamic vacuum.

Tetraglyme – A solution of 0.35 wt% tetraglyme in acetonitrile (ACN) was prepared in a volumetric flask. Sufficient tetraglyme/ACN solution was then added to the ionic liquid electrolyte to form a 0.2 wt% solution of tetraglyme. The acetonitrile was removed by evaporation. Finally, the solution was dried at 50 °C under dynamic vacuum.

Magnesium Iodide (Anhydrous) – Ten of the anhydrous MgI_2 beads were weighed and the average weight per bead was determined. A sufficient number of beads were added to the ionic liquid electrolyte to form a solution of approximately 500 ppm Mg^{2+} ions.

Silica (30 nm) – SiO_2 was added directly to the ionic liquid electrolyte to form a 5 wt% mixture. The mixture solidified to form a free standing gel.

LiPF_6 – The required amount of the dried LiPF_6 was added (e.g., LiPF_6 to $\text{P}_{13}(\text{TF})_2\text{N}$) to form a concentration (molality) in mol (lithium salt) per kg (solution) i.e., $0.5 \text{ mol kg}^{-1} \text{ LiPF}_6/\text{P}_{13}(\text{TF})_2\text{N}$.

LiAsF_6 – The required amount of the dried LiAsF_6 was added (e.g., LiAsF_6 to $\text{P}_{13}(\text{TF})_2\text{N}$) to form a concentration (molality) in mol (lithium salt) per kg (solution) i.e., $0.5 \text{ mol kg}^{-1} \text{ LiAsF}_6/\text{P}_{13}(\text{TF})_2\text{N}$.

LiSbF_6 – The required amount of the dried LiSbF_6 was added (e.g., LiSbF_6 to $\text{P}_{13}(\text{TF})_2\text{N}$) to form a concentration (molality) in mol (lithium salt) per kg (solution) i.e., $0.5 \text{ mol kg}^{-1} \text{ LiSbPF}_6/\text{P}_{13}(\text{TF})_2\text{N}$.

2.2 Cells:

2.2.1 Resealable stainless steel 'cup' cells:

The stainless steel cells, used in the project to simulate battery conditions were fabricated from 316 stainless steel and consisted of two half 'cups'. The two halves are separated by a Teflon spacer which also served to seal the cell. Inside the cell, a stainless steel piston on a spring within a polyvinyl chloride sleeve provided stack pressure. See Fig. 2.1.

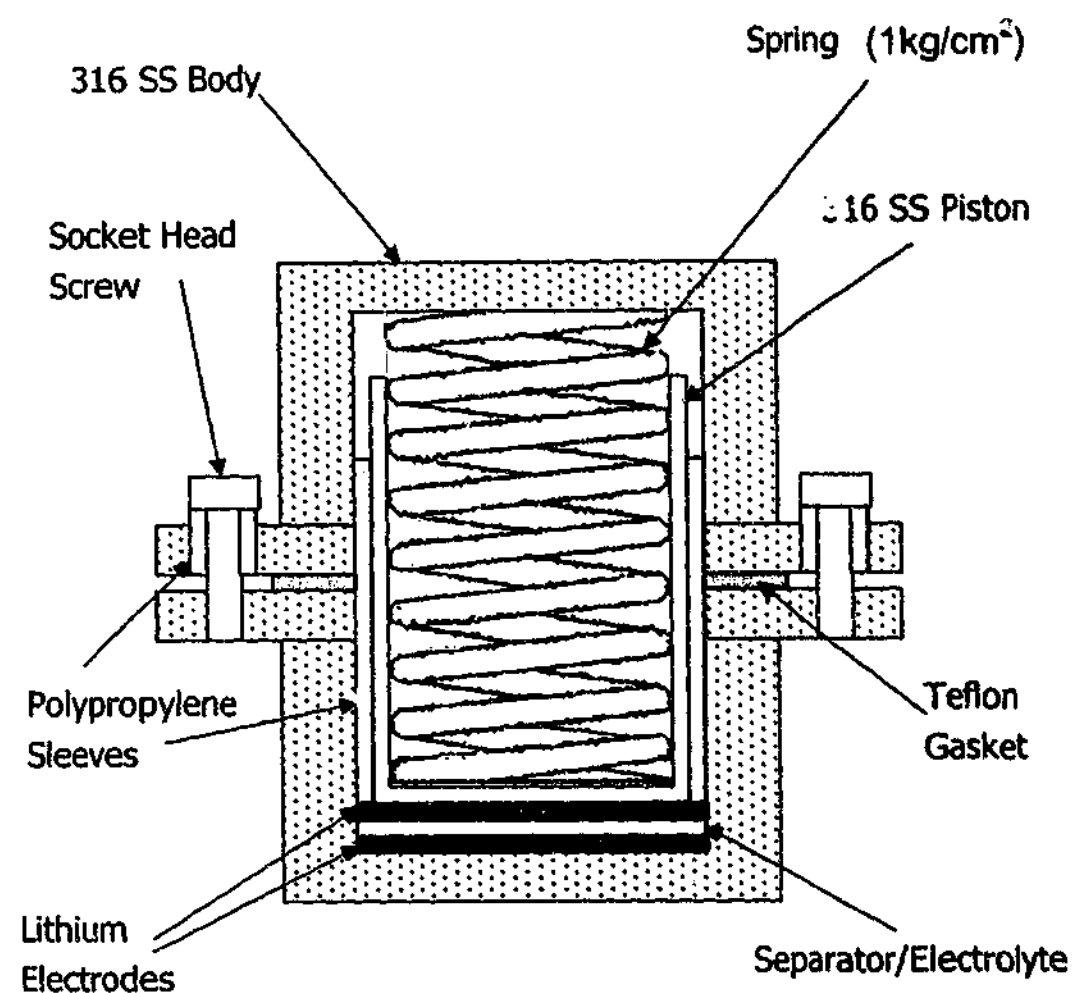


Fig. 2.1 Schematic of the resealable stainless steel 'cup' cell used in the project.

Before use the cells were washed successively in water, acetone and hexane prior to drying under vacuum at $\sim 50^\circ\text{C}$ for greater than 12 hours. Assembly of the cells (e.g., lithium symmetrical or lithium battery) was performed in the glovebox. The electrodes were formed by cutting the material with a 1.6 cm diameter stainless steel punch. Typically the negative electrode (e.g., lithium) was placed on the bottom of the cell. Four or five drops of the electrolyte were dropped onto the surface of the electrode and the separator was placed on top. Next the sleeve was positioned over the electrode and separator such that the electrode was centred in the sleeve and completely covered by the separator. Once the sleeve was in place five or six more drops of electrolyte were added and the 'top' electrode (i.e., lithium or positive electrode material) was dropped into place. Finally the piston, spring and Teflon gasket were fitted in place and the top half of the cell was secured. Once assembled the cell could be removed from the glovebox for study.

2.2.2 Optical cells:

The optical cells used in this study were designed and constructed specifically for the task of studying the evolution of lithium deposit morphology during cycling.

Materials:

Surlyn[®] (DuPont) was used as an adhesive sealant to bind the cell components together; Surlyn[®] is a transparent thermoplastic resin with good chemical resistance properties. Copper shim (Precision Brand; thickness: 0.025 mm) was used as a current-collector. The copper electrode was formed from a piece of electrolytic tough pitch copper 110 (ETP 110 Cu). All cell materials were washed successively in water, acetone and hexane prior to drying under vacuum (50°C) for 24 h. All materials were stored under a dry argon atmosphere in a glovebox.

Construction:

The following description refers to the final method developed to construct the optical cells. Early versions of the cells were quite different from that described here, typically design features were included to reduce the failure rate of the cells.

Construction of the optical cell was performed in a dry argon glovebox. Four pieces of copper current collector were made by cutting copper shim into strips ($4\text{ mm} \times 150\text{ mm}$), these were prepared outside of the glovebox and then washed and dried. Two small pieces of lithium foil ($\sim 2\text{ mm}$ by 25 mm , still wet with paraffin oil) were rolled into a polished stainless steel depression (see Fig. 2.2.a). After each successive roll excess lithium was trimmed from the edges as it filled the cavity. This eventually yielded two foils of uniform thickness of $100\mu\text{m}$ (4 mm wide \times 40 mm long). The resulting foil electrodes were washed in hexane, one was placed in contact with two pieces of copper shim at either end and then pressed in a Teflon lined press to form a single strip of metal (see Fig. 2.2.b). The other was similarly treated except only one piece of copper was used, then the lithium was trimmed and another piece of copper foil was placed so that it formed a juncture of lithium/copper. The copper electrode was formed by soldering a piece of copper foil ($4\text{ mm} \times 20\text{ mm} \times 100\mu\text{m}$) to a piece of the current collector. All of the strips were arranged adjacent to one another and sandwiched between two pieces of Surlyn[®] (approximately, $70\text{ mm} \times 25\text{ mm}$), placed in a Teflon-lined clamp (see Fig 2.2.c), and heated at 140°C for 30 min. After cooling the assembly was cut at the centre of the lithium foil using a double-edged punch (see Fig. 2.2.d), to create three exposed lithium surfaces and a copper surface of area $\sim 0.004\text{ cm}^2$ which were 2 mm apart. Thus one copper, and three sheathed lithium electrode surfaces, facing one another, with what would become an electrolyte cavity in between, were formed. Two more pieces of Surlyn[®] were cut (approximately, $70\text{ mm} \times 25\text{ mm}$) and a hole was cut at the centre similar to the electrode cut except slightly larger ($3\text{--}4\text{ mm} \times 15\text{ mm}$). The assembly was sandwiched between the two extra pieces of Surlyn[®] (so that the holes were lined up) and placed on a glass microscope slide. The additional pieces of Surlyn[®] were used as supports to stop the Surlyn[®] from flowing over the surface of the electrodes and closing off the surface. A borosilicate coverslip was carefully placed on top of the assembly, returned to the Teflon-lined clamp and (under gentle pressure) heated to 100°C for approximately 15 min. Two more pieces of Surlyn[®] and glass were added, to

reinforce the structural integrity of the cell, and the assembly was returned to the clamp at 100°C for 15 min (refer to the schematic shown in Fig. 2.3. a, b, c & d.). After cooling the cavity was filled with electrolyte using a syringe. The cavity was plugged by heating a small piece of Surlyn[®] with a soldering iron. The sealed cell could then be removed from the glovebox for study. Usually after removal from the glovebox the edges of the cell were glued with epoxy resin to ensure a good seal.

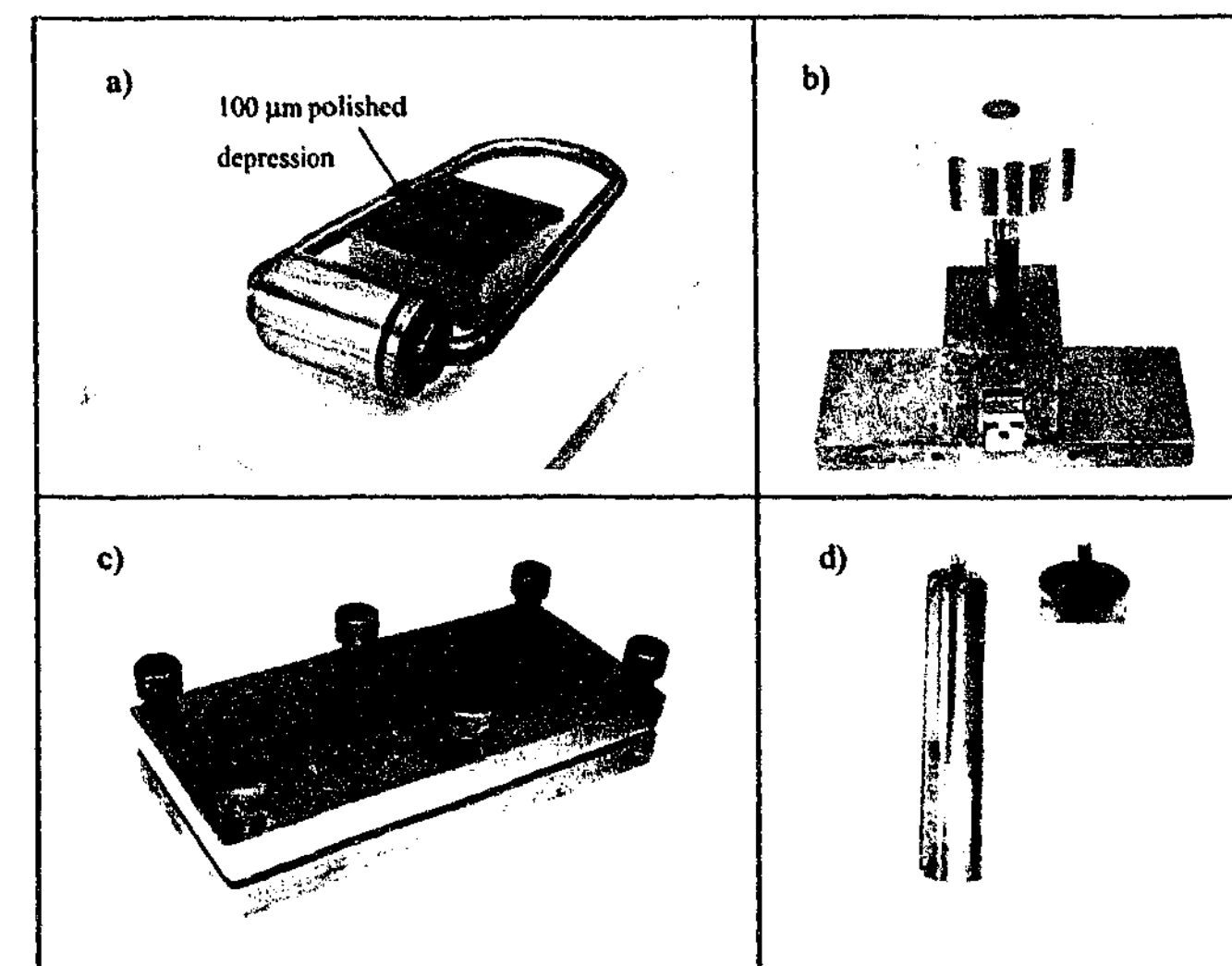


Fig. 2.2 Apparatus used in the fabrication of the optical cells, a) roller and stainless steel block b) Teflon-lined press c) Teflon-lined clamp d) double edged tool-steel punch.

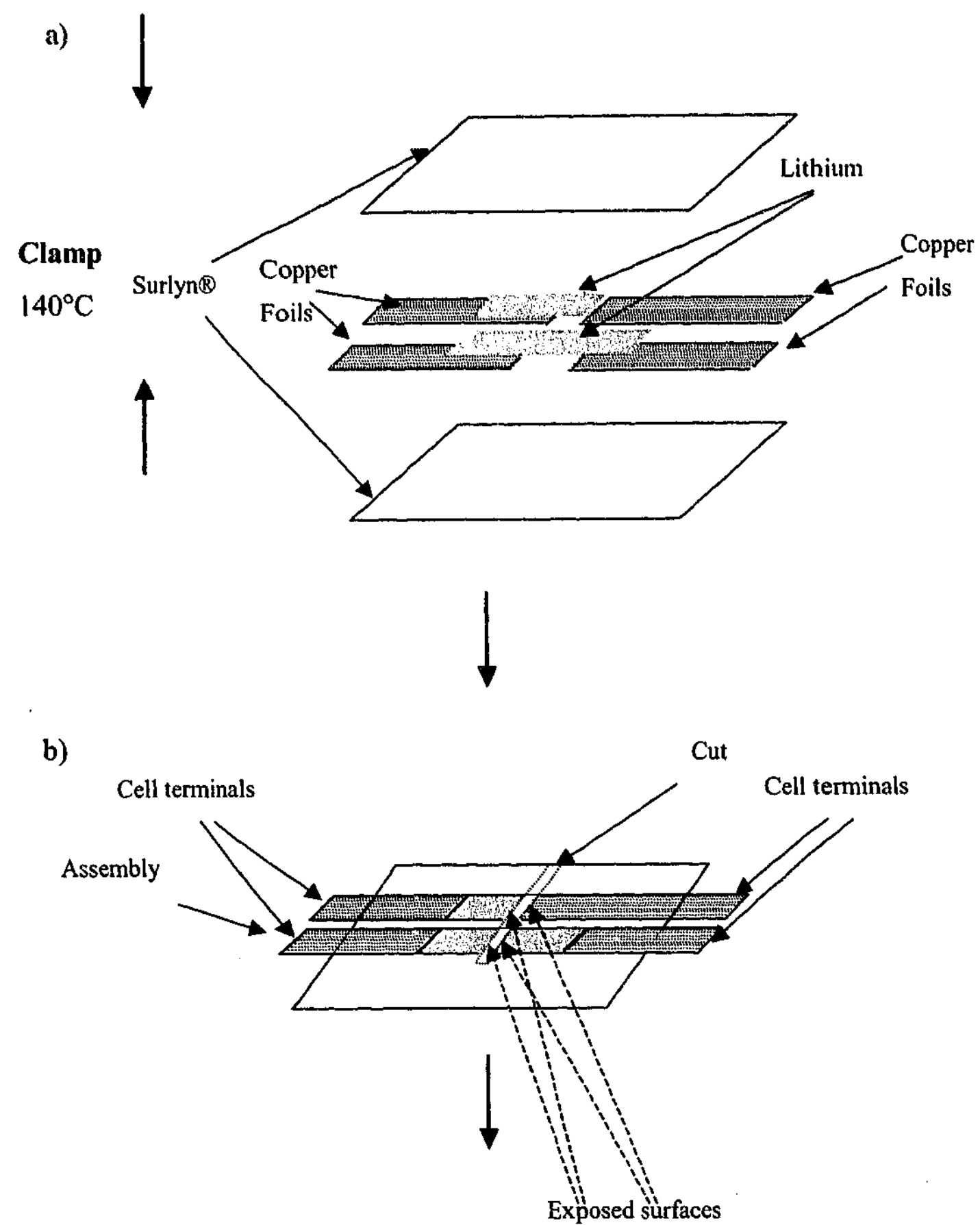


Fig. 2.3 Optical cell schematic, a) & b).

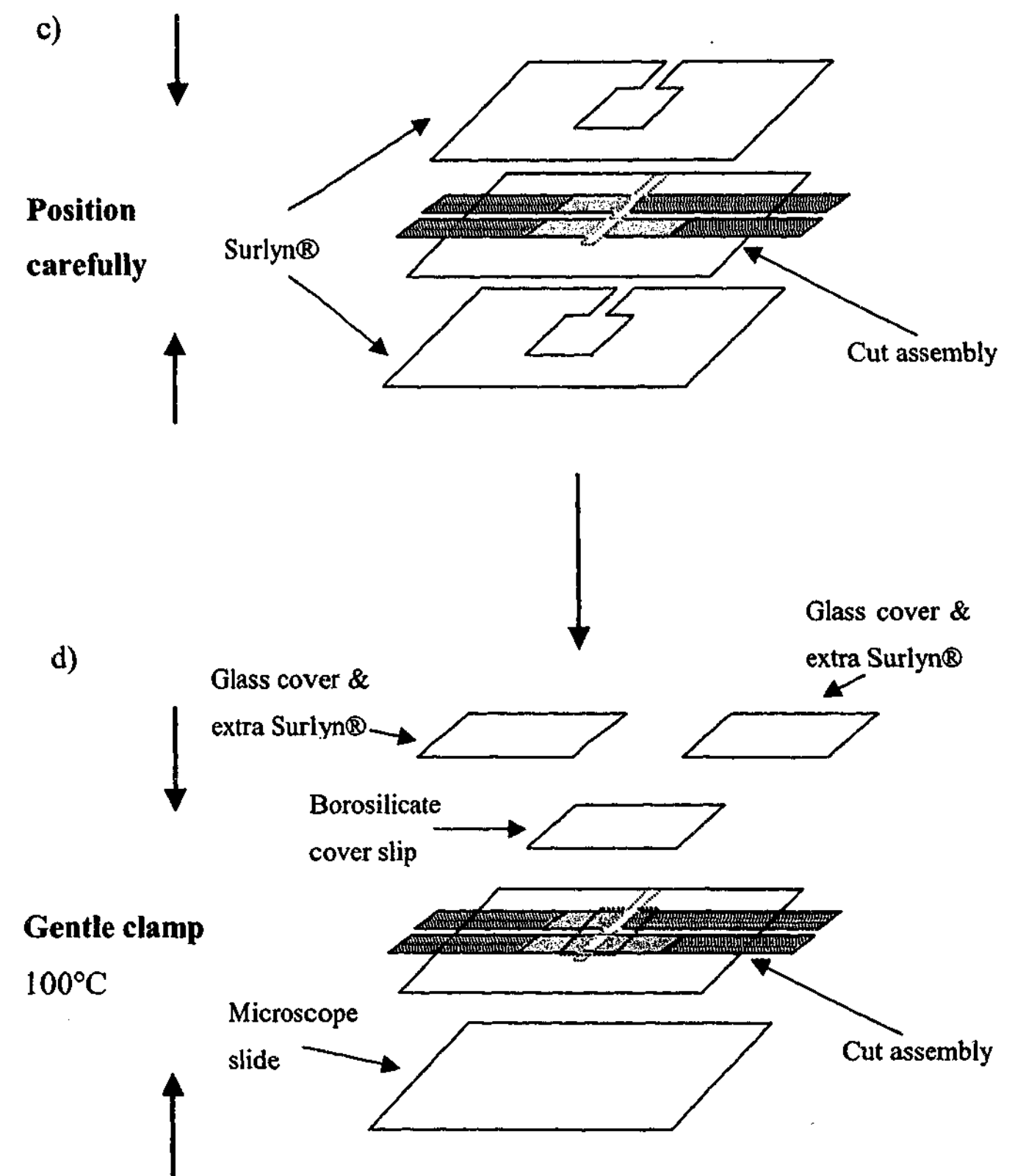


Fig. 2.3 (Cont.) Optical cell schematic, c) & d).

2.2.3 3-electrode cells:

A 3-electrode cell was used in various parts of the project, particularly where accurate knowledge of the working electrode surface area was required. The ionic liquids studied were generally available in small quantities. A specialised electrochemical cell was designed and built to allow experiments using small volumes to be performed in the glovebox. Fig. 2.4 shows an image of the cell apparatus, typically ~0.5 ml of sample was required. Many of the experiments were performed at elevated temperature, the temperature was monitored by inserting a K-type thermocouple into the cell stage adjacent to the cell.

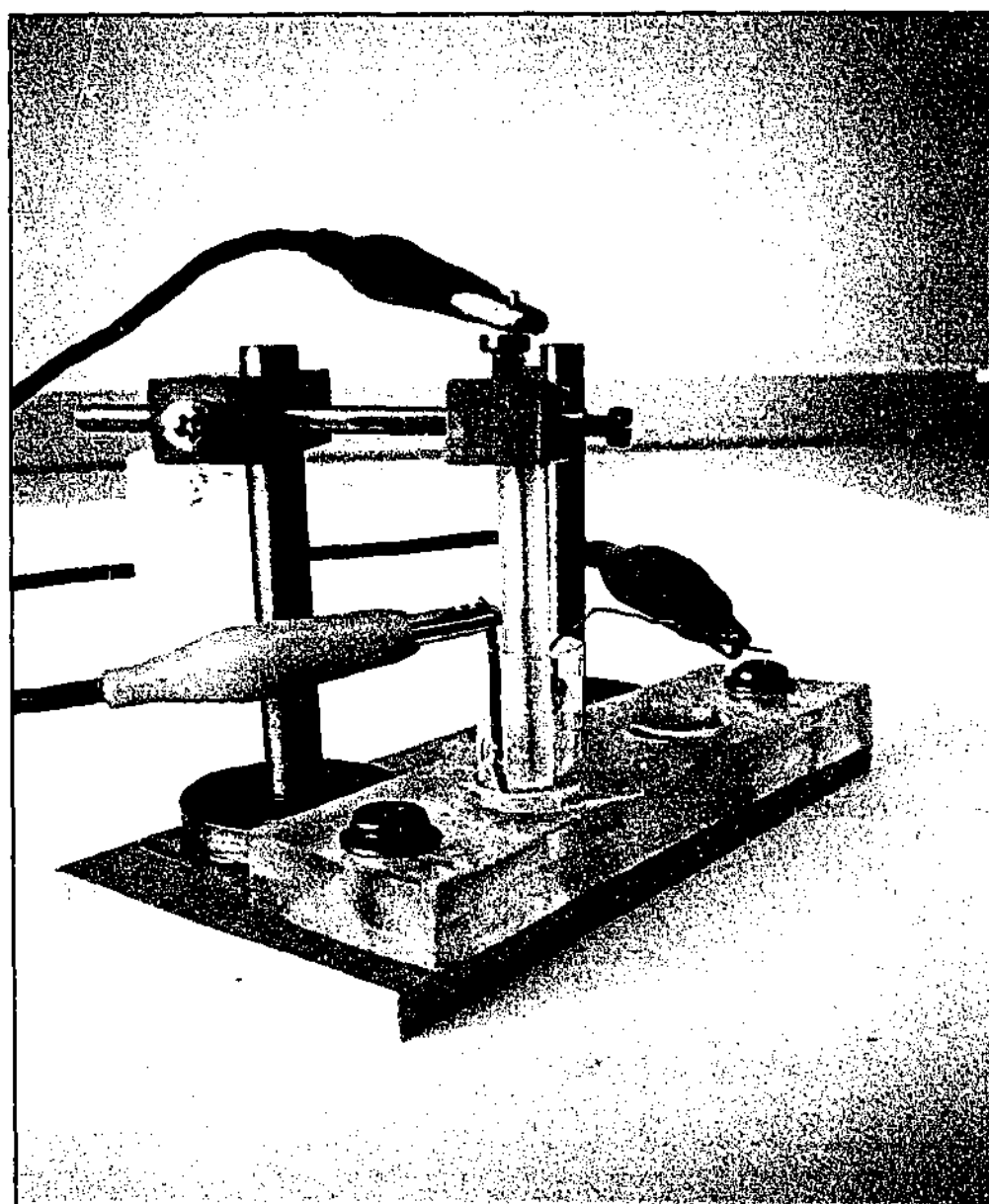


Fig. 2.4 3-electrode electrochemical used for small volume electrochemical measurements in the glovebox.

Working electrodes:

Platinum macroelectrode:

A commercially available 1 mm (nominal) platinum disk in PEEK (Poly ether ethyl ketone) electrode was polished before each measurement with 0.05 μm Al_2O_3 . The electrode was rinsed with deionised water and dried under a stream of heated air prior to admission to the glovebox.

Nickel and Copper macroelectrodes:

Working electrodes made from nickel and copper were fabricated in house. 99.999% Nickel rods (Aldrich) and OFHC (oxygen free high conductivity) copper were used respectively. The metal was machined into a rod having a tip of approximately 1 mm diameter. A piece of polyethylene (PE) was used as the sheath. The PE was machined to the shape of a rod and a hole of appropriate diameter was drilled through the centre. The disk electrode was formed by press fitting the metal rod into the sheath. The sheath was heated under hot air prior to press fitting. The electrode surface was exposed by cutting away excess PE, and the surface was prepared by polishing with successively finer grades

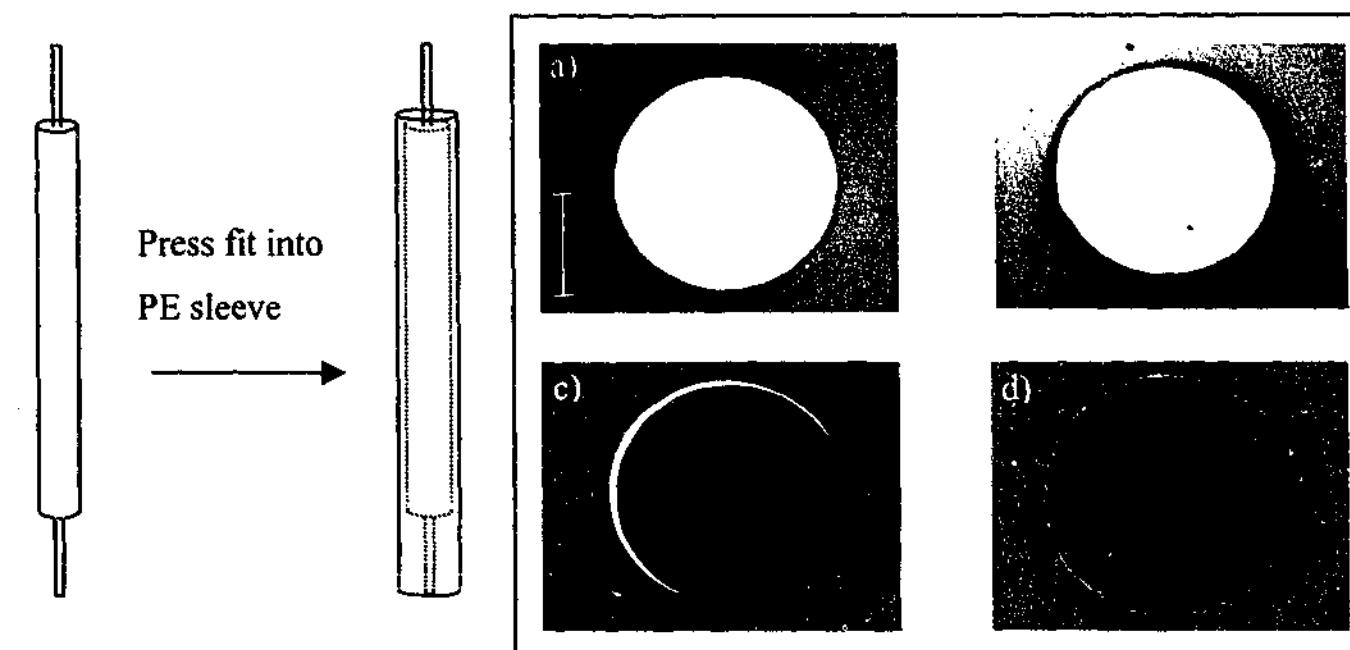
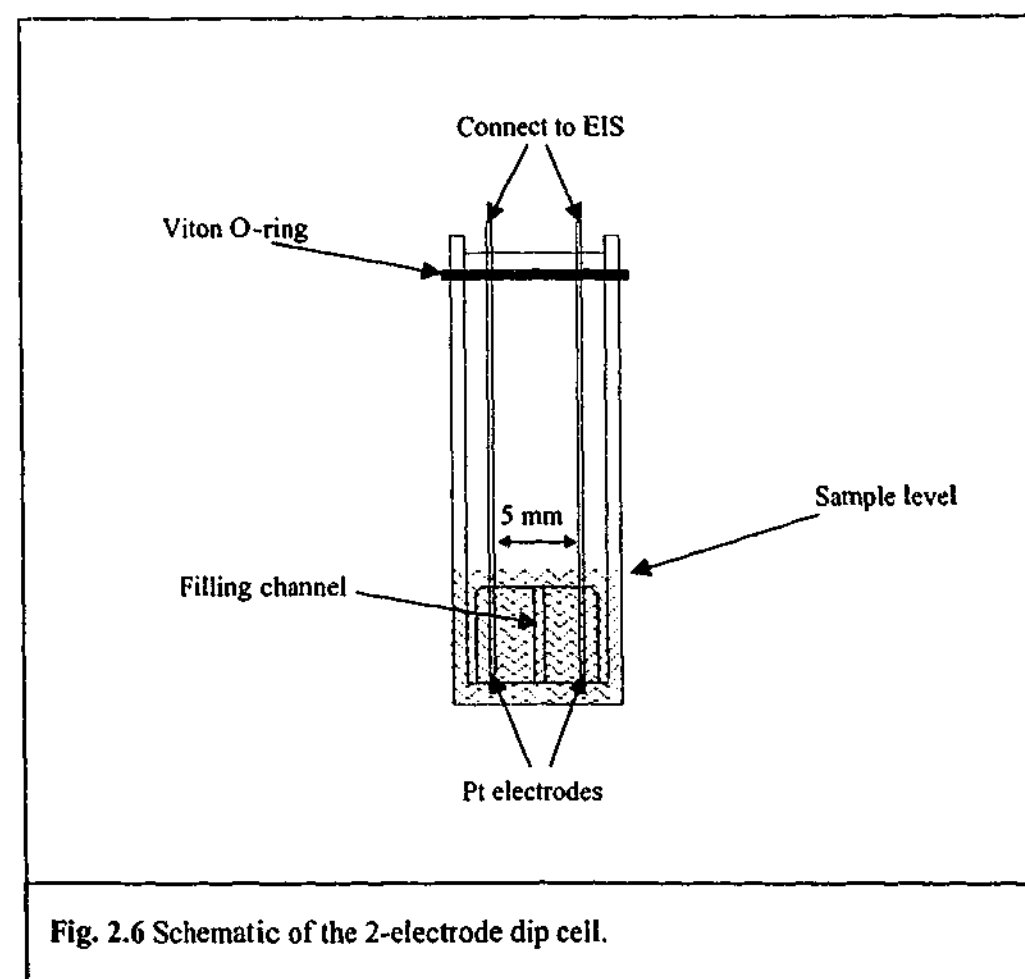


Fig. 2.5 PE sheathed working electrodes fabricated from nickel (a & b) and copper (c & d). Image d) is shown under dark-field illumination. Scale-bar shows 500 μm .

of Al_2O_3 until a smooth mirror like surface could be observed under a microscope. The interface between the PE and the metal observed under the microscope indicated that a tight fit had been obtained. Fig. 2.5 shows a schematic of the electrode design and optical micrographs of the electrode surfaces.

2.2.4 Conductivity cell:

A 2-electrode dip cell was used to determine the specific conductivity of selected solutions. The cell was comprised of two platinum electrodes sheathed in a single piece of glass, ~3 mm apart. Specially made vials with an O-ring at the mouth were used to provide a seal around the body of the electrode. A filling channel was cut into the side of the glass sheath to avoid bubbles being trapped against the electrode surfaces. The dimensions of the cell were minimized for small sample volumes, ~0.5 ml of sample was required. The design of the cell is shown schematically in Fig. 2.6. It was necessary to hold a fine piece of wire against the O-ring when inserting the electrode into the vial to allow atmosphere to escape past the seal and avoid pressurizing the seal. Once the electrode was in position, the wire was withdrawn from the cell.



2.3 Apparatus:

2.3.1 Electrochemical measurements:

Cypress:

The majority of the cyclic voltammetry and microelectrode work was performed on a Cypress Systems CYSY-1R potentiostat and a Cypress Systems faraday cage. The potentiostat was operated by a Cypress Systems Computer Controlled Electroanalysis System Version 6.1 / 4V.

Maclab:

The majority of the three electrode 'cycling efficiency' (described in section 1.3.4 & 2.6.3) experiments were performed on a Maclab potentiostat using Chart v3.1.4 software.

2.3.2 Cycling experiments:

Specialised cell cycling equipment was used to perform 'battery' cycling experiments on the cup cells and optical cells. In particular, the optical cells required a purpose built cell 'mount' and image acquisition apparatus.

PC:

All of the cell cycling experiments were controlled and recorded on a Pentium III 450 MHz PC (Windows NT). The PC operated CSIRO battery controller unit (BCU) software which wrote control profiles to, and recorded data from, a BCU. The profiles used to control the experiment were written in a simple programming language and downloaded to the BCU. The PC power supply was backed up by a Powerware Prestige EXT (800 P2HSVE) uninterruptible power supply.

CSIRO Battery Control Unit (BCU):

The CSIRO BCU, a programmable microprocessor, which operated on a downloaded profile, was interfaced to a potentiostat and a PC. The BCU was typically used to control and log cell current and cell voltage, as well as cell temperature, cycle number and time.

Interface:

An interface was required in order to allow the BCU to operate a 'standard' commercially available potentiostat. The interface amplified the signals to the required level (for the BCU), and adapted the physical connections to allow the units to be interfaced. In addition, the potentiostat produced bipolar voltages (i.e. both positive and negative), whereas the control and data-acquisition system, being designed for conventional batteries, could only accept monopolar (i.e., positive) voltages. To provide a quasi-bipolar voltage input, the interface added an additional 5V to the voltage from the potentiostat.

Potentiostats:

An EG&G PAR Model 362 scanning potentiostat and a Solartron Schlumberger 1186 electrochemical interface was used to apply current and voltage under the control of a BCU.

Cup cell heater:

A Perspex case wrapped in foil containing an incandescent globe as the heat source controlled by a thermocouple feedback loop was used as a heater during cup cell cycling. Most experiments were conducted at 50 °C. For higher temperatures, a Thermoline (VORS) vacuum oven was used.

Optical cell:*Mount & Stage:*

The cells were either placed on an XYZ stage which was mounted on a marble block on an anti-vibration bench or on the stage of a Nikon SMZ-2T microscope.

Heater and lighting:

A 16 V DC heater (to avoid noise in cell measurements), consisting of a single 'cement' resistor with a copper plate glued to its surface, was controlled by a feedback loop from a National Semiconductor LM35 temperature sensor mounted on the copper plate. The optical cell was attached to the heater surface using metal clips. A LM35 temperature sensor attached to the surface of the optical cell using a clip and thermal conductive paste monitored the cell temperature. Illumination was provided by a 12V DC dichroic light source; again, a DC power source was necessary to avoid noise in the cell measurements.

Image acquisition and analysis:

A PC running National Instruments IMAQ driver software and a PCI-IMAQ-1408 image acquisition card acquired digital images of the electrode surface from a Pulnix TM-6CN CCD camera fitted with a Navitar 1× adaptor lens. The experiments were also recorded on videotape. Alternatively, images were acquired on a PC running National Instruments IMAQ driver software and a PCI-IMAQ-1411 image acquisition card from a Sony Hyper HAD SSC-DC50P colour video camera fitted to Nikon SMZ-2T microscope with a TV lens C-0.6× adaptor. Figure 2.7 shows a schematic of the apparatus used to cycle and acquire images from the optical cell. A Labview™ program was developed that allowed automatic acquisition of images at specified intervals, this allowed high-speed animations to be compiled for lengthy experiments. Image areas and dimensions were determined using a 50 × 2 μm Graticules Ltd. (Tonbridge, England) graticule and Scion Image software.⁸ Scion Image for Windows is the Windows version of Scion Image, which is in turn a version of the popular Macintosh program, NIH Image, written at the National

Institutes of Health. Scion Image may be used to capture, display, analyse, enhance, measure, annotate, and output images.

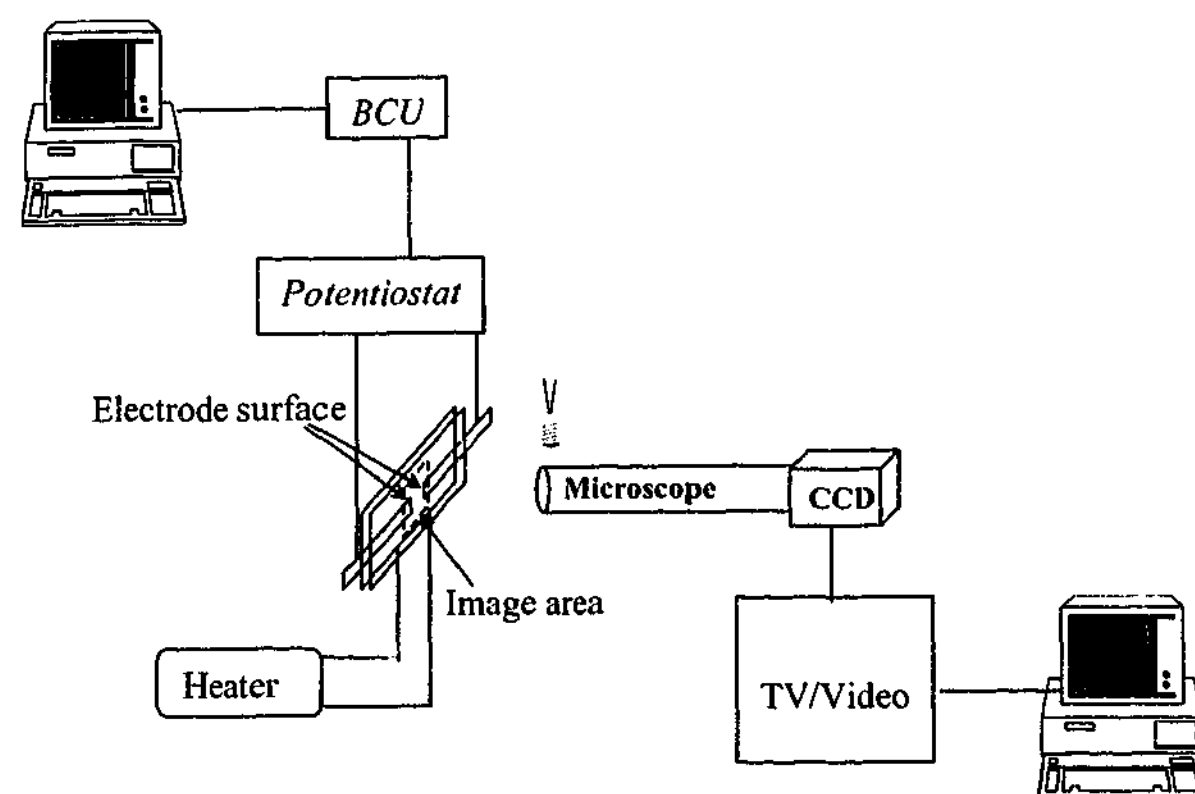


Fig. 2.7 Schematic of equipment used to study electrode processes within the optical cell.

2.4 Characterisation techniques:

2.4.1 Raman spectroscopy:

Raman spectra were acquired on a Renishaw RM2000 Raman spectrograph. The spectrograph was equipped with a HeNe 632.8 nm Spectraphysics laser source. In-situ and ex-situ spectra were acquired using an Olympus BH2 microscope attachment with 5 \times , 20 \times and 50 \times objective lenses. The system was controlled by a PC operating Renishaw WiRE (Windows Renishaw Environment) software V1.3.

In-situ spectra were acquired from the optical cell through the borosilicate window which was incorporated specifically for the purpose. Measurements were made by focusing on the surface of lithium deposits formed in the cell, typically spectra of the bulk electrolyte

were acquired by focusing at the same depth as the electrode deposits. Ex-situ spectra were acquired from a cup cell sample (i.e., an electrode taken from a cycled cup cell which had been dismantled in the glovebox) which was housed within a 'bolt cell'. The 'bolt cell' consisted of a nut with a sealed (Surlyn[®]) borosilicate window that could be sealed by screwing onto an O-ring (Fig. 2.8).

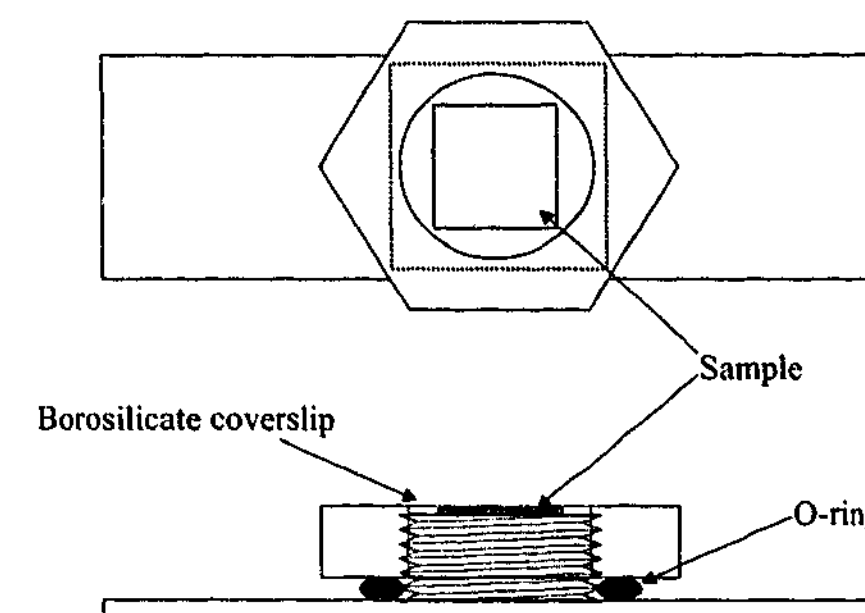


Fig. 2.8 Schematic of the 'Bolt cell' used for Raman spectra acquisition.

2.4.2 Fourier transform infrared spectroscopy:

Infrared spectra were acquired on a Digilab FTS 3000MX Excalibur series spectrometer using Digilab Win-IR Pro 3.2 software. Ex-situ Diffuse reflectance (DRFTIR) spectra were obtained using a Harrick DRFTIR accessory. To protect the sample surface from reaction with the atmosphere an hermetic transference chamber was designed and built, in which the DRFTIR accessory was housed. The chamber incorporated KBr O-ring sealed windows and an O-ring sealed access door. The chamber was aligned such that the windows and DRFTIR accessory could be positioned in the instrument beam path. It was necessary to align the mirrors prior to fitting the accessory into the chamber. Limited adjustment could be performed inside the chamber. A schematic detailing the basic features of the chamber is shown in Fig. 2.9. Transmission spectra for the electrolyte were obtained using NaCl windows.

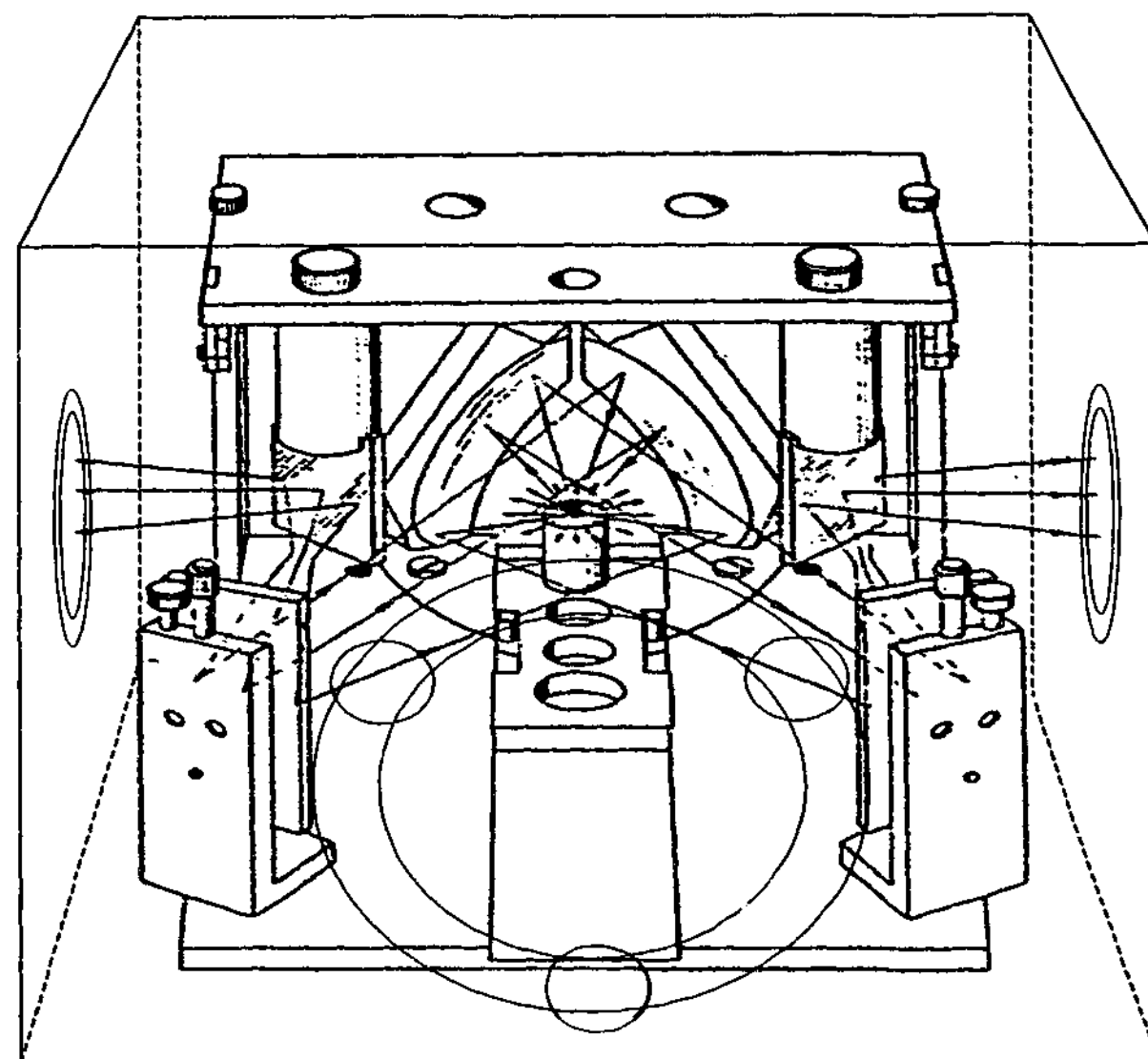


Fig. 2.9 Schematic of DRFTIR assembly and transfer chamber.

2.4.3 X-ray diffractometry (XRD):

An Inel XRG 3000 X-ray diffractometer fitted with an Inel CPS 120 position sensitive detector (PSD), a multilayer mirror and a cobalt X-ray source was used to acquire XRD spectra. Measurements were taken at 35 mA and 40 kV, acquisition times were typically 300s or 1200s. An environmental chamber was developed to protect the sample from the atmosphere during transfer and measurement. The environmental chamber is shown schematically in Fig. 2.10. The chamber was loaded with a cup cell sample, which had previously been mounted on a small electric motor and spun at high speed to remove as much of the excess electrolyte adhering to the sample surface as possible. The chamber was attached to a vacuum pump to remove the argon atmosphere and reduce the loss of X-ray intensity due to absorption; the vacuum was maintained throughout the measurement.

The instrument geometry was arranged so that measurements could be taken at various grazing angles to enable the detection of surface phases. The instrument geometry is shown schematically in Fig. 2.11.

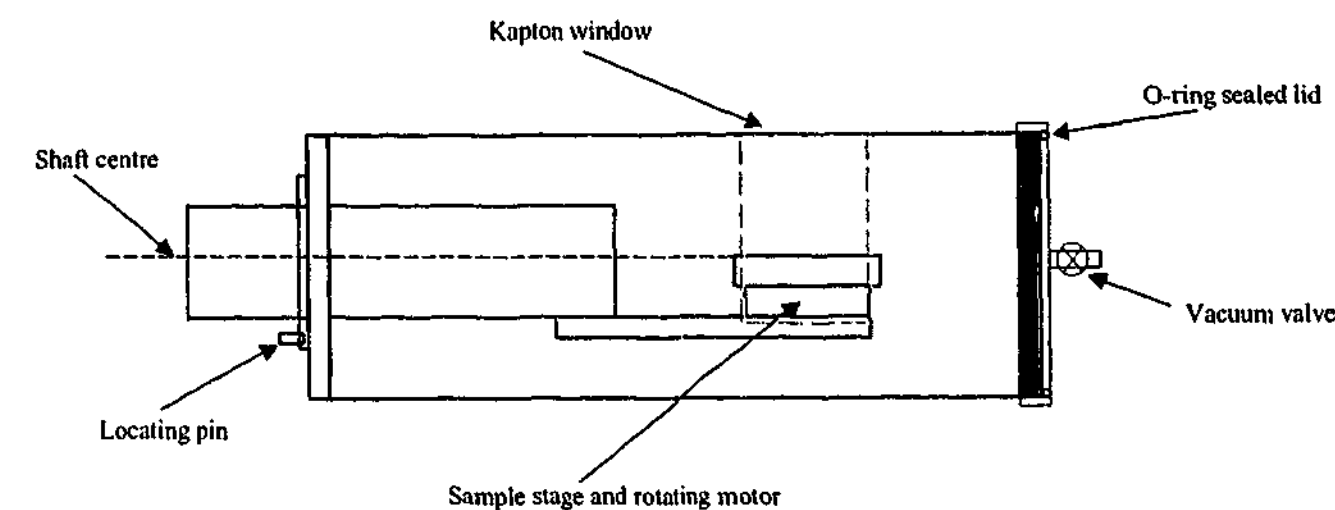


Fig. 2.10 GAXRD environmental chamber.

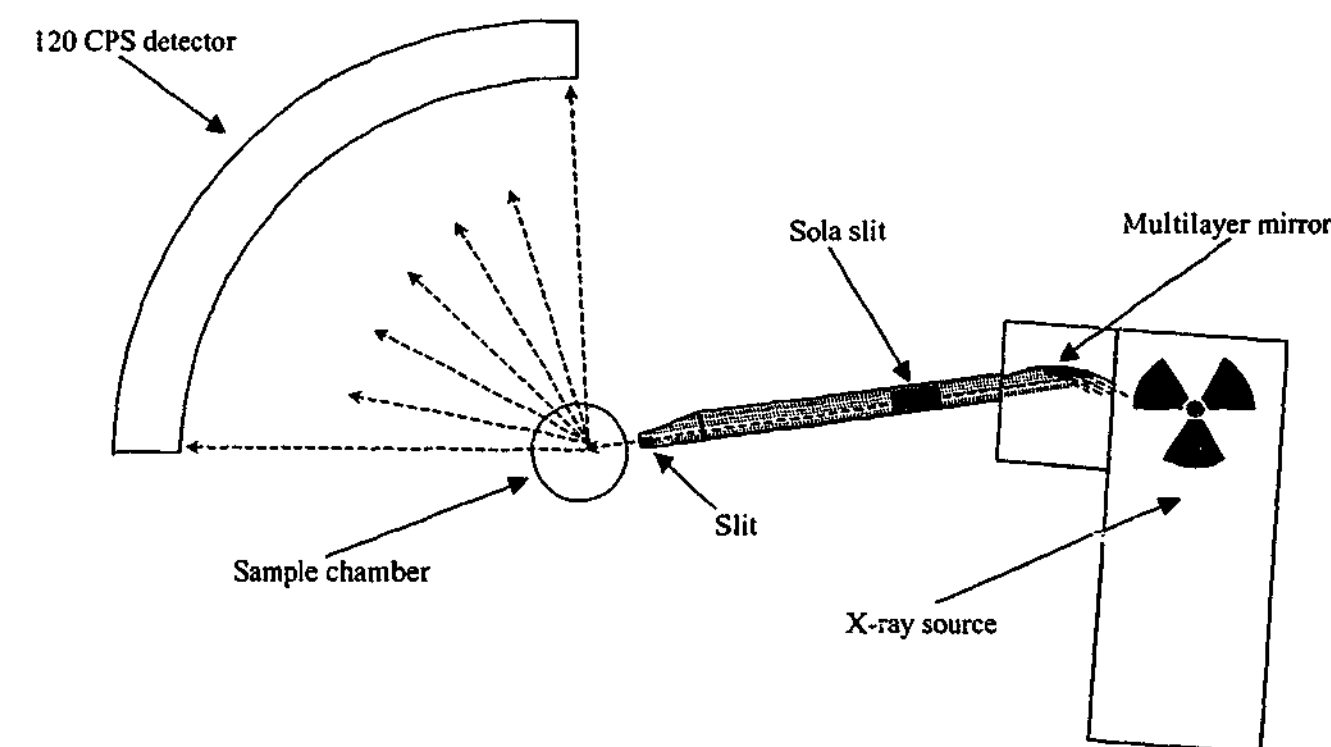


Fig. 2.11 Schematic of GAXRD geometry.

2.4.4 X-ray photoelectron spectroscopy (XPS):

Samples for XPS analysis were prepared (in the glovebox) from electrodes taken from cycled cup cells. The samples were mounted on a small electric motor and spun at high speed to remove as much of the excess electrolyte adhering to the sample surface as possible. After spinning the sample was mounted on an XPS sample stud using conductive carbon adhesive tape and placed in an hermetic transference vessel for transfer to the instrument. The samples were admitted to the XPS without access to the atmosphere by enclosing the instrument antechamber in an argon filled glovebag.

Spectra were acquired on a Kratos Axis ultra imaging XPS spectrometer. An aluminium monochromated X-ray source operating at 10 mA and 15 kV (150 W) was focused on the sample surface. The hybrid analysis mode was used which provided a sampling area of $300\text{ }\mu\text{m} \times 700\text{ }\mu\text{m}$. Survey spectra were acquired at 160 eV pass energy and high resolution region spectra were acquired at 20 eV pass energy. The instrument vacuum was maintained at $\sim 1.2 \times 10^{-8}$ torr. Etching experiments were performed on the sample surface using an argon ion beam gun operating at 15 mA and 5 kV – resulting in an estimated etching rate of $\sim 1\text{ }\text{\AA}\text{s}^{-1}$.

Instrument operation and peak fitting was performed using the XPS Axis ultra software. A 70 : 30 Gaussian : Lorentzian algorithm was used to fit the peaks to obtain quantitative results. The fit produced an estimated $\pm 10\%$ error in the atomic concentration determined for each peak.

2.4.5 Electrochemical impedance spectroscopy (EIS):

Two instruments were used to perform electrochemical impedance spectroscopy measurements.

1. A Solartron SI 1260 frequency response analyzer (FRA) and a Solartron SI 1255 electrochemical interface under GPIB control from a PC using Zplot v2 software.

2. A Solartron DI 1296 dielectric interface and a Solartron SI 1270 frequency response analyzer under GPIB control from a PC using Solartron Impedance Measurement software. A Eurotherm 2204e temperature controller under serial control was used to control a 240V cartridge heater for some experiments. The Eurotherm was under Solartron Impedance Measurement software control.

A 240V cartridge heater and a K type thermocouple mounted in a brass block, were used to heat the samples for dip cell conductivity and cup cell SEI impedance measurements. In the case of the dip cell, a cylindrical hole was made within the block in which the dip cell fit snugly.

2.4.6 Nuclear magnetic resonance spectroscopy:

Line spectra:

^{19}F , ^7Li , ^1H line spectra were recorded using a Bruker Avance 300 at 282.3MHz, 116.6MHz and 300.1MHz respectively and pulse length of 13 μsec , 9 μsec and 13 μsec respectively, from 300 to 345K. A minimum of 30 minutes was allowed for thermal equilibration at each temperature. A lithium tetrafluoroborate aqueous standard was used to determine the lineshape of the lithium and fluorine signals to ascertain whether any peak asymmetry was due to magnet inhomogeneity. Single lines were found for both cases with a FWHM of $\sim 75\text{Hz}$ for Lithium and $\sim 40\text{Hz}$ for Fluorine (slightly skewed).

Pulsed Field Gradient Diffusometry:

Pulsed Field Gradient spin echo (PFGSE) measurements were conducted using a Bruker Avance 300 spectrometer fitted with a water-cooled Bruker Diff30 diffusion probe. Measurements were taken from 300-345K. A minimum of 30 minutes was allowed for thermal equilibration at each temperature. A conventional spin echo pulse sequence [90° - τ - 180° - τ -echo] with two rectangular field gradients was used, separated by Δ . The echo amplitude was recorded at 2τ :

$$A = A_0 \exp\{-G^2 \gamma^2 D \delta^2 (\Delta - \delta/3)\} \quad (2.1)$$

where γ = magnetogyric ratio; D = self-diffusion coefficient; G = strength of applied field gradient. Diffusion time = 20 msec, gradient ramp time = 0.3 msec, the strength was varied up to 1800 G/cm over 16 steps. Samples were loaded in Schott NMR tubes (5mm OD, 178mm length), the tubes were sealed with paraffin film and Teflon tape.

2.5 Cycling Experiments:

Experiments designed to study the ability of the electrolyte to cycle under battery-like conditions were performed in a variety of configurations. Each cell was used for different reasons, in order to probe specific parameters important to battery operation.

2.5.1 Optical cell:

Early versions of the cell comprised a symmetrical cell, which was cycled at constant current, typically 1 mAcm⁻². The area of the electrode was estimated from the geometry of the foil, 4 mm × 100 μm giving an area of 0.004 cm². The amount of charge passed per cycle was estimated from the surface area to give a charge per unit area (typically 1 Ccm⁻²), and applied at constant current for a specified amount of time according to;

$$Q = I \times t \quad (2.2)$$

where Q is charge in coulombs (C), I is current in amps (A) and t is time in seconds (s).

Later versions of the optical cell comprised four electrodes, the cell was cycled using the copper electrode as the working electrode and the opposing lithium electrode as the counter electrode. The lithium electrode adjacent to the copper electrode was used as a reference. The amount of charge passed and the current density were estimated from electrode surface areas in the same manner as the symmetrical cell.

The majority of the optical cell experiments were performed at elevated temperature, typically 50 °C ± 2 °C. The temperature of the cell was logged during each experiment by attaching a National Semiconductors LM35 temperature sensor to the surface of the cell near the working electrode.

2.5.2 3-electrode cell:

A variety of working electrodes were used in the 3-electrode cell (Section 2.2.3). The majority of experiments employed either platinum wire counter and silver wire pseudo-references or prepared lithium foil for both the counter and reference electrodes.

The quality of the working electrode surface was monitored using an optical microscope at regular intervals. The surface areas of the working electrodes were determined by application of the Randles-Sevcik equation.⁹

$$I_p = 0.4463nFAc(nFvD/RT)^{1/2} \quad (2.3)$$

$$I_p = (2.687 \times 10^5) n^{3/2} v^{1/2} D^{1/2} Ac \text{ at } 25^\circ\text{C} \quad (2.4)$$

Where I_p is the peak voltammetric current (A), n is the number of electrons per reacting molecule, F is the Faraday constant (98485 Cmol⁻¹), A is the electrode area in cm², D is the apparent diffusion coefficient (cm²s⁻¹), v is the scan rate (Vs⁻¹) and c is the concentration (molcm⁻³). A solution of 5 mM ferrocene in acetonitrile with 0.1 M tetrabutylammonium hexafluorophosphate supporting electrolyte ($D = 2.30 \times 10^{-5}$ cm²s⁻¹)⁹ was used for the determination of the platinum macroelectrode surface area. Peak currents were determined at scan rates of 50, 100 and 200 mVs⁻¹. An example of the plots used to determine the macroelectrode surface area is given in Fig. 2.12.

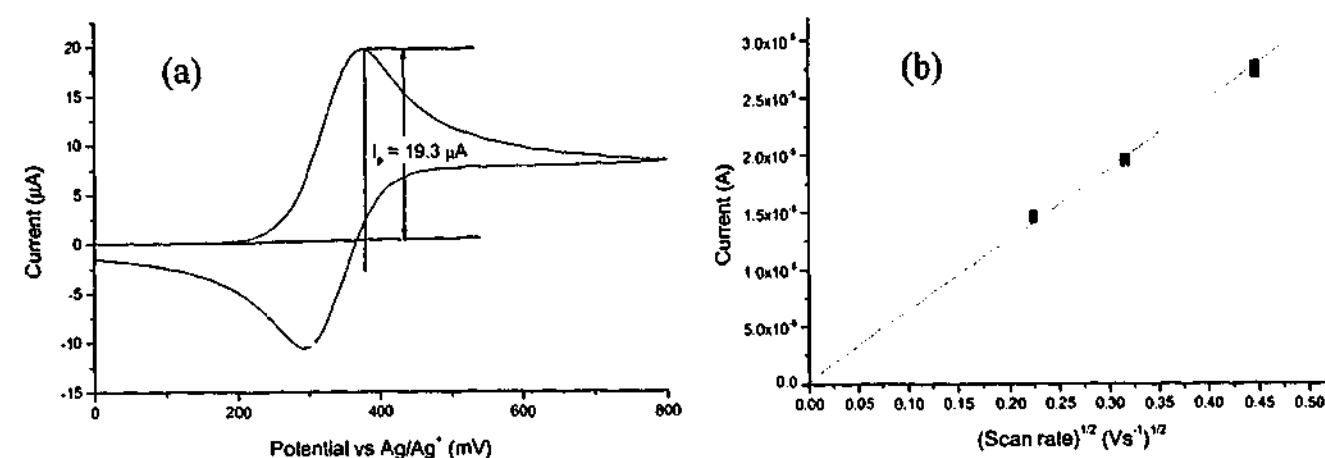


Fig. 2.12 (a) Cyclic voltammogram at 100 mVs^{-1} showing determination of peak current. (b) Plot of I_p vs. square root of the scan rate, the slope of the line is substituted into the Randles-Sevcik equation (2.4).

Alternatively, where electrochemical determination of the surface area was made difficult by surface reactions of the working electrode (e.g., in the case of copper), image analysis of optical micrographs using the Scion Image software was performed (section 2.2.3).

2.5.3 Resealable stainless steel cup cells:

Numerous cell configurations were employed. After assembly in the glovebox, the cup cells were removed and stored for approximately 24 hours at the temperature of the experiment prior to commencement of cycling.

Lithium symmetrical cell:

Lithium symmetrical cells were made from two pieces of lithium. A variety of separator materials were trialed. The electrode surface area was 2 cm^2 and both the current density and the charge were determined using equation (2.2) in the same manner as for the optical cell.

Lithium-copper half cell:

Lithium-copper half cells were made from a piece of lithium and a piece of copper with one of a variety of separator materials. The electrode surface area was 2 cm^2 and both the current density and the charge were determined using equation (2.2) in the same manner as for the optical cell.

'Battery' cell:

Battery cells were made from a piece of positive electrode material and either a piece of copper, platinum or lithium. The cells were cycled at various 'C' rates where 'C' refers to the current required to discharge or charge the limiting electrode in 1 hour. For the cells employed, the positive electrode constituted the limiting electrode in the cell. The 'C' rate was estimated from the amount of positive active material coating the electrode, multiplying the mass of the active material (in grams) by the specific capacity of the active material (in mAhg^{-1}) gave the capacity of the positive electrode. The specific capacity used was based on actual capacity values determined for conventional cells.¹⁰ Charge-discharge rates were denoted by either a multiple (e.g., 2C) or fraction (e.g., C/10) of C.

2.6 Methodology:

2.6.1 Electrochemical impedance spectroscopy:

Conductivity measurement:

The conductivity cell was connected to the Solartron DI 1296 dielectric interface and Solartron SI 1270 frequency response analyzer using two shielded BNC connectors. The cell heater was earthed to the temperature controller and seated in a bucket of vermiculite.

The cell constant of the dip cell was determined at 25 °C using an aqueous 0.01 M KCl solution. The measured conductance of solution was calculated from the real axis touchdown of the Nyquist plot using equation (2.6);

$$k_{\text{meas}} = 1/R \quad (2.6)$$

where R is the touchdown value in Ohms (Ω). The cell constant g (cm^{-1}) was determined from the solution conductance using equation (2.7);

$$g = \sigma_{\text{KCl}} / k_{\text{meas}} \quad (2.7)$$

where σ_{KCl} was the conductivity of the KCl solution at 25 °C (1409 Scm^{-1})¹¹ and k_{meas} was the measured conductance of the solution at 25 °C.

Measurements were generally made from 20 °C to 150 °C at 5 °C intervals, duplicate measurements were made as the cell cooled to room temperature. Each impedance spectrum was acquired using a 100 mV AC perturbation versus the cell open circuit voltage (OCV). The AC perturbation was varied from 10^7 Hz to 1 Hz for each temperature. The specific resistance of each solution was determined from the real axis touchdown in the Nyquist plot. The specific conductivity (σ , Scm^{-1}) of the solution was calculated using equation (2.8):

$$\sigma = g / R_{\text{meas}} \quad (2.8)$$

SEI vs. temperature:

Impedance spectroscopy was performed on cycled lithium symmetrical cup cells to examine the properties of the passivation film formed on the electrode surface. Each impedance spectrum was acquired using a 5 mV AC perturbation versus the cell open circuit voltage (OCV). The AC perturbation was varied from 10^7 Hz to 0.05 Hz for each temperature. Measurements were typically made from 25 °C to 80 °C in 10 °C steps (the

first step being 5 °C) on heating. A second spectrum was acquired at 10 °C intervals from 80 °C to 30 °C on cooling.

Fitting procedure:

Impedance spectra were fitted to equivalent circuits using ZView[®] version 2.3 (Scribner Associates 1999-2000). For most spectra, it was necessary to delete several points in the high frequency region of the spectrum due to the presence of inductance in the experimental setup. Typically, the solution resistance was estimated directly from the Nyquist plot, other circuit element resistances were also estimated from the real axis dimension of the arc. These values were 'fixed', and the capacitance (CPE values) were roughly estimated and set as 'free' variables. The iterative complex nonlinear least squares (CNLS) fitting engine was then used to refine the 'free' variables. With each successive fit, one or more of the fixed resistances was set to 'free' and the refinement was repeated, until finally all of the circuit elements were set to 'free'. A poor model was indicated by a failure of the model to converge with all elements 'free'. The model was judged to be of 'good fit' when a χ^2 value (square of the standard deviation between the original data and the calculated spectrum) of less than 0.001 was returned, and when the weighted sum of squares (proportional to the average percentage error between the original data points and the calculated values) was less than 0.1.

2.6.2 Voltammetry:

Macroelectrode area and diffusion:

Knowledge of the working electrode surface area allowed the determination of the lithium diffusion coefficient in the ionic liquid electrolyte solutions. The determination was carried out in a similar manner to the surface area measurements (section 2.5.2) using a modified Randles-Sevcik equation.

$$D^{1/2} = \frac{0.4463nFAC(nFv/RT)^{1/2}}{I_p} \quad (2.9)$$

The cyclic voltammograms were acquired by scanning from an upper potential (typically 2000 mV vs. Li/Li⁺) to a lower potential (typically -500 mV vs. Li/Li⁺) and back to the starting potential.

2.6.3 Cycling Efficiency:

The cycling efficiency measurements were performed as described in the literature.¹²⁻¹⁵ An excess of lithium was galvanostatically plated onto the surface of the working electrode followed by cycling of a fraction of the original excess. The number of cycles required to consume the original excess (indicated by a sharp change in dissolution potential) was used to calculate the 'average cycling efficiency' of the electrolyte. The cycling efficiency experiments were performed under a range of conditions in both the 3-electrode cell and the optical cell;

$$Av.Cyc.Eff = 100 \times NQ_{ps} / (NQ_{ps} + Q_{ex}) \quad (2.10)$$

where N is the number of cycles, Q_{ex} is the plated excess (1 Ccm⁻²) and Q_{ps} is the cycled fraction (0.25 Ccm⁻²). For the majority of experiments Q_{ex} = 1 Ccm⁻² and Q_{ps} = 0.25 Ccm⁻².

References

1. J. S. Wilkes and M. J. Zaworotko, *Chem. Commun.*, **13**, 965 (1992).
2. P. Bonhote, A. P. Dias, N. Papageorgiou, M. Armand, K. Kalyanasundaram and M. Gratzel, *Inorg. Chem.*, **35**, 1168 (1996).
3. D. R. MacFarlane, J. Golding, S. Forsyth, M. Forsyth and G. B. Deacon, *Chem. Commun.*, 1430 (2001).
4. D. R. MacFarlane, S. A. Forsyth, J. Golding and G. B. Deacon, *Green Chemistry*, **4**, 444 (2002).
5. S. Forsyth, J. Golding, D. R. MacFarlane and M. Forsyth, *Electrochim. Acta*, **46**, 1753 (2001).
6. D. R. MacFarlane, P. Meakin, J. Sun, N. Amini and M. Forsyth, *J. Phys. Chem. B*, **103**, 4164 (1999).
7. D. R. MacFarlane, J. Sun, J. Golding, P. Meakin and M. Forsyth, *Electrochim. Acta*, **45**, 1271 (2000).
8. Webmaster@scioncorp.com, Web Page, *Scion image* (Available: <http://www.scioncorp.com/index.htm>, July 2003).
9. R. N. Adams, *Electrochemistry at Solid Electrodes*, Marcel Dekker, Inc., New York (1969).
10. J. O. Besenhard (Ed.), *Handbook of Battery Materials*, Wiley-VCH, Weinheim (1999).
11. R. A. Robinson and R. H. Stokes, *Electrolyte Solutions*, Butterworths Publications Limited, Bath, UK (1965).
12. S. V. Sazhin, M. Yu. Khimchenko, Y. N. Trittenchenko, W. Roh and H. Y. Kang, *J. Power Sources*, **66**, 141 (1997).
13. D. Aurbach (Ed.), *Nonaqueous Electrochemistry*, Marcel Dekker, New York (1999).
14. A. T. Ribes, P. Beaunier, P. Willmann and D. Lemordant, *J. Power Sources*, **58**, 189 (1996).
15. M. Ishikawa, S. Machino and M. Morita, *J. Electroanal. Chem.*, **473**, 279 (1999).

Results & Discussion

3.1 Optical cell:

An optical cell was designed specifically for the study of novel electrolyte materials for use with lithium metal electrodes in secondary cells. Particular design focus was applied to allow image capture and analysis of the Li morphology at the Li | electrolyte interface with cycling. The design allowed cells to be assembled with very reproducible geometry. The cell configuration (i.e., thin, widely separated electrodes) was intended to give rise to a situation where the electrode surface could be viewed as a representative subsection of what would occur on the surface of a battery electrode. Moreover, sealed cells allow observation of gas evolution and build up. It is conceivable that gas pressure within the cell could influence the evolution of deposit morphology.

3.1.1 Initial studies in 2-electrode configuration:

During the initial development of the optical cell, a 1 M LiPF₆ solution in propylene carbonate (PC) was used as the electrolyte to establish a notion of 'typical behaviour' for a cycled lithium electrode in the optical cell. These experiments were used as a means to develop methods to ensure that the cells were fabricated with reproducible geometry, a good seal, to optimise the set up of the imaging apparatus and cycling equipment, as well as providing a platform for the preliminary investigation of RTILs as lithium battery electrolytes.

The original cell design comprised two symmetrical lithium electrodes and did not include a reference electrode. The electrode separation was 2mm for all cells. The majority of experiments were conducted at constant current for a set amount of charge. Deposit morphology was monitored throughout by video recording or by automated image acquisition. The cell design was continually being altered to improve the cell failure rate, which was initially very high, and to incorporate improved design features such as a borosilicate cover-slip to allow in-situ Raman measurements.

The initial investigation aimed to;

- develop an understanding of the problems associated with conventional electrolyte systems and the Li metal electrode, particularly with respect to the way they manifested in the optical cell.
- obtain a preliminary understanding of the behaviour of RTIL electrolytes when cycled with Li metal electrodes, particularly with reference to the behaviour of the electrode | electrolyte interface and the deposit morphology.

Cycling parameters such as current and charge densities were estimated values based on the geometrical surface area of the electrode. In some cases the geometrical surface area of the electrode departed significantly from the estimated value due to a tendency of the Surlyn[®] to flow over the electrode surface during cell construction, usually the extent of electrode coverage could be determined post-cycling from the appearance of the electrode surface. In-situ EIS and Raman measurements were also performed on some of the cells and will be discussed in a later section (3.4.3 and 3.4.4).

PC/LiPF₆:

The 1 M LiPF₆ solution of propylene carbonate (PC) used to develop the optical cell is not used in commercial cells. Usually a mixture of solvents is used to optimise the liquid range, conductivity and SEI properties (see Table 1.2). However, for the purpose of establishing an understanding of the behaviour of Li in a 'conventional' solvent and to develop the methodology for making and studying the cells, the PC/LiPF₆ system was seen as a suitable starting point.

Figure 3.1.1 displays the voltage profile of a PC/LiPF₆ optical cell undergoing galvanostatic cycling at 2 mAcm⁻² and 1 Ccm⁻² for 900 charge-discharge cycles. Inset into the plot are images of the optical cell showing evolution of the lithium deposit with cycling. Figure 3.1.2 displays the images inset into figure 3.1.1 in greater detail. On the first deposition cycle there are immediate observable changes on the electrode surface.

With continued cycling, both electrode surfaces became almost uniformly covered with voluminous deposits. It was found that deposition and growth of the deposits occur from the base, close to the electrode surface instead of from the surface of the deposits. As the deposits advance further into the cell, it was observed that the outermost deposits did not change in appearance. In some cases, it has been possible to follow the progress of individual, distinctly shaped deposits for several hundred cycles without significant changes in appearance. It appears that the deposits are no longer taking part in the charge-discharge process and are most likely examples of dead lithium. Occasionally, rapid motions occur within the mass of the deposit. These are probably a result of the deposits pushing against one another and are an indication of the presence of forces that are sufficient for the deposits to pierce a separator and lead to short-circuiting of a cell. It is not difficult to envisage similar behaviour at the surface of a battery electrode under stack pressure. All of these observations agree with the findings of other researchers investigating the processes of dendrite growth and the formation of dead lithium.¹⁻⁴

Examination of the voltage profile during cycling also indicates that dendritic growth and the formation of dead lithium have a marked effect on the impedance of the cell (Fig. 3.1.1). Initially, the potential required to pass the constant current (2 mAcm⁻²) is low and stable. After several hundred cycles, the cell begins to fill with deposit and the potential required to maintain the current increases substantially. This indicates an increase in resistance to the transport of lithium ions, possibly due to the presence of dead lithium acting as a physical barrier. It is feasible that this situation would precede a short circuit. Heat is generated as a result of the increased resistance which would soften the separator. The presence of deposits of dead lithium close to the surface may effectively reduce the active surface area of the electrode leading to an increase in current density. Increased deposition current density has been shown to promote dendritic deposition.^{2,4,5} The deposits will also significantly reduce the volume of electrolyte close to the surface leading to increased concentration gradients during current flow. Studies of polymer cells have linked the appearance of large concentration gradients close to the surface to the onset of dendritic deposition.^{1,6,7} It is also interesting to note that even when the deposits had completely filled the cell, and apparently made 'contact' between the two electrodes, there was no indication of a short circuit. This suggests that the surface film covering the deposits was not electron conducting and/or that the deposits were so finely divided

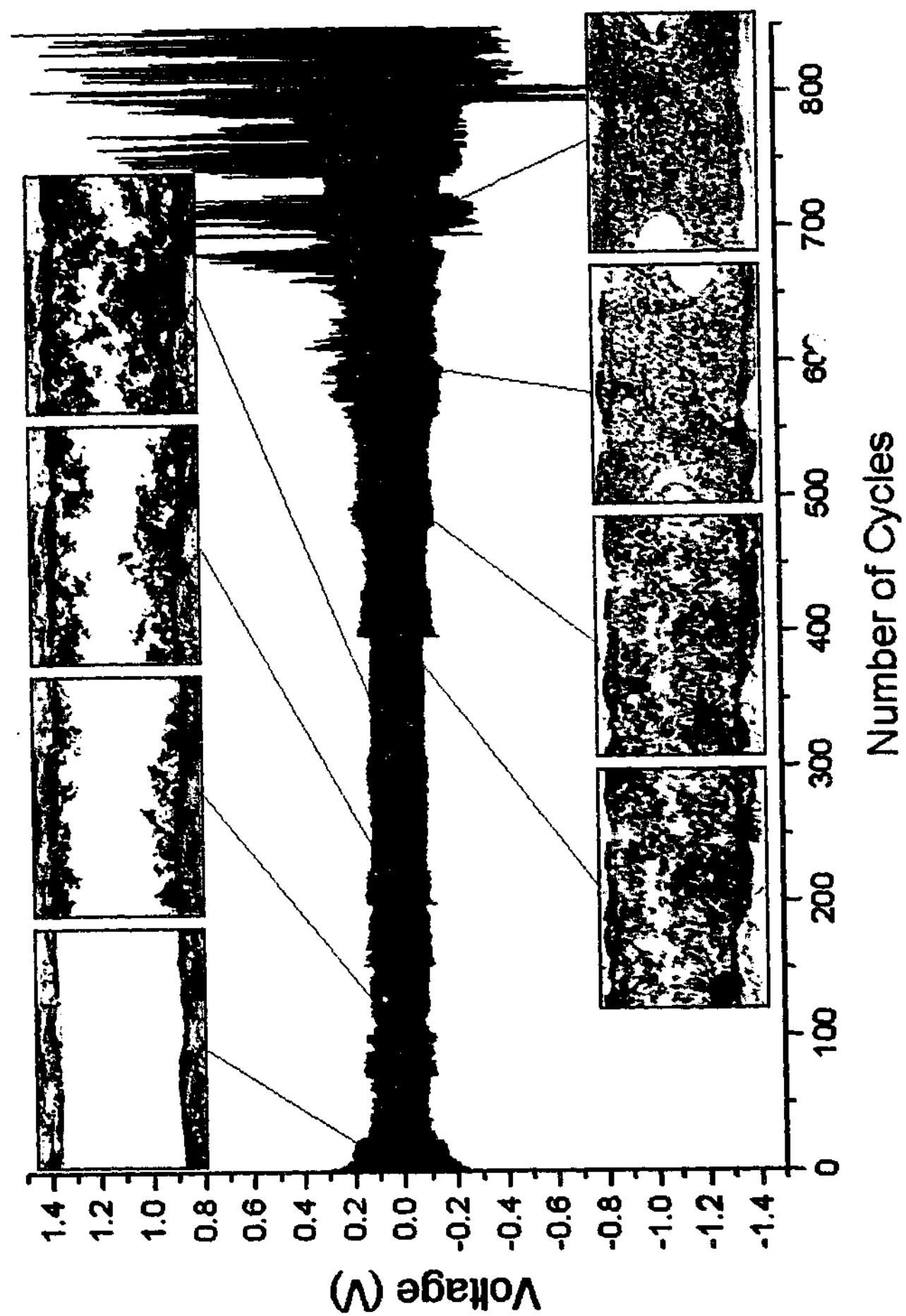


Fig. 3.1.1 PC/LiPF₆ cell cycled at 2 mAcm⁻², 1 Ccm⁻² and ambient temperature. Inset: 1st cycle and (consecutively) cycles 100, 200, 300, 400, 500, 600 & 700.

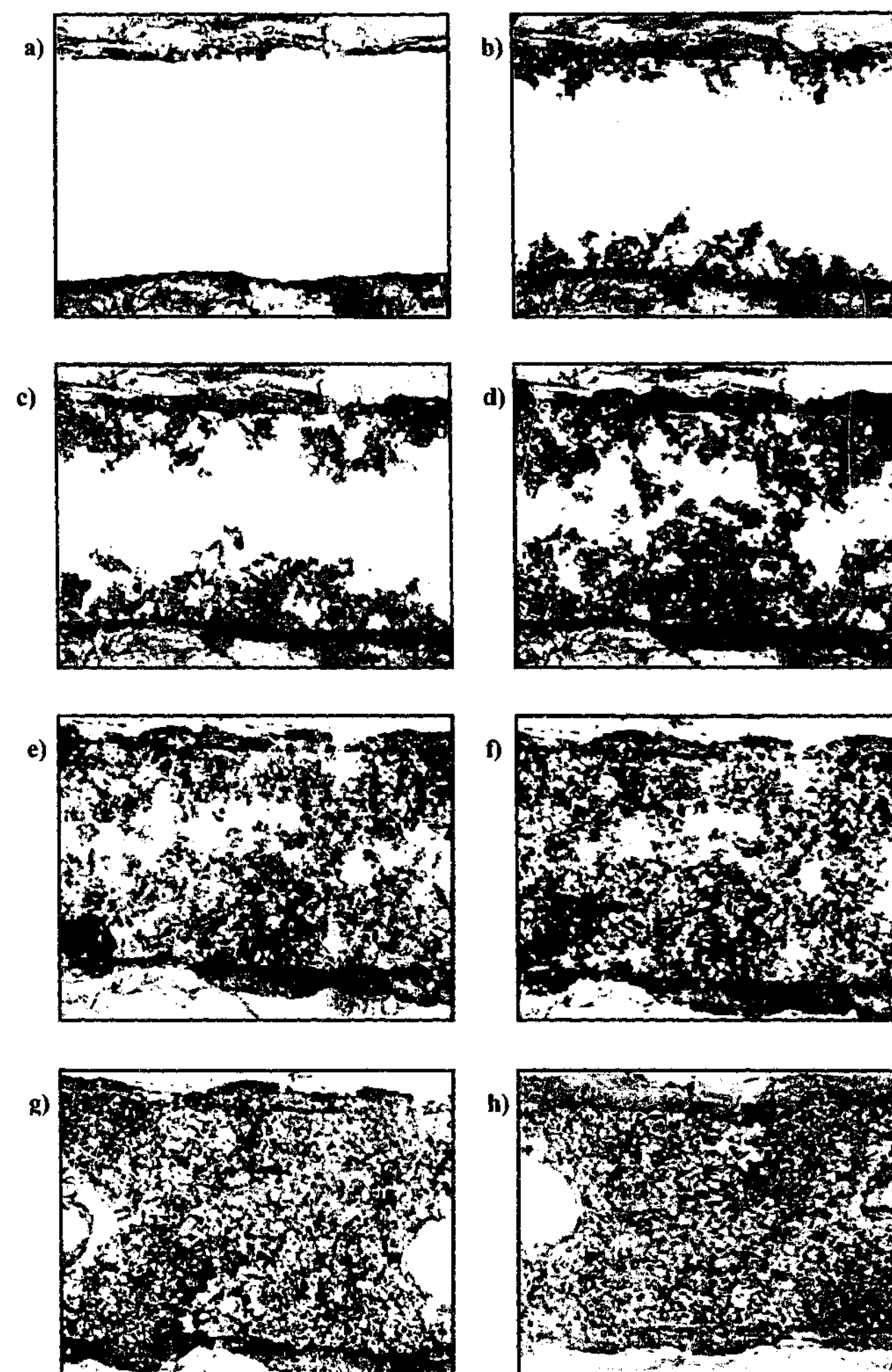


Fig. 3.1.2 PC/LiPF₆ cell cycled at 2 mAcm⁻², 1 Ccm⁻² and ambient temperature. (a-h) 1st cycle and cycles 100, 200, 300, 400, 500, 600 & 700 respectively.

that no path for electron conduction existed, even when the deposits become closely packed in the latter stages of the experiment.

Figure 3.1.3 displays the results of a similar experiment conducted at higher rates 6 mAcm^{-2} , and higher charge 20 Ccm^{-2} . Figure 3.1.4 displays images of the high rate cell in detail. The lithium deposit has a similar appearance to that of the cell operating at 2 mAcm^{-2} (Fig. 3.1.1 & 3.1.2). The deposit quickly fills the cell and the cell voltage increases rapidly after 2 cycles. The majority of the deposit becomes inactive (i.e., dead lithium) although it can be seen that portions are involved in cycling as seen for the deposit on the right hand electrode, Figs. 3.1.4 (d-h).

The images acquired for the conventional electrolyte system demonstrate the problems associated with operating a secondary battery with a lithium metal electrode. The finely divided deposit, likely to be a heterogeneous mass of metallic lithium and electrolyte reduction products, represents an extremely reactive mass. The likelihood of the heat generated by a short-circuit leading to ignition of the deposit (and, hence, the rest of the battery) in the presence of a volatile electrolyte makes the battery impractical for commercial use. Also, the evident loss of capacity with cycling indicates a short cycle-life for a battery without a large excess of lithium metal.

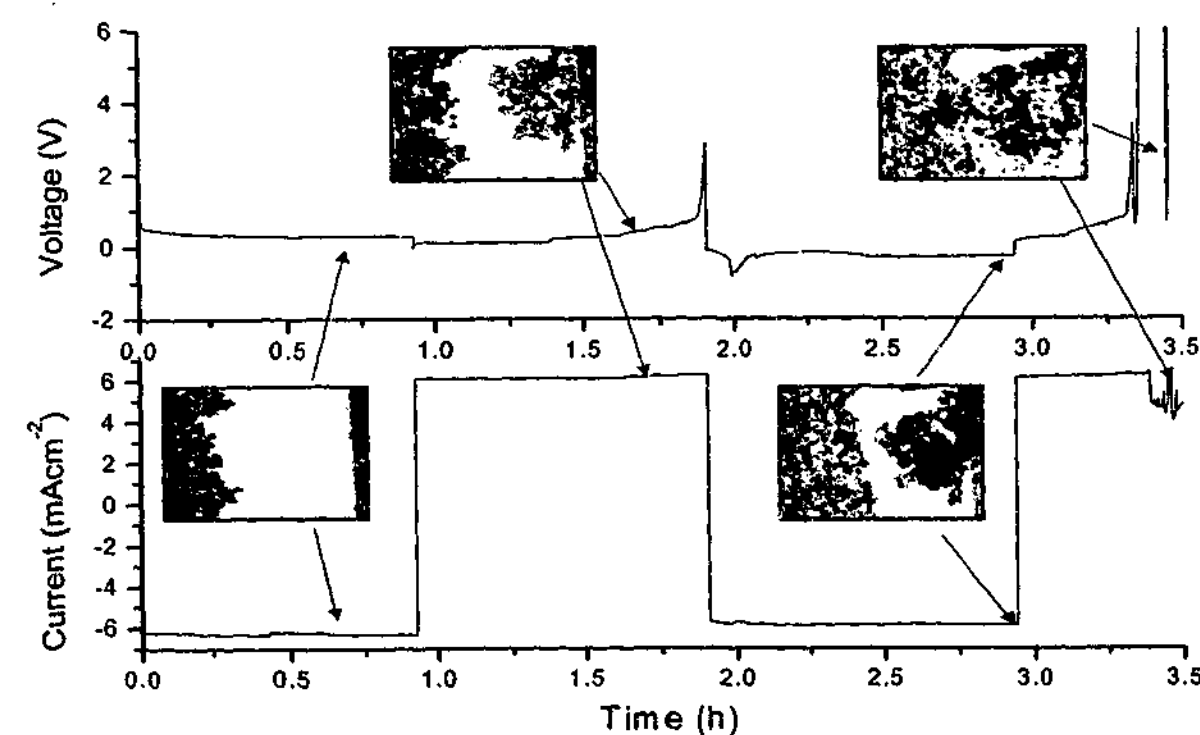


Fig. 3.1.3 PC/LiPF₆ optical cell cycled at 6 mAcm^{-2} and 20 Ccm^{-2} at ambient temperature.



Fig. 3.1.4 PC/LiPF₆ optical cell cycled at 6 mAcm^{-2} and 20 Ccm^{-2} at ambient temperature. Images were taken at $\frac{1}{2}$ hour intervals.

EMI(Tf)₂N:

Figure 3.1.5 shows a representative plot of the voltage profile obtained from an optical cell filled with a 0.5 mol kg⁻¹ EMI(Tf)₂N solution (refer to section 2.1.6 for RTIL nomenclature and conventions), cycled at 1 mA cm⁻² and 1 C cm⁻² at 70 °C. A very resistive component at the interface (discussed later section 3.4.4) required a large potential be applied for 1 mA cm⁻² of current to flow. The CSIRO BCU has a negative potential limit (for acquisition) of -5 V. In this case substantially greater negative potentials were applied, the actual values must be inferred from the positive potentials, which were measured up to 20 V. It was necessary to heat the cell to 70 °C for it to perform at the specified rates. Figure 3.1.6 displays images obtained from the cell during cycling. The 'stained' region in the electrolyte was produced when attempting to cycle the cell at room temperature. Its appearance did not change with subsequent cycling at elevated temperature. The electrolyte level slowly dropped during the experiment as can be seen by the progression of bubbles from left to right (i.e., left of the image is the top of the cell) in Fig. 3.1.6 (d-g). It was not clear if this was due to a leak (although none could be observed) or through some process that consumed the electrolyte. The change in electrolyte level could be accounted for by the observation of liquid pooled within spaces in the Surlyn[®], which had softened at elevated temperature. Gassing from the electrode surface was not observed during the experiment. The colour of the electrolyte was observed to darken as cycling progressed. As can be seen from the images in Figure 3.1.6 the electrode surface became covered in a thick deposit, presumably a product of the reaction between the electrolyte and lithium. The visible changes taking place on the electrode surface, and in the electrolyte itself, suggest that a significant portion of the charge passed was involved in some reaction other than the lithium deposition-dissolution process. The lithium surface morphology remained uniform and free of dendrites or mossy deposits, in stark contrast to the PC/LiPF₆ cell.

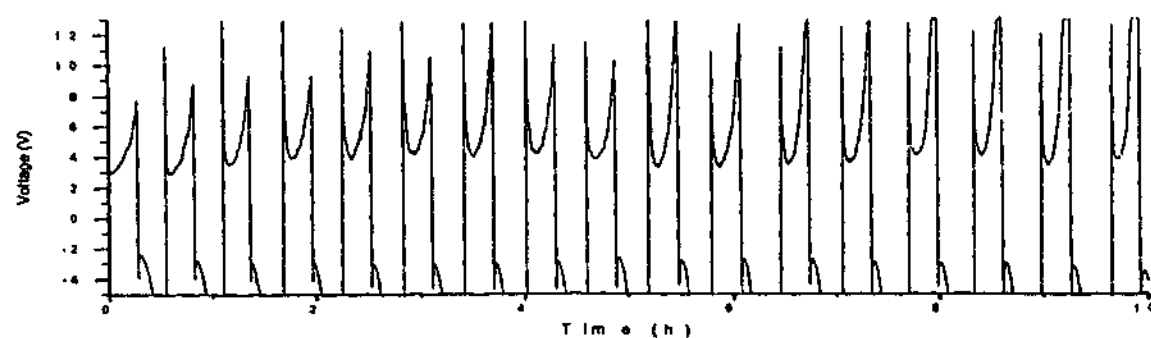


Fig. 3.1.5 Representative voltage profile plot for 0.5 mol kg⁻¹ EMI(Tf)₂N optical cell cycled at 1 mA cm⁻², 1 C cm⁻² and 75 °C.

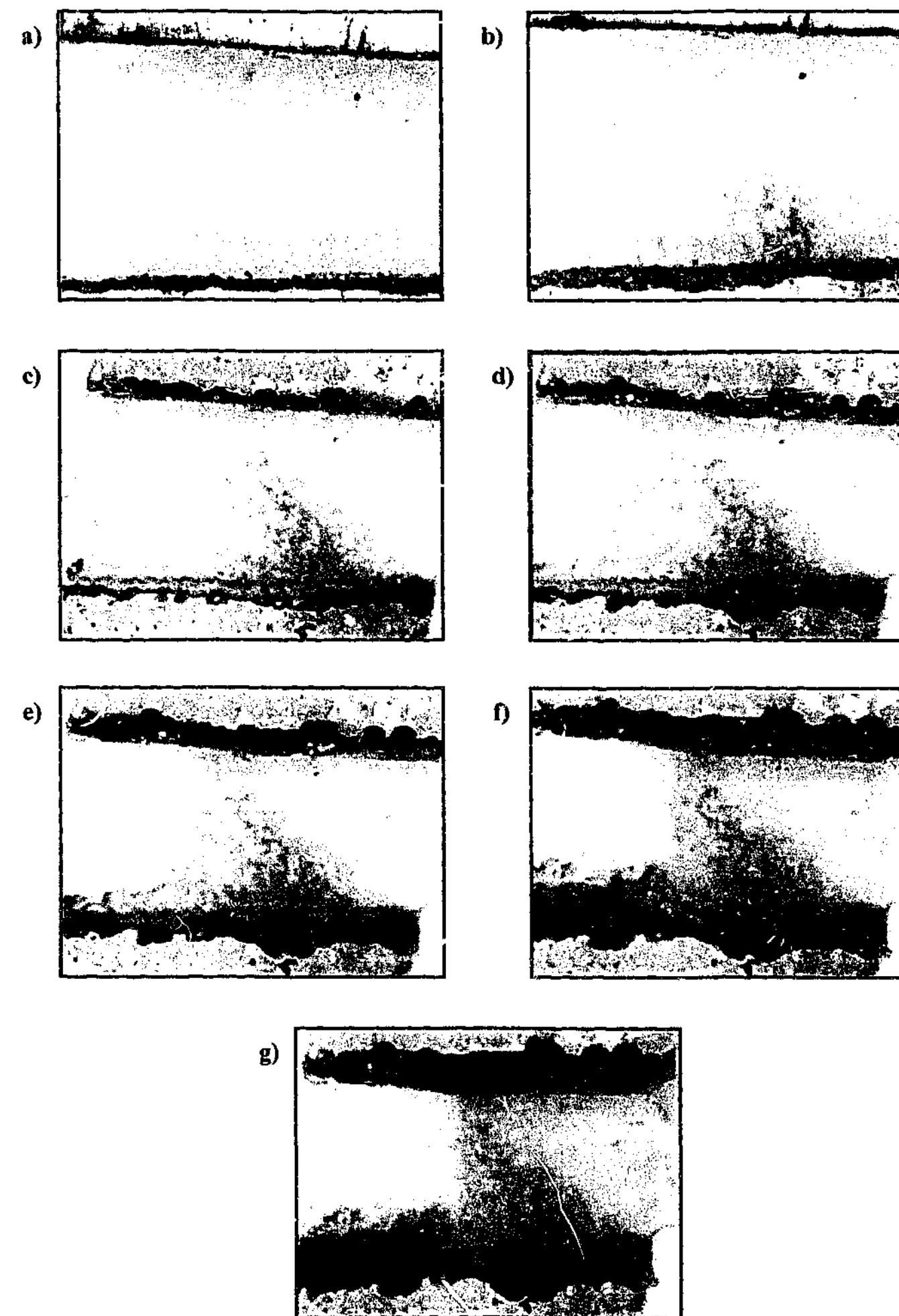


Fig. 3.1.6 Images acquired from a 0.5 mol kg⁻¹ EMI(Tf)₂N optical cell cycled at 1 mA cm⁻², 1 C cm⁻² and 75 °C (a-g) uncycled, 25, 50, 75, 100, 150, 200 cycles, respectively.

$P_{13}BF_4$

Figure 3.1.7 shows representative plots of the voltage profile of an optical cell, filled with a $0.25 \text{ mol kg}^{-1} P_{13}BF_4$ solution, cycled at 0.05 mA cm^{-2} and 0.1 C cm^{-2} at 80°C . Figure 3.1.7a shows ten initial cycles at 0.1 mA cm^{-2} and 0.1 C cm^{-2} at 80°C , a rapid increase in the impedance of the cell takes place in the early cycles. Figure 3.1.7b shows ten representative cycles at 0.05 mA cm^{-2} and 0.1 C cm^{-2} at 80°C after initial cycling at higher rates (0.1 mA cm^{-2}). The cell was able to maintain 0.05 mA cm^{-2} but required a substantial applied potential. Figure 3.1.8 displays images obtained from the cell during charge-discharge cycling. The $P_{13}BF_4$ solution was of particular interest because it forms a conductive plastic crystal phase at ambient temperatures. However, it was necessary to heat the cell to temperatures well above the melt to sustain 0.05 mA cm^{-2} .

The lithium electrode surface did not alter substantially in appearance, nor were there any noticeable changes in the appearance of the electrolyte. Gassing from the electrode surface was not observed. However, on heating, bubbles were observed close to the electrode surface when the solution melted. This possibly indicates the presence of gaseous reaction

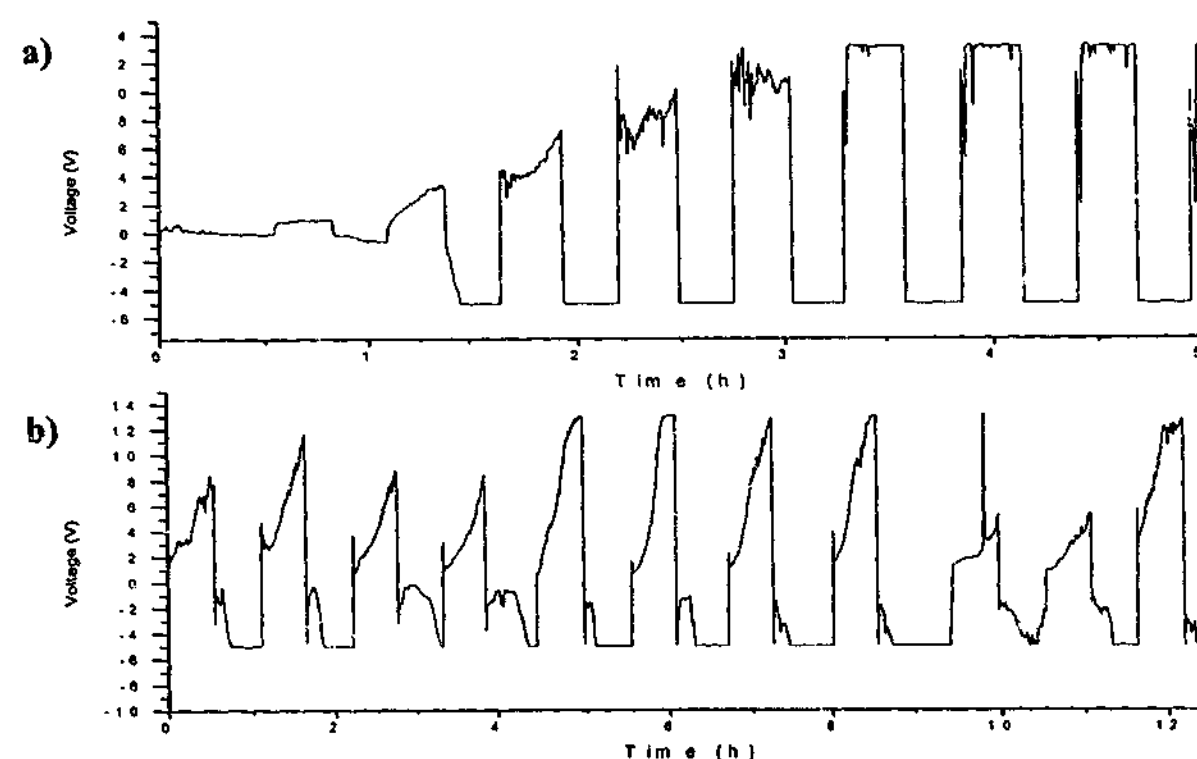


Fig. 3.1.7 Voltage profile obtained from a $0.25 \text{ mol kg}^{-1} P_{13}BF_4$ optical cell, a) initial cycles at 0.1 mA cm^{-2} and 0.1 C cm^{-2} at 80°C , b) representative cycles at 0.05 mA cm^{-2} and 0.1 C cm^{-2} at 80°C .

products trapped in the solid phase. The lithium surface morphology remained uniform and free of dendrites or mossy deposits in contrast to the $PC/LiPF_6$ cell. A noticeable aspect of the images acquired during the experiment was the lack of any change in the appearance of the interface, this indicates that the SEI formed in the $0.25 \text{ mol kg}^{-1} P_{13}BF_4$ electrolyte was stable and did not lead to the formation of dendritic or mossy deposits (at least at the rates used in the experiment). It was not clear from the experiment whether the high cell impedance resulted from the interface or the electrolyte, but it was clear that a compact, stable and 'safe' interface was formed.

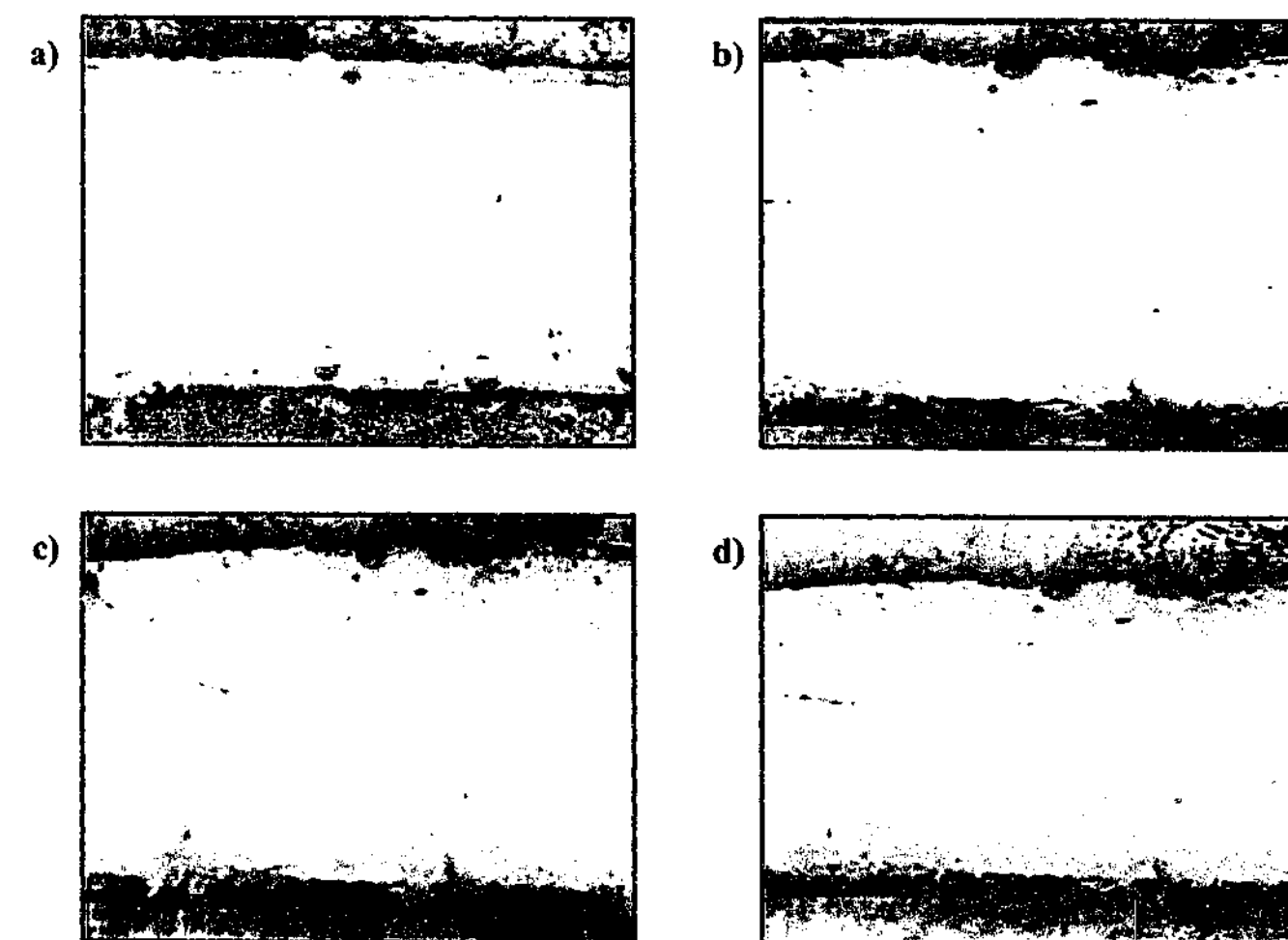


Fig. 3.1.8 Images acquired from a $0.25 \text{ mol kg}^{-1} P_{13}BF_4$ optical cell cycled at 0.05 mA cm^{-2} , 0.1 C cm^{-2} at 80°C , (a-d) uncycled and cycles 20, 30 & 40 respectively.

$P_{13}(Tf)_2N$:

The voltage profile obtained from an optical cell filled with a $0.4 \text{ mol kg}^{-1} P_{13}(Tf)_2N$ electrolyte is shown in Figure 3.1.9. The cell was cycled at 1 mAcm^{-2} and 1 Ccm^{-2} at 75°C for 1500 charge-discharge cycles. Inset into the plot are images of the optical cell showing changes at the lithium | electrolyte interface with cycling. Figure 3.1.10 displays the same images in detail. Figure 3.1.11 presents subsets of the data shown in Figure 3.1.9 in greater detail. Figure 3.1.11a shows the voltage profile from initial cycles at 0.1 mAcm^{-2} and 0.1 Ccm^{-2} at 75°C , the applied potential remained low and stable. Figure 3.1.11b displays the voltage profile obtained from initial cycling at 1 mAcm^{-2} and 1 Ccm^{-2} at 75°C after initial cycling at low rates (0.1 mAcm^{-2}). The cell was able to maintain 1 mAcm^{-2} at low and stable applied potentials. Figure 3.1.11c shows the voltage profile obtained from continued cycling at 1 mAcm^{-2} and 1 Ccm^{-2} at 75°C . An increasing applied potential was required to continue cycling. Continued cycling at high applied potentials resulted in a return to low and stable potentials, Figure 3.1.11d.

During the experiment it was noted that the colour of the electrolyte did not change appreciably. However, one electrode developed a thick brown deposit during charge-discharge cycling. The other electrode remained relatively free of deposit and its appearance did not change appreciably. The voltage profile displayed a corresponding asymmetry; positive potentials corresponded to dissolution at the 'top' electrode and deposition at the 'bottom' electrode. Regions of high applied potential (Fig 3.1.9) corresponded to times when rapid changes in the appearance of the 'bottom' electrode occurred. During periods where low and stable potentials were applied, the appearance of the electrodes changed very little. It seems that the thick deposit on the electrode surface had a strong influence on the cell impedance, indicating that it played a role in lithium transport. This suggests that an SEI was formed in the RTIL and that it was stable, although it exhibited increasing resistivity with cycling. The return to low applied potentials indicated that the SEI was susceptible to breakdown and repair. The lack of a significant change in appearance of one of the electrodes indicated that, under some conditions, a stable and possibly less resistive SEI could form.

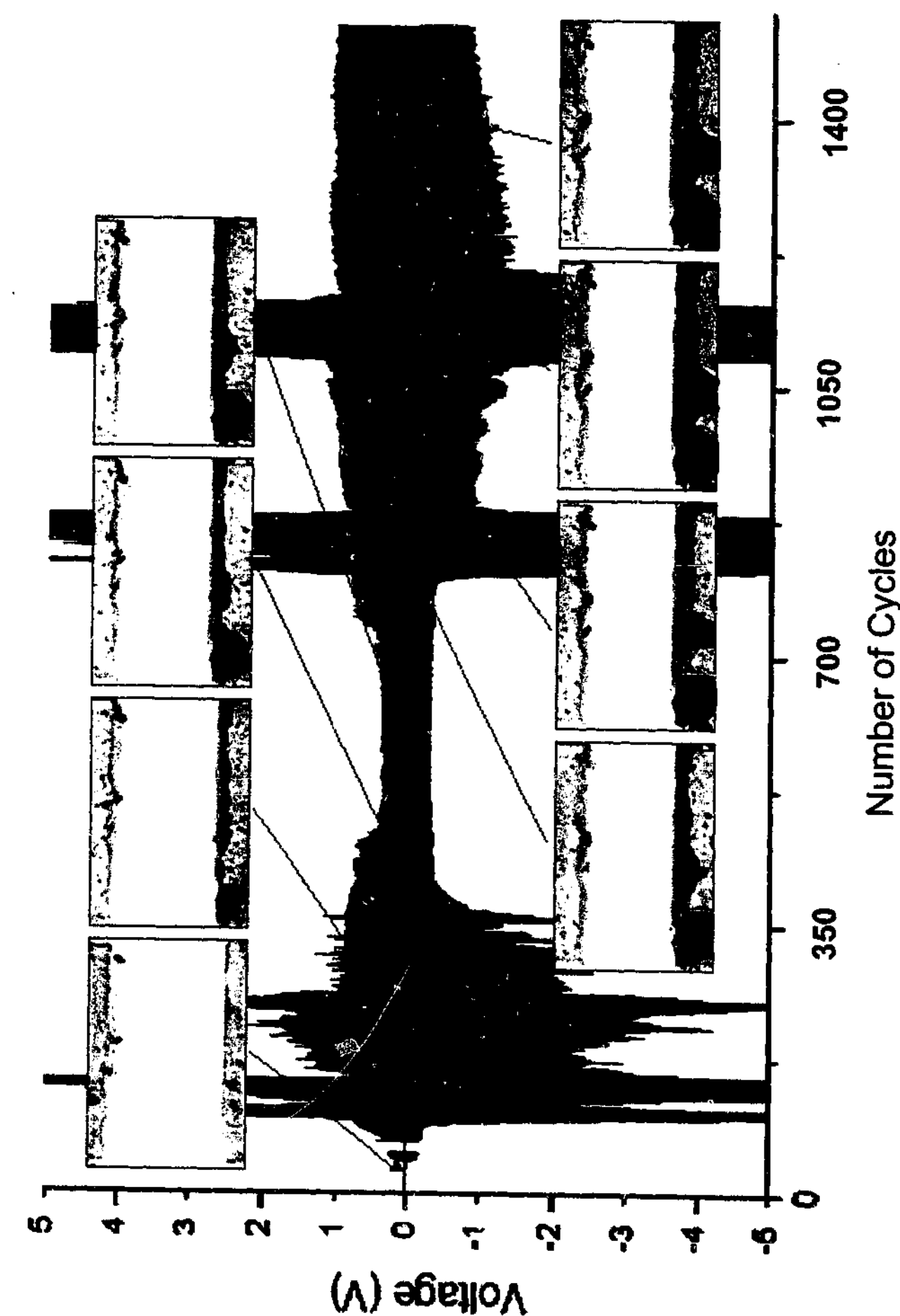


Fig. 3.1.9 Voltage profile for a $0.4 \text{ mol kg}^{-1} P_{13}(Tf)_2N$ cell, 1500 cycles at 1 mAcm^{-2} , 1 Ccm^{-2} and 75°C . Inset: 1st cycle and cycles 200, 400, 600, 800, 1000, 1200 & 1400, respectively.

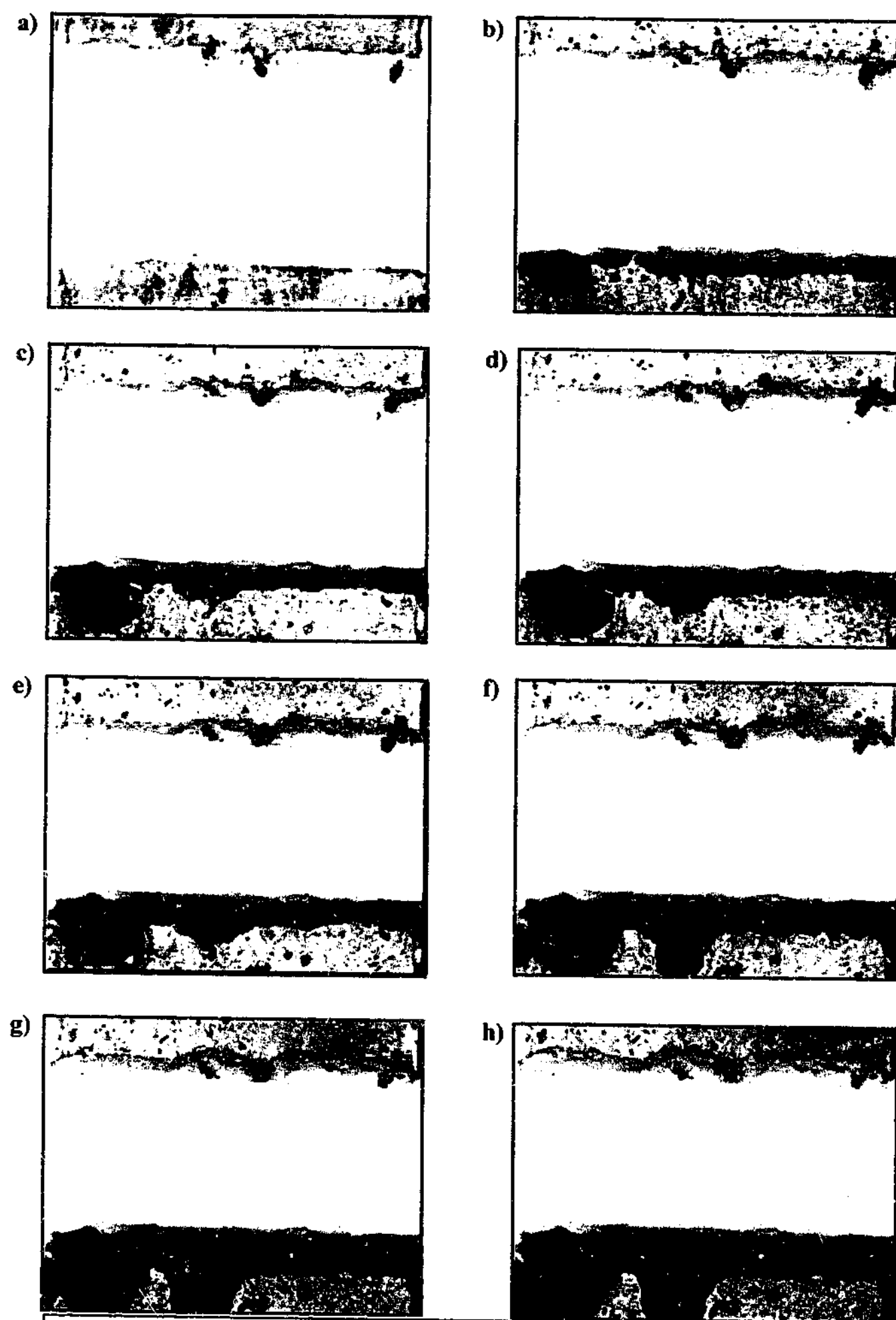


Fig. 3.1.10 Images acquired from a $0.4 \text{ mol kg}^{-1} \text{ P}_{13}(\text{Tf})_2\text{N}$ cell, cycled at 1 mA cm^{-2} , 1 C cm^{-2} and 75°C , a) 1st cycle and cycles 200, 400, 600, 800, 1000, 1200 & 1400, respectively (b-h).

High magnification colour micrographs revealed that the yellowish/brown deposit was largely composed of crystals. Several of these crystals were large and well-defined, Figure 3.1.12a-d. The colour micrographs (Fig. 3.1.12) also revealed the presence of large crystals distributed within the bulk of the lithium electrode. The micrograph in Figure 3.1.12d was obtained from a backlit sample and clearly shows a large crystal that had grown within the lithium foil, allowing light to pass through the sample. The location of the crystal indicates that the electrolyte had penetrated the electrode; most likely between the Surlyn[®] sheath and the foil surface. This situation was not seen to occur in the PC-LiPF₆ cell, which was cycled for a similar number of cycles.

In a cell where (an accidental) high current density was applied, $\sim 250 \text{ mA cm}^{-2}$, gassing from the dissolution electrode (anode) was observed. The lithium surface morphology in the $0.4 \text{ mol kg}^{-1} \text{ P}_{13}(\text{Tf})_2\text{N}$ cell remained uniform and free of dendrites or mossy deposits for 1500 cycles, again in contrast to the PC/LiPF₆ cell.

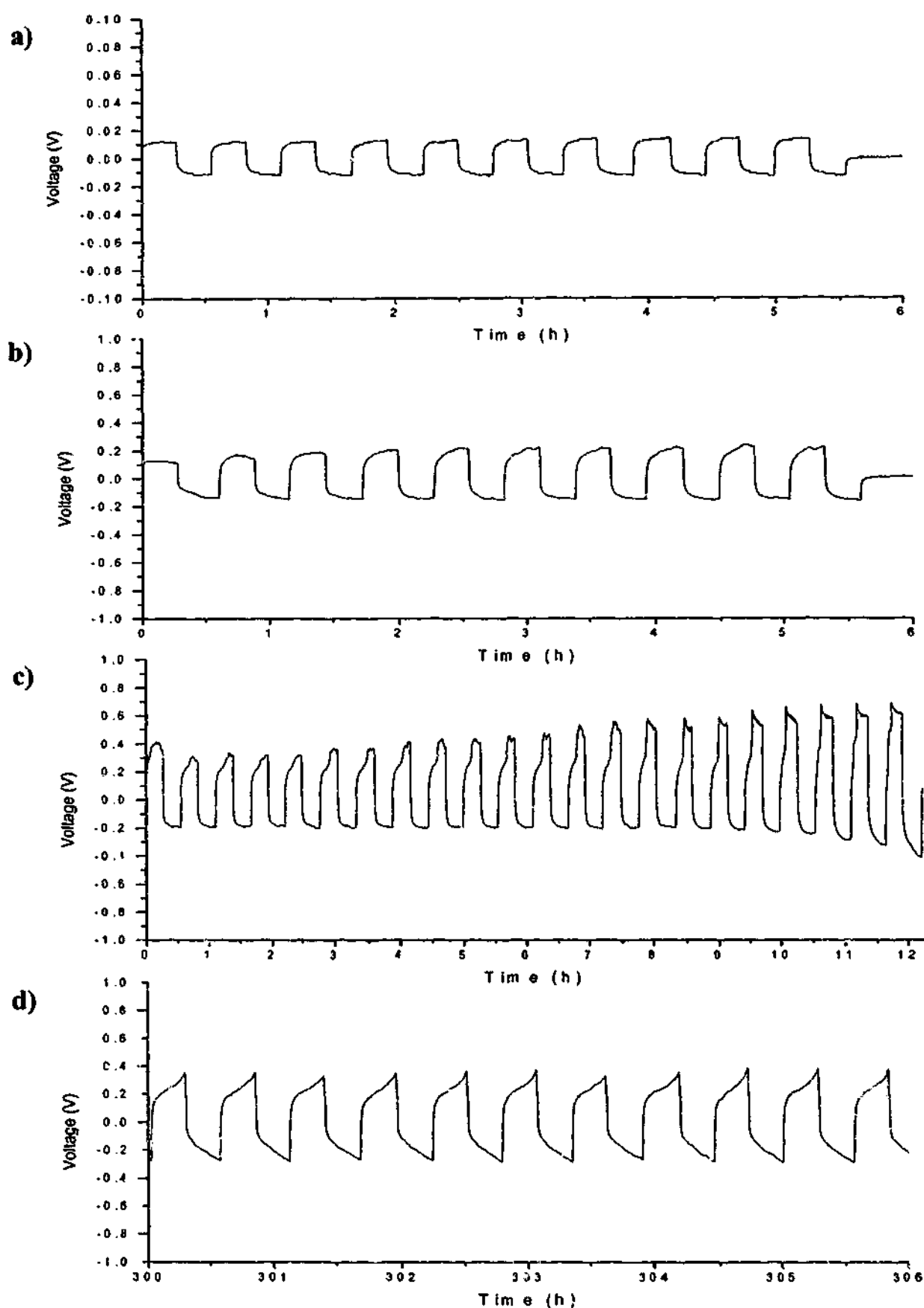


Fig. 3.1.11 Initial cycling of a 0.4 mol kg⁻¹ P₁₃(Tf)₂N optical cell at 75 °C. a) Initial cycling at low current, 0.1 mA cm⁻² & 0.1 C cm⁻² b) initial cycling at 1.0 mA cm⁻² & 1.0 C cm⁻² c) continued cycling at 1.0 mA cm⁻² & 1.0 C cm⁻² d) stable profile after over 500 charge-discharge cycles.

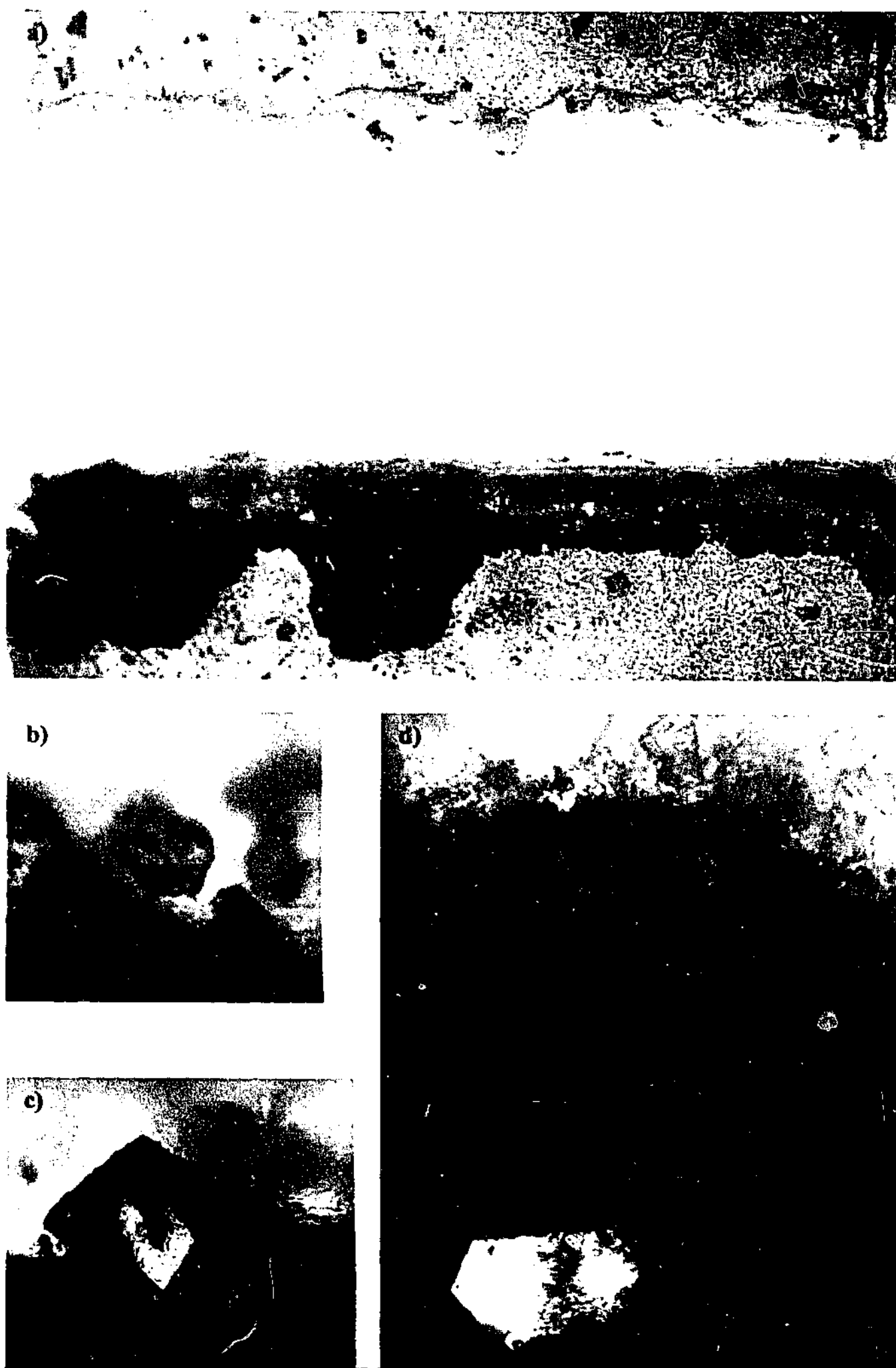


Figure 3.1.12 Colour micrographs obtained from a $0.4 \text{ mol kg}^{-1} \text{ P}_{13}(\text{Tf})_2\text{N}$ optical cell after 1500 charge-discharge cycles. a) $5\times$ magnification, b), c) & d) $40\times$ magnification.

Summary:

A 2-electrode symmetrical lithium optical cell was developed to study novel electrolytes for application with a lithium metal electrode in a secondary cell. Initially the cell failure rate through breakage, leaks, and loss of active electrode surface by overlap of the Surlyn[®] sheath, or other mishaps was unacceptably high. However, refinement of the fabrication method and continued practice reduced the failure rate to acceptable levels. The 2-electrode optical cell provided a sound method of qualitatively assessing the properties of novel electrolytes for application in secondary batteries incorporating a lithium metal electrode, particularly with respect to the evolution of lithium deposit morphology during charge-discharge cycling.

A 1 M LiPF₆ in propylene carbonate solution was studied to establish a measure of the behaviour of a conventional electrolyte when undergoing charge-discharge cycling with a lithium metal electrode. The PC/LiPF₆ electrolyte was found to easily maintain a current density of 2 mAcm⁻² at ambient temperature for a large number of cycles. However, voluminous mossy deposits were observed to develop during charge-discharge cycling. The evolution of the lithium deposit morphology was found to agree with the reports of other workers. The development of an increasing amount of disconnected deposit within the cell led to a loss of electrode active material, and apparently contributed to increased cell impedance, both of which would ultimately result in the failure of a secondary cell.

Several novel RTIL electrolytes were studied to assess their behaviour when undergoing charge-discharge cycling with a lithium metal electrode. None of the RTIL cells were able to operate at comparable rates to the PC/LiPF₆ cell and required heating to enable operation at reasonable rates. In all cases, charge-discharge cycling of the RTIL cells resulted in increased impedance in the cell, as displayed by the necessity to apply an increased potential to maintain a constant current. The 0.4 molkg⁻¹ P₁₃(Tf)₂N cell exhibited the best behaviour, able to continually undergo charge-discharge cycling for over 1500 cycles. However, at times the cell required the application of impractically high potentials to maintain current flow. The 0.4 molkg⁻¹ P₁₃(Tf)₂N cell displayed an ability of the electrolyte to penetrate the electrode and open up new, less resistive pathways for lithium ion transport. However, most importantly, none of the RTIL cells exhibited a tendency to

develop dendritic, or mossy, lithium deposit morphology as a result of charge-discharge cycling.

3.1.2 3-electrode optical cell experiments:

Following the 2-electrode optical cell experiments, a wider survey of RTILs with potential for Li cell applications was conducted. To facilitate comparison between the different systems the optical cell was redesigned to allow a quantitative cycling efficiency measurement to be carried out, as described in section 2.5.1 and 2.6.3. The cell design was modified to incorporate a copper working electrode and a lithium quasi-reference electrode. The conditions under which the majority of experiments were conducted are detailed in Table 3.1.1. Unless otherwise stated, all of the electrolytes were prepared at a concentration of 0.5 molkg⁻¹ of the lithium salt of the anion in solution. The cells were allowed to equilibrate for a period of 24 hours before cycling.

The convention used to plot the potential profiles recorded during the cycling efficiency experiments is that a positive current produces deposition and that deposition occurs at negative potentials. The potential axes of the plots were inverted so that 'up' corresponds to lithium deposition and 'down' corresponds to lithium dissolution.

It should be made clear that the acquisition and presentation of the images for this work suffered a reduction in clarity and resolution compared to that visible through the eyepiece of the microscope at the time of the experiment. Thus, at times, notes made during the acquisition of the images provide more information than the image itself.

Table 3.1.1 Parameters used in the optical cell cycling efficiency measurements.

Deposition current	(I _{dep})	0.25 mAcm ⁻²
Excess charge	(Q _{ex})	1 Ccm ⁻²
Dissolution current	(I _{diss})	0.25 mAcm ⁻²
Cycled fraction of charge	(Q _{ps})	0.25 Ccm ⁻²
Temperature		50 °C
Electrode separation		2 mm
Volume of electrolyte		~50 µL

EMIDCA:

Conductivity (@ 22 °C)	22 mScm ⁻¹	8
Viscosity (@25 °C)	21 cP	9,10
Density (@20 °C)	1.06 gcm ⁻³	9,10
Affinity for water	High	9,10
T _m (°C)	-21	9,10
T _{decomp} (°C)	275	11

EMIDCA is the least viscous (and most conductive) of all known ionic liquids^{9,10} and for this reason alone warrants investigation for electrolyte applications. Referring to Figure 3.1.13 it can be seen that the deposition potential did not reach a potential where lithium deposition was likely to occur, indicating that some other process was active. The experiment indicated a cycling efficiency for lithium of less than 3 %.

During the experiment it was noted that gassing occurred at the lithium reference electrode (RE), suggesting that a spontaneous process was occurring at the lithium surface. Figure 3.1.14 displays images taken during the cycling efficiency experiment, no obvious change can be seen other than gas evolution at the surface of the lithium counter electrode (Fig 3.1.14c), during dissolution, and pronounced gas evolution at the end of the experiment at open circuit (Fig. 3.1.14d). Figure 3.1.15 shows images acquired after the deposition phase of the experiment (Fig. 3.1.15a-d) and after the cycling phase of the experiment (Fig. 3.1.15e-h). Images a-c show features present on the surface of the copper electrode, there is no indication of the presence of a lithium deposit. Instead, a fine crystalline precipitate can be observed evenly distributed throughout the cell, in fact a large amount of precipitate had settled on the back glass of the cell (image c). The features visible in images a) and b) are characteristic of dendritic lithium deposits, possibly indicating that lithium deposition had occurred but had quickly reacted to form the crystalline deposit. Image d) shows the lithium counter electrode (CE) surface, showing a finely divided surface structure and non-metallic appearance. Images (e & f) show the surface of the copper working electrode (WE) after the cycling experiment. Not surprisingly, given the lack of any sign of a reversible process in Fig. 3.1.13, there is no obvious change in the appearance from the

post deposition images. Image g) shows the surface of the lithium counter electrode, the surface appeared corroded and was covered in a fine white precipitate. Image h) shows the surface of the lithium reference electrode which also appeared to have corroded. At the conclusion of the experiment it was noted that the colour of the electrolyte had changed from pale yellow to pale green.

Based on the observations made during the course of this experiment it was concluded that EMIDCA was not stable in contact with lithium and formed a poorly passivating surface film. Furthermore the EMIDCA electrolyte was not able to reversibly deposit and strip lithium to any appreciable degree and instead reacted with lithium to form a precipitate of unknown composition. On the basis of these conclusions EMIDCA was dismissed as a candidate electrolyte solvent.

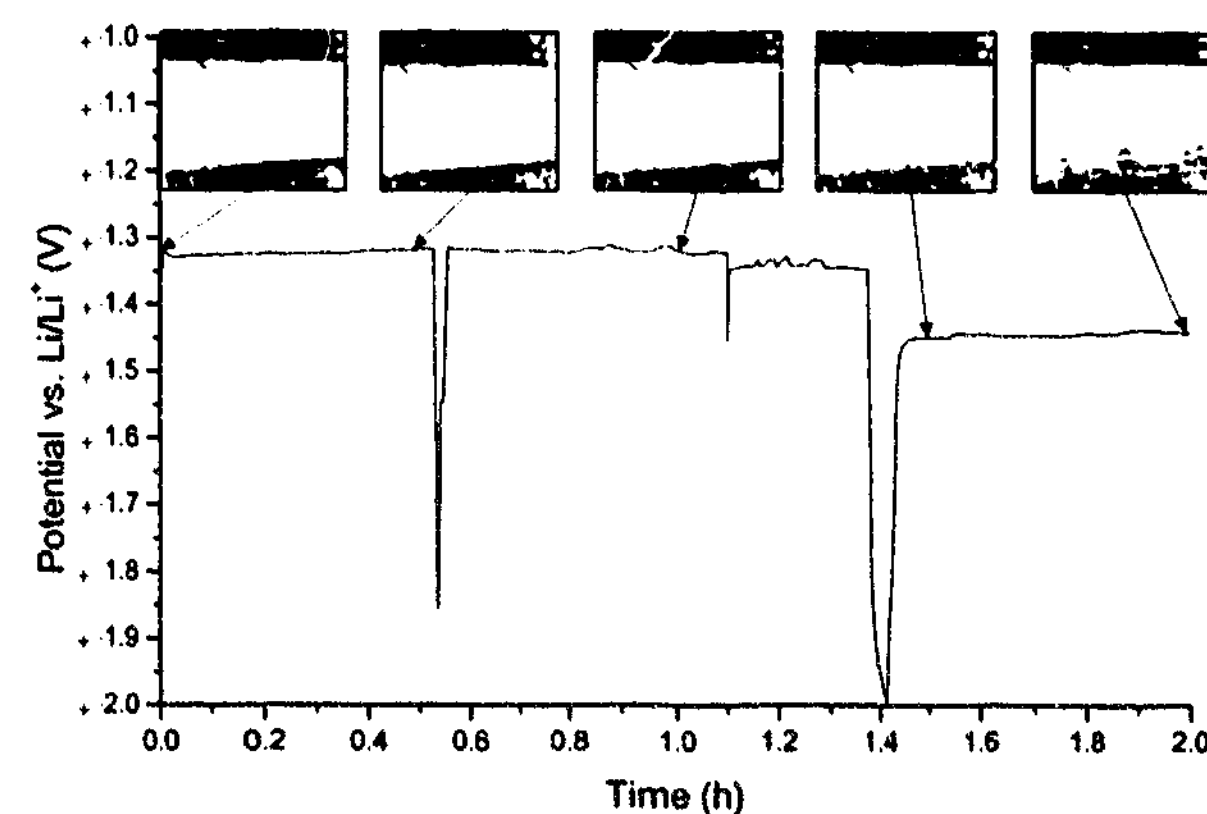


Fig. 3.1.13 0.5 mol kg⁻¹ EMIDCA cycling efficiency potential profile. Gassing at open circuit evident at counter electrode.

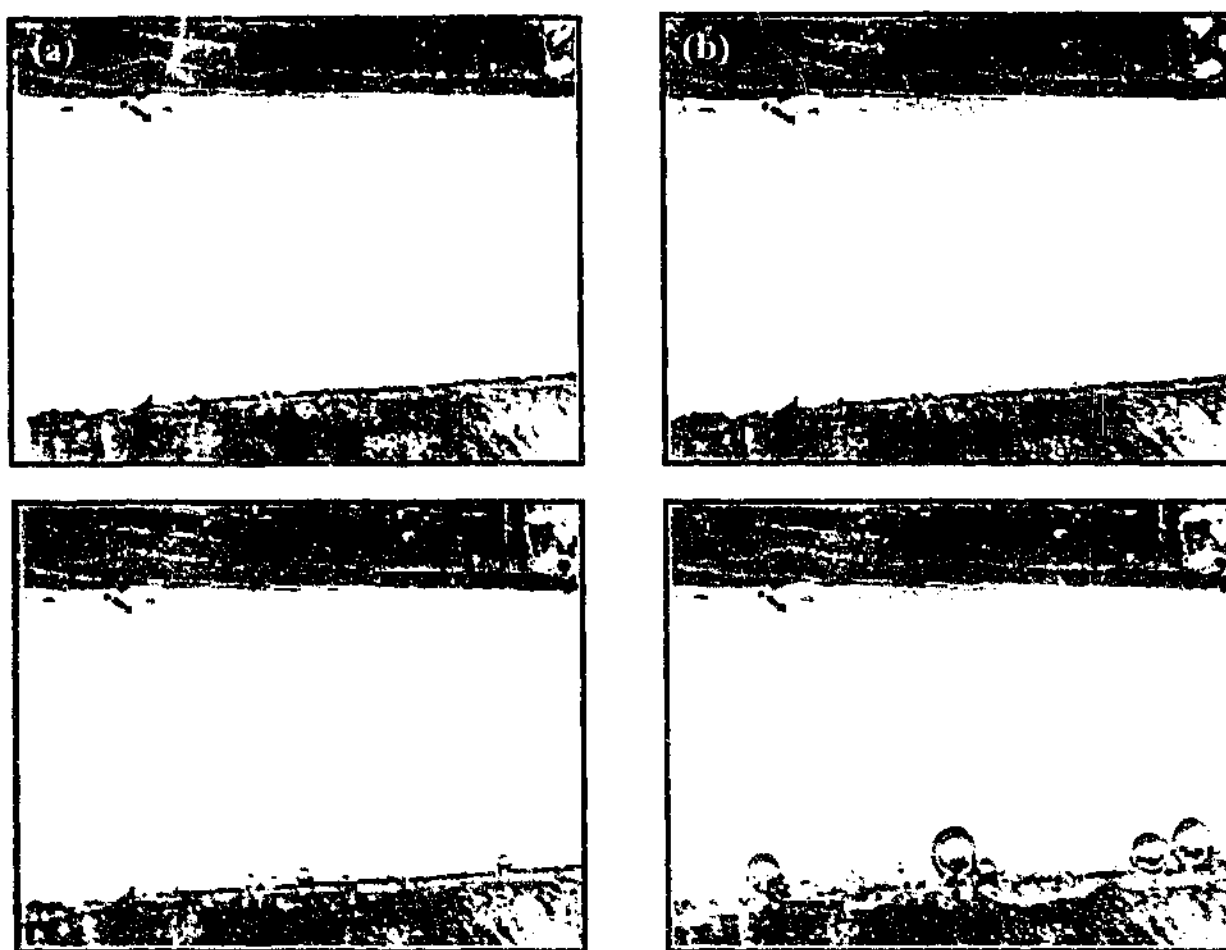


Fig. 3.1.14 0.5 mol kg⁻¹ EMIDCA cycling efficiency images, (a) Initial, (b) 60 min, (c) 90 min, (d) 120 min - gassing at open circuit.

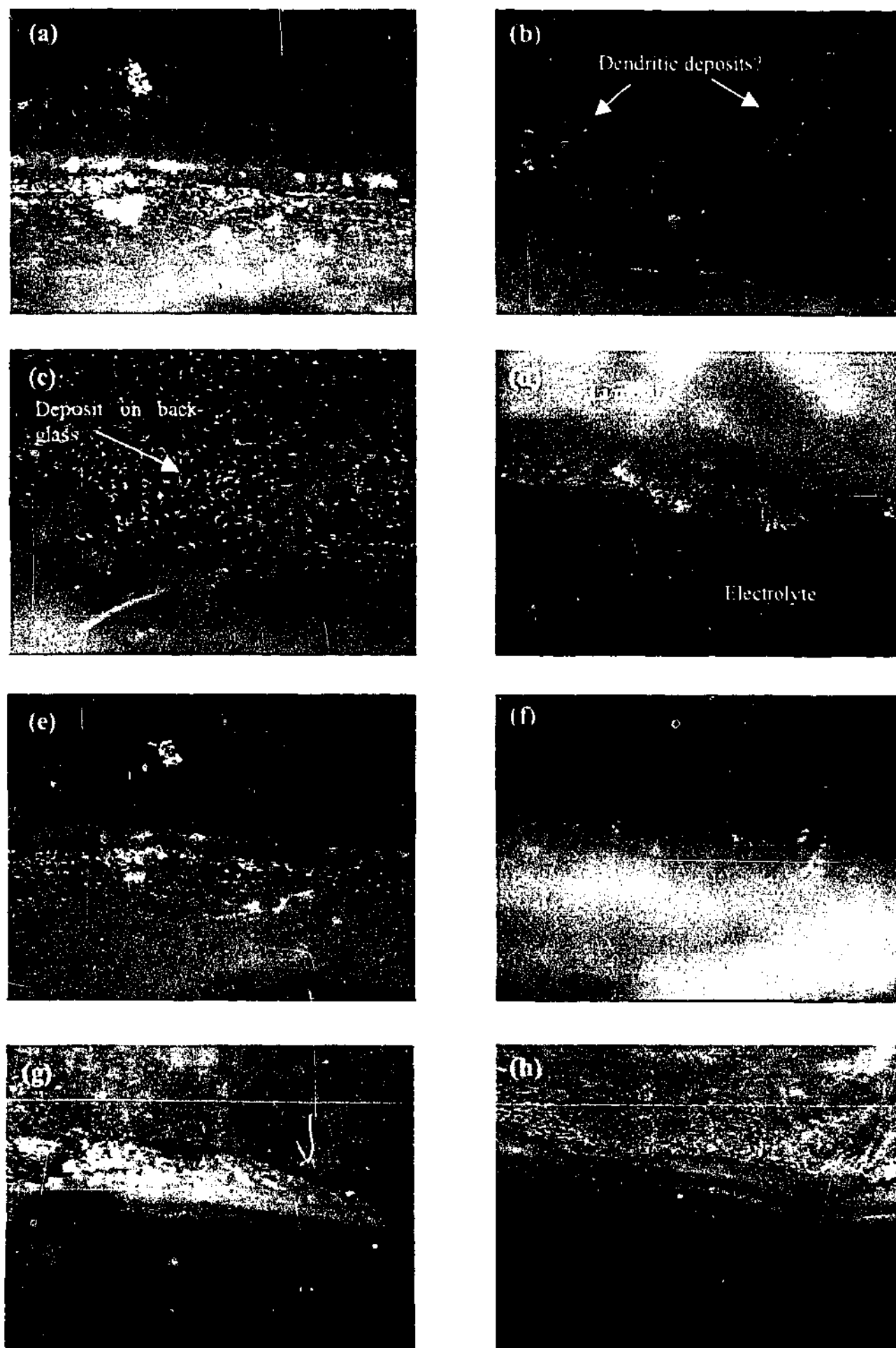


Fig. 3.1.15 0.5 mol kg⁻¹ EMIDCA (a-c) post deposition Cu working surface, (d) post deposition Li counter surface, (e & f) post cycling Cu working surface, (g) post cycling Li counter surface, (h) post cycling Li reference electrode.

EMIBF₄:

Conductivity (@ 25 °C)	9.8 mScm ⁻¹	12
Viscosity (@ 20 °C)	66.5 cP	13
Density (@ 25 °)	1.26 gmL ⁻¹	13
Affinity for water	Moderate	13,14
T _m (°C)	11	15
T _{decomp} (°C)	450	15

EMIBF₄ has previously been investigated as a potential electrolyte for lithium batteries^{16,17} and a patent¹⁸ exists that claims its use with water as an additive (to form a passivating film).

Figure 3.1.16 shows colour images of the lithium counter electrode surface prior to the cycling efficiency experiment. The surface had reacted with the electrolyte and appeared to be continuing to do so (image a). The images show evidence of substantial corrosion at the electrode surface. The bubbles visible at the surface differed in appearance to gas bubbles present elsewhere in the cell and seem to indicate a liquid reaction product that was not miscible with the RTIL. Figure 3.1.17 shows a plot of the potential profile from the cycling efficiency experiment. For this experiment a deposition charge (Q_{ex}) of 10 Ccm⁻² was used (as opposed to 1 Ccm⁻², used for the majority of experiments). The deposition potential rose continuously after an initial period of relative stability. This coincided with substantial gas evolution at the working electrode surface (Fig. 3.1.18). Extensive corrosion is visible at the lithium counter electrode surface along with the formation of a thick white surface film. Following deposition there was no evidence of a lithium deposit on the copper surface, a small amount of a fine crystalline deposit was scarcely visible. The experiment indicated a cycling efficiency of less than 1 %.

Both the lithium counter and reference electrode surfaces exhibited substantial corrosion although the reference exhibited a uniform surface, whereas large pits developed in the counter surface during dissolution (Fig. 3.1.18). It was noted that the lithium surface was discoloured close to the electrolyte interface (adjacent to the passivating film).

Based on the observations made during the course of this experiment it was concluded that EMIBF_4 was not stable in contact with lithium and formed a thick passivating surface film. Furthermore the EMIBF_4 electrolyte was not able to reversibly deposit and strip lithium to any appreciable degree and instead reacted with lithium to form a precipitate of unknown composition, as well as what appeared to be a liquid reaction product. On the basis of these conclusions EMIBF_4 was dismissed as a candidate electrolyte solvent.

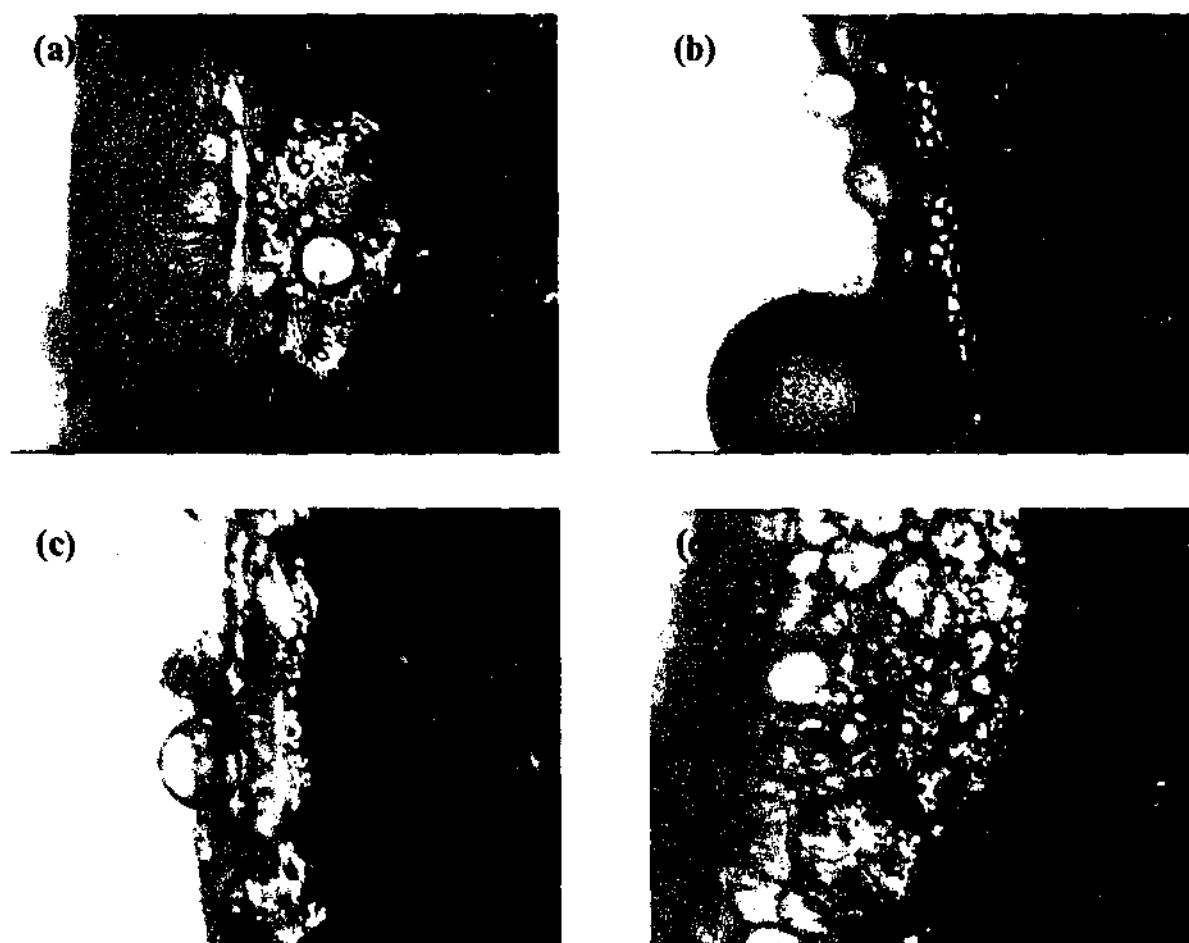


Fig. 3.1.16 0.5 mol kg^{-1} EMIBF_4 images uncycled Li CE surface (a) 40x, (b) 10x, (c) 10x, (d) 40x.

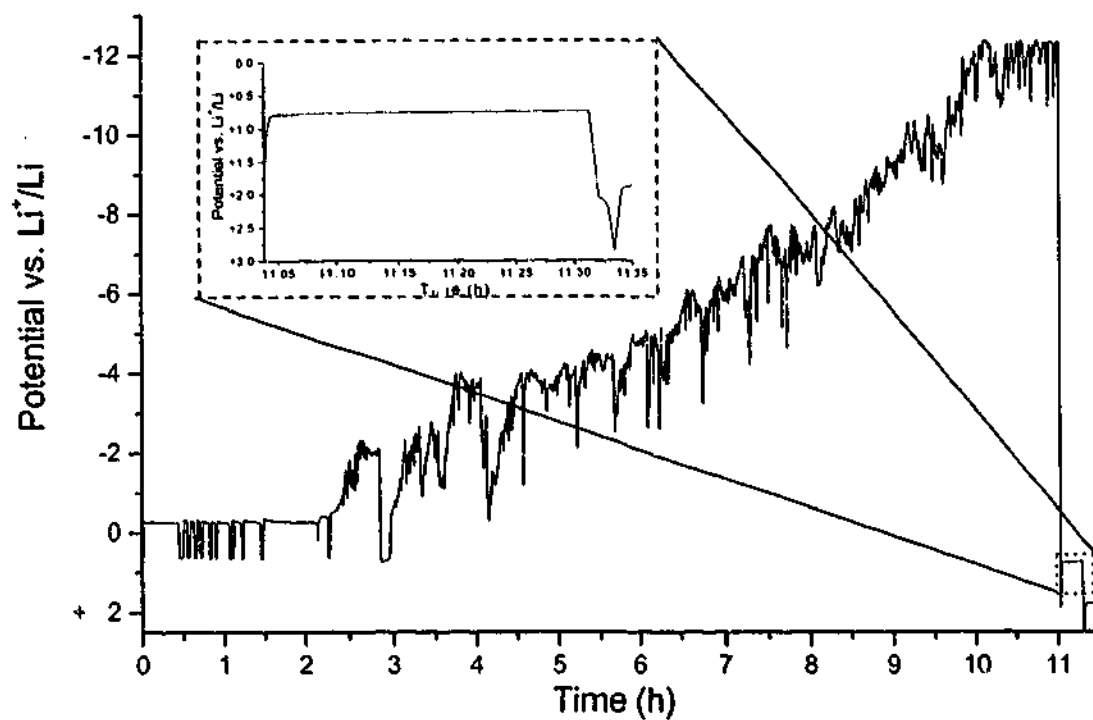


Fig. 3.1.17 0.5 mol kg⁻¹ EMIBF₄ cycling efficiency potential profile. Inset shows the cycling phase of the experiment.

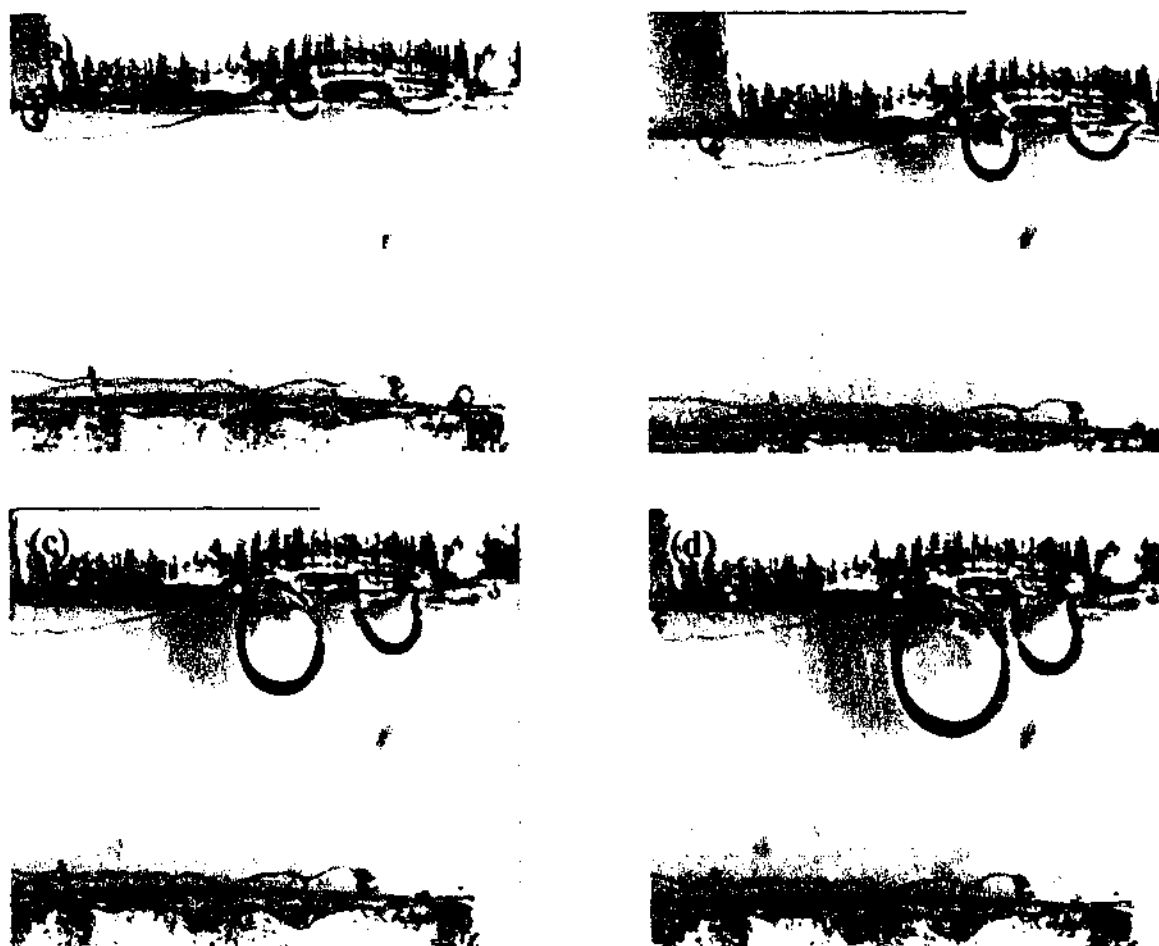


Fig. 3.1.18 0.5 mol kg⁻¹ EMIBF₄ cycling efficiency image (a) initial, (b) 3.75 h, (c) 7.5 h, (d) 11.25 h. Pronounced gas generation visible at the WE during deposition.

EMI(Tf)₂N:

Conductivity (@ 20 °C)	8.8 mScm ⁻¹	19
Viscosity (@20 °C)	34 cP	19
Density	1.52 gcm ⁻³	19
Affinity for water	hydrophobic	19
T _m (°C)	-3	19
T _{decomp} (°C)	420	20

Six consecutive cycling efficiency experiments were conducted in the EMI(Tf)₂N optical cell. By conducting a series of experiments in this manner, the influence of previous cycling experiments could be ascertained, particularly with respect to the influence of the presence of passivating films and irreversible surface deposits. The experiments can be viewed as being analogous to a cell where the anode had been completely consumed during discharge.

Figure 3.1.19 shows the potential profile recorded during the first experiment. The profile displays a significant process, at approximately 1.3 V 'above' the lithium potential, that occurred before lithium deposition could commence. This process could represent the reduction of a number of possible species;

1. the EMI⁺ cation,
2. the (Tf)₂N⁻ anion,
3. impurities such as moisture.

Given that the purity and moisture content of the RTILs have been carefully controlled (Experimental 2.1.6), it is unlikely that a process related to an impurity could consume such a large amount of charge, although a catalytic process could explain the behaviour. Thus, it is most likely that the process was related to either the anion or cation.

After approximately 10 minutes the potential shifted to values where lithium deposition should have occurred, this type of behaviour typifies the formation of a passivating film (or

SEI). The formation of a SEI and its likely composition will be the topic of a later section (section 3.4). From the data presented in Fig. 3.1.19, it can be deduced that a surface film that prevents (or at least slows) further reduction of the electrolyte was formed.

The images shown in Figure 3.1.20 clearly show that lithium deposition had occurred. The lithium deposit was uniformly distributed across the surface, had a 'bright' appearance and exhibited hemispherical morphology; the formation of dendrites was also visible (particularly in image c).

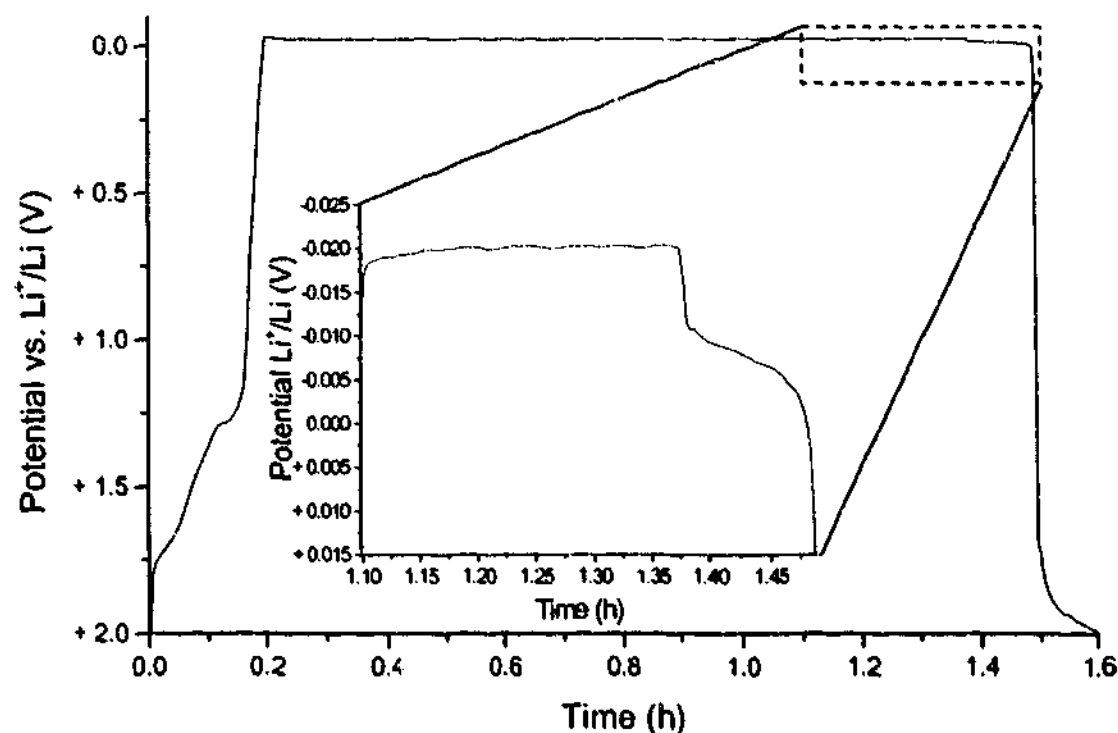


Fig 3.1.19 0.5 mol kg^{-1} $\text{EMI}(\text{Tf})_2\text{N}$ cycling efficiency potential profile. 1st experiment, inset shows the cycling phase of the experiment.

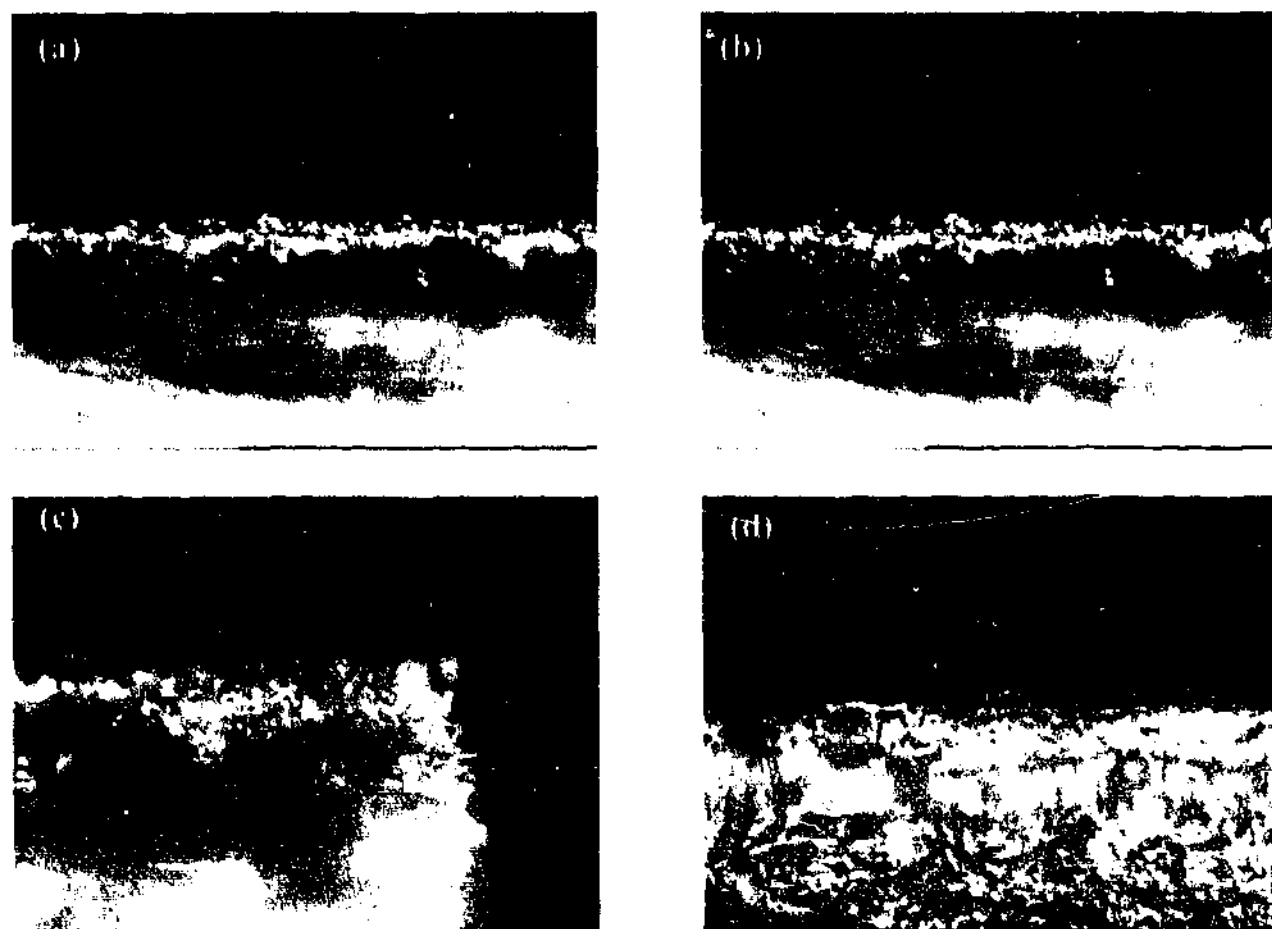


Fig. 3.1.20 0.5 mol kg⁻¹ EMl(Tf)₂N post deposition images (1st experiment), Cu working electrode surface (a) 20x, (b) 20x, (c) 40x, (d) 'backside' image 20x.

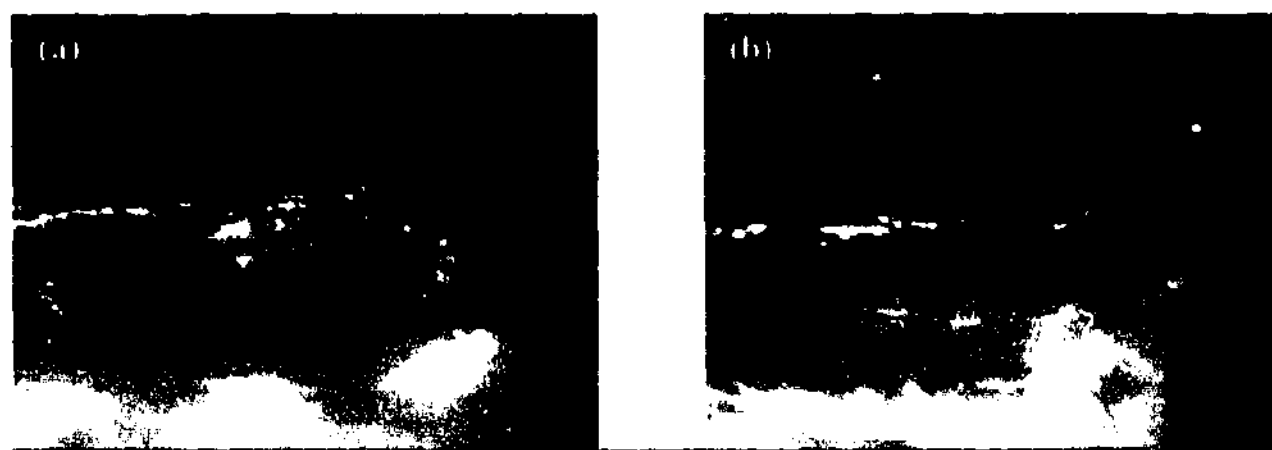


Fig. 3.1.21 0.5 mol kg⁻¹ EMl(Tf)₂N post cycling images (1st experiment), Cu working electrode surface (a) 40x, (b) 20x.

The images shown in Figure 3.1.21 were taken of the copper surface after the cycling phase of the experiment. The copper surface was relatively bare, the remnants of the lithium deposits that had existed previously being barely visible. The cell OCV was ~ 2 V. No obvious changes in the appearance of the lithium counter electrode were visible. The cycling phase of the experiment indicated dissolution of lithium for 0.4 of a cycle, giving a cycling efficiency of approximately 10 %.

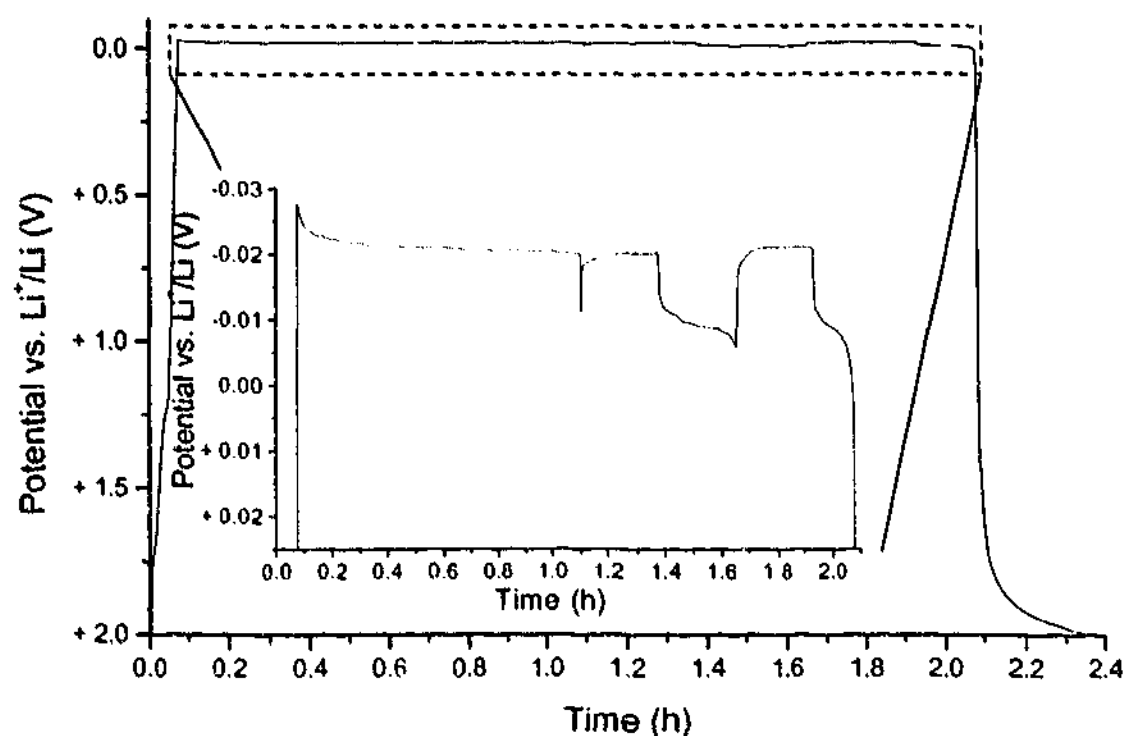


Fig. 3.1.22 0.5 molkg⁻¹ EMI(Tf)₂N cycling efficiency potential profile. 2nd experiment, inset shows the cycling phase of the experiment.

Figure 3.1.22 shows the potential profile recorded during the second experiment. Again the profile displays an initial plateau at approximately 1.3 V 'above' the lithium potential. In this case it did not last as long and the potential shifts to lithium deposition after approximately 5 minutes. The images shown in Figure 3.1.23 show that the lithium deposit had a similar appearance to that of the first experiment (Fig. 3.1.20), although perhaps slightly more uniform in appearance and distribution. The cycling phase of the experiment extended for 1.6 cycles, giving a cycling efficiency of approximately 30 %.

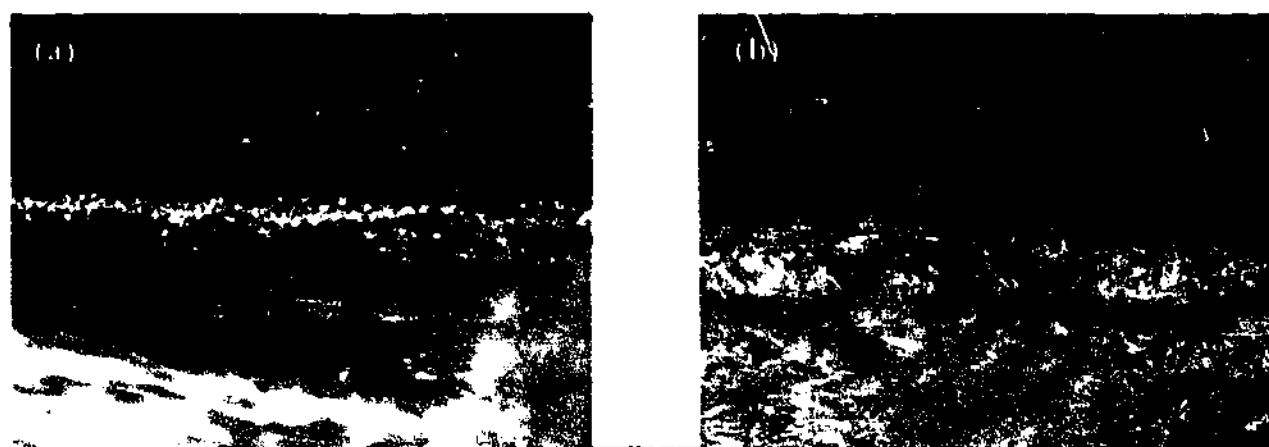


Fig. 3.1.23 0.5 molkg⁻¹ EMI(Tf)₂N post deposition images (2nd experiment) Cu working electrode surface (a) 20x, (b) 20x.

Figure 3.1.24 shows the potential profile recorded during the third experiment. Again the profile displays an initial plateau at approximately 1.3 V 'above' the lithium potential. The plateau extends for approximately 10 minutes. The cycling phase of the experiment extended for almost 5 cycles, giving a cycling efficiency of approximately 55 %. Figure 3.1.25 shows the potential profile recorded during the fourth experiment. The data for the deposition phase of the experiment was lost. The cycling phase of the experiment extended for 7.5 cycles, giving a cycling efficiency of approximately 65 %. The images presented in Figure 3.1.26 were acquired after the deposition phase of the fourth experiment and they display a marked difference to those presented previously (Fig. 3.1.20 & 3.1.23). The lithium deposit displays a significantly improved morphology, being more uniform and evenly distributed (images a-d). The individual particle sizes also appear significantly reduced, consistent with an increased number of nucleation sites. This is the first indication of what will become a recurring theme in these experiments, the close relationship of deposit morphology and cycling efficiency. In this case the improved morphology is coincident with increased cycling efficiency. Also shown in Figure 3.1.26 are micrographs displaying the onset of dendritic deposition (images e & f).

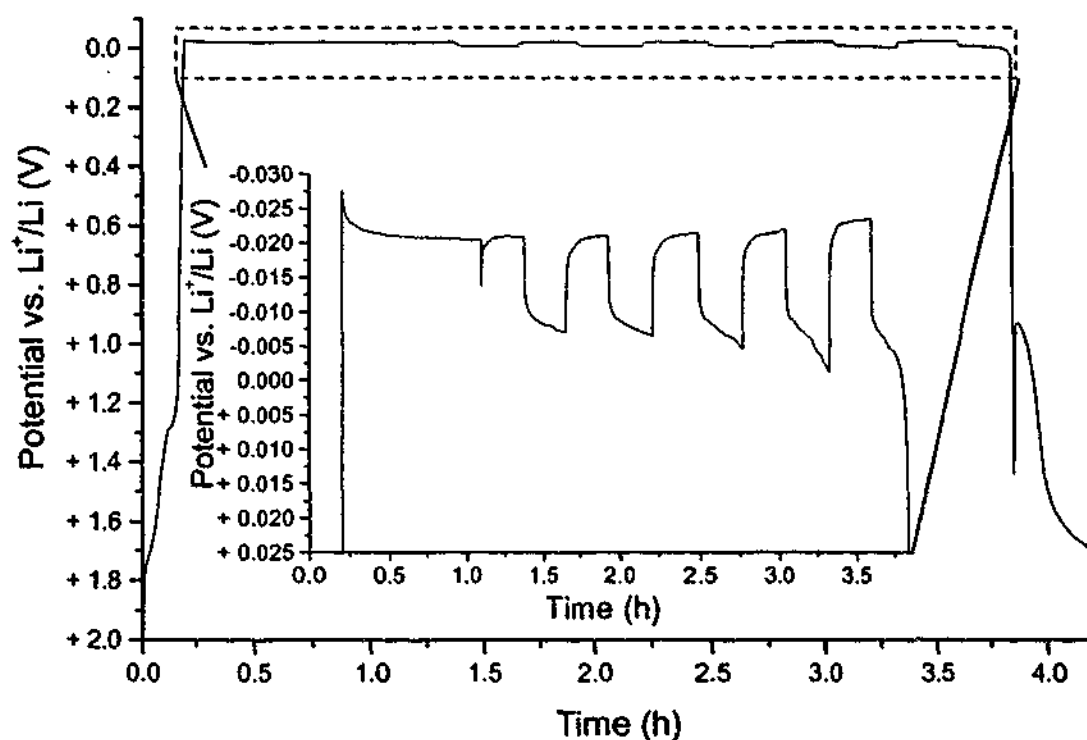


Fig. 3.1.24 0.5 molkg⁻¹ EMI(Tf)₂N cycling efficiency potential profile. 3rd experiment, inset shows the cycling phase of the experiment.

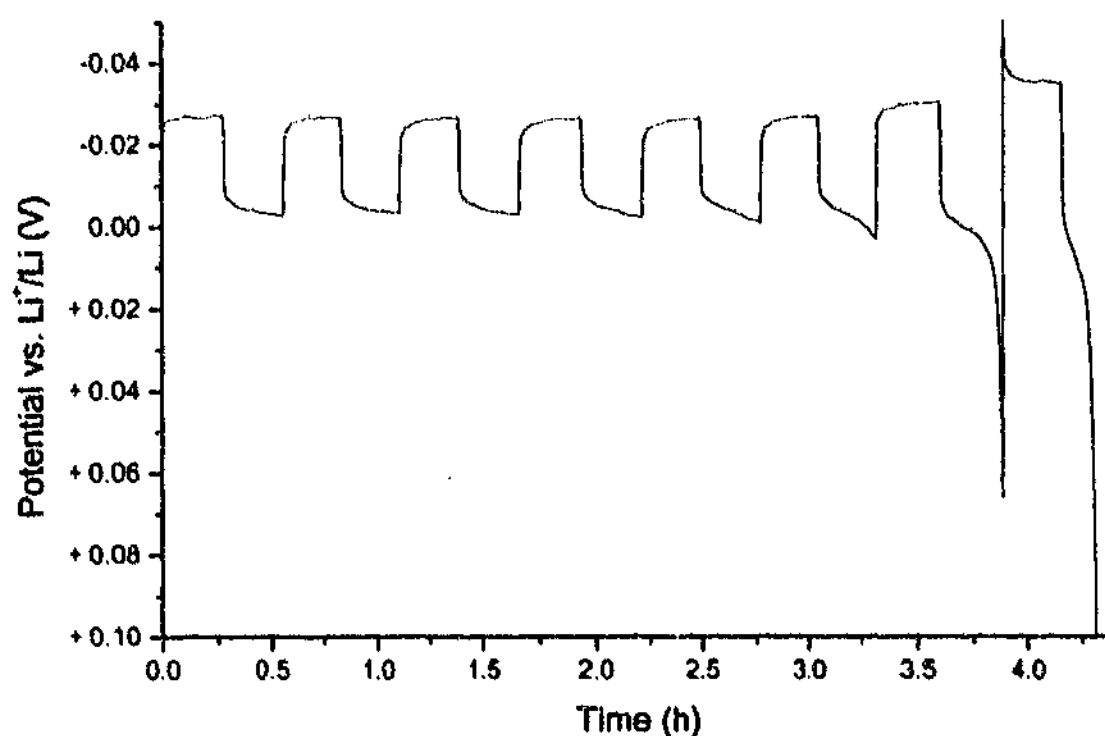


Fig. 3.1.25 $0.5 \text{ mol kg}^{-1} \text{ EMI(Tf)}_2\text{N}$ cycling efficiency potential profile. 4th experiment. Data for the deposition phase was lost.

The images in Figure 3.1.27 were acquired after the cycling phase of the experiment and are similar in appearance to those shown in Figure 3.1.21. However, a larger amount of material persisting on the electrode surface is visible, particularly in image d). Image c) shows the surface of the cycled lithium counter electrode, the image is not particularly clear; however no large features (e.g., dendrites) are in evidence. The surface in general (here notes made during examination of the sample under the microscope are being cited) is uniform and free of dendrites. The lithium counter electrode surface did not change markedly throughout the experiment. This is another recurring theme that became apparent throughout this series of experiments. The deposit morphology on the lithium electrode behaved differently to the copper electrode, generally exhibiting a reduced tendency to form dendrites. In fact, dendrites on the lithium surface were only observed on a couple of occasions. This observation will be investigated in greater detail in later sections (Sections 3.2 & 3.4) and highlighted in other examples in this section.

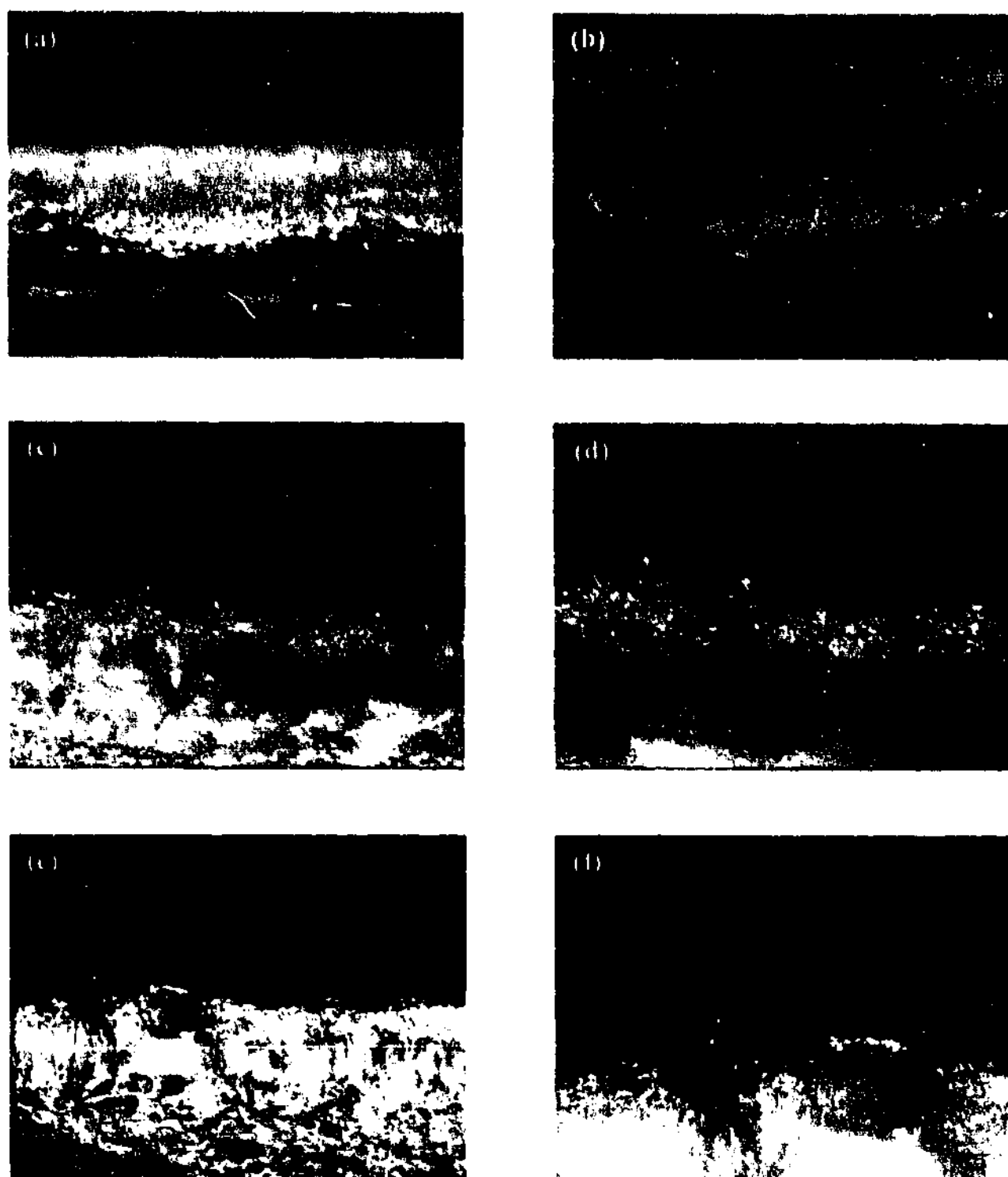


Fig. 3.1.26 0.5 mol kg⁻¹ EMI(Tl)₂N post deposition images (4th experiment), Cu working electrode surface (a) 20×, (b) 40×, (c) 20×, (d) 40×, (e) 20×, (f) 40×.

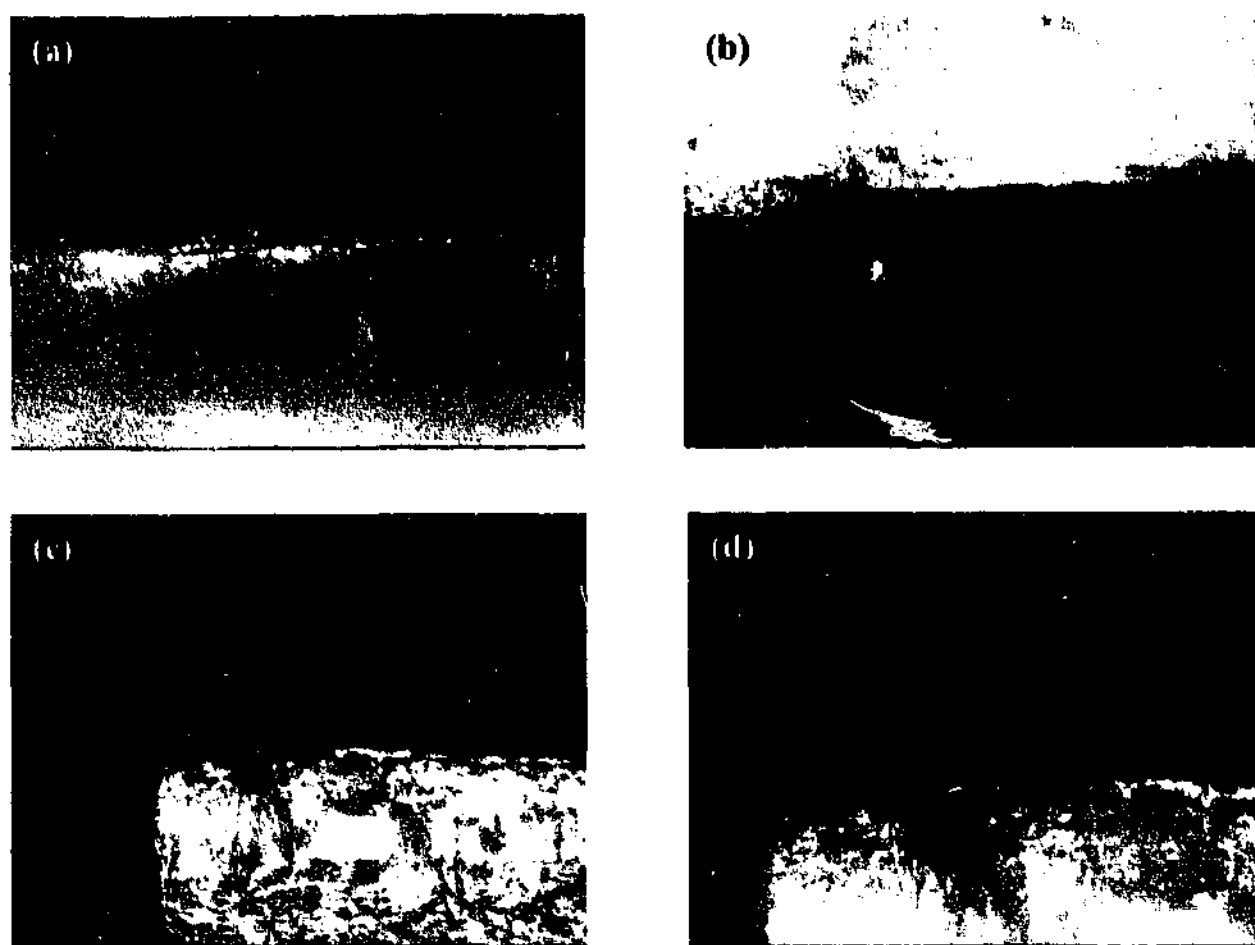


Fig. 3.1.27 0.5 mol kg^{-1} EMI(Tf)₂N post cycling images (4th experiment) Cu working electrode surface (a) 40 \times , (c) 20 \times & (d) 40 \times . Li counter electrode surface (b) 20 \times .

Figure 3.1.28 shows the potential profile recorded during the fifth experiment. The initial potential plateau had almost completely disappeared and the lithium deposition potential was reached almost immediately. The cycling phase of the experiment extended for 5.6 cycles, giving a cycling efficiency of approximately 58 %.

The images presented in Figure 3.1.29 display a marked difference to those presented in Figure 3.1.26. The morphology of the lithium deposit (images a-f) had become dominated by dendritic deposits which had previously been scarce and not as well developed. The appearance of the dendrites coincided with a change in the deposition and dissolution potential displayed in Fig. 3.1.28. Deposition occurred at $\sim 40 \text{ mV}$ as opposed to $20\text{--}25 \text{ mV}$ in previous experiments. Similarly the dissolution potential became progressively more negative (on the arbitrary scale) with each experiment. These changes most likely indicate either a change in the conductivity of the surface film (SEI), a change in the active surface area of the electrode or a change in the conductivity of the electrolyte. The observation of the build-up of crystalline deposits still present after cycling indicates that a combination

of the first two parameters offers the most likely explanation. The other significant change in the appearance of the potential profiles is the appearance of high initial deposition potentials indicated by the sharp peak at the start of the initial deposition phase of each experiment. The progressively higher values indicate that nucleation on the 'bare' copper surface had become progressively more difficult. Again, this is indicative of a change in active surface area and/or SEI resistance. Figure 3.1.29g shows the cycled lithium surface, which was largely unchanged in appearance although it did exhibit some signs of corrosion.

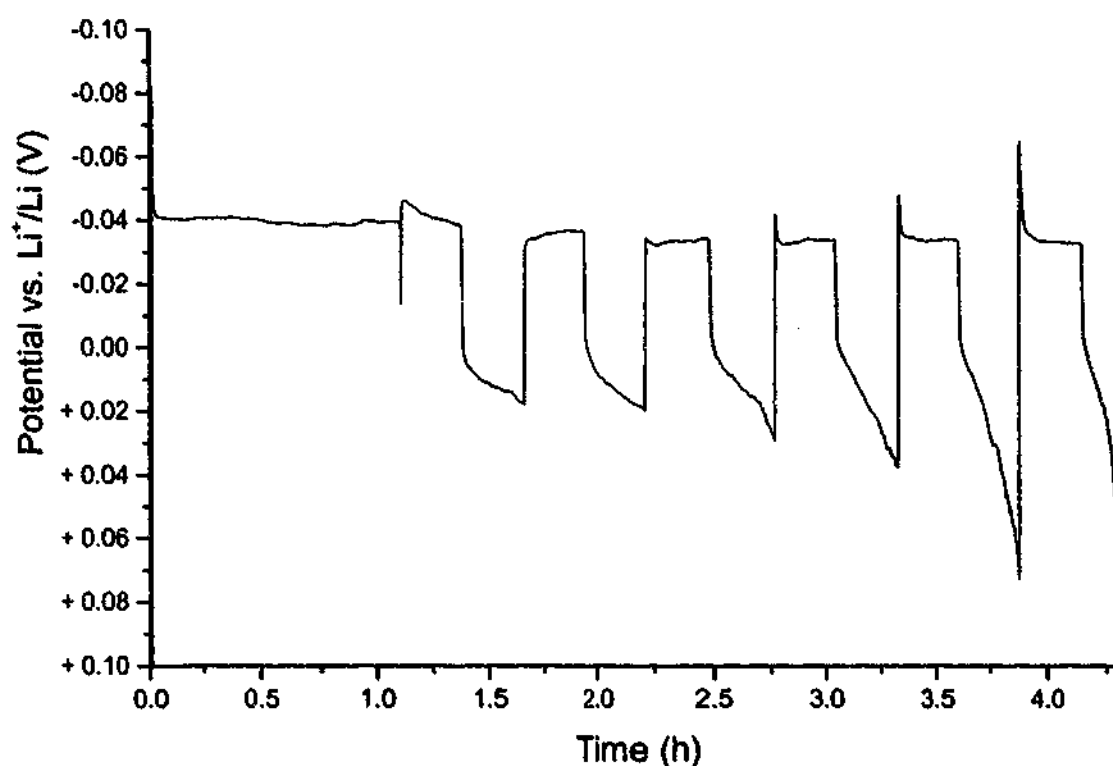


Fig. 3.1.28 0.5 mol kg^{-1} EMI(Tf)₂N cycling efficiency potential profile. 5th experiment.

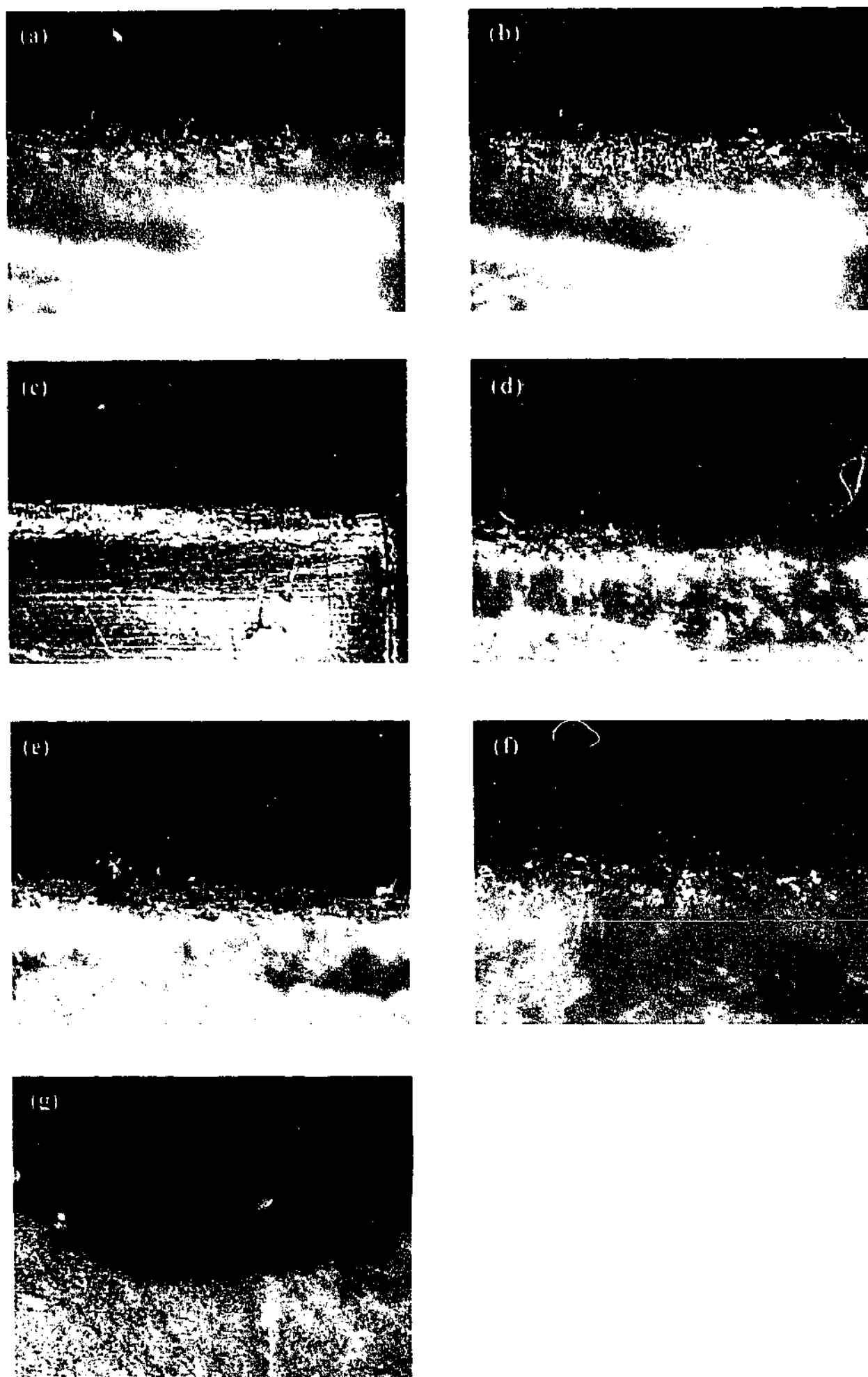


Fig 3.1.29 0.5 mol kg^{-1} EMI(Tf)₂N post deposition images (5th experiment) Cu working electrode surface (a) 20x, (b) 20x, (c) 5x & (d) 20x, (e) 20x, (f) 40x. Li counter electrode surface (g) 20x.

Figure 3.1.30 shows the potential profile recorded during the sixth experiment. The cycling phase of the experiment extended for almost 4 cycles, giving a cycling efficiency of approximately 50 %. There was also a notable increase in the initial nucleation potential.

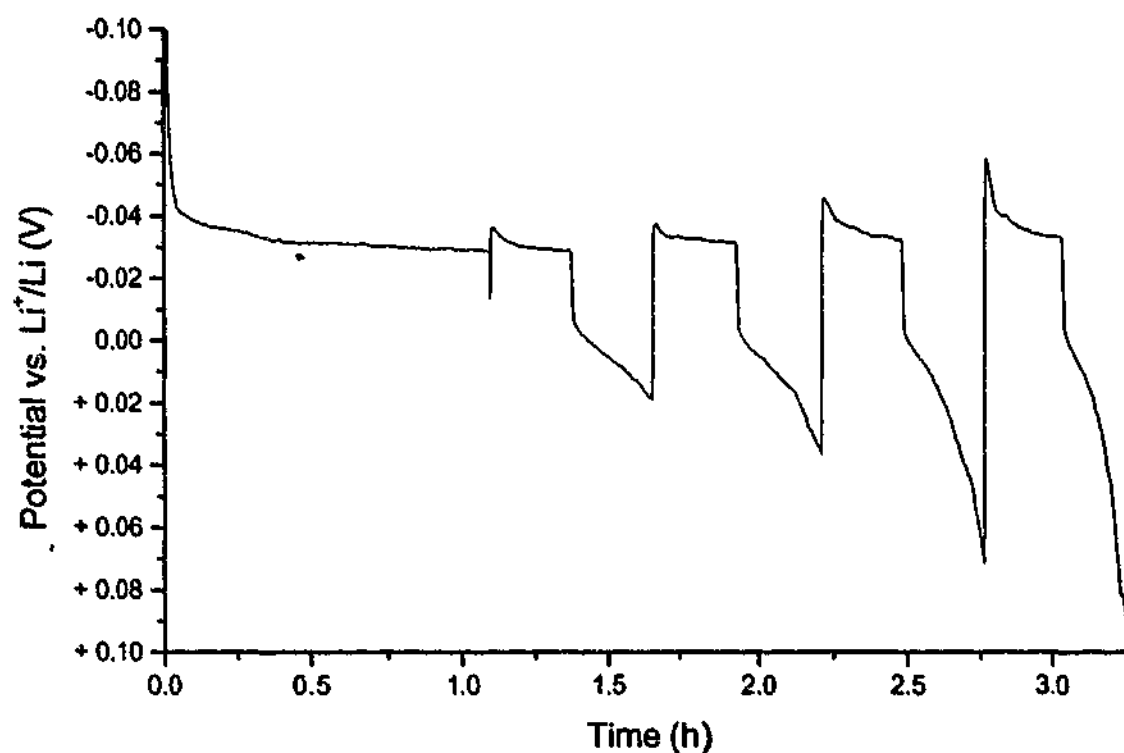


Fig. 3.1.30 0.5 mol kg⁻¹ EMI(Tf)₂N cycling efficiency potential profile. 6th experiment.

The images in Figure 3.1.31 were acquired after the cycling phase of the sixth experiment. A large amount of material was visible persisting on the electrode surface, some of the material had a crystalline appearance as previously described and is undoubtedly evidence of the continued reaction between lithium and some component of the electrolyte. Also in evidence are some pieces of bright metallic deposit, presumably lithium. These deposits most likely represent what has been termed 'dead lithium' (section 1.5.3), where a deposit had become disconnected from the substrate and was no longer electrochemically active. This is the first evidence of the generation of dead lithium in one of these cells.

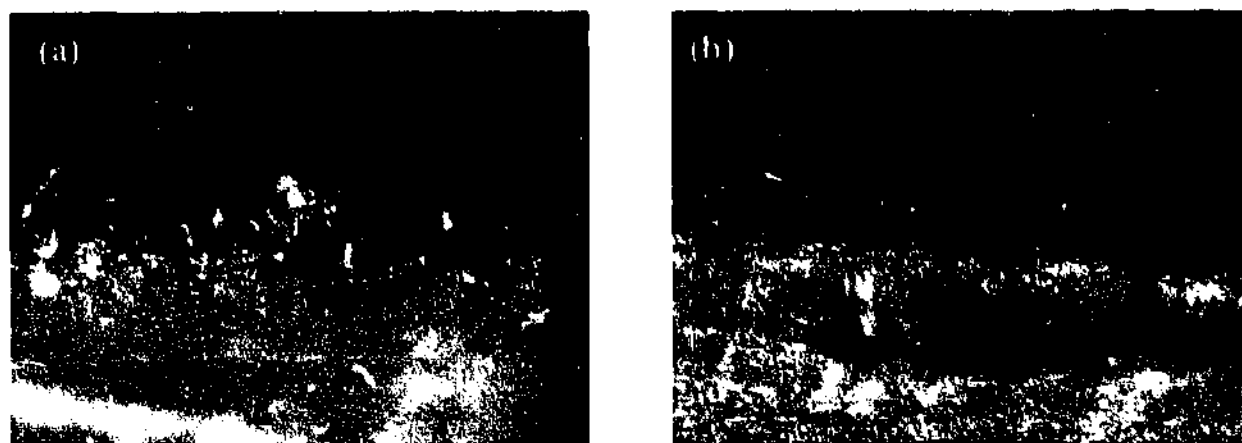


Fig. 3.1.31 0.5 mol kg^{-1} $\text{EMI}(\text{Tf})_2\text{N}$ post cycling images (6th experiment) Cu working electrode surface (a) $20\times$, (b) $20\times$.

The general course of the experiments saw an increase in cycling efficiency from low values initially to relatively high values, with a maximum of 65 % in the fourth experiment, followed by a decrease in cycling efficiency in subsequent experiments. Table 3.1.2 summarises the events that took place over the course of the six experiments.

Table 3.1.2 Summary of $\text{EMI}(\text{Tf})_2\text{N}$ optical cell experiments.

Exp. No.	Cyc. Eff. %	Deposit surface	Cycled surface
1	10	Discrete hemispherical	Bare, crystals just visible
2	30	Discrete hemispherical	-
3	55	-	-
4	65	Uniform hemispherical, some dendrites	Crystals becoming more visible
5	58	Uniform hemispherical, increasingly dendritic	-
6	50	-	Visible crystals, dead lithium

The most probable explanation for the behaviour of the cycled lithium deposit involves the formation and subsequent build-up of an SEI. The initial low cycling efficiency can be attributed to the consumption of a large portion of the deposition charge prior to the

formation of a protective SEI. The cycling efficiency then gradually improved as less charge was consumed before the deposit was passivated and because the SEI favoured a uniform lithium deposit, which exhibited better cycling behaviour. However, with continued cycling the copper surface became increasingly fouled with products of the reaction between lithium and the electrolyte. The fouled surface created a tendency to form dendritic deposits, which in turn formed dead lithium and led to a reduction in cycling efficiency. The cycling behaviour of the $\text{EMI}(\text{Tf})_2\text{N}$ was significantly better than that of EMIDCA or EMIBF_4 . This implicates the $(\text{Tf})_2\text{N}^-$ anion in a role as a SEI former which acts to improve cycling behaviour.

P_{13}BF_4 :

Conductivity (@ 25 °C)	0.1 mS cm^{-1}	21
Viscosity (@25 °C)	Solid	22
Affinity for water	Moderate/High	21,22
T_m (°C)	64	22
T_{decomp} (°C)	~340*	22

* Result determined for P_{11}BF_4 .

P_{13}BF_4 has been extensively investigated^{21,23-25} because of its interesting plastic crystal behaviour. The material exhibits fast ion conduction in the solid state, and, when doped with a salt (e.g., LiBF_4) conductivity is increased by several orders of magnitude²⁵ as has been reported for other plastic crystal materials.²⁶ To our knowledge this is the first time that experiments of this nature have been conducted in this type of material.

Figure 3.1.32 shows a plot of the potential profile from the cycling efficiency experiment. At 50 °C the electrolyte is a viscous liquid. Experiments were attempted in the solid state, but yielded only very low deposition currents. This most likely indicates that, although diffusion measurements show that lithium transport is quite facile (diffusion coefficient of Li in 2wt.% $\text{LiBF}_4/\text{P}_{13}\text{BF}_4 = 10^{-11} \text{ m}^2\text{s}^{-1}$ at 320K),²⁵ the number of mobile lithium ions is not sufficient to allow a substantial current to flow. In the liquid state, deposition occurred at a low and stable potential. The cycling phase of the experiment extended for 1.7 dissolution cycles giving a cycling efficiency of approximately 29 %.

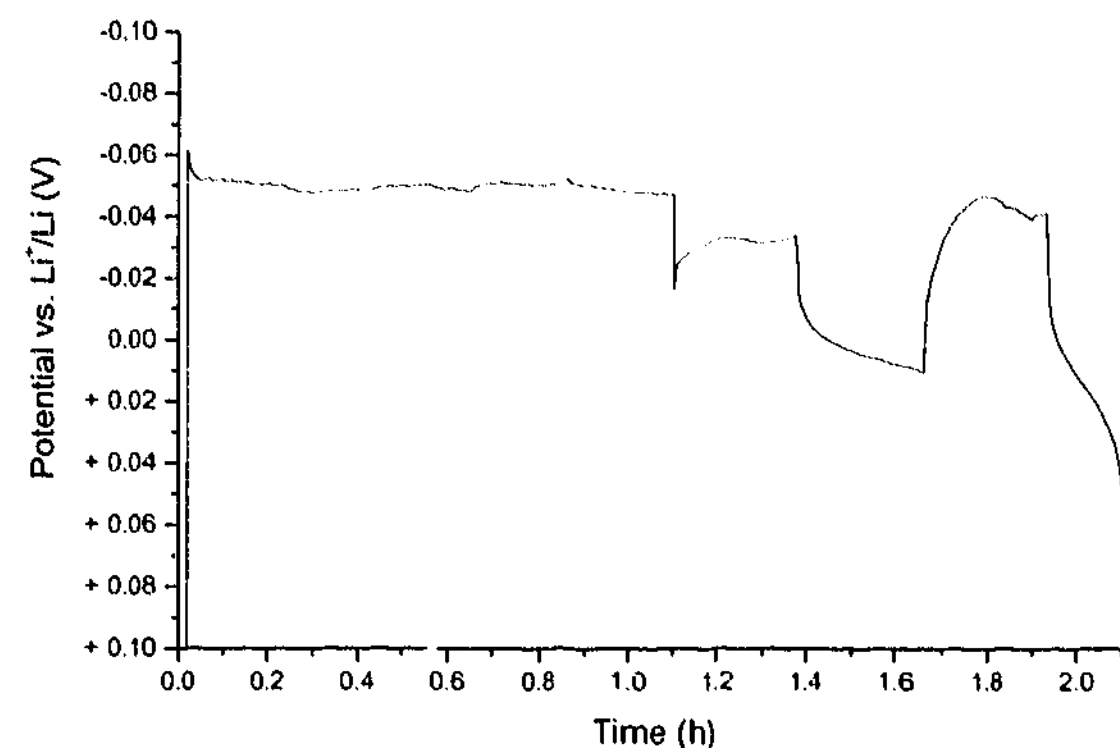


Fig. 3.1.32 0.5 molkg⁻¹ P₁₃BF₄ cycling efficiency potential profile.

Figure 3.1.33 shows images acquired after the deposition phase of the experiment. The electrolyte is a translucent solid at room temperature, which resulted in relatively poor quality images. The deposit was largely dendritic and had a 'bright' appearance.

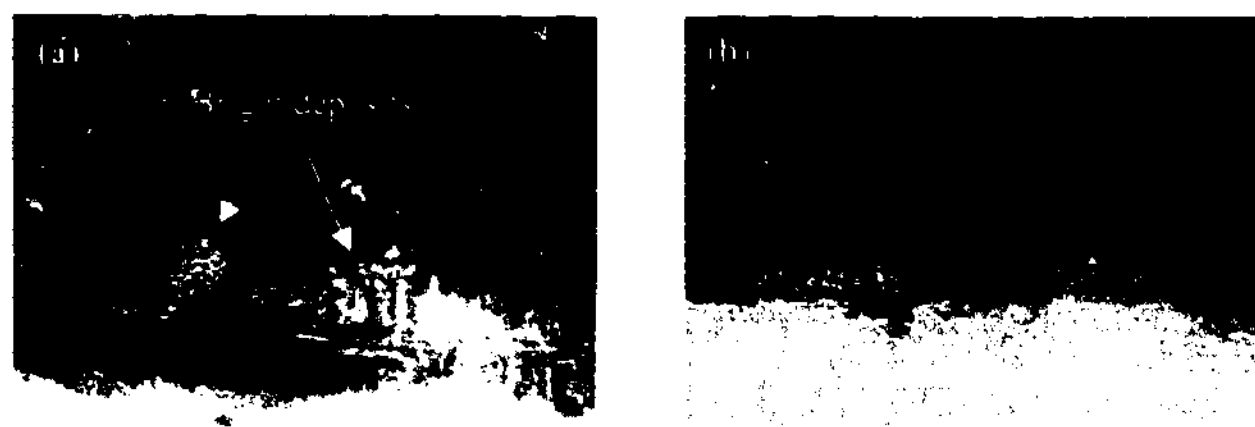


Fig. 3.1.33 0.5 molkg⁻¹ P₁₃BF₄ post deposition images, Cu working electrode surface (a) 20×, (b) 20×.

Figure 3.1.34 shows images acquired after the cycling phase of the experiment. The poor image quality is more difficult to interpret. However, it appears that the familiar theme of the appearance of a precipitate on the electrode surface is evident, along with the persistence of some 'dead' lithium on the electrode surface. On the basis of these observations P₁₃BF₄ would not seem suitable for application in a lithium cell, at least at these temperatures.

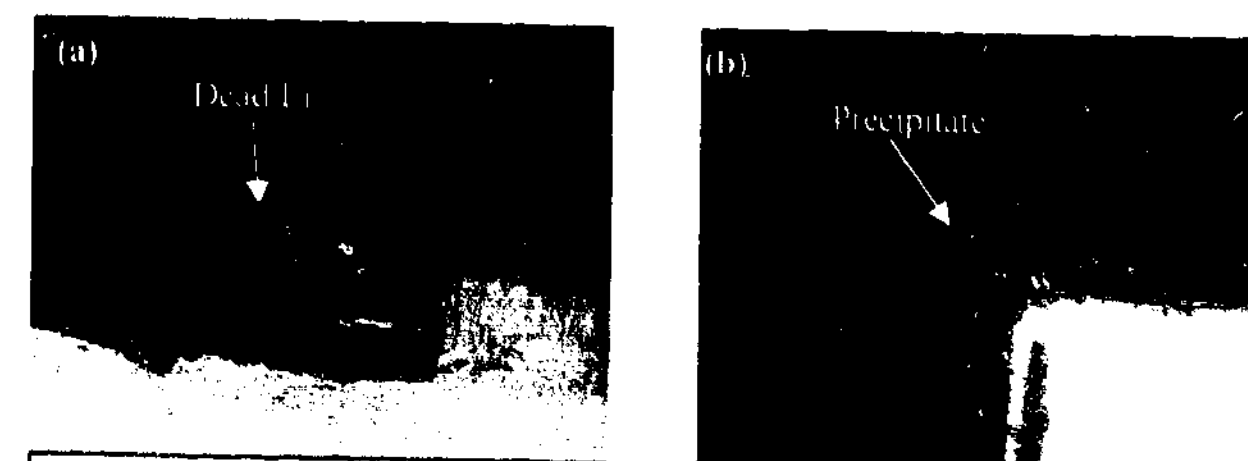


Fig. 3.1.34 0.5 molkg⁻¹ P₁₃BF₄ post cycling images, Cu working electrode surface (a) 20×, (b) 20×.

P₁₄DCA:

Viscosity (@ 20 °C)	50 cP	9,10
Density (@ 25 °C)	0.95 gcm ⁻³	9,10
Affinity for water	hydrophilic	9,10
T _m (°C)	-55	9,10
T _{decomp} (°C)	250*	11

* Result determined for P₁₂DCA

Figure 3.1.35 shows a plot of the potential profile from the cycling efficiency experiment. The potential moved quickly to a low and stable value where lithium deposition was likely to have occurred. The cycling phase of the experiment extended for 3.5 cycles, giving a cycling efficiency of approximately 47 %.

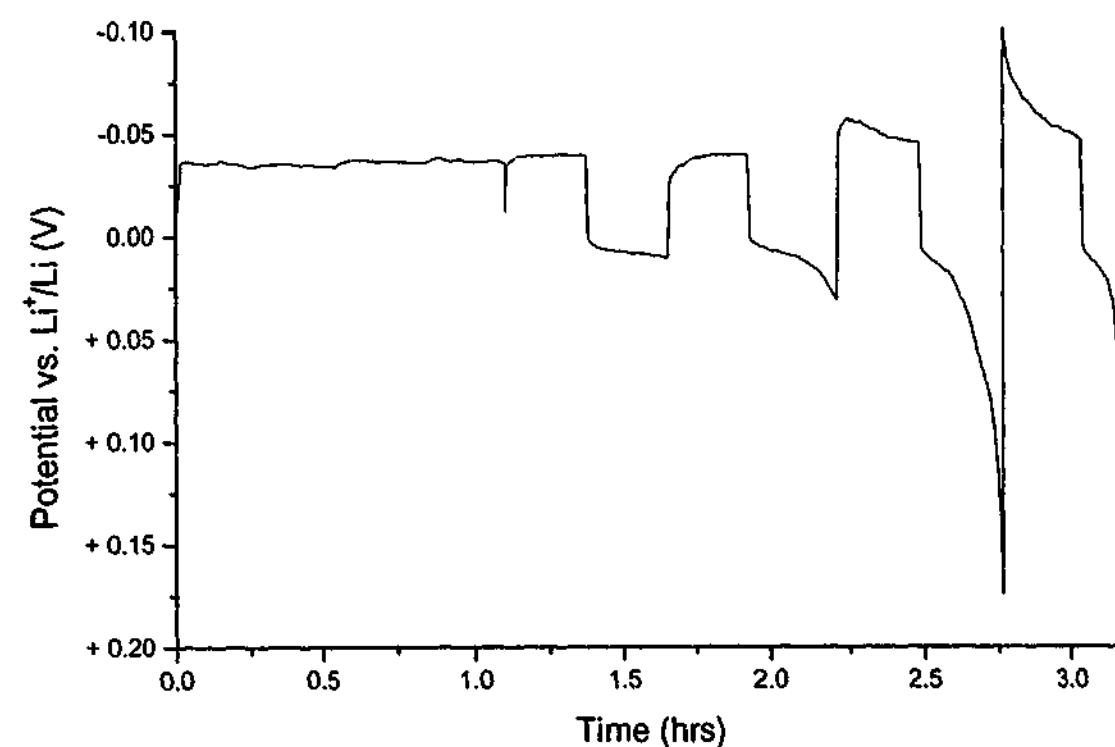


Fig 3.1.35 0.5 mol kg⁻¹ P₁₄DCA cycling efficiency potential profile.

The images shown in Figure 3.1.36 were acquired after the deposition phase of the experiment. The deposit was bright, had a hemispherical morphology and was uniformly distributed. There was no indication of dendrites anywhere on the electrode surface; in fact the deposit had the most favourable appearance of any of the deposits produced during this series of experiments. The other significant feature was a dark region between the deposit and the copper substrate.

The images shown in Figure 3.1.37 show the copper electrode surface after the cycling phase of the experiment. The appearance of the deposit was largely unchanged; a large portion had not taken part in the deposition / dissolution cycling indicating that it had become electrochemically inactive, presumably via the formation of an insulating surface film. The inactivation of the deposit appears to be the most likely cause of the relatively low cycling efficiency. It is possible that this was in some way related to the dark line at the base of the deposit, visible in Figure 3.1.36a-e and Figure 3.1.37a-c. The dark line is not visible in some of the images (Fig. 3.1.36f & g and Fig. 3.1.37e-g). The cycled images

indicate that, in the absence of the dark coloured deposit, the deposit had cycled more efficiently and there was no indication of a deposit related to a side reaction, the copper surface having a 'clean' appearance. The possibility that the dark region was related to an impurity must be considered. Image d) shows some of the deposit that had apparently reacted to form a dark coloured product. Image h) shows the cycled lithium surface which was discoloured.

P₁₄DCA exhibited excellent deposit morphology, but a relatively low cycling efficiency. It seems possible that improvements in cycling efficiency could be attained through the use of additives; the presence of impurities also raises questions that warrant further investigation. The possibility of application in lithium ion cells where conditions are less extreme is also worth considering.

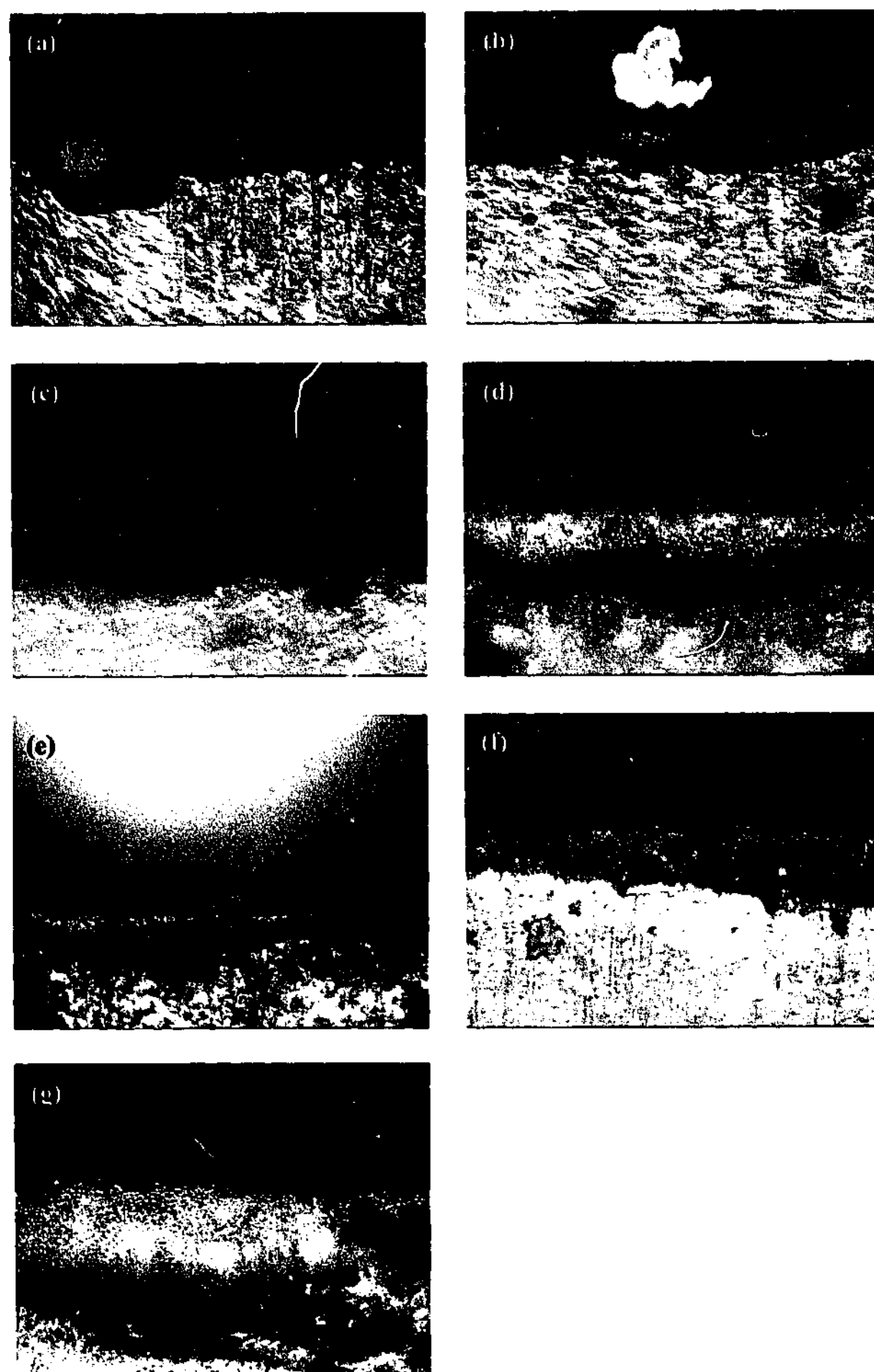


Fig 3.1.36 $0.5 \text{ mol kg}^{-1} \text{ P}_{14}\text{DCA}$ post deposition images Cu working electrode surface (a) 20 \times , (b) 20 \times , (c) 50 \times , (d) 50 \times , (e) 20 \times , (f) 20 \times , (g) 50 \times . *Note:* A software upgrade altered the colour balance for these images.

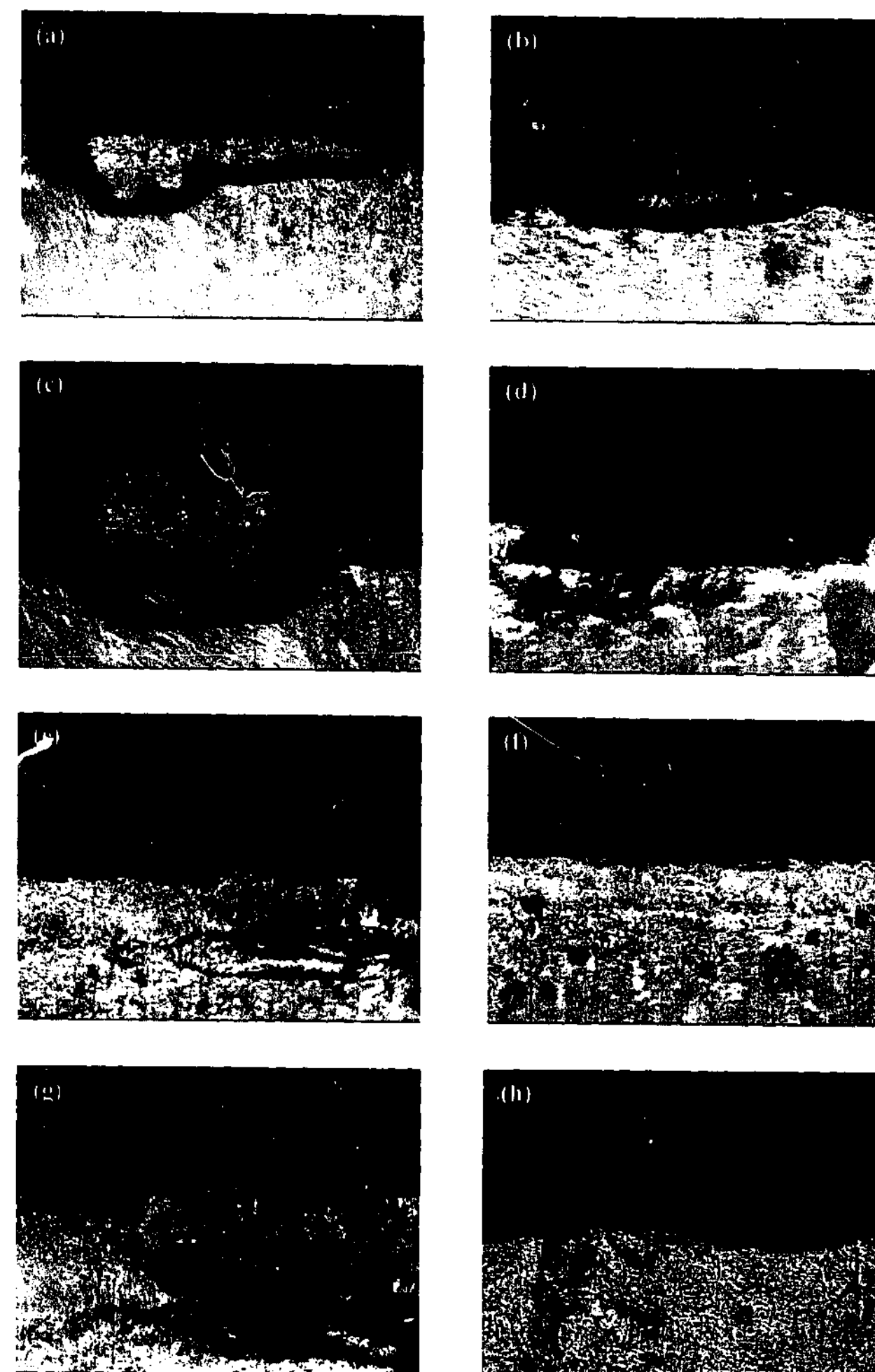


Fig 3.1.37 $0.5 \text{ mol kg}^{-1} \text{ P}_{14}\text{DCA}$ post cycling images. Cu working electrode surface (a) 20 \times , (b) 20 \times , (c) 5 \times , (d) 40 \times , (e) 20 \times , (f) 20 \times (g) 20 \times . Lithium counter electrode surface (h) 20 \times ((e-h) backside images). *Note:* A software upgrade altered the colour balance for these images.

BMImI:

Viscosity (@25 °C)	1110 cP	27
Density	1.44 g mL^{-1}	27
Affinity for water	Moderate/High	27
T _m (°C)	-72	27
T _{decomp} (°C)	265	27

BMImI was investigated because of the possibility that an SEI composed of LiI might be developed which enables good lithium passivation and has been exploited in primary cells (typically for application with pacemakers) for over 30 years.²⁸

Figure 3.1.38 displays the potential profile acquired during the cycling efficiency experiment. Deposition occurred at a relatively low and stable potential. During cycling, the impedance of the cell rose quite dramatically as was evidenced by the inability of the potentiostat to maintain the applied current. This can be seen in the potential profile during

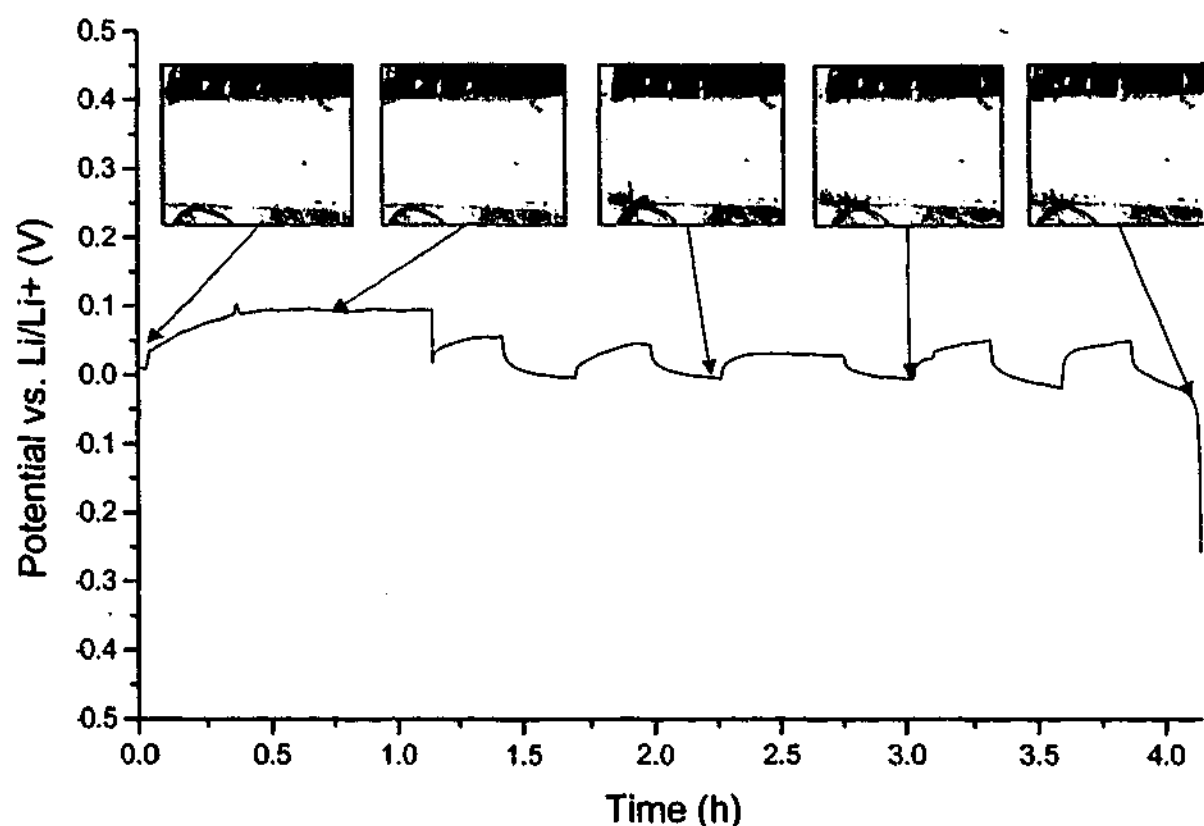


Fig. 3.1.38 0.5 mol kg^{-1} BMImI cycling efficiency potential profile.

the third deposition cycle where the time required to deposit 0.25 Ccm^{-2} of lithium increased. The increase in cell impedance coincided with gassing and discoloration of the electrolyte at the lithium counter electrode (visible in the lower left hand corner of the third image inset into the profile). To allow the experiment to continue the fourth (redundant) reference electrode was connected to the original counter electrode, thus effectively doubling the surface area of the counter electrode. The cycling phase of the experiment extended for almost 5 cycles giving a cycling efficiency of approximately 55 %.

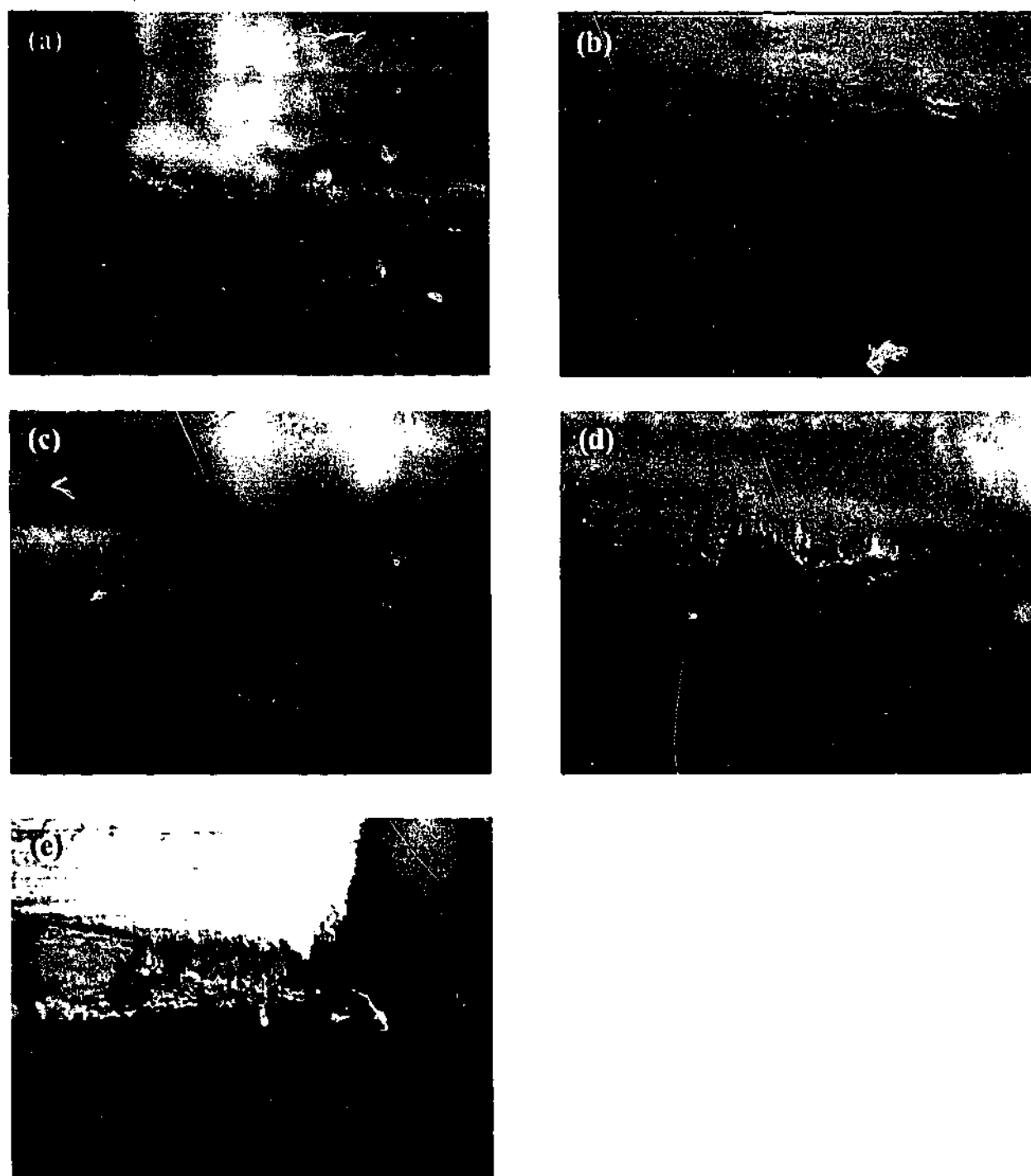


Fig. 3.1.39 0.5 mol kg^{-1} BMImCl post deposition images, Cu working electrode surface (a) 20x, (b) 20x, (c) 20x, (d) 20x & (e) 20x.

The images displayed in Figure 3.1.39 show the copper electrode surface after the deposition phase of the experiment. The deposit had a bright appearance and exhibited uniform morphology. The electrode was almost completely free of dendrites, the only dendrites in evidence occurred near the edge of the electrode surface (image e) where the electrode geometry would give rise to higher current density (i.e., increased lithium ion flux). The dendrites shown in image e) provide the first clue to the relationship between current density and the evolution of the lithium deposit morphology in RTILs. This relationship will be discussed at length in later sections.

The post cycling images shown Figure 3.1.40 indicate the presence of an irreversible product on the surface of the copper electrode. The formation of this deposit appeared to be the major contributing factor that reduced the cycling efficiency; there was no indication of unreacted (dead) lithium on the electrode surface.

The change in cell impedance during cycling, coupled with gas generation and electrolyte discolouration at the counter electrode, is indicative of oxidation of iodide and the formation of iodine. This process is likely to occur at the counter electrode in place of lithium dissolution. Oxidation of iodide renders the electrolyte unsuitable for a secondary cell although the electrolyte could find application in a primary cell.

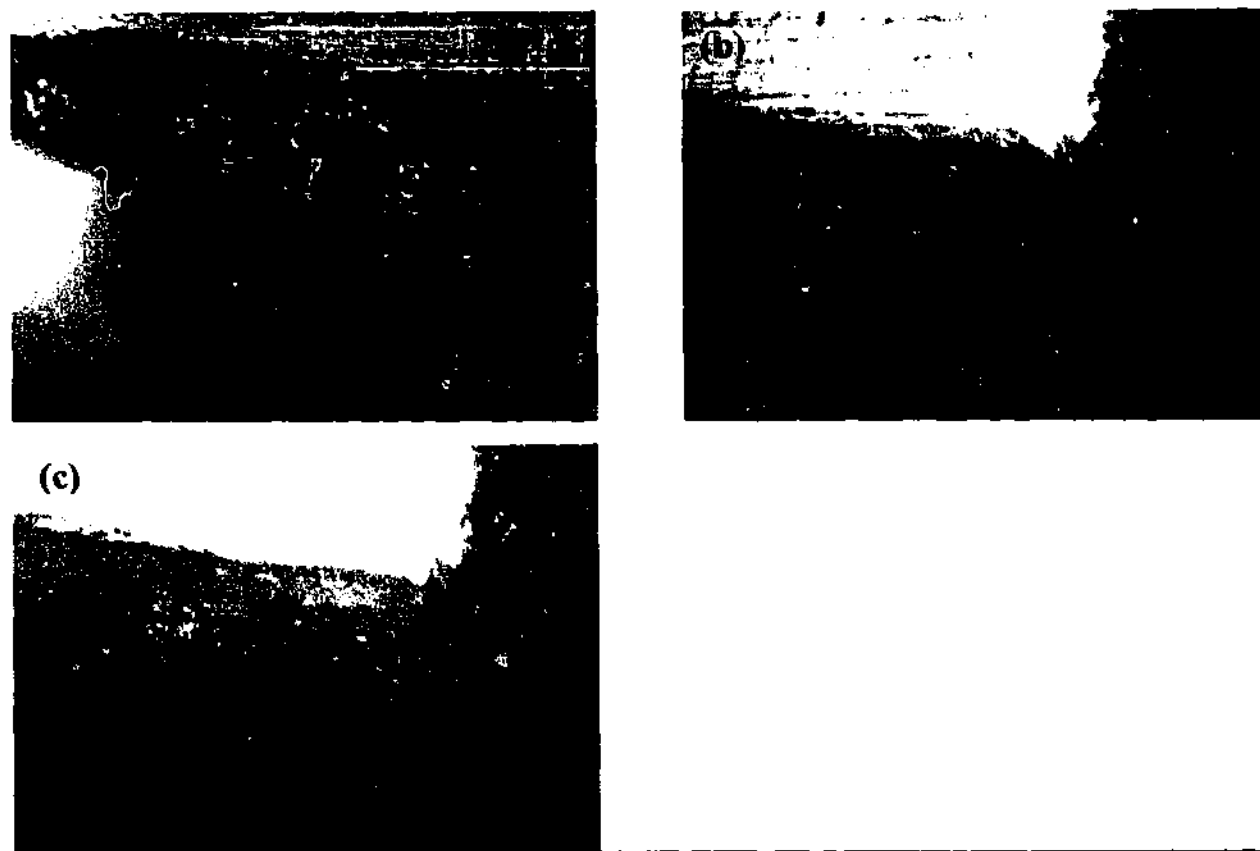


Fig. 3.1.40 0.5 molkg⁻¹ BMImI post cycling images. Cu working electrode surface (a) 20 \times , (b) 20 \times , (c) 20 \times .

$P_{14}(Tf)_2N$:

Conductivity (@ 25 °C)	2.2 mScm ⁻¹	29,30
Viscosity (@25 °C)	85 cP	29,30
Density (20 °C)	1.41 gcm ⁻³	29,30
Affinity for water	Low	29,30
T _m (°C)	-18	29,30
T _{decomp} (°C)	400	20

Four consecutive cycling efficiency experiments were conducted in the $P_{14}(Tf)_2N$ optical cell. As for the $EMI(Tf)_2N$ experiments, the series of experiments were conducted to examine the electrode cycling behaviour after the electrode had been completely discharged.

Figure 3.1.41 shows the potential profile recorded during the first experiment. The deposition potential remained low and stable after an initial (relatively) high nucleation potential. The cycling phase of the experiment extended for almost 5 dissolution cycles giving a cycling efficiency of approximately 55 %.

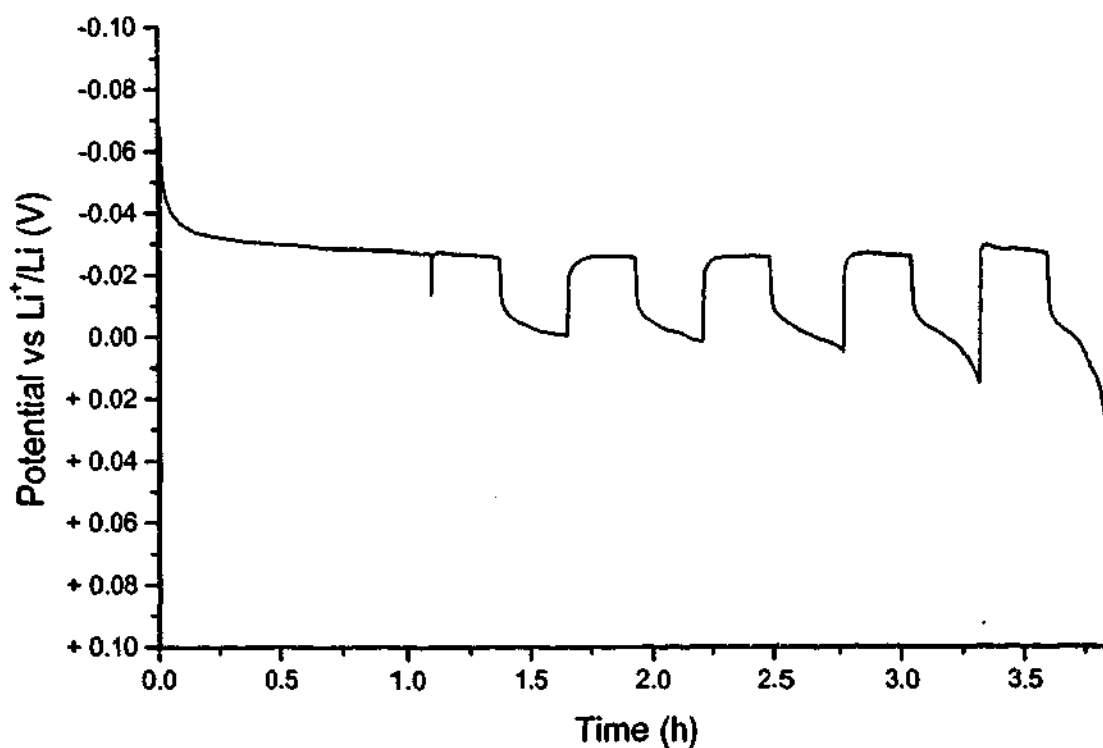


Fig. 3.1.41 0.5 molkg⁻¹ $P_{14}(Tf)_2N$ cycling efficiency potential profile, 1st experiment.

The images shown in Figure 3.1.42 clearly show that lithium deposition had occurred. The lithium deposit was uniformly distributed across the surface, had a 'bright' appearance and exhibited predominantly dendritic morphology.

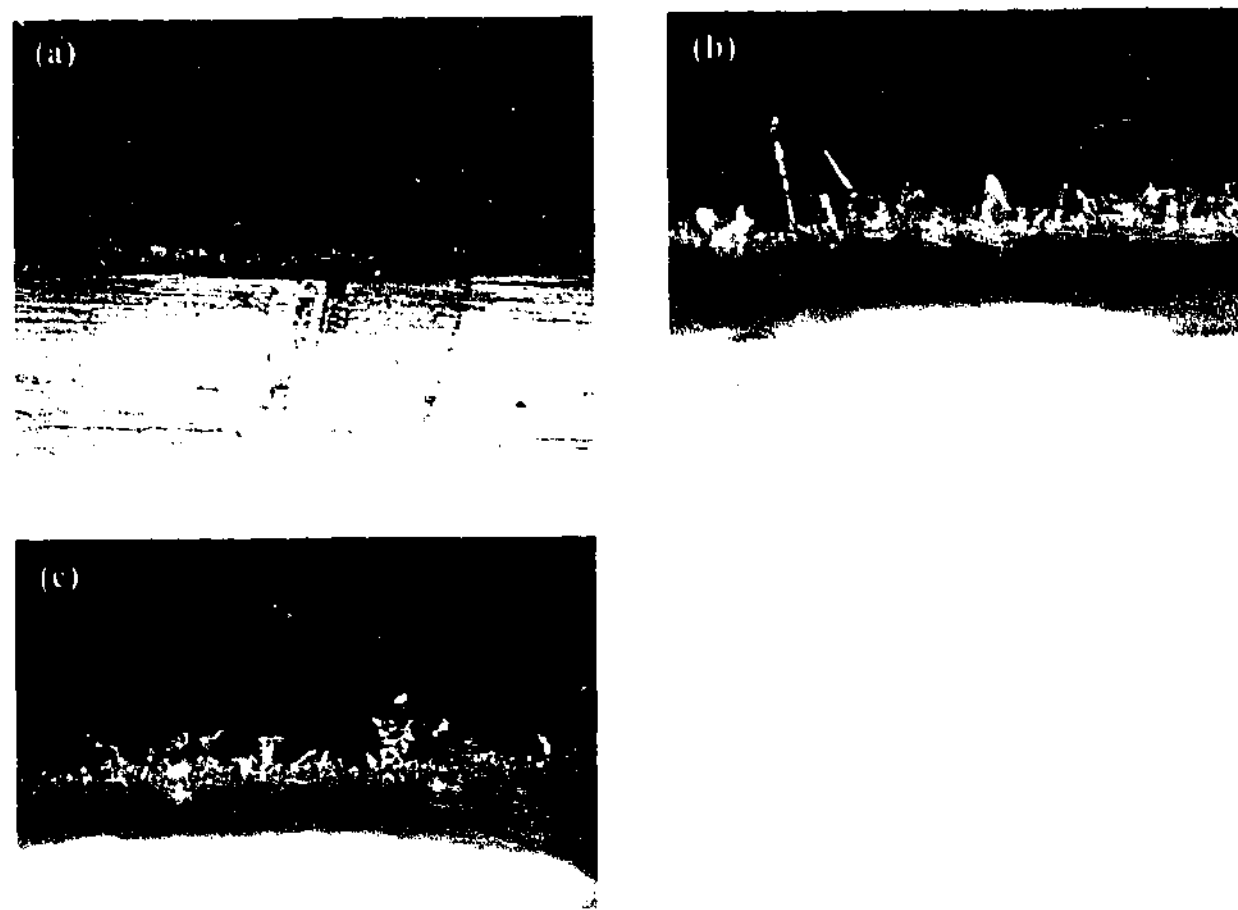


Fig. 3.1.42 0.5 mol kg⁻¹ P₁₄(Tf)₂N post deposition images (1st experiment), Cu working electrode surface (a) 5×, (b) 20×, (c) 20×.

The images shown in Figure 3.1.43 were acquired after the cycling phase of the experiment. The surface was largely covered in a crystalline material; there were no obvious signs of 'dead' lithium remaining on the surface. Although the material is difficult to discern in the images presented here, through the eyepiece of the microscope the material had the appearance of a translucent crystal and had a distinctly different appearance to the lithium deposits present prior to the cycling experiment. This indicates that the conversion of the lithium deposit into the precipitate represents the major contribution leading to a cycling efficiency of less than 100 %.

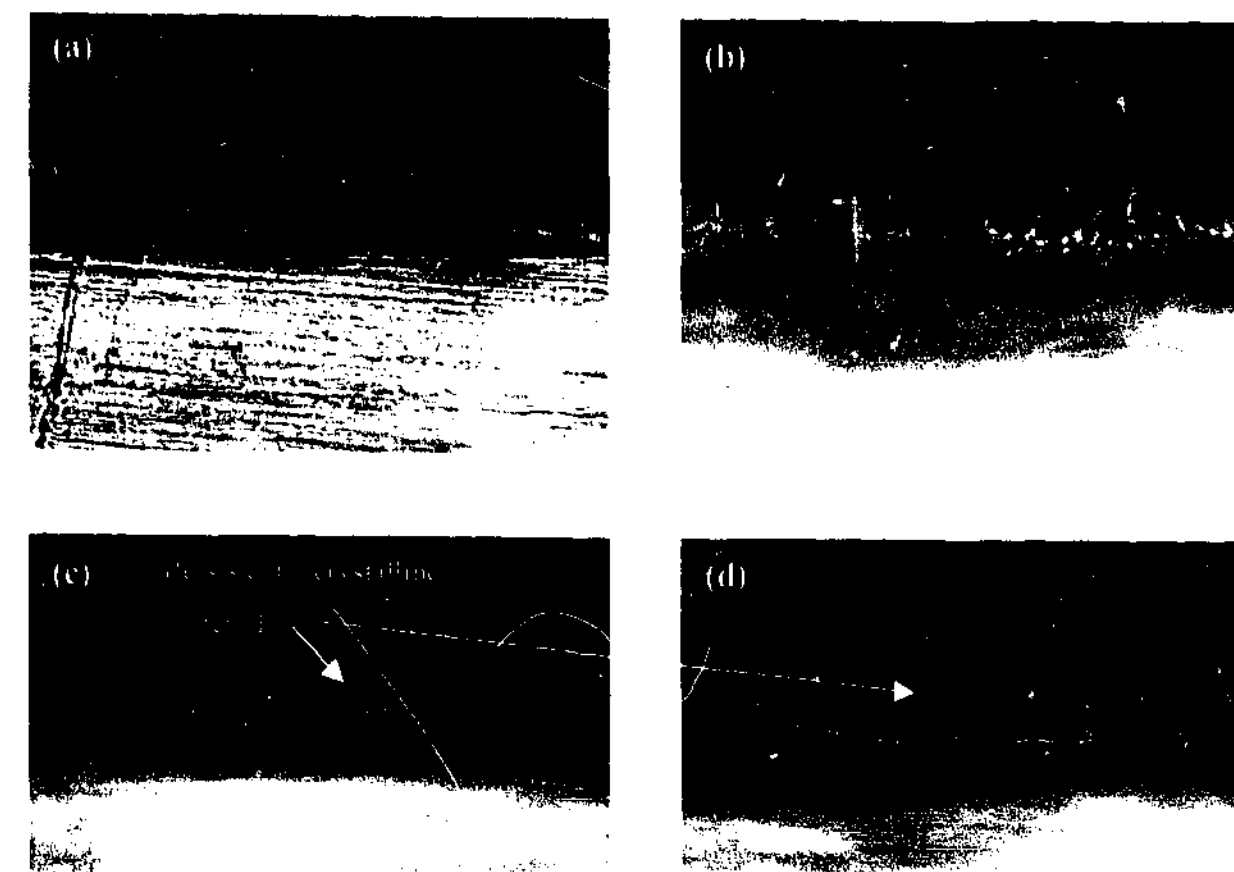


Fig. 3.1.43 0.5 mol kg⁻¹ P₁₄(Tf)₂N post cycling images (1st experiment), Cu working electrode surface (a) 5×, (b) 20×, (c) 20×, (d) 20×.

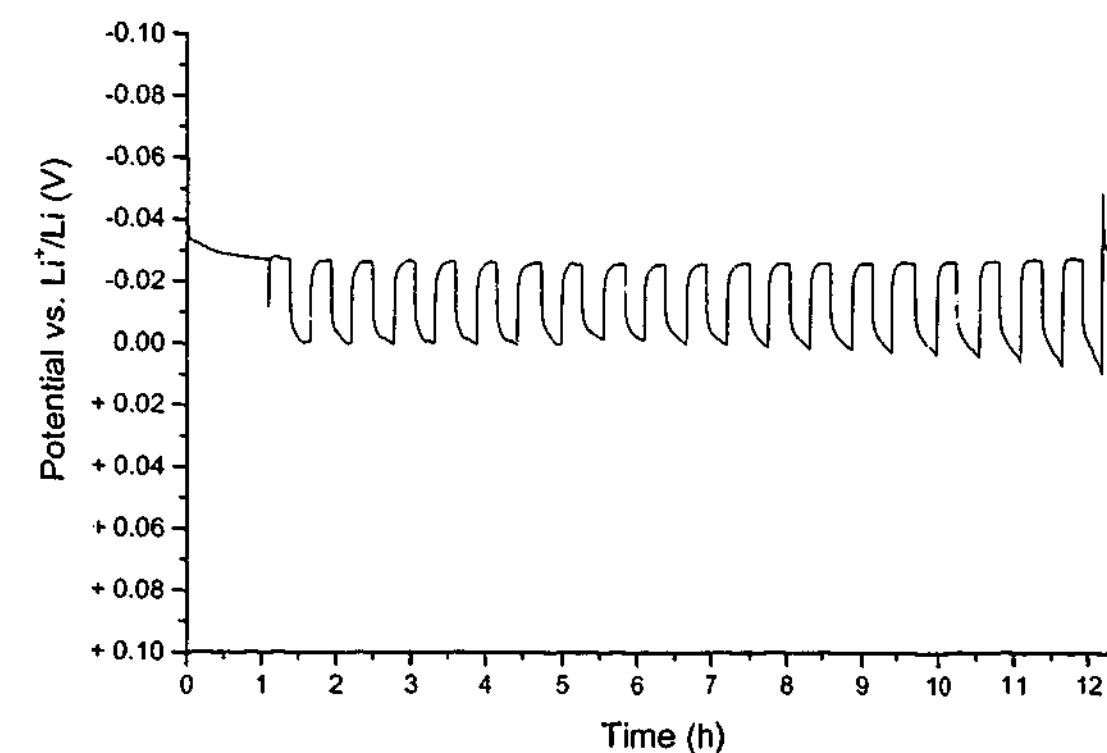


Fig. 3.1.44 0.5 mol kg⁻¹ P₁₄(Tf)₂N cycling efficiency potential profile, 2nd experiment.

Figure 3.1.44 shows the potential profile recorded during the second experiment. The initial nucleation potential was significantly reduced from the first experiment, but otherwise the cell behaved similarly. The cycling phase of the experiment extended for almost 21 dissolution cycles giving a cycling efficiency of approximately 84 %.

The images shown in Figure 3.1.45 were acquired after the deposition phase of the second experiment. The deposit had a similar appearance to that of the first experiment, although generally less dendritic. In addition there were regions of highly uniform, distributed small hemispherical deposits as shown in image c).

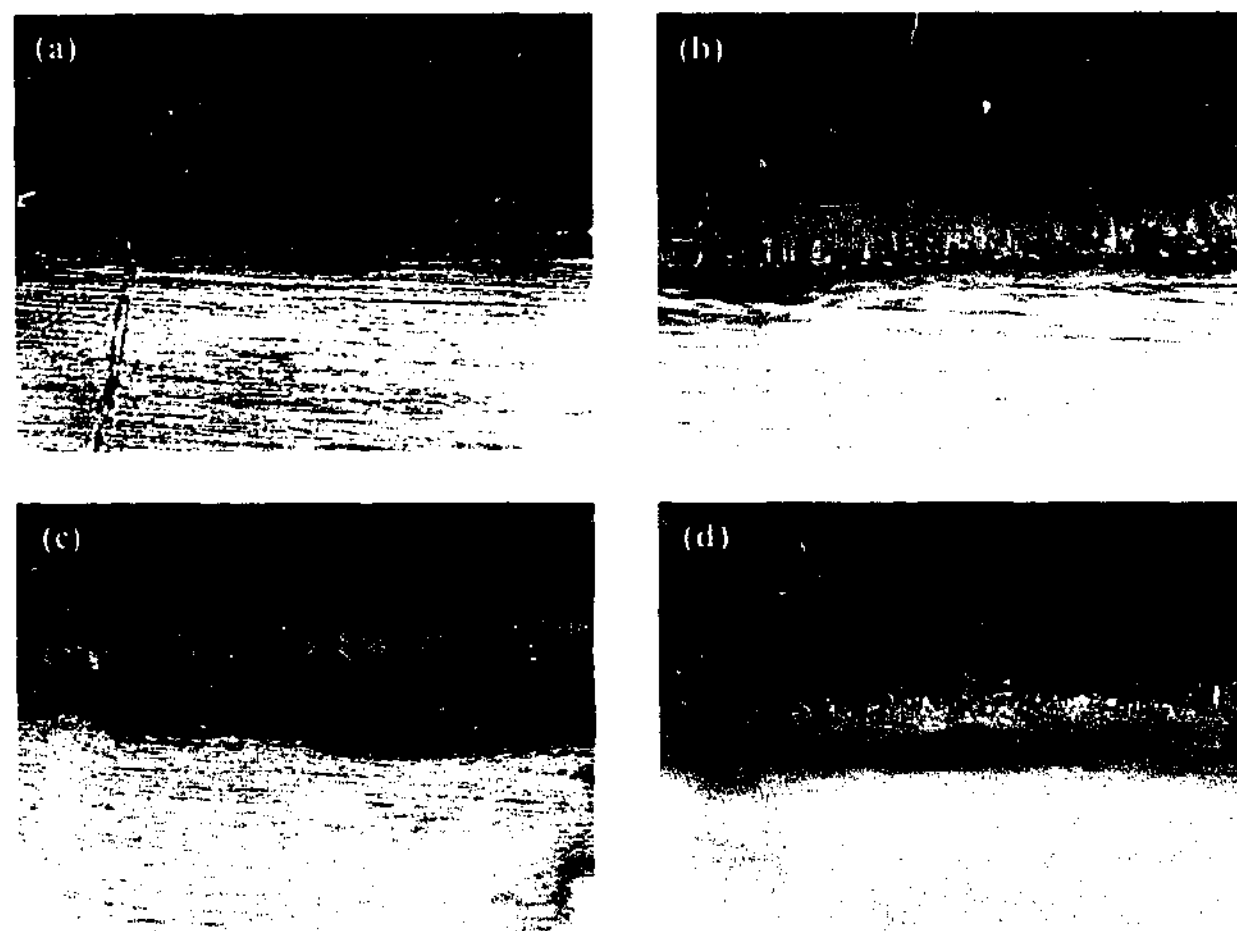


Fig. 3.1.45 $0.5 \text{ mol kg}^{-1} \text{ P}_{14}(\text{Tf})_2\text{N}$ post deposition images (2nd experiment), Cu working electrode surface (a) 5 \times , (b) 20 \times , (c) 20 \times , (d) 20 \times .

The images shown in Figure 3.1.46 were acquired after the cycling phase of the second experiment. The appearance of the copper electrode surface did not change markedly, although the consumption of 'bright' lithium is apparent by comparing images 3.1.45a & b with 3.1.46a & b. The fine deposits (i.e., image 3.1.45c and images 3.1.46c & d) did not

change markedly in appearance. The less dendritic deposit and uniform distribution appears to have contributed to the relatively high cycling efficiency achieved in this experiment.

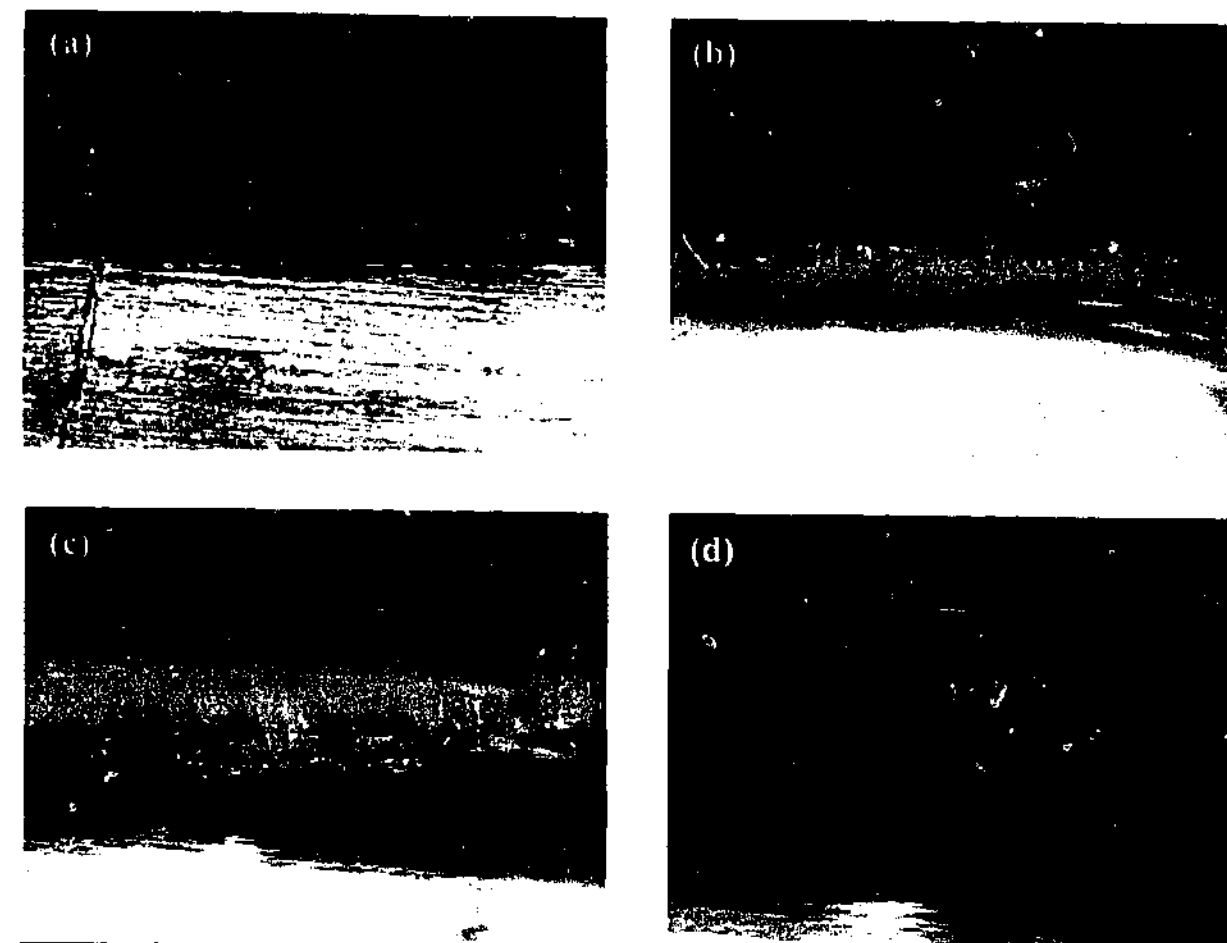


Fig. 3.1.46 $0.5 \text{ mol kg}^{-1} \text{ P}_{14}(\text{Tf})_2\text{N}$ post cycling images (2nd experiment), Cu working electrode surface (a) 5 \times , (b) 20 \times , (c) 20 \times , (d) 40 \times .

Figure 3.1.47 shows the potential profile recorded during the third experiment. The profile was similar in appearance to that of the second experiment. The cycling phase of the experiment extended for almost 12 dissolution cycles giving a cycling efficiency of approximately 75 %.

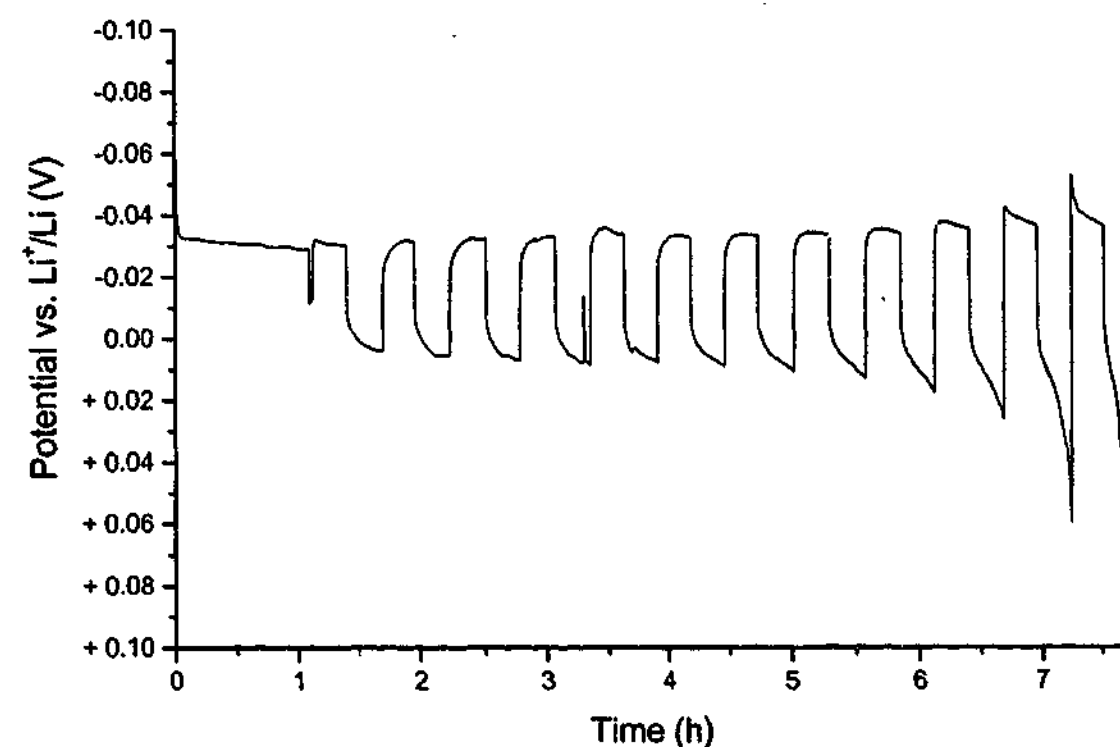


Fig. 3.1.47 0.5 mol kg⁻¹ P₁₄(Tf)₂N cycling efficiency potential profile, 3rd experiment.

The post deposition and post cycling images acquired after the third experiment did not show any significant differences to those acquired from the second experiment. A slight build-up in the amount of crystalline material persisting on the surface was evident at the end of the cycling phase of the experiment.

Figure 3.1.48 shows the potential profile recorded during the fourth experiment. The initial nucleation potential can be seen to have increased significantly, and the overall deposition potential had increased. The cycling phase of the experiment extended for almost 4 dissolution cycles giving a cycling efficiency of approximately 49 %.

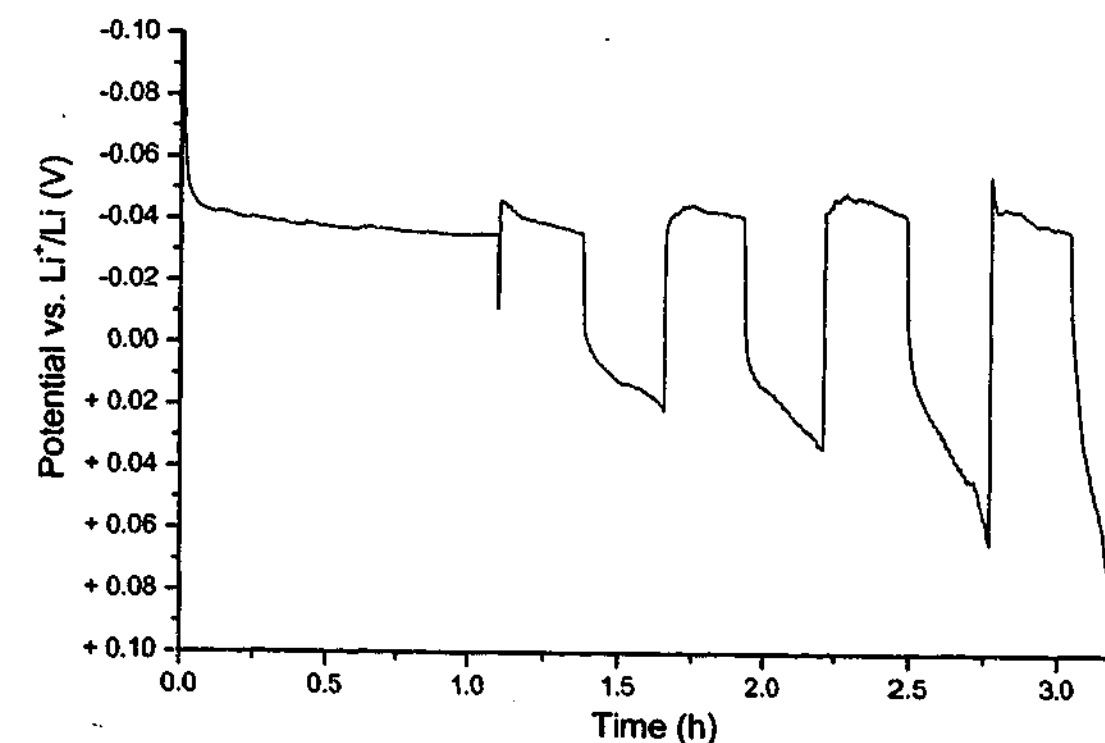


Fig. 3.1.48 0.5 mol kg⁻¹ P₁₄(Tf)₂N cycling efficiency potential profile, 4th experiment.

The images shown in Figure 3.1.49 were acquired after the deposition phase of the fourth experiment. The overall appearance of the deposit had become more dendritic, as exemplified by image c).

The images shown in Figure 3.1.50 were acquired after the cycling phase of the fourth experiment. A significant quantity of unreacted lithium was evident on the lithium surface; bright, dendritic deposits can be seen persisting on the lithium surface particularly in images b) and d). Image e) shows the cycled lithium surface which did not exhibit any dendritic features; the surface had a crystalline appearance.

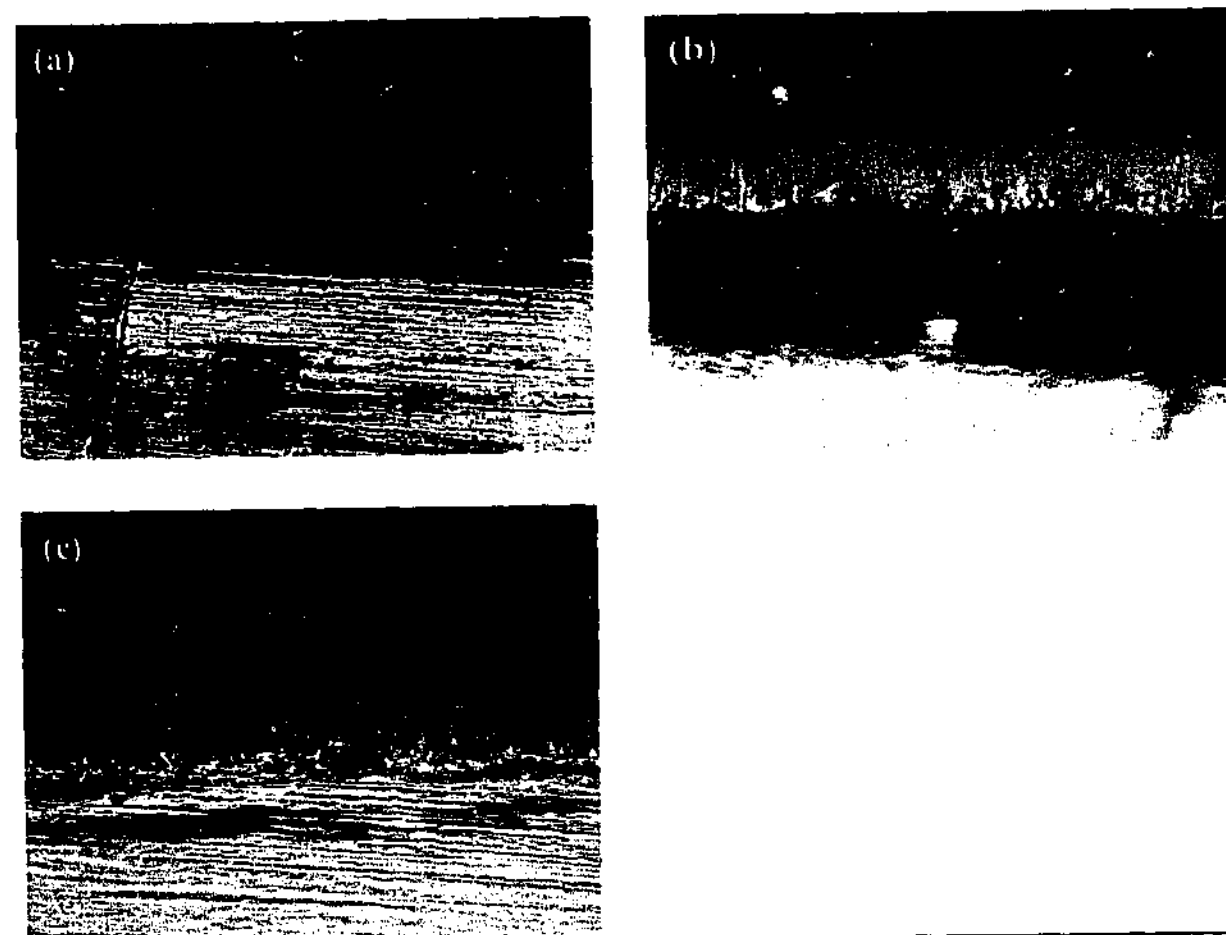


Fig. 3.1.49 $0.5 \text{ mol kg}^{-1} \text{ P}_{14}(\text{Tf})_2\text{N}$ post deposition images (4th experiment), Cu working electrode surface (a) 5 \times , (b) 20 \times , (c) 20 \times .

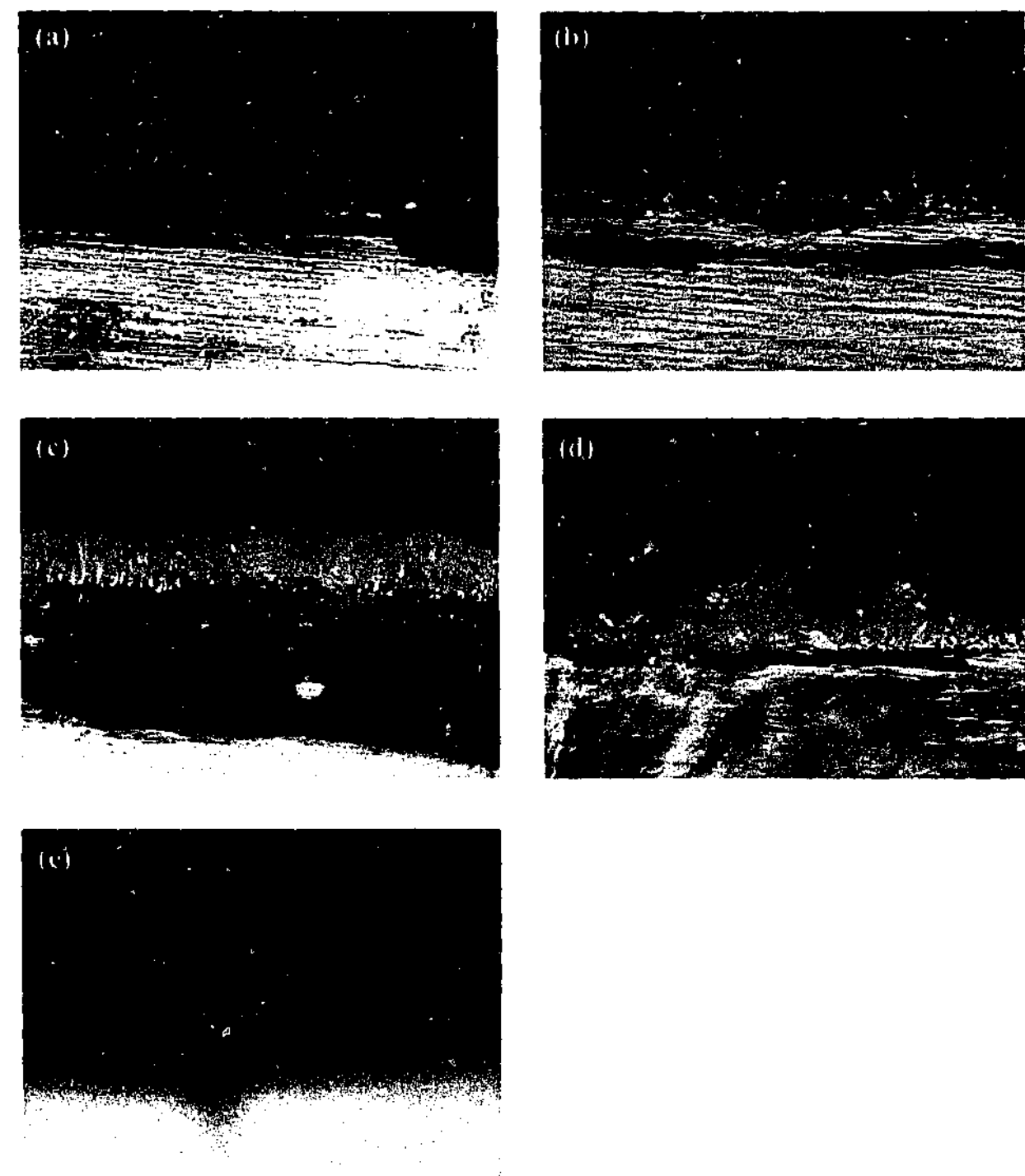


Fig. 3.1.50 $0.5 \text{ mol kg}^{-1} \text{ P}_{14}(\text{Tf})_2\text{N}$ post cycling images (4th experiment), Cu working electrode surface (a) 5 \times , (b) 20 \times , (c) 20 \times , (d) 20 \times . Li counter electrode surface (e) 20 \times .

The general course of the experiments saw an increase in cycling efficiency from low values initially to high values, with a maximum of 84 % in the second experiment, followed by a decrease in cycling efficiency in subsequent experiments. Table 3.1.3 summarises the events that took place over the course of the six experiments.

Table 3.1.3 Summary of $P_{14}(Tf)_2N$ optical cell experiments.

Exp. No.	Cyc. Eff. %	Deposit surface	Cycled surface
1	55	Uniform, dendritic	Crystalline deposit
2	84	Less dendritic, some hemispherical	Crystalline deposit
3	75	Less dendritic, some hemispherical	Crystalline deposit (build-up)
4	48	Increasingly dendritic	'Dead' lithium visible

A similar mechanism to that which occurred for $EMI(Tf)_2N$ appeared to be active in dictating the cycling efficiency for $P_{14}(Tf)_2N$. However, there was no plateau at low potentials (during the initial deposition phase) and a higher overall efficiency was attained. Initially the deposit was quite dendritic, which coincided with a relatively high initial nucleation potential. The second experiment exhibited a reduced initial potential and the deposit was less dendritic. Again, there was interplay between the amount of crystalline material fouling the electrode surface and the morphology of the subsequent deposit. When the deposit was dendritic the cycling efficiency was significantly reduced.

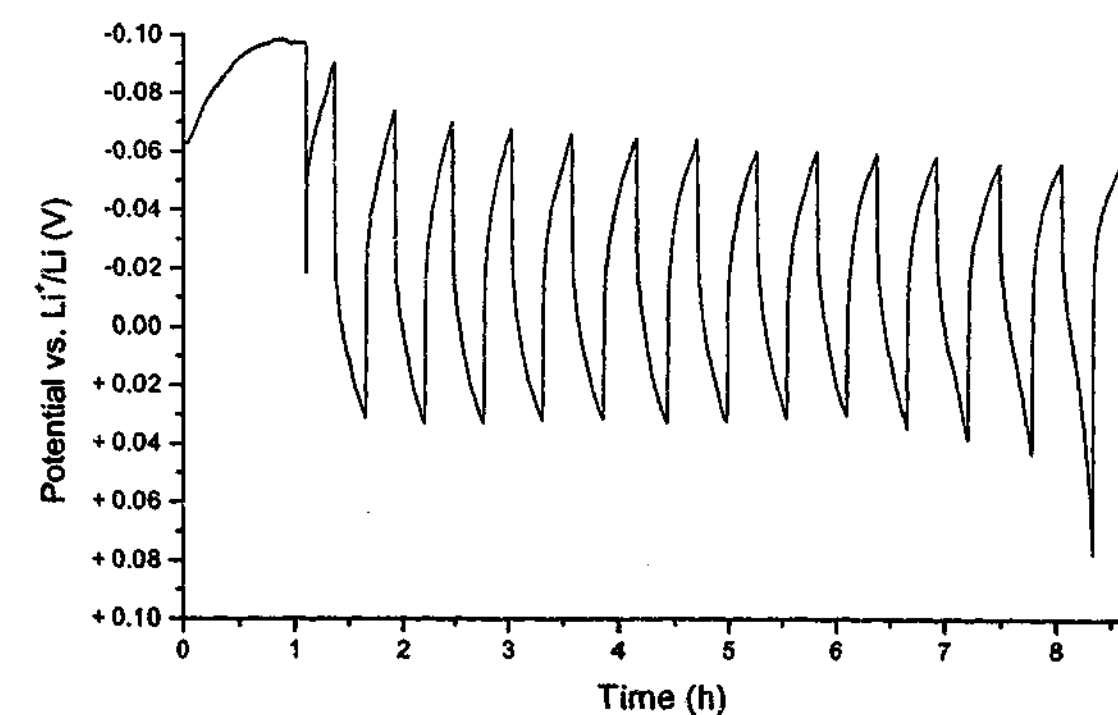
 $P_{13}(Tf)_2N$:

Conductivity (@ 25 °C)	1.4 mScm ⁻¹	29,30
Viscosity (@25 °C)	6.3 cP	29,30
Density (@20 °C)	1.45	29,30
Affinity for water	Low	29,30
T_m (°C)	12	29,30
T_{decomp} (°C)	400	20

Four consecutive cycling efficiency experiments were conducted in the $P_{13}(Tf)_2N$ optical cell.

Figure 3.1.51 shows a plot of the potential profile from the first cycling efficiency experiment. The deposition potential rose to relatively high values before reaching a plateau around 100mV. The cycling phase of the experiment extended for almost 14 cycles, giving a cycling efficiency of approximately 78 %.

The image shown in Figure 3.1.52 was acquired after the deposition phase of the experiment. The deposit was bright, had a hemispherical morphology and was uniformly

Fig. 3.1.51 0.5 mol kg⁻¹ $P_{13}(Tf)_2N$ cycling efficiency potential profile, 1st experiment.

distributed across the electrode surface. There was no indication of dendrites anywhere on the electrode surface.

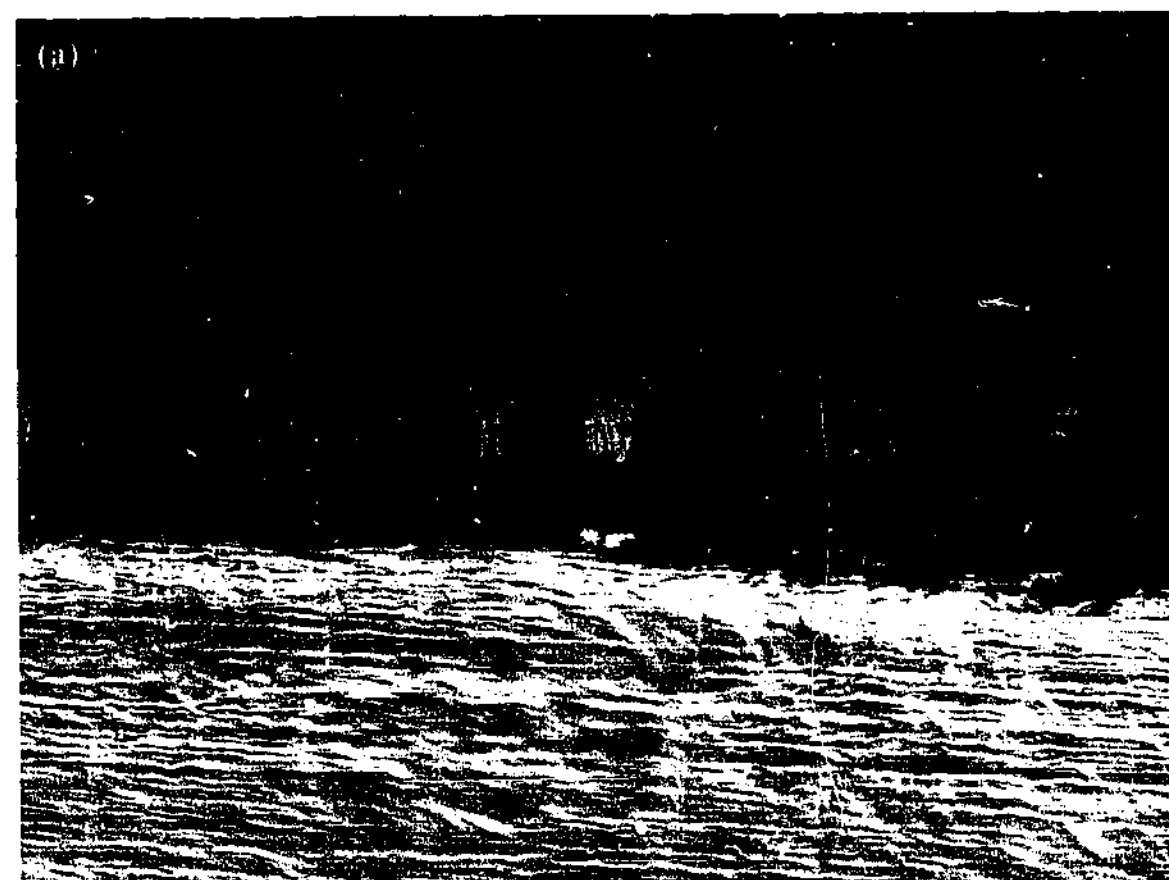


Fig. 3.1.52 $0.5 \text{ mol kg}^{-1} \text{ P}_{13}(\text{Tf})_2\text{N}$ post deposition image (1st experiment), Cu working electrode surface (a) 20 \times .

The images shown in Figure 3.1.53 show the copper electrode surface after the cycling phase of the experiment. A material of crystalline appearance uniformly covered the surface. There was no indication of any unreacted lithium.

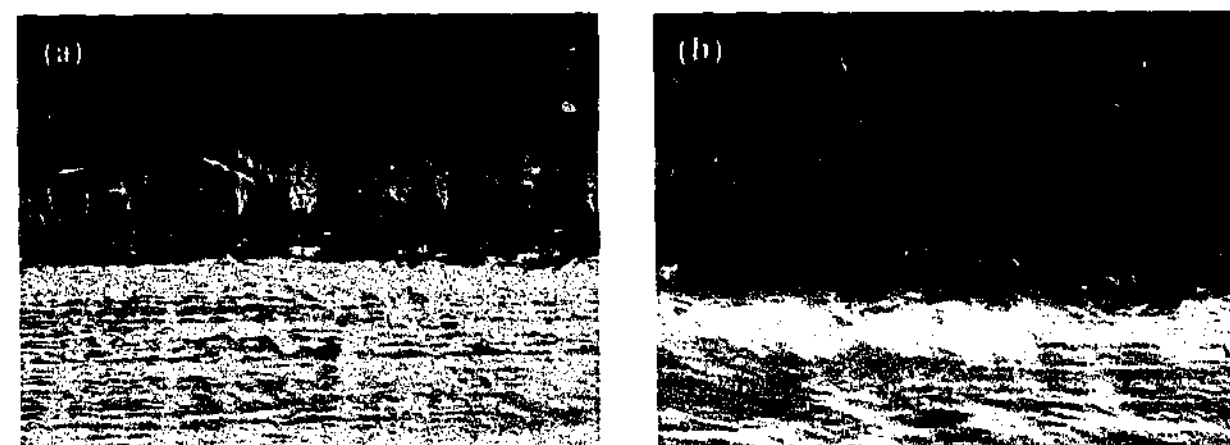


Fig. 3.1.53 $0.5 \text{ mol kg}^{-1} \text{ P}_{13}(\text{Tf})_2\text{N}$ post cycling images (1st experiment), Cu working electrode surface (a) 20 \times , (b) 40 \times .

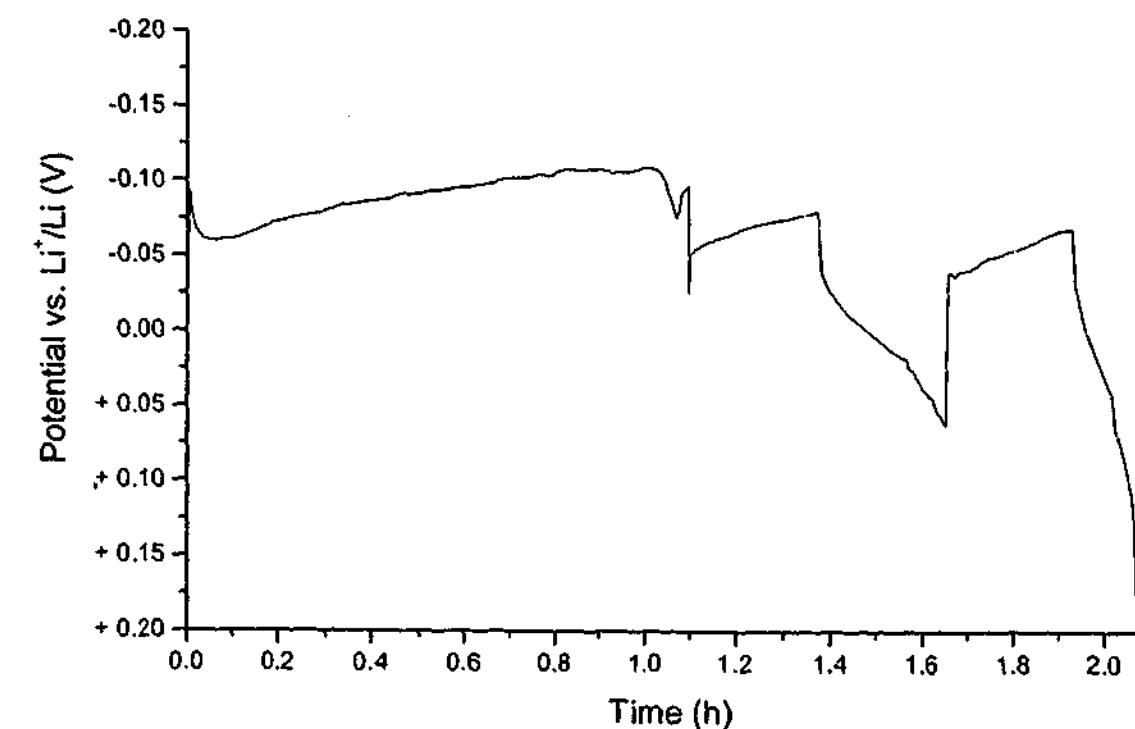


Fig. 3.1.54 $0.5 \text{ mol kg}^{-1} \text{ P}_{13}(\text{Tf})_2\text{N}$ cycling efficiency potential profile, 2nd experiment.

Figure 3.1.54 shows a plot of the potential profile from the second cycling efficiency experiment. Again the deposition potential rose to relatively high values before reaching a plateau around 100mV. The cycling phase of the experiment extended for 1.7 cycles, giving a cycling efficiency of approximately 30 %.

The images shown in Figure 3.1.55 were acquired after the deposition phase (a), and after the cycling phase (b), of the experiment. Image a) shows an example of the lithium deposit, which had deposited as fine, branched dendrites. Image b) shows the same deposit after cycling. Its appearance had not changed to any noticeable extent. Deposits exhibiting this morphology did not seem to participate in cycling at all, presumably because the 'thin' connection to the substrate was easily broken.

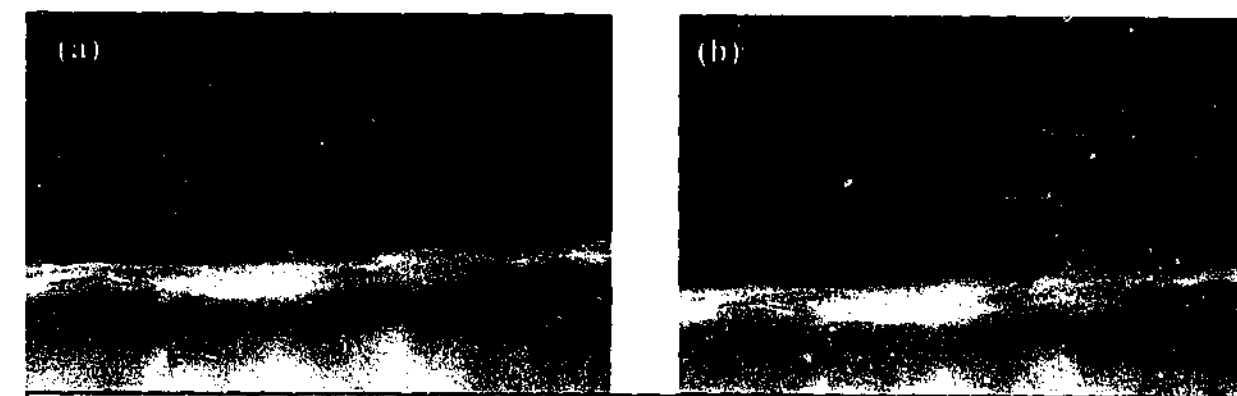


Fig. 3.1.55 $0.5 \text{ mol kg}^{-1} \text{ P}_{13}(\text{Tf})_2\text{N}$ Cu working electrode surface (2nd experiment), (a) post deposition image, 20 \times , (b) post cycling image, 20 \times .

Figure 3.1.56 shows a plot of the potential profile from the third cycling efficiency experiment. The cycling phase of the experiment extended for less than 0.5 dissolution cycles, giving a cycling efficiency of less than 10 %.

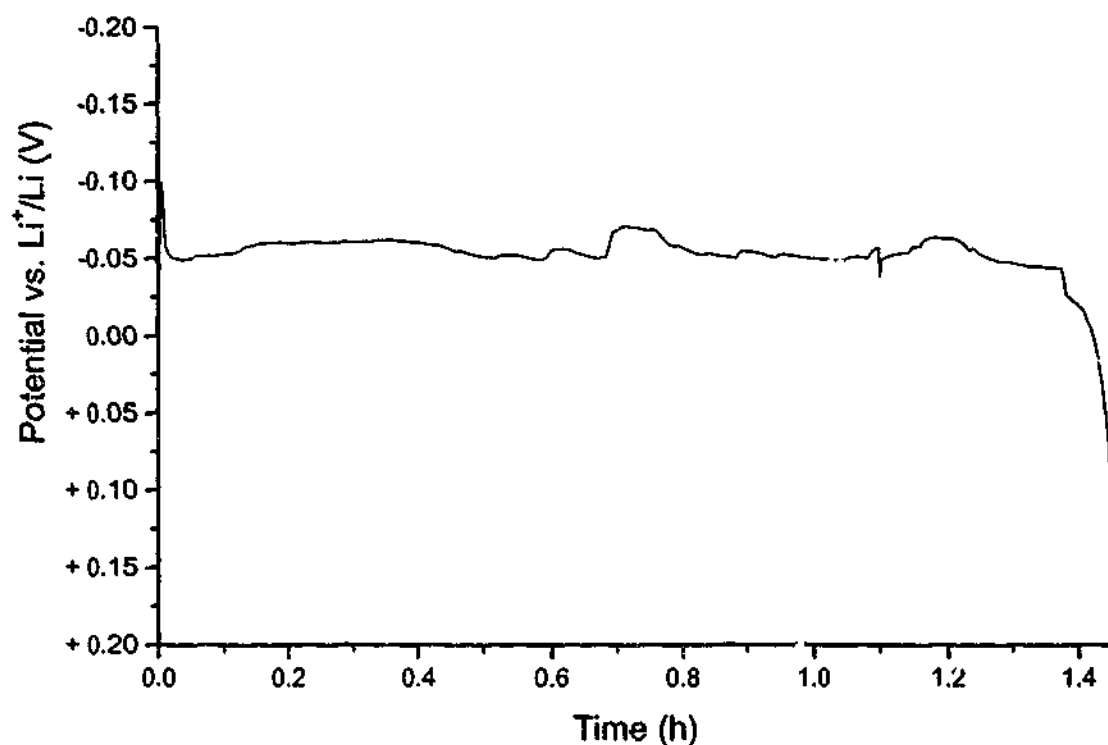


Fig. 3.1.56 $0.5 \text{ mol kg}^{-1} \text{ P}_{13}(\text{Tf})_2\text{N}$ cycling efficiency potential profile, 3rd experiment.

The images shown in Figure 3.1.57 were acquired after the cycling phase of the experiment. Again unreacted deposits having a fine, branched dendritic morphology were visible. The formation of this type of deposit appears to have been the principal cause of the rapid reduction in cycling efficiency exhibited by this cell.

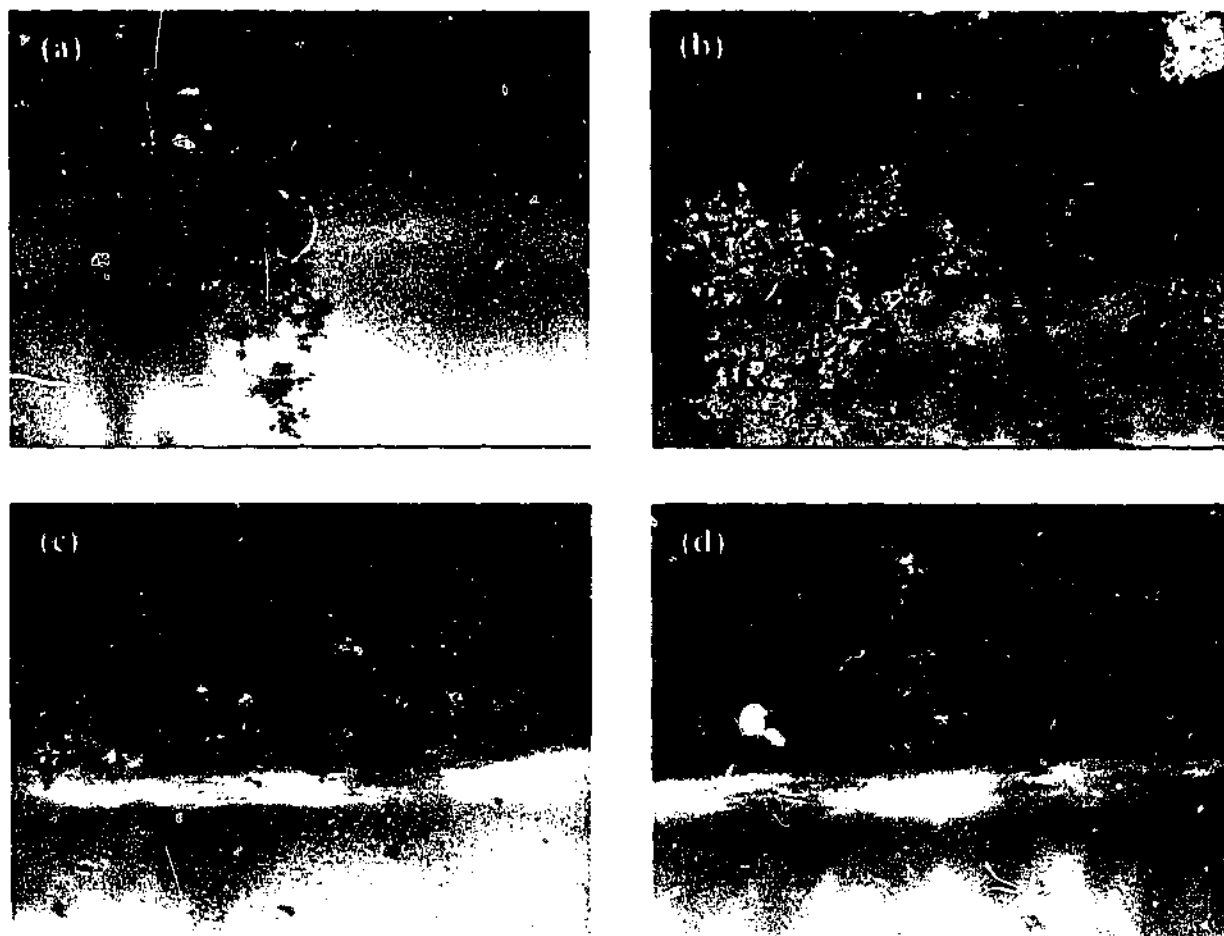


Fig. 3.1.57 $0.5 \text{ mol kg}^{-1} \text{ P}_{13}(\text{Tf})_2\text{N}$ post cycling images (3rd experiment), Cu working electrode surface (a) $20\times$, (b) $20\times$, (c) $20\times$, (d) $20\times$.

High rate experiment:

Figure 3.1.58 shows a plot of the potential profile from the first cycling efficiency experiment conducted at higher rates. The deposition dissolution current was set at $\sim 2 \text{ mA cm}^{-2}$, the amount of excess charge plated initially was 10 C cm^{-2} , and the fraction of charge cycled was 1 C cm^{-2} . The cycling profile of the experiment extended for almost 18 cycles, giving a cycling efficiency of approximately 67 %.

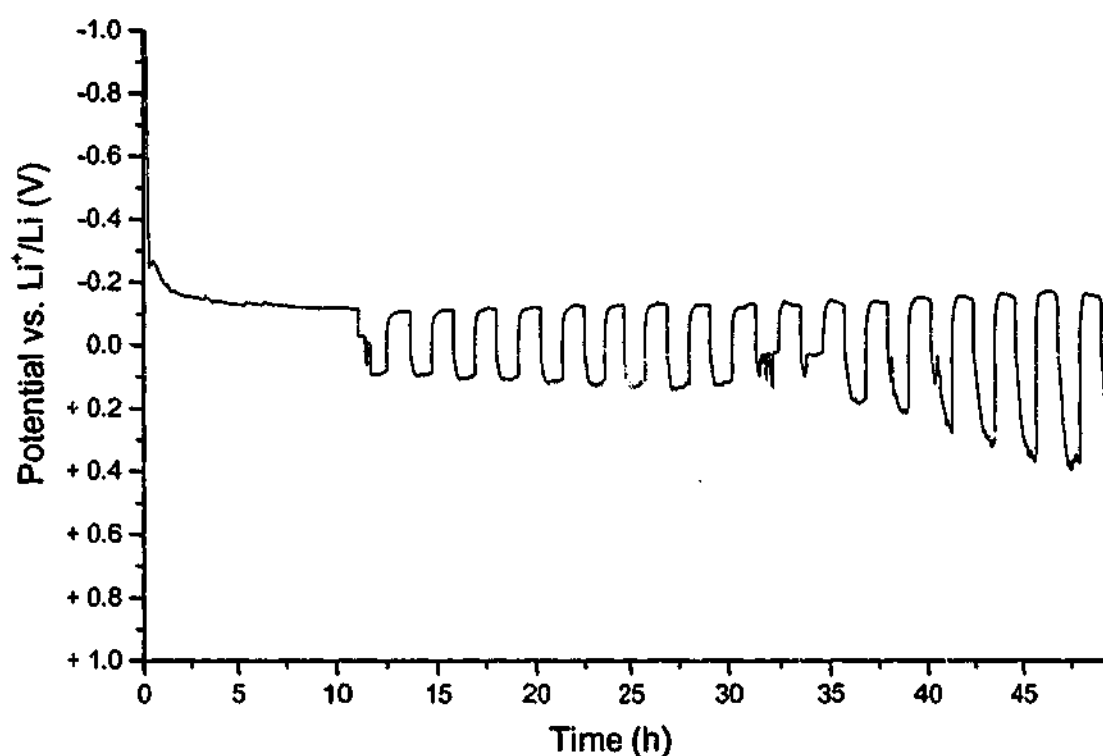


Fig. 3.1.58 0.5 mol kg⁻¹ P₁₃(Tf)₂N cycling efficiency potential profile (1st experiment). $I_{\text{dep/diss}} = \sim 2 \text{ mA cm}^{-2}$, $Q_{\text{ex}} = 10 \text{ C cm}^{-2}$, $Q_{\text{ps}} = 1 \text{ C cm}^{-2}$.

Figure 3.1.59 shows the evolution of the surface deposit morphology during the deposition phase of the experiment. The images show a highly dendritic deposit.

Figure 3.1.60 show images acquired after the deposition phase of the experiment. The deposits (images a & b) display a highly dendritic structure with some branching. The surface of the dendrites was bright and had a very smooth appearance. The dendrites were in the order of 3-5 μm in diameter, significantly thicker than the majority of dendrites previously observed which had been generated after consecutive cycling efficiency experiments. The lithium counter electrode surface (images c & d) shows the presence of a white deposit of crystalline appearance; uniformly distributed across the surface. Image c) shows some evidence of pitting/corrosion.

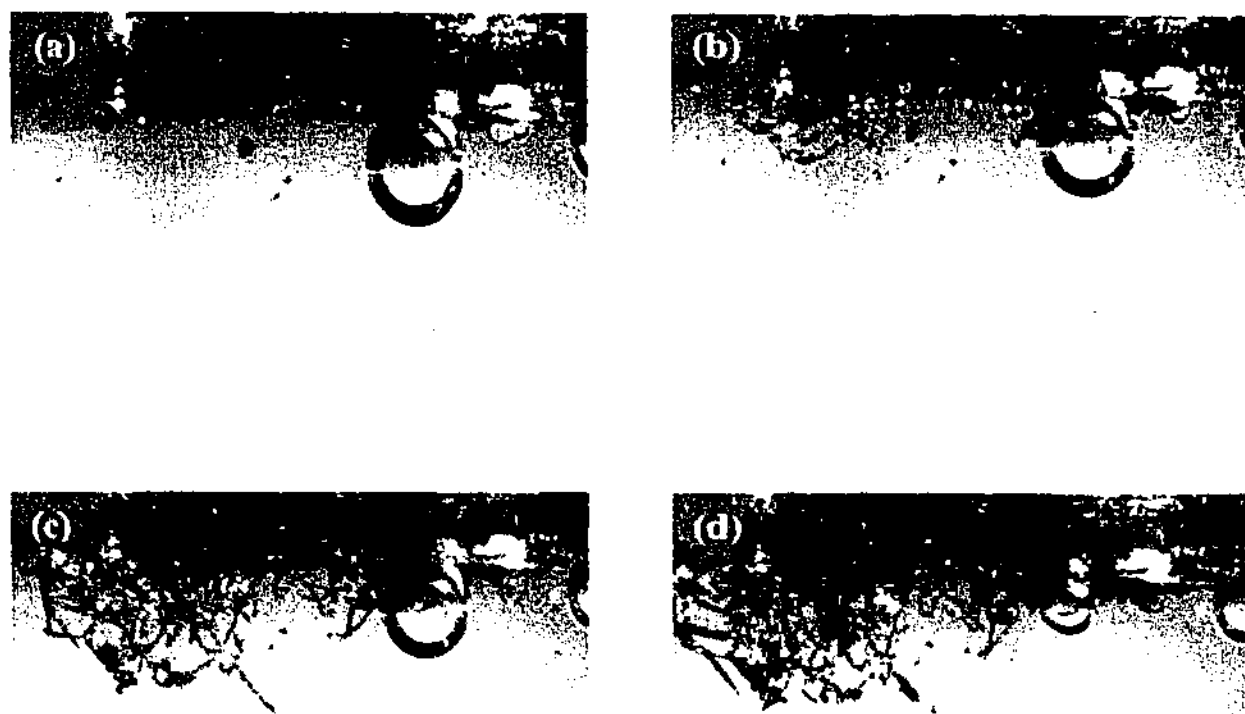


Fig. 3.1.59 $0.5 \text{ mol kg}^{-1} \text{ P}_{13}(\text{Tf})_2\text{N}$ in-situ deposition images (1st experiment), (a) Initial, (b) 3.7 h, (c) 7.4 h and (d) 11 h.

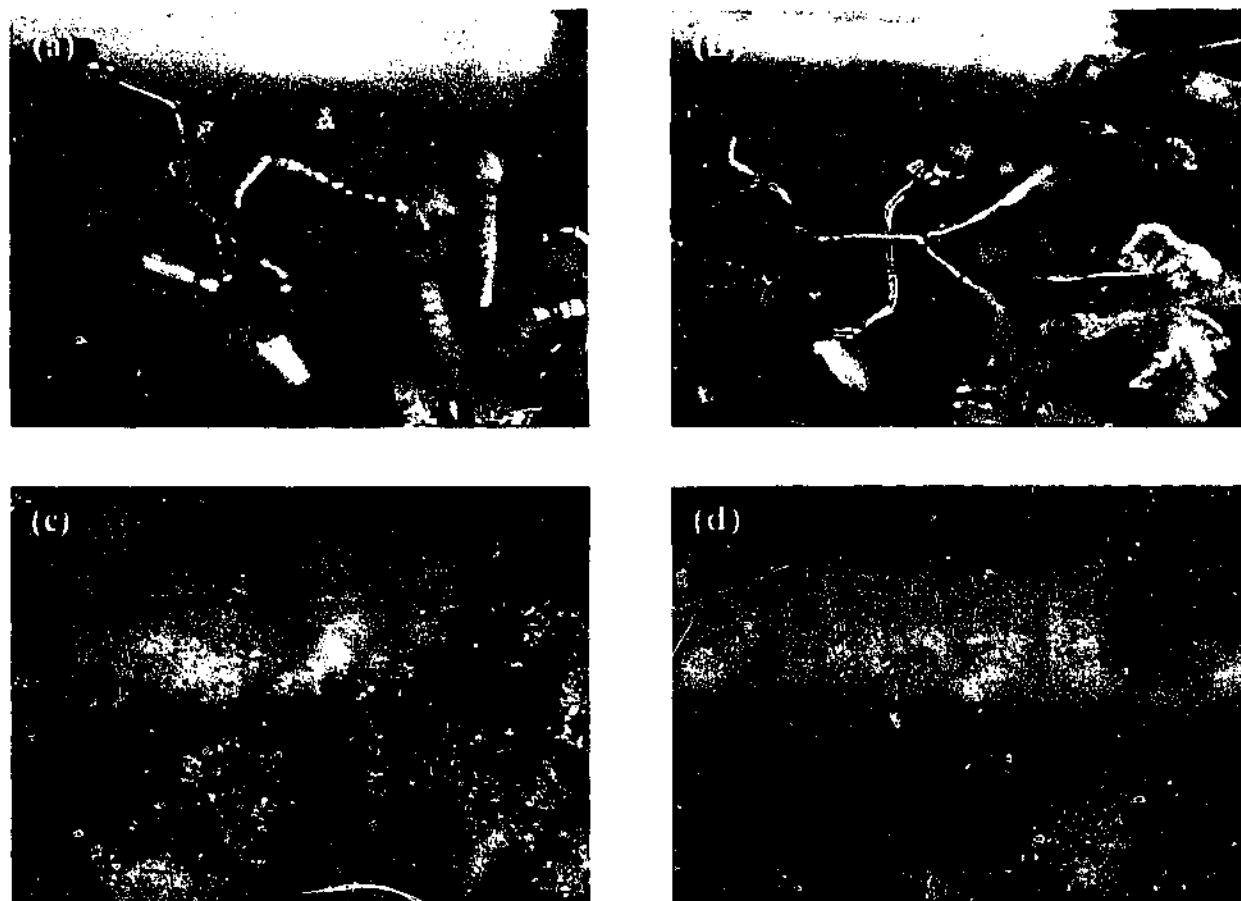


Fig. 3.1.60 $0.5 \text{ mol kg}^{-1} \text{ P}_{13}(\text{Tf})_2\text{N}$ post deposition images (1st experiment), Cu working electrode surface (a) 20 \times , (b) 20 \times . Li counter surface (c) 20 \times , (d) 20 \times .

Figure 3.1.61 shows images acquired during the cycling phase of the experiment. The dendritic structure 'pulsed' (i.e., exhibited a breathing-like change in shape) during cycling, possibly as a result of convection currents in the RTIL or possibly because of changes that occurred at the deposit | substrate interface. The bright appearance of the dendrites gradually faded and was replaced by a dulled grey appearance. Deposits were observed to become disconnected from the substrate (or from the rest of the dendritic structure), an obvious example is indicated by the arrow in image b).

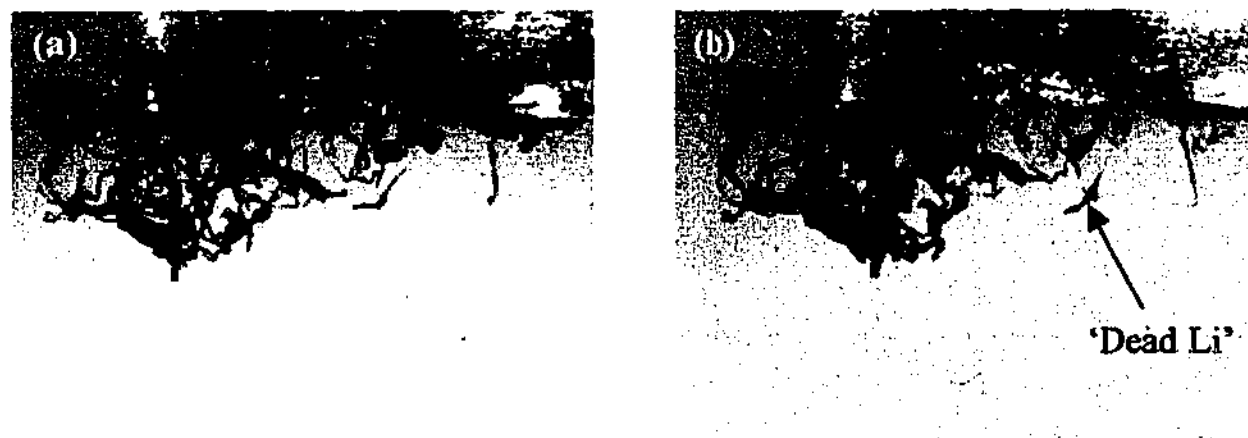


Fig. 3.1.61 $0.5 \text{ mol kg}^{-1} \text{ P}_{13}(\text{Tf})_2\text{N}$ in-situ cycling images, (a) 23.5 h, (b) 36 h.

Figure 3.1.62 shows images acquired after the cycling phase of the experiment. Image a) shows a finely branched dendritic deposit, the surface of which had developed a crystalline appearance after cycling; dendrites of this nature were not present after the deposition phase and must have been generated during the cycling phase of the experiment. Image b) shows an image of the surface of a 'bulk' dendrite (as opposed to a fine, branched dendrite). The surface was dulled and had a crystalline appearance, indicating that the dendrite surface had been active during cycling. The fact that the large deposit remained after the completion of the cycling phase of the experiment suggests that it had become disconnected from the substrate. Image d) shows a fine dendrite that clearly indicates the manner by which 'bulk' deposits can become disconnected. Image c) shows the presence of a precipitate on the surface of the cycled copper electrode.

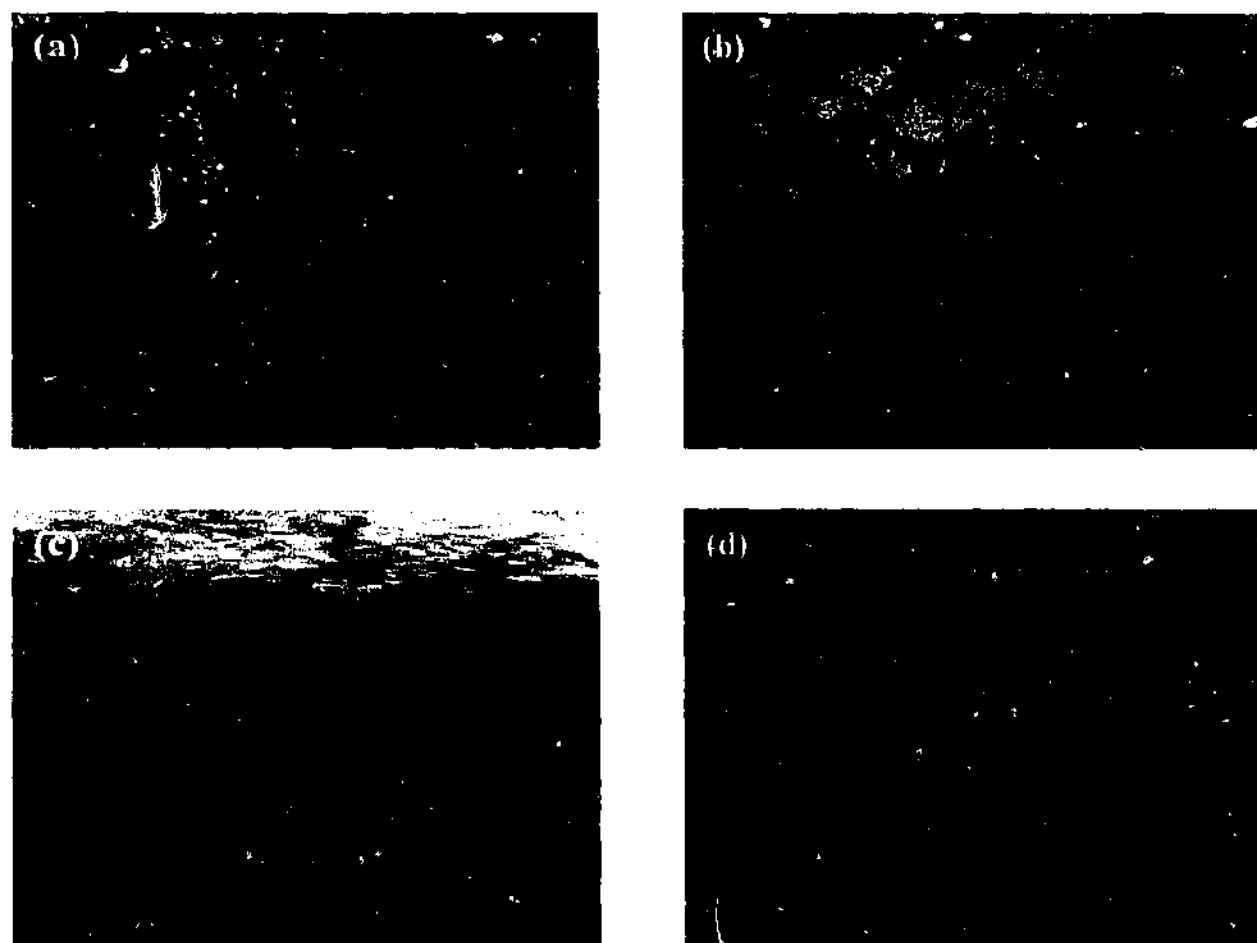


Fig. 3.1.62 $0.5 \text{ mol kg}^{-1} \text{ P}_{13}(\text{Tf})_2\text{N}$ post cycling images (1st experiment), Cu working electrode surface (a) 20 \times , (b) 20 \times , (c) 20 \times , (d) 20 \times .

Figure 3.1.63 shows a plot of the potential profile from the second cycling efficiency experiment conducted at higher rates. The cycling parameters were the same as the first experiment. The cycling phase of the experiment extended for 0.5 cycles, giving a cycling efficiency of less than 10 %.

Figure 3.1.64 shows the evolution of the surface deposit morphology during the deposition phase of the experiment. Deposition activity was located in the same region as in the first experiment; however the deposit exhibited a much finer dendritic structure. Once the deposit had 'filled' the initial region, deposition commenced in a different location (right-hand side of images b), c) & d)). The deposit had a similar appearance to the original deposit in the first experiment.

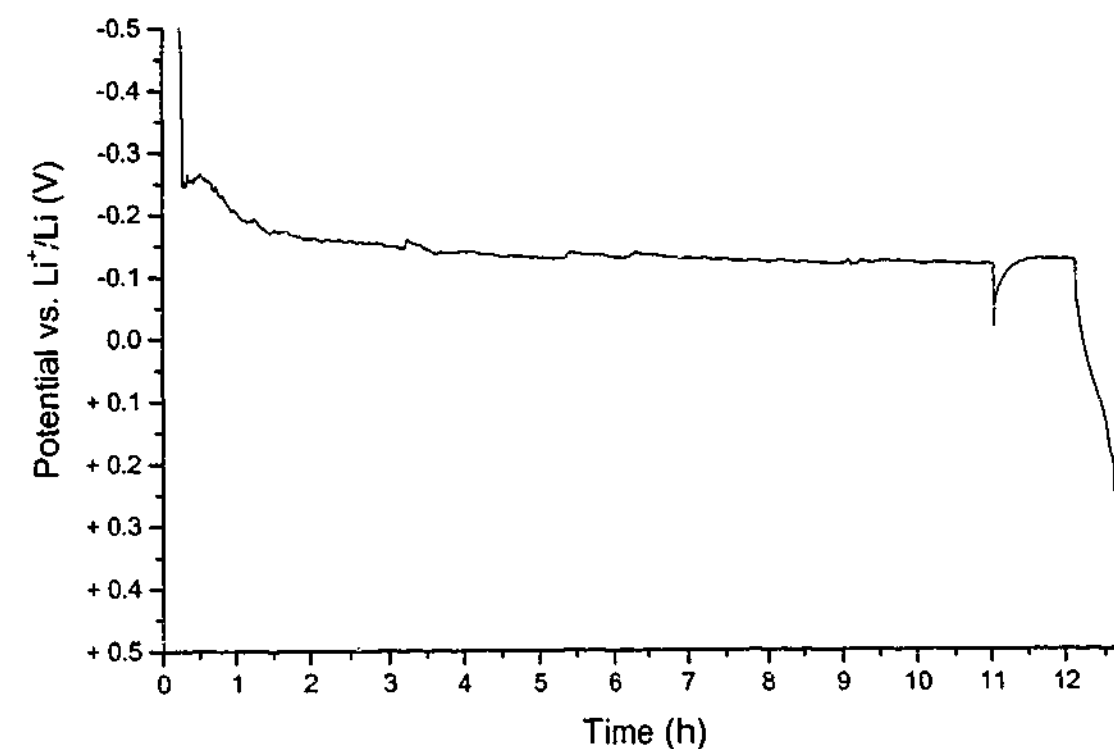


Fig. 3.1.63 0.5 mol kg⁻¹ P₁₃(Tf)₂N cycling efficiency potential profile (2nd experiment). $I_{\text{dep/diss}} = \sim 2 \text{ mA cm}^{-2}$, $Q_{\text{ex}} = 10 \text{ C cm}^{-2}$, $Q_{\text{ps}} = 1 \text{ C cm}^{-2}$.

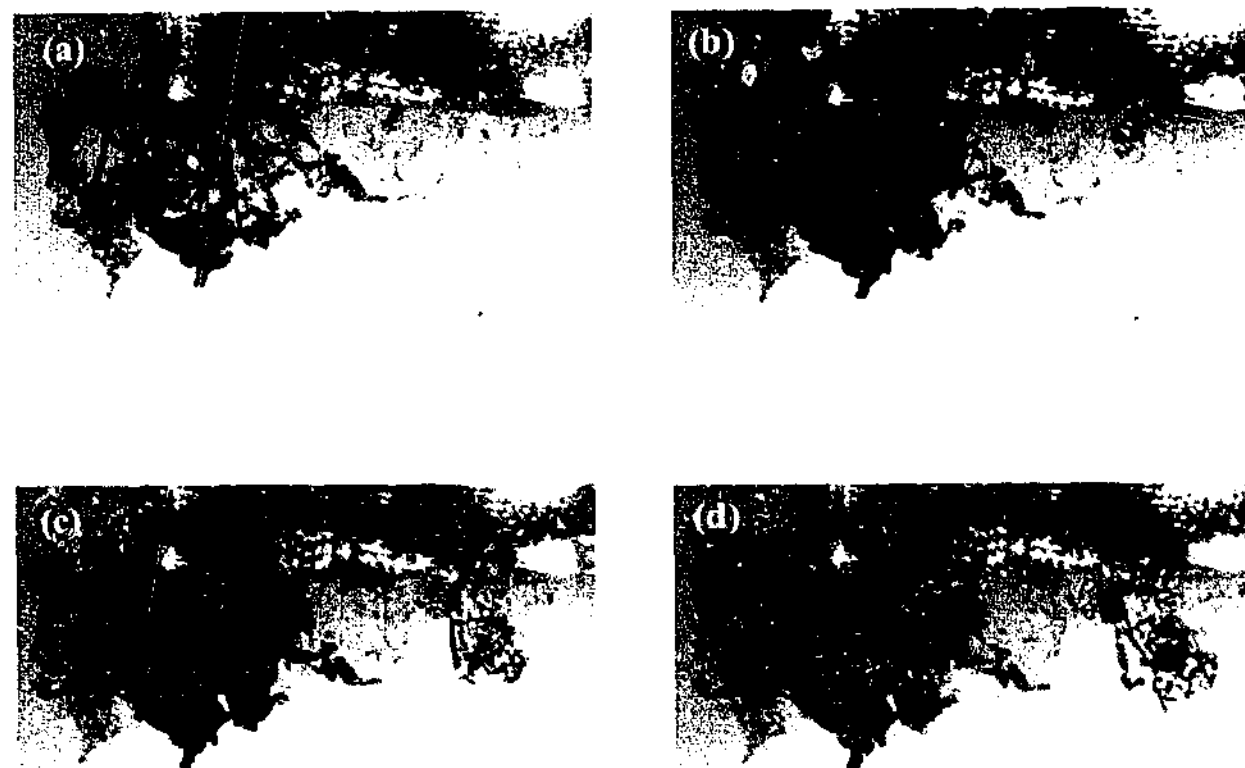


Fig. 3.1.64 0.5 mol kg⁻¹ P₁₃(Tf)₂N in-situ deposition images (2nd experiment), (a) Initial, (b) 3.7 h, (c) 7.4 h and (d) 11 h.

Figure 3.1.65 shows colour images acquired after the deposition phase of the experiment. The deposits display a highly branched, fine dendritic structure. The dendrites were significantly less than 10 μm in diameter. As had been seen in previous experiments (Fig. 3.1.59), this type of deposit cycled very poorly.

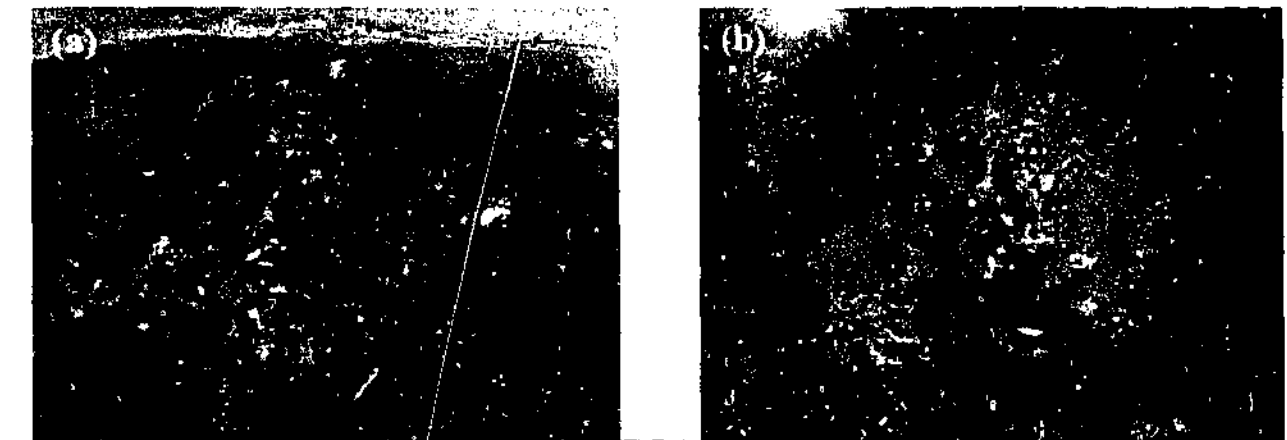


Fig. 3.1.65 0.5 mol kg⁻¹ P₁₃(Tf)₂N post deposition images (2nd experiment), Cu working electrode surface (a) 20 \times , (b) 20 \times .

Figure 3.1.66 shows images acquired after the cycling phase of the experiment. Image a) shows an excellent example of a piece of disconnected lithium that, presumably, would have otherwise been active during cycling. Other examples of bright lithium deposits that persisted after cycling are shown. Image e) shows an image of the surface of the lithium counter electrode which was covered in a deposit of crystalline appearance. Again there was no sign of any dendritic deposit on the counter electrode surface.

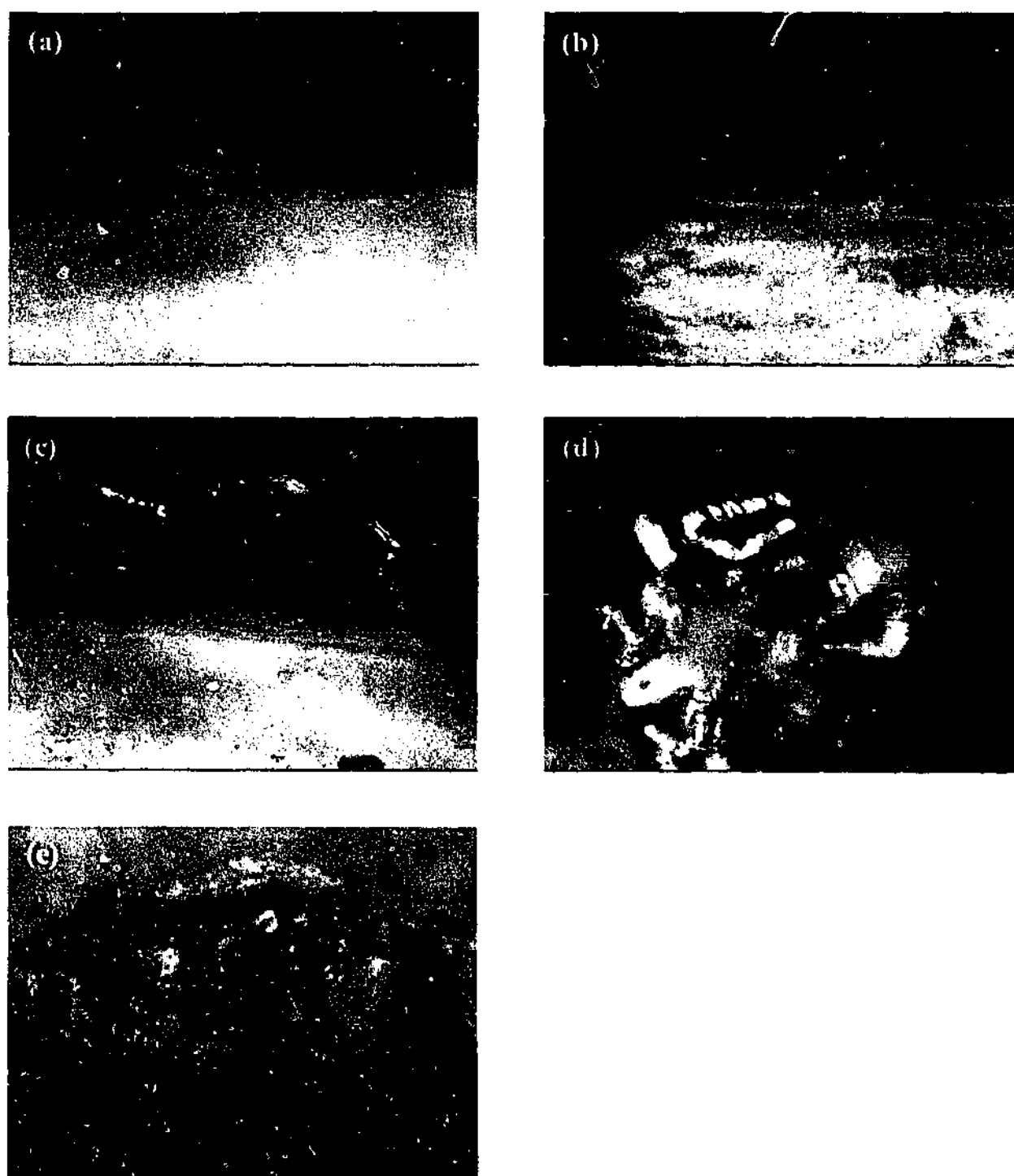


Fig. 3.1.66 $0.5 \text{ mol kg}^{-1} \text{ P}_{13}(\text{Tf})_2\text{N}$ post cycling images (2^{nd} experiment), Cu working electrode surface (a) $20\times$, (b) $20\times$, (c) $20\times$, (d) $20\times$. Li counter surface (e) $20\times$.

Very high rate experiment:

The images shown in Figure 3.1.67 were acquired during a high rate deposition experiment ($\sim 12 \text{ mAcm}^{-2}$ and 10 Ccm^{-2}). The deposit was highly dendritic and had a fine, branched structure. As expected, the deposit cycled very poorly.

Figure 3.1.68 shows the lithium counter electrode surface after the deposition phase of the experiment. The presence of a dendritic deposit on the surface (where only dissolution should have occurred) is difficult to explain. The deposit is perhaps evidence of the formation of large potential differences across the counter electrode surface when a high current density is flowing. Inhomogeneities in the SEI could lead to the formation of transient local regions that are 'relatively cathodic'. Moreover, the lithium concentration in this region is likely to be very high and would favour lithium deposition/precipitation in regions of relatively cathodic potential and/or high concentration.

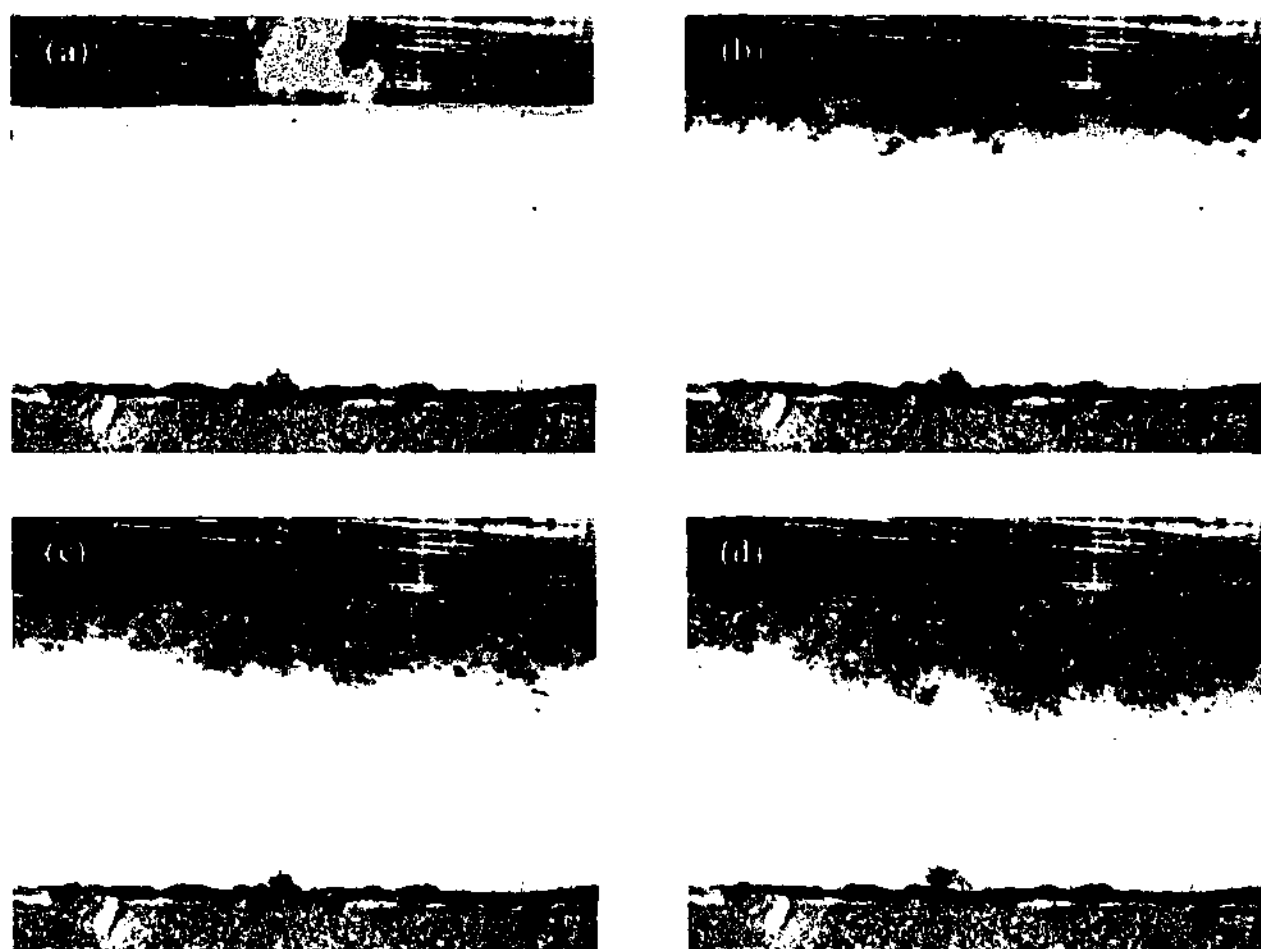


Fig. 3.1.67 $0.5 \text{ molkg}^{-1} \text{ P}_{13}(\text{Tf})_2\text{N}$ in-situ deposition images. High rate experiment, $\sim 12 \text{ mAcm}^{-2}$ & 10 Ccm^{-2} (a) Initial, (b) 5 min, (c) 10 min and (d) 15 min.



Fig. 3.1.68 $0.5 \text{ mol kg}^{-1} \text{ P}_{13}(\text{Tf})_2\text{N}$ post deposition image (high rate experiment), Li counter electrode surface – dendrites formed during dissolution (20 \times).

Deposition on a sputtered gold substrate:

Recently, the deposition of metals on an insulating substrate was reported.³¹ By using a specially designed cell (Fig. 3.1.69), it was possible to propagate the growth of a thin metallic film on a glass (or teflon) substrate at high rates. By using a gold 'edge' which lays on the surface of the substrate to be coated and acts as a starting point for the deposition, under certain conditions a uniform, 'covering' deposit can be created. The

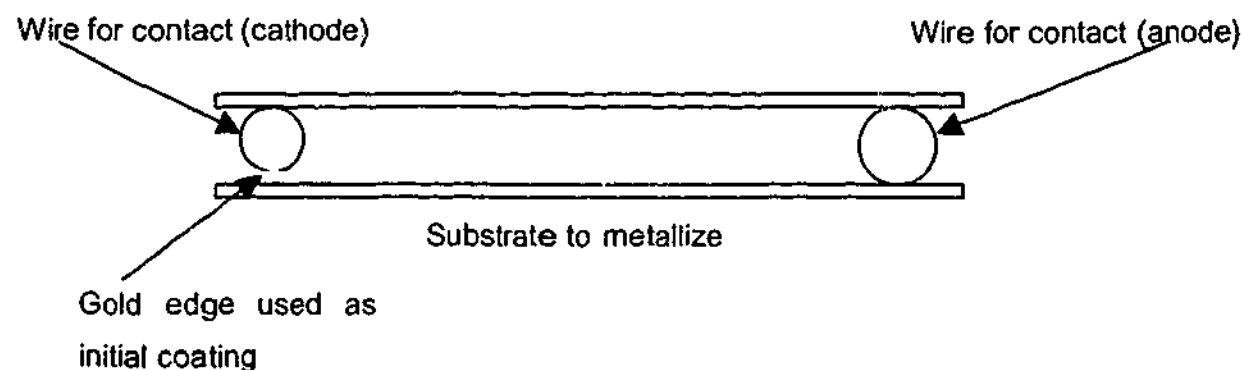


Fig. 3.1.69 Cell for deposition on an insulating substrate, taken from ref. ³¹

authors suggest this type of plating as a way to control lithium deposit morphology and as a way to achieve high deposition rates. A similar experiment was attempted in the optical cell; primarily because the optical cell design lent itself to such an experiment.

The experiment was performed in a modified optical cell (i.e., incorporating a sputtered gold edge) filled with $0.5 \text{ mol kg}^{-1} \text{ P}_{13}(\text{Tf})_2\text{N}$. The experiment was unsuccessful in duplicating the reported phenomenon. The gold edge needed to be thin enough to be non-conducting, in practice this was difficult to achieve and deposition occurred on the gold substrate as well as on the exposed copper surface. However, the lithium deposit on the gold sputtered substrate had a striking appearance, Fig. 3.1.70. A cycling efficiency measurement was not meaningful in this cell because the bulk of the deposit formed as a dendritic mass on the exposed copper surface (indicated by the arrow in image a), Fig. 3.1.70). Thus, a cycling efficiency measurement would have involved an unknown current density at the copper and the gold surface, in addition, the fraction of charge on each surface was unknown. However, the deposit on the gold substrate was very uniform and had a hemispherical morphology. Images c) and d) show the 'front' of the gold substrate (i.e., the edge of the sputtered coating that was closest to the counter electrode), here the coverage of the lithium deposits is relatively dense. The feature extending beyond the front of the gold substrate possibly represents the successful deposition of lithium on the glass substrate, as had been reported.³¹ Image f) shows the deposit after cycling; the deposit morphology had remained remarkably smooth. This experiment, while not achieving its intended goal, indicates an avenue worthy of further investigation. It is possible that the use of different substrate compositions (pure metals and alloys) could allow improved control of the lithium deposit morphology in an RTIL.

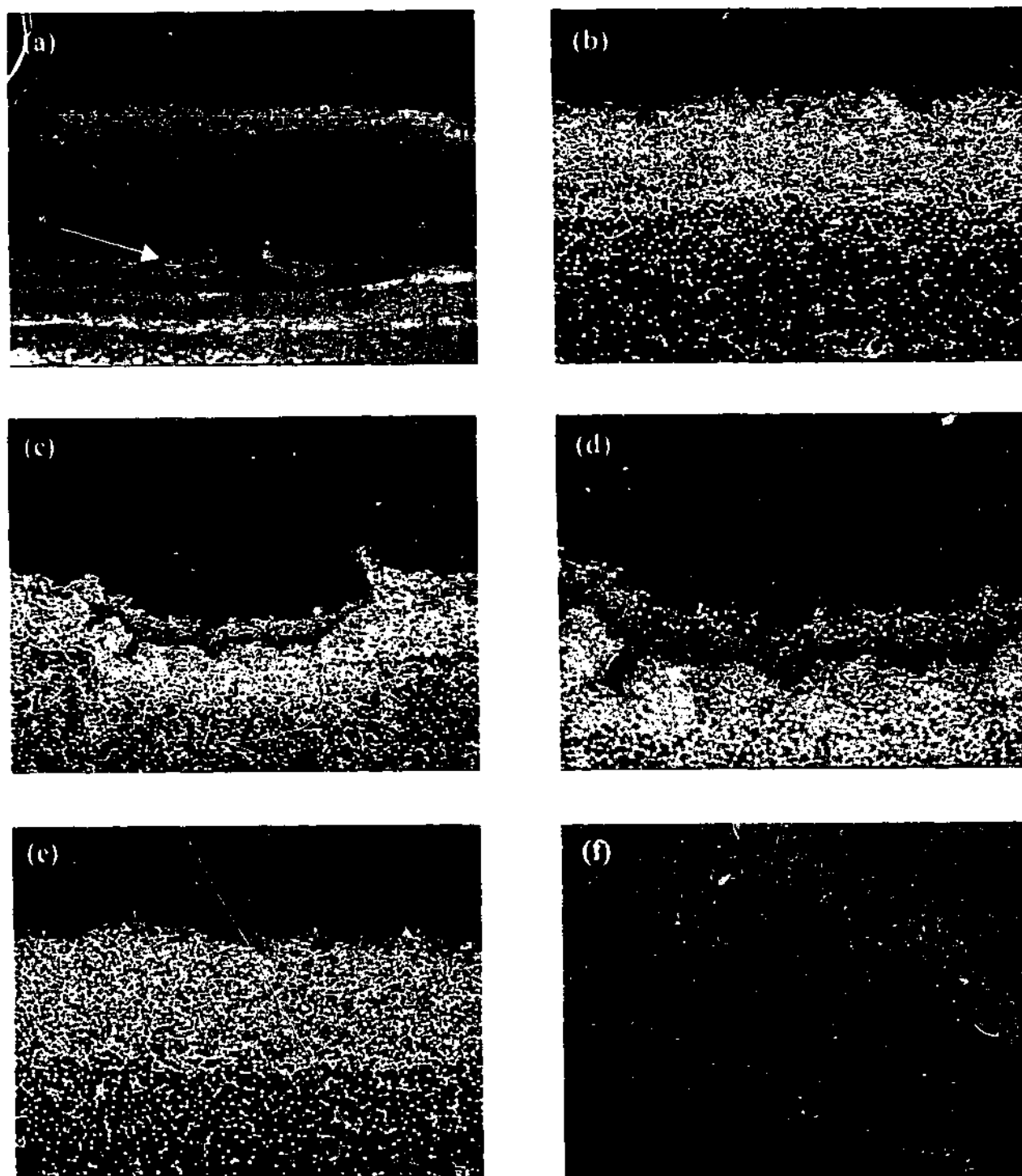


Fig. 3.1.70 Lithium deposited on a gold sputtered substrate (a) 5 \times , (b) 20 \times , (c) 20 \times , (d) 40 \times , (e) 20 \times , (f) 20 \times .

PVP additive in $0.5 \text{ mol kg}^{-1} \text{ P}_{13}(\text{Tf})_2\text{N}$:

The final series of experiments conducted in the optical cell involved the use of polyvinylpyrrolidone (PVP) as an additive, which has been shown to improve lithium cycling efficiency in 0.25 M LiBF_4 and $0.25 \text{ M Li}(\text{Tf})_2\text{N}$ EC:PC (1:1) solutions.³² The use of additives has been a common avenue of investigation for the improvement of cycling efficiency for conventional solvents. A more extensive investigation of a number of additives in $\text{P}_{13}(\text{Tf})_2\text{N}$ will be presented in a later section (Section 3.5).

Four consecutive experiments were performed in the optical cell and they followed the by now familiar theme of a gradual increase in the amount of dendritic deposit with each consecutive experiment.

Figure 3.1.71 shows the potential profile recorded during the first experiment. The deposition potential was low, and remained low throughout the experiment. The cycling phase of the experiment extended for almost 37 dissolution cycles giving a cycling efficiency of approximately 90 %.

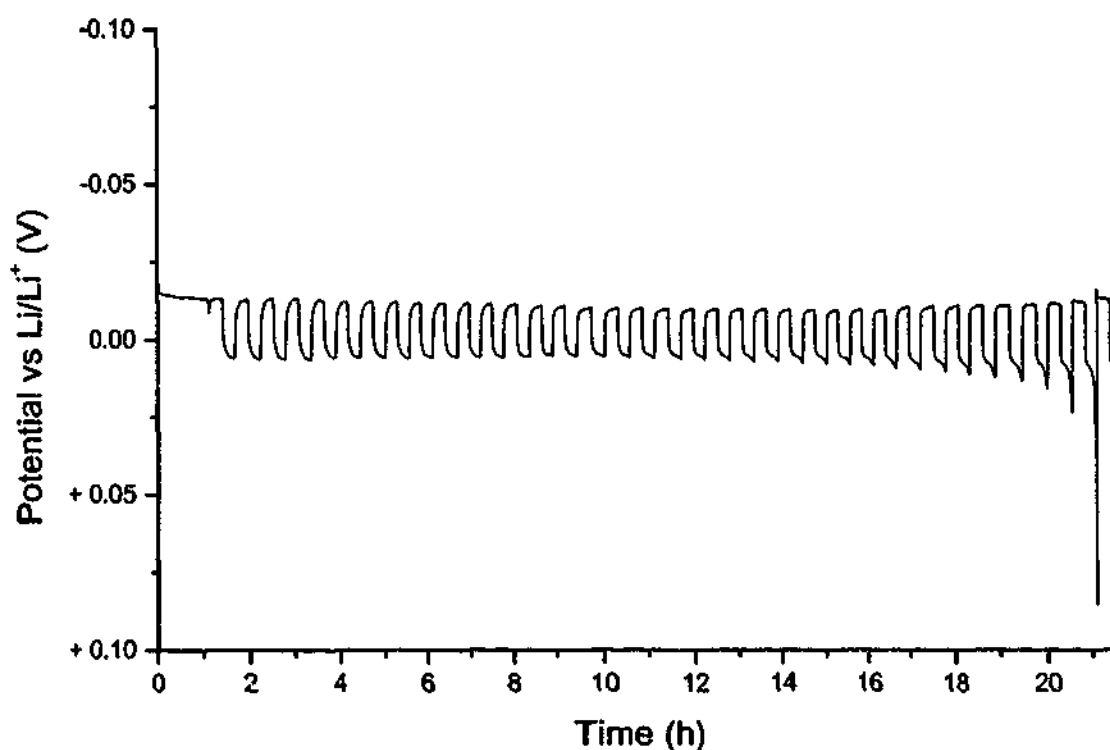


Fig. 3.1.71 $0.5 \text{ mol kg}^{-1} \text{ P}_{13}(\text{Tf})_2\text{N}$ / 0.30 wt\% PVP cycling efficiency potential profile, 1st experiment.

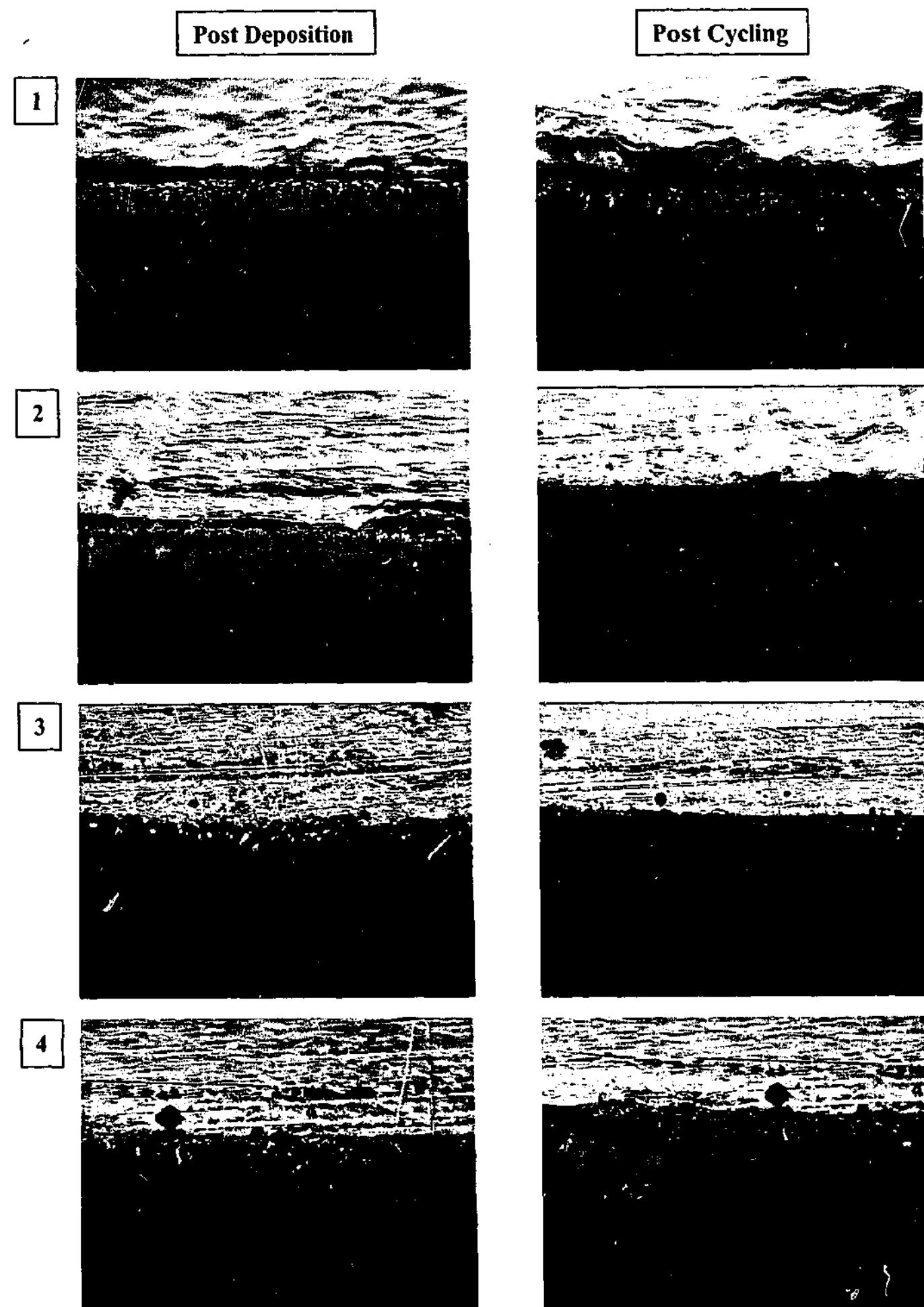


Fig. 3.1.72 Representative images obtained post deposition and post cycling for four consecutive experiments in $0.5 \text{ mol kg}^{-1} \text{ P}_{13}(\text{Tf})_2\text{N} / 0.3 \text{ wt\% PVP}$. All images are at $20\times$ magnification.

The images shown in Figure 3.1.72 show that the initial lithium deposit was uniform and non-dendritic. With each successive cycling efficiency experiment, the deposit became increasingly more dendritic and the presence of dead lithium after the cycling phase had been completed became more obvious.

The images presented in Fig. 3.1.73 show the lithium surface in the cycled $0.5 \text{ mol kg}^{-1} \text{ P}_{13}(\text{Tf})_2\text{N} / 0.3 \text{ wt\% PVP}$ cell. The surface exhibits an unusual appearance; image a) shows a porous deposit which appears to be an agglomerate of lithium and lithium reaction products. Given that this type of feature was not observed in other cells it is reasonable to assume that it is related to the polymer additive. Image b) shows similar features present on the reference electrode surface, indicating that a spontaneous process formed the agglomerates. It was noted that some gas evolution occurred at the counter and reference electrodes.

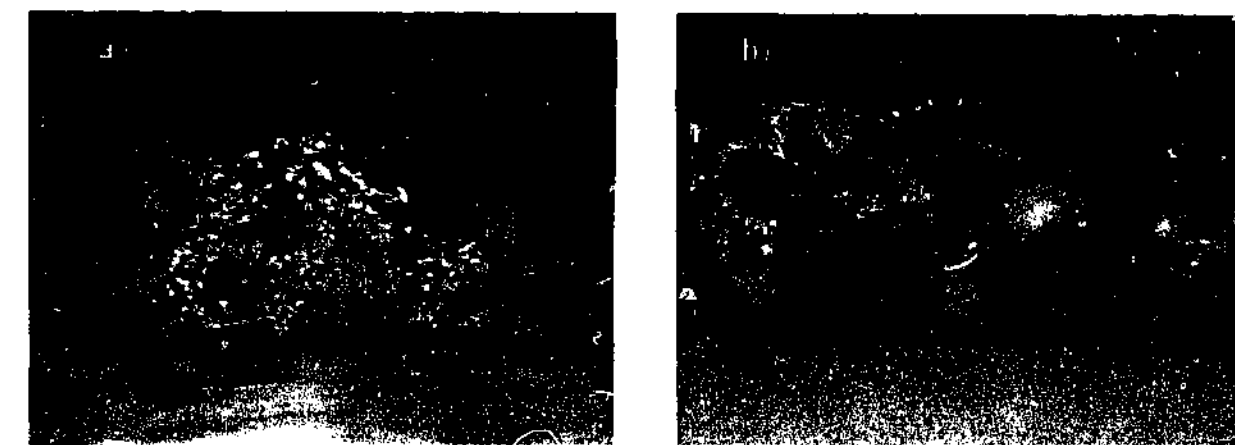


Fig. 3.1.73 Images of the lithium counter (a) and lithium reference electrode (b) surface in the $0.5 \text{ mol kg}^{-1} \text{ P}_{13}(\text{Tf})_2\text{N} / 0.3 \text{ wt\% PVP}$ cell. Both images at $20\times$ magnification.

The general course of the experiments saw decreasing cycling efficiency values with each consecutive experiment, the first experiment giving a maximum of 90 %. Table 3.1.4 summarises the events that took place over the course of the four experiments.

Table 3.1.4 Summary of $P_{13}(Tf)_2N/PVP$ optical cell experiments.

No.	Cyc. Eff. %	Deposit surface	Cycled surface
1	90	Uniform, hemispherical	Crystalline deposit
2	65	Uniform, hemispherical, some dendrites	Crystalline deposit, dead lithium
3	43	Increasingly dendritic	Crystalline deposit, dead lithium
4	38	Dendritic, fine branched	Large quantities of dead lithium visible

The $P_{13}(Tf)_2N$ was the most extensively investigated system using the optical cell. The highest cycling efficiency was obtained (with the addition of PVP) of all of the RTILs investigated. The deposit morphology was found to be dependent upon current density and on the amount of charge-discharge cycling that the surface had been subjected to. The cycling efficiency was highly dependant on the deposit morphology. The deposit morphology also appeared to be influenced by the choice substrate material.

3.1.3 Conclusions:

Strengths/weaknesses of optical cell:

The use of the modified optical cell enabled quantitative determination of the cycling efficiency of the electrolyte. It also enabled the observation of the evolution of the deposit morphology throughout the course of the experiment. High quality images were obtained. The combination of a quantitative measurement and the ability to observe the electrode | electrolyte interface provided a powerful tool for understanding the processes contributing to a cycling efficiency of less than 100 %. In addition, the cell also allowed in-situ Raman spectra to be obtained. This data will be presented in a later section (section 3.4.3)

However, fabrication of the cell was difficult and time consuming, which made duplicate measurements impractical. Also, it was not possible to accurately control the surface area

of the working electrode. This meant that the applied current density was an estimate only. Given the observed sensitivity of the measurement to current density this was a major weakness of the cell.

An important consideration derives from the fact that the measurements were sensitive to the presence of atmospheric contaminants. The seal of the cell was generally good, but imperfect. All of the cells slowly exhibited changes associated with reaction with the atmosphere, generally over a period of 3 – 6 months, occasionally longer. The variation in the quality of the seal (along with the need to estimate the current density) made the reproducibility of the measurements difficult to estimate. Without performing multiple experiments, requiring the fabrication of multiple cells, the cycling efficiencies obtained can only be considered to be semi-quantitative.

In general terms the optical cell experiments were very successful and provided valuable insight into the behaviour of a new class of electrolytes, RTILs, when cycled with a lithium electrode. The general cell design could find application in a multitude of other studies where electrodeposition and deposit morphology are of interest, particularly where atmospheric contaminants are a consideration. Accurate determination of the working electrode area could be achieved with the addition of a low concentration of analyte of known diffusion coefficient, allowing for the geometry of the cell, a surface area could be determined using cyclic voltammetry or a similar technique. Alternatively, the presence of two reference electrodes allows for the determination of the area of the working and counter electrodes if the electrolyte conductivity is known. Subtle variations in measurements caused by the access of atmospheric contaminants and by changes in the quality of the glovebox atmosphere cannot be entirely eliminated. All conclusions drawn pertaining to the behaviour of the cells must therefore consider the impact of these variations as a determining factor.

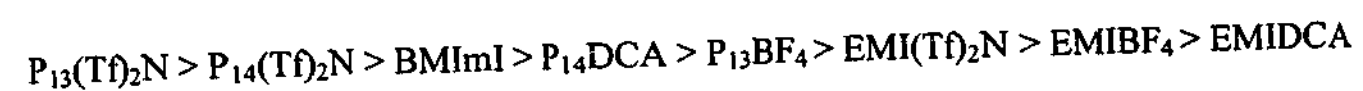
Summary of RTIL electrolyte behaviour:

The series of experiments conducted in the optical cell allows for the relative cycling efficiencies of the systems studied to be compared. Table 3.1.5 summarises the cycling efficiencies obtained from the first experiment for each system.

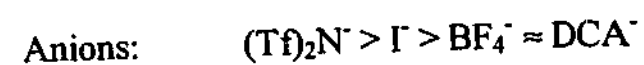
Table 3.1.5 Summary of optical cell measurements.

RTIL	Cycling efficiency (%)	Deposit morphology	Post cycling surface
EMIDCA	< 5	N/A	N/A
EMIBF ₄	< 5	N/A	N/A
EMI(Tf) ₂ N	10 (65)	Hemispherical/Dendritic	Crystals
P ₁₃ BF ₄	29	Dendritic	Crystals/Dead Li
P ₁₄ DCA	47	Fine hemispherical	Bare/Dead Li
BMImI	55	Fine hemispherical	Crystals
P ₁₄ (Tf) ₂ N	55	Hemispherical/Dendritic	Crystals/Dead Li
P ₁₃ (Tf) ₂ N	78	Hemispherical	Crystals
P ₁₃ (Tf) ₂ N/PVP	90	Hemispherical	Crystals

The RTILs can be ranked according to their relative ability cycle lithium reversibly. Ranking the electrolytes in this way reflects not only their relative electrochemical stability, but also their ability produce a uniform deposit. The ranking also reflects the nature of the SEI formed in the RTIL and its ability to passivate the lithium surface, but still allow lithium transport.



From the ranking of the various RTILs, the ranking of the cations and anions can be inferred;



The relative ranking of the RTILs is noted to correlate to their relative hydrophobicity / hydrophilicity. The more hydrophobic systems (e.g., P₁₃(Tf)₂N) exhibit superior cycling behaviour. A possible explanation for the relationship lies in the fact that the more hydrophilic systems, given that all RTILs were all dried under the same conditions, will contain a greater proportion of water as a contaminant. However, it seems unlikely that trace levels of water could have such a significant effect. This leads to the more interesting possibility that the properties dictating relative affinity for water could also be important in dictating lithium cycling behaviour. It has been noted that properties such as hydrophobicity / hydrophilicity are generally dictated by the anion.³³

Another significant observation that can be made of the relative behaviour of the RTILs studied here pertains to the morphology of the lithium deposit. The most favourable morphologies (uniform, fine hemispheres) were obtained in the most conductive/least viscous RTILs. Thus, for the systems studied here, P₁₄DCA and BMImI (EMIDCA and EMIBF₄ were more conductive but not sufficiently stable) produced the most favourable deposits. The correlation between morphology and conductivity suggests that, at least initially, the nature of the deposit is dictated largely by the transport of lithium from the bulk electrolyte and not by the properties of the SEI. The SEI becomes significant with repeated cycling and will be discussed shortly. This observation suggests that, in order to achieve a deposit that is uniform and free of dendrites in a RTIL, transport of lithium to the electrode surface that is not limited by diffusion from the bulk electrolyte is a key requirement. Furthermore, in the absence of any evidence to the contrary, it suggests that, if the transport of lithium to the electrode surface is not diffusion limited, the lithium deposit will *always be uniform and hemispherical in a RTIL* – at least initially.

This leads to a discussion of the influence of current density on the morphology of the deposit. It was demonstrated that the deposit was very sensitive to current density, and that the deposit became increasingly dendritic as the current density was increased. Undoubtedly this is related to the preceding discussion of the influence of electrolyte conductivity. The influence of current density in conventional solvents has been reported by numerous authors.^{2,4,34,35} The reports of Brissot *et. al.*^{1,3,6,7,36}, in particular, refer to the way in which the diffusion of lithium from the electrolyte (in their case, a polymer) to the electrode surface influences deposit morphology. The authors contend that the onset of dendritic deposition is closely related to the Sands time, when the concentration of lithium

close to the electrode surface approaches zero. It appears that a similar process occurs in RTILs. When a large concentration gradient is present at the surface, nucleation at a relatively small number of thermodynamically favoured sites is favoured – the result being dendritic deposition morphology. This occurrence should not be confused with the appearance of dendritic deposits after repeated charge-discharge cycling, which is more closely related to transport through the SEI.

The relative electrochemical stabilities of imidazolium and pyrrolidinium cations are available in the literature.^{30,37-39} Pyrrolidinium RTILs are reduced at $\sim -3.0\text{V}$ vs. Ag^+/Ag and imidazolium is reduced at $\sim -2.0\text{V}$ vs. Ag^+/Ag , indicating that the negative potential limit in these materials is governed by the cation. Thus, it is not surprising that the pyrrolidinium RTILs are superior lithium electrolyte solvents. However, the observation of a stable lithium deposit in an imidazolium RTIL, $\text{EMI}(\text{Tf})_2\text{N}$ and BMImI , indicates that, under certain conditions, the imidazolium cation at an RTIL | lithium interface can be kinetically stable. This type of behaviour is likely to occur because of the presence of an SEI, the formation of which can be deduced from the behaviour exhibited by the $\text{EMI}(\text{Tf})_2\text{N}$ potential profile, as discussed earlier. For the systems presented here, relatively poor cycling behaviour is exhibited by all of the RTILs comprised of anions other than $(\text{Tf})_2\text{N}^-$. This implies that, for the systems investigated here, the most favourable SEI (for cycling) is formed in $(\text{Tf})_2\text{N}^-$ RTILs. The way in which repetitive cycling attempts led to an improved cycling efficiency in the $\text{EMI}(\text{Tf})_2\text{N}$ cell suggested that the passivating film gradually became sufficiently protective only after prolonged periods at reducing potentials. Apart from this initial process, the $\text{EMI}(\text{Tf})_2\text{N}$ and $\text{P}_{18}(\text{Tf})_2\text{N}$ cells exhibited marked similarity in the appearance of the lithium deposits and in their behaviour with repeated cycling experiments. This similarity can best be explained by the formation of an SEI from the reaction of the anion with lithium. The imidazolium RTIL required a thicker, more protective SEI before reversible lithium cycling could be achieved. If the cations were to play a significant role in the formation of an SEI, then similar passivating behaviour would have been observed in the other RTILs.

The preceding discussion outlines a clear role for the cation and anion with respect to the application of RTILs in a lithium battery. The role of the cation is to be inert and unreactive, while the anion appears to play a crucial role in the formation of an SEI, which

protects both the cation and anion from further reduction reactions. This assertion implies a very distinct advantage of RTILs over other solvent systems, because it allows for an SEI to be formed (in the absence of impurities) from *one reactant only*, as opposed to conventional solvent systems where the SEI will usually be formed from both the solvent and salt. For this ideal to occur, a cation that is truly unreactive at the lithium interface would be required. Clearly this is not the case for the imidazolium cation; however the pyrrolidinium cation is significantly more stable.

Mechanisms contributing to reduced efficiency:

After considering the behaviour of the various RTILs in the optical cells it becomes apparent that the mechanisms which are acting to reduce the cycling efficiency to less than 100% are complex. Depending on the experimental conditions, a different mechanism may be dominating, and it is likely that several processes will have been occurring simultaneously. However, it is possible to draw some general conclusions about the processes occurring.

Side reactions: In all of the cells studied it was apparent that a side reaction (i.e., a process other than the oxidation and reduction of lithium) was active. The extent to which the side reaction occurred ultimately dictated the cycling efficiency of the electrolyte. The side reaction could have involved either the cation or the anion and probably involved both; the situation is likely to have been aggravated by the generation of species which could undergo further reduction. Referring to the discussion above, this side reaction appeared to be the least significant in the $(\text{Tf})_2\text{N}^-$ RTILs, resulting in relatively high cycling efficiencies. Also referring to the discussion above it is apparent that in some cases the side reactions led to the formation of a SEI. The SEI then acted to eliminate or reduce the side reactions. That the protection afforded by the SEI is not completely effective in stopping the reactions is apparent from the cycling efficiency values of the less than 100%. The build-up of crystalline deposits observed in many of the cells, particularly the $(\text{Tf})_2\text{N}^-$ cells, are evidence that the side reactions continue throughout the experiment.

SEI build-up/surface fouling: Apart from the primary impact of the side reactions on the cycling efficiency it is apparent that the fouling of the surface with these products has secondary effects on the way in which the cycling process can proceed. As was observed in

numerous experiments, repetitive cycling often led to an increase in the potential required to initiate deposition. It is likely that this was a result of a reduction in the active surface area of the electrode and/or the build-up of more resistive pathways to the electrode surface. The models proposed for dendrite formation in conventional solvents follow similar lines of reasoning, where, as a result of the formation of the SEI, the subsequent impediment of lithium transport to the electrode surface results in preferential deposition at a small number of sites. It is apparent from the repeated cycling experiments conducted in the $(\text{Tf})_2\text{N}^-$ cells that the continued fouling of the surface (which is evident from increasing quantities of crystalline deposit on the electrode surface) is the cause of the increasingly dendritic deposits. This leads to a rapid reduction in the cycling efficiency because of the tendency of the deposits to become disconnected, as was witnessed on numerous occasions. In addition, it was apparent that the dendrites formed in this way were more prone to appear only after all of the active lithium on the electrode surface had been exhausted (i.e., after each consecutive cycling efficiency measurement). This implies that nucleation on the 'bare' (although fouled) copper surface was more difficult than when an active lithium deposit was present. This coincided with a significant increase in the potential required to initiate deposition, and, in all cases this resulted in the onset of the appearance of dendritic deposits on the copper surface.

Previously the influence of current density and its interplay with electrolyte conductivity to produce dendritic deposits was discussed. The result of the formation of dendrites as a result of this process is significantly different to that of the formation of dendrites due to surface fouling. The dendrites formed at high rates tended to be more robust and exhibited a different appearance and cycling behaviour to those produced by surface fouling. Effectively they were formed by the same process, but in the case of dendrites formed by surface fouling the current densities involved became very high and the dendrites formed were very thin. The thicker, more robust dendrites produced by (moderately) high rate deposition tended to cycle more effectively and exhibited a reduced tendency to become disconnected.

The other significant observation that can be drawn from the optical cell experiments is the marked difference in the behaviour of the native lithium surface to that of the deposited lithium surface. While the deposited lithium exhibited behaviour varying from uniform hemispherical deposits to extremely dendritic deposits, the lithium surface exhibited very

few features other than the build-up of a layer of crystalline material. Dendritic deposits were observed on a number of occasions, which involved extreme currents or contamination due to a leaking cell. This has a number of implications, the most important of which being the likelihood that the SEI on the lithium surface is significantly different to that of the deposited lithium formed in-situ. Whether or not this leads to a difference in the cycling efficiency of a lithium electrode is worthy of consideration, but is a difficult quantity to determine. Alternatively, the fact that deposition was occurring on a lithium substrate, as opposed to the 'bare' copper surface discussed above, could have been the reason for the difference in behaviour.

Considering all of these observations in the context of a thin film battery, it is apparent that a cell would need to operate under defined charging conditions to avoid dendrite formation. Also the likelihood of dendrite formation would increase toward the end of cell life. However, it appears that a cell incorporating a lithium electrode, as opposed to a deposited electrode, would be significantly less likely to fail as a result of dendritic deposition.

The optical cell experiments indicated that the pyrrolidinium bis(trifluoromethanesulfonyl)amides were the most suitable candidates for further investigation as materials for application in lithium battery systems. The experiments also provided valuable information on the behaviour and mechanisms occurring at the lithium electrode | electrolyte interface during deposition / dissolution cycling. However, because of limitations imposed by the cell design it became necessary to continue the investigation using more traditional apparatus where accurate control over current density could be established. The following section details the results obtained from 3-electrode cell experiments on the $\text{P}_{1x}(\text{Tf})_2\text{N}^-$ system.

References

1. C. Brissot, M. Rosso, J.-N. Chazalviel and S. Lascaud, *J. Power Sources*, **81**, 925 (1999).
2. J. Yamaki, S. Tobishima, K. Hayashi, S. Keiichi, Y. Nemoto and M. Arakawa, *J. Power Sources*, **74**, 219 (1998).
3. C. Brissot, M. Rosso, J.-N. Chazalviel, P. Baudry and S. Lascaud, *Electrochim. Acta*, **43**, 1569 (1998).
4. M. Arakawa, S. Tobishima, Y. Nemoto, M. Ichimura and J. Yamaki, *J. Power Sources*, **43**, 27 (1993).
5. I. Yoshimatsu, T. Hirai and J. Yamaki, *J. Electrochem. Soc.*, **135**, 2422 (1988).
6. M. Rosso, T. Gobron, C. Brissot, J.-N. Chazalviel and S. Lascaud, *J. Power Sources*, **97-98**, 804 (2001).
7. C. Brissot, M. Rosso, J.-N. Chazalviel and S. Lascaud, *J. Power Sources*, **94**, 212 (2001).
8. C. Tiyaipiboonchaiya, J. M. Pringle, D. R. MacFarlane, M. Forsyth and J. Sun, *Macromolecular Chemistry and Physics*, **204**, 2147 (2003).
9. D. R. MacFarlane, S. A. Forsyth, J. Golding and G. B. Deacon, *Green Chemistry*, **4**, 444 (2002).
10. D. R. MacFarlane, J. Golding, S. Forsyth, M. Forsyth and G. B. Deacon, *Chem. Comm.*, 1430 (2001).
11. Stewart Forsyth, Ph.D Thesis, Monash University, 2003.
12. M. Egashira, S. Okada and J. Yamaki, *Solid State Ionics*, **148**, 457 (2002).
13. L. C. Branco, J. N. Rosa, J. J. Moura Ramos and C. A. M. Afonso, *Chemistry - A European Journal*, **8**, 3671 (2002).
14. J. S. Wilkes and M. J. Zaworotko, *Chem. Comm.*, **13**, 965 (1992).
15. H. L. Ngo, K. LeCompte, L. Hargens and A. B. McEwen, *Thermochim. Acta*, **357-358**, 97 (2000).
16. J. Fuller, R. T. Carlin and R. A. Osteryoung, *J. Electrochem. Soc.*, **143**, L145-L147 (1996).
17. H. Nakagawa, S. Izuchi, K. Kuwana, T. Nukuda and Y. Aihara, *J. Electrochem. Soc.*, **150**, A695-A700 (2003).
18. R. T. Carlin and J. Fuller, US5589291-A (1996).
19. P. Bonhôte, A.-P. Dias, N. Papageorgiou, K. Kalyanasundaram and M. Grätzel, *Inorg. Chem.*, **35**, 1168 (1996).
20. J. M. Pringle, J. Golding, K. Baranyai, C. M. Forsyth, G. B. Deacon, J. L. Scott and D. R. MacFarlane, *New J. Chem.*, **27**, 1504 (2003).
21. J. Efthimiadis, S. J. Pas, M. Forsyth and D. R. MacFarlane, *Solid State Ionics*, **154-155**, 279 (2002).
22. S. Forsyth, J. Golding, D. R. MacFarlane and M. Forsyth, *Electrochim. Acta*, **46**, 1753 (2001).
23. A. J. Hill, J. Huang, J. Efthimiadis, P. Meakin, M. Forsyth and D. R. MacFarlane, *Solid State Ionics*, **154-155**, 119 (2002).
24. J. Efthimiadis, M. Forsyth and D. R. MacFarlane, *J. Mater. Sci.*, **38**, 3293 (2003).
25. J. Efthimiadis, G. J. Annat, J. Efthimiadis, M. Forsyth and D. R. MacFarlane, *Physical Chemistry Chemical Physics (PCCP)*, **5**, 5558 (2003).
26. D. R. MacFarlane, J. H. Huang and M. Forsyth, *Nature*, **402**, 792 (1999).
27. J. G. Huddleston, A. E. Visser, W. M. Reichert, H. D. Willauer, G. A. Broker and R. D. Rogers, *Green Chemistry*, **3**, 156 (2001).
28. A. Cisak and L. Werblan, *High-Energy Non-Aqueous Batteries*, Ellis Horwood limited, west Sussex, England (1993).

29. D. R. MacFarlane, J. Sun, J. Golding, P. Meakin and M. Forsyth, *Electrochim. Acta*, **45**, 1271 (2000).
30. D. R. MacFarlane, P. Meakin, J. Sun, N. Amini and M. Forsyth, *J. Phys. Chem. B*, **103**, 4164 (1999).
31. V. Fleury, W. A. Watters, L. Allam and T. Devers, *Nature*, **416**, 716 (2002).
32. Y. Matsuda, T. Takemitsu, T. Tanigawa and T. Fukushima, *J. Power Sources*, **97-98**, 589 (2001).
33. K. R. Seddon, *Symposium and Workshop on Ionic Liquids, Monash University: Personal Communication* (2003).
34. F. Orsini, A. Du Pasquier, B. Beaudoin, J. M. Tarascon, M. Trentin, N. Langenhuizen, E. De Beer and P. Notten, *J. Power Sources*, **76**, 19 (1998).
35. D. Aurbach, I. Weissman, H. Yamin and E. Elster, *J. Electrochem. Soc.*, **145**, 1421 (1998).
36. E. Chassaing, J.-N. Chazalviel, T. Gobron and M. Rosso, *Electrochim. Acta*, **47**, 1267 (2002).
37. J. S. Wilkes, J. A. Levisky, R. A. Wilson and C. L. Hussey, *Performer: Frank J. Seiler Research Lab., United States Air Force Academy, CO. Mar 1982. 2p. Report: FJSRL-JR-82-0008(1982)*.
38. B. M. Quinn, Z. Ding, R. Moulton and A. J. Bard, *Langmuir*, **18**, 1734 (2002).
39. H. Sakaebe and H. Matsumoto, *Electrochemistry Communications*, **5**, 594 (2003).

3.2 3-electrode cell:

Measurements using a conventional 3-electrode electrochemical cell were undertaken to allow greater control over the current density. The work presented in this section details the results of a cyclic voltammetry (CV) study and a survey of the influence of current density on the cycling efficiency of $P_X(Tf)_2N$ electrolytes (where X is 2, 3 or 4) under galvanostatic conditions.

Figure 3.2.1 shows a CV obtained for a neat sample of $P_{14}(Tf)_2N$ at room temperature. An electrochemical window approaching 6 V is obtained, in agreement with published results.¹ No significant features are observed other than a reduction process at ~ 0 V vs. Li/Li^+ (ascribed to reduction of the cation) and an oxidation process at + 6 V vs. Li/Li^+ (ascribed to oxidation of the anion).¹ Minor features appear when the voltage range is extended beyond 0 V and + 6 V vs. Li/Li^+ . With respect to the cathodic process, it is apparent that the potential at which the cation is reduced is very similar to that of lithium.

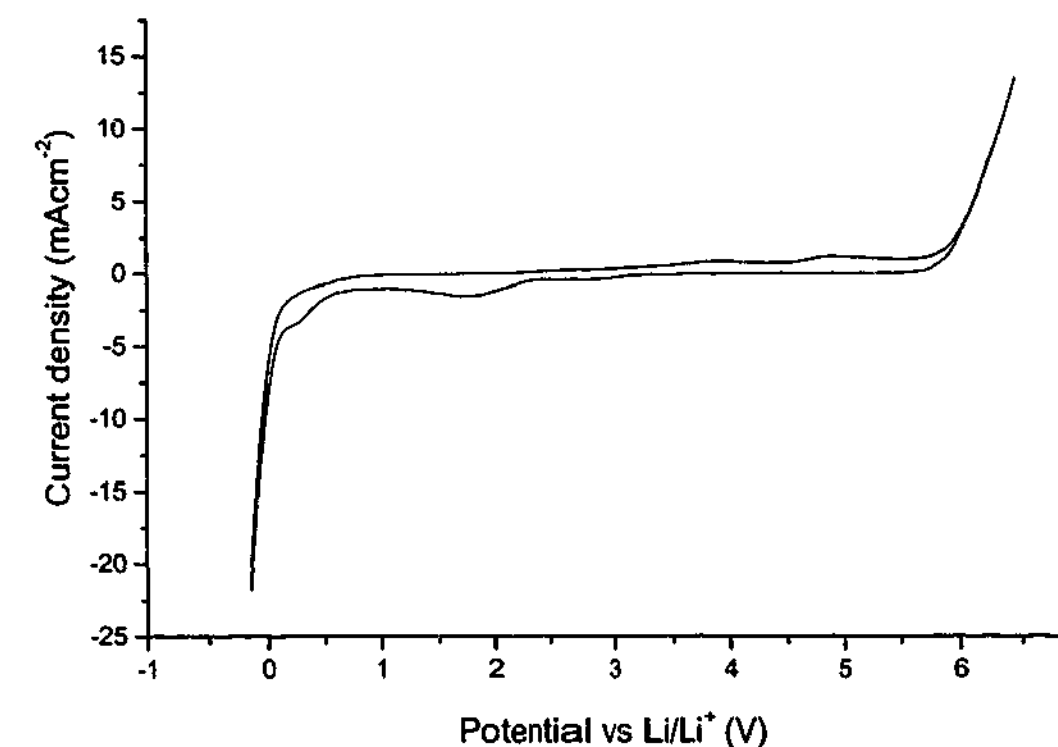


Fig. 3.2.1 Electrochemical window of $P_{14}(Tf)_2N$ on a Pt substrate, 100 mVs^{-1} at 25°C .

The addition of a lithium salt ($\text{Li}(\text{Tf})_2\text{N}$) to the RTIL results in very different behaviour at reducing potentials. Figure 3.2.2 shows a CV obtained for a 0.5 mol kg^{-1} $\text{P}_{14}(\text{Tf})_2\text{N}$ electrolyte, a reduction peak at -0.5 V (vs. Li/Li^+) and a corresponding oxidation peak at $+0.5 \text{ V}$ (vs. Li/Li^+) appear. Based on the evidence provided by the optical cells and standard reduction potentials the peaks are assumed to arise from the deposition and dissolution of lithium metal. The peak separation of $\sim 1 \text{ V}$ is much greater than the 60 mV expected for a fully reversible one electron charge transfer process and is indicative of the presence of a resistive surface film.² By integrating all of the negative and positive currents, an estimate of the coulombic efficiency can be obtained. For the CV presented in Fig. 3.2.2 the coulombic efficiency was 83% .

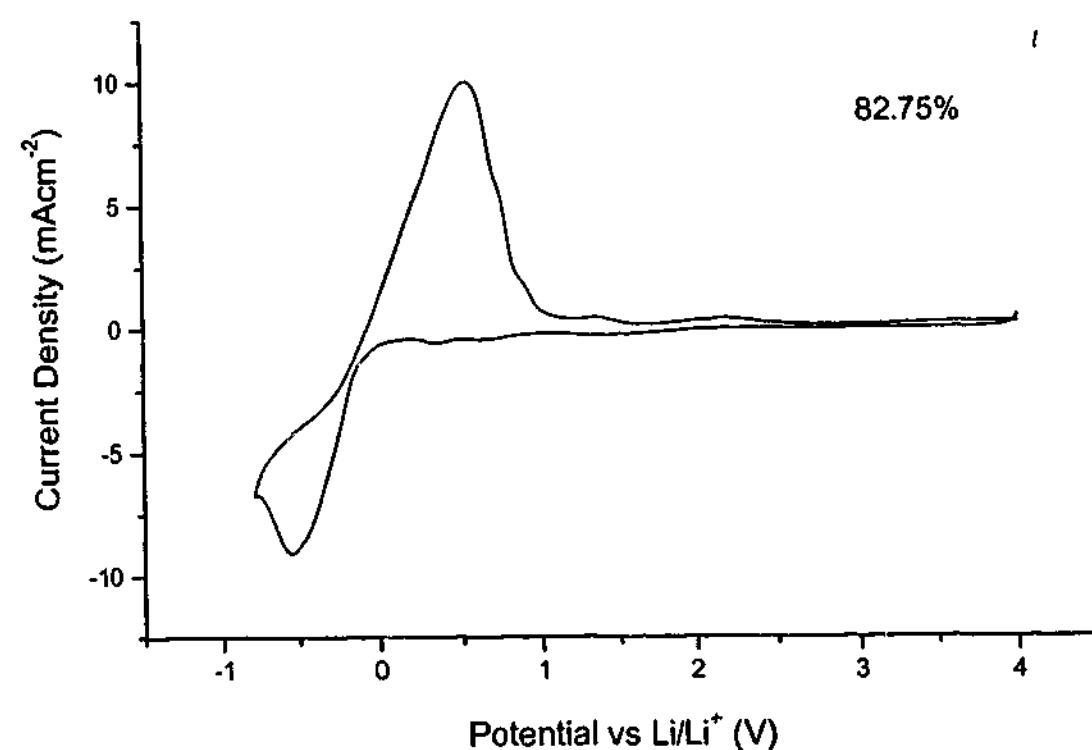


Fig. 3.2.2 Cyclic voltammogram of 0.5 mol kg^{-1} $\text{P}_{14}(\text{Tf})_2\text{N}$ at 25°C , 100 mVs^{-1} on a platinum substrate.

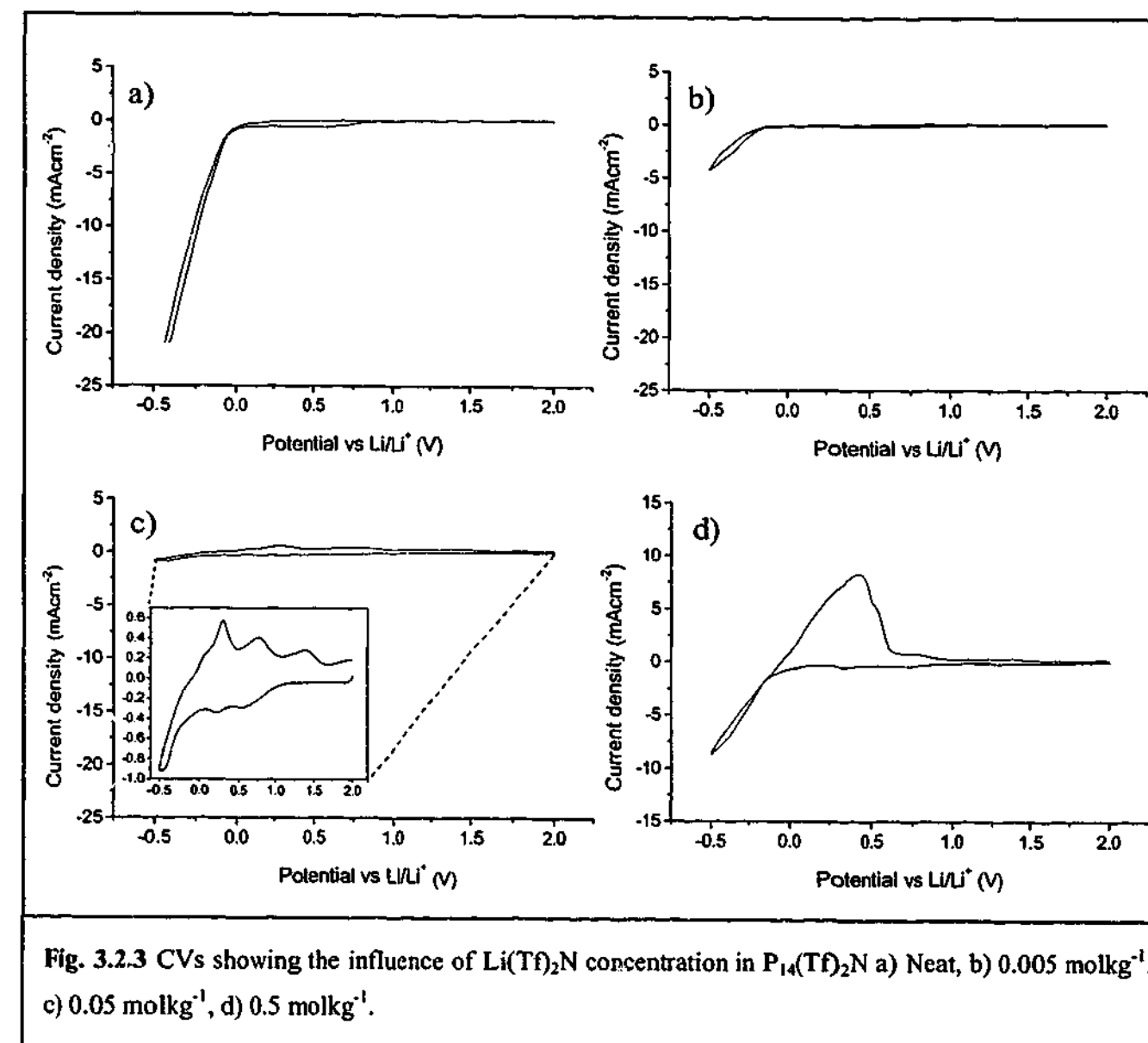


Fig. 3.2.3 CVs showing the influence of $\text{Li}(\text{Tf})_2\text{N}$ concentration in $\text{P}_{14}(\text{Tf})_2\text{N}$ a) Neat, b) $0.005 \text{ mol kg}^{-1}$, c) 0.05 mol kg^{-1} , d) 0.5 mol kg^{-1} .

Figure 3.2.3 shows the dramatic influence of increasing $\text{Li}(\text{Tf})_2\text{N}$ concentration on the nature of the cathodic processes occurring in the electrolyte. The neat electrolyte (a) shows the onset of a cathodic process at $\sim 0 \text{ V}$ vs. Li/Li^+ (as seen in Fig 3.2.1), at low concentrations (b - $0.005 \text{ mol kg}^{-1}$) the rate of reduction of the cation is significantly reduced and at higher concentrations (c - 0.05 mol kg^{-1}) the process is almost entirely absent. The 0.5 mol kg^{-1} sample (d) shows chemically reversible lithium deposition and dissolution. Again, this type of behaviour is indicative of the presence of a passivating film. The measurements presented in Fig. 3.2.3 indicate that the formation of the passivating film is associated with the presence of lithium in the electrolyte and that the film properties are likely to be related to the lithium concentration. It appears that the reaction that forms the surface film is kinetically dependant upon the lithium concentration in the bulk solution, at higher concentrations the reaction proceeds more quickly and/or favours a more protective film.

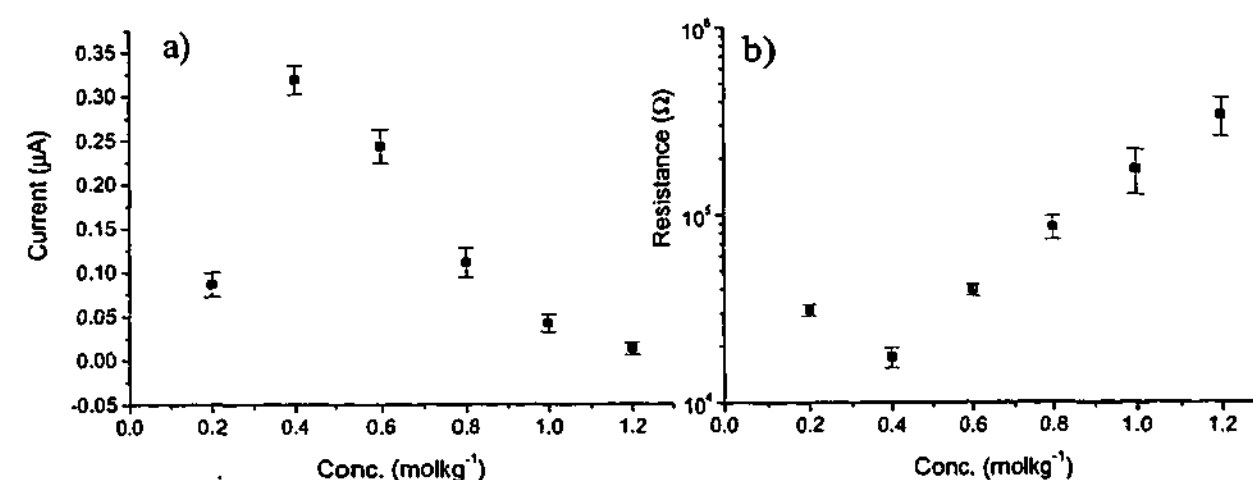


Fig. 3.2.4 Steady state current (a) and low frequency impedance touchdown (b) for equivalent $\text{P}_{13}(\text{Tf})_2\text{N}$ cells at varying $\text{Li}(\text{Tf})_2\text{N}$ concentrations.

Figure 3.2.4 shows the average results obtained from triplicate experiments for a set of equivalent lithium symmetrical cells (i.e., same cell geometry, temperature etc.) made using different concentration $\text{P}_{14}(\text{Tf})_2\text{N}$ electrolytes. Fig. 3.2.4a shows a plot of the steady state current obtained when a potential of 10 mV was applied across the cell. Fig. 3.2.4b shows a plot of the real axis touchdown of the low frequency part of a Nyquist impedance plot (for more discussion of impedance spectra, see section 3.4.4). The steady state current exhibited a maximum at 0.4 mol kg^{-1} , which corresponded to a minimum in the interfacial resistance of the cell. These results indicate that an electrolyte concentration near 0.4 mol kg^{-1} produces the least resistive film (at room temperature) and that lithium transport through the SEI is a dominant factor dictating lithium transport, and hence limiting currents.

Figure 3.2.5 presents CVs obtained at a scan rate of 100 mV s^{-1} at room temperature for $\text{P}_{12}(\text{Tf})_2\text{N}$, $\text{P}_{13}(\text{Tf})_2\text{N}$ and $\text{P}_{14}(\text{Tf})_2\text{N}$ electrolytes. Similar features are observed for all three systems, the main difference being the magnitude of the lithium deposition and dissolution peaks. Based on the CVs in Fig. 3.2.5 it can be concluded the lithium transport in 0.5 mol kg^{-1} $\text{P}_{14}(\text{Tf})_2\text{N}$ is the most rapid. It is apparent that the lithium dissolution peak is composed of more than one peak, this is most obvious in the $\text{P}_{12}(\text{Tf})_2\text{N}$ CV but is also evident in the $\text{P}_{13}(\text{Tf})_2\text{N}$ and $\text{P}_{14}(\text{Tf})_2\text{N}$ CVs. The additional peak(s) are thought to arise from the alloying of lithium with platinum,³ the lithium platinum

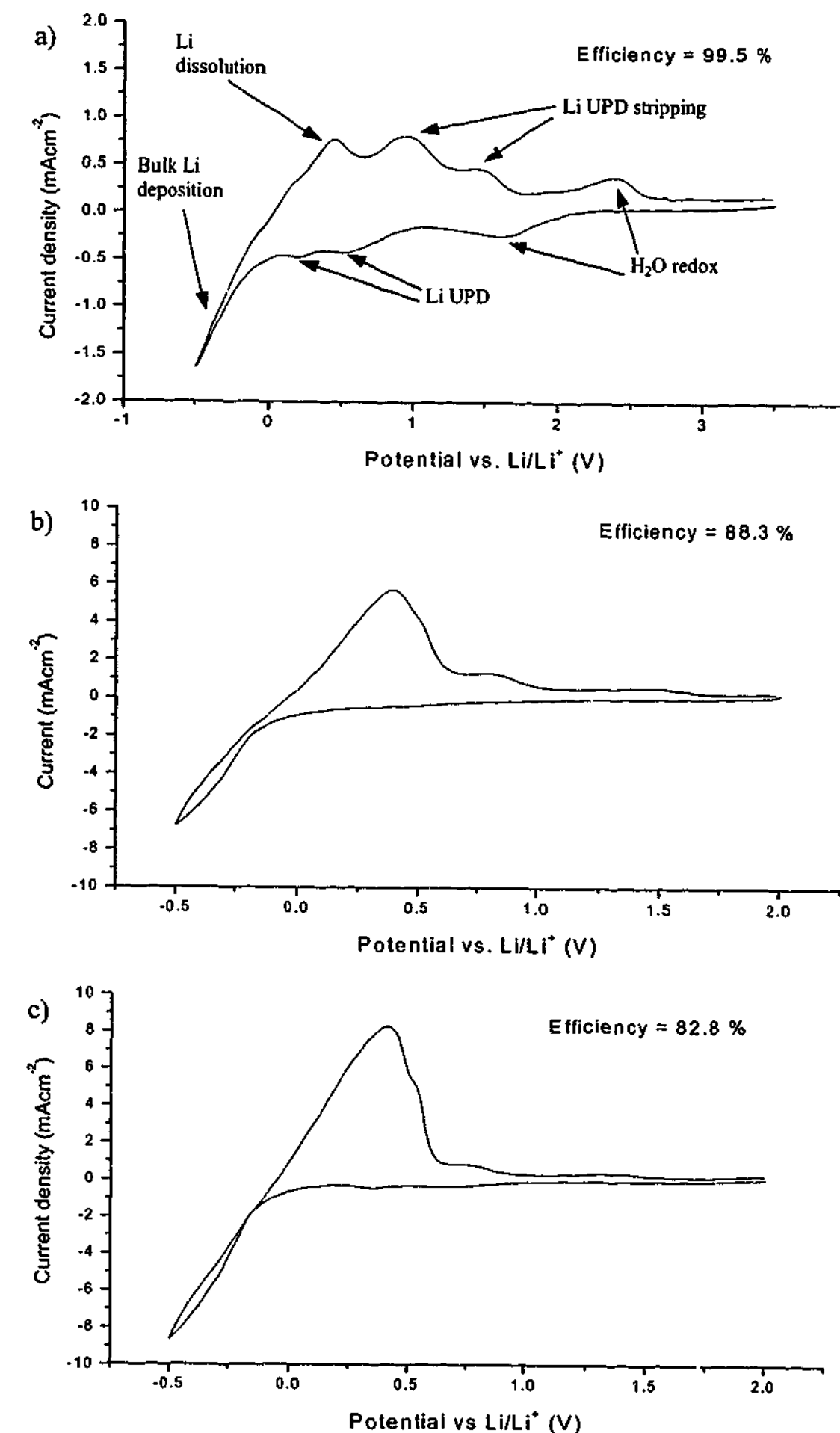


Fig. 3.2.5 CVs for a) 0.25 mol kg^{-1} $\text{P}_{12}(\text{Tf})_2\text{N}$, b) 0.5 mol kg^{-1} $\text{P}_{13}(\text{Tf})_2\text{N}$ & c) 0.5 mol kg^{-1} $\text{P}_{14}(\text{Tf})_2\text{N}$. 100 mV s^{-1} , 25°C , Pt substrate.

system exhibits rich phase behaviour.⁴ Lithium electrochemistry at a platinum electrode is characterised by several features;³

- Under potential deposition (UPD): two peaks at 0.7 V and 0.3 V (vs. Li/Li⁺), and corresponding anodic stripping peaks at 1.1 V and 1.3 V (vs. Li/Li⁺).
- Below 0 V (vs. Li/Li⁺), bulk lithium deposition occurs.
- In the presence of water (tens of ppm), a water reduction peak appears at 1.6 V (vs. Li/Li⁺) with a corresponding anodic peak at ~2.2 V (vs. Li/Li⁺). The behaviour is unique to platinum and may be related to its catalytic properties and affinity for hydrogen adsorption. Trace water is reduced to LiOH and hydrogen, which remain absorbed on the metal, and is oxidised to H⁺ on the reverse sweep. H⁺ reacts further with LiOH to form H₂O and Li⁺.

The above processes are most notable in the P₁₂(Tf)₂N CV (3.2.5a), their presence is less obvious for the other systems, presumably due the higher lithium currents. The peaks and their corresponding processes are labelled in Fig 3.2.5a.

The estimated coulombic efficiency for each CV is also provided. The P₁₂(Tf)₂N system exhibits the highest efficiency, approaching 100%. The P₁₃(Tf)₂N and P₁₄(Tf)₂N systems, exhibit lower efficiencies, at around 90 % and 80 % respectively. One reason for the improved efficiency for the P₁₂(Tf)₂N system could be the lower current densities, which were related to improved deposit morphology, and hence improved lithium cycling efficiencies, in the previous section (3.1.2). Extending the potential range beyond -0.5 V vs. Li/Li⁺ typically resulted in a decay in efficiency, presumably because of the onset of a solvent decomposition process. An efficiency of less than 100 % for the first cycle (as shown in Fig. 3.2.5) may reflect the irreversible formation of a passivating film, indicating that the film forming reactants become more reactive with increasing length of the alkyl group on the cation. This may occur because of the difference in physical properties introduced by the change in the cation, e.g., changes in viscosity and the relative mobility of the ionic species.

Figures 3.2.6, 3.2.7 and 3.2.8 show multiple scan CVs for P₁₂(Tf)₂N, P₁₃(Tf)₂N and P₁₄(Tf)₂N electrolytes respectively. Plots of the coulombic efficiency and the

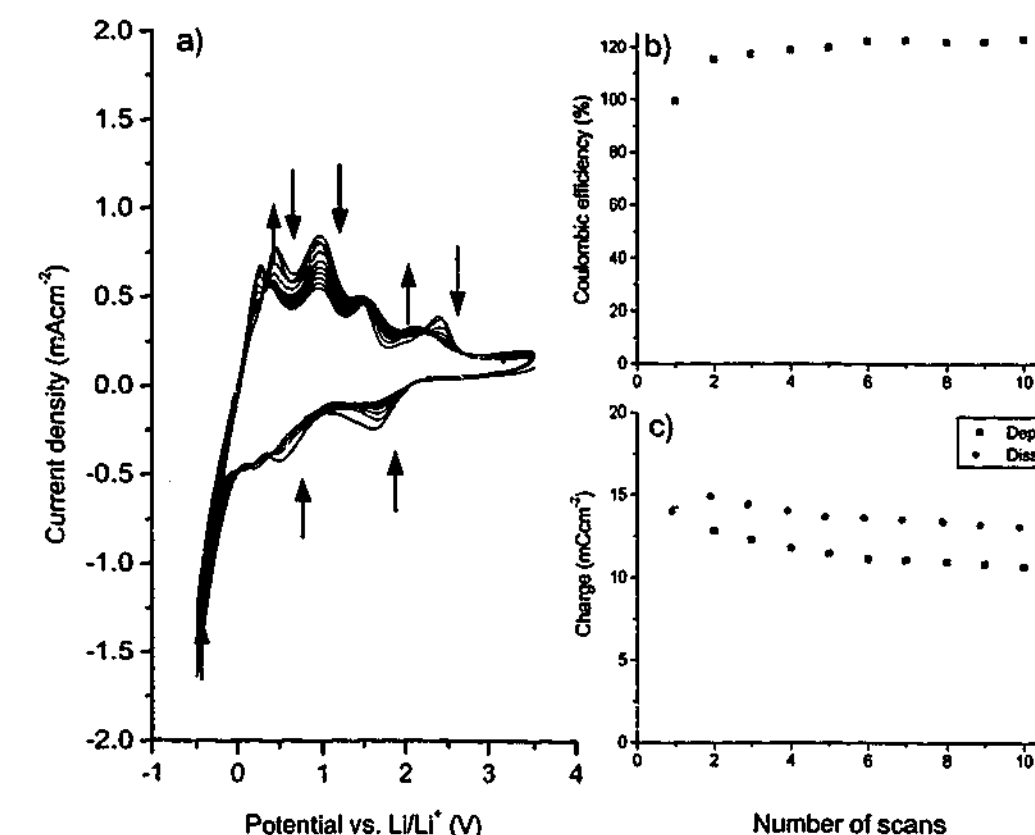


Fig. 3.2.6 Multiple cyclic voltammogram of 0.25 mol kg⁻¹ P₁₂(Tf)₂N, Pt substrate, 100 mVs⁻¹ at 25 °C. a) CV, b) Efficiency, c) Charge. Arrows indicate the direction of peak current evolution with each successive scan.

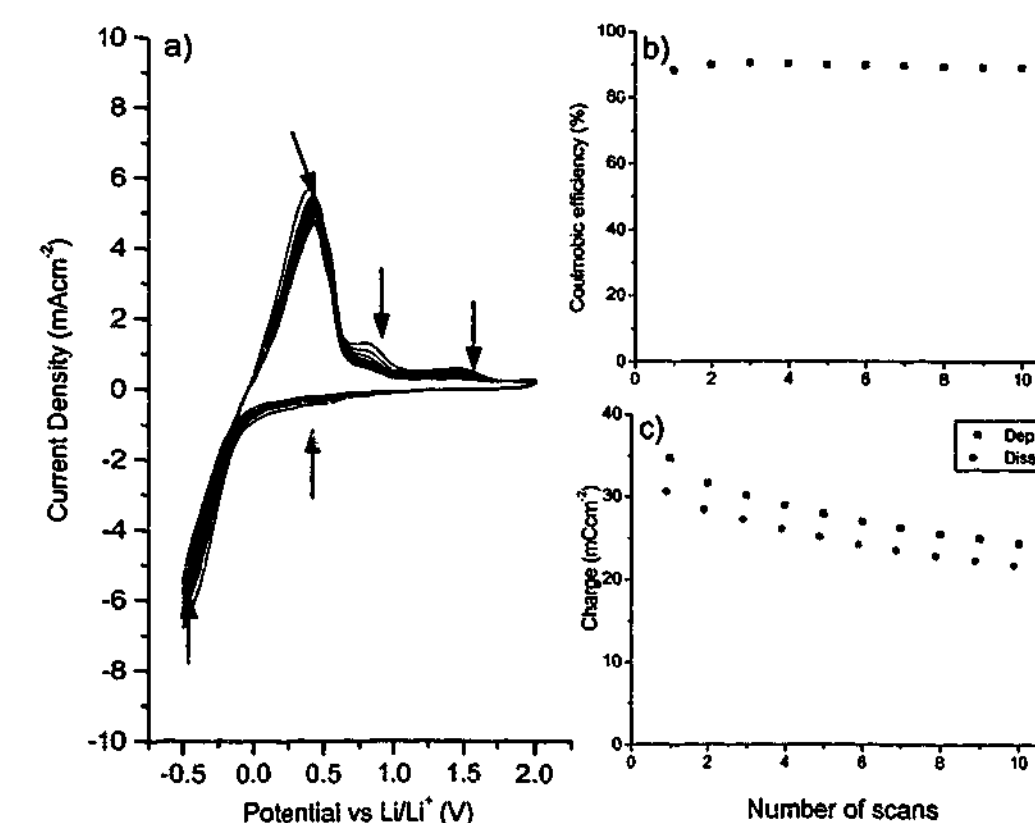


Fig. 3.2.7 Multiple cyclic voltammogram of 0.5 mol kg⁻¹ P₁₃(Tf)₂N, Pt substrate, 100 mVs⁻¹ at 25 °C. a) CV, b) Efficiency, c) Charge. Arrows indicate the direction of peak current evolution with each successive scan.

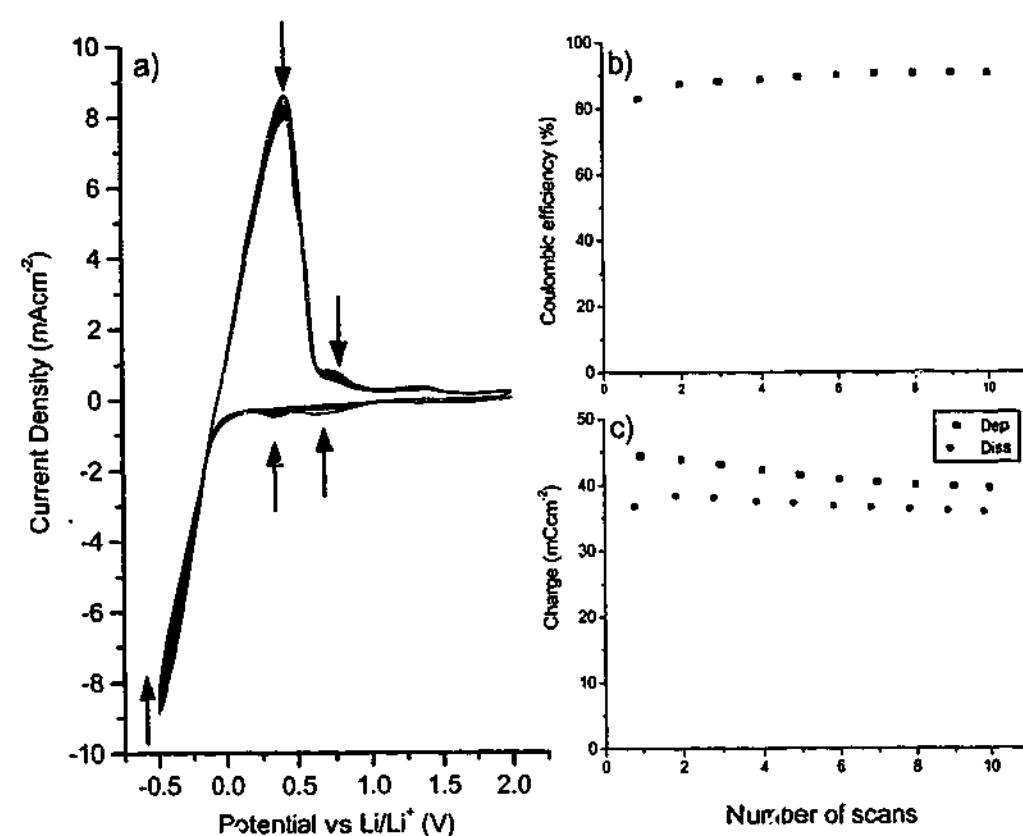


Fig. 3.2.8 Multiple cyclic voltammogram of 0.5 mol kg⁻¹ P₁₄(Tf)₂N, Pt substrate, 100 mVs⁻¹ at 25°C. a) CV, b) Efficiency, c) Charge. Arrows indicate the direction of peak current evolution with each successive scan.

'deposition' and 'dissolution' charge (i.e., the charge values may also represent contributions from other processes not associated with lithium deposition/dissolution) versus cycle number are also shown.

The P₁₂(Tf)₂N electrolyte (Fig. 3.2.6) rapidly reaches steady state behaviour and displays minimal reduction in the amount of charge passed per scan. The efficiency however, quickly reached 120 %, indicating an oxidation process other than the dissolution of deposited lithium. Most likely, this is an indication of electrolyte oxidation processes. These processes did not appear to be significant in the other systems, P₁₃(Tf)₂N and P₁₄(Tf)₂N, presumably because the lithium electrochemistry is much more dominant. In addition, the potentials were scanned to more positive regions for the P₁₂(Tf)₂N sample, this would also have contributed to a greater fraction of oxidative currents. The lithium dissolution/alloy decomposition peaks exhibited complex changes as the scans progressed; their progression towards a steady state indicates that a stable lithium/lithium alloy composition was reached.

The P₁₃(Tf)₂N electrolyte (Fig. 3.2.7) exhibited increasing efficiency with each scan, reaching plateau at approximately 90 %. The charge passed per scan exhibited a steady decrease. The P₁₄(Tf)₂N electrolyte (Fig. 3.2.8) also exhibited increasing efficiency and reached a plateau at 90 %. Of the three systems, the P₁₄(Tf)₂N system passed the greatest amount of charge per scan and exhibited the least amount of change in appearance with each successive scan.

On the basis of these measurements the P₁₄(Tf)₂N system appears to have the most favourable properties for lithium electrochemistry, yielding higher peak currents and more stable cycling behaviour.

Figures 3.2.9 and 3.2.10 show the influence of different substrates on the lithium electrochemistry in a P₁₄(Tf)₂N electrolyte. The behaviour on both nickel and copper substrates was similar, and was distinctly different from the behaviour on a platinum substrate. The CVs exhibit less features and the alloying behaviour and water peaks present in the platinum substrate CVs are noticeably absent, overall resulting in a less complex CV. The onset of bulk lithium deposition shifts to negative values (~ -0.15 V vs. Li/Li⁺) on the nickel and copper electrodes compared to the platinum electrode (~ +0.1 V vs. Li/Li⁺), indicating that nucleation is more difficult on the copper and nickel substrates. The initial efficiency is significantly reduced compared to that obtained on platinum and a peak at 0.35 V (vs. Li/Li⁺) is evident, an increase in coulombic efficiency and a decrease in the magnitude of the peak coincide, suggesting the formation of a passivating film. Both electrodes exhibit a rapid decline in efficiency after peaking at 85-90 %; the loss in efficiency is mainly due to a decrease in the dissolution charge, which steadily declined, while the deposited charge tended to plateau. The amount of charge deposited on the nickel and copper electrodes was also significantly reduced after the first cycle in comparison to the platinum electrode.

The decline in efficiency exhibited by the copper and nickel electrodes can be explained with reference to the optical cell experiments presented in section 3.1.2. It was noted that a deposit built up on the electrode surface each time the lithium was completely stripped and that there was a tendency for the subsequent lithium deposit to have a dendritic morphology. In addition, a tendency for dendritic deposits to form at high current

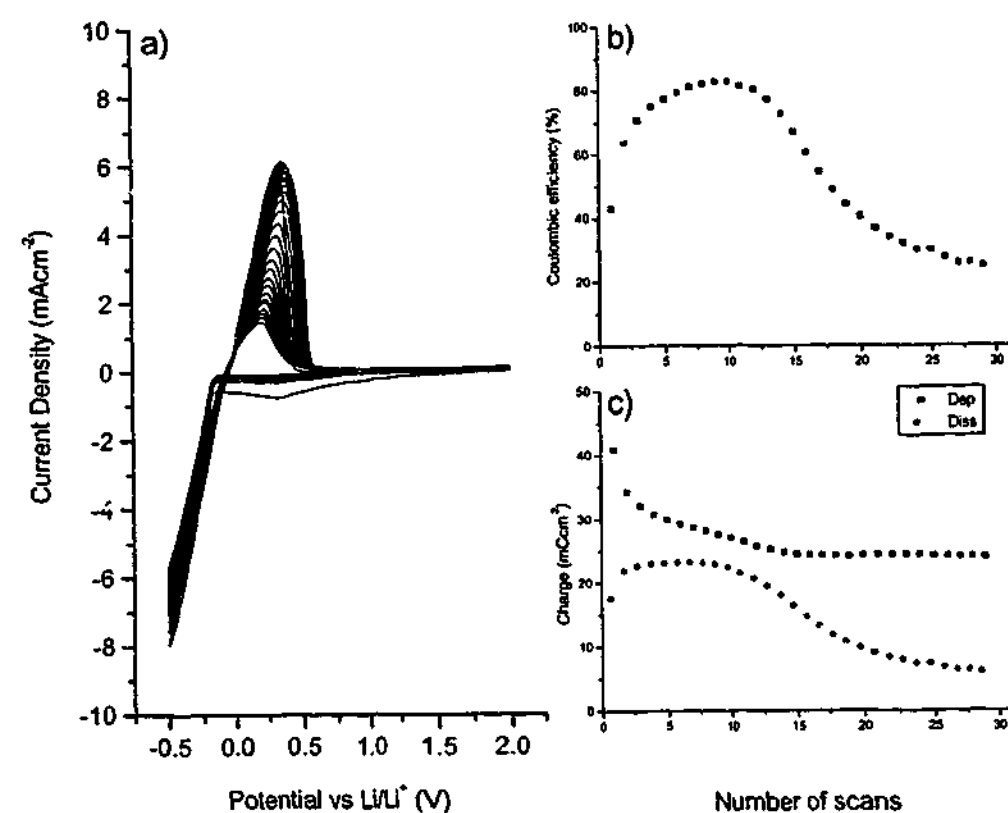


Fig. 3.2.9 Multiple cyclic voltammogram of $0.5 \text{ mol kg}^{-1} \text{ P}_{14}(\text{Tf})_2\text{N}$, Ni substrate, 100 mVs^{-1} at 25°C . a) CV, b) Efficiency, c) Charge.

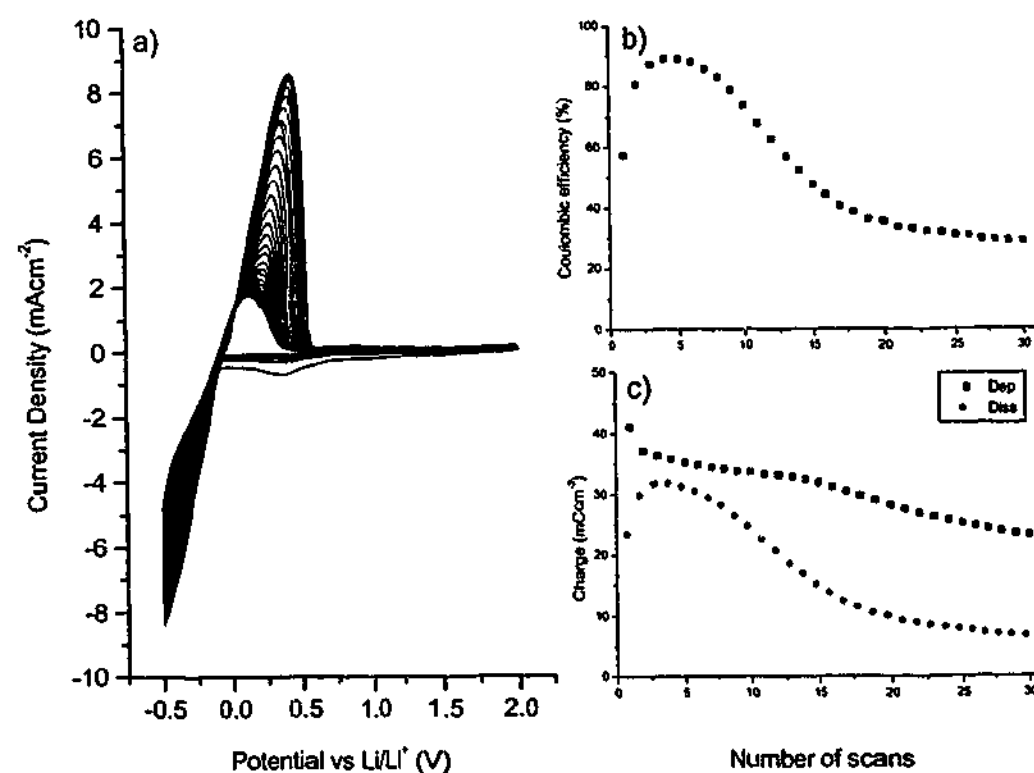


Fig. 3.2.10 Multiple cyclic voltammogram of $0.5 \text{ mol kg}^{-1} \text{ P}_{14}(\text{Tf})_2\text{N}$, Cu substrate, 100 mVs^{-1} at 25°C . a) CV, b) Efficiency, c) Charge.

densities was demonstrated. Considering the CV experiment, after the completion of each scan the electrode surface would gradually become fouled, reducing the active surface area and hence increasing the actual current density during the subsequent scan. The peak currents, approaching 10 mAcm^{-2} , would be likely to result in dendritic deposit morphology. From these considerations it seems most likely that the decline in efficiency seen in the CV experiments results from unfavourable deposit morphology. Figure 3.2.11 compares multiple CVs of the three systems, $\text{P}_{12}(\text{Tf})_2\text{N}$, $\text{P}_{13}(\text{Tf})_2\text{N}$, $\text{P}_{14}(\text{Tf})_2\text{N}$, showing a zoomed view on platinum of the regions where the SEI formation and UPD are thought to occur. It is clear that all of the systems exhibit similar features, the UPD peaks (0.3 and $0.7 \text{ V vs. Li/Li}^+$) and UPD stripping peaks (0.7 – $0.8 \text{ V vs. Li/Li}^+$) decreased with cycling. By comparison, the features of the $\text{P}_{12}(\text{Tf})_2\text{N}$ CV were spread over a wide potential range. The appearance of the CVs became progressively more compact going from $\text{P}_{13}(\text{Tf})_2\text{N}$ to $\text{P}_{14}(\text{Tf})_2\text{N}$, possibly reflecting more facile lithium transport to the electrode surface as the cation alkyl chain length increased. The $\text{P}_{13}(\text{Tf})_2\text{N}$ and $\text{P}_{14}(\text{Tf})_2\text{N}$ CVs were very similar in appearance, particularly after several cycles, when their appearance had reached a steady state. The onset of negative current typically began at around 1.5 – $2.0 \text{ V (vs. Li/Li}^+)$, on the platinum electrode it is not clear whether this is a result of UPD or from the formation of the SEI.

Figure 3.2.12 compares multiple CVs for $0.5 \text{ mol kg}^{-1} \text{ P}_{14}(\text{Tf})_2\text{N}$ on nickel and copper electrodes, again showing a zoomed view. The features are almost identical for both substrates. Given that nickel and copper electrodes have a low tendency to alloy with lithium (particularly nickel),^{3,4} the peak at $0.35 \text{ V (vs. Li/Li}^+)$ can be assigned to the formation of a passivating film. The peak onset occurs at ~ 1.5 – $2.0 \text{ V (vs Li/Li}^+)$, which is indicative of the reduction of the $(\text{Tf})_2\text{N}^-$ anion.³ The other feature worthy of note is the progression of the dissolution peak end-potential towards higher potentials, the peak gradually becoming broader. This is another indication of the formation of a passivating film and indicates that the lithium deposit became progressively more difficult to strip from the electrode surface due to the presence of a resistive surface film.

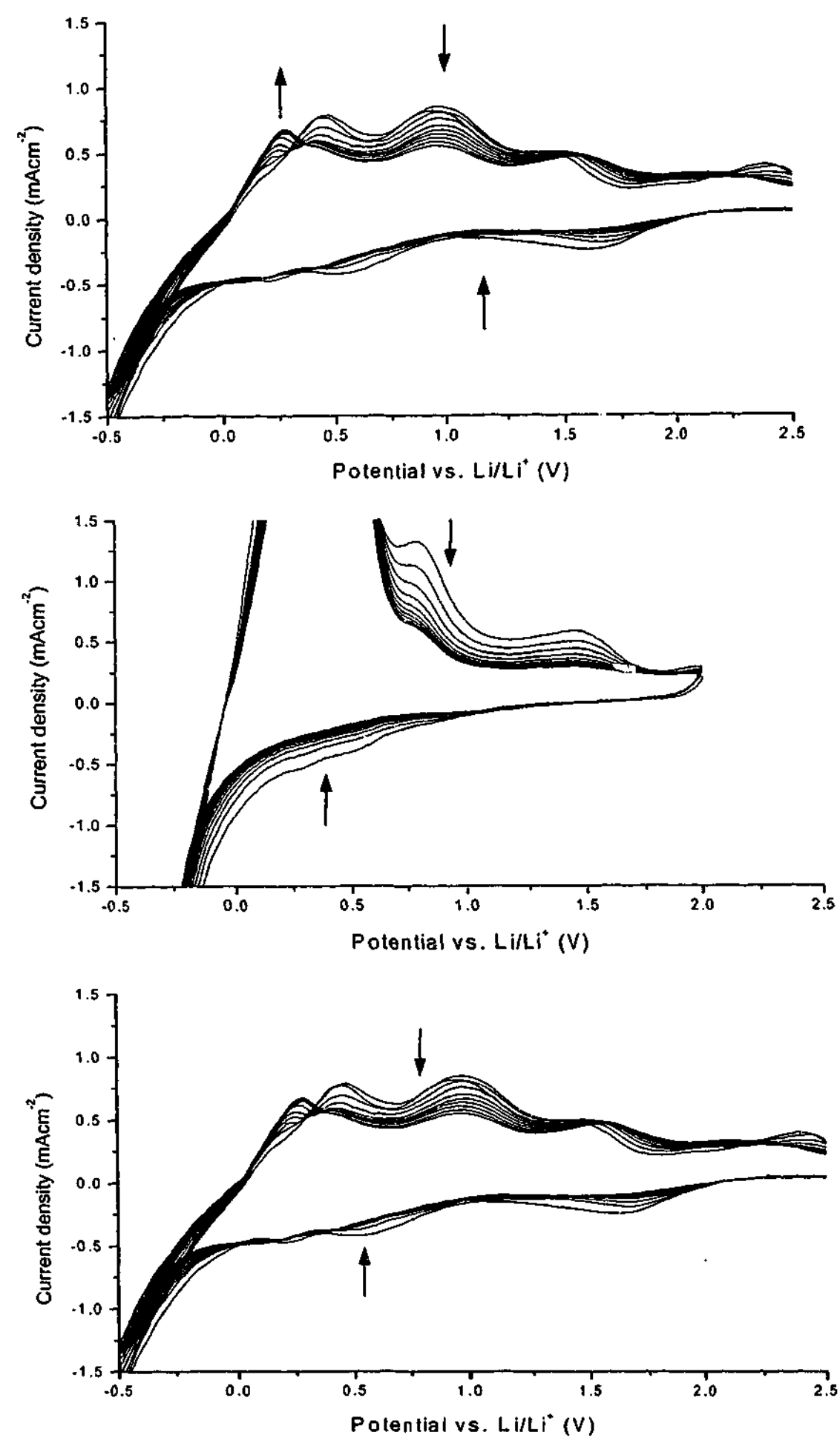


Fig. 3.2.11 Multiple CVs for a) $0.25 \text{ mol kg}^{-1} \text{ P}_{12}(\text{Tf})_2\text{N}$, b) $0.5 \text{ mol kg}^{-1} \text{ P}_{13}(\text{Tf})_2\text{N}$ & c) $0.5 \text{ mol kg}^{-1} \text{ P}_{14}(\text{Tf})_2\text{N}$. 10 scans at 100 mVs^{-1} , 25°C on a Pt electrode.

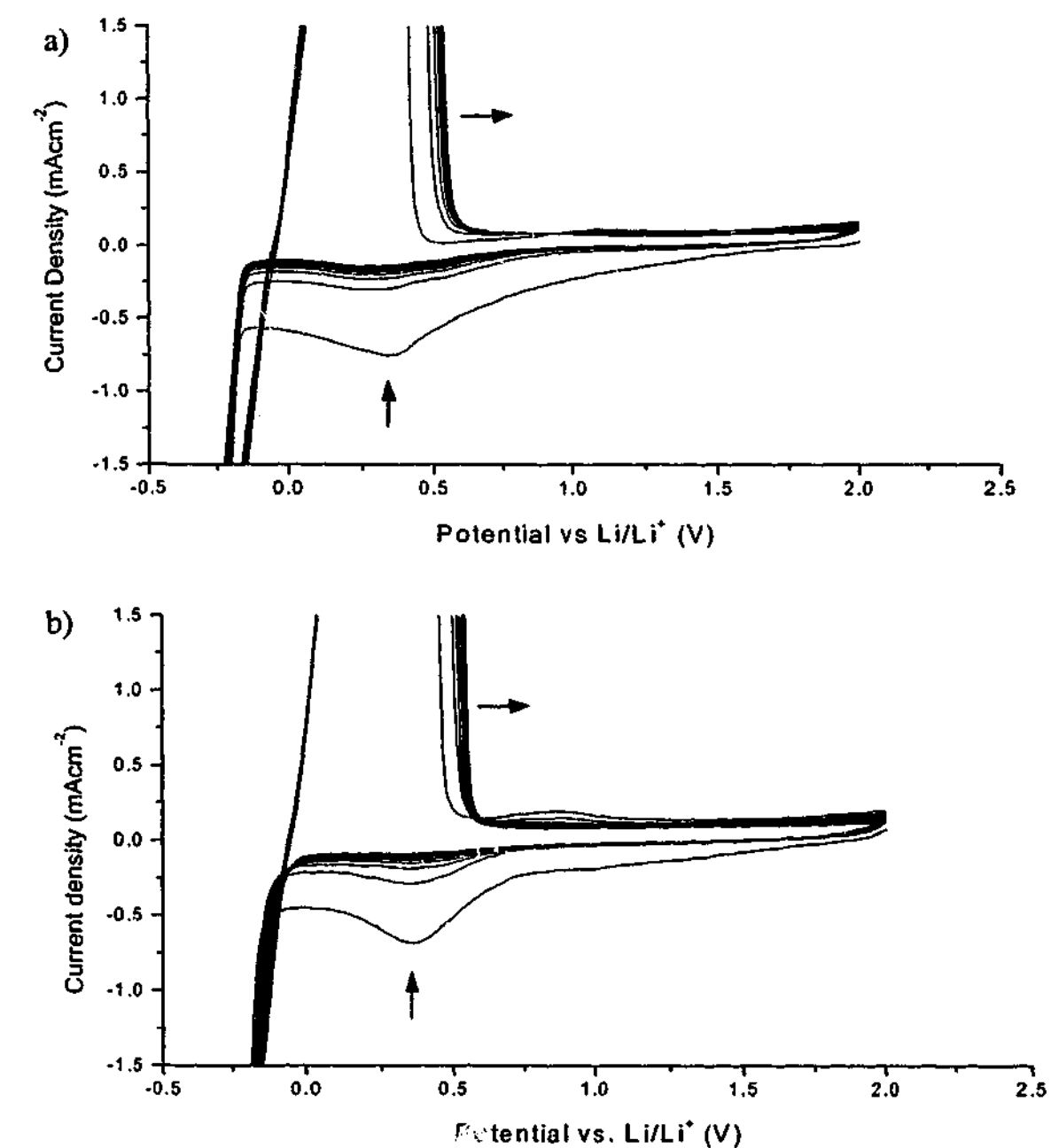


Fig. 3.2.12 Multiple CVs for $0.5 \text{ mol kg}^{-1} \text{ P}_{14}(\text{Tf})_2\text{N}$, a) Ni substrate, b) Cu substrate. 10 scans at 100 mVs^{-1} .

Summary:

The cyclic voltammograms indicated a clear difference in the behaviour of the lithium electrochemistry on different substrates (Pt, Ni & Cu), the differences mainly arose from the formation of alloys with the substrate.

Clear evidence for the formation of a SEI is provided by the CVs, particularly for the Ni and Cu substrates. The potential at which the reduction process occurs suggests the reduction of the $(\text{Tf})_2\text{N}^-$ anion based on reports in the literature.^{3,5}

Initial CVs indicate a coulombic efficiency of 100 % for $\text{P}_{12}(\text{Tf})_2\text{N}$, 90 % for $\text{P}_{13}(\text{Tf})_2\text{N}$ and 80 % for $\text{P}_{14}(\text{Tf})_2\text{N}$. The 'steady state' voltammograms exhibit increased efficiency. The evolution of the coulombic efficiency with repeated cycling is dominated by the influence of the deposit morphology which was dictated by surface fouling and the current density. Galvanostatic cycling efficiency measurements offer greater control over the deposit morphology and a better indication of the electrolytes' ability to cycle a lithium deposit reversibly.

3.2.1 $\text{P}_{14}(\text{Tf})_2\text{N}$ – Cycling efficiency:

Platinum electrode:

Galvanostatic cycling efficiency experiments (as described in section 2.6.3 and employed in the optical cells, section 3.1.2) were performed using a platinum electrode for 0.5 mol kg^{-1} $\text{P}_{14}(\text{Tf})_2\text{N}$ electrolytes. A typical voltage profile is presented in Fig. 3.2.13, indicating an efficiency of 94 % for a 0.25 mA cm^{-2} experiment at 50°C . The profiles exhibit a significant difference in appearance to those acquired from the optical cells (section 3.1.2), the dissolution potential extended to high positive potentials, and described a sloping potential curve (inset Fig. 3.2.13). This reflects the higher positive potentials required to strip the lithium/platinum alloys as indicated by the CVs in the previous section. The higher dissolution potentials translate to poor cell performance in a battery, where they would result in a sloping discharge curve, because the majority of electronic devices require a constant discharge potential. The change in dissolution potential, which indicated the end of the experiment, was less sharp on the platinum electrode; an endpoint of 2.5 V (vs. Li/Li^+) was chosen to determine the cycling efficiency.

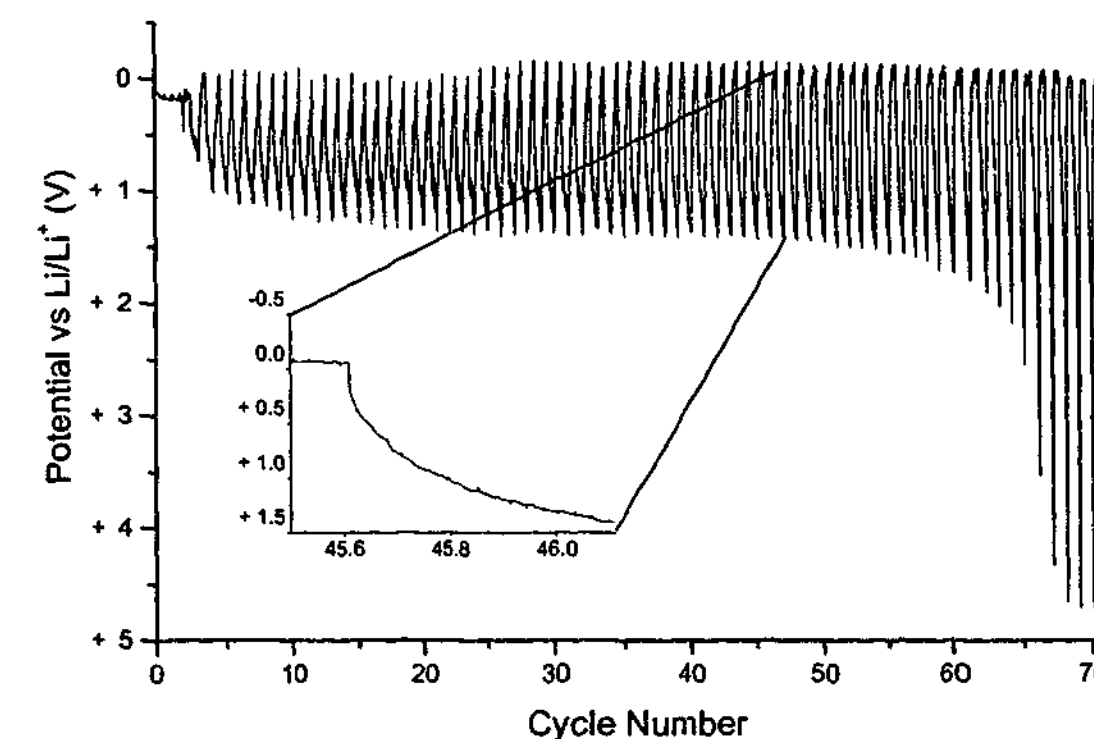


Fig. 3.2.13 Potential profile obtained from a 0.5 mol kg^{-1} $\text{P}_{14}(\text{Tf})_2\text{N}$ cycling efficiency experiment, 0.25 mA cm^{-2} , 1 C cm^{-2} excess & 0.25 C cm^{-2} cycling capacity at 50°C on a Pt electrode.

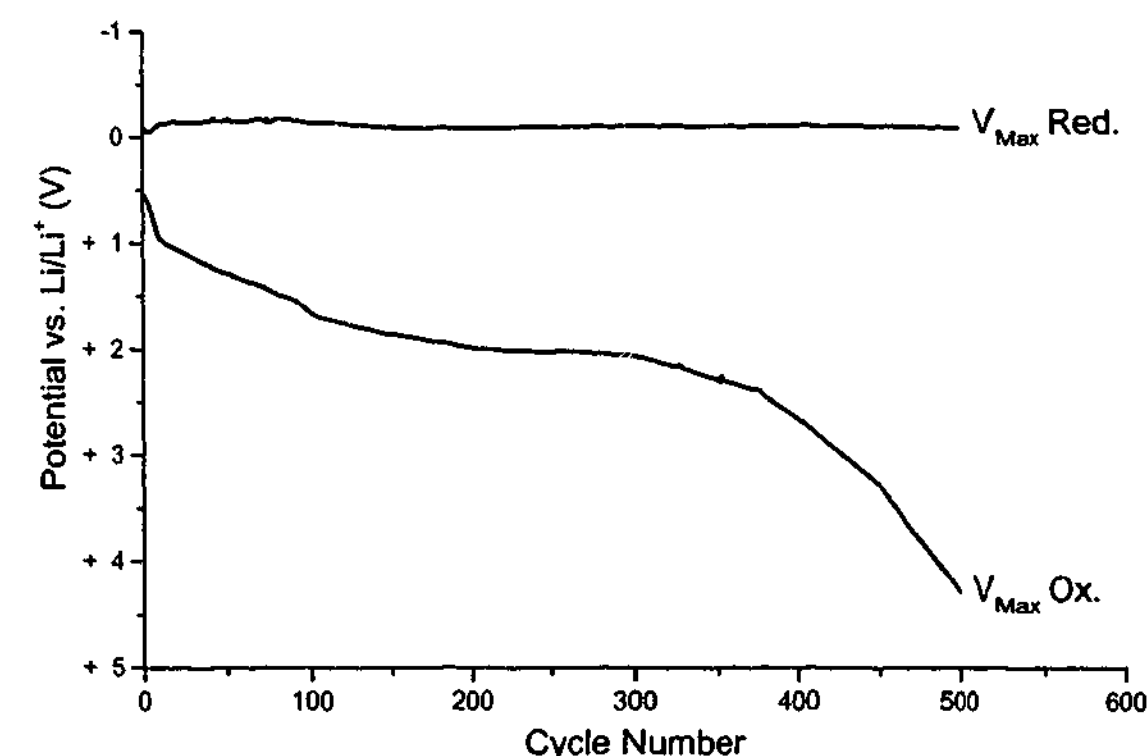


Fig. 3.2.14 Potential profile obtained from a 0.5 mol kg^{-1} $\text{P}_{14}(\text{Tf})_2\text{N}$ cycling efficiency experiment, 1.0 mA cm^{-2} , 1 C cm^{-2} excess & 0.25 C cm^{-2} cycling capacity at 50°C on a Pt electrode.

Figure 3.2.14 shows a voltage profile recorded for a 1 mAcm^{-2} experiment, because of the large number of cycles, only the maximum (V_{max}) and minimum (V_{min}) potentials are shown. The dissolution end-potential extended to a stable region of ~ 1.5 to 2 V (vs. Li/Li^+), within which the deposit cycled reversibly for many cycles. The experiment continued for approximately 390 cycles, indicating an average cycling efficiency of 99.0 % under these conditions.

Figure 3.2.15 shows a voltage profile recorded for a 1.75 mAcm^{-2} experiment; the profile exhibits two clear endpoints, one giving an efficiency of 64 % and the other an efficiency of 97 %. The recovery of the cycling performance of the electrode is most likely an example of the recombination of dead lithium at high dissolution rates, as demonstrated by Arakawa *et al.*⁶ Disconnected lithium may be reconnected at high dissolution rates because of the presence of a large potential gradient formed between the lithium anode and the disconnected Li. Under these conditions it is possible that the disconnected Li could be at sufficiently cathodic potentials for deposition of lithium to occur on its surface, thus forming a bridge back to the Li electrode and 'recombining'.

Figure 3.2.16 shows a plot of the average cycling efficiency determined for a range of current densities on a platinum electrode. The errors are assumed to arise from the choice of the endpoint and were determined from equation 2.10 using $N = N \pm 1$. The efficiency rapidly declines at approximately 1.75 mAcm^{-2} , the decline is attributed to the onset of dendritic deposition morphology. Two points are plotted for the 1.75 mAcm^{-2} experiment, reflecting the two endpoints that were determined. The maximum at 1 mAcm^{-2} is most likely a result of the competing influences of deposition/dissolution current density. At low values, deposition is uniform and at high values, the deposit becomes dendritic. Low dissolution current density results in pitting and promotes the formation of dendrites during the subsequent deposition cycle. The maximum value at 1 mAcm^{-2} indicates that, under these conditions, deposition is not dendritic and that dissolution is not resulting in pitting.

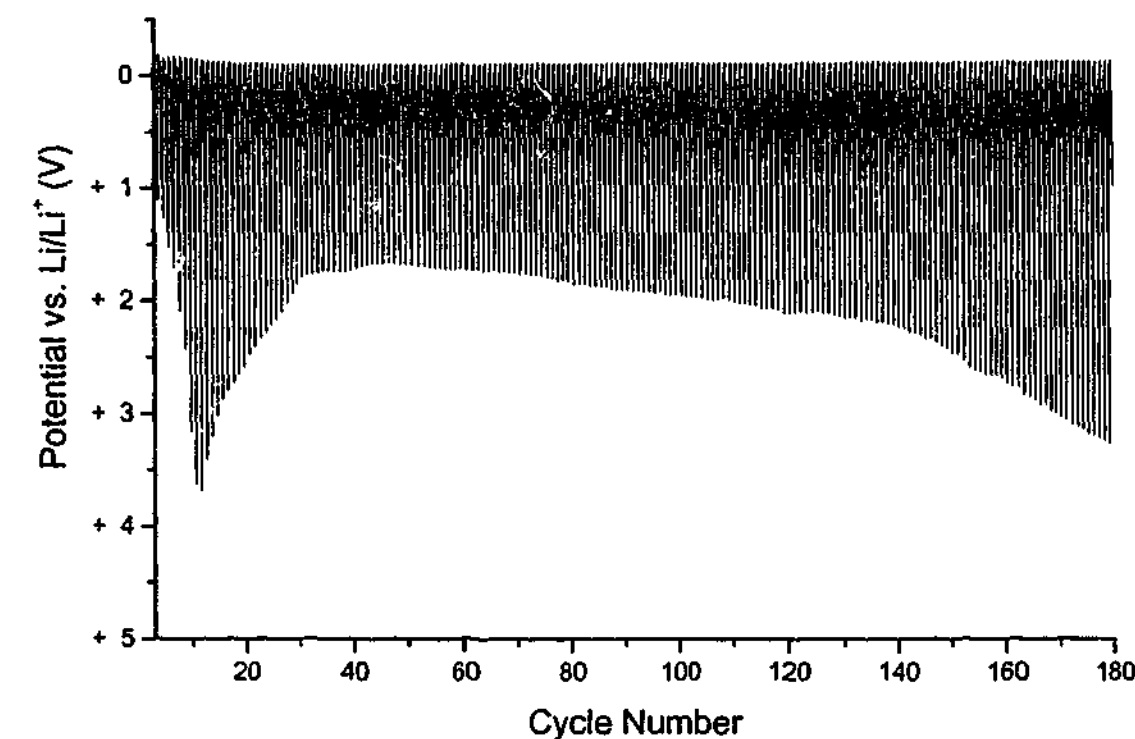


Fig. 3.2.15 Potential profile obtained from a $0.5 \text{ molkg}^{-1} \text{ P}_{14}(\text{Tf})_2\text{N}$ cycling efficiency experiment, 1.75 mAcm^{-2} , 1 Ccm^{-2} excess & 0.25 Ccm^{-2} cycling capacity at 50°C on a Pt electrode.

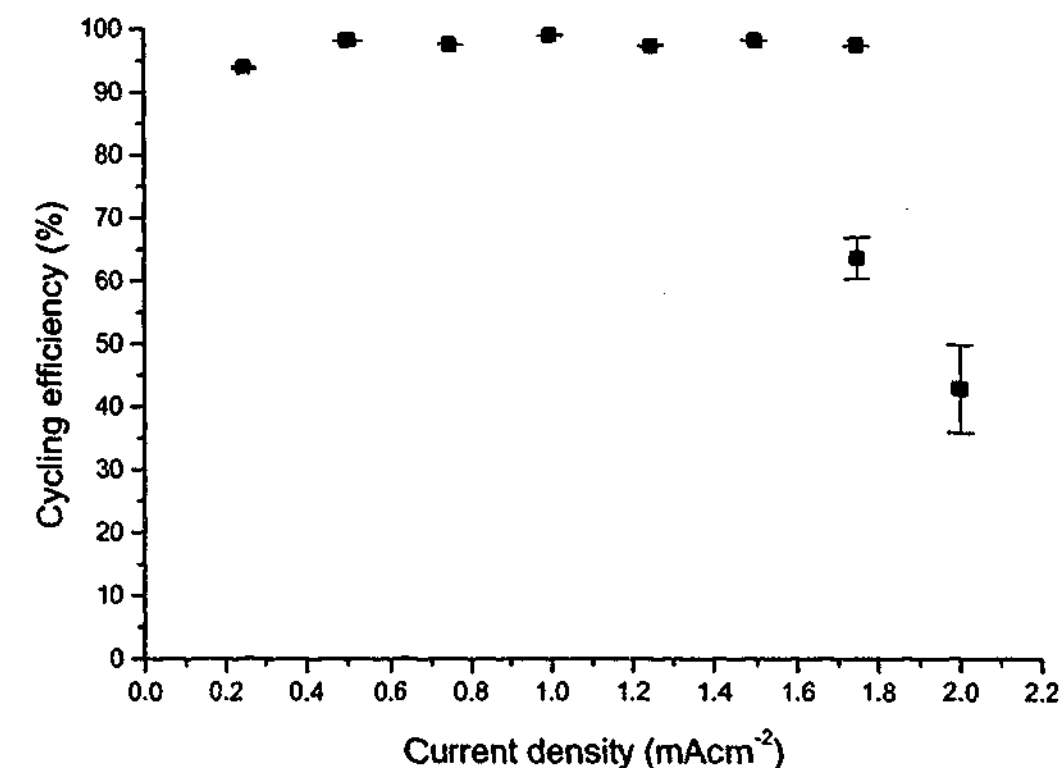


Fig. 3.2.16 Average cycling efficiency (%) for $0.5 \text{ molkg}^{-1} \text{ P}_{14}(\text{Tf})_2\text{N}$ at various current densities on a Pt electrode. 1 Ccm^{-2} excess charge & 0.25 Ccm^{-2} cycling charge at 50°C .

Copper electrode:

A similar set of experiments was performed using a copper electrode. Figure 3.2.17 shows an example of a typical potential profile recorded for a 0.25 mAcm^{-2} experiment. The appearance of the profile was similar to those obtained for the optical cell experiments (section 3.1.2), characterised by deposition and dissolution potentials of 50-70 mV (vs. Li/Li^+) and a sharp endpoint.

Generally, the cycling efficiencies obtained for a copper electrode were lower than those obtained using a platinum electrode. However, high efficiencies were obtained in some experiments. Figure 3.2.18 shows portions of the potential profile obtained for a 0.1 mAcm^{-2} experiment. The first thirty cycles are shown, followed by cycles 150-180 and 300-330. The deposit was still cycling after 330 cycles indicating an average efficiency of 98.8 %. In addition, it is clear from the voltage profile that the deposition and dissolution potentials were decreasing from approximately 150 cycles onwards. Under these conditions, the deposit gave every indication that it would continue to cycle indefinitely.

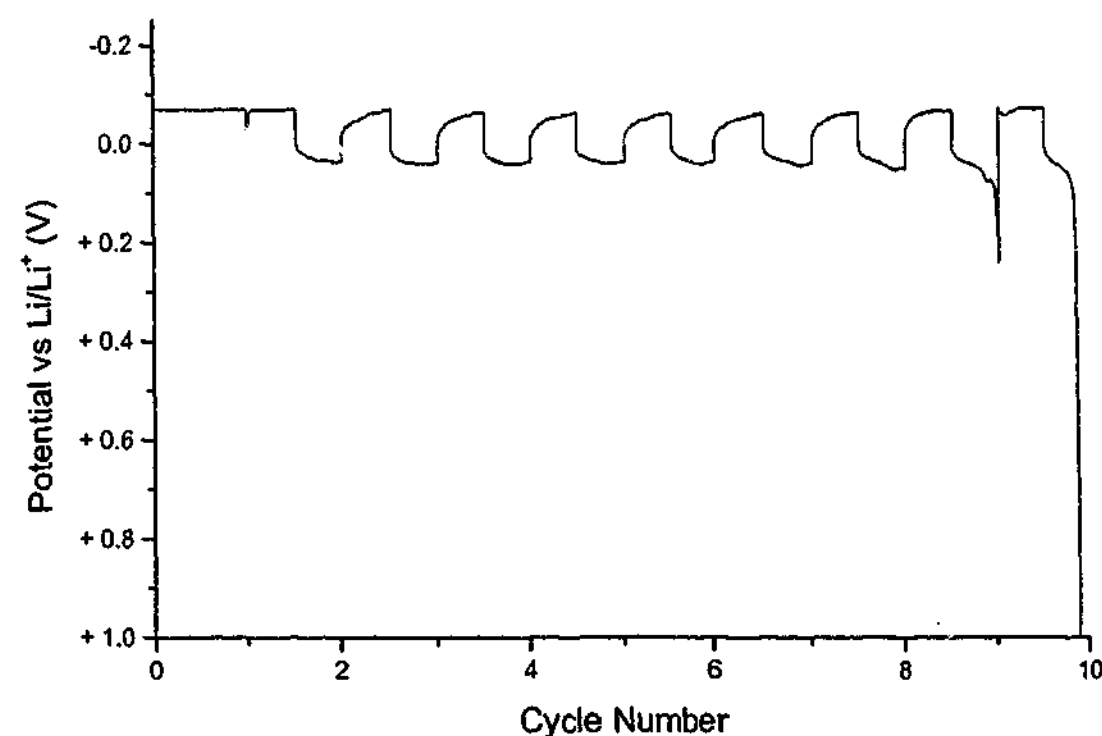


Fig. 3.2.17 Potential profile obtained from a $0.5 \text{ molkg}^{-1} \text{ P}_{14}(\text{Tf})_2\text{N}$ cycling efficiency experiment, 0.25 mAcm^{-2} , 1 Ccm^{-2} excess & 0.25 Ccm^{-2} cycling capacity at 50°C on a Cu electrode.

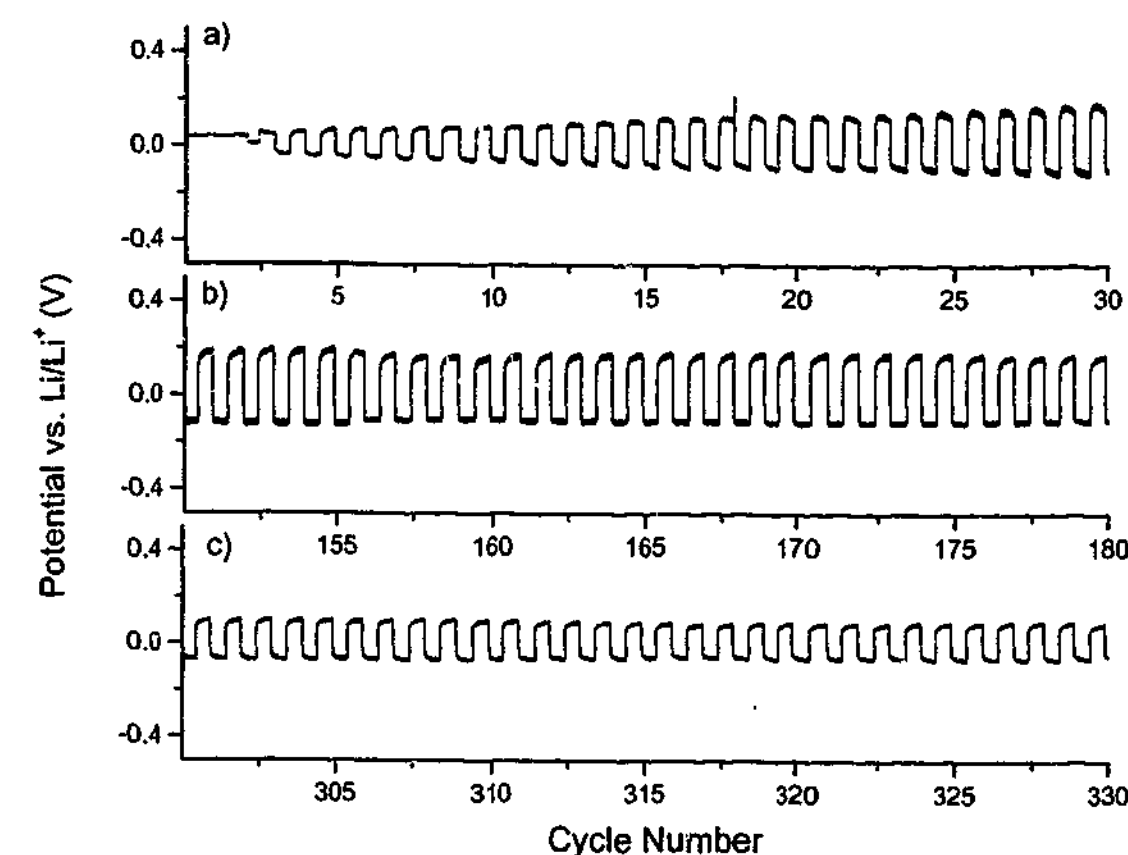


Fig. 3.2.18 Potential profile obtained from a $0.5 \text{ molkg}^{-1} \text{ P}_{14}(\text{Tf})_2\text{N}$ cycling efficiency experiment, 0.1 mAcm^{-2} , 1 Ccm^{-2} excess & 0.25 Ccm^{-2} cycling capacity at 50°C on a Cu electrode, a) Cycles 1-30, b) cycles 150-180, c) cycles 300-330.

To examine the influence of higher current densities on the deposit the current density was increased to 0.25 mAcm^{-2} after 330 cycles (Fig. 3.2.19a). The deposit continued to cycle at low and decreasing deposition and dissolution potentials for another 72 cycles (99.0% total and $>95.0\%$ at 0.25 mAcm^{-2}). The current density was increased again to 0.5 mAcm^{-2} (Fig. 3.2.19b, the deposit cycled for another 62 cycles ($>93.9\%$ at 0.5 mAcm^{-2}) before the experiment terminated. The deposit cycled for a total of 464 cycles (99.1%). The experiment indicates that very high cycling efficiencies can be obtained at low rates on copper. Given that the initial deposit cycled continuously for over 20 days, this experiment also indicates that the rate of any self-discharge process that may have been occurring was negligible. More significantly, the experiment demonstrates that after the formation of a deposit with a suitable SEI and morphology, improved cycling efficiencies can be obtained at higher rates. It is worth noting that the efficiencies obtained for the cycled deposit, cycled at higher rates (i.e., 0.25 mAcm^{-2} and 0.5 mAcm^{-2}) were higher than those obtained for any other experiment on a copper substrate.

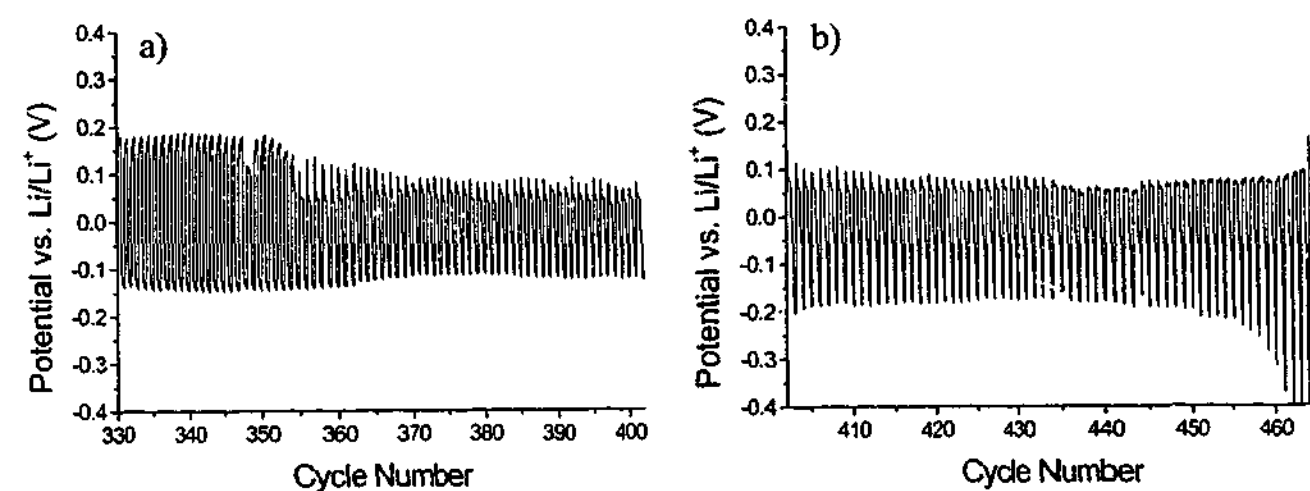


Fig. 3.2.19 Potential profile obtained from a $0.5 \text{ mol kg}^{-1} \text{ P}_{14}(\text{Tf})_2\text{N}$ cycling efficiency experiment, 1 C cm^{-2} excess & 0.25 C cm^{-2} cycling capacity at 50°C on a Cu electrode, a) Cycles 330-402 at 0.25 mA cm^{-2} , b) cycles 402-465 at 0.5 mA cm^{-2} .

Figure 3.2.20 shows a plot of the average cycling efficiency determined for a range of current densities on a copper electrode. The highest values, for pairs of experiments, are shown in red. The efficiency shows a decline with increasing current density and a large amount of scatter. The differences in behaviour when compared to the results for a

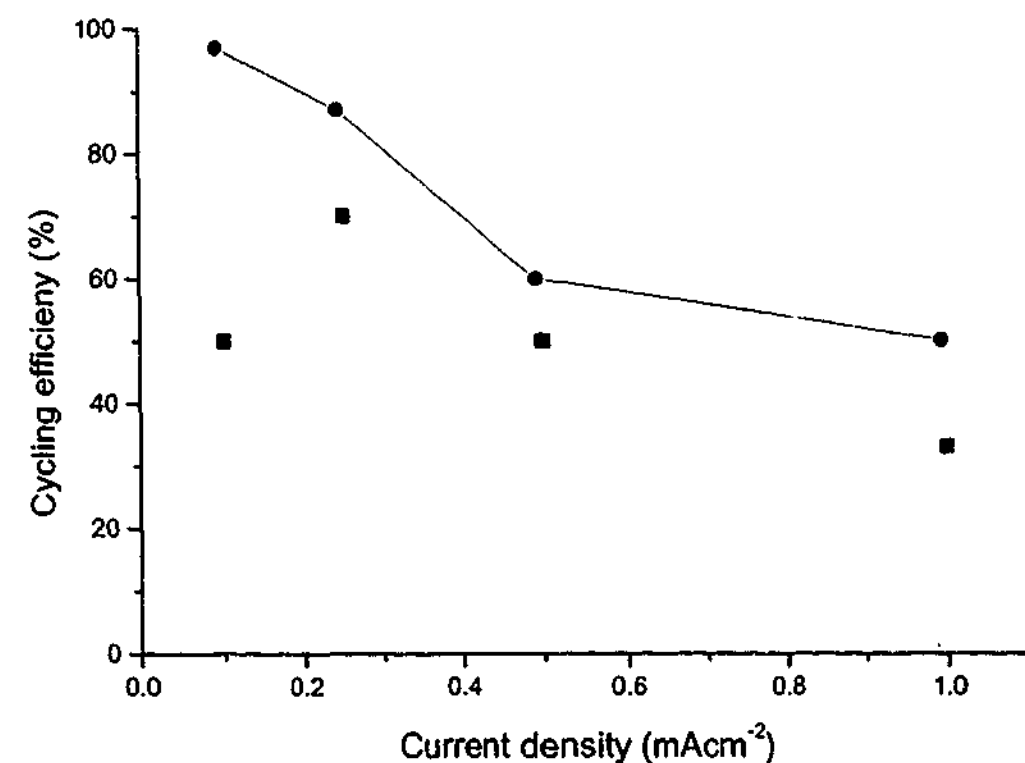


Fig. 3.2.20 Cycling efficiency (%) for $0.5 \text{ mol kg}^{-1} \text{ P}_{14}(\text{Tf})_2\text{N}$ at various current densities on a Cu electrode, two experiments. 1 C cm^{-2} excess charge & 0.25 C cm^{-2} cycling charge at 50°C .

platinum electrode are attributed to the nucleation conditions on the copper electrode. The nucleation potential on the copper electrode was significantly more negative than on the platinum electrode and it appears that this resulted in a greater tendency for dendritic deposits to form on the copper surface, and hence greater scatter in the results.

3.2.2 $\text{P}_{13}(\text{Tf})_2\text{N}$ – Cycling efficiency:

The influence of current density on the cycling efficiency of $\text{P}_{13}(\text{Tf})_2\text{N}$ electrolyte was also investigated for a copper electrode. An example of the potential profile obtained for a 1.0 mA cm^{-2} experiment is shown in Fig. 3.2.21. The profile exhibits a similar appearance to the $\text{P}_{14}(\text{Tf})_2\text{N}$ experiments. Figure 3.2.22 shows a plot of the average cycling efficiency determined for a range of current densities on a copper electrode. The highest values, for pairs of experiments, are shown in red. The results are similar to those obtained for $\text{P}_{14}(\text{Tf})_2\text{N}$, although the overall performance is more consistent and the efficiencies at higher current densities are higher. The difference in behaviour is difficult to explain, and at this point must be attributed to the complexities involved in the formation of a

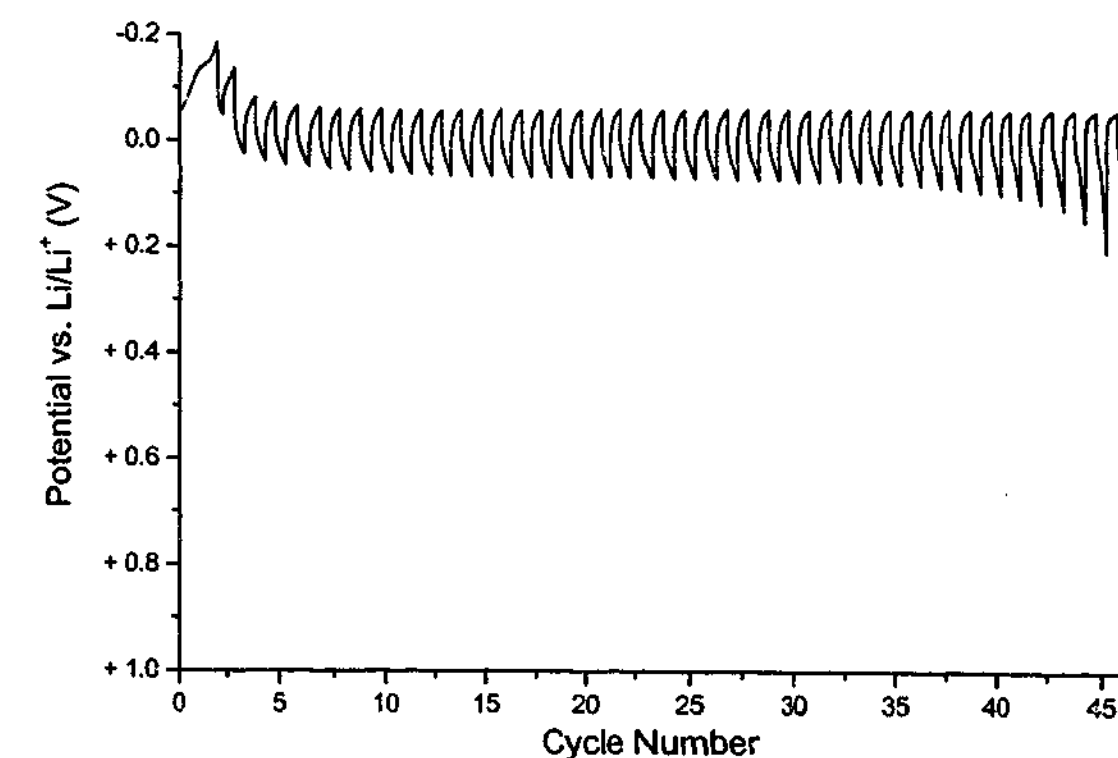


Fig. 3.2.21 Potential profile obtained from a $0.5 \text{ mol kg}^{-1} \text{ P}_{13}(\text{Tf})_2\text{N}$ cycling efficiency experiment, 1.0 mA cm^{-2} , 1 C cm^{-2} excess & 0.25 C cm^{-2} cycling capacity at 50°C on a Cu electrode.

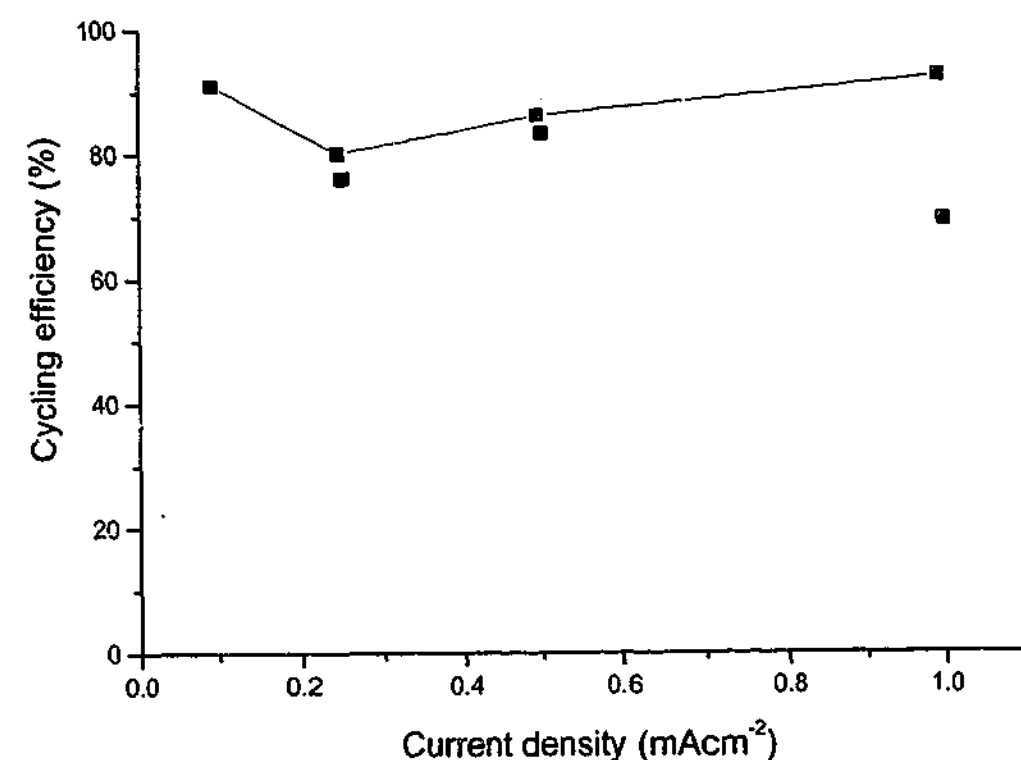


Fig. 3.2.22 Cycling efficiency (%) for $0.5 \text{ mol kg}^{-1} \text{ P}_{13}(\text{Tf})_2\text{N}$ at various current densities on a Cu electrode, two experiments. 1 C cm^{-2} excess charge & 0.25 C cm^{-2} cycling charge at 50°C .

favourable SEI. The improved efficiencies suggest that in $\text{P}_{13}(\text{Tf})_2\text{N}$ the deposit tends to a less dendritic morphology on a copper substrate, than in $\text{P}_{14}(\text{Tf})_2\text{N}$.

3.2.3 $\text{P}_{12}(\text{Tf})_2\text{N}$ – Cycling efficiency:

Experiments were also performed using the $\text{P}_{12}(\text{Tf})_2\text{N}$ electrolyte, however, reversible cycling was not possible at any of the current densities attempted (down to 0.1 mA cm^{-2}). The potential profiles indicated that a diffusion limit was preventing deposition at appreciable current densities, as can be seen in Fig. 3.2.23, where a transition to another process (presumably reduction of the P_{12}^+ cation) occurs early in the deposition phase of the experiment.

Application of the Sand equation (Section 1.3.1) to the transition times determined for 0.1 mA cm^{-2} and 0.25 mA cm^{-2} allows an estimate of the lithium diffusion coefficient to be obtained. The experiments reproducibly gave a value of $8 \times 10^{-8} \text{ cm}^2 \text{ s}^{-1}$. This value is less

than that obtained from NMR measurements (section 3.3.3) and agrees with the observations from conductivity measurements, which indicate that not all of the Li^+ cations in the sample are mobile (section 3.3.4). Recalculating the concentration term in the Sand equation using the diffusion coefficient obtained from the NMR measurements gives a concentration of $4 \times 10^{-5} \text{ mM}$ for Li^+ , suggesting that only $1:10^7$ lithium ions are mobile for a 0.5 mol kg^{-1} sample at 60°C .

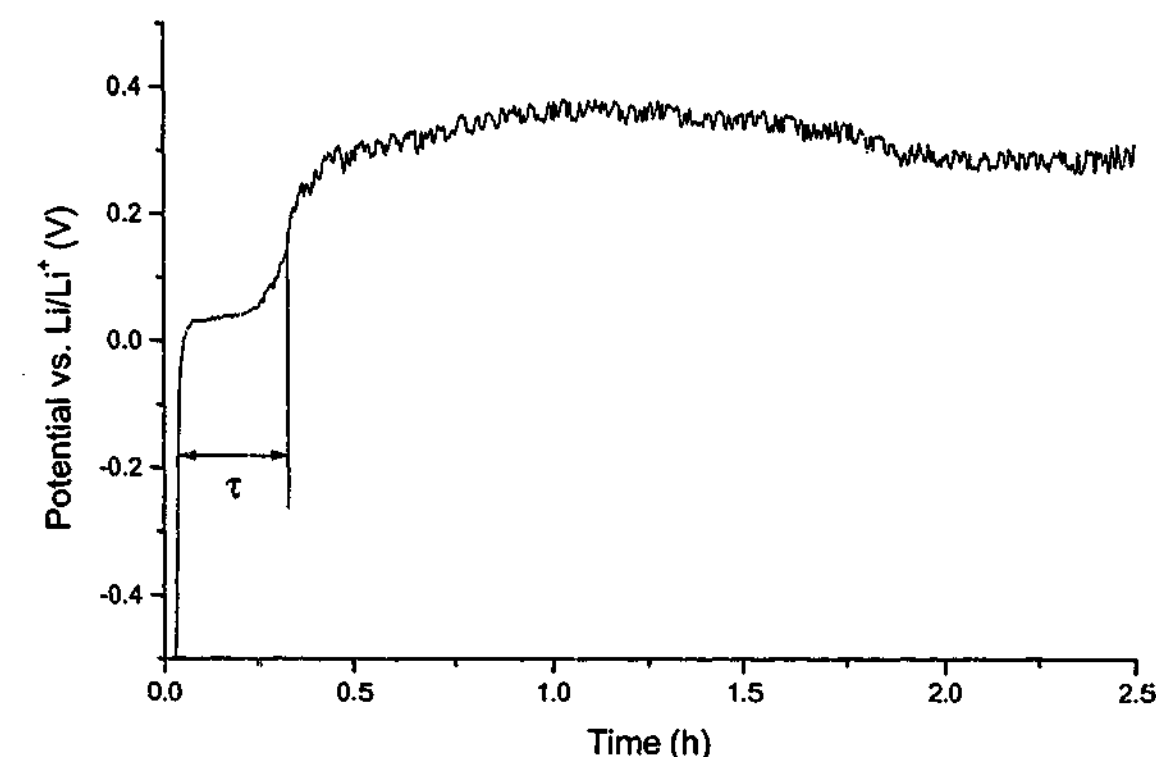


Fig. 3.2.23 Potential profile obtained from the excess deposition phase of a $0.5 \text{ mol kg}^{-1} \text{ P}_{12}(\text{Tf})_2\text{N}$ cycling efficiency experiment, 0.1 mA cm^{-2} , 1 C cm^{-2} excess 60°C on a Cu electrode.

3.2.4 Conclusions:

Reversible lithium deposition and dissolution was demonstrated in all three systems, appreciable currents were obtained in the $\text{P}_{13}(\text{Tf})_2\text{N}$ and $\text{P}_{14}(\text{Tf})_2\text{N}$ systems. The addition of a lithium salt to the neat RTIL resulted in a significant increase in the cathodic stability of the system by favouring lithium deposition over reduction of the pyrrolidinium cation. Steady state current measurements, in combination with impedance measurements,

indicated an optimum lithium concentration of $\sim 0.4 \text{ mol kg}^{-1}$ $\text{Li}(\text{Tf})_2\text{N}$ and that lithium transport was dominated by the properties of the interface.

Evidence for the formation of an SEI was provided by cyclic voltammetry, which indicated that the reversibility of the lithium deposition/dissolution process was improved, after a significant reduction peak at 0.35 V (vs. Li/Li^+) had reduced in magnitude (with successive scans). Literature values indicated that the peak could be related to the reduction of the $(\text{Tf})_2\text{N}^-$ anion.

The lithium electrochemistry was significantly affected by the choice of substrate, a platinum substrate exhibited underpotential deposition and alloy formation, which appeared to improve the overall reversibility of the lithium deposition/dissolution process. The copper and nickel substrates did not exhibit the same features in their CVs and the SEI formation peak was more pronounced on these substrates, indicating that the SEI properties are likely to differ, depending on the substrate.

The cycling efficiency was investigated on platinum and copper electrodes for a $\text{P}_{14}(\text{Tf})_2\text{N}$ electrolyte. The platinum substrate gave very high and consistent efficiencies (exceeding 99 %) and a sloping dissolution potential profile. The copper substrate gave less consistent results, which was attributed to the stochastic nature of the nucleation process on copper and the influence of deposit morphology. However, at low current densities (0.1 mA cm^{-2}) very high efficiencies were obtained, exceeding 99 %. Under these conditions, the deposit appeared to be capable of cycling indefinitely, and furthermore, the cycled deposit gave higher efficiencies at higher rates than was possible for deposits plated at higher rates.

The $\text{P}_{13}(\text{Tf})_2\text{N}$ and $\text{P}_{12}(\text{Tf})_2\text{N}$ systems were also investigated for their cycling efficiencies on a copper substrate. The $\text{P}_{13}(\text{Tf})_2\text{N}$ system exhibited more consistent cycling efficiencies and higher efficiencies at high rates than the $\text{P}_{14}(\text{Tf})_2\text{N}$ system. The $\text{P}_{12}(\text{Tf})_2\text{N}$ electrolyte was not capable of cycling lithium at appreciable rates. Diffusion coefficients calculated from the Sand equation were of the order of $8 \times 10^{-8} \text{ cm}^2 \text{ s}^{-1}$ and comparison with NMR values indicated that only a small fraction of the lithium ions were mobile. Work undertaken to characterise and compare the transport properties of each system is presented in the following section.

References

1. D. R. MacFarlane, P. Meakin, J. Sun, N. Amini and M. Forsyth, *J. Phys. Chem. B*, **103**, 4164 (1999).
2. A. J. Bard and L. R. Faulkner, *Electrochemical Methods, Fundamentals and Applications*, John Wiley and Sons, New York (1980).
3. D. Aurbach (Ed.), *Nonaqueous Electrochemistry*, Marcel Dekker, New York (1999).
4. T. B. Massalski, *Binary Alloy Phase Diagrams*, ASM International, Materials Park, Ohio (1990).
5. D. Aurbach, I. Weissman, A. Zaban and O. Chusid, *Electrochim. Acta*, **39**, 51 (1994).
6. M. Arakawa, S. Tobishima, Y. Nemoto, M. Ichimura and J. Yamaki, *J. Power Sources*, **43**, 27 (1993).

3.3 Diffusion & transport in $\text{Li}(\text{Tf})_2\text{N} / \text{P}_{1x}(\text{Tf})_2\text{N}$:

For any electrolyte system, an understanding of the way in which the analyte (in this case Li^+) is transported to the electrode surface is critical. RTILs present some unusual transport properties and differ significantly from conventional electrolytes. The concentration of charge in RTILs is orders of magnitude greater than that of other systems, which results in very different behaviour when a process is occurring at an electrode surface. The work presented in this section aims to characterise the transport behaviour of the $\text{Li}(\text{Tf})_2\text{N} / \text{P}_{1x}(\text{Tf})_2\text{N}$ system and gain an understanding of the roles of the various forces at work within the liquid.

3.3.1 Diffusion by 3-electrode cell (Randles-Sevcik):

The diffusion coefficient of an electrochemically active species can be determined by electrochemical experiments if transport does not contain a migration or convection component. In the viscous RTIL, the convection component can be discounted. The migration component poses another problem. In conventional solvents, transport is only considered to be diffusion controlled in situations where the analyte is at low concentration (e.g., mM) and in the presence of a supporting electrolyte. The situation in RTILs can be considered analogous, in that for a 0.5 mol kg^{-1} solution there is one lithium ion for every nine solvent ions. Given the high concentration of 'indifferent' (i.e., electrochemically inactive) ionic charge present in the RTIL electrolyte, it is likely that an applied electric field would not extend far into the bulk solution from the electrode surface, thus reducing the influence of a migration current.

If the migration current in RTILs were negligible, then electrochemical methods usually reserved for solutions with low analyte concentration and added supporting electrolyte should be applicable to the solutions used in this study. For example, Figure 3.3.1 shows a series of cyclic voltammograms obtained at varying scan rates in a $0.5 \text{ mol kg}^{-1} \text{ P}_{14}(\text{Tf})_2\text{N}$ solution (*Note*: concentration notation has been described previously, section 2.1.6). A plot of the deposition peak currents (I_p) versus the square root of the scan rate (Fig. 3.3.2)

allows the calculation of the lithium diffusion coefficient via the application of the Randles-Sevcik equation (as described in section 2.5.2 & 2.6.2).

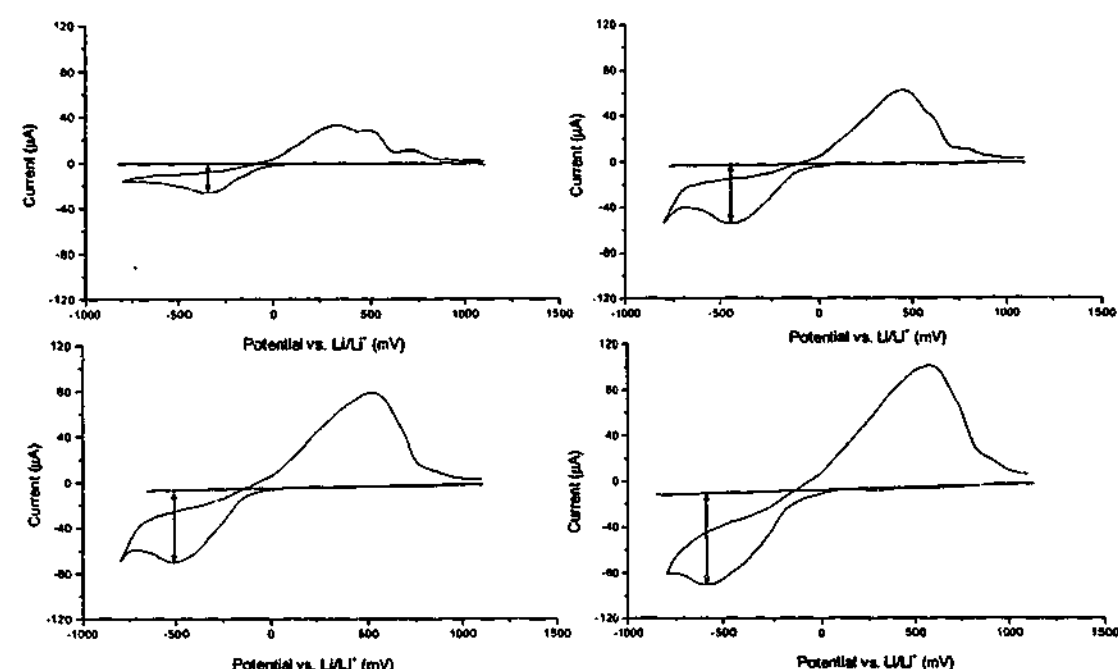


Fig. 3.3.1 Cyclic voltammograms obtained at 300K in 0.5 mol kg⁻¹ P₁₄(Tf)₂N at varying scan rates, a) 10 mVs⁻¹, b) 50 mVs⁻¹, c) 100 mVs⁻¹, d) 200 mVs⁻¹.

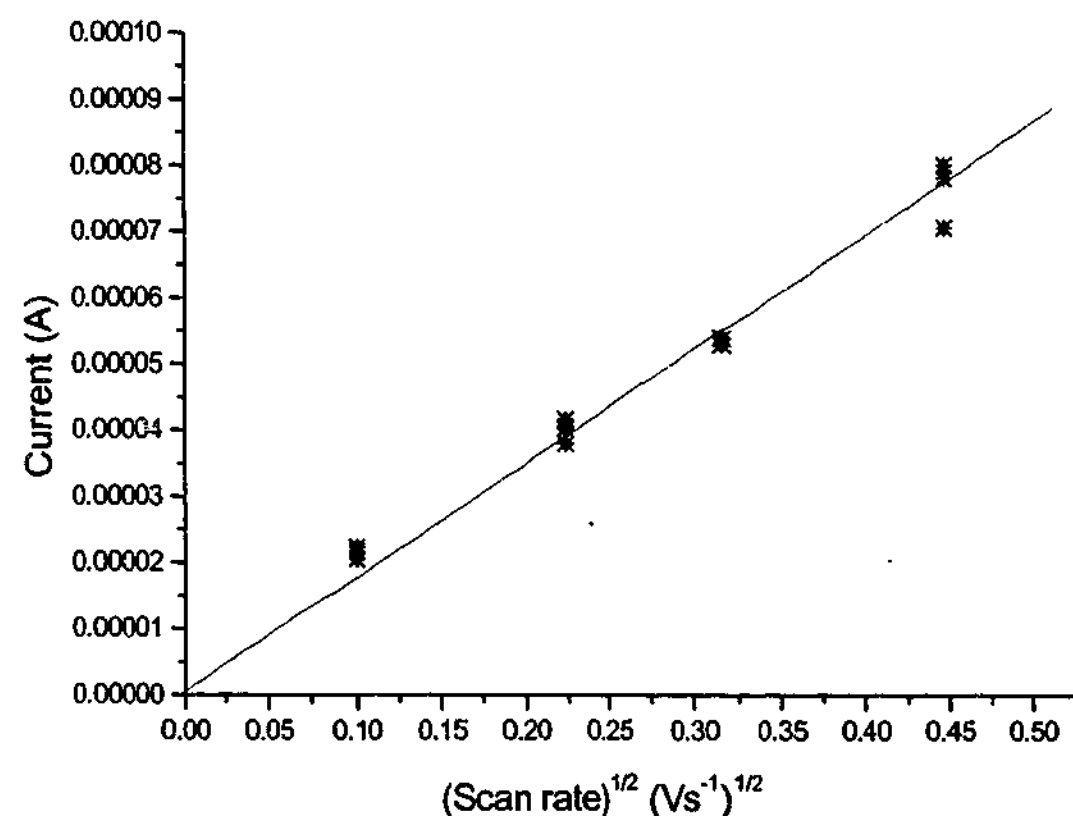


Fig. 3.3.2 Plot of current versus (Scan rate)^{1/2} for determination of the diffusion coefficient of lithium in 0.5 mol kg⁻¹ P₁₄(Tf)₂N.

The magnitude of the peak currents was reproducible (as shown in Fig. 3.3.2) and a linear fit of the data (correlation coefficient of 0.993) provided a value of $1.0 (\pm 0.1) \times 10^{-8} \text{ cm}^2 \text{ s}^{-1}$ for the diffusion coefficient of lithium in 0.5 mol kg⁻¹ P₁₄(Tf)₂N at 300K. The deposition peak was used to avoid complications due to the influences of SEI transport during dissolution; deposition on a freshly polished electrode surface allows the influence of changes in the electrode area and the formation of passivation films to be minimized.

The validity of this experiment, and hence the validity of the assumptions made about the nature of lithium transport in the RTIL, can be verified by determining the diffusion coefficient by other means. This has been achieved by a combination PFGSE-NMR and conductivity measurements and will be presented in the following sections.

3.3.2 Conductivity:

The specific conductivity of P₁₂(Tf)₂N, P₁₃(Tf)₂N and P₁₄(Tf)₂N with and without added lithium salt was determined over a range of temperatures. The conductivity was obtained from the first real axis touchdown in the impedance spectrum complex plane plot, an example is shown in figure 3.3.3.

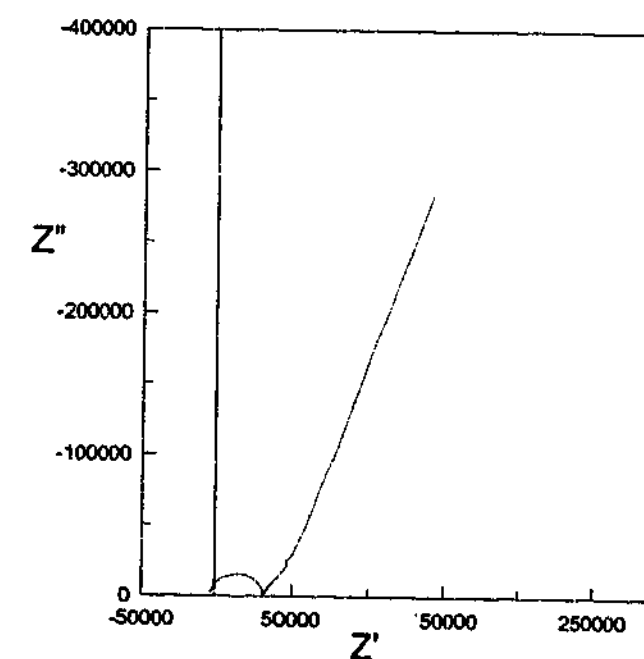


Fig. 3.3.3 0.25 mol kg⁻¹ P₁₂(Tf)₂N EIS complex plane plot, real axis touchdown used to determine the specific conductivity

Figure 3.3.4 shows a plot of the specific conductivity of a 0.25 mol kg^{-1} and 0.5 mol kg^{-1} solution of $\text{Li}(\text{Tf})_2\text{N}$ in $\text{P}_{12}(\text{Tf})_2\text{N}$. Both systems undergo fusion in the temperature range of the measurements, as indicated by the distinct change in the slope of both plots. The relationship between phase behaviour and conductivity of the doped solids has been characterised by other workers.^{1,2} The doped solids have been found to exhibit plastic crystal behaviour due to the presence of significant rotational disorder arising from the rotation of the pyrrolidinium cation. The disorder results in a high concentration of vacancies and transport is thought to occur via a vacancy mechanism.³⁻⁶ The conductivity exhibited by both solutions in the solid state is significant, the 0.5 mol kg^{-1} sample exhibiting higher conductivity below the melting point. The conductivity has been found to increase with the addition of a dopant (in this case $\text{Li}(\text{Tf})_2\text{N}$) reaching a maximum at 33 mol% ($\sim 0.9 \text{ mol kg}^{-1}$). The conductivity behaviour of the solid is complicated by supercooling; in these measurements, the sample is melted in order to load the conductivity cell and the presence of supercooled liquid phases in the solid must be considered. Solid-state conductivity behaviour in these materials has been found to be reproducible, but only after the doped system has been fused (reproducibility is indicated by the duplicate 0.5 mol kg^{-1} measurements, which are indistinguishable). In the melt, the conductivity of the

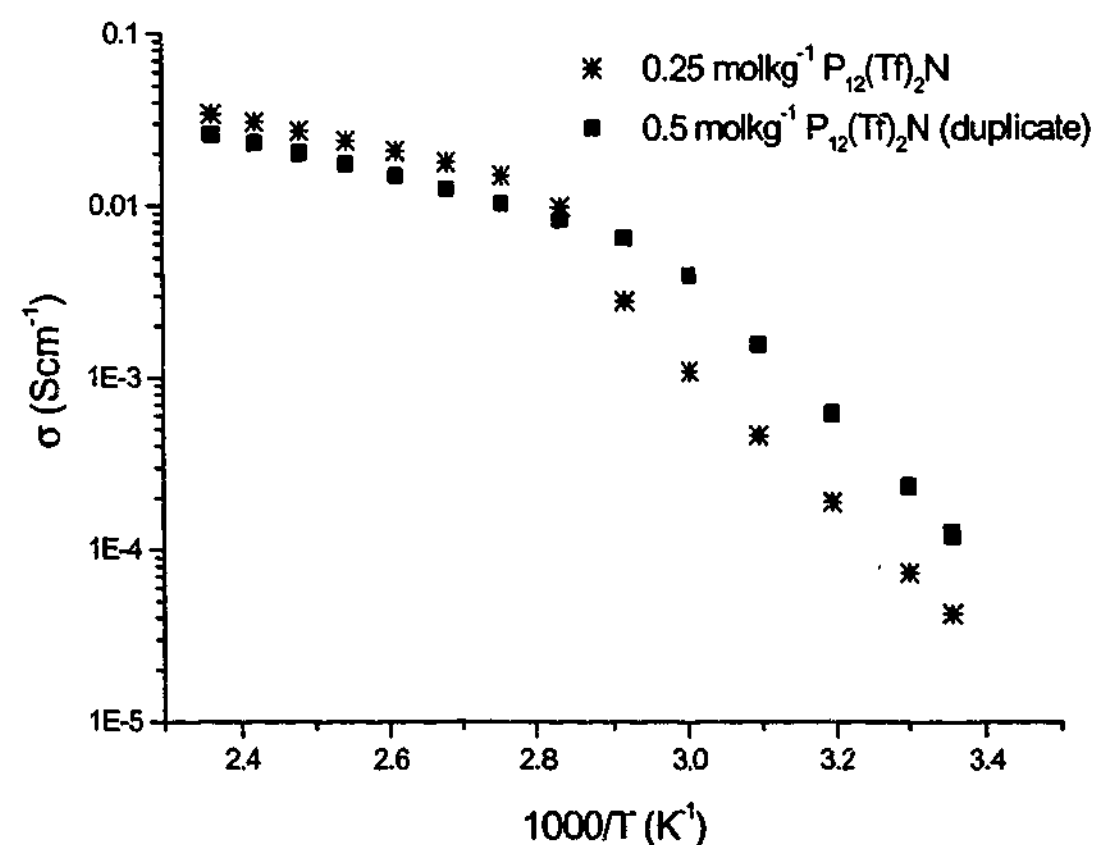


Fig. 3.3.4 0.25 and $0.5 \text{ mol kg}^{-1} \text{P}_{12}(\text{Tf})_2\text{N}$ specific conductivity. Error bars are within the data points.

0.25 mol kg^{-1} sample is higher than that of the 0.5 mol kg^{-1} sample, this is the result of increased ion interactions occurring in the presence of higher concentrations of the lithium cation.

Figure 3.3.5 shows an Arrhenius plot of neat and $0.5 \text{ mol kg}^{-1} \text{P}_{13}(\text{Tf})_2\text{N}$ specific conductivity. Again, the addition of the lithium salt causes a considerable reduction in conductivity. It is apparent that at elevated temperatures the difference in conductivities becomes less pronounced, indicating that the relative influence of lithium on the ion-ion interactions is reduced at higher temperatures.

A similar plot of the P_{14} system at various lithium salt concentrations is shown in Figure 3.3.6. Similar behaviour is observed when compared to the $\text{P}_{13}(\text{Tf})_2\text{N}$ samples. The conductivities of the neat and low concentration samples are virtually indistinguishable. As observed for the P_{13} samples, the addition of the lithium salts causes a decrease in conductivity, which becomes less significant at higher temperatures. The inset shows the data over a narrower temperature range to highlight the slight difference in the conductivity of the low concentration samples.

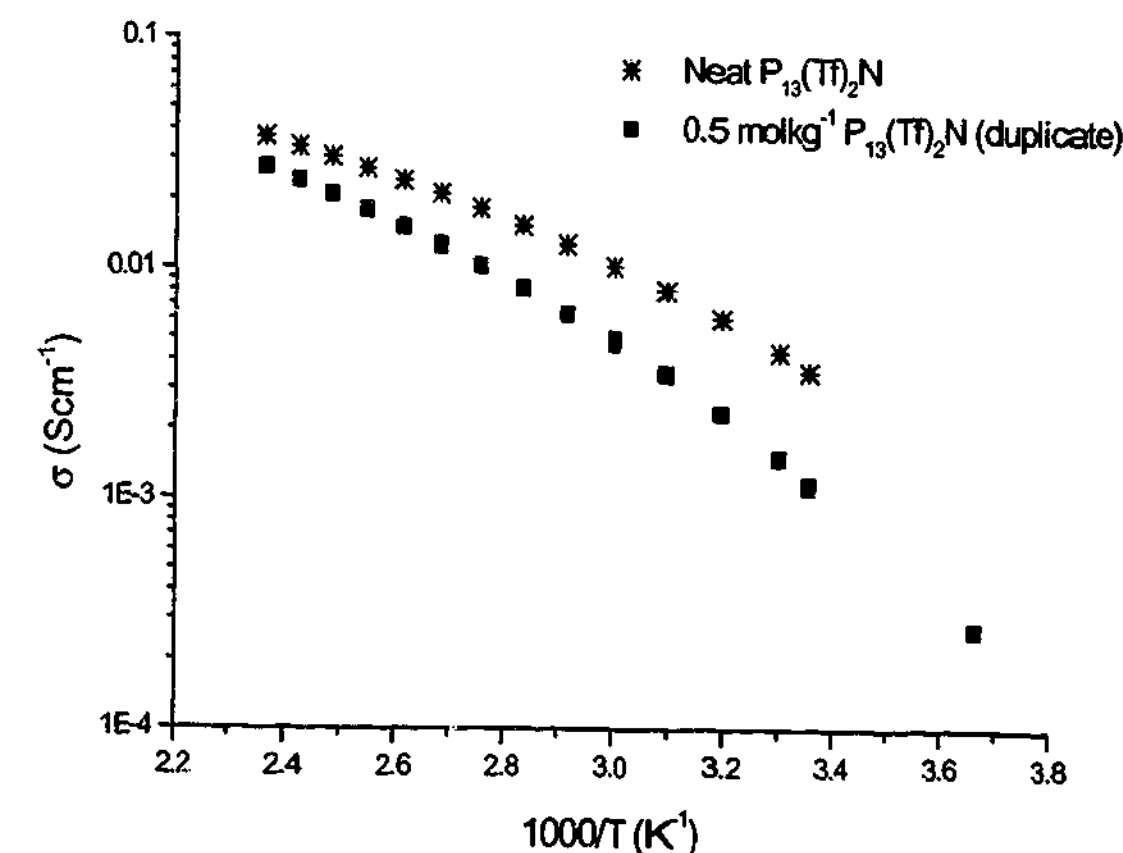


Fig. 3.3.5 Neat and $0.5 \text{ mol kg}^{-1} \text{P}_{13}(\text{Tf})_2\text{N}$ specific conductivity. Error bars are within the data points.

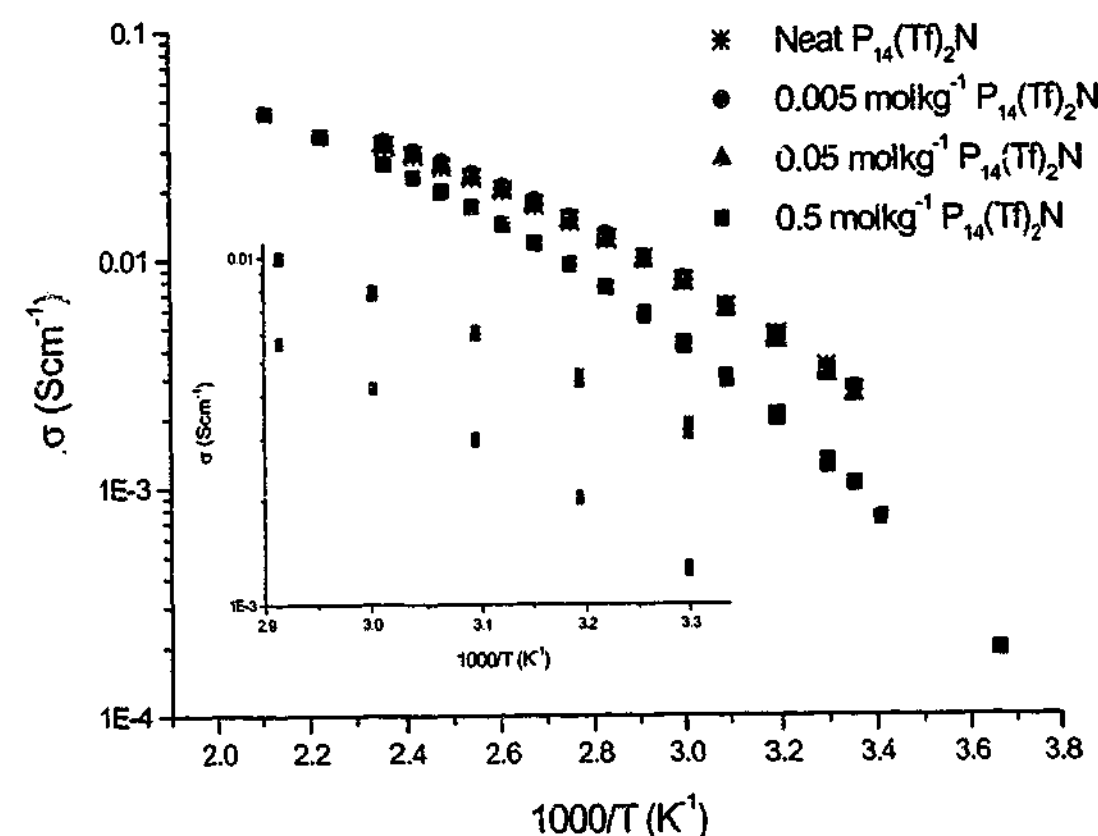


Fig. 3.3.6 Neat, 0.005, 0.05 & 0.5 molkg⁻¹ P₁₄(Tf)₂N specific conductivity. Error bars are within the data points. Inset: same data with an expanded scale

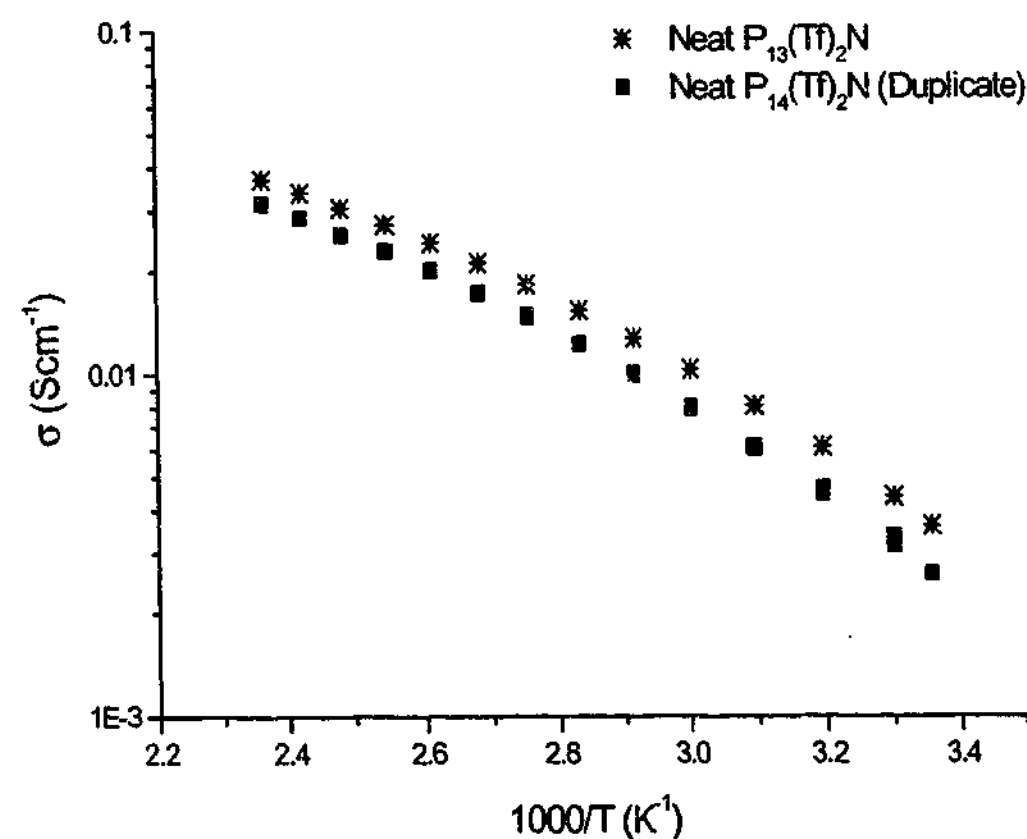


Fig. 3.3.7 Comparison of the specific conductivity of neat P₁₃(Tf)₂N and neat P₁₄(Tf)₂N. Error bars are within the data points.

Figure 3.3.7 shows a comparison of the conductivity of neat P₁₃(Tf)₂N and P₁₄(Tf)₂N RTILs. For the entire temperature range the conductivity of P₁₃(Tf)₂N is slightly greater than that of P₁₄(Tf)₂N. This reflects the smaller ionic radius of the P₁₃ cation compared to that of P₁₄. In contrast, the melting point of P₁₄(Tf)₂N is lower than that of P₁₃(Tf)₂N (-18 °C vs. 12 °C).³

For the majority of the samples presented, duplicate runs were performed on heating and on cooling. The results were found to be highly reproducible.

Figure 3.3.8 shows an Arrhenius plot comparing the conductivity of 0.5 molkg⁻¹ solutions of Li(Tf)₂N in P₁₂(Tf)₂N, P₁₃(Tf)₂N and P₁₄(Tf)₂N. The conductivity of the three solutions is almost identical in the melt, as can be seen more clearly in the inset. It is surprising that the conductivity of the P₁₃(Tf)₂N is highest, given that the P₁₂ cation has the lowest ionic radius. This possibly reflects the limits of the accuracy of the measurements. The overall similarity of the conductivities of the doped samples indicates that the strength of the interactions imparted by the presence of the lithium ions overrides the difference in interactions imparted by the differing sizes (and flexibilities) of the pyrrolidinium cations.

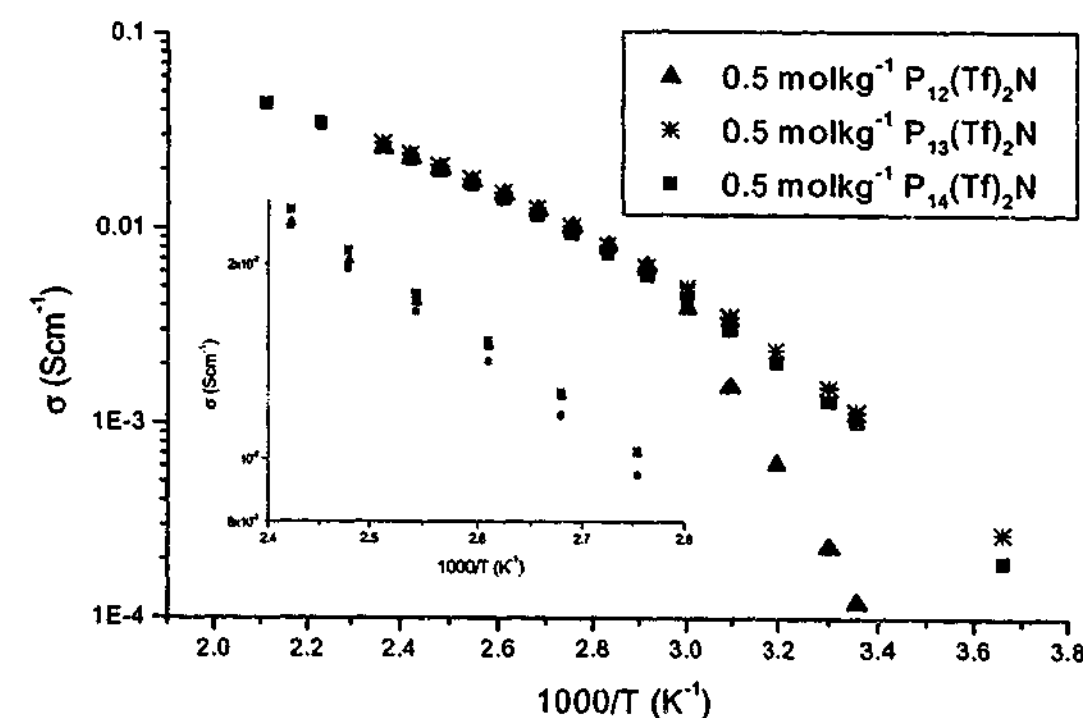


Fig. 3.3.8 0.5 molkg⁻¹ P₁₂(Tf)₂N, P₁₃(Tf)₂N & P₁₄(Tf)₂N specific conductivity comparison. Inset: Zoom of the main plot above the P₁₂ melting point. Error bars are within the data points.

Table 3.3.1 provides values of the specific conductivity of all of the samples measured at 25 °C and 50 °C. It is interesting to note that the 0.005 mol kg⁻¹ P₁₄ sample exhibits slightly higher conductivity than the neat sample. The difference is close to the limit of the accuracy of the measurement, and could reflect systematic errors arising from the determination of the cell constant. Alternatively, it could indicate that at low concentrations, the increase in the amount of charge (per unit volume) available for conduction outweighs the increased ion-ion interactions due to the presence of the lithium ion.

Table 3.3.1 Specific conductivity (mS cm⁻¹) of all samples at 25 °C and 50 °C.

	P ₁₂ (Tf) ₂ N		P ₁₃ (Tf) ₂ N		P ₁₄ (Tf) ₂ N			
	0.25 mol kg ⁻¹	0.5 mol kg ⁻¹	Neat	0.5 mol kg ⁻¹	Neat	0.005 mol kg ⁻¹	0.05 mol kg ⁻¹	0.5 mol kg ⁻¹
25 °C	<0.1	0.1	3.6	1.1	2.6	2.7	2.5	1.0
50 °C	0.5	1.5	8.0	3.5	6.1	6.2	5.9	3.0

The curvature present in all of the plots indicates that the conductivity-temperature relationship does not exhibit strictly Arrhenius behaviour; it has been found that the conductivity of RTILs can be more adequately described by the VTF equation.⁷ However, the behaviour of the samples over a relatively narrow temperature range can be described by the Arrhenius equation, as indicated by the linearity of the plots in Fig. 3.3.8 (Inset).

Table 3.3.2 provides *apparent* Arrhenius activation energies for each sample calculated for the 300-340K temperature range. The apparent activation energies exhibited by the solids are significantly higher than those of the liquids, implying a different conduction mechanism. For the RTILs the addition of a lithium salt causes an increase in the apparent activation energy. This, and the observed convergence of conductivity values at higher temperatures (Figs. 3.3.5 & 3.3.6) indicates that the relative influence of the lithium ion-solvent ion interactions (most likely (Tf)₂N⁻) decreases at higher temperatures.

Table 3.3.2 Apparent Arrhenius activation energies for all samples (300-340K).

Electrolyte	State	Apparent Arrhenius Act. Energy (kJ mol ⁻¹)	Correlation coefficient (R)
0.25 mol kg ⁻¹ P ₁₂ (Tf) ₂ N	Solid	79 ± 1	0.9994
0.5 mol kg ⁻¹ P ₁₂ (Tf) ₂ N	Solid	79 ± 1	0.9998
Neat P ₁₃ (Tf) ₂ N	Liquid	23 ± 1	0.9987
0.5 mol kg ⁻¹ P ₁₃ (Tf) ₂ N	Liquid	31 ± 1	0.9978
Neat P ₁₄ (Tf) ₂ N	Liquid	24 ± 1	0.9986
0.005 mol kg ⁻¹ P ₁₄ (Tf) ₂ N	Liquid	24 ± 1	0.9991
0.05 mol kg ⁻¹ P ₁₄ (Tf) ₂ N	Liquid	25 ± 1	0.9987
0.5 mol kg ⁻¹ P ₁₄ (Tf) ₂ N	Liquid	32 ± 1	0.9980

Table 3.3.3 summarises the best-fit parameters obtained from a VTF (equation 1.15[†]) fit of the conductivity data for the liquid (i.e., P₁₃ & P₁₄) samples. Apart from the 0.5 mol kg⁻¹ P₁₃(Tf)₂N sample (where the fit to the data was not as good as for the other samples), the *T*₀ values were almost identical. This indicates that the difference in ionic transport properties (between the different RTILs as well as the different Li concentrations) was dictated mainly by the *B* term (i.e., by activation energies). Thus, the difference in the temperature dependence of the ionic conductivity of the samples most likely reflects a temperature dependence of concentration (activity) arising from shifts in the state of aggregation. The findings agree with those of Noda *et al.*⁸ who reported VTF fits for a variety of transport properties (viscosity, diffusion, conductivity) for imidazolium and pyridinium cations with tetrafluoroborate and bis(trifluoromethanesulfonyl)amide anions. Although the properties of these RTILs were significantly different, the reported *T*₀ values were similar, particularly for the conductivity data.

[†] At temperatures in the low-fluidity region (i.e., where non-Arrhenius behaviour is most evident, between *T*₀ and 2*T*₀) the *T*^{-1/2} term can be omitted because the exponential term easily accommodates the rapid changes in transport properties that occur in this region.⁹

Table 3.3.3 VTF equation parameters for conductivity data for liquid samples (i.e., excludes $P_{12}(Tf)_2N$ samples).

Electrolyte	$\sigma_o (S\text{cm}^{-1})$	$B (K)$	$T_o (K)$	R^2
Neat $P_{13}(Tf)_2N$	0.32 (± 0.005)	520 (± 6)	181 (± 1)	0.9999
0.5 molkg ⁻¹ $P_{13}(Tf)_2N$	0.9 (± 0.1)	960 (± 67)	150 (± 8)	0.9998
Neat $P_{14}(Tf)_2N$	0.31 (± 0.01)	550 (± 15)	184 (± 3)	0.9999
0.005 molkg ⁻¹ $P_{14}(Tf)_2N$	0.36 (± 0.01)	590 (± 6)	178 (± 1)	0.9999
0.05 molkg ⁻¹ $P_{14}(Tf)_2N$	0.34 (± 0.01)	570 (± 10)	182 (± 2)	0.9999
0.5 molkg ⁻¹ $P_{14}(Tf)_2N$	0.53 (± 0.01)	720 (± 7)	183 (± 1)	0.9999

3.3.3 Multinuclear PFGSE-NMR diffusion:

The use of the pulsed field gradient spin echo nuclear magnetic resonance (PFGSE-NMR) technique allows the determination of self-diffusion coefficients for various nuclei. In the case of the samples studied here, determination of the 1H , ^{19}F and 7Li nuclei self-diffusion coefficients gives the average self-diffusion coefficients for each of the mobile species.

Figure 3.3.9 provides examples of the 1H , ^{19}F and 7Li line spectra and of the fits of the spin echo pulse sequence for various samples. Generally, the fits to the pulse sequence did not contribute a significant error to the measurement (typically $< \pm 0.5\%$ when a good fit is obtained). To estimate the errors present in the values obtained for each of the self-diffusion coefficients, the standard error for each of the values determined for the 1H spectrum was used. The example shown in Fig. 3.3.9a allows for seven peaks to be fitted, and hence, seven diffusion coefficients (all from the same species) to be determined. The standard error determined in this way (for each sample at each temperature) was then applied to the ^{19}F and 7Li values as a percentage error. Error margins ranging from $\pm 1\%$ to $\pm 15\%$ were obtained. Typically, the scatter in the data increased with temperature. An error of $\pm 1K$ was estimated for the sample temperature control.

For most of the systems measured, two separate samples obtained from different batches of RTILs were measured at 300 K, 325K & 340K or at 310K, 320K & 330K. In this way, the significance of variations due to sample purity and lithium salt concentration could be determined.

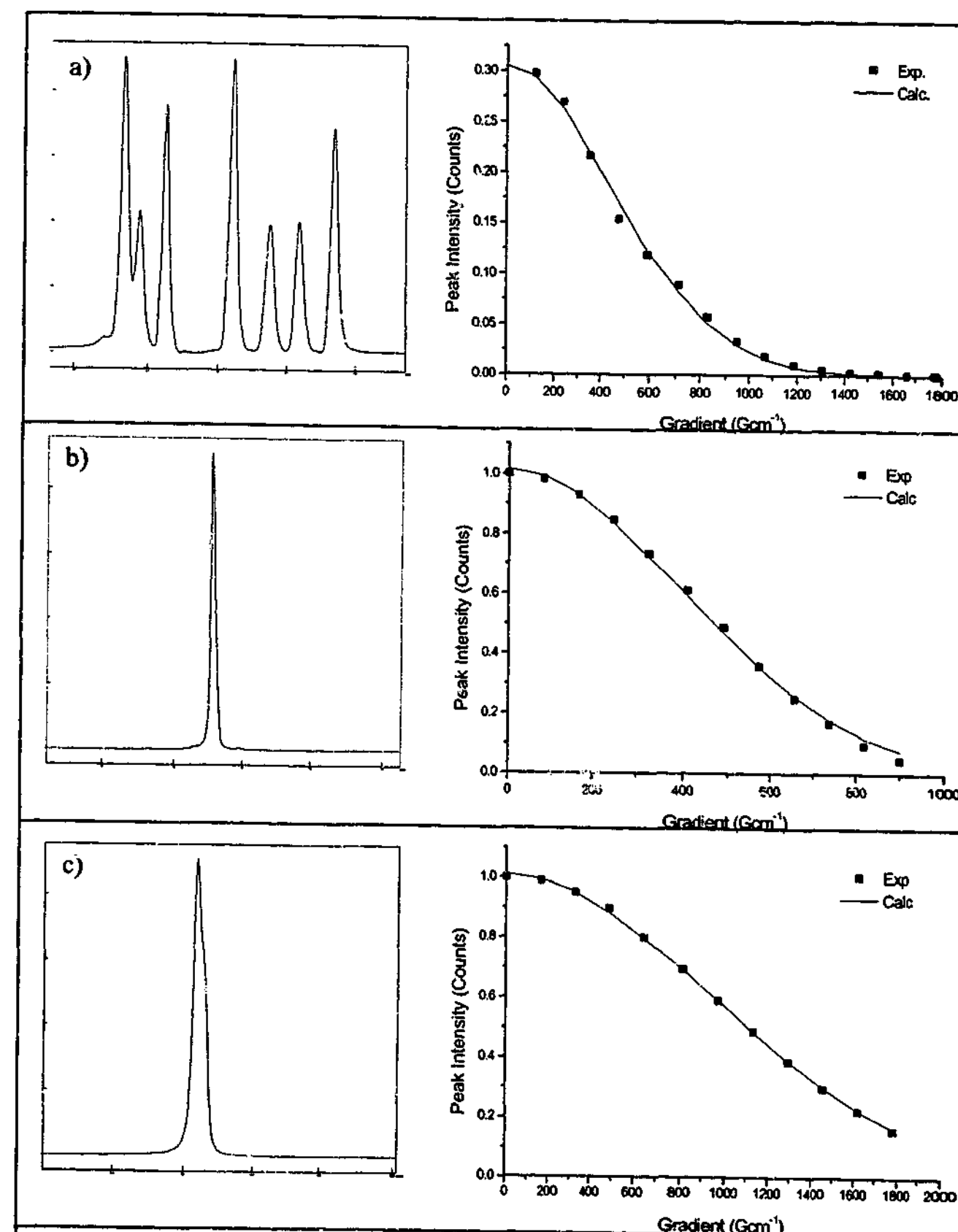


Fig. 3.3.9 Representative 1D Spectra and fits for $Li(Tf)_2N / P_{13}(Tf)_2N$ PFGSE-NMR experiments. a) 1H 0.05 molkg⁻¹ $P_{14}(Tf)_2N$ at 300 K, b) ^{19}F 0.5 molkg⁻¹ $P_{14}(Tf)_2N$ at 340 K and c) 7Li 0.5 molkg⁻¹ $P_{13}(Tf)_2N$ at 320 K.

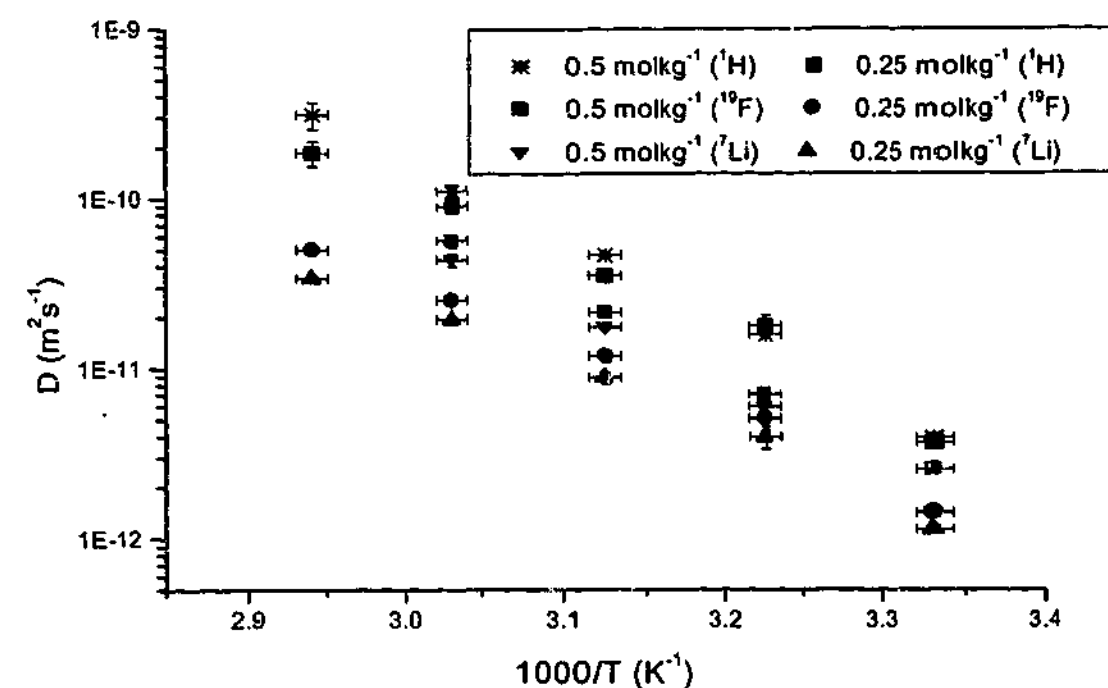


Fig. 3.3.10 0.25 & 0.5 mol kg⁻¹ P₁₂(Tf)₂N Arrhenius plot of multinuclear PFGSE-NMR diffusion coefficients.

Figure 3.3.10 shows an Arrhenius plot of the diffusion data obtained for two P₁₂(Tf)₂N systems, 0.25 mol kg⁻¹ and 0.5 mol kg⁻¹ Li(Tf)₂N. Both samples are in the solid state for the majority of measurements, the 0.25 mol kg⁻¹ sample melting at ~340K and the 0.5 mol kg⁻¹ sample melting at ~325K. Some general trends can be observed in the data. In both systems, the pyrrolidinium cation was the most rapidly diffusing species, and their rate of diffusion was similar. For both systems the (Tf)₂N⁻ anion was generally diffusing more quickly than the lithium cation (~ 1.5 times as quickly). The rate of (Tf)₂N⁻ and Li⁺ diffusion was greater in the 0.5 mol kg⁻¹ sample than in the 0.25 mol kg⁻¹ sample, exhibiting approximately a two-fold increase in both cases. Referring to the conductivity data shown in Fig. 3.3.4, this suggests that the increased conductivity of the 0.5 mol kg⁻¹ sample (above that of the 0.25 mol kg⁻¹ sample), in the solid state, results from the increased mobility of Li⁺ and (Tf)₂N⁻. It is not clear whether this derives from a fast ion conduction mechanism in the plastic crystal phase or from the presence of a greater proportion of a eutectic liquid phase known to be present in these samples at these temperatures.⁵ It is apparent that the changes in the diffusivity of the pyrrolidinium cation do not contribute significantly to the enhanced conductivity.

Figure 3.3.11 shows an Arrhenius plot of the diffusion data obtained for neat P₁₃(Tf)₂N and 0.5 mol kg⁻¹ P₁₃(Tf)₂N. In the neat sample the rate of cation and anion diffusion was similar. The addition of 0.5 mol kg⁻¹ Li(Tf)₂N resulted in a decrease in the diffusivity of all of the species. Pyrrolidinium diffusion was decreased approximately two-fold and (Tf)₂N⁻ diffusion was decreased approximately four-fold. Lithium diffusion in the 0.5 mol kg⁻¹ sample behaved similarly to that of (Tf)₂N⁻, generally the rate of diffusion of the anion was ~1.5 times greater than that of lithium. The apparent activation energy for the pyrrolidinium cation was less than that of the other species.

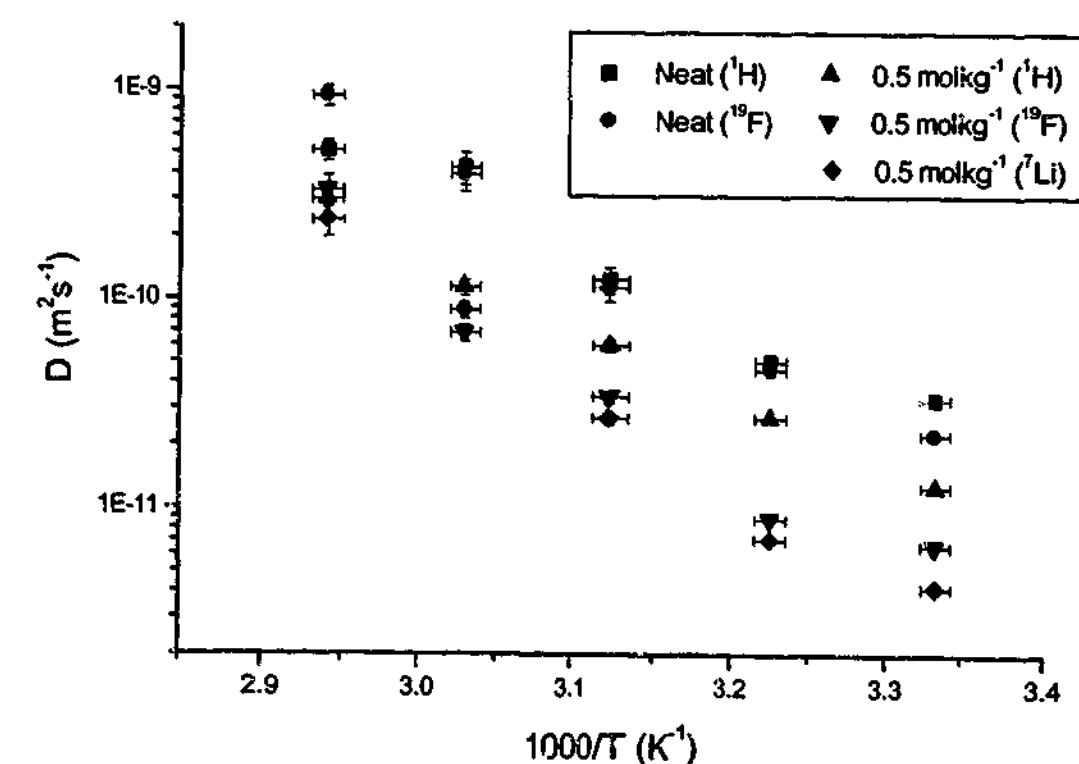


Fig. 3.3.11 Neat & 0.5 mol kg⁻¹ P₁₃(Tf)₂N Arrhenius plot of multinuclear PFGSE-NMR diffusion coefficients.

Figure 3.3.12 shows an Arrhenius plot of the diffusion data obtained for $0.005 \text{ mol kg}^{-1}$ $\text{P}_{14}(\text{Tf})_2\text{N}$. The data highlights the differences that were observed between samples at this $\text{Li}(\text{Tf})_2\text{N}$ concentration; the dashed lines indicate the data obtained for two different batches (1 & 2). The data obtained for batch 1 exhibited diffusivities approximately two to three times greater than that of batch 2. This significant discrepancy most likely derives from differences in the concentration of the lithium salt (the availability of small quantities of sample made accurate preparation of sample concentrations at this level difficult) and from varying levels of impurities in each batch. In addition, the amount of scatter in the measurements tended to increase for higher values of the diffusion coefficient. This possibly reflects the presence of stray convection currents in the sample, which becomes more likely as the sample viscosity decreases. Discrepancies of this level were not evident at higher concentrations of lithium salt (Figs. 3.3.13 & 3.3.14). The scatter in the relative diffusivities of all three mobile species indicates that they are diffusing at similar rates at this concentration.

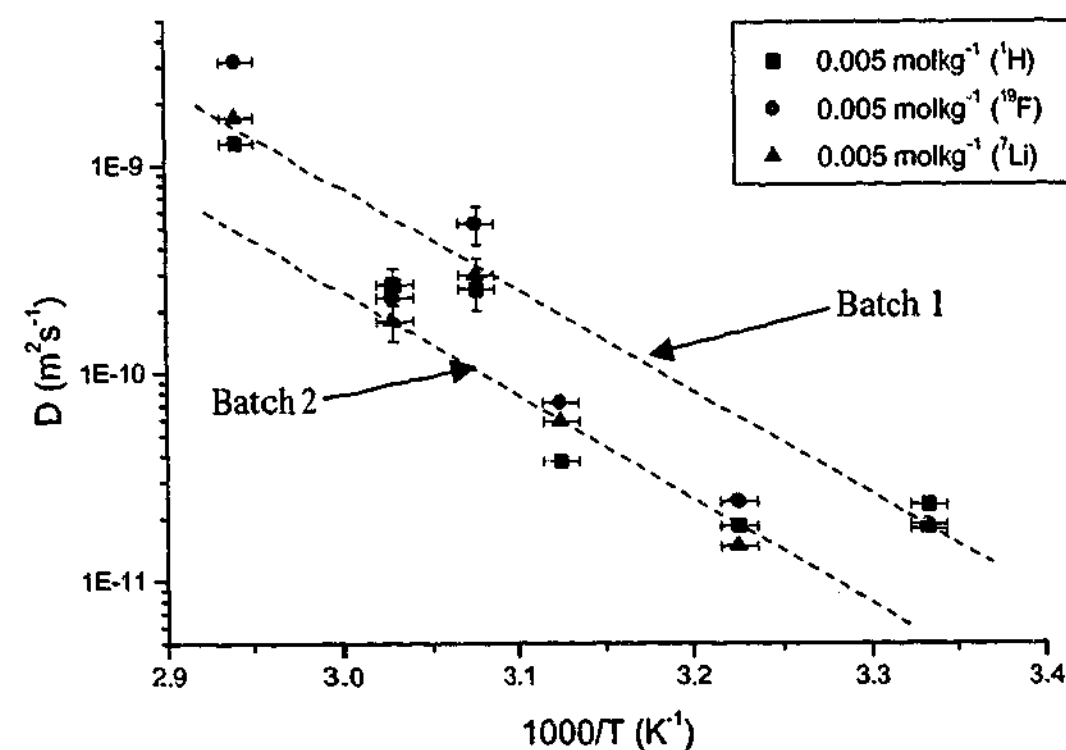


Fig. 3.3.12 $0.005 \text{ mol kg}^{-1}$ $\text{P}_{14}(\text{Tf})_2\text{N}$ Arrhenius plot of multinuclear PFGSE-NMR diffusion coefficients (dashed lines are to guide the eye).

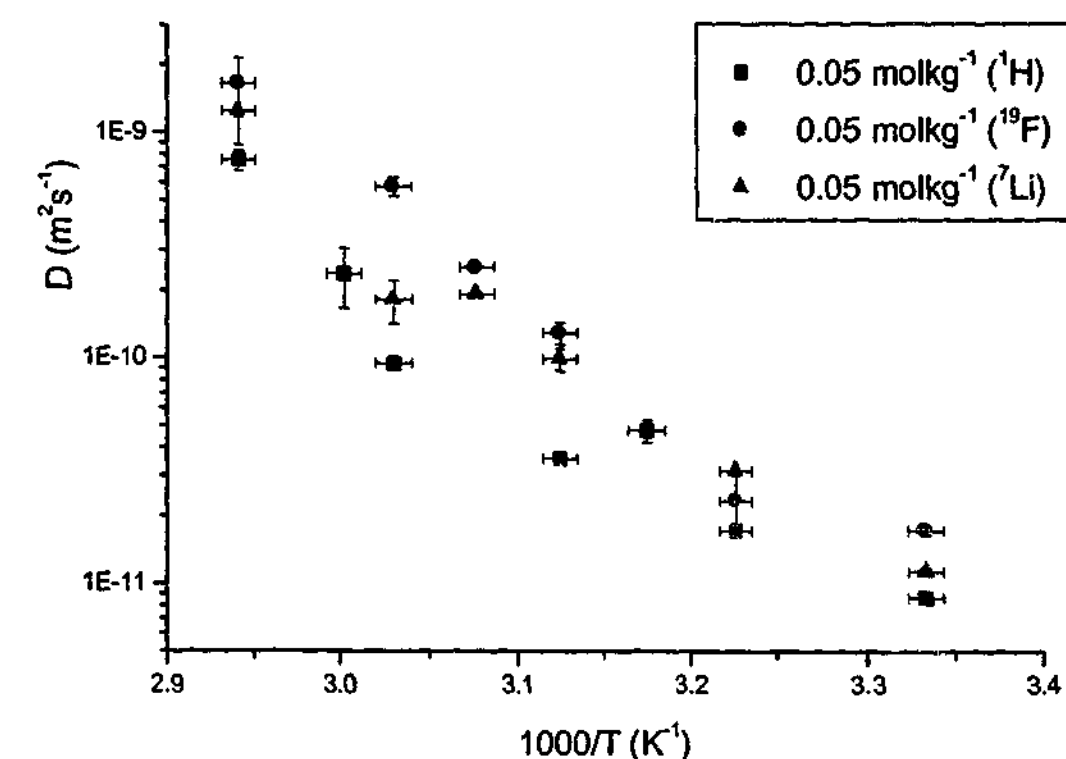


Fig. 3.3.13 0.05 mol kg^{-1} $\text{P}_{14}(\text{Tf})_2\text{N}$ Arrhenius plot of multinuclear PFGSE-NMR diffusion coefficients.

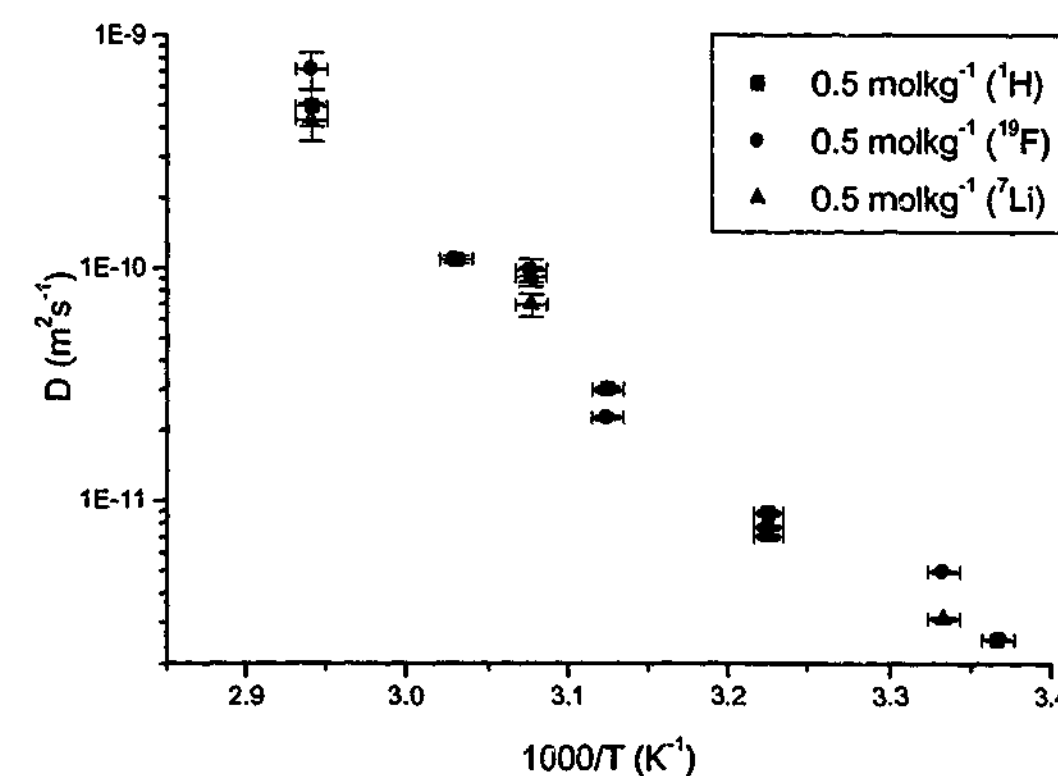


Fig. 3.3.14 0.5 mol kg^{-1} $\text{P}_{14}(\text{Tf})_2\text{N}$ Arrhenius plot of multinuclear PFGSE-NMR diffusion coefficients.

Figures 3.3.13 and 3.3.14 show Arrhenius plots of 0.05 mol kg^{-1} and 0.5 mol kg^{-1} $\text{P}_{14}(\text{Tf})_2\text{N}$ samples. The 0.05 mol kg^{-1} samples shows significant scatter in the data points, although less than was present in the $0.005 \text{ mol kg}^{-1}$ sample. Examining the two less concentrated samples it appears that generally, the diffusivities of the lithium ions and the $(\text{Tf})_2\text{N}^-$ anions were higher than that of the pyrrolidinium cation. In the 0.5 mol kg^{-1} sample, the diffusivities of the three species were of similar magnitude.

For all of the diffusion data, although most obvious in the low $\text{Li}(\text{Tf})_2\text{N}$ concentration samples, there is a notable departure from Arrhenius behaviour. Typically, the rate of increase in diffusivity with temperature increases over the temperature range, resulting in discernible curvature in the plots. Other workers have noted VTF behaviour for the diffusivity of ions in neat RTILs.⁸ The diffusion behaviour of the pyrrolidinium RTILs (at least for the temperature range studied here) cannot be described by the VTF equation. It is apparent that some other mechanism is influencing the diffusivities in these samples. The most likely explanation for the behaviour lies in considering the state of ionic aggregation in the samples and how that changes with temperature. As already mentioned (section 3.3.2), VTF fits for the conductivity data indicated that shifting states of aggregation might play a role in the observed temperature dependence of the conductivity. If it is considered that the ions in the sample are diffusing as 'free' species (i.e., lone ions) or as 'clusters' (i.e., as groups of ions), then it follows that there are species present in the sample that are diffusing at different rates. The free ions will tend to diffuse at a greater rate because of the smaller ionic radius. However, NMR measurements cannot distinguish between either of the diffusing species. Thus, the diffusion coefficient will reflect an average value, which will depend on the relative populations of the free or clustered species. The curvature in the data suggests that the proportion of free (more diffusive) species increases at higher temperatures.

Figure 3.3.15 shows plots of the diffusion data for each nucleus at each concentration. Generally, the diffusivities decrease with increasing lithium salt concentration as expected. The less concentrated samples show significant scatter and the trend is barely discernible. The 0.5 mol kg^{-1} sample exhibits consistently lower diffusivities.

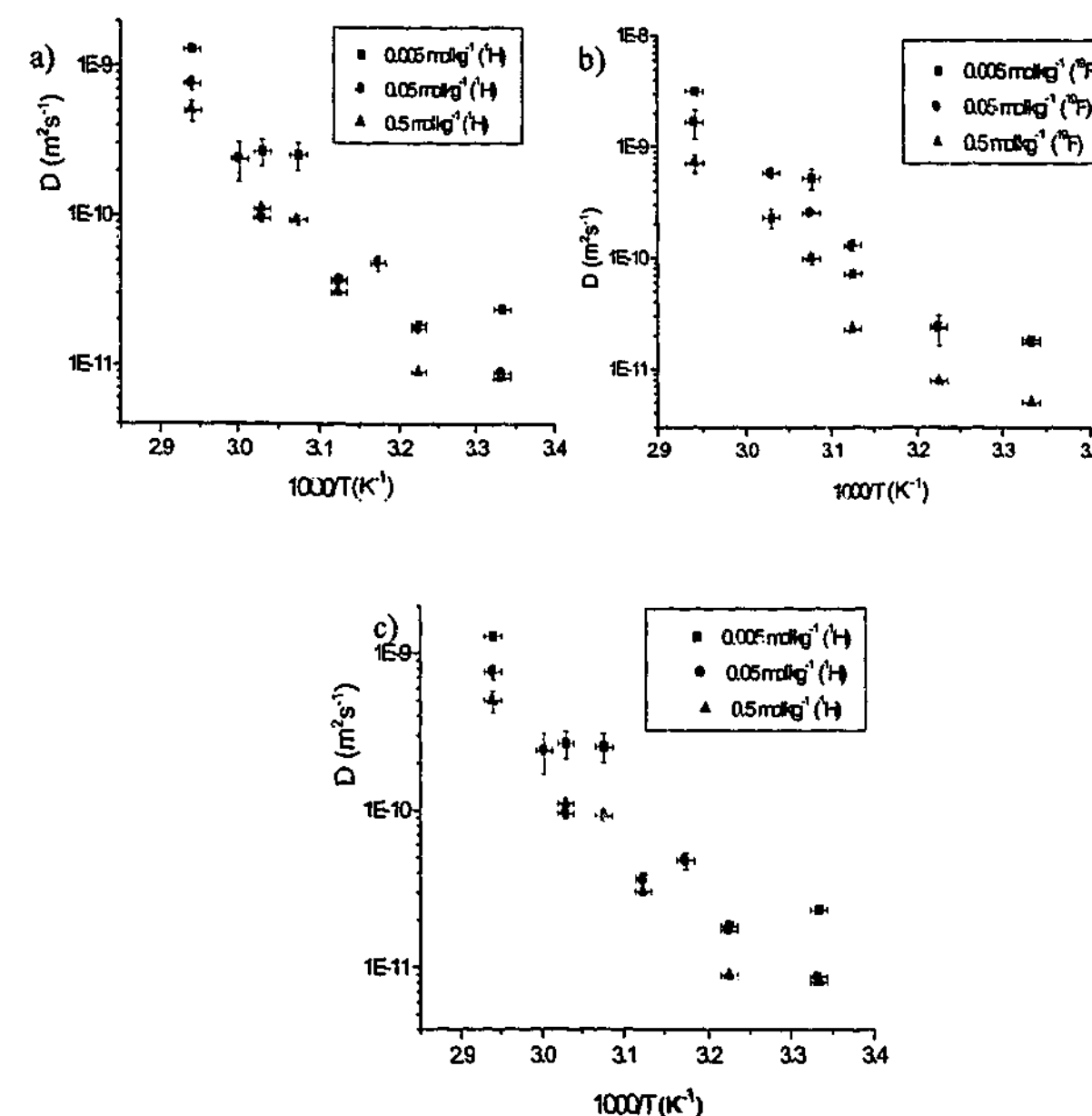


Fig. 3.3.15 Data from Figs 3.3.11, 3.3.12 & 3.3.13 replotted to compare nuclei at different $\text{Li}(\text{Tf})_2\text{N}$ concentrations, a) ^1H , b) ^{19}F & c) ^7Li .

3.3.4 Nernst-Einstein calculations:

The use of the Nernst-Einstein equation allows comparison of the observed conductivities with those calculated from the diffusion coefficients obtained from NMR measurements (as described in section 1.4.5). Fused salts have been found to deviate significantly from the Nernst-Einstein relation^{7,9,10} and, as will be shown here, RTILs behave in a similar manner.

The calculation of the molar conductivities of the samples required that the density of the samples be assumed to remain constant with temperature. In reality, this will not be the case and density changes will occur; however, over the temperature range studied the deviations are not likely to be large. Calculations allowing for reasonable changes in the density of the sample ($\pm 0.1 \text{ g cm}^{-3}$) indicate that the resultant molar conductivities did not alter significantly for the purpose of comparison with the value calculated from the Nernst-Einstein equation.

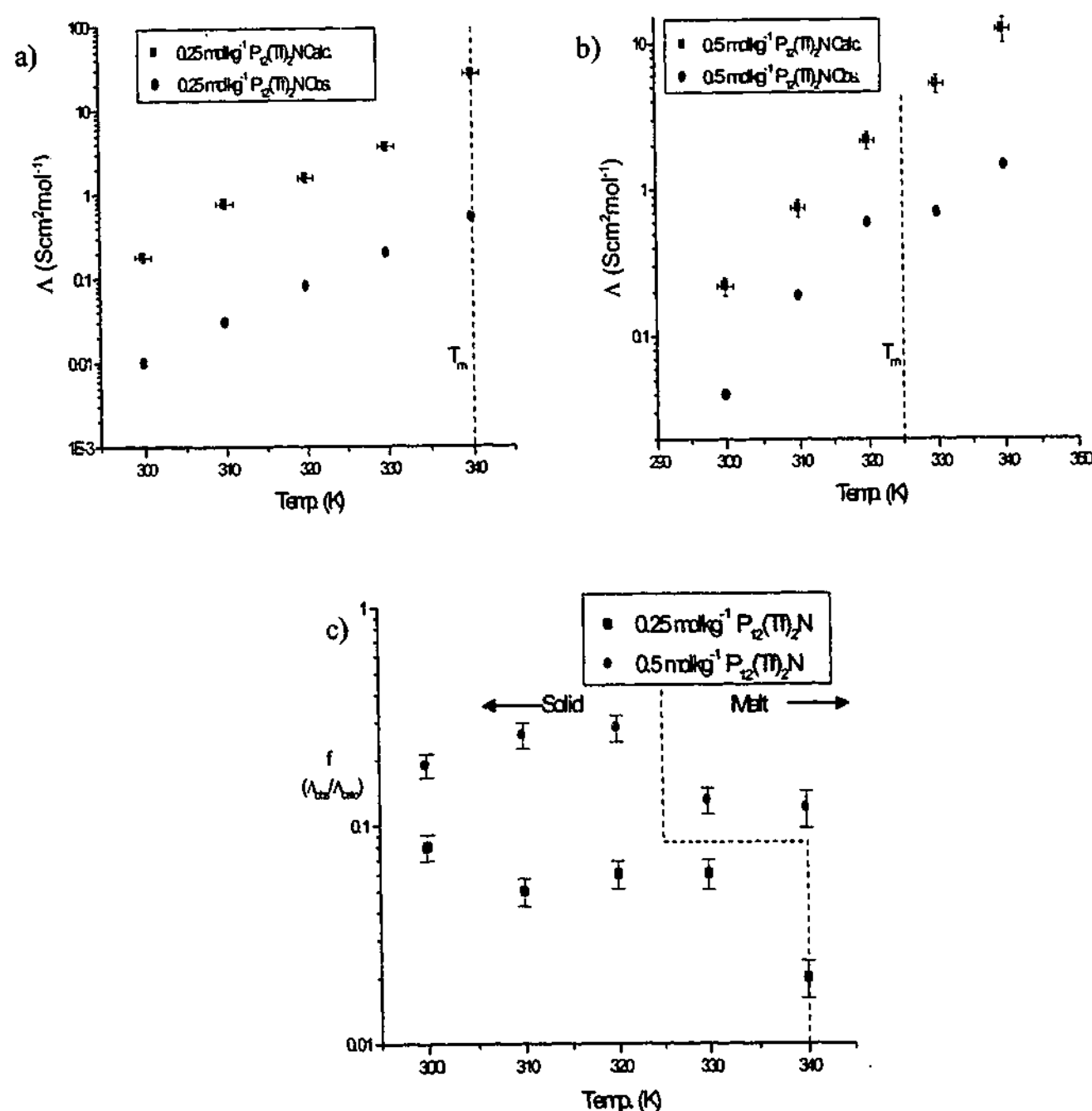


Fig. 3.3.16 Comparison of observed and calculated molar conductivities for $\text{P}_{12}(\text{Tf})_2\text{N}$ samples, a) 0.25 mol kg⁻¹, b) 0.5 mol kg⁻¹ and c) f - observed/calculated fraction.

Figure 3.3.16 shows plots for comparison of observed versus calculated values for 0.25 mol kg⁻¹ and 0.5 mol kg⁻¹ $\text{P}_{12}(\text{Tf})_2\text{N}$ (a and b respectively). It is apparent from the plots that the Nernst-Einstein equation adequately models the sample response to temperature in the solid state. Deviations are apparent in the 0.5 mol kg⁻¹ sample above the melting point. However, the actual conductivities differ by more than one order of magnitude. This can be accounted for by the fact that the Nernst-Einstein relation requires that all of the charge carriers in the sample be mobile. Obviously, for the solid sample, this will not be true and only a small fraction of the charged species in the sample are likely to be mobile at any given time. This is demonstrated by the improved agreement between observed and calculated values for the 0.5 mol kg⁻¹ sample (calc./obs. ~ 4) versus the 0.25 mol kg⁻¹ sample (calc./obs. ~ 20). As has been mentioned previously (3.3.2) the addition of greater quantities of lithium salt results in increased conductivity in the $\text{P}_{12}(\text{Tf})_2\text{N}$ sample which is ascribed to an increase in the number of mobile charge carriers.

Figure 3.3.16c shows a plot of the fraction observed/calculated for both samples versus temperature. The fraction may represent the fraction of species present in the sample that are contributing to conduction. Figure 3.3.16c indicates that the fraction of mobile species contributing to conduction in the solid state remains relatively static with temperature. Thus, the increase in conductivity with temperature in solid state $\text{P}_{12}(\text{Tf})_2\text{N}$ is due either to the increased diffusivity of the charge carriers or to an increase in the total number of mobile species. The plot also indicates that there is a greater fraction of mobile charge carriers contributing to conduction in the solid phase than in the melt.

Alternatively, the fraction can be a measure of the amount of interference experienced by the charge carriers in the sample due to the motions of other charge carriers under an electric field (i.e., charges moving in opposite directions in an electric field may interfere with one another, causing the electrical mobilities to fall below the diffusional mobilities).⁹ Figure 3.3.16c indicates that, in the solid state, the influence of the interference remains relatively static with the increase in diffusivity due to temperature. In addition, the amount of interference experienced by the mobile species is more significant in the melt than in the solid phase.

Figure 3.3.17 shows a similar set of data for a neat sample of $P_{13}(Tf)_2N$ and a 0.5 mol kg^{-1} sample of $P_{13}(Tf)_2N$. These samples are liquid at all temperatures studied. The comparison of observed and calculated molar conductivities differs from the case of the solid samples in that the disparity increases with increasing temperature (Fig. 3.3.17a, b & c).

Increasing divergence between calculated and observed conductivities with increased temperature is typical for fused salts.⁹ The divergence can be understood in terms of the hole theory of the liquid state (section 1.4.5), where the rate of transport is effectively determined by the rate of transport of 'holes'. At higher temperatures, the amount of free volume in the liquid is predicted to increase, and thus, the likelihood of holes large enough

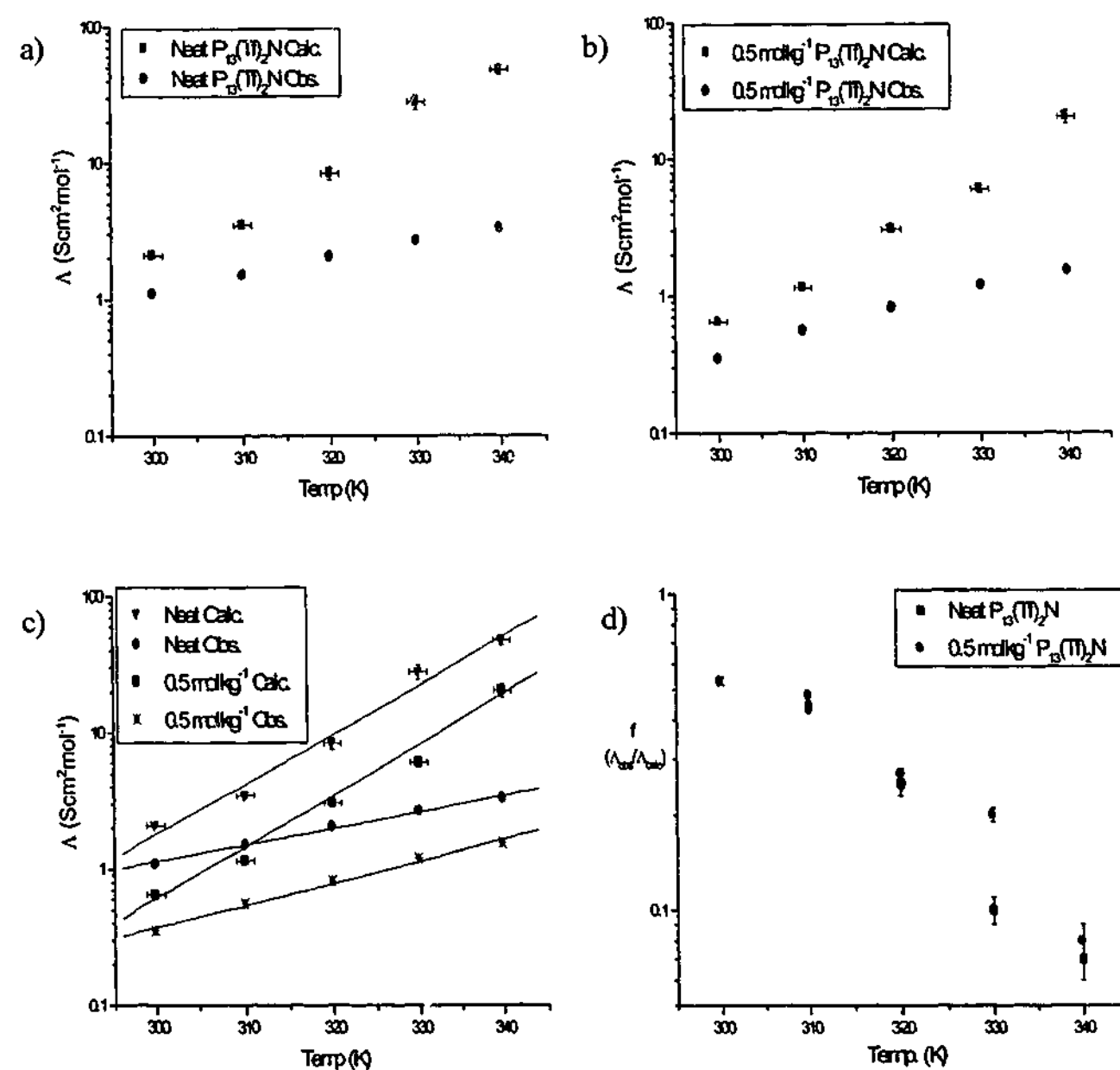


Fig. 3.3.17 Comparison of $P_{13}(Tf)_2N$ observed and calculated molar conductivities, a) Neat, b) 0.5 mol kg^{-1} , c) Neat and 0.5 mol kg^{-1} comparison and d) f – observed/calculated fraction.

to allow diffusion of paired charges also increases. Diffusion occurs but there is no net migration of charge, causing the observed deviation from the Nernst-Einstein equation, this situation has been described as a 'current-less' mode of diffusion.^{9,10}

Both samples (neat and $0.5 \text{ mol kg}^{-1} P_{13}(Tf)_2N$) exhibit reasonable agreement at low temperatures. The observed and calculated conductivity is higher for the neat sample than the sample with added lithium salt. The fourth plot (Fig. 3.3.17d) shows a plot of the fraction (f) versus temperature for both samples, which exhibit similar behaviour. Again, depending on the school of thought, the decrease in the value of the fraction (f) can be thought to represent a reduction in the fraction of mobile charge carriers (and hence an increase in current-less modes of diffusion, as described above). Alternatively, it may reflect an increase in the level of interference due to the motion of oppositely charged species in the electric field, due to an increase in the number of ions migrating at any instant.⁹ The similarity in behaviour of both samples indicates that the presence of lithium ions does not play a significant role in this type of behaviour, although there is some deviation at higher temperatures.

Figure 3.3.18 shows a similar set of plots for three samples of $P_{14}(Tf)_2N$ (0.005 , 0.05 and 0.5 mol kg^{-1}). The behaviour is very similar to that observed in the $P_{13}(Tf)_2N$ samples, exhibiting reasonable agreement at low temperatures and increasing disparity at higher temperatures. The value of the fraction (f) decreases with temperature. There is some variation between the low concentration samples and the 0.5 mol kg^{-1} sample. This suggests that the addition of a lithium salt does reduce the influence of the phenomenon that causes the observed conductivity to depart from its theoretical value, although the influence is relatively minor and increased error in the results at higher temperatures weaken the argument.

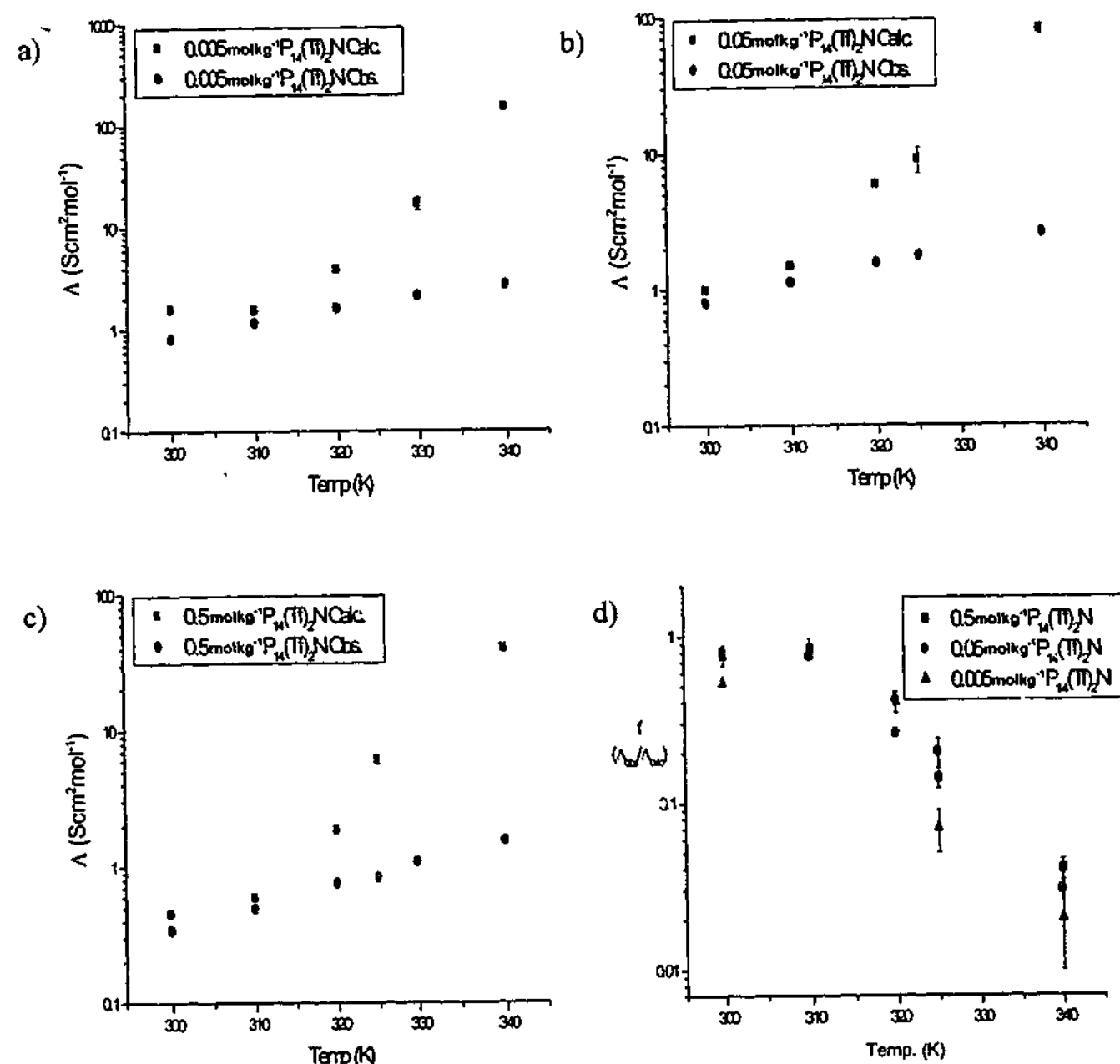


Fig. 3.3.18 Comparison of $P_{14}(Tf)_2N$ observed and calculated molar conductivities, a) $0.005 \text{ mol kg}^{-1}$, b) 0.05 mol kg^{-1} , c) 0.5 mol kg^{-1} and d) f – observed/calculated fraction.

3.3.5 Transport number:

The application of the information obtained from the diffusion coefficient measurements in combination with the specific conductivity measurements can provide an indication of the relative contribution of each ionic species to the conduction flux, as represented by the transport number. Section 1.4.5 provides a description of the calculation used to determine the transport number from conductivity and diffusion measurements.

The calculation involves the use of a 'cross coefficient' to account for the difference between the observed and calculated conductivities. The cross coefficient is applied to the measured diffusion coefficients and effectively adjusts their values to represent the relative contribution to the conduction flux. The method was proposed by Borucka *et al.* and is based on assumptions derived from the hole model of transport in the liquid state.¹⁰⁻¹² The use of the cross coefficient was described in terms of a model whereby the Nernst-Einstein deviation was assumed to result from current-less diffusion modes due to the presence of uncharged ionic aggregates (see section 1.4.5). However, as a subtractive term used to adjust diffusion coefficients to account for Nernst-Einstein deviations, it seems applicable to either model, and could equally be thought of as a 'drag coefficient'. With this in mind the term has been used to determine transport numbers for the samples studied here.

Figure 3.3.19 presents the transport numbers obtained versus temperature for neat $P_{13}(Tf)_2N$, $0.5 \text{ mol kg}^{-1} P_{13}(Tf)_2N$ and $0.5 \text{ mol kg}^{-1} P_{14}(Tf)_2N$. For the samples described here, where the concentration of mobile species is not equal (e.g., the 0.5 mol kg^{-1} samples), the magnitude of the cross coefficient was adjusted according to their relative concentrations. Therefore, for $(Tf)_2N^-$ the calculated cross coefficient was used unadjusted. For Li^+ a factor of 0.2 was applied, according to its fraction of the cations in the sample. Similarly, a factor of 0.8 was applied to P_{1X}^+ according to its fraction of the cations in the sample. The use of this factor assumes that each of the cationic species will deviate proportionately from the Nernst-Einstein equation, relative to its concentration. Given the difference in the size and charge density of the P_{1X}^+ and Li^+ cations it is unlikely that their mobility will deviate in the exactly the same manner. However, it is reasonable to assume that the deviation will be of similar magnitude and the correction factor serves to adjust the cross coefficient according to the number of species to which it is applied. Transport numbers for the $P_{12}(Tf)_2N$ samples could not be calculated because the calculation requires knowledge of the number of mobile charge carriers in the sample, the cross coefficient is applied with the assumption that all charged species are mobile and that the only reason they do not contribute to conduction is because of current-less modes of diffusion or drag effects. A further complication is introduced by the fact that a different fraction of the Li^+ , $(Tf)_2N^-$ or P_{12}^+ species could be mobile relative to the other species.

Before discussing the results presented in Figure 3.3.19, some comment should be made about the magnitude of the errors present in the data. At higher temperatures, the error becomes very large, in some cases larger than the value itself. This is in part due to the increased scatter in the data at higher temperatures. The other dominant factor contributing to the error is its propagation through the calculation. As the difference between the calculated and observed conductivities becomes large, the value of the cross coefficient also becomes large, approaching that of the measured diffusion coefficient. The calculated value of 'independent diffusion' becomes small but retains the error present in the cross coefficient and the measured diffusion coefficient (e.g., according to equation 1.27 - $D_{+,ind} = D_{+,obs} - D_{+}$). At higher temperatures, the error dominates the calculated value and the result becomes meaningless.

Figure 3.3.19 presents calculated transport numbers plotted against temperature for neat $P_{13}(Tf)_2N$, $0.5 \text{ mol kg}^{-1} P_{13}(Tf)_2N$ and $0.5 \text{ mol kg}^{-1} P_{14}(Tf)_2N$. The plot for the neat sample indicates that cation transport is dominant ($t_{P_{13}^+} \sim 0.6$ and $t_{(Tf)_2N^-} \sim 0.4$) and that there is no significant trend in the values as temperature is increased. Considering the 0.5 mol kg^{-1} samples, although the errors rapidly become significant as the temperature is increased, both samples show similar trends with increasing temperature. Specifically, the Li^+ and $(Tf)_2N^-$ transport numbers increase with increasing temperature and the pyrrolidinium transport number decreases with increasing temperature. These results agree with observations from electrochemical cycling experiments where significantly better lithium cycling behaviour was observed at higher temperatures (sections 3.1 & 3.2). Comparing the 0.5 mol kg^{-1} samples, the $P_{13}(Tf)_2N$ sample exhibits consistently higher pyrrolidinium transport numbers, which is consistent with the smaller ionic radius of the cation. The lower pyrrolidinium transport numbers in $P_{14}(Tf)_2N$ coincide with an increase in the $(Tf)_2N^-$ transport number and a slight increase in the lithium transport number.

The increase in t_{Li^+} with temperature suggests a shift in the level of interaction of Li^+ with $(Tf)_2N^-$. Interactions between $(Tf)_2N^-$ and Li^+ have been indicated as the cause of Li^+ transport numbers of less than 0.5 in polymer electrolytes incorporating this salt.^{13,14} In addition, the work presented here suggests that Li^+ and $(Tf)_2N^-$ transport are 'linked', based on the similarity of the behaviour of their diffusion coefficients. A weakening of the interactions at elevated temperatures would cause an increase in both the Li^+ and $(Tf)_2N^-$

transport numbers (due to a decrease in their effective ionic radius), which would cause a corresponding decrease in the P_{13}^+ transport number.

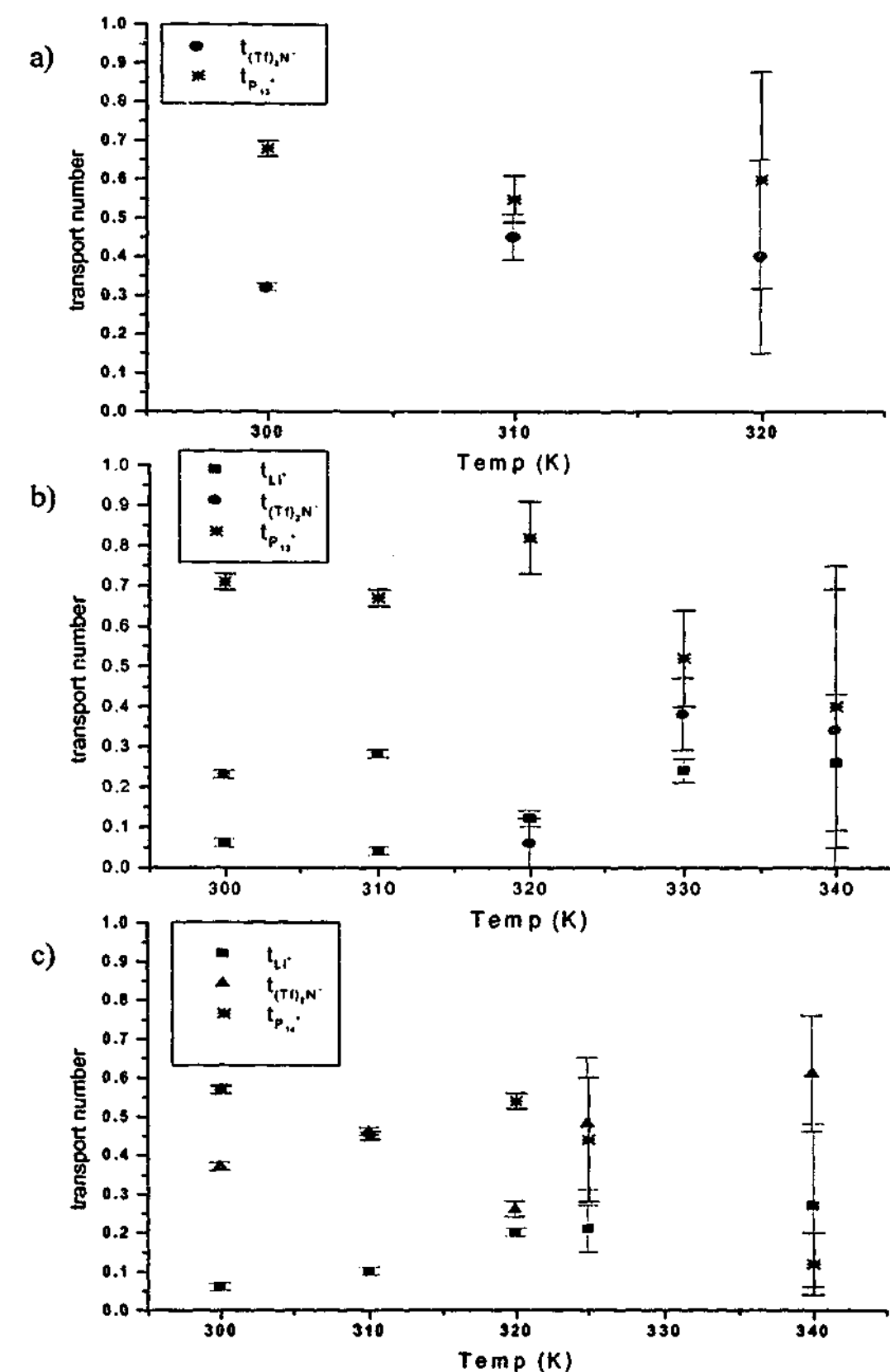


Fig. 3.3.19 Plots showing transport number versus temperature, a) Neat $P_{13}(Tf)_2N$, b) $0.5 \text{ mol kg}^{-1} P_{13}(Tf)_2N$ and c) $0.5 \text{ mol kg}^{-1} P_{14}(Tf)_2N$

3.3.6 Conclusions:

The transport properties of some $P_{1X}(Tf)_2N$ electrolytes were investigated using a combination of electrochemical and PFGSE-NMR techniques. The diffusion coefficient of lithium in a 0.5 mol kg^{-1} $P_{14}(Tf)_2N$ sample was determined by the application of the Randles-Sevcik equation to be $1.0 \times 10^{-8} \text{ cm}^2 \text{ s}^{-1}$ at 300K. The diffusion coefficient of lithium determined by PFGSE-NMR was $3.1 \times 10^{-8} \text{ cm}^2 \text{ s}^{-1}$ at 300K. The two techniques are very different, the electrochemical measurement pertaining to diffusion along a concentration gradient produced by a process at the electrode surface, and the NMR value measures diffusion produced by Brownian motion arising from local concentration gradients. The use of a cross coefficient was designed to account, in part, for the difference between the NMR and electrochemical measurements. After the application of a cross coefficient the PFGSE-NMR diffusion coefficient was adjusted to $2.8 \times 10^{-8} \text{ cm}^2 \text{ s}^{-1}$ at 300K. The two techniques provide reasonable agreement; the discrepancy can be accounted for by considering the difference between the two electrochemical measurements. In the case of the application of the Randles-Sevcik equation, the measurement pertains to a limiting current to an electrode surface where a stable concentration gradient is established. In the case where a cross coefficient is applied, the electrochemical impedance measurement used to determine it represents a transient situation where the concentrations of all of the species at the electrode surface are changing. Thus, the adjusted PFGSE-NMR value pertains to lithium diffusion at an electrode surface when the concentrations of the mobile species are changing.

The agreement obtained between the two techniques suggests that the assumption that the migration current to the electrode surface was negligible was valid. In fact, if there had been an appreciable migration current, then the Randles-Sevcik diffusion coefficient would be expected to be higher than that obtained from the NMR measurements. Hence, for a 0.5 mol kg^{-1} solution of $P_{14}(Tf)_2N$ at 300 K, lithium deposition can be expected to be diffusion controlled.

The specific conductivity of a range of $P_{1X}(Tf)_2N$ samples was determined as a function of temperature. The solid state conductivity of lithium doped $P_{12}(Tf)_2N$ samples was substantial and found to increase with added lithium salt (0.25 mol kg^{-1} to 0.5 mol kg^{-1}). The

liquid state conductivity was found to decrease with the addition of lithium salt, presumably because of increased ion-ion interactions. The specific conductivities of all of the samples were found to converge at higher temperatures. The conductivity of the $P_{13}(Tf)_2N$ samples were found to be slightly higher than the $P_{14}(Tf)_2N$ samples.

Diffusion coefficients for all of the mobile species in the samples were determined by PFGSE-NMR. Overall, the diffusivities of all species were similar for all of the samples in the liquid state.

Arrhenius activation energies for samples in the liquid state determined from diffusion coefficients were significantly higher than those determined from conductivity data, suggesting that a force opposing conductive modes of transport was increasing with temperature. The observed molar conductivity was significantly lower than that calculated from the Nernst-Einstein equation for all samples. In the solid state, the Nernst-Einstein equation effectively predicted the activation energy for conduction; the overestimation of the actual molar conductivities was partly because all of the species in the sample were assumed to be mobile for the calculation.

The disparity between the calculated and observed molar conductivities increased with temperature, as has been reported for fused salts.⁹ There has been substantial debate over the origins of deviations from the Nernst-Einstein equation. Generally, two models have been proposed, neither of which has been clearly shown to be correct. The explanation of Bockris and Hooper proposed that current-less modes of diffusion arising from simultaneous diffusion of oppositely charged species reduced the observed conductivity.¹² The second explanation, by Laity, suggested that mutual interference caused by a large number of charged species moving in opposite directions in response to an applied field causes the electrical mobilities to fall below the diffusional mobilities.¹⁵ Both explanations predict an increase in the disparity between observed and calculated values with increasing temperature. Current-less modes of diffusion may increase at higher temperature because of an increase in the number of paired vacancies arising from thermal expansion. Interference from charged species will increase at higher temperatures because greater numbers of ions will be migrating at any instant. Angell compared the packing ratio ($V_{\text{melt}}/V_{\text{ions}}$) for alkali nitrates and halides and found that, at equal fractions above T_g , the

halides are more loosely packed than the nitrates. However, the nitrates exhibit greater deviations from the Nernst-Einstein equation, this favours the inter-ionic interference explanation because loose packing should favour paired diffusion and reduce inter-ionic interference.¹⁶

The diffusion coefficients obtained from PFGSE-NMR measurements were adjusted using a cross coefficient and used to calculate internal transport numbers for each of the mobile species.¹⁰ The transport numbers indicated an increase $(\text{Ti})_2\text{N}^+$ and Li^+ transport and a corresponding decrease in pyrrolidinium transport with increasing temperature. The Li^+ transport number was low, ranging from 0.05 to 0.2. The values reported need to be verified using another technique before the method can be applied with confidence. However, the results obtained were reasonable with respect to expectations. Attempts were made to determine the transport number for lithium using the DC polarisation technique,¹⁷ however a large value for the impedance at the interface introduced a significant error, making the results meaningless. Recent reports of transport numbers determined using electrophoretic PFGSE-NMR offer an alternative method to verify the values reported here.^{14,18}

References

1. J. Huang, Ph. D Thesis, Monash University, 2002.
2. H. Every, Ph. D Thesis, Monash University, 2001.
3. D. R. MacFarlane, P. Meakin, J. Sun, N. Amini and M. Forsyth, *J. Phys. Chem. B*, **103**, 4164 (1999).
4. D. R. MacFarlane, J. H. Huang and M. Forsyth, *Nature*, **402**, 792 (1999).
5. J. Huang, M. Forsyth and D. R. MacFarlane, *Solid State Ionics*, **136**, 447 (2000).
6. A. J. Hill, J. Huang, J. Efthimiadis, P. Meakin, M. Forsyth and D. R. MacFarlane, *Solid State Ionics*, **154-155**, 119 (2002).
7. B. R. Sundheim (Ed.), *Fused Salts*, McGraw-Hill Book Company, New York (1964).
8. A. Noda, K. Hayamizu and M. Watanabe, *Journal of Physical Chemistry B*, **105**, 4603 (2001).
9. S. Petrucci (Ed.), *Ionic Interactions: From Dilute Solutions to Fused Salts*, Academic Press, New York and London (1971).
10. J. O. Bockris and Reddy Amulya K. N., *Modern Electrochemistry 1: Ionics*, Plenum Press, New York (1998).
11. A. Borucka, J. O. M. Bockris and J. A. Kitchener, *Proc. Roy. Soc. Lond.*, **A241**, 554 (1957).
12. J. O. M. Bockris and G. W. Hooper, *Discussions Faraday Soc.*, **32**, 218 (1967).
13. S. J. Wen, T. J. Richardson, D. V. Ghanous, K. A. Striebel, P. N. Ross and E. J. Cairns, *J. Electroanal. Chem.*, **408**, 113 (1996).
14. H. Dai and T. A. Zawodzinski, *J. Electroanal. Chem.*, **459**, 111 (1998).
15. R. W. Laity, *Discussions Faraday Soc.*, **32**, (1962).
16. C. A. Angell, *J. Phys. Chem.*, **69**, 399 (1965).
17. J. Evans, C. A. Vincent and P. G. Bruce, *Polymer*, **28**, 2324 (1987).
18. H. J. Walls and T. A. Zawodzinski, *Electrochemical and Solid-State Letters*, **3**, 321 (2000).

3.4 Surface Characterisation:

Information pertaining to the characteristics of the SEI formed on the lithium surface in a RTIL is not present in the literature. The following section of work describes the results of efforts to characterise the SEI formed in $P_{1X}(Tf)_2N$ electrolytes.

Techniques developed and implemented specifically for the task of characterising the SEI include; X-ray photoelectron spectroscopy (XPS), grazing angle XRD (GAXRD), diffuse reflectance FTIR (DRFTIR), in-situ Raman microscopy, and electrochemical impedance spectroscopy.

The samples were prepared by cycling a cell (generally Li symmetrical or Li/Cu) under a galvanostatic regime. Fig. 3.4.1 shows examples of typical voltage profiles recorded during cycling. Lithium and lithium deposited on copper (denoted Li-Cu) samples were investigated in an effort to determine if the observed difference in behaviour noted in section 3.1 could be attributed to differences in the SEI composition.

One of the principal difficulties encountered in the analytical work (aside from the reactivity of the lithium surface) was presented by the RTIL itself. Because of the non-volatile nature of the RTIL, it was not possible to remove it from the surface of the sample

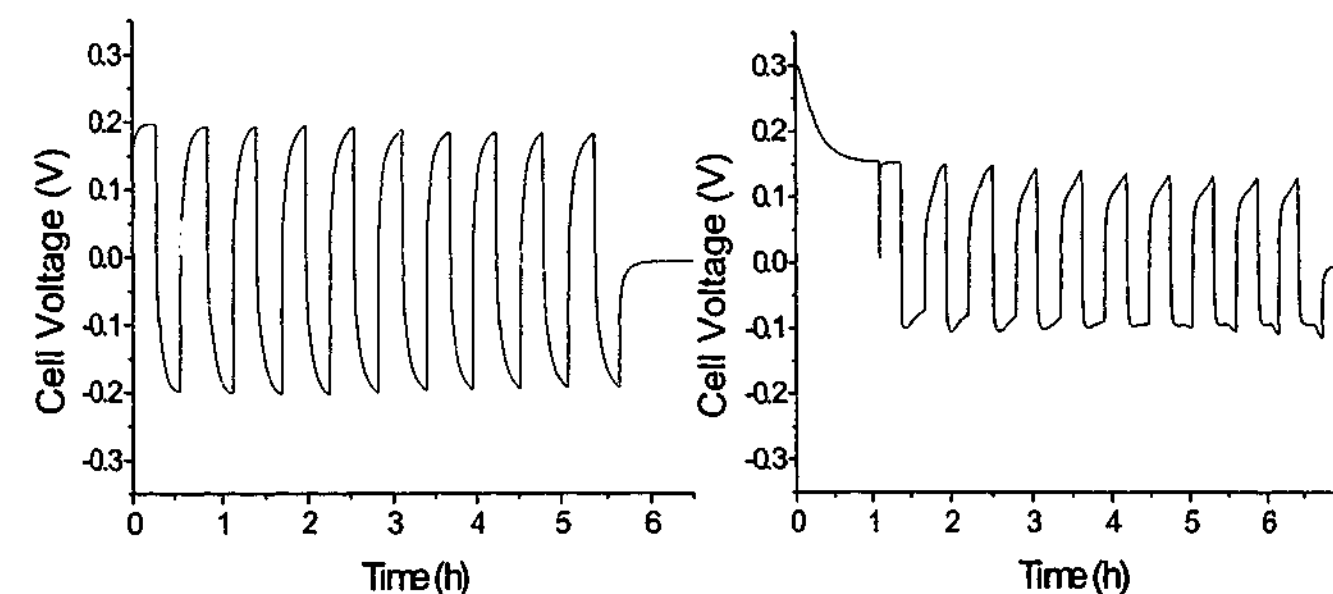


Fig. 3.4.1 Examples of the voltage profile obtained from galvanostatic cycling of $P_{1X}(Tf)_2N$ cells at 50 °C; a) Li/0.5 mol kg⁻¹ $P_{13}(Tf)_2N/Li$, 0.25 mAcm⁻² & 0.25 Ccm⁻² b) Li/0.5 mol kg⁻¹ $P_{14}(Tf)_2N/Cu$, 0.25 mAcm⁻², 1 Ccm⁻² excess and 0.25 Ccm⁻² cycling.

by evaporation prior to characterisation. Any solvent capable of removing the RTIL from the surface was also likely to compromise the sample. Instead, the bulk of the RTIL was removed by physical means. Thus, all of the measurements were conducted with the RTIL persisting on the sample, often complicating the interpretation of the results.

3.4.1 X-ray photoelectron spectroscopy (XPS):

Typical XPS survey spectra and high resolution region spectra are presented in Fig. 3.4.2. The chemical species assigned to each peak is shown for the high resolution region spectra. The peak identities were determined from published standard values¹ and from reports from XPS studies of the lithium surface.²⁻⁸ The results clearly indicate that the RTIL is present on the surface of the sample in significant quantities, as expected after sample preparation (comments above). This is testament to the lack of volatility of these materials, given that the results indicate that the RTIL is present, apparently unchanged, under ultra high -vacuum ($\sim 10^{-8}$ torr).

A series of experiments were conducted to determine if the technique was suitable for the RTIL samples, to determine the sensitivity of the samples to brief exposure to the atmosphere, and to see if the technique could detect differences between Li and Li-Cu samples. A lithium sample that had been exposed to a $P_{1X}(Tf)_2N$ electrolyte for several hours and transferred under argon was included as a control. The results of the measurements are presented graphically in Fig 3.4.3a-f. The electrolyte contains a $Li^+ : P_{1X}^+ : (Tf)_2N^-$ ratio of 1 : 4 : 5. By determining a mass balance for each of the species present, it is possible to account for the RTIL and gain an indication of which species are present in excess (or deficit) on the surface. Generally, it was found that there was excess $(Tf)_2N^-$, lithium (as salts) and in the case of the lithium surface, excess oxygen, fluoride and carbonate species. With respect to the P_{1X}^+ cation there was generally a small excess of C-N species and a slight deficit for C-C/C-H, this was more pronounced on the Li-Cu surface than it was on the Li surface. The $(Tf)_2N^-$ anion exhibited an excess in the amount of CF_3 and a deficit in the amount of SO_2 on the Li-Cu surface and a large excess of O (as Li_2O) and a deficit of SO_2 on the Li surface.

The samples exposed to atmosphere did not exhibit a clear difference to those transferred under argon. This indicates that the RTIL film protected the surface during the brief exposure to air or that the fast initial reactions with glovebox contaminants had already occurred during the transfer process.

Overall, the results clearly indicated that the surface was largely composed of lithium salts (covered by persistent RTIL), the majority of which appeared to be reaction products of the $(Tf)_2N^-$ anion. In addition, the results indicated a clear difference between the Li and Li-Cu surfaces. Carbonate and carbonyl species were present on the Li surface and absent on the Li-Cu surface; presumably, these were components of the native film. The Li-Cu surface also contained a larger fraction of $(Tf)_2N^-$ products than the Li surface, possibly due to the absence of the native film components. The Li surface contained a higher ratio of Li^+ (as salt) than the Li-Cu surface, indicating that the components of the film were in a lower oxidation state i.e., a greater proportion of components such as Li_2O , Li_2CO_3 and LiF .

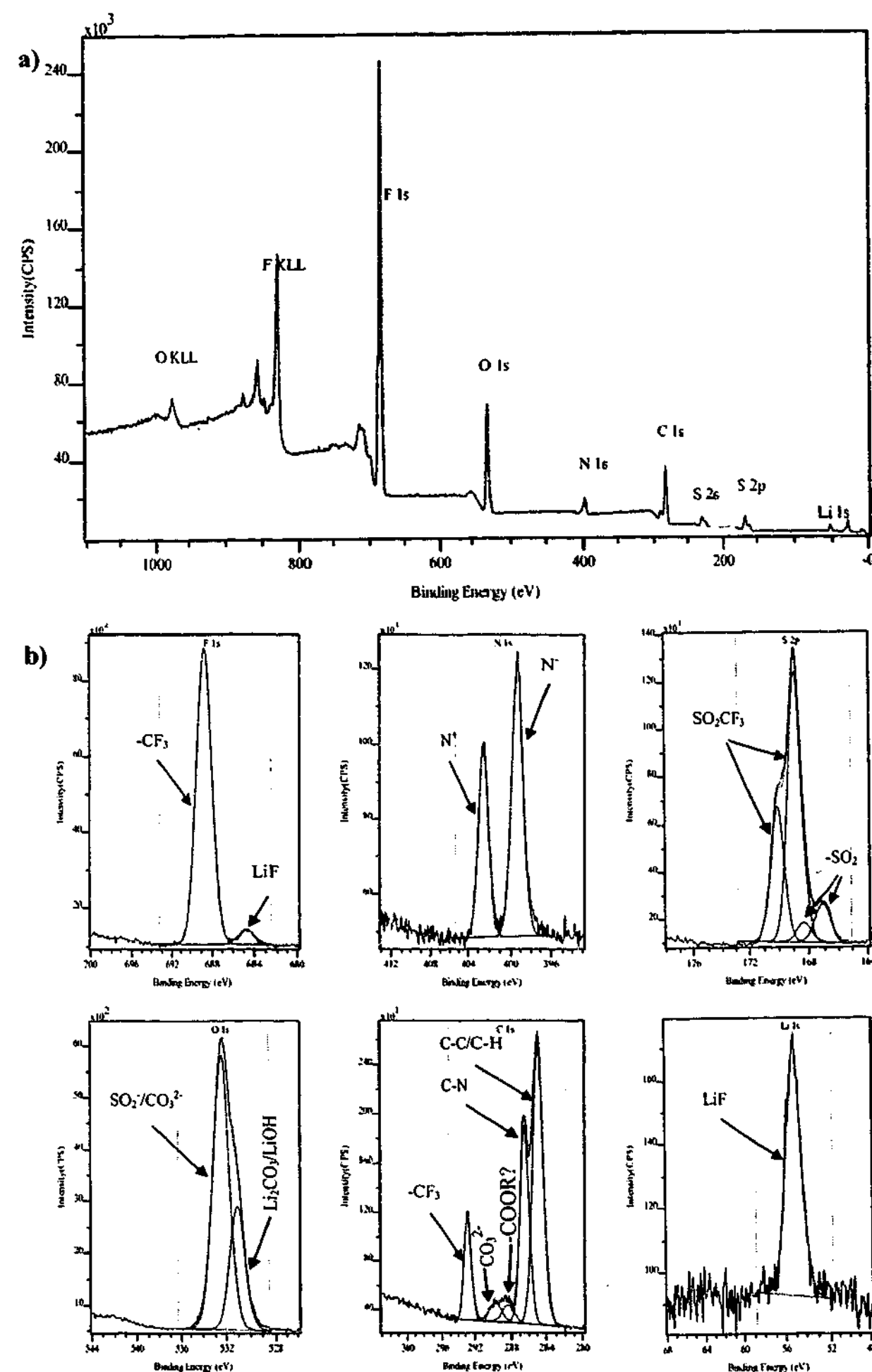


Fig. 3.4.2 Representative XPS scans; a) Survey scan b) Region scans F 1s, N 1s, S 2p, O 1s, C 1s and Li 1s.

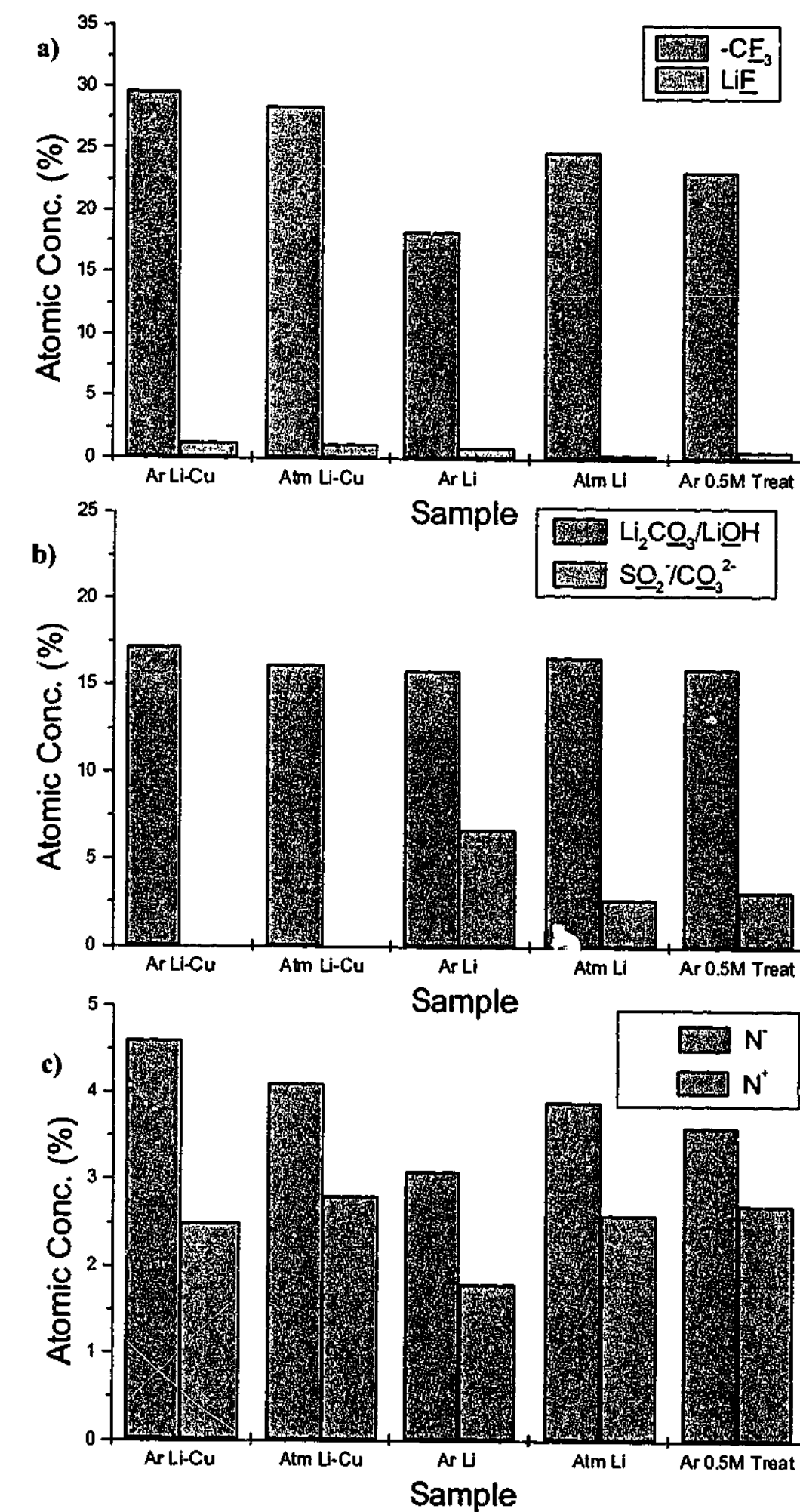


Fig. 3.4.3 Region scan summary for atmosphere and argon transferred Li and Li-Cu samples; a) F 1s region b) O 1s region c) N 1s region.

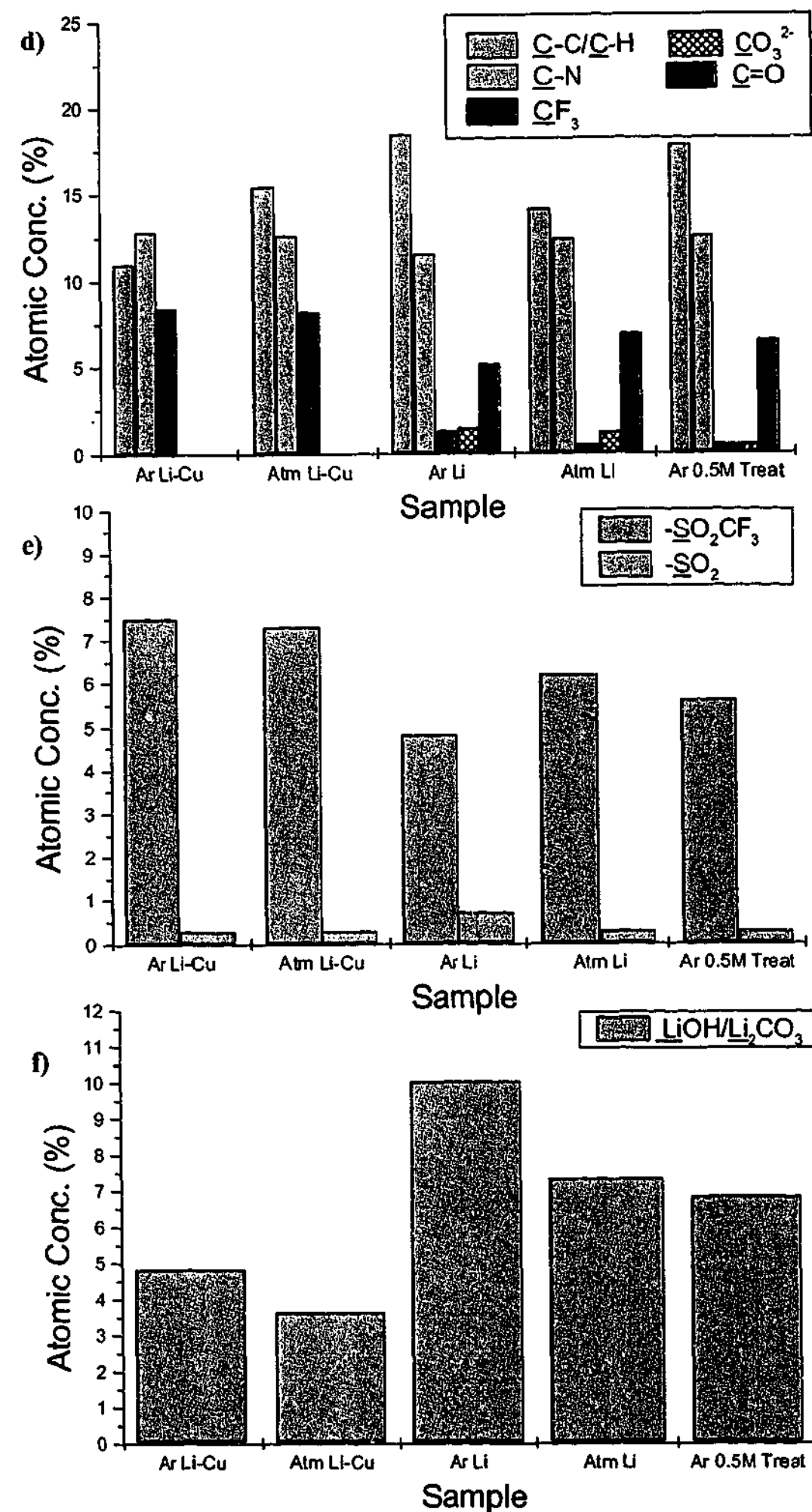


Fig. 3.4.3 (cont.) Region scan summary for atmosphere and argon transferred Li and Li-Cu samples; d) C 1s region e) S 2p region f) Li 1s region.

Etching experiments:

It must be remembered that the data obtained from the previous experiments is only indicative of the outer surface of the sample. Photoelectrons are statistically only likely to be ejected from the outer few atomic layers of the sample (tens of Angstroms), thus much of the SEI structure was not accessed in the previous experiments. However, by bombarding the sample surface with sputtered argon ions, it is possible to etch the surface, thereby revealing the material underneath.

Before discussing the results obtained from the etching experiments, it is important to review some of the pitfalls of the etching process. Effectively, the etching process is a destructive technique and as such, the process can alter the sample composition. Thus, the identification of changes in chemical states with depth may not reflect the true sample composition. Broadly, the complicating factors are as follows:¹

1. Smearing or elemental mixing: sample components may be 'pushed' around the sample surface instead of etched, resulting in mixing.
2. Preferential sputtering: some components of the sample may be etched more easily.
3. Sample reduction: components of the sample may be reduced by the argon ions.
4. X-ray degradation: repetitive measurements on one spot may result in components of the sample being degraded by the x-ray beam.

The results from the etching experiments must be considered in light of these factors and conclusions drawn about the structure of the SEI can only be tentative at best and must be supported by evidence from other techniques. However, many of the new species revealed by the etching process are likely to represent the true composition of the SEI providing important insight into the nature of the film. The etching rate is estimated at roughly 1 \AA s^{-1} , thus the etching experiments are estimated to have removed approximately 200-300 nm of material; notwithstanding the points mentioned above.

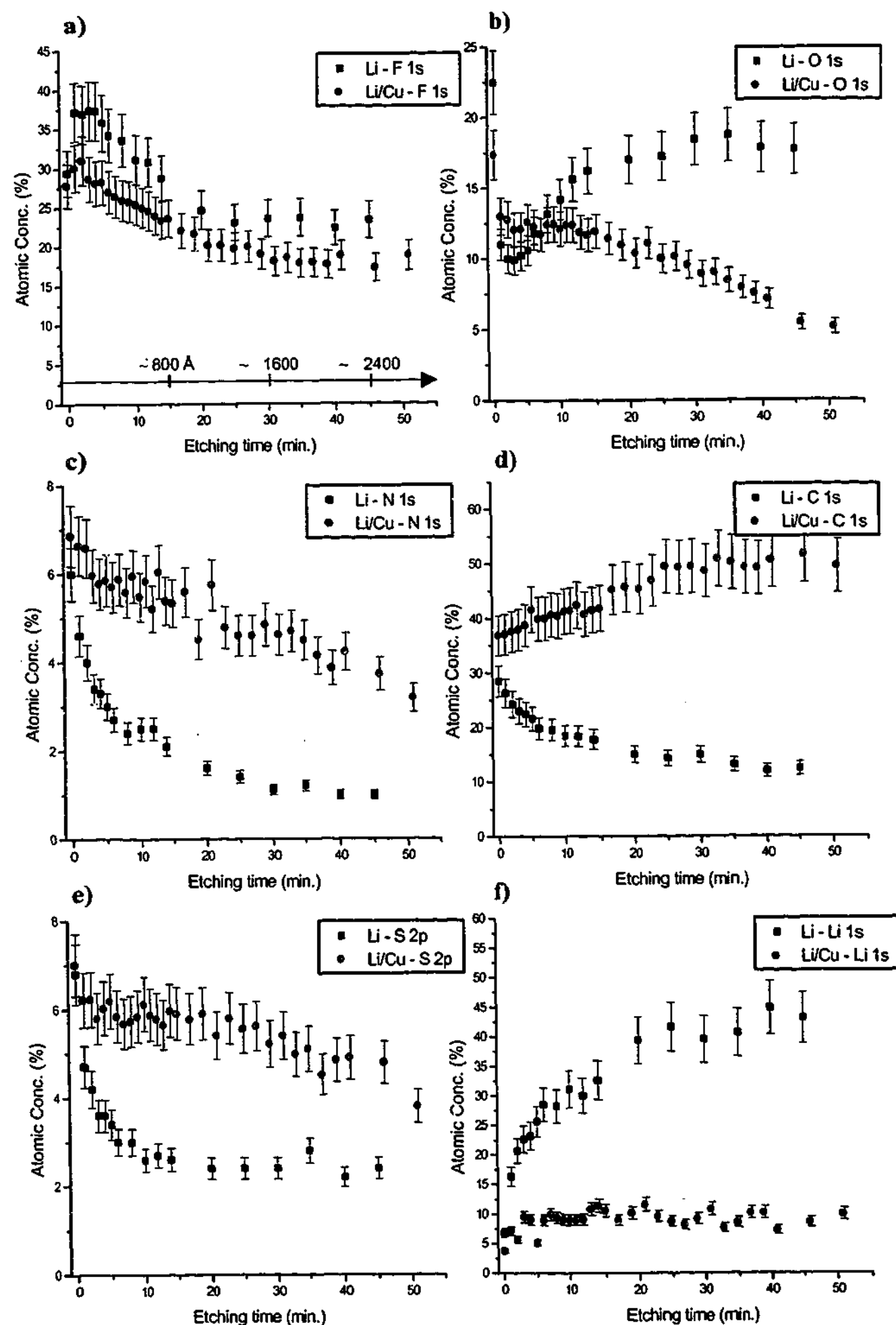


Fig. 3.4.4 Atomic concentration for each photoelectron line versus etching time for Li (black) and Li-Cu (red) samples; (a) F 1s (b) O 1s (c) N 1s (d) C 1s (e) S 2p (f) Li 1s.

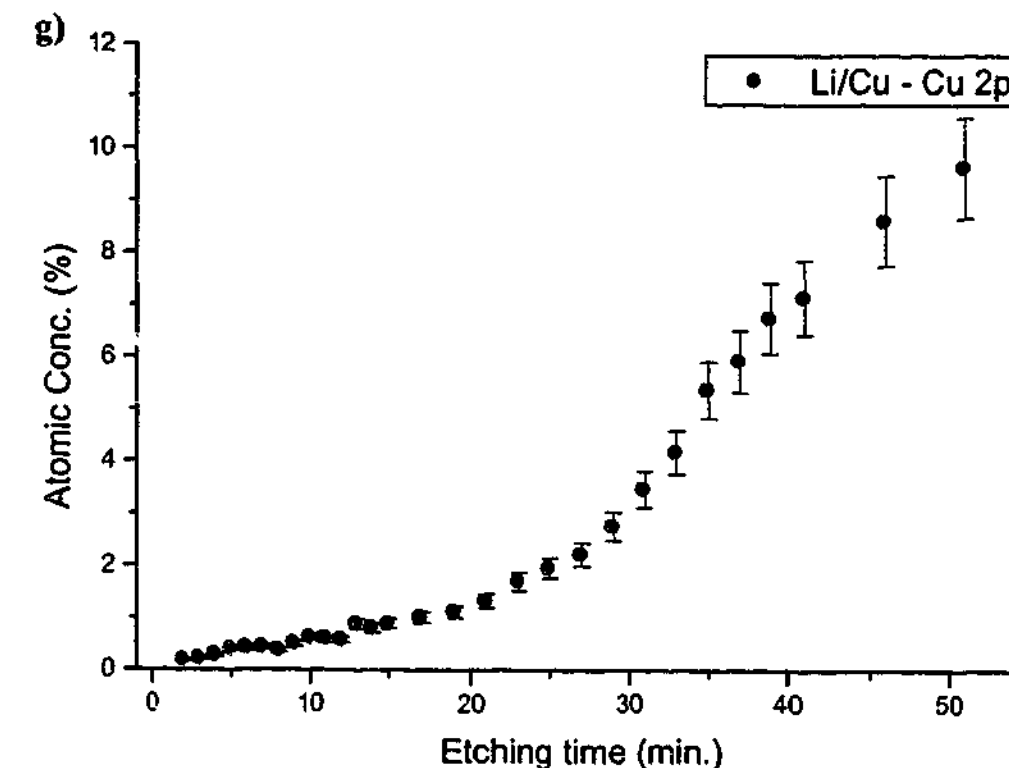


Fig. 3.4.4 (cont.) Atomic concentration versus etching time for the Li-Cu (red) sample; (g) Cu 2p.

Survey spectra were acquired at intervals throughout the etching process, the atomic concentration determined for each photoelectron line for both the Li surface and the Li-Cu surface is presented in Fig. 3.4.4a-g. The etching process reveals further differences between the Li surface and that of the Li-Cu sample. The F 1s spectra display a similar trend of reducing fluorine content, the Li surface containing a slightly greater quantity than the Cu. The amount of oxygen containing species increases with etching for the Li sample and decreases with etching for the Li-Cu sample. The Li-Cu sample contains a larger quantity of nitrogen containing species than the Li sample, which decreases with etching. The sulphur containing species exhibit similar behaviour. A much larger amount of carbon containing species is present on the Li-Cu sample with etching than is present on the Li sample. The Li sample contains a larger fraction of lithium containing species than the Li-Cu sample. Figure 3.4.4 (g) shows the increasing amount of Cu species that were encountered with continued etching.

The survey spectra provide only limited information as to the chemical nature of the species present on the sample surface. By acquiring high resolution region spectra at intervals during the etching process, more information about the nature of the changes in chemical states that occurred can be obtained. Combining this information with the trends observed in the survey spectra provides an understanding of the relative quantities of chemical species making up each of the photoelectron lines.

High resolution region spectra were acquired initially, after 15 minutes and after 30 minutes for the Li sample and after 41 minutes for the Li-Cu sample. Figure 3.4.5 summarises the results obtained from the F 1s high resolution region spectra for both samples.

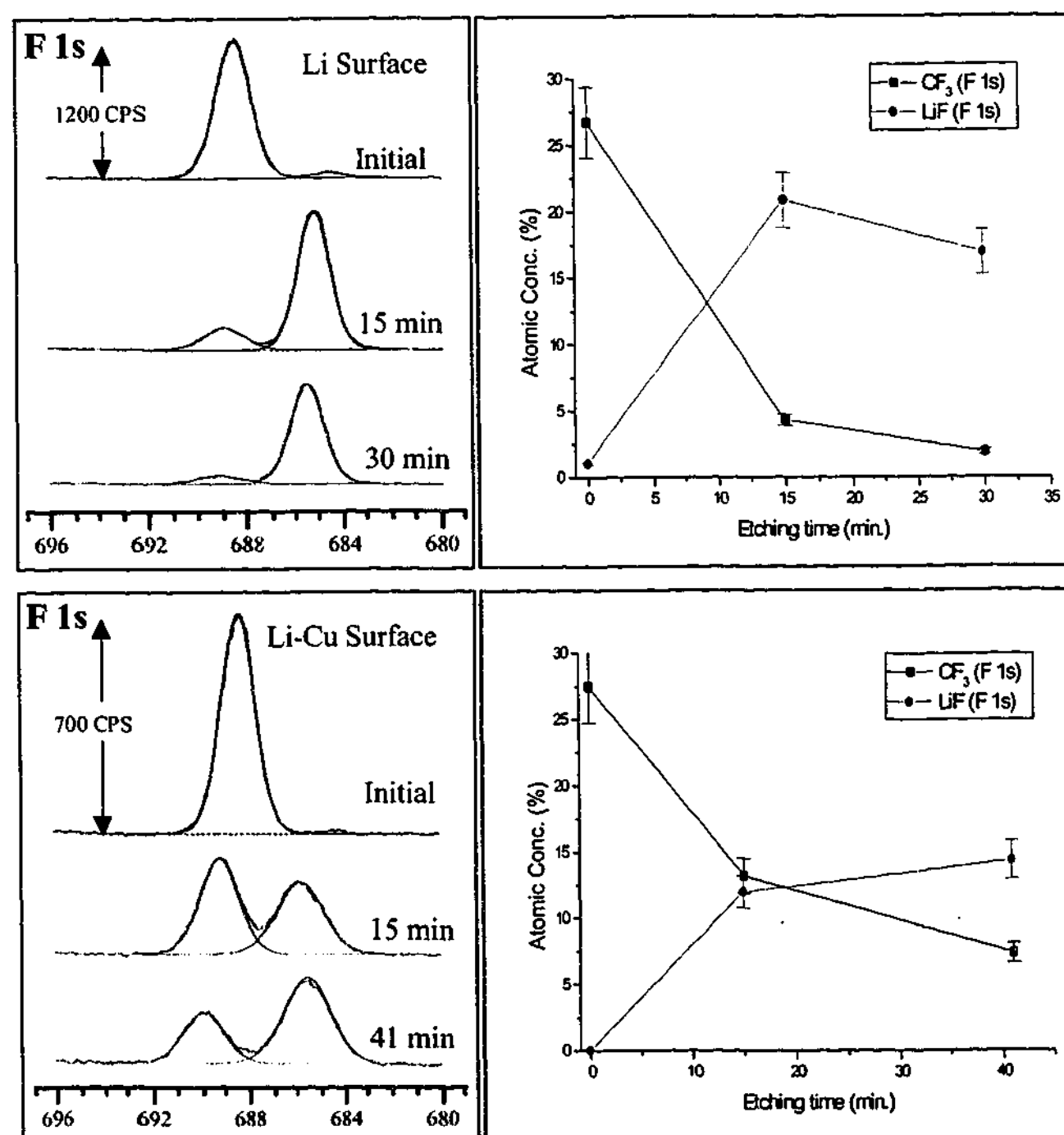


Fig. 3.4.5 F 1s high resolution region spectra with etching for Li and Li-Cu samples.

It is immediately apparent that the decreasing quantity of fluorine in the sample is completely accounted for by the decreasing amount of CF₃ present in the sample, and that there is in fact an increase in the quantity of LiF. The results suggest that a layer of LiF is present close to the lithium surface. There is also a significant difference between the samples, the Li surface quickly becoming dominated by LiF whereas the Li-Cu sample exhibits a more steady change, suggesting that the Li-Cu SEI may be thicker, or that a significant quantity of another species may be present on the Li surface, displacing the LiF.

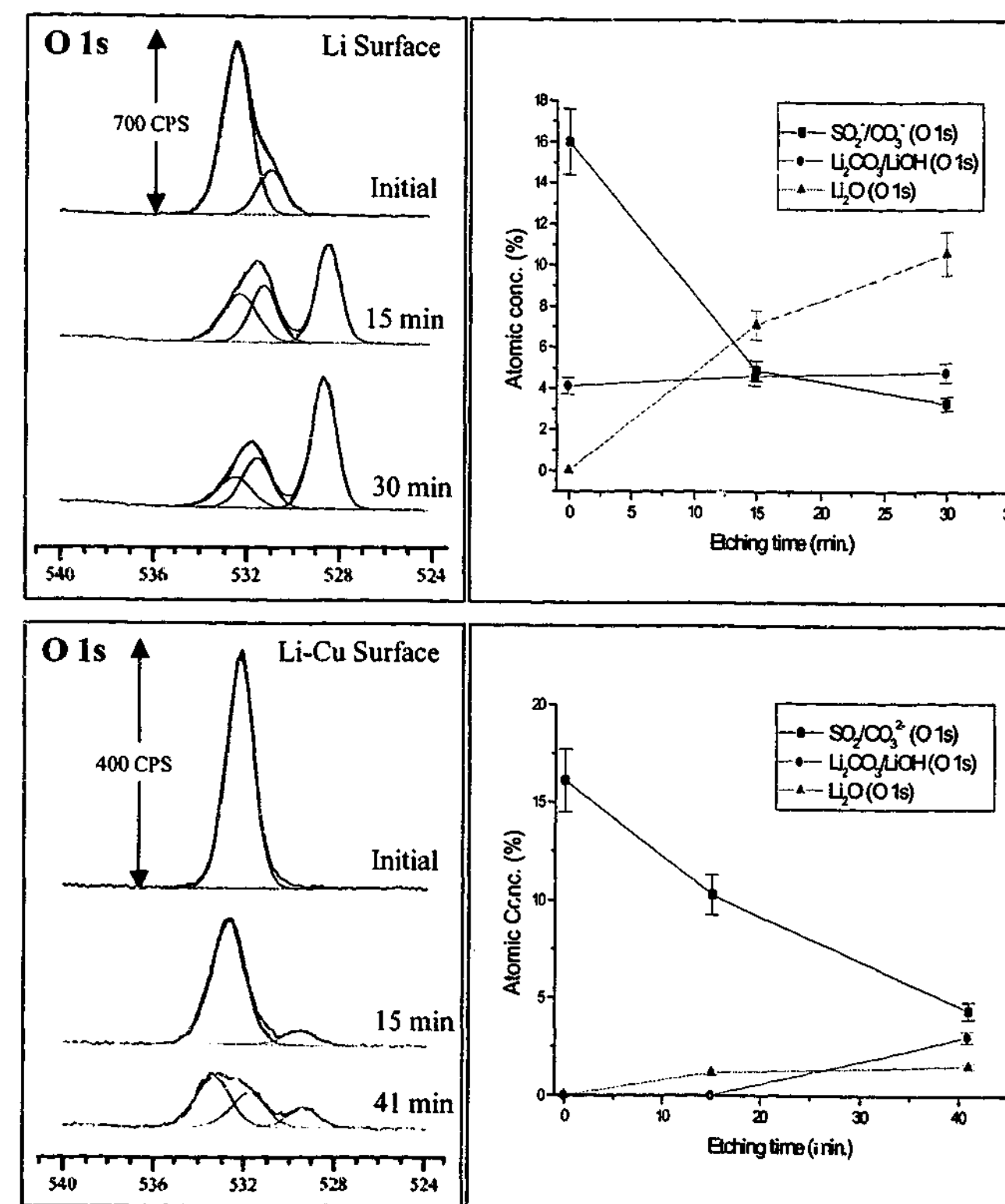


Fig. 3.4.6 O 1s region spectra with etching for Li and Li-Cu samples.

Figure 3.4.6 summarises the results obtained for the O 1s high resolution region spectrum. The results clearly indicate that the amount of CO_3^{2-} and SO_2 (predominately SO_2 – referring to the S 2p and C 1s spectra) decreased and that the quantity of Li_2O was increasing. The Li sample showed a much larger quantity of Li_2O present in the sample. Li_2CO_3 or LiOH (not distinguishable) was also present, the Li surface containing a more significant quantity than the Li-Cu surface.

Figure 3.4.7 summarises the results obtained for the N 1s spectrum. The results are consistent with the removal of the RTIL along with the surface during etching. Again, the Li concentration changes more quickly suggesting a thinner surface dominated by more reduced species. The Li surface also contained a small quantity of nitride species, possibly

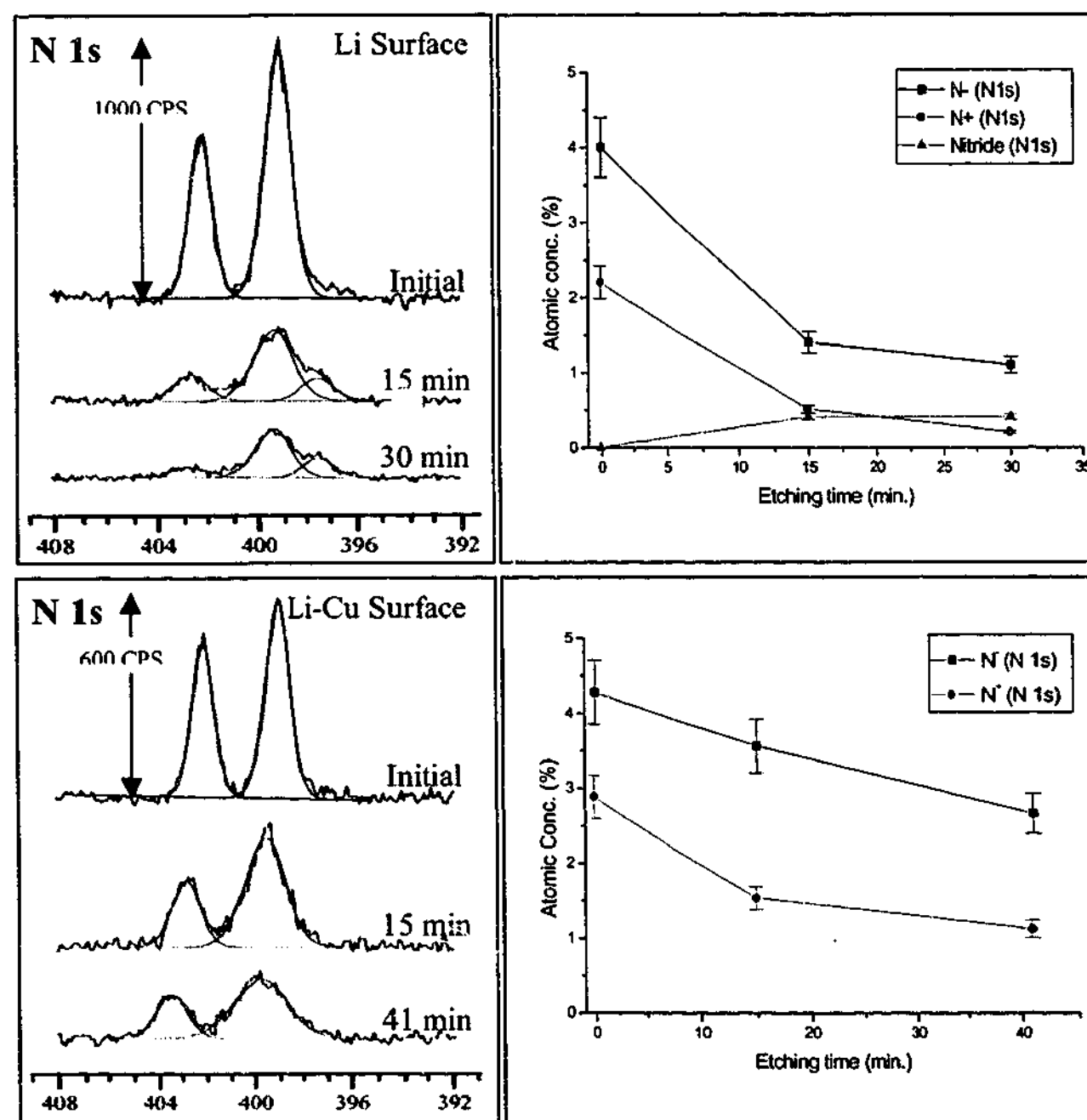


Fig. 3.4.7 N 1s region spectra with etching for Li and Li-Cu samples.

related to the native film.

Figure 3.4.8 summarises the results obtained for the C 1s high resolution region spectrum. There is a marked difference between the two surfaces, the Li surface showing steady removal of the carbons associated with the RTIL and the appearance of carbonate/carbonyl species. The Li-Cu surface displays an increase for carbon, derived either from the cation or from the anion, although it seems most likely to be related to the organic cation. The other species, CF_3 and the carbonate/carbonyls show similar distribution to those found for the Li surface.

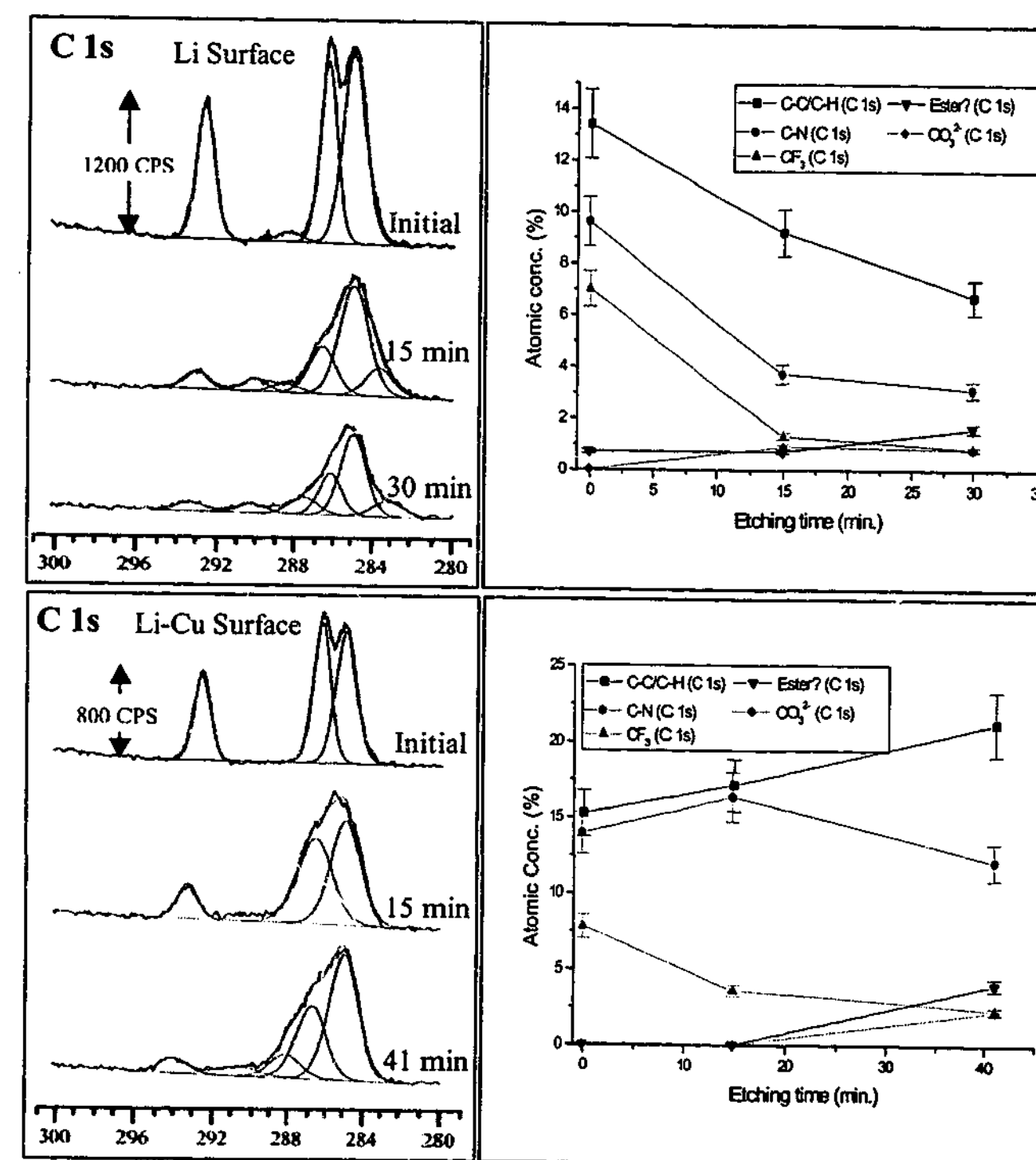


Fig. 3.4.8 C 1s region spectra with etching for Li and Li-Cu samples.

Figure 3.4.9 summarises the results obtained for the S 2p high resolution region spectrum. The results show that the $-\text{SO}_2\text{CF}_3$ moiety dissipates rapidly with etching, the high initial value partly consists of reduced S^{2-} , as well as contributions from the RTIL persisting on the surface. At longer etching times, both samples display a complex mixture of reduced sulphur species, which adhere to the fitting parameters surprisingly well (i.e., a S 2p species produces a doublet arising from spin orbit splitting, the doublet should be separated by 1.18 eV and have a ratio of $\sim 2:1$). The overall quantity of sulphur species remains the same, becoming progressively more reduced, which is suggestive of changes due to the etching process. However, this could also reflect a progressively more reducing environment, close to the lithium surface. A small amount of oxidised sulphur ($-\text{SO}_2$) is present throughout the experiment.

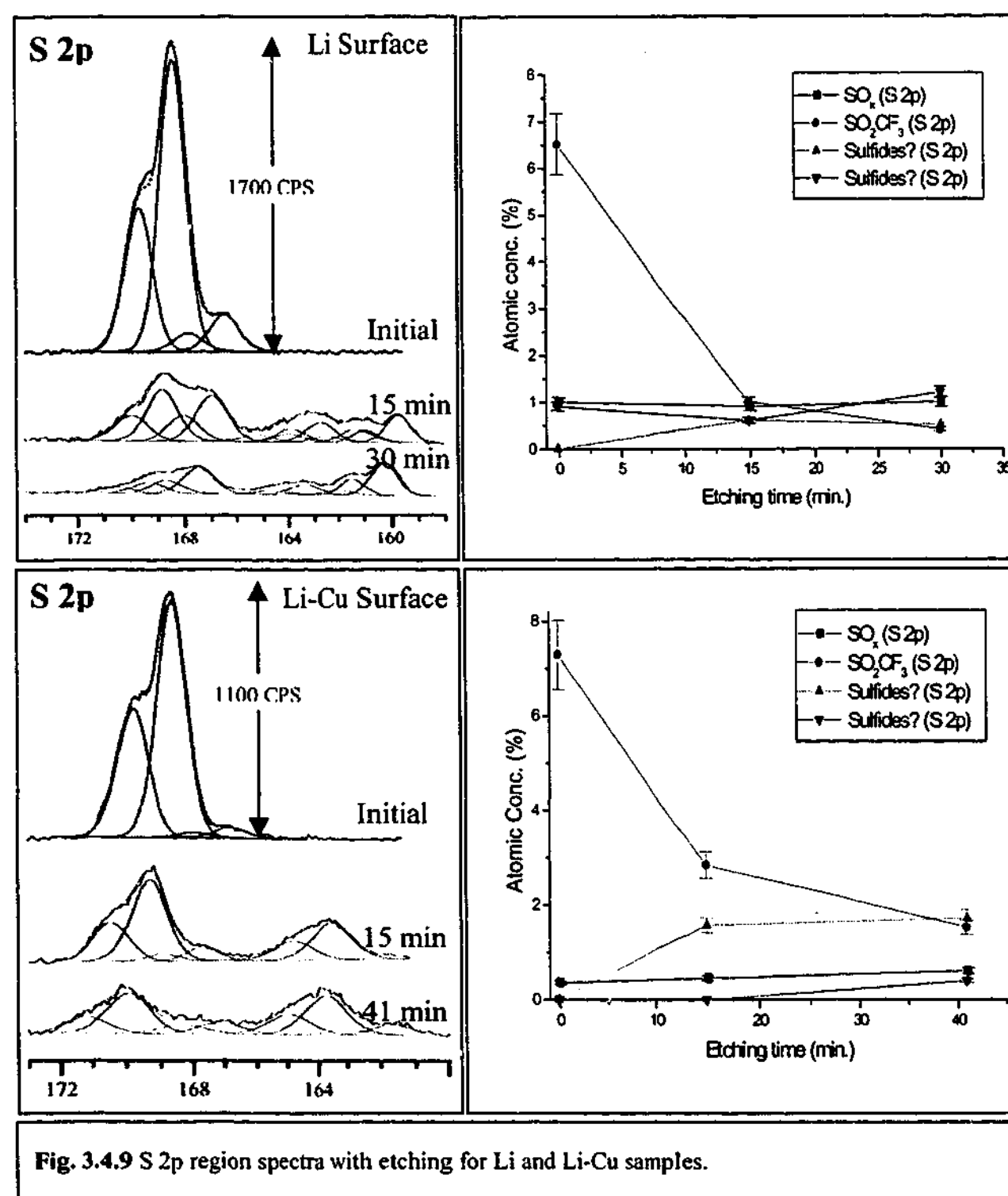
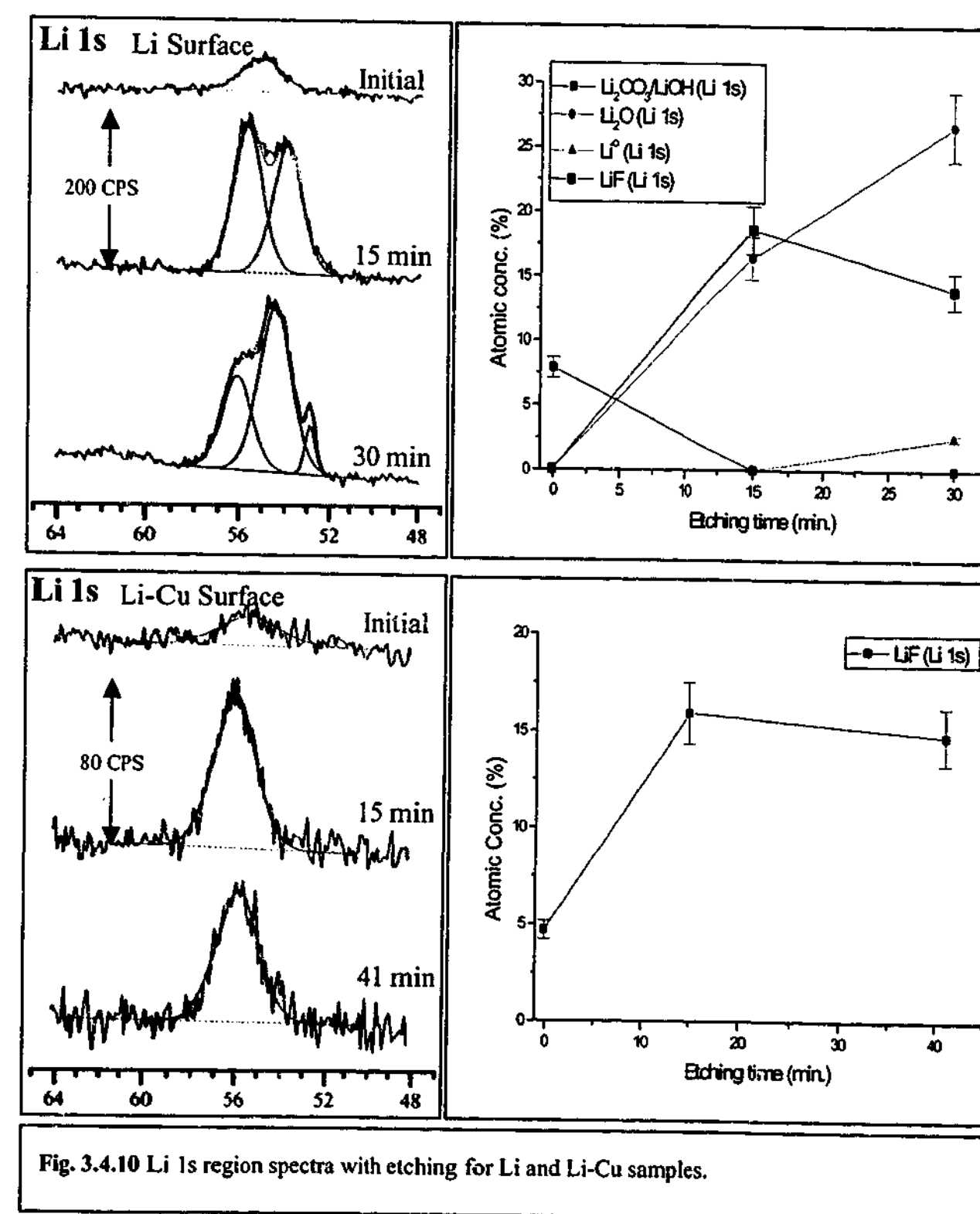


Figure 3.4.10 summarises the results obtained for the Li 1s high resolution region spectrum. The initial Li surface spectrum indicated the presence of a significant quantity of $\text{Li}_2\text{CO}_3/\text{LiOH}$ which did not persist with etching, and is possibly present as a contaminant arising from sample exposure to the glovebox atmosphere. A large quantity of Li_2O is indicated for the Li surface, as well as substantial amount of LiF , the quantity of Li_2O continued to increase with etching. The Li-Cu surface exhibited a single peak associated with LiF , which quickly reached a maximum concentration and stabilised in a similar manner to the Li surface.



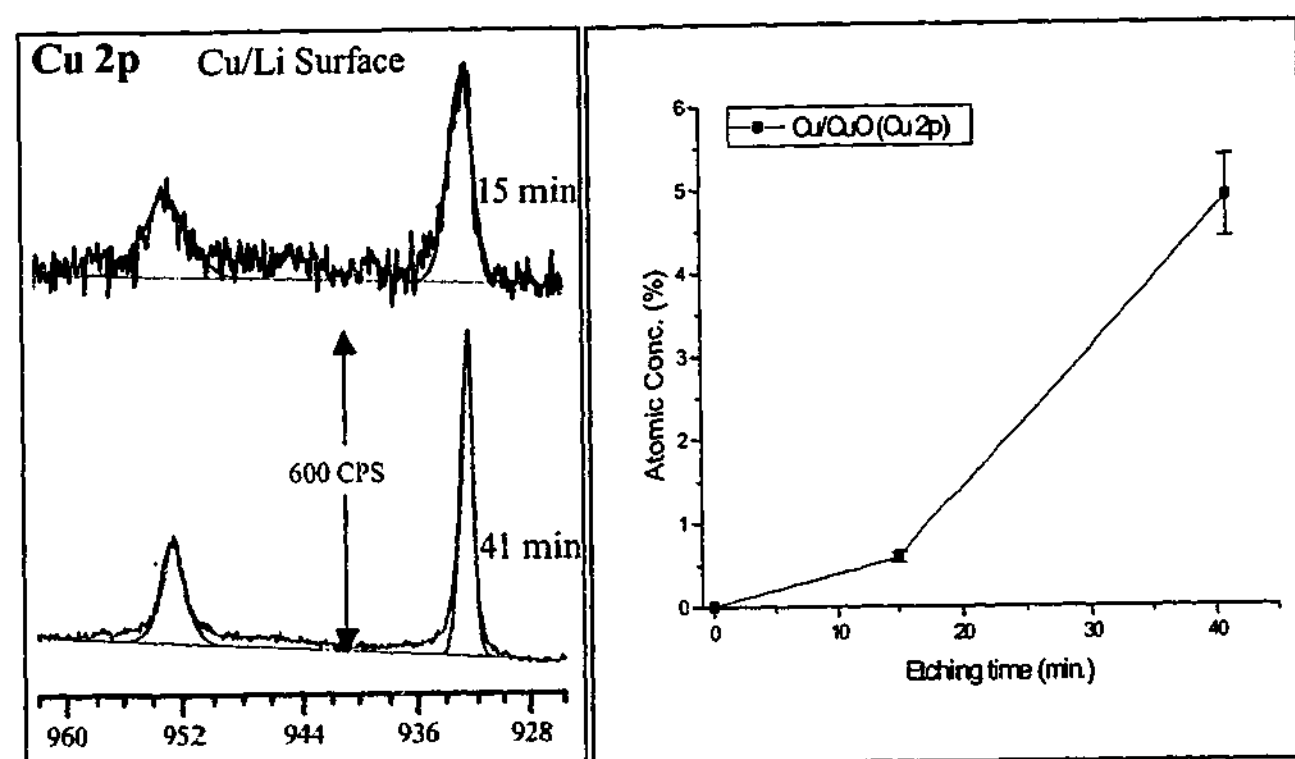


Fig. 3.4.11 Cu 2p region spectra with etching for Li-Cu sample.

Figure 3.4.11 summarises the results obtained for the Cu 2p high resolution region spectrum. Initially copper (as Cu or CuO) was not detected, with continued etching the Cu/CuO peak appeared and grew progressively more prominent. The appearance of the Cu/CuO peak indicated that material was in fact being removed by the etching process.

Summary:

The XPS measurements clearly indicated that the cycled lithium surface was dominated by reduction products of the $(\text{Tf})_2\text{N}^-$ anion. A clear difference between the lithium surface and the surface of electrochemically deposited lithium was also evident. If the etching process was assumed to result in gradual removal of material and hence progressively uncovered surface species closer to the lithium surface, then a picture of the structure of the SEI can be developed. The SEI formed on lithium metal was composed of an outer layer of less reduced $(\text{Tf})_2\text{N}^-$ reduction products, e.g., $\text{Li}_2\text{S}_2\text{O}_4$, $\text{Li}_2\text{NSO}_2\text{CF}_3$, $\text{Li}_y\text{C}_2\text{F}_x$ etc. as well as Li_2O , LiOH , Li_2CO_3 and LiF . Products of this type have been proposed by Aurbach *et al.*⁹ as reduction products of $\text{Li}(\text{Tf})_2\text{N}$ containing electrolytes and will be discussed later. Further in, the SEI becomes dominated by LiF and Li_2O , ultimately Li_2O appears to become the dominant species.

The deposited lithium surface (Li-Cu) presents a different surface structure. The Li_2O species is mostly absent and while there is a similar structure arising from reduced $(\text{Tf})_2\text{N}^-$ species, progressing towards a LiF dominated SEI, there is also a significant quantity of hydrocarbon and C-N species. These most likely arise from the P_{1X}^+ cation, and are present as either reduced species or as cations physically entrained within the salt structure. The presence of Li_2O and Li_2CO_3 species is associated with a native film on the lithium surface (more discussion later).

3.4.2 Grazing angle X-ray diffraction (GAXRD):

A grazing angle x-ray diffraction technique was developed for analysis of the lithium surface. Initial experiments were carried out in air to determine if the technique was sensitive enough to detect changes on the surface of a piece of lithium metal. In addition, these experiments provided information about the relative rates of reaction of lithium with components of the atmosphere. Figure 3.4.12 presents the results obtained for a piece of lithium metal after exposure to air. The experiment shows that the technique was sensitive to changes on the sample surface and that the dominant product was LiOH , formed from the reaction of lithium with moisture in the air. After 4.5 hours, another (unidentified) phase had become apparent, indicated by the peaks at 24.9, 35.5 and 77.3 degrees (2θ).

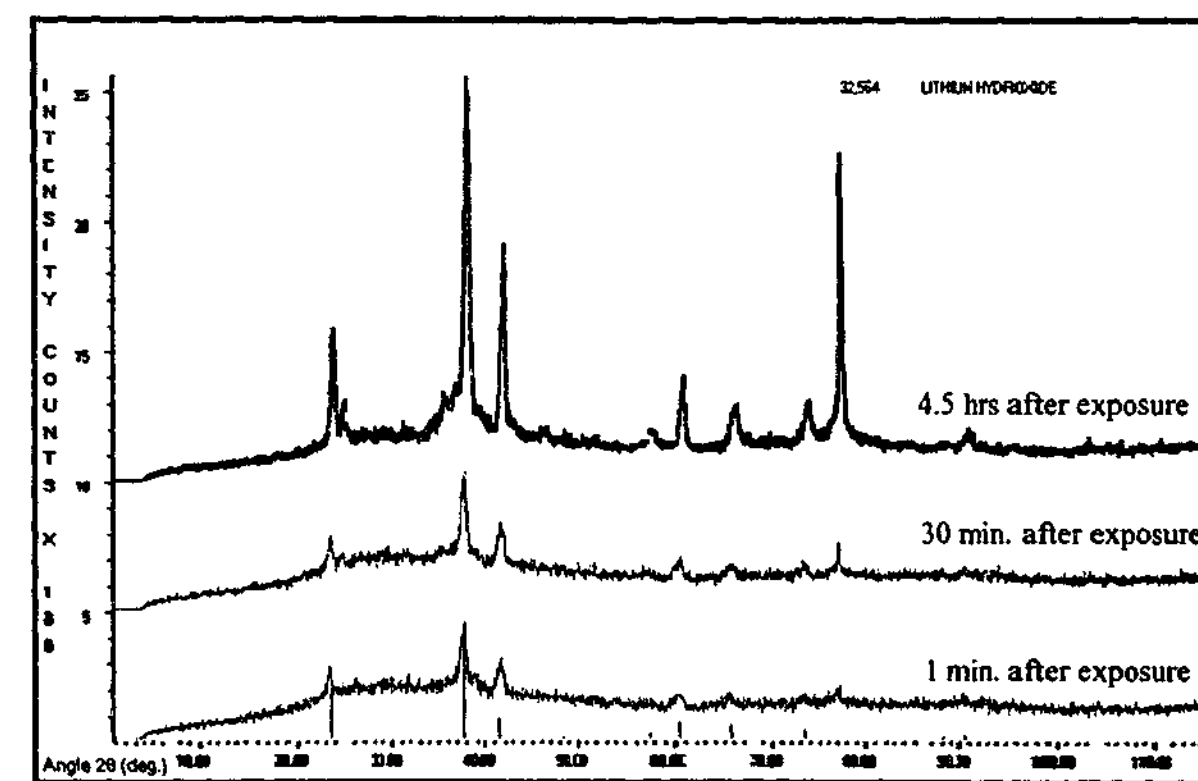


Fig. 3.4.12 Phase transformations on the lithium surface within several hours of exposure to air (ageing process).

Figure 3.4.13 shows the results of a similar experiment, but with varied incident angles (labelled). It can be seen that by varying the incident angle the relative intensity response of the phases present varied. The main phases were identified as LiOH and Li_2CO_3 (Zabuyelite). Generally, the intensity response of a phase is dictated by the incident angle such that at low incident angles the outer surface will give the strongest response. At higher incident angles, the x-ray beam will penetrate further into the sample, and the intensity response from 'deeper' phases will increase. Hence the results presented in Fig. 3.4.13 indicate Li_2CO_3 at the surface, and then LiOH as the dominant component. At higher incident angles the intensity of the Li_2CO_3 begins to increase again, this is thought to be due to penetration through to the bottom side of the sample. At high incident angle (10 degrees), where it is assumed all of the sample is being analysed, after 24 hours the sample was determined to be composed of a mixture mainly composed of LiOH and Li_2CO_3 .

The results confirmed the ability of the technique to detect subtle changes in the composition of the surface film and to provide information about the distribution of the phases present in the surface film. A chamber was constructed to allow measurements to be obtained without the influence of the atmosphere (section 2.4.3), selected results from measurements of lithium surfaces cycled in $\text{P}_{18}(\text{Tf})_2\text{N}$ electrolytes are shown in Fig. 3.4.14. The diffraction pattern was dominated by the lithium and/or copper substrate. However, low intensity, reproducible peaks were found that did not belong to any of the phases previously encountered on the lithium surface. These were assumed to result from the presence of phases that constituted the SEI formed on the cycled surface. The peaks could not be matched to any known phase and, hence, the identity of the phase(s) could not be determined. The peaks were very sharp, indicating that components of the SEI were crystalline, as was indicated in the optical micrographs presented in section 3.1.2. The broad peak at 21 degrees (2θ) indicates a large amorphous component; this was attributed to persistent RTIL on the surface of the sample, although an amorphous component of the SEI could also be present. There was no significant difference displayed by the Li or Li-Cu surface in contrast to the XPS data. This most likely reflects a lack of sensitivity of the technique to the small quantities of materials that make up the SEI.

Overall, the technique did not provide very useful information, however, its application to other lithium surfaces could prove more fruitful. In addition, the technique could be applied to the study of cathode materials where a much larger body of work has been published, and where the diffraction patterns obtained are likely to be more intense and well defined because of their high crystalline component and the fact that they are present in greater quantities than the materials which make up the lithium SEI.

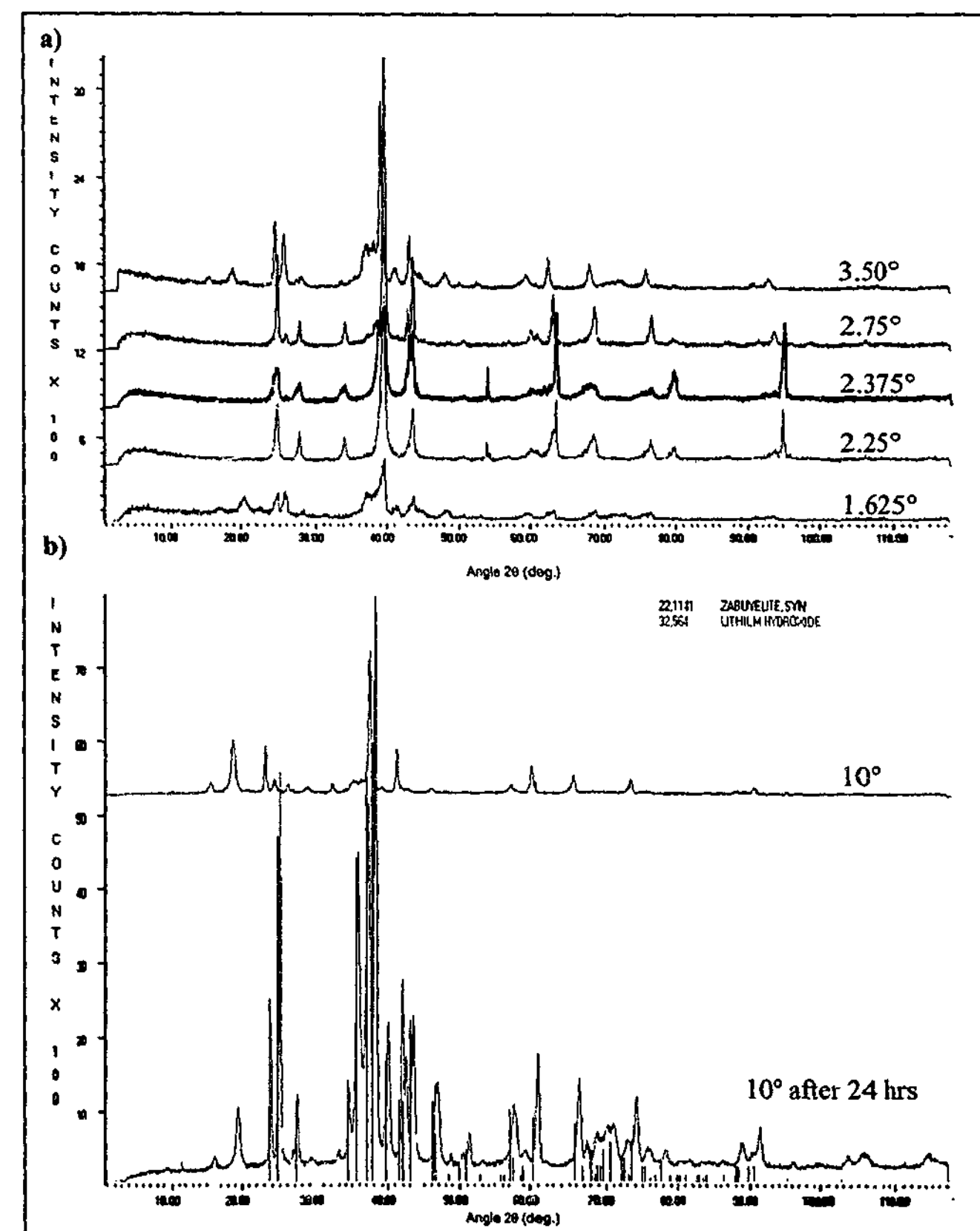


Fig. 3.4.13 Phase transformations and phase dependence of the lithium surface at different incident angles immediately and 24 hours after exposure to the atmosphere.

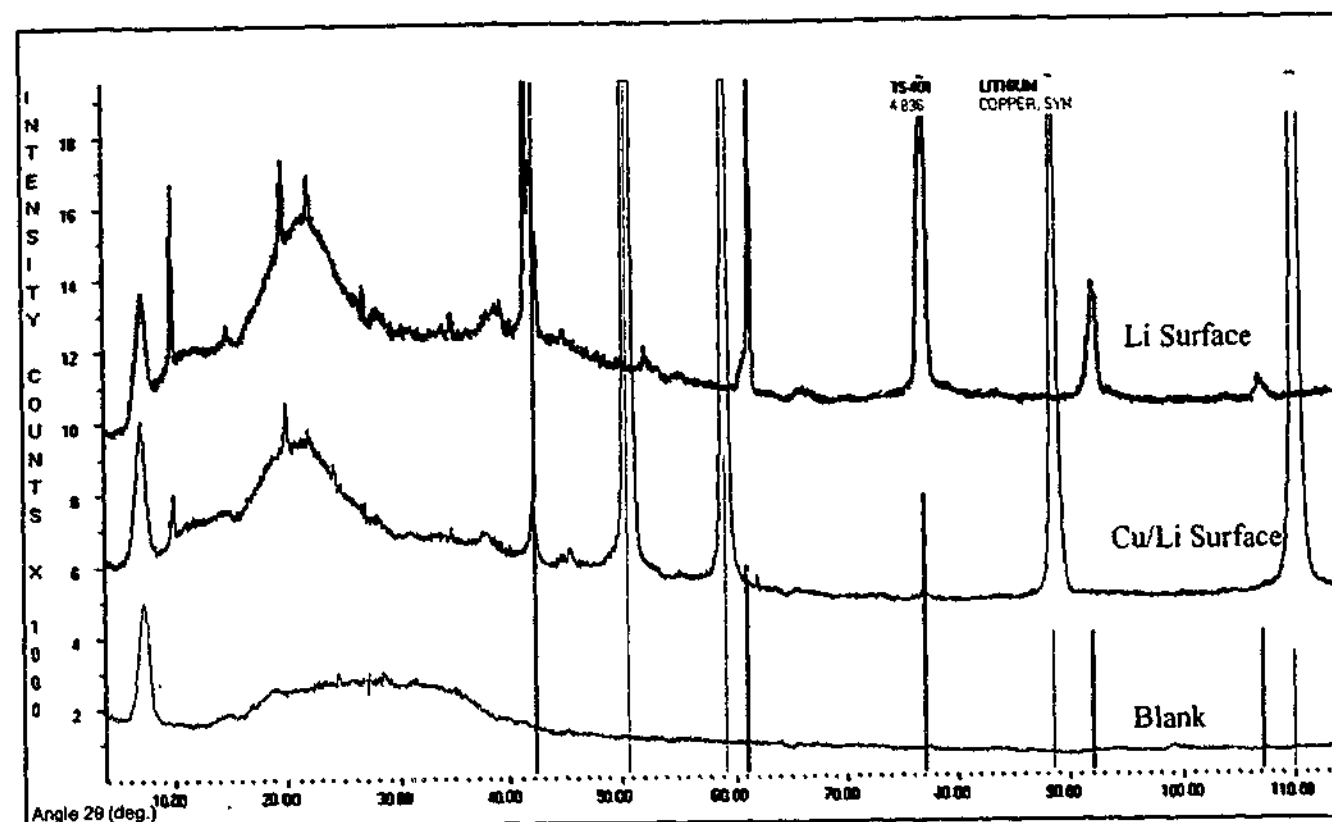


Fig. 3.4.14 Representative diffraction patterns obtained from lithium surfaces cycled in $P_{1X}(Tf)_2N$ electrolytes at 7 degrees incident angle. The response from the empty chamber is also shown

3.4.3 Diffuse reflectance FTIR - (DRFTIR) and Raman spectroscopy:

Table 3.4.1 shows the Raman and IR spectrum peak positions and their assignments for $P_{1X}(Tf)_2N$ electrolytes. The majority of the most significant peaks have been assigned. Both techniques were used to investigate the SEI formed in a $P_{1X}(Tf)_2N$ electrolyte.

Table 3.4.1 Peak position and assignment for Raman and FTIR spectra of $P_{1X}(Tf)_2N$ electrolytes.

Assignment	Raman (cm^{-1})	IR (cm^{-1})	Reference(s)
	314 (m)		
ρSO_2	327 (m)		10
	339 (m)		
ωSO_2	404 (m)		10
	437 (w)		
	496 (w)		
$\delta_s CF_3$		514 (m)	10
$\nu N-C, \delta_s SO_2$	553 (m)		11
$\nu N-C, \delta_s CF_3$	571 (w)	574 (m)	11
	590 (w)		
$\delta_s SO_2$		618 (s)	10
	636 (w)		
δSNS	657 (w)	655 (m)	10
	678 (w)		
$\delta_s CF_3$	743 (vs)	740 (m)	10,12,13
νSNS		762 (w)	10,13
νCS	798 (w)	790 (m)	10
	823 (w)		
Ring mode	889 (sh)	887 (w)	11,14
Ring mode	903 (m)	905 (w)	14
Ring mode		939 (w)	11,14
Ring mode		970 (w)	14
	1011 (w)	1004 (w)	
νSNS	1041 (m)	1057 (s)	10
$\nu_s SO_2$	1138 (m)	1139 (s)	10
		1193 (s)	
$\nu_s CF_3$		1234 (sh)	10
$\tau CH_2, \nu CF_3$	1243 (s)		11
$\nu_s SO_{2(o.p.)}$	1332 (m)	1335 (sh)	10,13
$\nu_s SO_{2(i.p.)}$	1354 (m)	1354 (s)	10,13
δCH_2	1457 (m)	1434 (w)	11,14
$\nu CH_2, \nu CH_3$		1470 (m)	
δCH_2 (ring)	1493 (w)		11
νCH_2	2850 (w)		15
νCH_2	2889 (m)	2890 (m)	14
νCH_2		2949 (m)	15
νCH_2	2976 (s)	2981 (s)	14
νCH_2	2997 (s)		14
		3041 (w)	

DRFTIR:

Li-Cu surface

Figure 3.4.15 presents comparative spectra obtained from an uncycled $P_{14}(\text{Tf})_2\text{N}$ electrolyte (transmission mode) and a cycled Li-Cu surface. Significant differences can be observed that distinguish the spectra. The spectrum obtained from the surface is dominated by that of the RTIL still present on the sample. As such, the differences between the spectra will indicate the presence of surface species as well as changes that have occurred to the electrolyte itself. Comparison of spectra of the electrolyte taken from cycled cells and of the uncycled electrolyte revealed that they were indistinguishable, indicating that the electrolyte composition was unchanged with respect to its IR spectrum. Thus, the differences in appearance can be attributed to surface species and to differences in the spectral response of the two techniques. The two techniques should be comparable and peak positions should not change. However, changes in peak intensity are likely due to changes in the frequency response of the reflectivity of the sample surface. In addition, baseline correction will have introduced some differences in the intensity response, particularly at lower wavenumbers where the DRFTIR response was sloping.

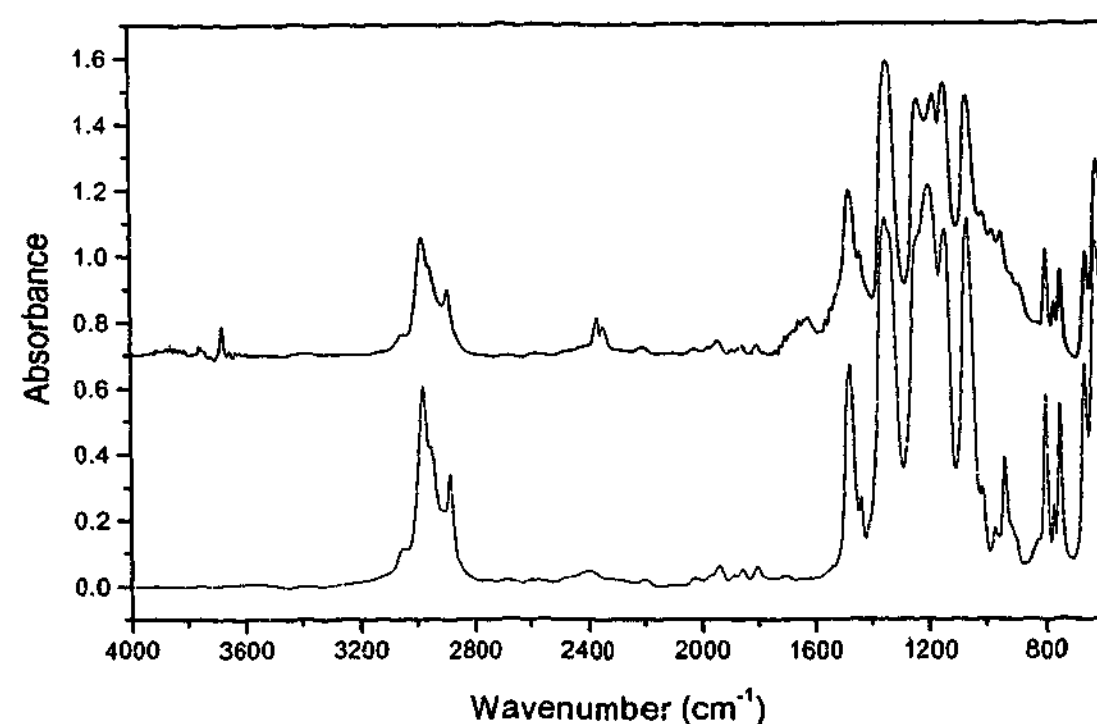


Fig. 3.4.15 Comparison of $P_{14}(\text{Tf})_2\text{N}$ (red) and the cycled Li-Cu surface (blue) IR spectra (baseline corrected).

The most informative way to compare spectra of this type is by subtraction, where a difference spectrum is obtained. In this case, the spectra were baseline corrected and normalised to the intensity of a single peak, and then the spectrum of the electrolyte was subtracted from the DRFTIR spectrum of the lithium surface. Interpretation of the difference spectrum is complicated by the comparison of the two different techniques and by the choice of the normalisation peak. Normalising the spectrum to a peak that has changed due to the presence of surface species could result in misinterpretation of the results. To avoid this a number of different peaks were used to normalise the spectra. The results for the Li-Cu surface are presented in Figure 3.4.16. Tables 3.4.2 and 3.4.3 provide tentative assignments for the peaks which consistently appeared in the difference spectrum.

Positive peaks most likely represent the presence of new species on the surface of the sample, either due to the formation of new bonds or due to the presence of larger amounts of materials with the same types of chemical bonds. The negative peaks most likely represent broken or missing/lost bonds and hence a loss in the intensity of a particular band, which indicates the species that have reacted to form the new surface compounds.

Table 3.4.2 Position and assignment for the most consistently prominent positive peaks in the difference spectrum for the cycled Li-Cu surface.

Pos. Peak (cm^{-1})	Assignment	Reference(s)
875	Li_2CO_3	7,9,16,17
905	Ring mode, C=C	14,15,18
944	Ring mode, C=C	14,15,18,18
977	Ring mode, C=C	14,15
1013	δSO_2	9,10,19
1065	$\nu_s\text{SNS}$	9,10,19
1145	$\nu_s\text{SO}_2$	9,10,19
1171	$\nu_s\text{CF}_3(?)$	9,10,19
1229	$\nu_s\text{CF}_3$	9,10,19
1338	$\nu_s\text{SO}_2$	9,10,19
1440	Li_2CO_3	7,16,17
1508	Li_2CO_3	7,9,16,17
1618	Amide, C=C	15
3675	LiOH	7,16,20

Table 3.4.3 Position and assignment for the most consistently prominent negative peaks in the difference spectrum for the cycled Li-Cu surface.

Neg. Peak (cm^{-1})	Assignment	Reference(s)
1057	$\nu_s\text{SO}_2$	21
1202	$\nu_s\text{CF}_3$	9,10,19
1253	$\nu_s\text{CF}_3$	9,10,19
1372	sulphonamide	15
2880	νCH_2	15

The peak assignments clearly indicate the presence of reaction products of the $(\text{Tf})_2\text{N}^-$ anion on the surface of the electrode, providing strong support for the XPS results. The number of altered peaks indicates that the $(\text{Tf})_2\text{N}^-$ anion had reacted in a complex manner, considering the functional groups that could be reduced by lithium (e.g., $-\text{CF}_3$, $-\text{SO}_2$, S-N) the spectral evidence suggests that the anion had undergone reaction via a number of different pathways. The presence of Li_2CO_3 and LiOH is also indicated, supporting the XPS results. The presence of modes associated with the pyrrolidinium ring is also indicated, and the band at 1618 cm^{-1} suggests that the cation had also been reduced. The reduction could have occurred at the nitrogen, resulting in the formation of an amide, or possibly via the formation of a CF_3 radical²² which could extract an alkyl hydrogen, thus forming a $\text{C}=\text{C}$ bond. The evidence for the reaction of the cation is not clear and its presence could be due to physical entrainment within the SEI structure or by the precipitation of solid pyrrolidinium salts with reaction products of the $(\text{Tf})_2\text{N}^-$ anion (e.g., pyrrolidinium triflate).

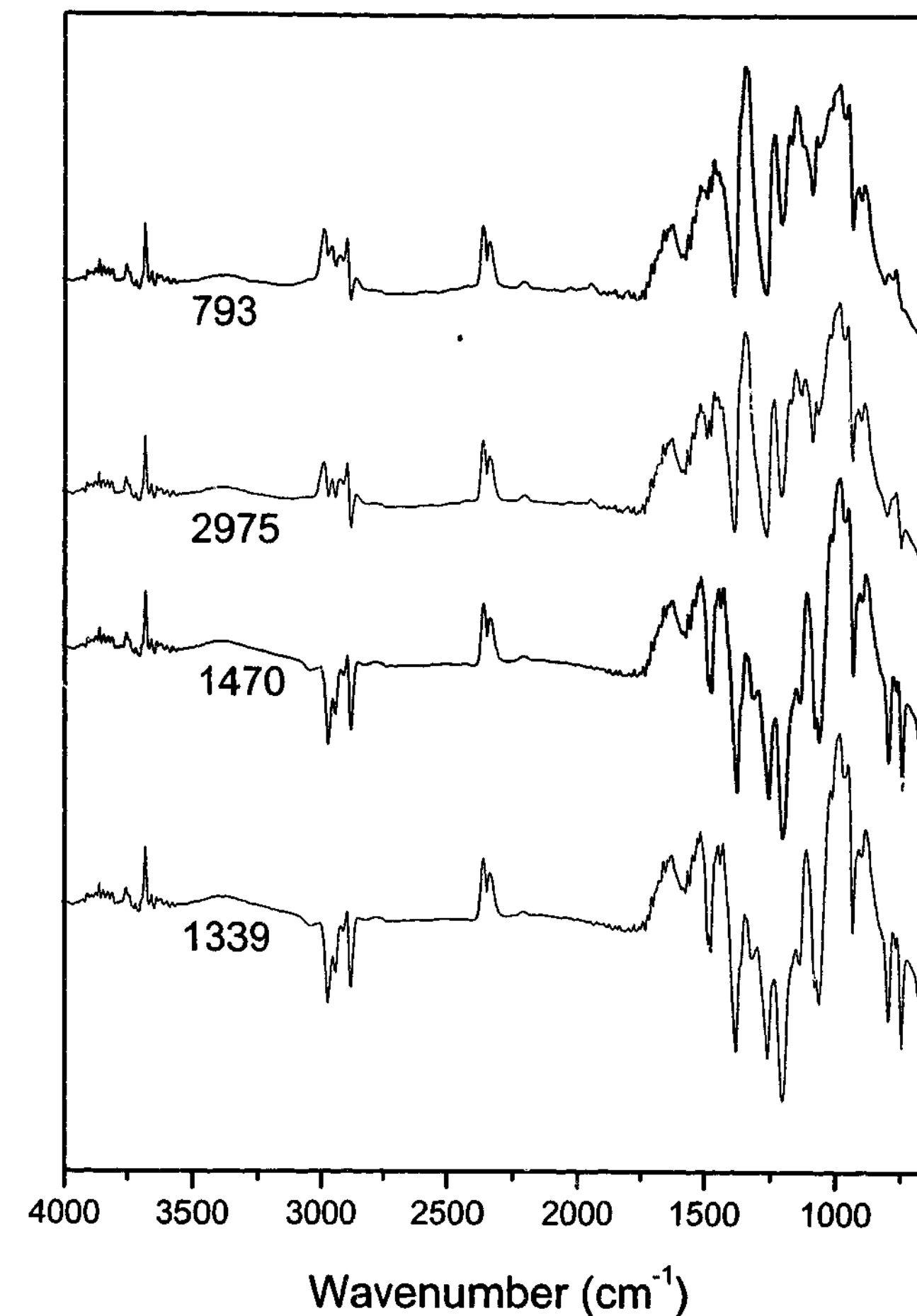


Fig. 3.4.16 Difference spectra obtained for the cycled Li-Cu surface, peaks used to normalise the spectra are indicated.

Li surface

Figures 3.4.17 and 3.4.18 provide similar spectra for the cycled Li surface. Tentative peak assignments are given in Tables 3.4.4 and 3.4.5. The difference spectra indicate the presence of reaction products of the $(\text{Tf})_2\text{N}^-$ anion as well as LiOH and Li_2CO_3 . The spectra are also clearly different from those obtained from the Li-Cu surface, although exhibiting similar features. The evidence for the presence/reaction of the pyrrolidinium cation is less compelling, indicating that the pyrrolidinium cation was either not present or present in significantly smaller quantities.

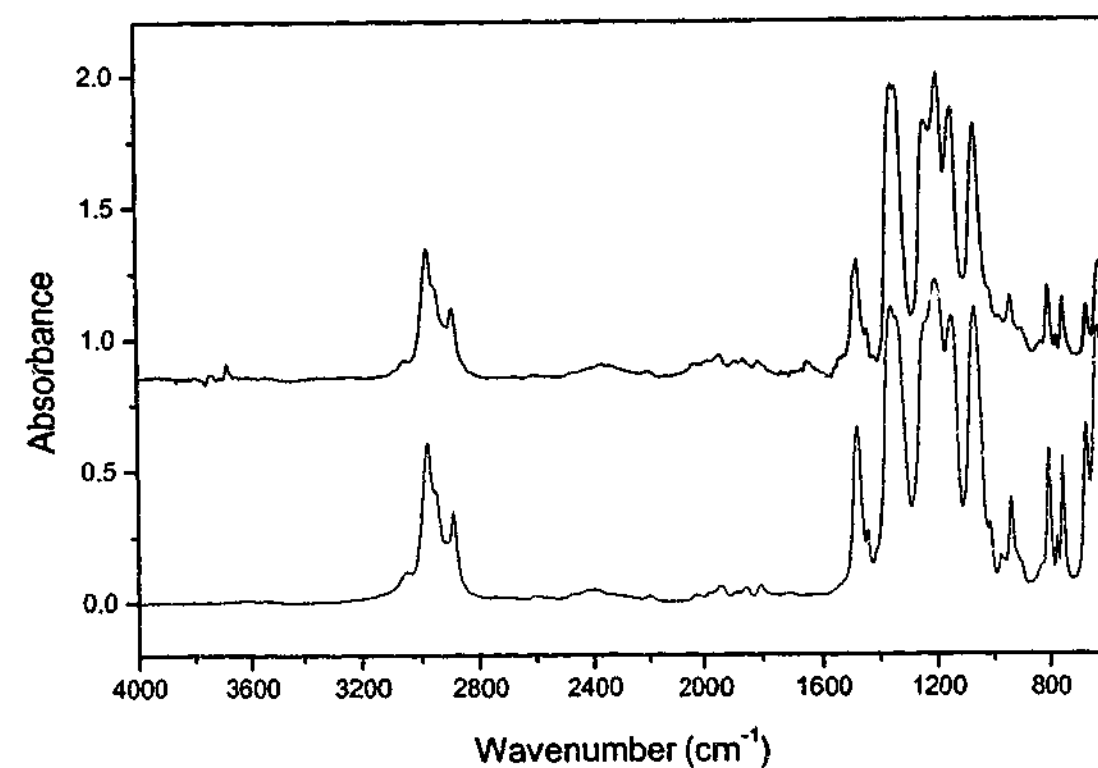


Fig. 3.4.17 Comparison of $\text{P}_{14}(\text{Tf})_2\text{N}$ (red) and the cycled Li surface (blue) IR spectra (baseline corrected).

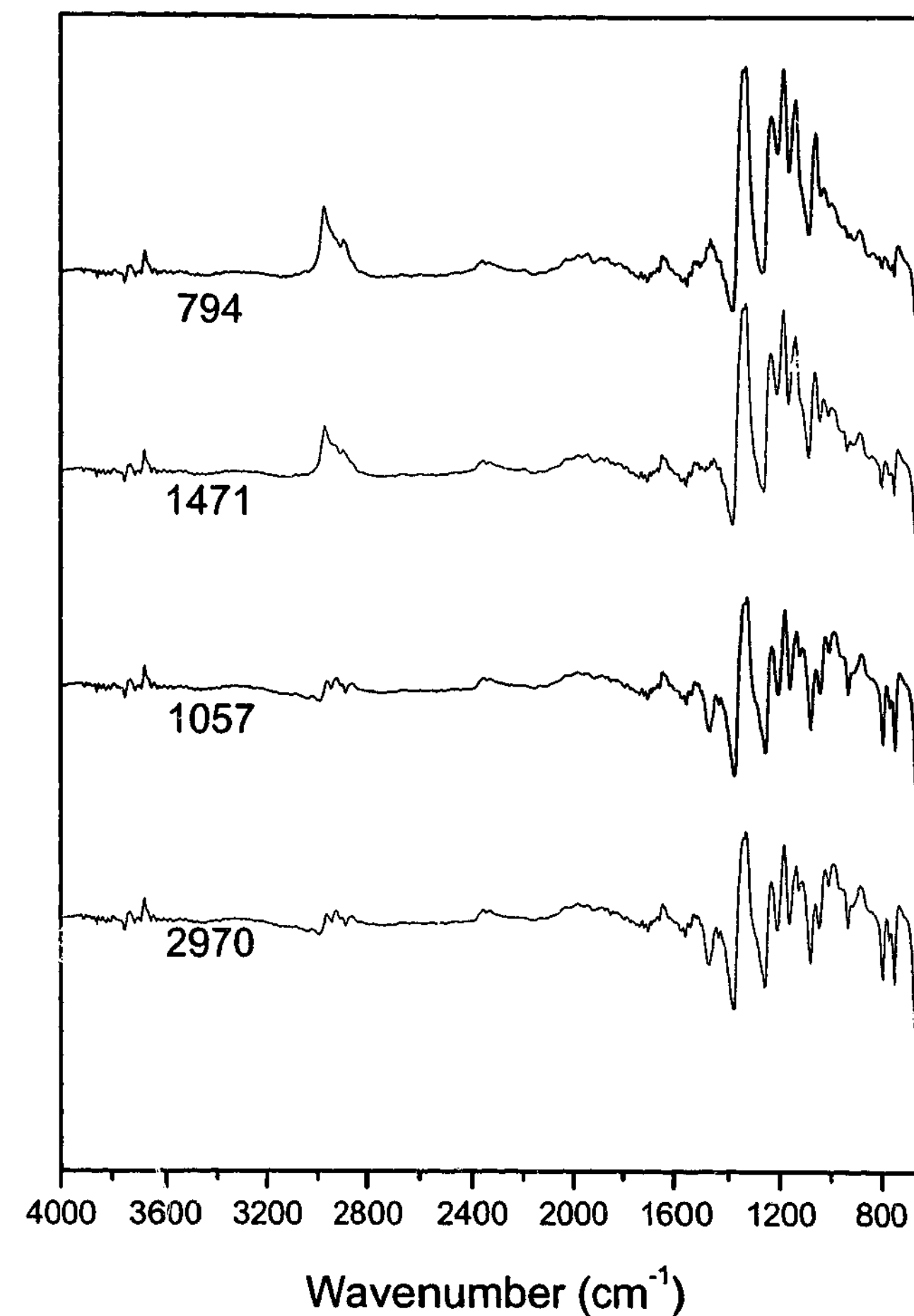


Fig. 3.4.18 Difference spectra obtained for the cycled Li surface ($0.5 \text{ mol kg}^{-1} \text{ P}_{13}(\text{Tf})_2\text{N}$), peaks used to normalise the spectra are indicated.

Table 3.4.4 Position and assignment for the most consistently prominent positive peaks in the difference spectrum for the cycled Li surface.

Pos. Peak (cm ⁻¹)	Assignment	Reference(s)
879	Li ₂ CO ₃	7,9,16,17
984		
1018	δSO ₂	9,10,19
1057	ν _s SO ₂	21
1110		
1136	ν _s SO ₂	9,10,19
1184	ν _a CF ₃	9,10,19
1332	ν _a SO ₂	9,10,19
1345	ν _a SO ₂	9,10,19
1530	Li ₂ CO ₃	7,9,16,17
1642	Amide, C=C	15
2851	νCH ₂	14
2919	νCH ₂	14
2962	νCH ₂	14
3676	LiOH	7,16,20

Table 3.4.5 Position and assignment for the most consistently prominent negative peaks in the difference spectrum for the cycled Li surface.

Neg. Peak (cm ⁻¹)	Assignment	Reference(s)
1254	ν _s CF ₃	9,10,19
1377	sulphonamide	15

Separator sample

Figure 3.4.19 presents comparative spectra from an alternative method of sampling the cycled lithium surface. It was noted when dismantling the cells that a significant amount of material would often adhere to the separator surface, particularly when a glass fibre filter paper was used as a separator. The spectrum shown in Fig 3.4.19 was obtained by wiping a

NaCl IR plate with the Li facing surface of the separator. Figure 3.4.20 shows the difference spectrum obtained from the wipe and P₁₃(Tf)₂N, the difference spectra all exhibited the same features regardless of the normalisation peak.

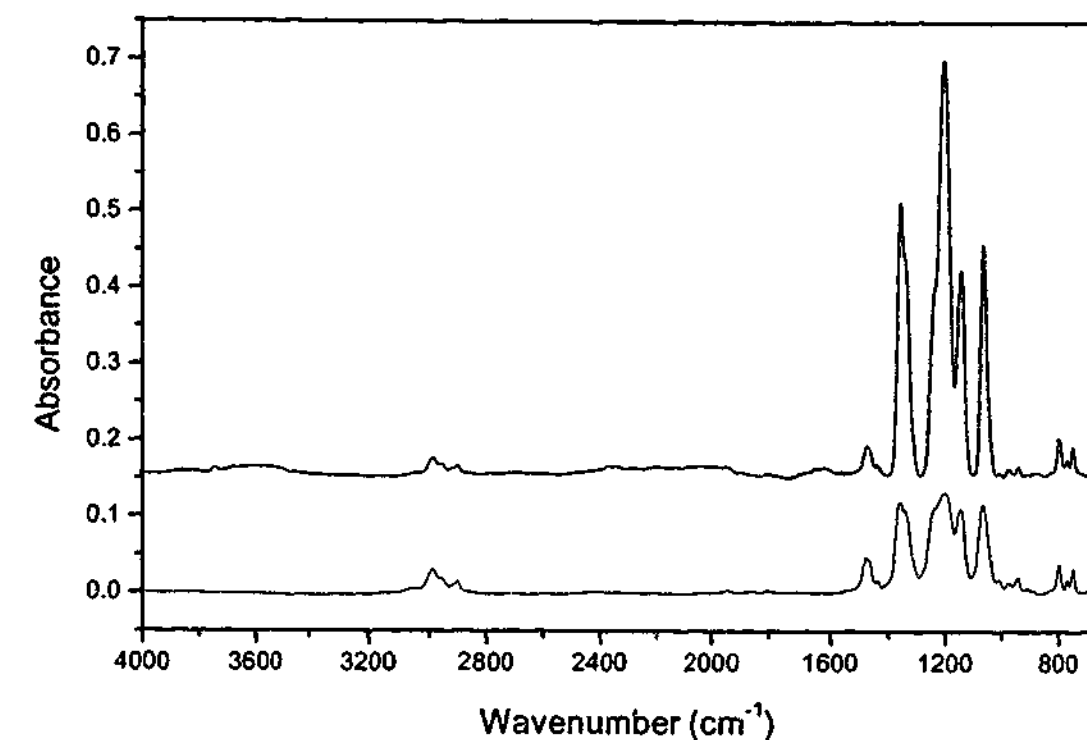


Fig. 3.4.19 Spectra obtained from a separator surface wipe (blue) and uncycled 0.5M P₁₃(Tf)₂N (red).

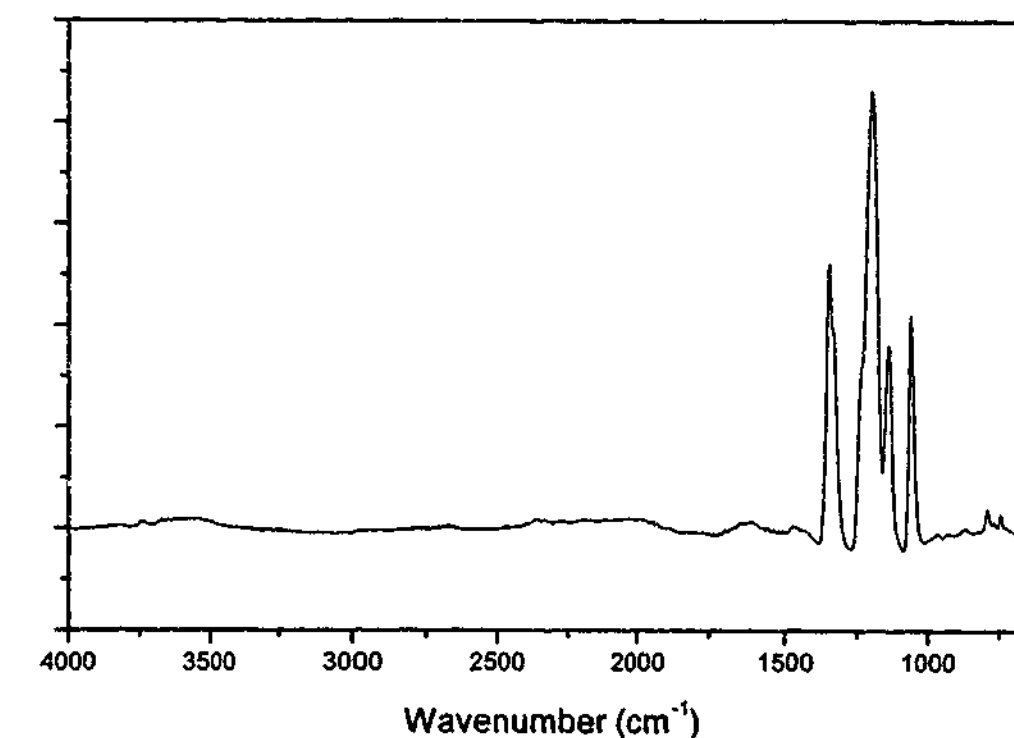


Fig. 3.4.20 Difference spectrum obtained from a separator from a cycled P₁₃(Tf)₂N cell and uncycled P₁₃(Tf)₂N.

Table 3.4.6 Position and assignment for peaks in the difference spectrum for the separator sample.

Pos. Peak (cm ⁻¹)	Assignment	Reference(s)
615	$\delta_s\text{SO}_2$	9,10,19
1060	$\nu_s\text{SO}_2$	21
1135	$\nu_s\text{SO}_2$	9,10,19
1193	$\nu_s\text{CF}_3$	9,10,19
1234	$\nu_s\text{CF}_3$	9,10,19
1331	$\nu_s\text{SO}_2$	9,10,19
1349	$\nu_s\text{SO}_2$	9,10,19

The peak positions and assignments are summarised in Table 3.4.6. The difference spectrum indicates that the sample obtained from the surface of the separator was composed entirely of $\text{P}_{13}(\text{Tf})_2\text{N}$ electrolyte and reduction products of the $(\text{Tf})_2\text{N}^-$ anion. This simple method is more robust because the difference spectrum is generated from two transmission spectra. Whether the sample obtained is representative of the entire SEI is debatable, however, taken with the results from the DRFTIR measurements, clear evidence for the reduction of the $(\text{Tf})_2\text{N}^-$ anion is provided.

Raman Spectroscopy:

An important feature of the optical cell was the ability to acquire in-situ Raman spectra. This enabled the electrolyte composition to be monitored as a function of cycling and allowed spectra to be obtained from the lithium surface. Selected spectra are presented here to support the XPS and FTIR evidence.

Figure 3.4.21 shows normalised Raman spectra obtained from a 1M LiPF_6/PC optical cell in the 300-2400 cm⁻¹ region. The three spectra displayed are that of the bulk electrolyte, the surface of a deposit (i.e., a precipitate, of crystalline appearance and with no sign of metallic lithium – as seen in section 3.1.) and that of the lithium surface. It can be seen that the spectra obtained from the bulk electrolyte and the surface of the deposit do not exhibit any significant differences in this region of the spectrum. However, the spectrum obtained from the lithium surface exhibits several additional features, the difference spectrum (effectively removing the contribution of the electrolyte) is shown in Fig. 3.4.22.

Presumably, the additional peaks are associated with the lithium surface and represent vibrational modes of one or more of the components of the SEI.

The Raman spectrum for Li_2CO_3 has been reported;²³⁻²⁵ peaks were recorded at 711, 748, 1091 and 1459 cm⁻¹. The difference spectrum shown in Figure 3.4.22 has features that indicate the presence of Li_2CO_3 . The formation of lithium alkoxide (ROCO_2Li) components of the SEI in alkyl carbonate electrolytes has been reported by numerous authors.²⁶ Raman peaks at 1015, 1156, 1248, 1390, 1519 and 2130 cm⁻¹ have been reported on the surface of lithium in LiPF_6/PC electrolytes.²³⁻²⁵ The peaks were assigned to ROCO_2Li . Surface enhanced Raman scattering from LiF cluster-based nanofilms has been observed and peaks were reported at 614 and 950-960 cm⁻¹.²⁷ Figure 3.4.22 exhibits features that could be assigned to Li_2CO_3 , LiF and ROCO_2Li as expected from prior literature reports. Recently, a report in the literature dealt with the appearance of the peak at 1850 cm⁻¹ on lithium surfaces.²⁸ The authors demonstrated that the peak was associated with the thermal degradation of Li_2CO_3 (due to local heating of the Li surface by the laser). The peak was assigned to the stretching vibration of the $\text{C}\equiv\text{C}$ bond; evidence was presented which indicated that the species formed was Li_2C_2 .

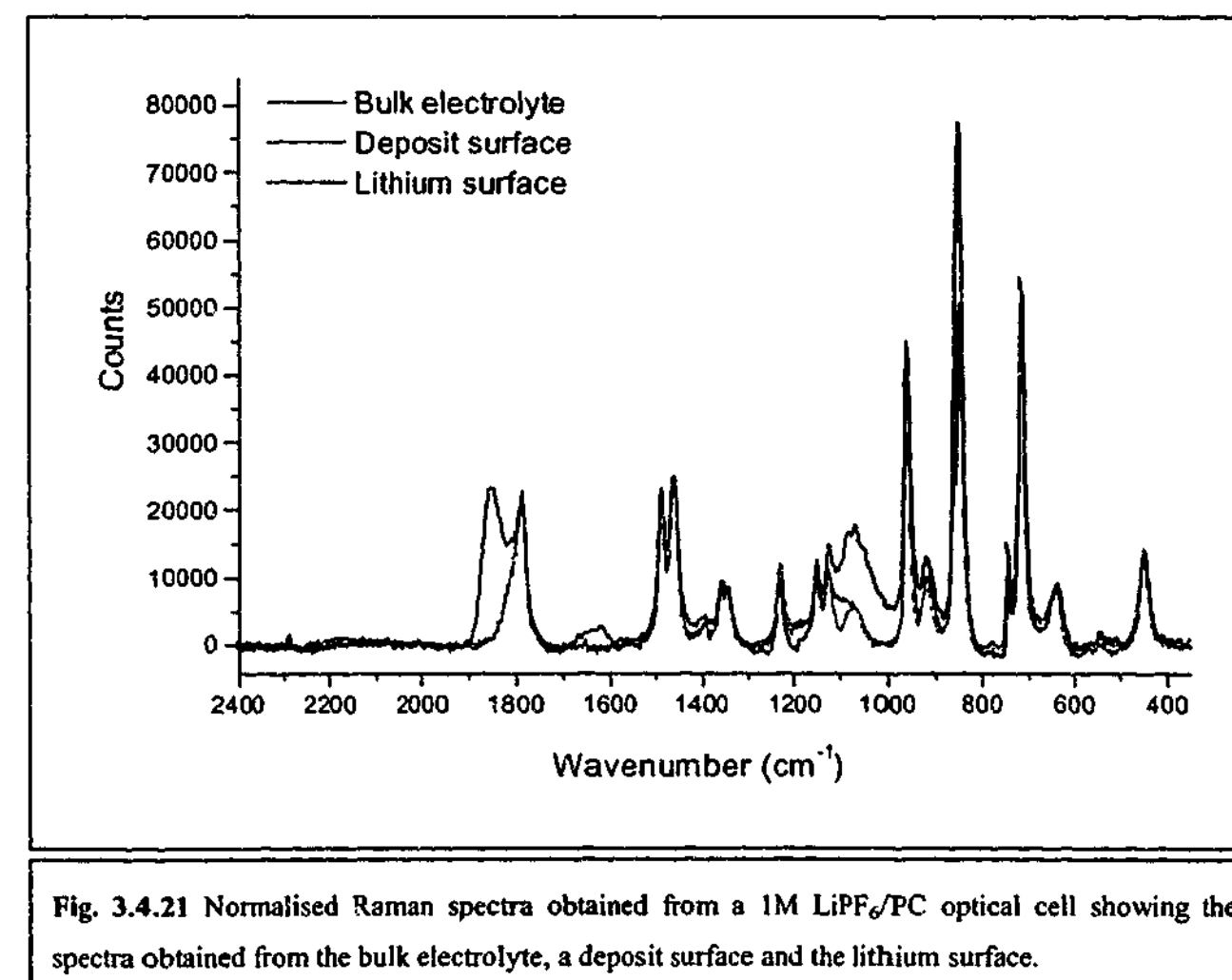


Fig. 3.4.21 Normalised Raman spectra obtained from a 1M LiPF_6/PC optical cell showing the spectra obtained from the bulk electrolyte, a deposit surface and the lithium surface.

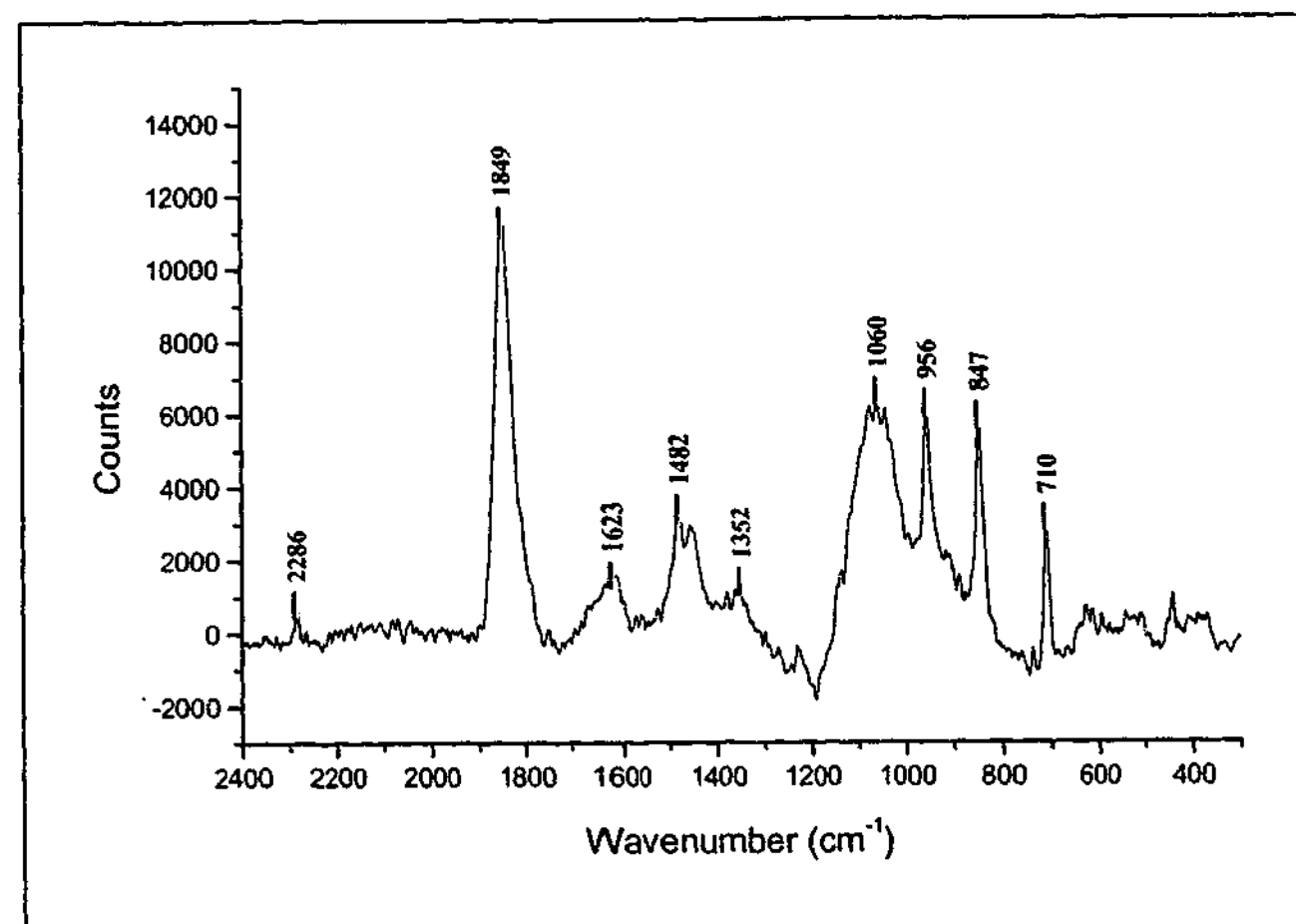


Fig. 3.4.22 Raman difference spectrum obtained for the Li surface, in-situ optical cell measurement.

The spectra shown in Fig. 3.4.23 provide supporting evidence that the peak at 1850 cm^{-1} is associated with the native film formed in the glovebox. Referring to the GAXRD experiments presented previously (section 3.4.2) the lithium surface exposed to air rapidly reacts to form LiOH, before less rapid conversion to Li_2CO_3 . The spectra acquired after exposure to air (exposed 1) show a reduction in the intensity of the peak at 1850 cm^{-1} followed by an increase in intensity after 20 minutes (exposed 2). This suggests that the peak is due to the presence of Li_2CO_3 , in agreement with the results of Naudin *et al.*²⁸

Figure 3.4.24 shows in-situ Raman spectra acquired from $0.5\text{ mol kg}^{-1}\text{ P}_{13}(\text{Tf})_2\text{N}$ optical cells before and after cycling. There are no major discernible differences in the spectra indicating that significant chemical changes to the electrolyte composition had not occurred. Slight differences in the peaks at ~ 300 and 500 cm^{-1} are likely to be artefacts due to a sloping baseline at low wavenumbers.

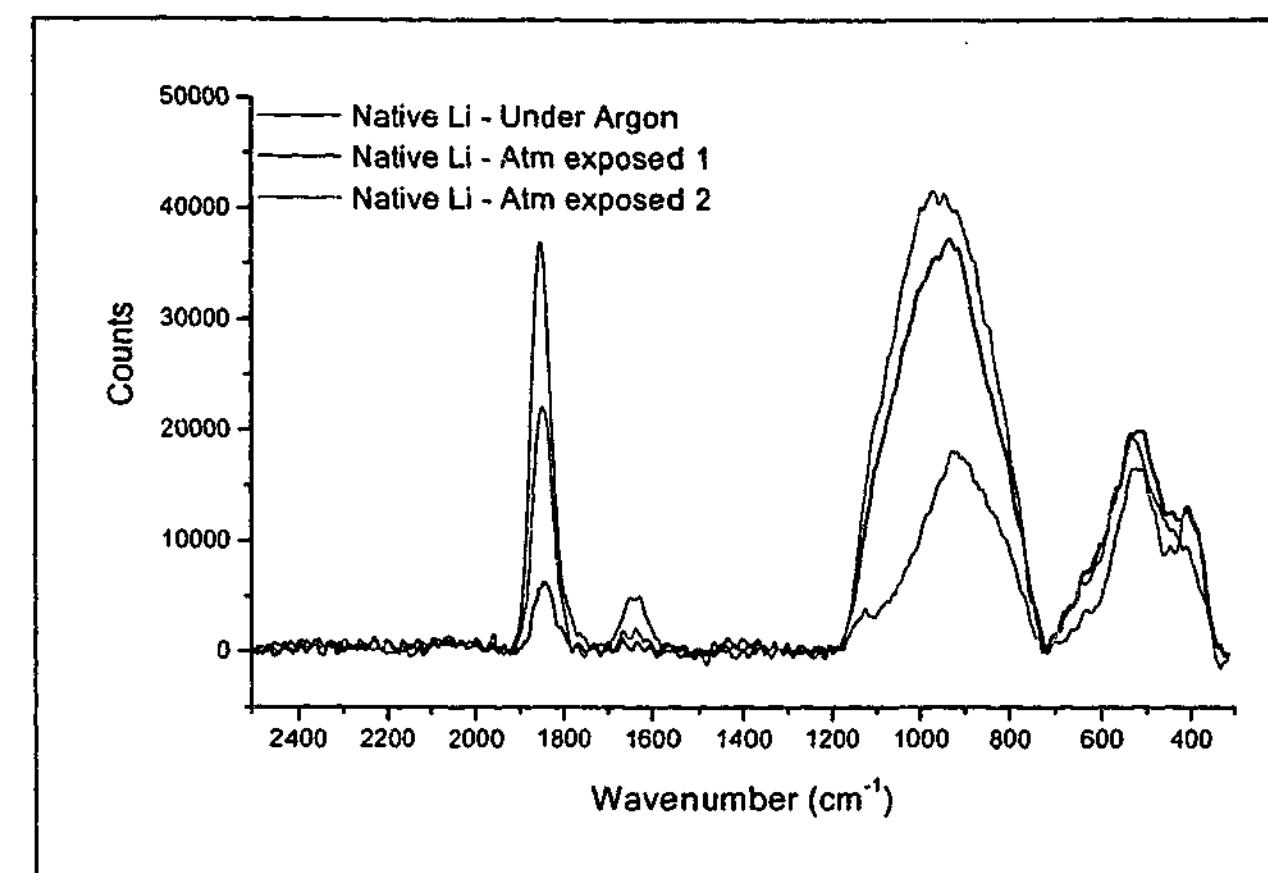


Fig. 3.4.23 Raman spectra of the lithium surface 'native glovebox film', (acquired using the bolt cell) before and after exposure to the atmosphere.

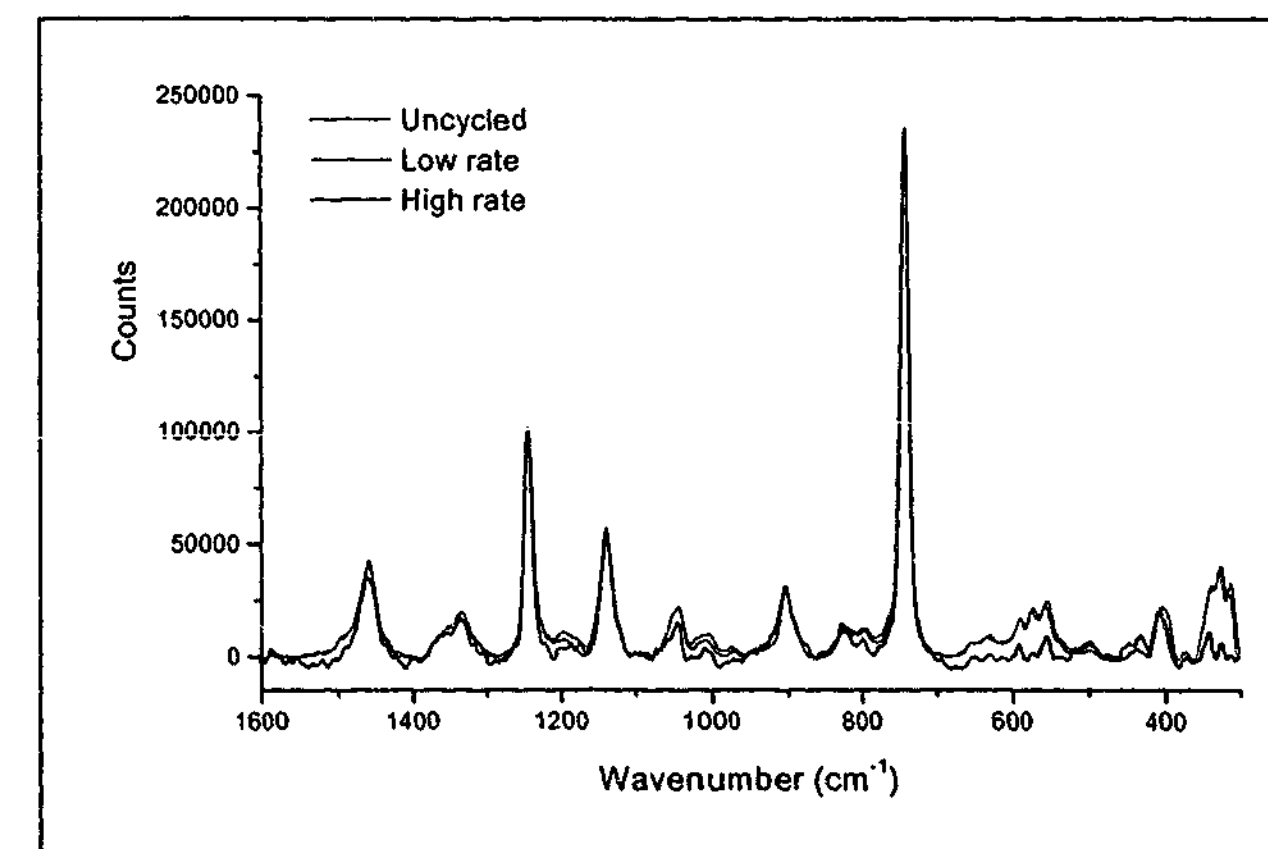


Fig. 3.4.24 Normalised Raman spectra obtained from a $0.5\text{ mol kg}^{-1}\text{ P}_{13}(\text{Tf})_2\text{N}$ optical cell showing the spectra obtained from the uncycled bulk electrolyte, after cycling at low rate (potentiostatic) and after cycling at high rates ($\sim 2\text{ mA cm}^{-2}$).

Figure 3.4.25 presents in-situ Raman spectra acquired from a cycled $0.5 \text{ mol kg}^{-1} \text{ P}_{13}(\text{Tf})_2\text{N}$ optical cell. Spectra were acquired from the cycled lithium surface (Li), a dendrite deposited on Cu (Li-Cu) and from bulk electrolyte. The difference spectrum for the Li surface and for the Li-Cu surface is shown in Fig. 3.4.26 and Fig. 3.4.27 respectively. The prominent peaks and their tentative assignments are given in Table 3.4.7 and 3.4.8 respectively.

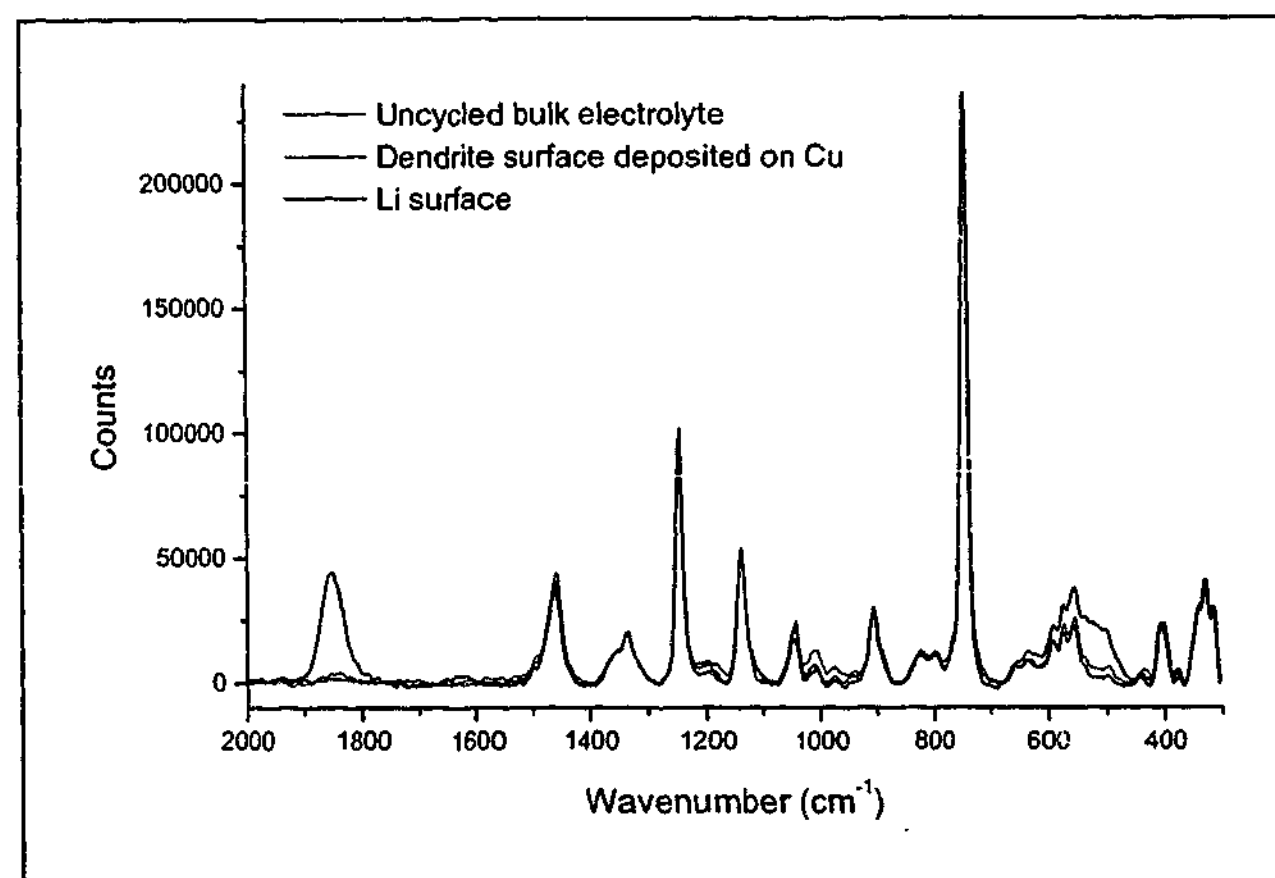


Fig. 3.4.25 Normalised Raman spectra obtained from a $0.5 \text{ mol kg}^{-1} \text{ P}_{13}(\text{Tf})_2\text{N}$ optical cell showing the spectra obtained from the uncycled bulk electrolyte, from the surface of a dendrite (Li-Cu) and from the Li surface.

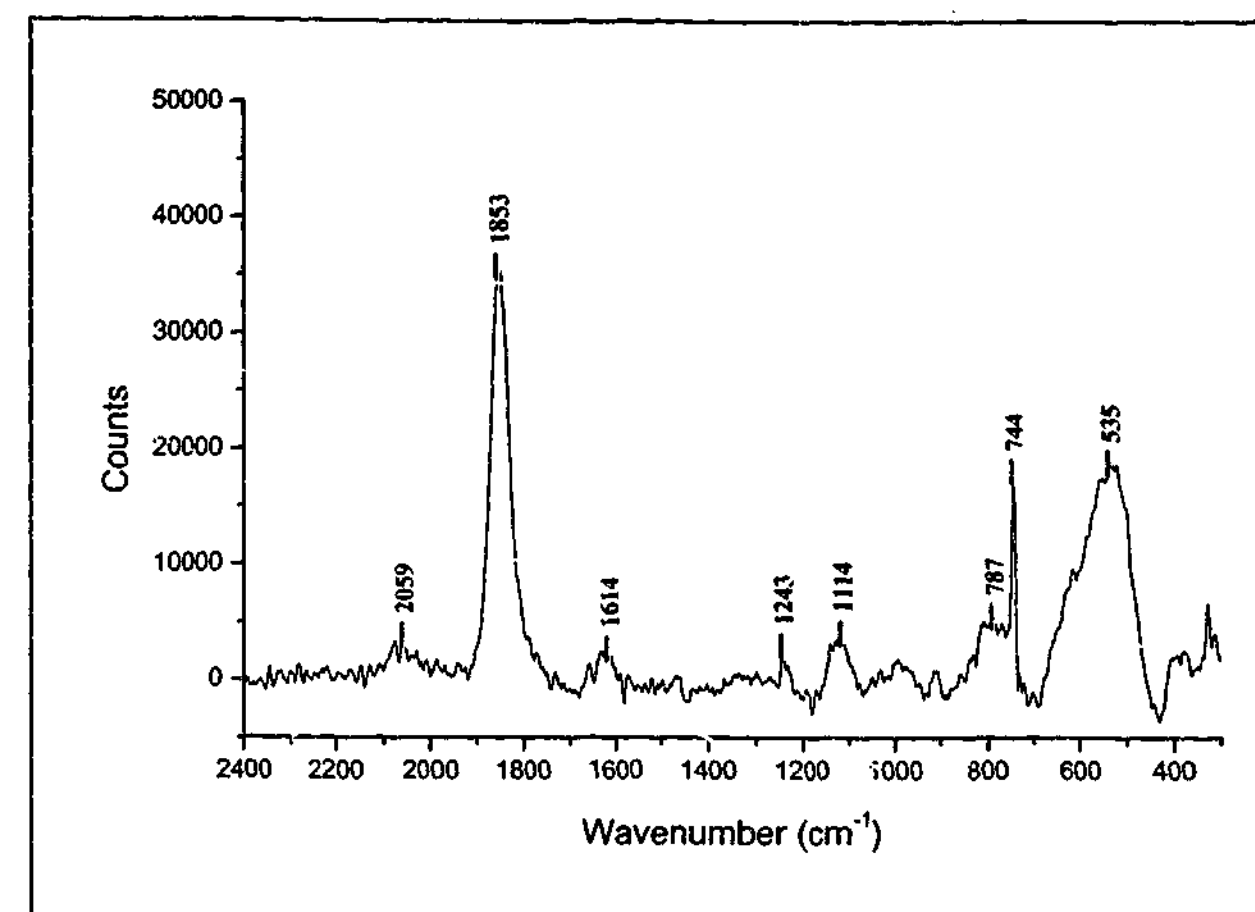


Fig. 3.4.26 $0.5 \text{ mol kg}^{-1} \text{ P}_{13}(\text{Tf})_2\text{N}$ optical cell Li surface difference spectrum.

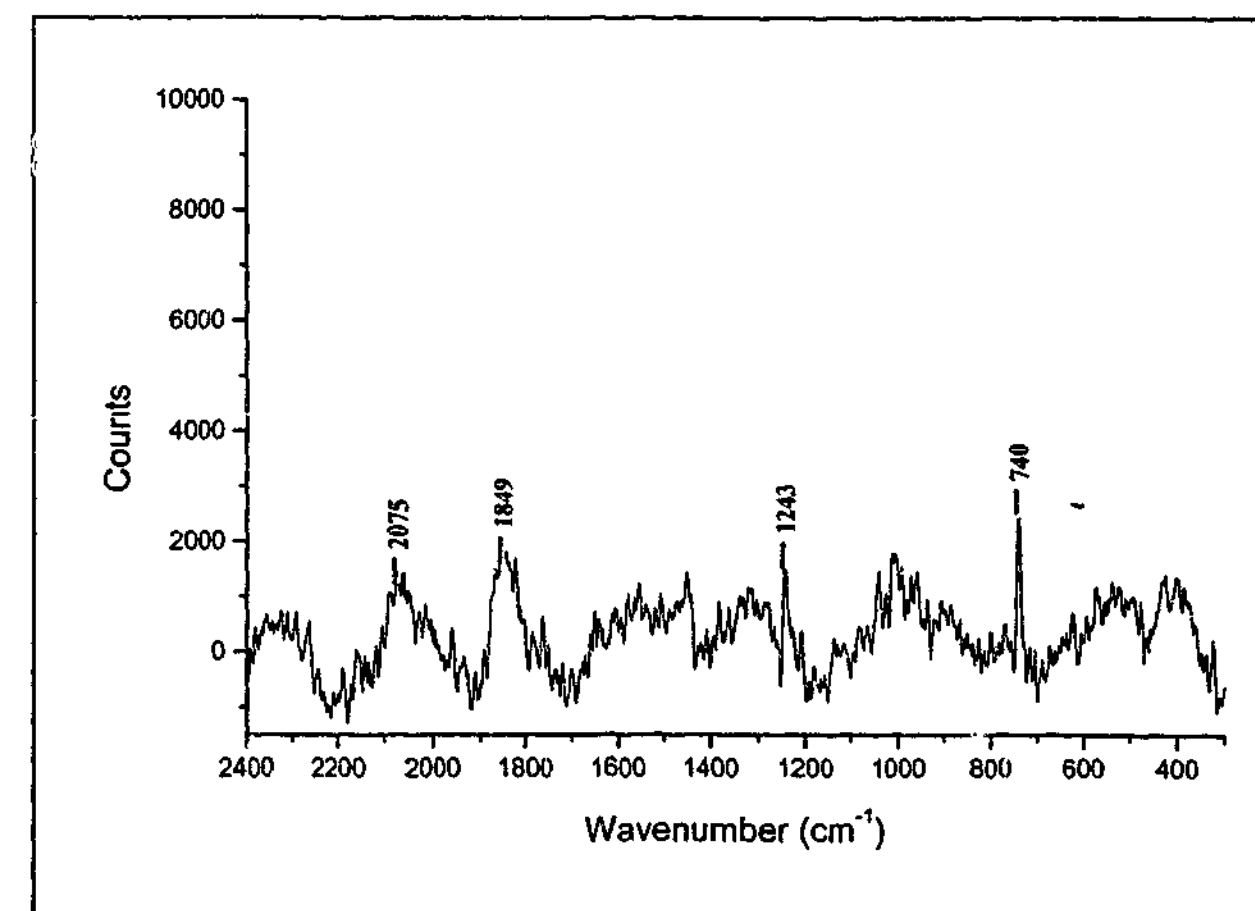


Fig. 3.4.27 $0.5 \text{ mol kg}^{-1} \text{ P}_{13}(\text{Tf})_2\text{N}$ optical cell dendrite (Li-Cu) surface difference spectrum.

Table 3.4.7 Prominent peaks and tentative assignments for the Li surface difference spectrum.

Pos. Peak (cm ⁻¹)	Assignment	Reference(s)
535	Li ₂ O (IR)	16,29
744	δ_s CF ₃	10,12,13
787	CF ₃ , C-S, S-O etc.	9
1114		
1243	τ CH ₂ , ν_s CF ₃	11
1614	Amide, C=C	15
1853	ν C \equiv C	28
2059	Cyano (?)	9,10,19

Table 3.4.8 Prominent peaks and tentative assignments for the Li-Cu surface difference spectrum.

Pos. Peak (cm ⁻¹)	Assignment	Reference(s)
740	δ_s CF ₃	10,12,13
1243	τ CH ₂ , ν_s CF ₃	11
1849	ν C \equiv C	28
2075	Cyano (?)	9,10,19

The Li surface difference spectrum exhibits some peaks that could be associated with (Tf)₂N⁻ reduction products as well as a broad peak at 535 cm⁻¹ that IR studies have reported to arise from Li₂O. The most prominent feature is the familiar peak at 1853 cm⁻¹, related to Li₂CO₃. The Li-Cu difference spectrum is virtually featureless; the sharp peaks at 740 and 1243 cm⁻¹ are likely to be due to band shifts in the peak position due to interactions with the lithium surface. The peak at 1849 cm⁻¹ is very weak by comparison. This supports the assertion that the composition of the Li and Li-Cu surface films are significantly different, and that the differences arise from the presence of native film species persisting on the Li surface.

3.4.4 Electrochemical impedance spectroscopy (EIS):

Fitting:

Electrochemical impedance spectroscopy (EIS) can be used to gain information about the electrical properties of the surface film formed in lithium cells. Figures 3.4.28, 3.4.29 and 3.4.30 show fitted impedance spectra for a cycled symmetrical lithium cell using a 0.5 molkg⁻¹ P₁₃(Tf)₂N electrolyte. The error for each fit is included in the figure.

The models used to fit the data were taken from the literature:

- The polymer electrolyte interphase (PEI) model, proposed by Thevenin and Muller,³⁰ corresponds to a compact mixture of polymeric and inorganic compounds with the properties of a polymer electrolyte. The equivalent circuit is determined by three impedances:
 - (i) The conduction impedance defined by the bulk resistance R_b and the geometric capacitance C₁ (or CPE₁).
 - (ii) The charge transfer impedance represented by the charge transfer resistance and the double layer capacitance C_{dl} (or CPE_{dl})
 - (iii) The diffusion impedance Z_d determined by the finite thickness of the diffusion layer.
- The layer model, which was proposed and applied extensively by Aurbach *et al.*^{26,31,32} The model corresponds to a layered structure where the impedance is dominated by the diffusion of lithium ions through each discrete layer. The layers possess different physicochemical properties and are represented by discrete RC elements in series.

Fig. 3.4.28a shows a simple circuit employing constant phase elements. The constant phase elements are used, in this case, to account for the departure from ideality of the capacitance behaviour of the interface. Distributed elements, in this case a constant phase element, are often used to describe real systems where the microscopic material properties are themselves distributed. For example, a solid electrode | solid electrolyte interface may have defects such as kinks, jags, ledges, local charge inhomogeneities, two and three-phase

regions, adsorbed species, and variations in composition and stoichiometry.³³ Thus, reaction resistance and capacitance differ with position and vary over a certain range around a mean, but only their average effects over the entire electrode surface can be observed, resulting in a distributed response. Microscopically smooth liquid metal-aqueous interfaces do not show dispersion.³³ In addition, a distribution of relaxation times has been suggested as the origin of the CPE response that is often seen in impedance studies of solid electrolytes and the solid-solid interface. In disordered solids, frequency dependent transport is expected to be of the form exhibited by a CPE if certain statistical properties of the distribution functions associated with time and distance (i.e., of ion hopping) are fulfilled.³³ Fig. 3.4.28b & c employs circuits provided in the literature based on the polymer electrolyte interphase (PEI) model.⁵⁰ The models have been modified to include a constant phase element to improve the fit.

Figures 3.4.29 and 3.4.30 show variations on the layer model proposed and applied extensively by Aurbach *et al.*^{26,31,32} Constant phase elements are used to improve the fit of the low frequency arc (of the Nyquist plot). Figure 3.4.29c differs from 3.4.29b in that the value for the electrolyte resistance (R_e) was set at 4.5 Ω .

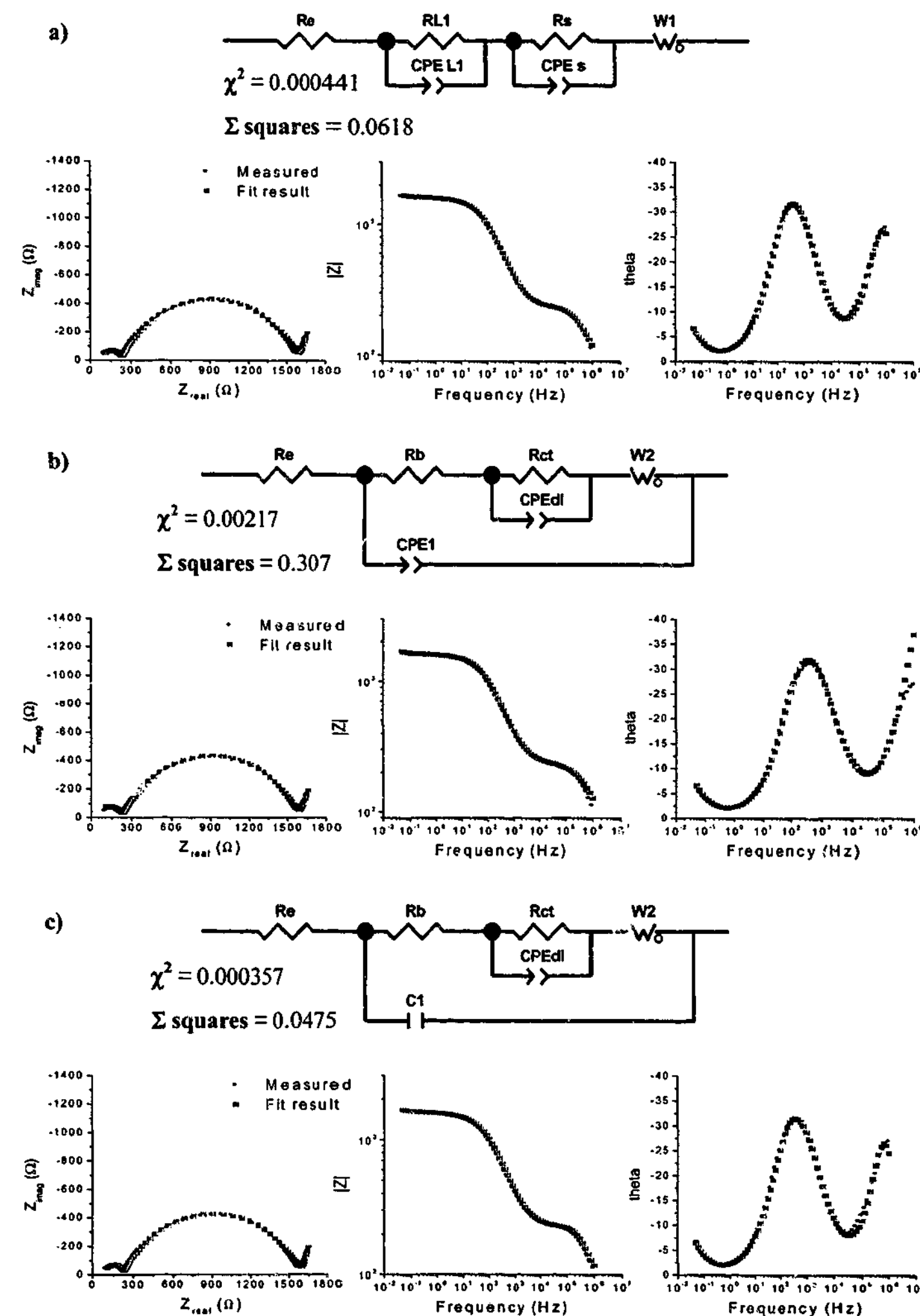


Fig. 3.4.28 Fitted impedance data for a cycled Li/0.5 mol kg⁻¹ P₁₃(Tf)₂N/Li cell a) simple model b) PEI model A c) PEI model B.

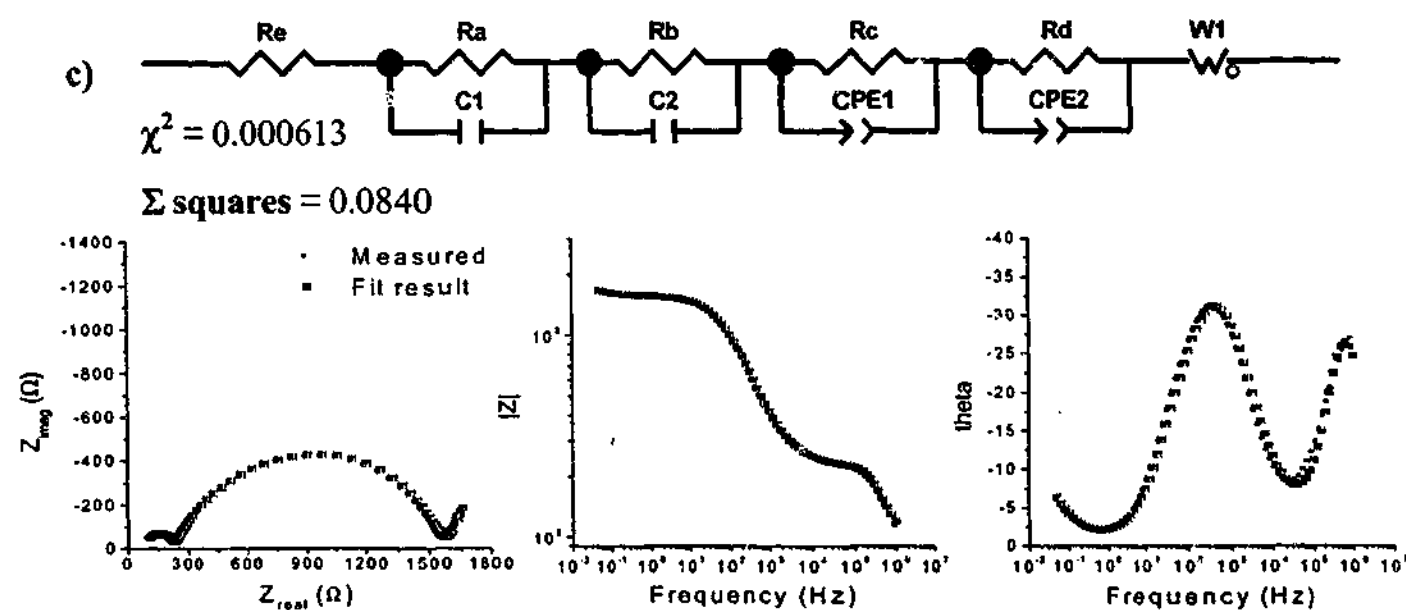
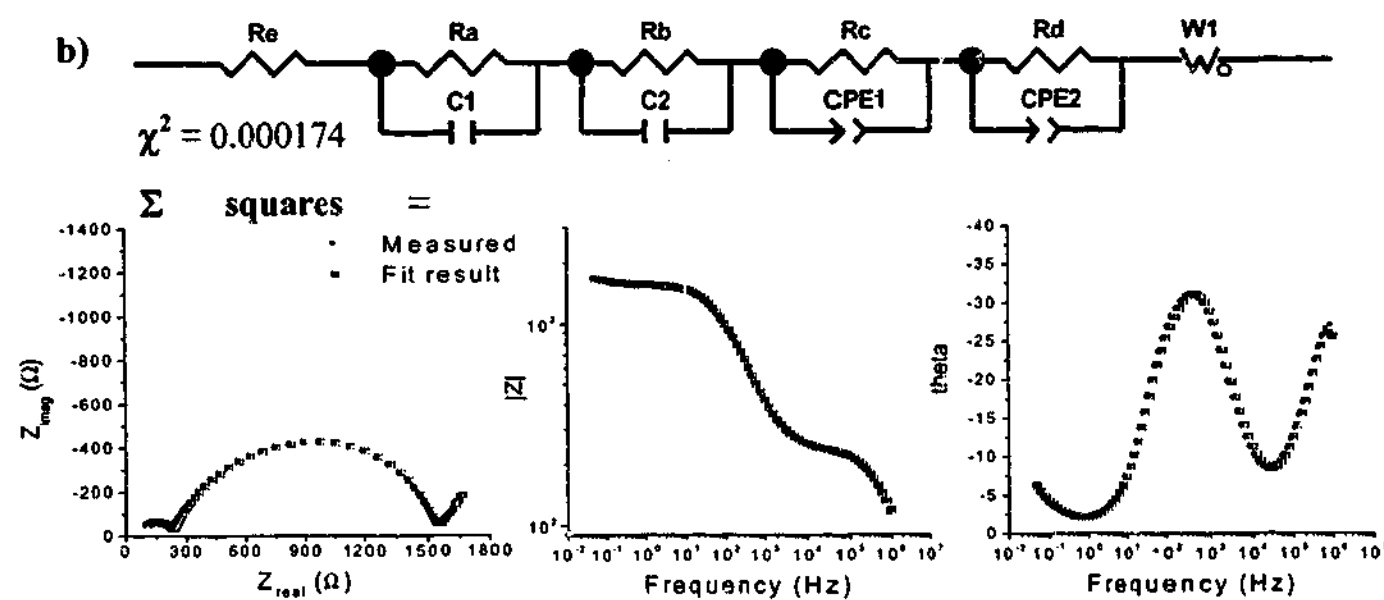
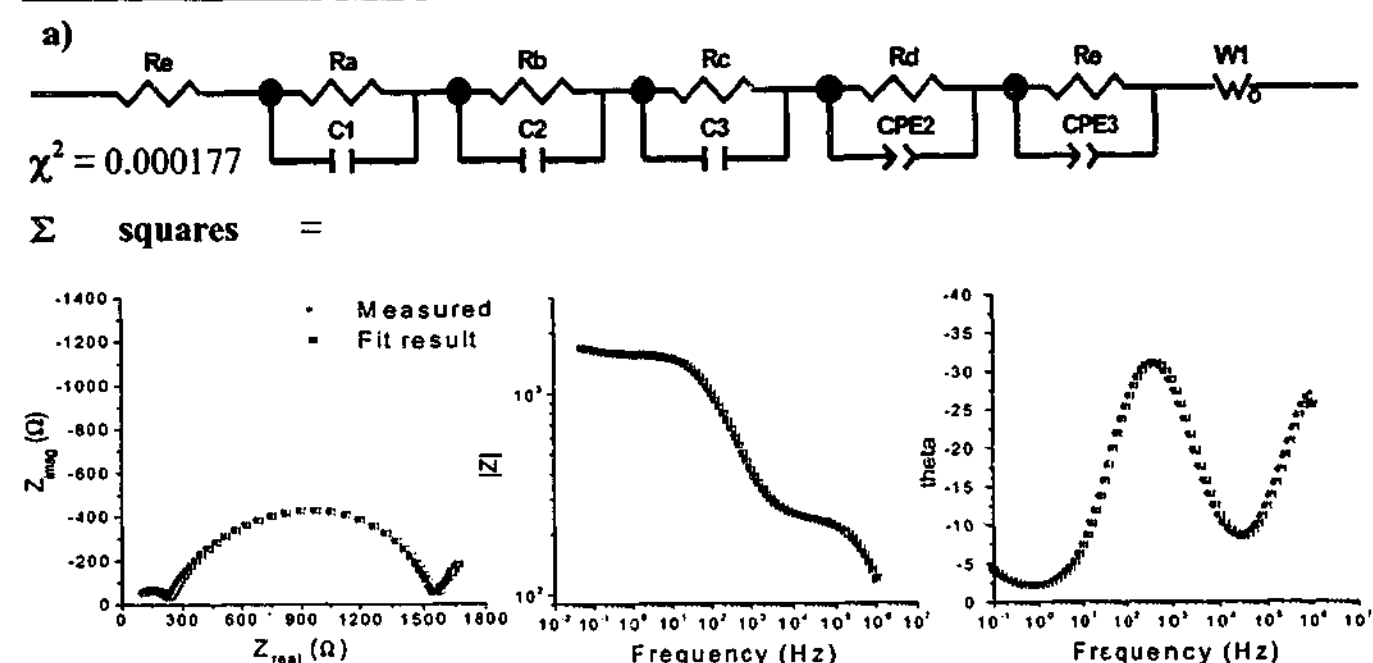


Fig. 3.4.29 Fitted impedance data for a cycled $\text{Li}/0.5 \text{ mol kg}^{-1} \text{ P}_{13}(\text{Tf})_2\text{N}/\text{Li}$ cell a) 5 element layer model b) 4 element layer model c) 4 element layer model (locked).

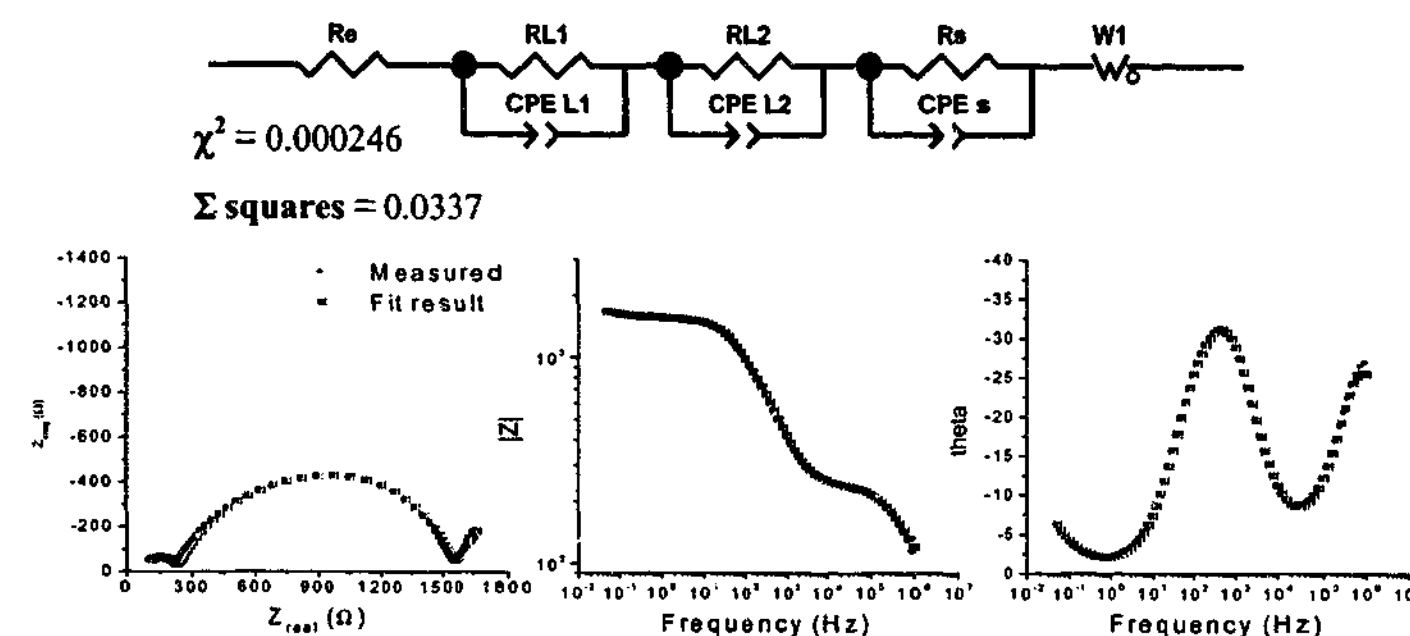


Fig. 3.4.30 Fitted impedance data for a cycled $\text{Li}/0.5 \text{ mol kg}^{-1} \text{ P}_{13}(\text{Tf})_2\text{N}/\text{Li}$ cell, 3 element layer model.

Generally, all of the equivalent circuits were able to fit the data reasonably well. Data recorded at high frequencies was subject to significant induction currents; rendering the points recorded above 1 MHz meaningless. The data between 100 KHz and 1 MHz is also likely to be compromised. The majority of the error in the fits arose from contributions from fitting the high frequency data. From this perspective, it is difficult to assert the superiority of one model over another. Hence, in this case using a model to derive a picture of the physical structure of the SEI is questionable. In the literature, there has been some contention about the contribution of the charge transfer resistance (R_{ct}) to the impedance response of the lithium electrode.³⁴ Aurbach²⁶ has asserted that the contribution from R_{ct} is negligible, based on potentiodynamic measurements using microelectrodes to obtain exchange current densities³⁵⁻³⁹ (e.g., 32 mA cm^{-2} for $1 \text{ M LiClO}_4/\text{PC}^{40}$), in addition Aurbach asserts that the PEI model is too simplified. Based on these arguments, it seems unlikely that the charge transfer resistance will play a significant role in charge transport to the lithium surface in $\text{P}_{13}(\text{Tf})_2\text{N}$ electrolytes, particularly in comparison to the resistive process observed at low frequencies.

The best fits were obtained for the layer models, particularly the 4-element circuit (Fig. 3.4.29b & c) and for the 3-element model employing constant phase elements. The five element equivalent circuit (Fig. 3.4.29a) did not show any improvement over the 4-element circuit. Equivalent circuits of this type suggest a film in which the conduction process is

composed of distinct time constants. The use of CPEs to describe the low frequency arc suggests a homogeneous dispersion of time constants,³³ indicating a complex composition where varied conduction pathways exist in parallel. The ability to fit the high frequency arc with a resistance/capacitance (RC) type circuit elements suggests a structure which has distinct elements (or layers), perpendicular to the electrode surface.³² A layer model is attractive because it agrees with evidence suggesting the formation of surface films comprised of inner compact and outer diffuse layers.⁴¹

The contribution from induction currents at high frequency prevents adequate modeling of the electrode response above 1 MHz. However, by using the conductivity values presented in section 3.3.2, and accounting for the cell geometry and separator tortuosity it is possible to estimate the resistance contribution of the electrolyte (R_e). Values of approximately 4.5 Ω at 25 °C are obtained, which is negligible compared to the resistance contribution of the high frequency arc (~225 Ω). Setting the value of R_e to 4.5 Ω resulted in the best fit being obtained by the 4-element layer model, providing additional support for this model.

Considering the impedance plot in general terms, it is apparent that the bulk of the cell resistance arises from the process corresponding to the low frequency arc (~1425 Ω). By comparison, the contribution for the high frequency arc and the electrolyte resistance is trivial. By using the capacitance values obtained for each arc, it is possible to estimate the thickness of each layer according to equation 3.4.1;

$$l = \frac{\epsilon_o K A}{C} \quad (3.4.1)$$

where ϵ_o is the dielectric constant for vacuum, K is the films' dielectric constant, C is its capacitance, and A is the electrode geometric area.²⁶ The real capacitance (C_i) for a CPE can be calculated from equation 3.4.2;⁴²

$$C_i = R_i^{(1-n)/n} Y_i^{1/n} \quad (3.4.2)$$

where R_i is the resistance described by the arc and Y_i is a pseudocapacitance. The capacitance for the high frequency arc was of the order of 5×10^{-8} F, and the low frequency arc was 5×10^{-7} F. Assuming a value of 5 for K for the high frequency arc

(based on Li_2O , LiF etc.)³² and a value of 10 for K for the low frequency arc (based on ϵ ranging from 5-20 for most materials)⁴² and a geometric area of 2cm^2 for the electrode area, the film thickness can be estimated. These capacitance values reflect a layer ~180 nm thick for the high frequency arc and ~40 nm thick for the low frequency arc.

The resistivity for each arc can be calculated from equation 3.4.3;

$$\rho = \frac{RA}{l} \quad (3.4.3)$$

where ρ is the resistivity and R is the diameter of each of the semicircles in the Nyquist plot (e.g., Fig 3.4.28). The low frequency arc corresponds to a calculated resistivity of $2.6 \times 10^7 \Omega\text{cm}$ and the high frequency to $7.4 \times 10^8 \Omega\text{cm}$ (both at 25 °C). These values are comparable with those published for compact surface films formed in alkyl carbonates and ethers.²⁶

$\text{P}_{13}(\text{Tf})_2\text{N}$ – EIS vs. temperature:

A structure composed of discrete layers, which are related to time constants represented by the elements of the equivalent circuit, should show varied response to temperature changes according to the physical properties of the individual layers. Measuring the impedance response of a cell at varied temperatures allows Arrhenius plots of resistance versus temperature to be constructed and, hence, determination of activation energies for each of the time constants corresponding to the high frequency and low frequency arcs in the Nyquist plot.

Figures 3.4.31 and 3.4.32 presents Arrhenius plots obtained from a cycled $\text{P}_{13}(\text{Tf})_2\text{N}$ cell for the high frequency and low frequency arcs respectively. The plots indicate that Li^+ transport through the surface film occurs by at least two distinct conduction mechanisms, reflected by activation energies for conduction of 45 kJmol^{-1} and 60 kJmol^{-1} . It was not possible to resolve the high frequency arc into its individual RC components because the influence of the induction currents extended to lower frequencies as the temperature was increased. However, it was possible to estimate the resistance of the high frequency arc

from its low frequency touchdown and from the electrolyte resistance (section 3.3.2) as described earlier. Thus, it is likely that the activation energy of the low frequency arc is an average of those derived from two or more time constants. The low frequency arc could not be resolved into its individual elements, rather the component resistances altered randomly to allow the best fit; this is further indication of a phase where the time constants are dispersed homogeneously. The calculated capacitances for each arc remained relatively constant over the temperature range.

The presence of distinct conduction mechanisms has been rationalised by Aurbach *et al.*^{26,31,32} in terms of the layer model, which was applied extensively to alkyl carbonate and ether electrolytes with varying lithium salts. The SEI was viewed as a multi-layer structure, comprised of an inner compact interphase and an outer diffuse interphase. The compact interphase was composed of several distinct layers, which were found to exhibit distinct physicochemical properties. The inner layers of the compact interphase, which corresponded to the high frequency part of the Nyquist plot, were found to be thickest, to have the lowest resistivity and to exhibit a low activation energy for conduction. Layers further from the lithium surface, and closer to the solution side, were thinner, more resistive and had higher activation energies for conduction. The properties of the layers were discussed in terms of their proximity to the reactive lithium surface; the inner layers are formed rapidly under less selective conditions and are expected to be composed of species with less complex chemical structures (i.e., Li_2O , LiF etc.). These conditions produce a layer that is expected to be the most conductive because it has the greatest amount of defects present in its structure (due to the less selective formation conditions). By the same reasoning, the activation energy for conduction is also expected to be low. The factors that facilitate Li^+ migration through the film (e.g., defects) are also expected to facilitate electron transfer,³² thus the layer which is the most disordered should also be the thickest. The outer layers form under more selective conditions and are expected to be composed of species with more complex chemical structures. The outer layers are expected to be more homogeneous, and are also expected to exhibit higher activation energies.^{31,32}

All of the above observations agree well with the results presented here for the lithium surface in the RTIL. The calculated film thickness in the RTIL appears to be greater than those reported in the literature, which range from 10-100 nm.⁴³ The other distinct difference between the data presented here seems to be the absence of the porous outer

layer, which has been characterised by high capacitance (as a result of its high surface area), high resistivity ($>10^{10} \Omega\text{cm}$) and low activation energy. The outer layer in the RTIL (corresponding to the low frequency arc), while being highly resistive, exhibits high activation energy.

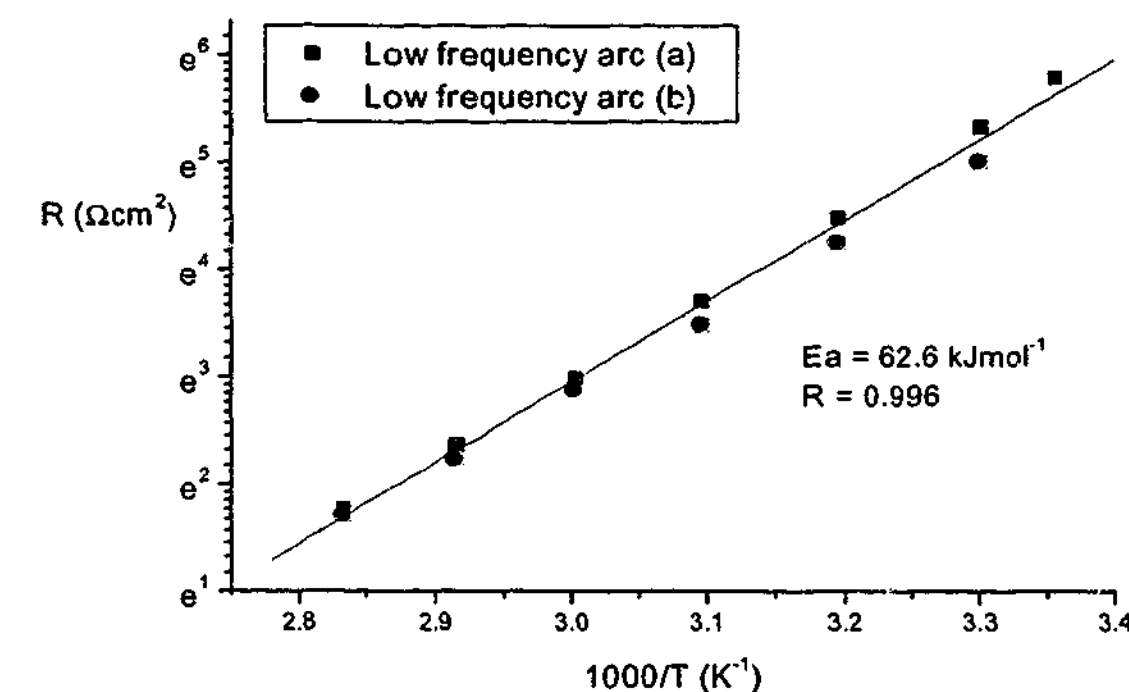


Fig. 3.4.31 Arrhenius plot of the low frequency arc resistance versus temperature for a cycled $\text{Li}/0.5 \text{ mol kg}^{-1} \text{ P}_{13}(\text{Tf})_2\text{N}/\text{Li}$ cell a) temperature increasing b) temperature decreasing.

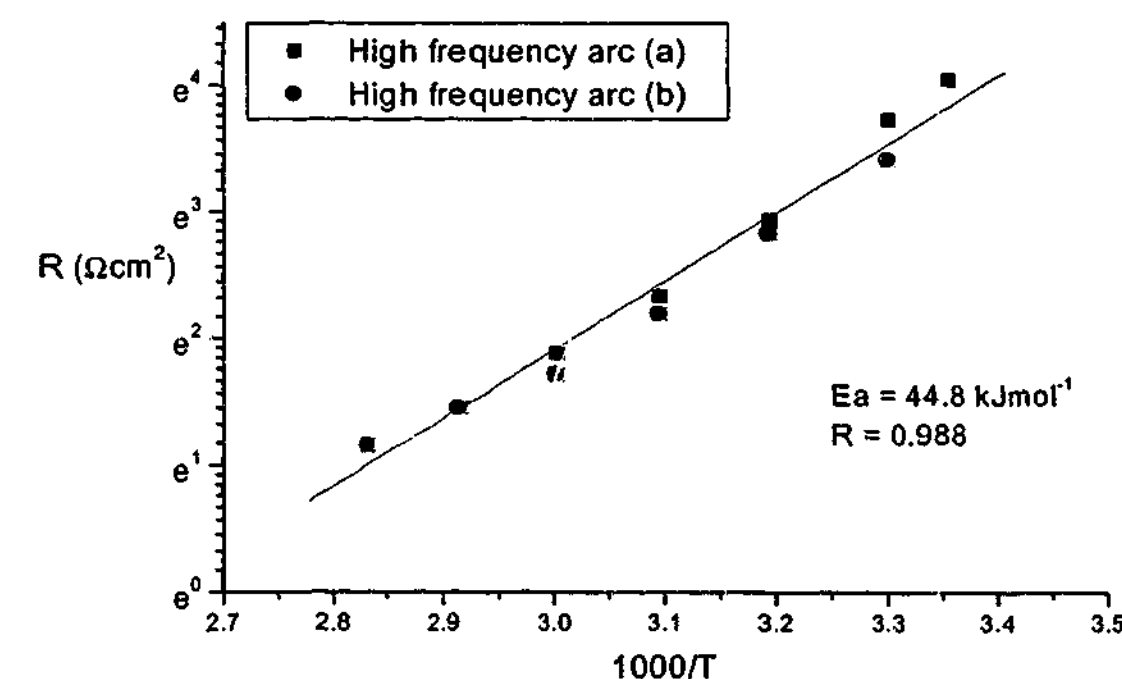


Fig. 3.4.32 Arrhenius plot of the high frequency arc resistance versus temperature for a cycled $\text{Li}/0.5 \text{ mol kg}^{-1} \text{ P}_{13}(\text{Tf})_2\text{N}/\text{Li}$ cell a) temperature increasing b) temperature decreasing.

Figure 3.4.33 shows a plot of the low frequency touchdown resistance versus time for a cycled symmetrical lithium cell using a $P_{13}(\text{Tf})_2\text{N}$ electrolyte. The interfacial resistance reached a stable value and did not change significantly over a period of two months. This indicates a stable interface and should translate to a charged cell where self-discharge (of the negative electrode) is not significant. The stability of the interfacial resistance is indicative of an absence of electrolyte reactions and buildup of the passivation film. This reflects a film that is sufficiently passivating to protect the lithium surface from further reaction.

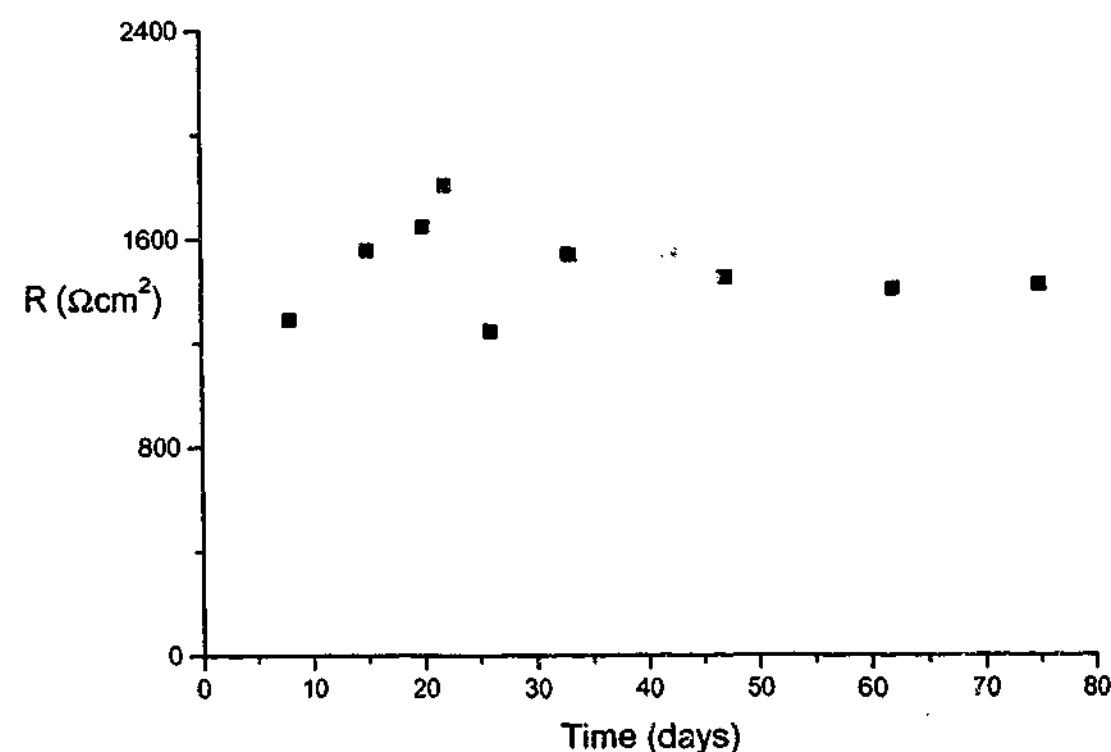
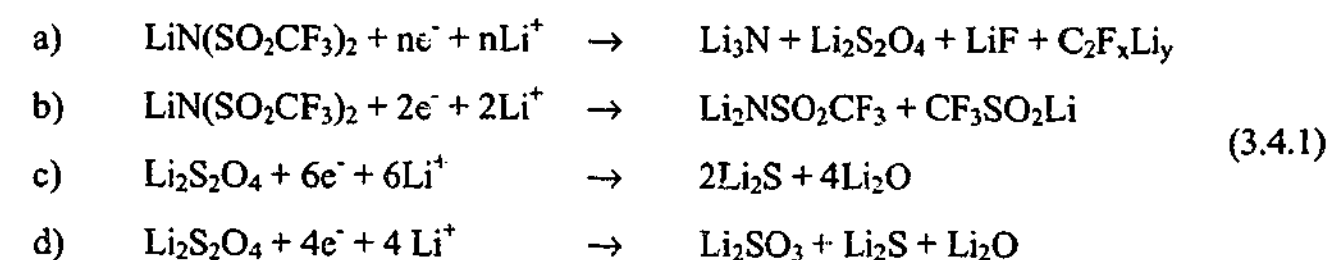


Fig. 3.4.33 Plot of the low frequency touchdown resistance versus time for a cycled Li/0.5 molkg⁻¹ $P_{13}(\text{Tf})_2\text{N}$ /Li cell.

3.4.5 Conclusions:

The SEI formed on the lithium electrode in a $P_{13}(\text{Tf})_2\text{N}$ electrolyte was characterised using XPS, GAXRD, FTIR, Raman and EIS techniques. Each technique contributed to the understanding of the composition and structure of the SEI.

The SEI was found to be composed of reduction products of the anion. Reduction patterns for the $(\text{Tf})_2\text{N}^-$ anion on Li have been proposed in the literature and are presented in Scheme 3.4.1;²⁶



The evidence provided by XPS, FTIR and Raman spectroscopy strongly supports the presence of the products presented in scheme 3.4.1.

A pronounced difference in composition was observed between the SEI formed on the lithium surface and that formed in-situ during deposition. This had been expected from differences observed in the cycling properties and deposit morphologies exhibited in the optical cells (Section 3.1.1 and 3.1.2). The native species present on the lithium surface appeared to persist in the SEI and to dominate the SEI composition. The surface film formed on the lithium deposit did not contain species associated with the lithium native film. Instead, significant quantities of species associated with the cation were observed. The role of the cation in the formation of the SEI is not clear from the results. Some evidence of reduced species of the cation was indicated by the FTIR measurements but the results were not conclusive.

The cation could be present in the surface film, trapped within the crystal structure of the anion reduction products. Alternatively, the cation could precipitate as solid P_{13} salts of the reduction products of the anion. Kariv-Miller *et al.*^{44,45} studied the reduction of quaternary ammonium cations on the surface of metals and reported the formation of metastable metal

amalgams (Sn, Bi, Pb, Hg & Sb). The amalgams were typically electrochemically reversible. The formation of a $P_{1X}(Li)_y$ amalgam should also be considered.

The difference in the composition of the films (Li & Li-Cu) can be rationalised by considering the conditions under which they were formed;

1. The Li surface was usually allowed to equilibrate for 24 hrs prior to cycling. Under these conditions, it appears that the passivating film already present on the lithium prevented any reduction/incorporation of the cation. The cation is unlikely to react, being stable at the lithium potential. Instead the $(Tf)_2N^-$ anion reacted, forming a protective film composed entirely of native film plus anion reduction products.
2. The Li-Cu surface was formed under more extreme conditions, the potential being at the lithium potential plus the overpotential necessary to maintain the current density. Under these conditions, reduction of the P_{1X}^+ cation is possible, although not definite. The $(Tf)_2N^-$ anion will definitely be reduced, commencing at approximately +1.5V vs. Li/Li^+ .²⁶ In addition, the concentration of P_{1X}^+ at the electrode surface will be high, because of electrostatic attraction. Thus, the formation of a film comprised of $(Tf)_2N^-$ reduction products with either reduced or entrapped P_{1X}^+ species is more likely on the copper surface. The rate of lithium deposition is likely to have a pronounced effect on the composition and structure of the film.

GAXRD indicated a highly crystalline component of the SEI, as well as the presence of amorphous species (possibly the RTIL). The crystalline component was not a known phase.

EIS indicated varied lithium conduction pathways through the film. Equivalent circuit modelling indicated that the pathways were in series and suggested a layered structure. Calculated activation energies, resistivity and thickness values were comparable to literature values and indicated that the layered structure became progressively more conductive (i.e., more disordered) close to the lithium surface.

Combining the information gathered from the different techniques allows the construction of a general model for the structure of the SEI formed on the Li and Li-Cu surface; the

models are shown in Fig. 3.4.34. The different techniques complemented one another well, providing a more detailed picture of the SEI structure and properties. Furthermore, the various techniques did not show any significant inconsistencies, thus providing supporting evidence for one another.

The simplified models shown in Fig. 3.4.34 highlight the principal differences between the Li and Li-Cu SEIs. The models indicate a layered structure, based on XPS and EIS evidence, and the relative thickness of each layer is shown. The presence of significant quantities of Li_2O on the Li surface is indicated, as opposed to a LiF dominated inner layer on the Li-Cu surface. The presence of species related to P_{1X}^+ is also indicated for the Li-Cu surface.

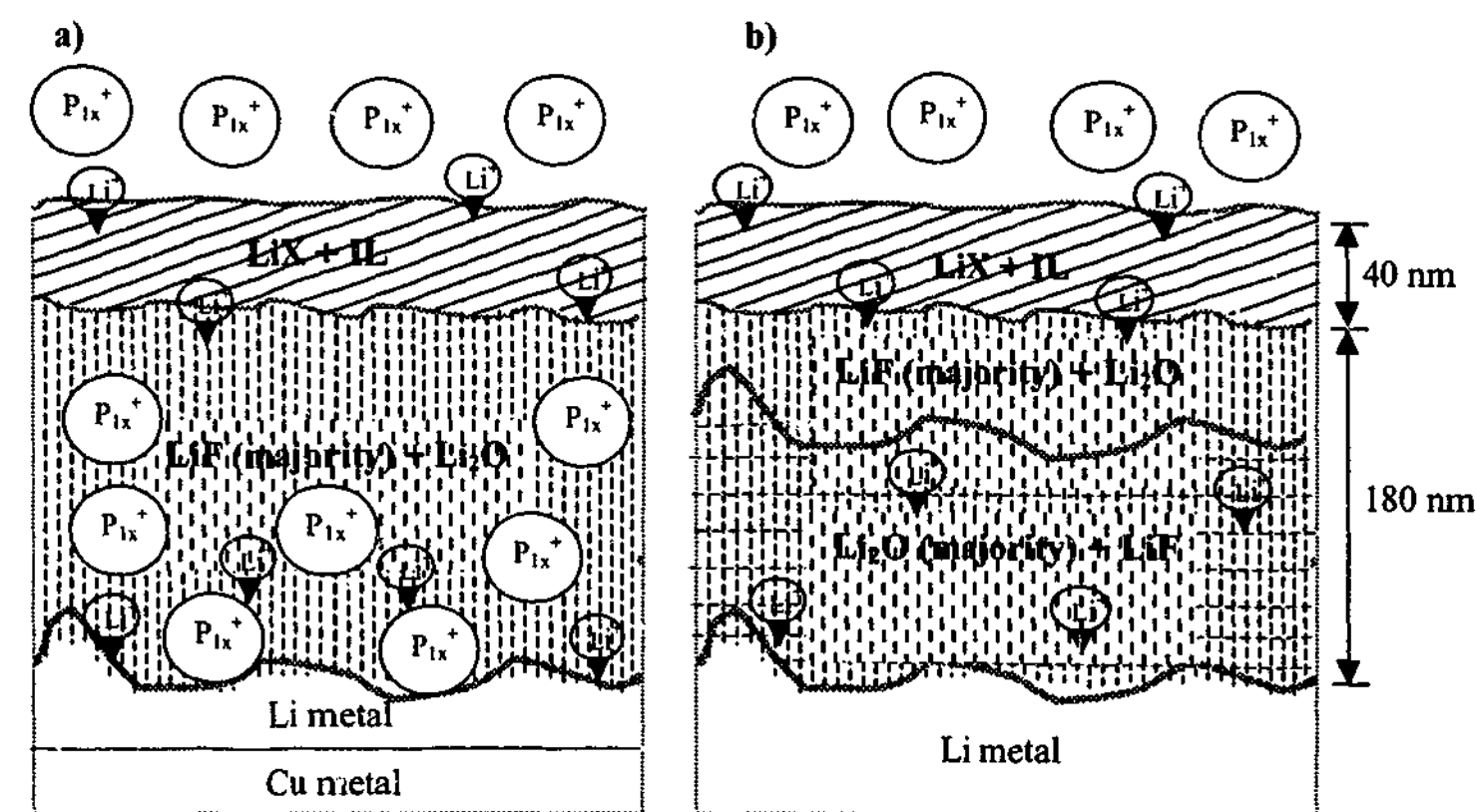


Fig. 3.4.34 Simple models of the SEI structure on the Li (a) and Li-Cu (b) surfaces. LiX: X might be S_2O_4 , F, SO_3CF_3 , NSO_2CF_3 , SO_3 , S, O, OH.

References

1. J. F. Moulder, W. F. Stickle, P. E. Sobol and K. D. Bomben, *Handbook of X-Ray Photoelectron Spectroscopy*, Perkin-Elmer Corporation, Eden Prairie (1992).
2. D. Aurbach, M. Daroux, P. Faguy and E. Yeager, *J. Electroanal. Chem.*, 297, 225 (1991).
3. L. J. Rendek, G. S. Chottiner and D. A. Scherson, *J. Electrochem. Soc.*, 149, E408-E412 (2002).
4. K. Kanamura, S. Shiraishi, H. Tamura and Z. Takehara, *J. Electrochem. Soc.*, 141, 2379 (1994).
5. I. Ismail, A. Noda, A. Nishimoto and M. Watanabe, *Electrochim. Acta*, 46, 1595 (2001).
6. K. Kanamura, H. Tamura, S. Shiraishi and Z.-I. Takehara, *Electrochim. Acta*, 40, 913 (1995).
7. K. Morigaki and A. Ohta, *J. Power Sources*, 76, 159 (1998).
8. K. Kanamura, H. Tamura and Z. Takehara, *J. Electroanal. Chem.*, 333, 127 (1992).
9. D. Aurbach, I. Weissman, A. Zaban and O. Chusid, *Electrochim. Acta*, 39, 51 (1994).
10. I. Rey, P. Johansson, J. Lindgren, J. C. Lassègues, J. Grondin and L. Servant, *J. Phys. Chem. A*, 102, 3249 (1998).
11. J. Adebahr, P. Johansson, P. Jacobsson, D. R. MacFarlane and M. Forsyth, *Electrochim. Acta*, 48, 2283 (2003).
12. I. Rey, J. L. Bruneel, J. Grondin, L. Servant and J. C. Lassegues, *J. Electrochem. Soc.*, 145, 3034 (1998).
13. Z. Wang, W. Gao, X. Huang, Y. Mo and L. Chen, *J. Raman Spectrosc.*, 32, 900 (2001).
14. B. Bednarska-Bolek, R. Jakubas, G. Bator and J. Baran, *J. Mol. Struct.*, 614, 151 (2002).
15. D. H. Williams and I. Fleming, *Spectroscopic Methods in Organic Chemistry*, McGraw-Hill Book Company (UK) Limited, Maidenhead (1980).
16. D. Aurbach, *J. Electrochem. Soc.*, 136, 1611 (1989).
17. J. Li, H. Li, Z. Wang, L. Chen and X. Huang, *J. Power Sources*, 107, 1 (2002).
18. C. N. R. Rao, *Chemical Applications of Infrared Spectroscopy*, Academic Press, New York (1963).
19. O. Chusid, Y. Gofer, D. Aurbach, M. Watanabe, T. Momma and T. Osaka, *J. Power Sources*, 97-98, 632 (2001).
20. K. Nakamoto, *Infrared Spectra of Inorganic and Coordination Compounds*, Wiley-Interscience, New York (1970).
21. H. Every, A. G. Bishop, M. Forsyth and D. R. MacFarlane, *Electrochim. Acta*, 45, 1279 (2000).
22. M. Le Granvalet-Mancini, T. Hanrath and D. Teeters, *Solid State Ionics*, 135, 283 (2000).
23. H. Li, G. Li, Y. Mo, X. Huang, and L. Chen, *Solid State Ionics*, [Proc. Asian Conf.], 7th, 377. Chowdari, B. (Ed.), *World Scientific Publishing Co. Pty. Ltd. Singapore, Singapore* (2000).
24. G. Li, H. Li, Y. Mo, X. Huang and L. Chen, *Chem. Phys. Lett.*, 330, 249 (2000).
25. G. Li, H. Li, Y. Mo, L. Chen and X. Huang, *J. Power Sources*, 104, 190 (2002).
26. D. Aurbach (Ed.), *Nonaqueous Electrochemistry*, Marcel Dekker, New York (1999).
27. G. Wang, F. Liu, G. Cheng, M. Han and J. Ma, *Solid State Commun.*, 99, 369 (1996).
28. C. Naudin, J. L. Bruneel, M. Chami, B. Desbat, J. Grondin, J. C. Lassègues and L. Servant, *J. Power Sources*, 124, 518 (2003).
29. D. Aurbach, M. L. Daroux, P. W. Faguy and E. Yeager, *J. Electrochem. Soc.*, 134, 1611 (1987).

30. J. G. Thevenin and R. H. Muller, *J. Electrochem. Soc.*, 134, 273 (1987).
31. A. Zaban, E. Zinigrad and D. Aurbach, *J. Phys. Chem.*, 100, 3089 (1996).
32. D. Aurbach and A. Zaban, *J. Electroanal. Chem.*, 367, 15 (1994).
33. J. R. Macdonald, *Impedance Spectroscopy: Emphasizing Solid Materials and System*, Wiley-Interscience, New York (1987).
34. N. Munichandraiah, L. G. Scanlon and R. A. Marsh, *J. Power Sources*, 72, 203 (1998).
35. K. S. Aojula, J. D. Genders, A. D. Holding and D. Pletcher, *Electrochim. Acta*, 34, 1535 (1989).
36. D. Pletcher, J. F. Rohan and A. G. Ritchie, *Electrochim. Acta*, 39, 2015 (1994).
37. D. Pletcher, J. F. Rohan and A. G. Ritchie, *Electrochim. Acta*, 39, 1369 (1994).
38. J. Xu and G. C. Farrington, *Solid State Ionics*, 74, 125 (1994).
39. J. Xu and G. C. Farrington, *J. Electrochem. Soc.*, 142, 3303 (1995).
40. M. W. Verbrugge and B. J. Koch, *J. Electroanal. Chem.*, 367, 123 (1994).
41. Y. Geronov, F. Schwager and R. H. Muller, *J. Electrochem. Soc.*, 129, 1422 (1982).
42. R. Bouchet, S. Lascaud and M. Rosso, *J. Electrochem. Soc.*, 150, p A1385-A1389 (2003).
43. E. Peled, D. Golodnitsky, and J. Penciner, in *Handbook of Battery Materials*, 419, J. O. Besenhard (Ed.), Wiley-VCH, Weinheim, Germany (1999).
44. E. Kariv-Miller, P. B. Lawin and Z. Vajtner, *J. Electroanal. Chem.*, 195, 435 (1985).
45. C. M. Ryan, V. Svetlicic and E. Kariv-Miller, *J. Electroanal. Chem.*, 219, 247 (1987).

3.5 Additives:

A common approach to improving the cycling efficiency of electrolytes for rechargeable lithium metal batteries has been with additives. The use of additives to modify deposition morphology and hence improve cycling efficiency was discussed earlier (section 1.5.3). Numerous additives, in a variety of solvents, have demonstrated improved cycling behaviour for the lithium metal electrode. The results of a survey of the literature pertaining to the application of additives in lithium battery electrolytes are presented in Table 3.5.1.

A study was undertaken to assess the use of additives in a $0.5 \text{ mol kg}^{-1} \text{ P}_{13}(\text{Tf})_2\text{N}$ electrolyte. A number of additives were chosen from Table 3.5.1, to trial in the RTIL electrolyte. The choice of material was made with deference to ease of availability, and to cover the various types of additive (i.e., polymers, inorganic salts, fillers etc.). The aim of the experiments was to identify if it was possible to substantially influence the cycling performance of the RTIL by adding small quantities of impurities designed to modify the properties of the SEI.

The study also incorporated an assessment of different lithium salts, other than $\text{Li}(\text{Tf})_2\text{N}$. The salts chosen were LiPF_6 , LiAsF_6 and LiSbF_6 . The salt concentration and the temperature of the experiment were varied in some cases. These experiments were designed to test the influence of the anion in altering the cycling performance of the electrolyte.

A cycling efficiency experiment, using a 3-electrode cell (copper working-electrode, Li counter and quasi-reference), was used to assess each of the additive solutions. The experiments were conducted at 1 mA cm^{-2} , 1 C cm^{-2} excess charge and 0.25 C cm^{-2} cycling charge at 50°C allowing comparison with previous measurements (section 3.2.2). The additive solutions and their cycling efficiencies are presented in Table 3.5.2.

Table 3.5.1 Literature survey of additives demonstrated to have improved the cycling behaviour of the lithium metal electrode.

ADDITIVE	REF.	EFFECT	PROPOSED MECHANISM	SYSTEM STUDIED	COMMENTS
Nitrile Sucrose (Li Salt ~ 1wt%)	1	Reduced interfacial film R		EC/PC/LiPF ₆ PVDF/EC/PC/LiPF ₆	No cycling exp., EIS & CV only. No effect on electrochemical window
Nitrile Cellulose (Li Salt ~ 1wt%)	1	Reduced interfacial film R		EC/PC/LiPF ₆ PVDF/EC/PC/LiPF ₆	
AlI ₃ (100-600ppm M ⁺)	2	Reduced efficiency and cycle life	Alloy, Side reactions (Phosphoric)	PC/DMC/LiPF ₆ PC/DMC/LiClO ₄	Effective for LiClO ₄ , blocking interface
MgI ₂ (100-600ppm M ⁺)	2	Increased efficiency and cycle life	Alloy, no side reactions	PC/DMC/LiPF ₆ PC/DMC/LiClO ₄	Compact conductive interface
HF (5x10 ⁻³ M)	3	No dendrites	Uniform surface film composed of LiF (mainly)	PC/LiClO ₄	Maintained for 5 cycles
BTE (1,2-bis-(trifluoroacetoxy)-ethane) (20%v/v)	4	Increased efficiency	Reduced at 1.75V vs Li/Li ⁺	PC/BTE/LiN(SO ₂ CF ₃) ₂	Examined only with carbon anodes to negate solvent intercalation
ES (Ethylene sulfite) (3-5%v/v)	4	Increased efficiency	Reduced at ~2V vs Li/Li ⁺	PC/ES/LiClO ₄	
Perfluoropolyether (PFPE 500-2000ppm)	5	Increased efficiency	Less dendritic	PC/LiAsF ₆ PC/EC/LiAsF ₆	Optimum at 2000 ppm
Polyvinylpyrrolidone (PVP - MW 40000) (0.02-2 g/50 mL)	6	Increased efficiency Decreased int. resistance	Thin film, facile Li ⁺ transport	PC/EC/LiBF ₄ PC/EC/LiN(CF ₃ SO ₂) ₂	Optimum at 0.1-0.2 g /50 mL
Polyethyleneoxide (PEO - MW 400000) (0.02-0.2g/50mL)	6	Increased efficiency Decreased int. resistance	Thin film, facile Li ⁺ transport	PC/EC/LiBF ₄ PC/EC/LiN(CF ₃ SO ₂) ₂	Optimum at 0.1-0.2 g /50 mL, not as effective as PVP
Polyacrylonitrile (PAN - MW 150000) (0.02-0.2g/50mL)	6	Increased efficiency Decreased int. resistance	Thin film, facile Li ⁺ transport	PC/EC/LiBF ₄ PC/EC/LiN(CF ₃ SO ₂) ₂	Optimum at 0.1-0.2 g /50 mL, not as effective as PEO
Tris[(cyanoethoxy)methyl]aminomethane (TCEMAM) 5mol per 20mol ACN in PAN	7	Inc. exchange current density	Improved Li ⁺ dissolution	PAN/LiClO ₄ /PC	Dissolution enhancer gives significant conductivity increase
Tetrakis[(cyanoethoxy)methyl]methane (TCEMM) 5mol per 20 mol ACN in PAN	7	Inc. exchange current density	Improved Li ⁺ dissolution	PAN/LiClO ₄ /PC	
Tetraethylammonium heptadecafluorooctanesulfonate (TEAFOS 0.01-0.05M)	8	Increased efficiency	Li deposit morphology effects	PC/LiClO ₄ PC/EC/DME/LiClO ₄	Optimum at 0.025M, most effective with PC/EC/DME
Lithium heptadecafluorooctanesulfonate (LiFOS 0.005-0.05M)	8	Increased efficiency	Li deposit morphology effects	PC/LiClO ₄ PC/EC/DME/LiClO ₄	Optimum at 0.025M, most with PC/LiClO ₄

Table 3.5.1 (cont.) Literature survey of additives demonstrated to have improved the cycling behaviour of the lithium metal electrode.

ADDITIVE	REF.	EFFECT	PROPOSED MECHANISM	SYSTEM STUDIED	COMMENTS
CO ₂ /Ar (20%) Mixed Gas	9	Reduced voltage delay	Forms protective initial film	PC/LiClO ₄	Even dissolution of Li
Tetraethylammonium fluoride- tetrakis hydrogen fluoride (TEAFHF - (C ₂ H ₅) ₄ NF(HF) ₄ , 1.25 -10.0 x 10 ⁻³ M)	10	Increased efficiency, Hemispherical deposition	LiF/Li ₂ O bi-layer	PC/LiClO ₄ DME/LiClO ₄	Also studied H ₂ O addition - DME best solvent.
Dilithiumpthalocyanine (Li ₂ PC-10 ⁻³ M)	11	Increase exchange current density	Thin film, increased ion migration	PC/LiClO ₄	Unstable anion is favoured (LiAsF ₆), homogeneous film
Polysulfide (S _x ²⁻ 3x10 ⁻⁴)	12	Improves cycle efficiency	Compact deposition, less dendritic	PC/LiClO ₄	Also studied carbon electrodes
Propylene sulfite (PS - 5%v/v)	13	Suppresses co-intercalation of PC	SEI prevents co-intercalation	PC/LiClO ₄	Studied carbon electrodes only
2-methylfuran (2MeF - 1%v/v)	14	Reduced polarisation resistance		EC/DMC/LiPF ₆	
2-methyltetrahydrofuran (2MeTHF - 5%v/v)	14	Reduced polarisation resistance		EC/DMC/LiPF ₆	Similar effect to 2-MeF
2-Methylthiophene (2MeTp - 5%v/v)	14	Reduced polarisation resistance		EC/DMC/LiPF ₆	Similar effect to 2-MeF
Polyethylene oxide (MW 70000 - 1g in 50mL)	14	Reduced polarisation resistance		EC/DMC/LiPF ₆	Most effective
AlI ₃ (100-500ppm)	15	Increased efficiency, uniform current density across surface	Formation of high conductivity alloy at interface	PC/DME/LiClO ₄ PC/2MeTHF/LiClO ₄	Iodide adsorption, LiI formation.
SnI ₂	15	Not effective, current distribution more uniform than without additive	Alloy not very conductive	PC/DME/LiClO ₄ PC/2MeTHF/LiClO ₄	Additive had slight effect
LiI (100-300ppm)	16	Increased coulombic efficiency after 10 th cycle	I ⁻ adsorption inhibits interfacial SEI formation, conductive LiI layer	PC/LiClO ₄	R (EIS) increasing with cycling
SnI ₂ (100ppm)	16	Improved efficiency	Alloy formation plus iodide	PC/LiClO ₄	R (EIS) increasing with cycling
AlI ₃ (100ppm)	16	Improved efficiency	Alloy formation plus iodide	PC/LiClO ₄ PC/2MeF(0.5%v/v)/LiClO ₄	R stable with cycling. Synergy with 2MeF. AL-2MeF>Al>Sn>LiI

Table 3.5.2 Additive $P_{15}(Tf)_2N$ electrolyte systems and their cycling efficiencies at various temperatures and rates.

Additive	Temp. (°C)	Rate (mAcm ⁻²)	Number of cycles			Cyc. Eff. (%)	
			1	2	3	Av.	Max.
PEO (MW 100000 0.2 wt%)	50	1.0	9	35	21	84.4	89.7
PVP (MW 40000 0.15 wt%)	50	1.0	27	14	10	81.0	87.1
Tetraglyme (0.2 wt%)	50	1.0	9	5	10	66.7	71.4
SiO ₂ (5wt%)	50	1.0	5	5	3	52.0	55.6
SiO ₂ (5wt%)	50	0.5	20			83.3	83.3
MgI ₂ (100ppm)	50	1.0	4			50.0	50.0
MgI ₂ (500ppm)	50	1.0	15	7	10	72.7	78.9
MgI ₂ (100ppm)	50	1.0	6	9		64.6	69.2
MgI ₂ (100ppm)	50	0.5	26	9		78.0	86.7
LiPF ₆ (0.5 molkg ⁻¹)	50	1.0	<1			<20.0	<20.0
LiPF ₆ (0.5 molkg ⁻¹)	50	0.5	3	6	3	48.5	60.0
LiAsF ₆ (0.5 molkg ⁻¹)	50	1.0	1			20.0	20.0
LiAsF ₆ (0.5 molkg ⁻¹)	50	0.5	43	36	26	89.7	91.5
LiAsF ₆ (1.0 molkg ⁻¹)	50	0.5	61			93.8	93.8
Li(Tf) ₂ N (0.5 molkg ⁻¹)	75	1.0	7	4	5	57.1	63.6
Li(Tf) ₂ N (1.0 molkg ⁻¹)	50	1.0	10			74.2	74.2
Li(Tf) ₂ N (1.0 molkg ⁻¹)	75	1.0	13			76.5	76.5
LiAsF ₆ (1.0 molkg ⁻¹)	75	1.0	49	51		92.6	92.7
LiAsF ₆ (1.5 molkg ⁻¹)	100	0.5	36	33		89.6	90.0
LiAsF ₆ (1.5 molkg ⁻¹)	125	1.0	28			87.5	87.5

The polymeric additives did not alter the cycling behaviour of the electrolyte in any significant way. The addition of tetraglyme to the RTIL resulted in a consistent decrease in the cycling efficiency.

The 5 wt% SiO₂ sample formed a stable gel; the rate performance of the gel was slightly reduced, at lower rates the gel performed comparably to the original electrolyte. This approach appears to hold some merit; by optimising the amount of filler added it may be possible to reduce the impact on lithium transport indicated by the lower rate capability. Whether or not the addition of filler produces improved interfacial properties (as has been reported for polymer electrolytes, section 1.4.3) remains to be determined. Even in the event that the filler addition did not result in improved interfacial properties, a quasi-solid electrolyte of this type could allow the removal of the separator or its replacement with an open-weave support material, creating the opportunity for closer electrode spacing. A quasi-solid electrolyte also offers practical advantages for flexibility of design.^{17,18}

The addition of MgI₂ resulted in a substantial increase in the viscosity of the electrolyte, which severely reduced the performance of the electrolyte. At lower rates and at reduced concentration its behaviour was comparable to that of the original electrolyte.

None of the additives produced a significant improvement in the performance of the electrolyte, and overall a slight reduction in performance was the typical result. It must be recognised that the additives were trialled under a narrow range of conditions and their performance could differ at lower rates or at different temperatures. However, although a wide variety of additives remain that could be trialled; it seems that the mechanism leading to reduced efficiency is unlikely to be influenced by slight changes in the SEI composition.

The addition of a different lithium salt (i.e., other than Li(Tf)₂N) to the electrolyte effectively creates a mixture of four different ions. The properties of a mixture such as this can be difficult to predict, a eutectic may significantly reduce the melting point, and some mixtures can result in significantly enhanced conductivity.¹⁹ In this respect, the use of 'hetero-anions' as additives in the RTIL offers many possibilities. In addition, it has been shown in this work that the properties of the SEI are largely dictated by the anion (section 3.4).

The LiPF_6 salt gave significantly reduced performance under the conditions of the experiment and the LiSbF_6 salt failed to dissolve in the RTIL. The addition of LiAsF_6 resulted in an increase in viscosity and low cycling efficiency at 1 mAcm^{-2} ; however significant improvements were encountered at reduced rates, particularly at high salt concentrations. Apart from the low rate experiments described in section 3.2.1, the LiAsF_6 electrolytes gave the highest cycling efficiencies yet obtained on a copper substrate. The improvement of lithium metal cycling efficiency by the use of a LiAsF_6 has been demonstrated on numerous occasions. The improvement has been attributed to the doping of lithium with arsenic and arsenic compounds, which reduce the Li reactivity.²⁰⁻²³

The influence of temperature on the cycling efficiency of $\text{Li}(\text{Tf})_2\text{N}/\text{P}_{13}(\text{Tf})_2\text{N}$ and $\text{LiAsF}_6/\text{P}_{13}(\text{Tf})_2\text{N}$ electrolytes was very pronounced. Apparently the rate of the electrolyte decomposition / film formation reaction was significantly increased at higher temperatures. The improved performance of higher concentration samples at high temperatures suggests that a more protective SEI is formed at high concentrations, in agreement with the impedance measurements shown in section 3.2. The transport limitations imposed by the more resistive SEI are less significant at elevated temperatures. The LiAsF_6 samples exhibited significantly higher cycling efficiencies at elevated temperatures than the $\text{Li}(\text{Tf})_2\text{N}$ electrolytes.

The data shown in Table 3.5.3 provides cycling efficiencies for the most successful conventional electrolyte systems. The results were obtained under similar conditions to those presented for $\text{P}_{1X}(\text{Tf})_2\text{N}$ in this work. It is clear that the $\text{P}_{1X}(\text{Tf})_2\text{N}$ RTILs offer comparable performance, in terms of their cycling efficiency, to the best of the conventional systems. With this in mind, it is important to recognise that the results presented in Table 3.5.3 represent more than twenty years of concerted research into molecular solvent systems by numerous research groups worldwide.

The cycling behaviour of the lithium in $\text{P}_{1X}(\text{Tf})_2\text{N}$ electrolytes can be altered through the use of additives, but no significant improvement in efficiency was found for any of the additives tested here. The significant changes produced by the addition of a different Li salt, and by variations in the salt concentration and temperature, suggest that further

optimisation is probable and a systematic and concerted effort is required to account for the complex array of parameters which must be considered.

The performance of the $\text{P}_{1X}(\text{Tf})_2\text{N}$ RTILs as electrolytes for the lithium metal electrode is adequate for use in a lithium metal rechargeable battery. The next section will detail the results of a study of their behaviour in cells incorporating various battery chemistries.

Table 3.5.3 Typical Li cycling efficiency values obtained for various molecular solvent based electrolytes. Applied current density = 1 mAcm⁻², excess charge = 5 Ccm⁻² and cycling charge = 1.25 Ccm⁻². (Reproduced from Nonaqueous Electrochemistry²³)

Solvent	Salt	Additives	Cyc. Eff. (%)
1,3-Dioxolane	LiClO ₄		>95
	LiAsF ₆	Tributyl amine	96-97
	Li(Tf) ₂ N	Tributyl amine	<50
2Me-THF	LiAsF ₆		>95
	LiClO ₄		<50
THF	LiAsF ₆		>90
Glyme family (DG,EG)	LiClO ₄		80
	Li(Tf) ₂ N		<50
	LiSO ₃ CF ₃		<50
γ-Butyrolactone	LiClO ₄		<50
	LiAsF ₆		>80
	LiAsF ₆	O ₂ saturated	>85
Methyl formate (MF)	LiAsF ₆		<50
	LiAsF ₆	CO ₂	>90
MF-EC or MF-PC	LiAsF ₆	CO ₂	>90
Propylene carbonate (PC)	LiClO ₄		>70
	LiAsF ₆		>70
	LiAsF ₆		>80
	LiAsF ₆	CO ₂	>95
	LiPF ₆		>80
Ethers + PC	LiAsF ₆		<70
EC-Ethers	LiAsF ₆		>70
EC-Ethers	LiAsF ₆	CO ₂ or trace H ₂ O	>95
EC-PC	LiAsF ₆		>80
EC-DEC	LiAsF ₆		>90
EC-DMC (1:5)	LiAsF ₆		>90
EC-DMC (1:1)	LiPF ₆	CO ₂	>90

References

1. G. Nagasubramanian and D. Doughty, *J. Power Sources*, **96**, 29 (2001).
2. M. Ishikawa, S. Machino and M. Morita, *J. Electroanal. Chem.*, **473**, 279 (1999).
3. K. Kanamura, S. Shiraishi and Z. Takehara, *J. Electrochem. Soc.*, **141**, L108-L110 (1994).
4. M. Winter, *Monatshefte fuer Chemie/Chemical Monthly*, **132**, 473 (2001).
5. E. Eweka, J. R. Owen and A. Ritchie, *J. Power Sources*, **65**, 247 (1997).
6. Y. Matsuda, T. Takemitsu, T. Tanigawa and T. Fukushima, *J. Power Sources*, **97-98**, 589 (2001).
7. H. Tsutsumi, K. Takase, K. Onimura and T. Oishi, *J. Power Sources*, **104**, 40 (2002).
8. A. T. Ribes, P. Beaunier, P. Willmann and D. Lemordant, *J. Power Sources*, **58**, 189 (1996).
9. T. Fujieda, N. Yamamoto, K. Saito, T. Ishibashi, M. Honjo, S. Koike, N. Wakabayashi and S. Higuchi, *J. Power Sources*, **52**, 197 (1994).
10. K. Kanamura, S. Shiraishi and Z. Takehara, *J. Fluorine Chem.*, **87**, 235 (1998).
11. D. Rahner, S. Machill and K. Siury, *J. Power Sources*, **68**, 69 (1997).
12. M. W. Wagner, C. Liebenow and J. O. Besenhard, *J. Power Sources*, **68**, 328 (1997).
13. G. H. Wrodnigg, T. M. Wrodnigg, J. O. Besenhard and M. Winter, *Electrochemistry Communications*, **1**, 148 (1999).
14. Y. Matsuda and M. Sekiya, *J. Power Sources*, **81-82**, 759 (1999).
15. M. Ishikawa, M. Morita and Y. Matsuda, *J. Power Sources*, **68**, 501 (1997).
16. Y. Matsuda, M. Ishikawa, S. Yoshitake and M. Morita, *J. Power Sources*, **54**, 301 (1995).
17. J. O. Besenhard (Ed.), *Handbook of Battery Materials*, Wiley-VCH, Weinheim (1999).
18. E. Stathatos, P. Lianos, S. M. Zakeeruddin, P. Liska and M. Gratzel, *Chem. Mater.*, **15**, 1825 (2003).
19. H. Every, A. G. Bishop, M. Forsyth and D. R. MacFarlane, *Electrochim. Acta*, **45**, 1279 (2000).
20. D. Aurbach, A. Zaban, Y. Gofer, Y. E. Ely, I. Weissman, O. Chusid and O. Abramson, *J. Power Sources*, **54**, 76 (1995).
21. D. Aurbach, A. Zaban, Y. Gofer, O. Abramson and M. Benzion, *J. Electrochem. Soc.*, **142**, 687 (1995).
22. D. Aurbach, *J. Power Sources*, **68**, 91 (1997).
23. D. Aurbach (Ed.), *Nonaqueous Electrochemistry*, Marcel Dekker, New York (1999).

3.6 Cell studies:

The resealable stainless steel cells used to prepare cycled lithium surfaces for characterisation were also used to assess RTIL electrolyte cycling behaviour in 'battery-like' conditions. A range of cells were prepared including lithium symmetrical cells, lithium/copper asymmetrical cells and rechargeable cells incorporating a positive intercalation electrode.

Table 3.6.1 presents a summary of some of the cells studied in this work. Ultimately the work was directed to assess $P_{1X}(Tf)_2N$ electrolytes in a rechargeable lithium cell. However, there is very little information in the literature pertaining to the application of RTILs in secondary cells. Thus, factors such as the cell geometry, the presence of the separator, the stack pressure and the electrolyte volume could significantly alter the rate capability and the reversibility of the lithium electrochemistry, compared with the previous experiments in the optical cell and the 3-electrode cell. The results presented here are intended as a general survey of the cycling behaviour of $P_{1X}(Tf)_2N$ 'battery' cells under a range of conditions.

The main parameters that were varied were the type of electrode material and the rates at which the cells were cycled. The separator material, the temperature and the type of cycling experiment were also varied.

Of the separator materials that were used in the cells, the glass fibre filter paper (GFFP) was favoured. The cell cycling results did not indicate a clear superiority of one type over the other, however it was noted that the Solupor and particularly the Celgard separators did not appear to wet as readily as the GFFP. The polyolefin separators were generally wetted under vacuum to ensure penetration of the RTIL. The polyolefin separators were favoured for sample preparation (for surface characterisation) because the disassembled cells came apart more easily.

Generally, the current density that could be maintained in the resealable cells was lower than in the 3-electrode cell (section 3.2). This could be due to the separator tortuosity and interactions between the separator and the RTIL impeding lithium transport. In addition,

the difference in diffusion geometry could have resulted in a reduced rate of lithium transport to the electrode surface. Cells that were cycled at rates above 0.25 mAcm^{-2} generally performed poorly. Cells cycled at around 0.1 mAcm^{-2} performed very well.

Table 3.6.1 Summary of 'Battery' cells incorporating $\text{P}_{1x}(\text{Tf})_2\text{N}$ electrolytes studied in this work. Some $\text{PP}_{13}(\text{Tf})_2\text{N}$ cells are also shown.

Cell	Cycling Parameters	Remarks
Li / 0.5 molkg^{-1} $\text{P}_{14}(\text{Tf})_2\text{N}$ - Celgard TM / Cu	1 mAcm^{-2} and 0.5 mAcm^{-2} deposition at 50°C	Rapid increase in cell potential, cell unable to maintain applied currents. Sands time gives $D = 7 \times 10^{-7} \text{ cm}^2\text{s}^{-1}$.
Li / 0.5 molkg^{-1} $\text{P}_{14}(\text{Tf})_2\text{N}$ - Celgard TM / Pt	Cycling Eff. 0.25 mAcm^{-2} , 1 Ccm^{-2} at 50°C	Steady increase in both deposition and dissolution potentials. Possibly related to Pt alloying.
Li / 0.5 molkg^{-1} $\text{P}_{14}(\text{Tf})_2\text{N}$ - Solupor TM / Li	Initial 0.5 mAcm^{-2} , then 0.1 mAcm^{-2} , 1 Ccm^{-2} at 50°C	Cell unable to maintain initial current, at 0.1 mAcm^{-2} cell voltage at $\sim 100 \text{ mV}$ and increasing after 20 cycles.
Li / 0.5 molkg^{-1} $\text{P}_{14}(\text{Tf})_2\text{N}$ - Solupor TM / Li	0.1 mAcm^{-2} and 1 Ccm^{-2} at 50°C	Cell voltage at $\sim 70 \text{ mV}$ stable cycling for greater than 20 cycles.
Li / 0.5 molkg^{-1} $\text{P}_{13}(\text{Tf})_2\text{N}$ - Solupor TM / Li	0.1 mAcm^{-2} and 1 Ccm^{-2} at 50°C	Cell voltage at $100\text{--}150 \text{ mV}$, steady increase after 10 cycles.
Li / 0.5 molkg^{-1} $\text{P}_{13}(\text{Tf})_2\text{N}$ - Solupor TM / Li	0.25 mAcm^{-2} and 0.25 Ccm^{-2} at 50°C	Cell voltage at 200 mV and decreasing (180 mV after 10 cycles).
Li / 0.5 molkg^{-1} $\text{P}_{14}(\text{Tf})_2\text{N}$ - Celgard TM / Cu	Coulombic. Eff. 1 mAcm^{-2} , 1 Ccm^{-2} (plate & strip), 50°C	70-80 % Coulombic. Eff., failure after 4 cycles (limited quantity of electrolyte $\sim 0.04\text{g}$).
Li / 0.5 molkg^{-1} $\text{P}_{14}(\text{Tf})_2\text{N}$ - Celgard TM / Cu(Au)	Coulombic. Eff. 1 mAcm^{-2} , 1 Ccm^{-2} (plate & strip), 50°C	96 % (max.) Coulombic Eff., steady decay to 60 % after 20 cycles (limited quantity of electrolyte $\sim 0.04\text{g}$).
Li / 0.5 molkg^{-1} $\text{P}_{14}(\text{Tf})_2\text{N}$ - Celgard TM / Cu	Coulombic. Eff. 1 mAcm^{-2} , 1 Ccm^{-2} (plate & strip), 50°C	90 % (max.) Coulombic Eff., steady decay to 75 % after 40 cycles (excess electrolyte $\sim 0.5\text{g}$).

Cell	Cycling Parameters	Remarks
Li / 0.5 molkg^{-1} $\text{P}_{14}(\text{Tf})_2\text{N}$ - Celgard TM / Cu(Au)	Coulombic. Eff. 1 mAcm^{-2} , 1 Ccm^{-2} (plate & strip), 50°C	91 % (max.) Coulombic Eff., steady decay to 57 % after 40 cycles (excess electrolyte $\sim 0.5\text{g}$)
Li / 0.5 molkg^{-1} $\text{P}_{14}(\text{Tf})_2\text{N}$ - Celgard TM / Cu	Cycling Eff. 0.25 mAcm^{-2} , 1 Ccm^{-2} at 50°C	84 % and 76 % (duplicate)
Li / 0.5 molkg^{-1} $\text{P}_{14}(\text{Tf})_2\text{N}$ - Celgard TM / LMO(Al)	C/2 at ambient temp. then increased to 50°C , 4.3 V (charge) to 2.5 V (discharge)	80 % initial utilization, rapid decay to $\sim 5\%$, increase at 50°C (75 %), rapid decay to $\sim 1\%$
Li / 0.5 molkg^{-1} $\text{P}_{14}(\text{Tf})_2\text{N}$ - Celgard TM / LMO(Al)	C/10 at 50°C , 4.3 V (charge) to 2.5 V (discharge)	Low utilization (10 %), rapid decay to $\sim 2\%$. Efficiency initially 40 % increased to $\sim 80\%$.
Li / 0.5 molkg^{-1} $\text{P}_{13}(\text{Tf})_2\text{N}$ - GFFP / LMO(Pt)	C/10 at 80°C , 4.3 V (charge) to 3.8 V (discharge)	Initial utilization $\sim 70\%$, decay to 22 % by cycle 40 (17% by cycle 120). Initial efficiency at 80 %, increased to $>99\%$ by cycle 40.
Li / 0.5 molkg^{-1} $\text{P}_{13}(\text{Tf})_2\text{N}$ - GFFP / LMO(Pt)	C/10 at 80°C , 4.2 V (charge) to 3.8 V (discharge)	Initial utilization 40 %, decay to 13 % by cycle 40 (10% by cycle 100). Initial efficiency at 93 %, increased to $>99\%$ by cycle 4, very slow decay after cycle 20.
Li / 0.5 molkg^{-1} $\text{P}_{13}(\text{Tf})_2\text{N}$ - GFFP / LCO(Pt)	C/10 at 80°C , 4.3 V (charge) to 3.0 V (discharge)	Initial utilization 71 %, decay to 42 % by cycle 40 (26% by cycle 100). Initial efficiency at 75 %, increased to 93 % by cycle 5, plateau at 92-94% to cycle 100
Li / 0.5 molkg^{-1} LiAsF ₆ $\text{P}_{13}(\text{Tf})_2\text{N}$ - GFFP / LCO(Pt)	C/10 at 80°C , 4.3 V (charge) to 3.0 V (discharge)	Initial utilization 70 %, decay to 19 % by cycle 40 (9 % by cycle 75). Initial efficiency at 78 %, increased to 83 % by cycle 10, plateau at 80-88% to cycle 100
Li / 0.5 molkg^{-1} $\text{PP}_{13}(\text{Tf})_2\text{N}$ - GFFP / LCO(Pt)	C/10 at 80°C , 4.3 V (charge) to 3.0 V (discharge)	Initial utilization 52 %, decay to 30 % by cycle 40 (24% by cycle 100). Initial efficiency at 58 %, increased to 90 % by cycle 20, plateau at 95% after cycle 50
Li / 0.5 molkg^{-1} $\text{P}_{13}(\text{Tf})_2\text{N}$ - GFFP / Li	C/10 (0.0625 mAcm^{-2} , 2.25 Ccm^{-2}) at 80°C	Cell voltage 6 mV (Initial), plateau at 11 mV after 50 cycles - very stable cycling 100+ cycles.
Li / 0.5 molkg^{-1} $\text{PP}_{13}(\text{Tf})_2\text{N}$ - GFFP / Li	C/10 (0.0625 mAcm^{-2} , 2.25 Ccm^{-2}) at 80°C	Cell voltage 10 mV (Initial), gradual increase to 22 mV by cycle 100 - consistent increase in cell resistance.

3.6.1 Asymmetrical (Li/Cu) cells:

Cycling efficiency measurements were performed in the resealable cells using a copper substrate and values of approximately 80 % were obtained. These are lower than the results obtained using the 3-electrode cell (section 3.2). This suggests that the application of stack pressure does not significantly enhance cycling efficiency in RTILs (at these rates) as has been demonstrated for conventional systems.¹⁻³ Coulombic efficiency measurements were also performed; these measurements involved plating a set charge onto a copper substrate and then stripping until the cell voltage departed significantly from zero, in this case to a cut-off of 2 V. Figure 3.6.1 shows the results obtained from four cells designed to investigate the influence of the quantity of electrolyte as well as the influence of a gold sputtered substrate (i.e., Cu(Au) – copper sputter-coated with gold at 25 mA for 120s).

The cell voltage during deposition (positive during deposition on the Cu or Cu(Au) electrode) increased with cycling. The difference in the maximum potentials (Fig. 3.6.1 a & c vs. b & d) is due to the use of different potentiostats. Some clear differences can be observed between the behaviour of the cells. The cells that had a small amount of electrolyte did not perform as well as the cells with excess electrolyte. For the cells that had a small amount of electrolyte, the Cu(Au) substrate gave higher efficiencies. The highest coulombic efficiencies were obtained on the Cu(Au) substrate and the efficiencies ranged from 90-95 % for all of the cells except for the electrolyte-starved Cu cell (cell a). The increase in voltage during deposition is most likely a result of the build-up of anion reduction products on the electrode surface (section 3.4), resulting in increased cell impedance. The corresponding dissolution phase is limited to 2 V to prevent dissolution of copper. The results suggest that a minimum quantity of electrolyte is necessary to enable prolonged cycling. If it is assumed that the electrolyte is consumed to form the SEI, then the increase in cell resistance could also be due to the separator 'drying out'. In addition, the difference in behaviour between the two substrates suggests that the electrolyte in the Cu(Au) cell was not consumed as quickly, suggesting that the SEI formation process was not as rapid. The reduced potentials required for deposition on a gold substrate, where underpotential deposition is likely to occur,⁴ could lead to the formation of a thinner SEI. Overall, the coulombic efficiencies were quite high, and remained high for a large number of cycles, given that the substrate was being stripped back to a bare surface with each

cycle. The optical cell experiments (section 3.1) showed quite clearly that the bare surface was fouled with a layer of what was found to be mostly anion reduction products (section 3.4), and that the fouled surface tended to produce a dendritic deposit. The improvement of the coulombic efficiency under these conditions is probably a result of electrode stack pressure.

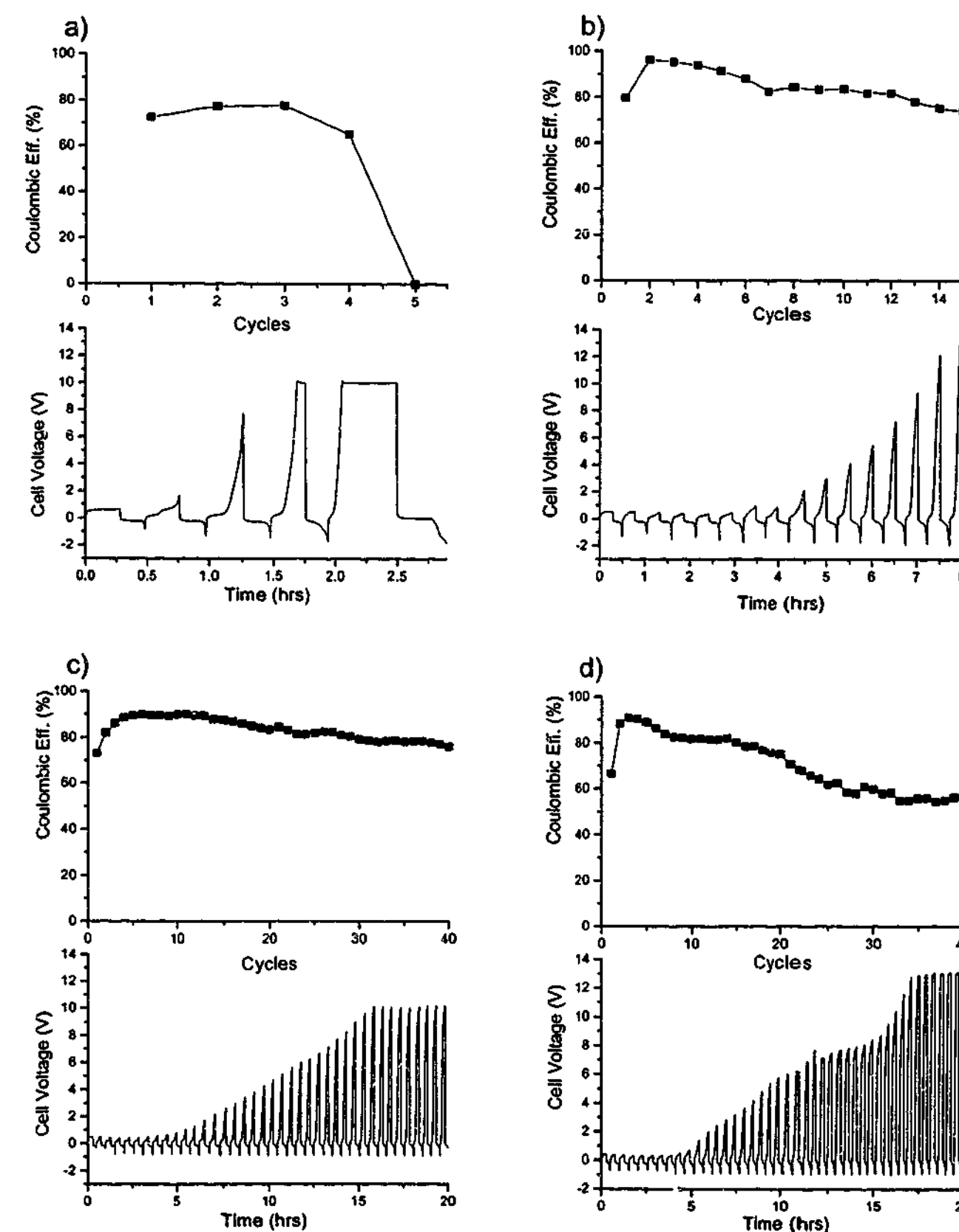


Fig. 3.6.1 Coulombic efficiency for $0.5 \text{ mol kg}^{-1} \text{ P}_{14}(\text{Tf})_2\text{N}$ cells deposition and dissolution at 1 mA cm^{-2} and 1 C cm^{-2} charge at 50°C , a) Li/Cu cell, 0.05g electrolyte b) Li/Cu(Au) cell, 0.05 g electrolyte c) Li/Cu cell, 0.5g electrolyte d) Li/Cu(Au), 0.5g electrolyte.

3.6.2 Lithium metal ionic liquid (LMIL) rechargeable cells:

An investigation into the cycling behaviour of $P_{1X}(Tf)_2N$ electrolytes in a rechargeable cell using common transition metal oxide cathode materials was undertaken. The principal aim was to determine if the cells would cycle reversibly at all, and to gain an indication of their cycle life. The cells were cycled at elevated temperatures, where it has been determined that good lithium metal cycling behaviour can be obtained. In addition, rechargeable lithium cells that are capable of operating under these conditions are perceived to have an advantage, for some applications, over commercially available lithium-ion / lithium polymer cells.

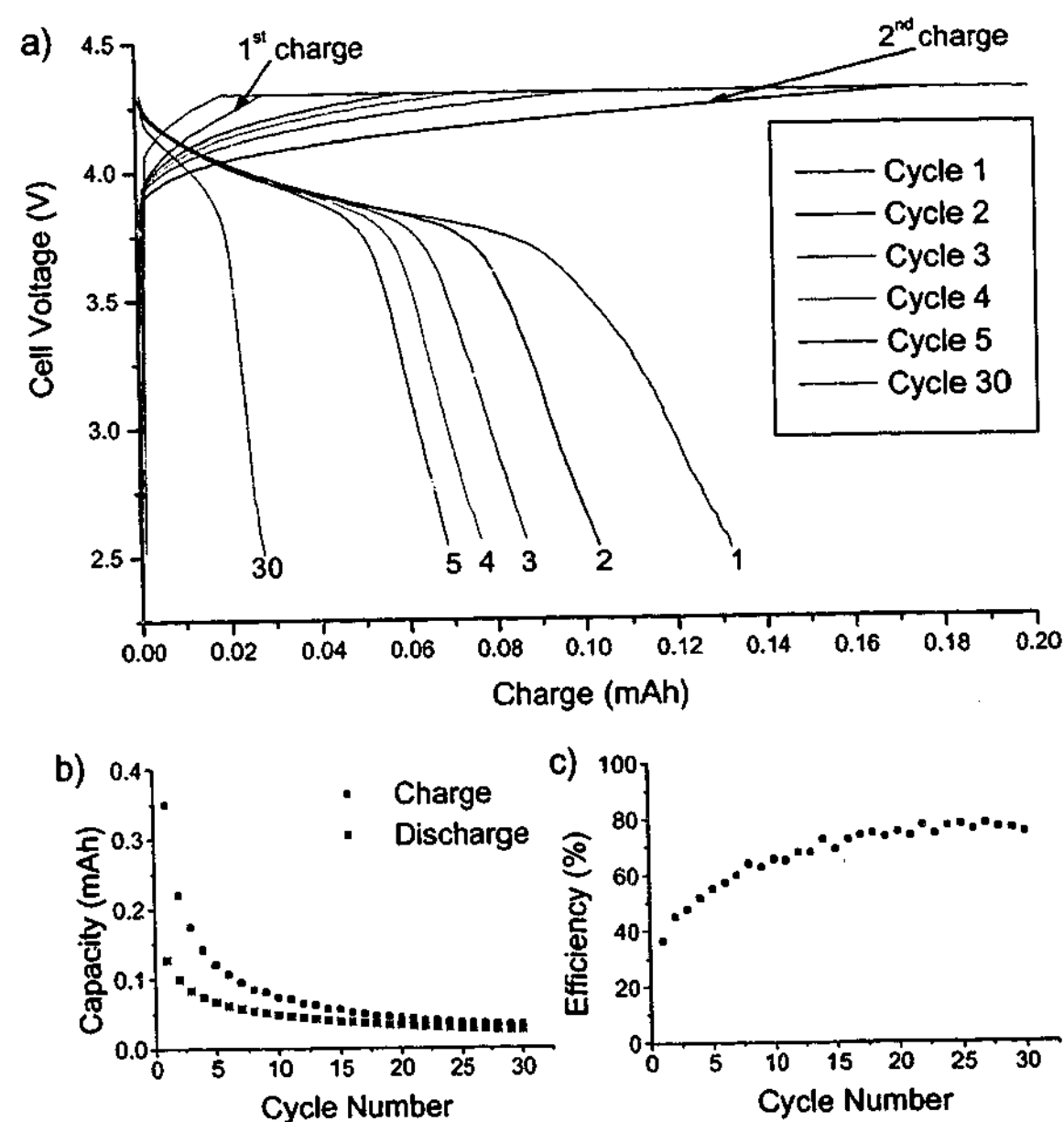


Fig. 3.6.2 Cycling behaviour of a Li / $P_{14}(Tf)_2N$ - Celgard™ / $LiMn_2O_4(Al)$ cell cycled at C/10 at 50 °C. a) Voltage profile b) Cell capacity c) Cell efficiency (discharge cap./charge cap.).

Figure 3.6.2 shows plots of the voltage profile, charge/discharge capacity and cell efficiency of a $Li/P_{14}(Tf)_2N/LiMn_2O_4$ cell cycled at C/10 (for a nominal 1.5 mAh cell based on 100% utilization of $150 \text{ mAhg}^{-1} LiMn_2O_4$)⁵ at 50 °C. The cell exhibited low utilization (initially ~ 10 % of theoretical) and rapid fade to very low values. The overall efficiency was low, increasing to close to 80 % by the 30th cycle. The experiment indicates that the electrolyte is capable of delivering stored charge, but that there is a rapid loss in capacity. The voltage profile indicates that there is no significant change in the cell resistance. The use $Li(Tf)_2N$ as an electrolyte salt in rechargeable lithium cells has been reported to result in corrosion of the aluminium current collector at the positive electrode.⁶⁻⁸ In light of these reports, the aluminium current collector was replaced with platinum. Platinum was chosen because it is unlikely to corrode, offering a way to eliminate the corrosion of the current collector as a contributing factor to the capacity fade exhibited by the cell. It is not suggested as a practical alternative to aluminium.

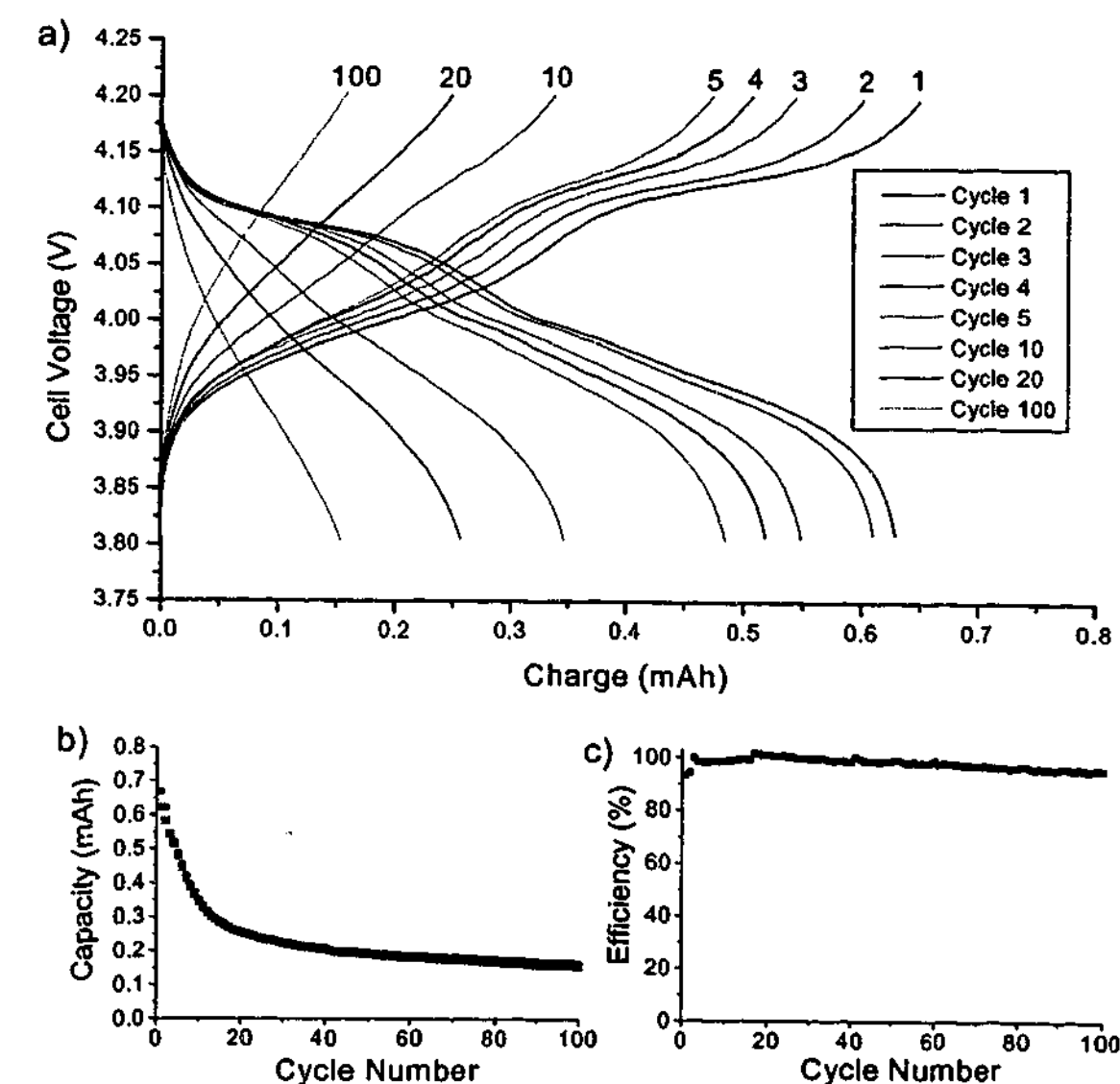


Fig. 3.6.3 Cycling behaviour of a Li / $P_{13}(Tf)_2N$ - GFFP / $LiMn_2O_4(Pt)$ cell cycled at C/10 at 80 °C. a) Voltage profile b) Cell capacity c) Cell efficiency (discharge cap./charge cap.).

Figure 3.6.3 shows plots of the voltage profile, charge/discharge capacity and cell efficiency of a $\text{Li/P}_{13}(\text{Tf})_2\text{N/LiMn}_2\text{O}_4$ cell cycled at $C/10$ (for a nominal 1.5 mAh cell based on 100% utilization of $150 \text{ mAhg}^{-1} \text{ LiMn}_2\text{O}_4$)⁵ at 80°C . The cell exhibited low utilization (initially $\sim 40\%$ of theoretical), and the discharge capacity faded rapidly to $\sim 0.25 \text{ mAh}$ by the 20th cycle, after which the rate of fade slowed. The overall efficiency was very high, exceeding 100% for a short period around the 20th cycle. The cell performance was generally better, indicating that corrosion of the aluminium current collector could have been contributing to the capacity fade; however, it is apparent that another process was leading to a reduction in the ability of the cell to store charge. Again, there was no indication of a change in the cell resistance.

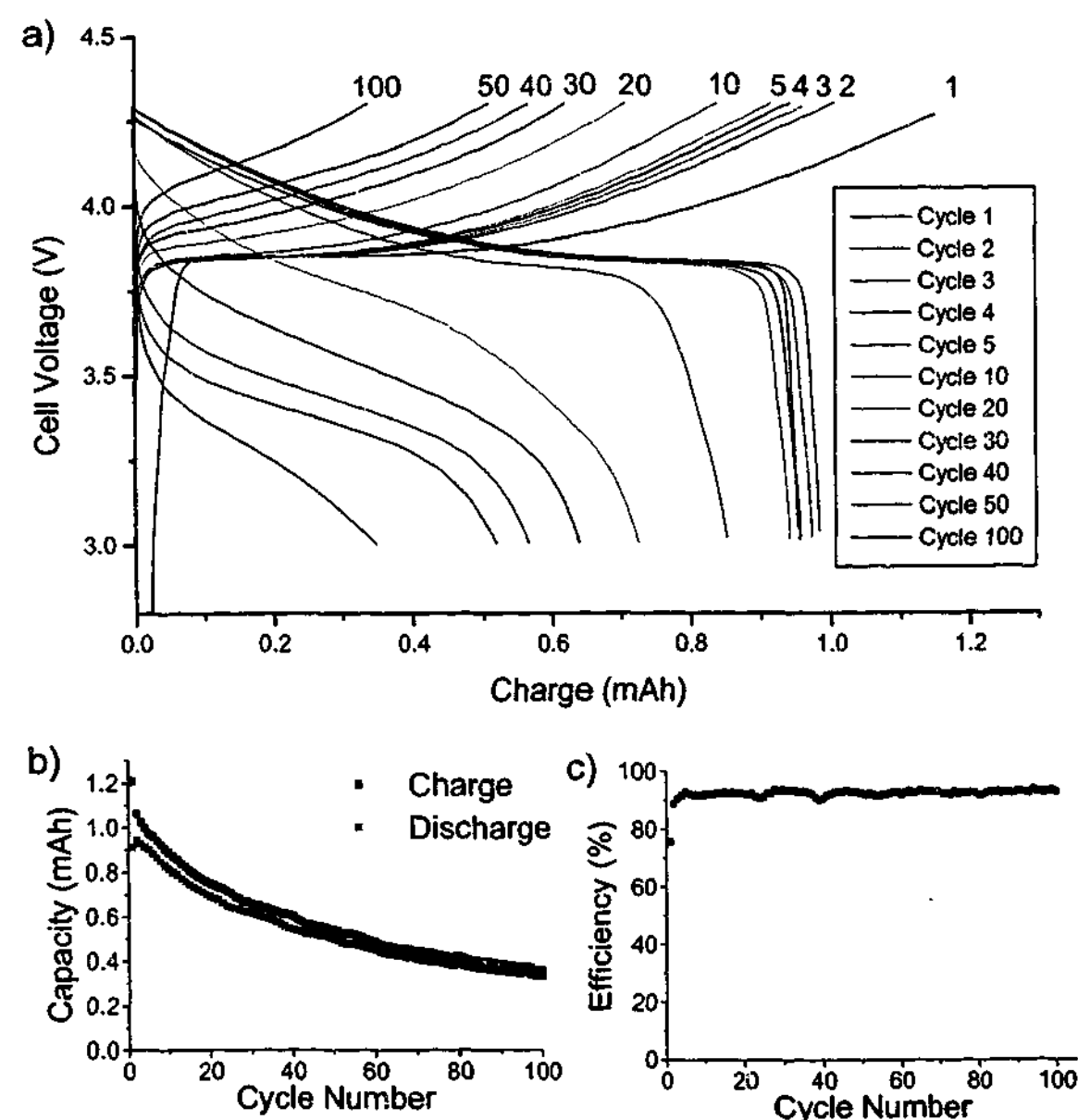
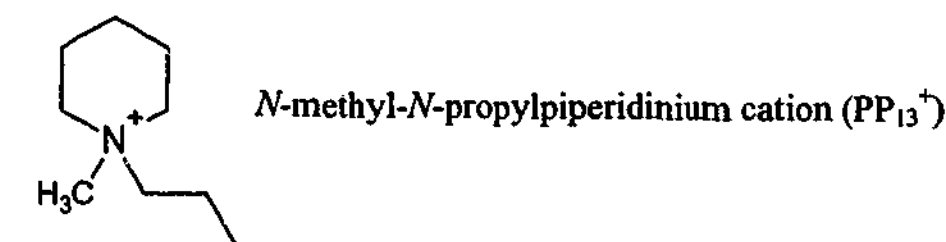


Fig. 3.6.4 Cycling behaviour of a $\text{Li} / \text{P}_{13}(\text{Tf})_2\text{N} - \text{GFFP} / \text{LiCoO}_2(\text{Pt})$ cell cycled at $C/10$ at 80°C . a) Voltage profile b) Cell capacity c) Cell efficiency (discharge cap./charge cap.).

To investigate the influence of the choice of positive electrode active material and because of concerns arising from reports of capacity fade of LiMn_2O_4 electrodes at elevated temperatures,⁹⁻¹¹ LiCoO_2 was used as a replacement. Figure 3.6.4 shows plots of the voltage profile, charge/discharge capacity and cell efficiency of a $\text{Li/P}_{13}(\text{Tf})_2\text{N/LiCoO}_2$ cell cycled at $C/10$ (for a nominal 1.25 mAh cell based on 100% utilization of $150 \text{ mAhg}^{-1} \text{ LiCoO}_2$)⁵ at 80°C . The cell exhibited high initial capacity and a significantly reduced rate of capacity fade, compared with the previous cells. The initial discharge capacity was $\sim 75\%$ of theoretical, which faded to $\sim 30\%$ by the 100th cycle. The cell efficiency was lower than that exhibited by the LiMn_2O_4 cells, reaching a plateau at $\sim 95\%$. The charge on the first cycle was close to theoretical, and a low voltage plateau was evident during the initial part of the voltage profile, indicative of SEI formation. The first discharge capacity was also lower than the subsequent (2nd) discharge, again reflecting the formation of a SEI. Unlike the previous cells, the discharge plateau in the voltage profile exhibited a steady decrease, indicating an increase in resistance to lithium transport within the cell, which could suggest a different mechanism for the capacity fade exhibited by this cell.

3.6.3 Comparison with $\text{PP}_{13}(\text{Tf})_2\text{N}$:

Recently, a study comparing the cycling behaviour of several RTILs composed of quaternary ammonium cations and the $(\text{Tf})_2\text{N}^-$ anion was reported.¹² The paper reported that the piperidinium cation (shown below) imparted superior cycling behaviour to Li/LiCoO_2 cells.



A study was undertaken to compare the properties of the $\text{PP}_{13}(\text{Tf})_2\text{N}$ and $\text{P}_{13}(\text{Tf})_2\text{N}$ ionic liquids, specifically, their conductivity, lithium cycling efficiency and the cycling behaviour of a Li/LiCoO_2 cell.

The $\text{PP}_{13}(\text{Tf})_2\text{N}$ RTIL can be expected to exhibit very similar properties to $\text{P}_{13}(\text{Tf})_2\text{N}$. The PP_{13}^+ cation could be expected to be slightly less reactive owing to the reduced ring strain

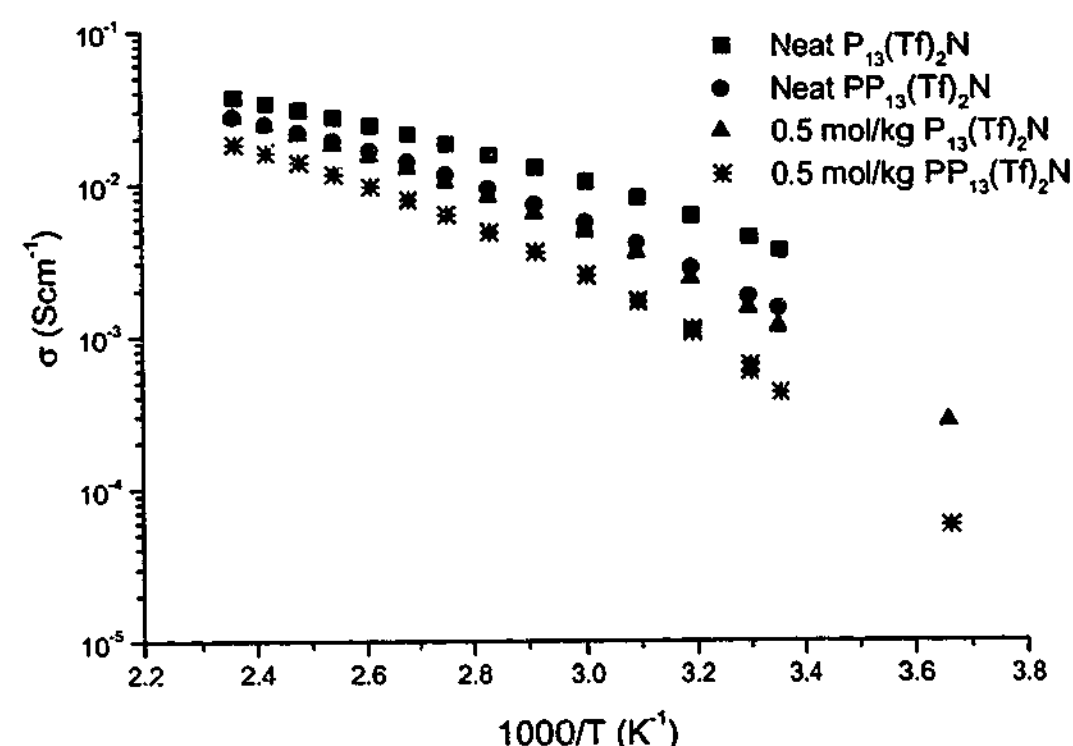


Fig. 3.6.5 Arrhenius plot showing a comparison of neat and 0.5 mol kg⁻¹ samples of P₁₃(Tf)₂N and PP₁₃(Tf)₂N.

imparted by the six-membered ring. The larger ionic radius of the PP₁₃⁺ cation should result in reduced conductivity. Figure 3.6.5 shows an Arrhenius plot comparing the conductivity of the two RTILs. Over the entire temperature range, the P₁₃(Tf)₂N ionic liquid was significantly more conductive.

Table 3.6.2 shows values for the cycling efficiency obtained on a copper electrode for PP₁₃(Tf)₂N. Comparison with the values obtained for P₁₃(Tf)₂N indicate that the P₁₃(Tf)₂N RTIL provides superior lithium electrode cycling performance, particularly at higher rates. The most likely explanation for the difference in cycling efficiencies exhibited by the two systems, given their similarity in terms of chemical reactivity, is that the deposit morphology in PP₁₃(Tf)₂N at higher current densities becomes dendritic. As has already been shown (section 3.1 & 3.2), the cycling efficiency and deposit morphology of lithium in RTIL electrolytes are closely related and are strongly dependent on the applied current density. The significant difference in conductivities exhibited by the two systems indicates that lithium transport to the electrode surface will become diffusion limited at much lower current densities in the PP₁₃(Tf)₂N electrolyte than it would in the P₁₃(Tf)₂N electrolyte. Thus the current density threshold above which the deposit morphology becomes

unfavourable for high cycling efficiency will be lower in the less conductive PP₁₃(Tf)₂N system. This difference highlights an important requirement for the improvement of the rate capability of RTIL electrolytes, given that the cycling efficiency is dictated not only by their chemical stability but also by the electrolytes' ability to transport lithium ions to the electrode surface.

Table 3.6.2 Cycling efficiencies determined on a copper electrode at 50 °C for 0.5 mol kg⁻¹ PP₁₃(Tf)₂N at various current densities. Excess charge = 1 C cm⁻², cycling charge = 0.25 C cm⁻². Values for 0.5 mol kg⁻¹ P₁₃(Tf)₂N are included for comparison.

RTIL	1.0 mAcm ⁻²	0.5 mAcm ⁻²	0.1 mAcm ⁻²
0.5 mol kg ⁻¹ PP ₁₃ (Tf) ₂ N	50 %	50 %	87 %
0.5 mol kg ⁻¹ P ₁₃ (Tf) ₂ N	92 %	86 %	>91 %

Figure 3.6.6 shows plots of the voltage profile, charge/discharge capacity and cell efficiency of a Li/PP₁₃(Tf)₂N/LiCoO₂ cell cycled at C/10 (for a nominal 1.25 mAh cell based on 100% utilization of 150 mAhg⁻¹ LiCoO₂)⁵ at 80 °C. The cell behaved similarly to the P₁₃(Tf)₂N cells, although its performance was slightly inferior to the equivalent P₁₃(Tf)₂N cell shown in Fig. 3.6.4, exhibiting a more rapid rate of capacity fade in the early cycles, contrary to the report of Sakaebe and Matsumoto.¹² The cell efficiency and utilization was also lower than that of the P₁₃(Tf)₂N cell. Under the conditions of the experiment, the applied current density was low (0.06 mAcm⁻²), thus the lithium cycling efficiency could be expected to be very high for both electrolytes. This indicates that any difference in the behaviour of the two systems is most likely related to interactions with the positive electrode. In addition, the cell used by Sakaebe and Matsumoto had a thin film configuration, thus the applied current to produce C/10 (calculated to be ~ 0.02 mAcm⁻², based on 1-1.5 mgcm⁻² of active material) in their experiment was even lower than in the experiments used here. Unlike the P₁₃(Tf)₂N cell (Fig. 3.6.4), the cell did not exhibit a decrease in the voltage of the discharge plateau.

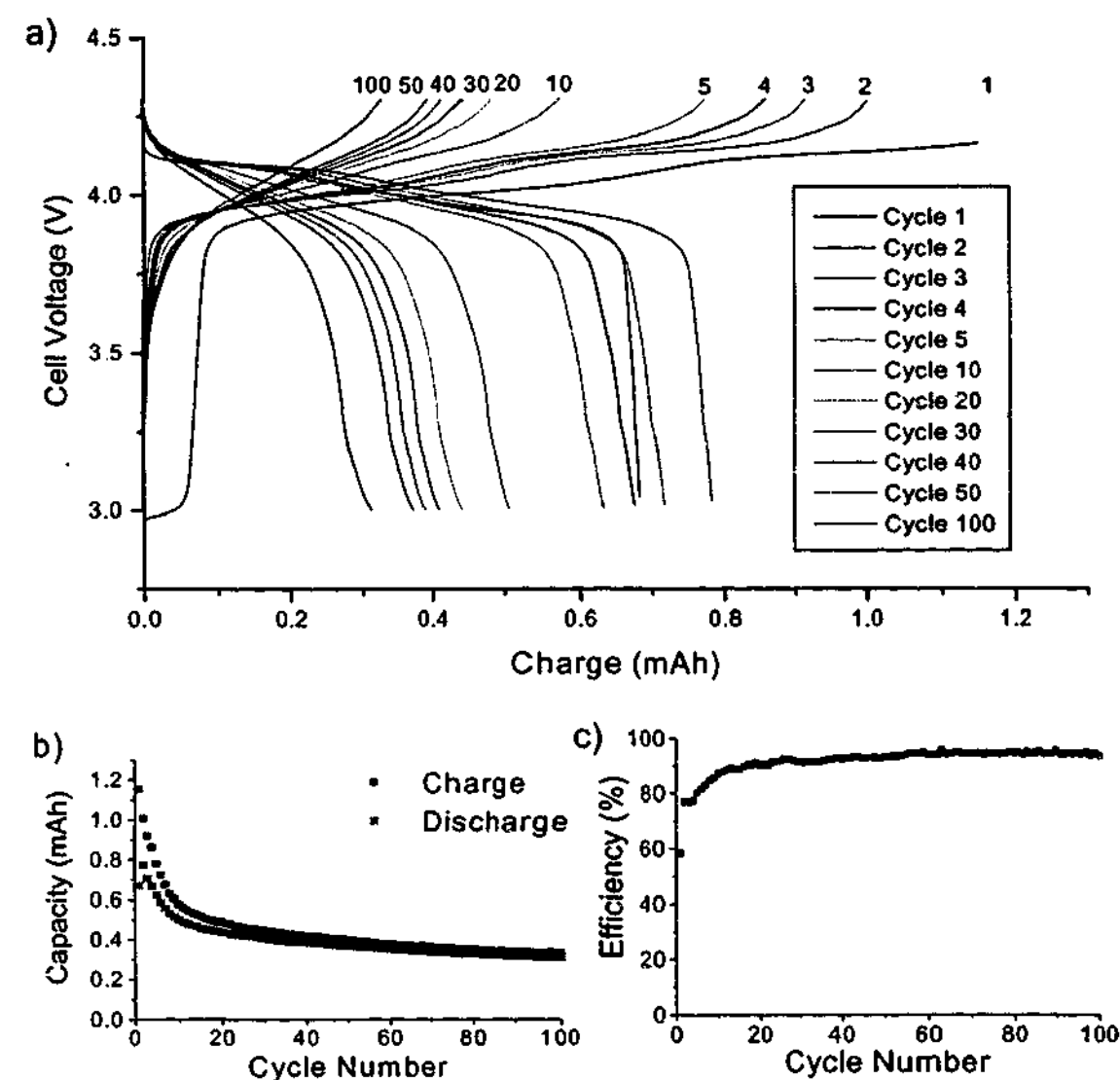


Fig. 3.6.6 Cycling behaviour of a Li / $\text{PP}_{13}(\text{Tf})_2\text{N}$ - GFFP / $\text{LiCoO}_2(\text{Pt})$ cell cycled at C/10 at 80 °C. a) Voltage profile b) Cell capacity c) Cell efficiency (discharge cap./charge cap.).

To compare the behaviour of the two systems with respect to the lithium electrode and to confirm the suspicion that the capacity fade exhibited by all of the cells was related to the positive electrode (based on the high lithium metal cycling efficiencies already determined), symmetrical lithium cells were made using the $\text{P}_{13}(\text{Tf})_2\text{N}$ and $\text{PP}_{13}(\text{Tf})_2\text{N}$ electrolytes. Both cells were cycled at the equivalent of a C/10 rate and under the same conditions as the Li/LiCoO₂ cells. Figure 3.6.7 shows the voltage profile recorded for both cells for 100 'charge-discharge' cycles. The profiles show a clear superiority of the $\text{P}_{13}(\text{Tf})_2\text{N}$ system over the $\text{PP}_{13}(\text{Tf})_2\text{N}$ system under the conditions of the experiment. The $\text{P}_{13}(\text{Tf})_2\text{N}$ cell, in particular, gave every indication that it would continue to cycle indefinitely. More importantly, the profiles clearly indicate that the electrolyte interactions at the lithium electrode would not have contributed to the capacity fade for any of the cells in this study. Thus, there is no doubt that the capacity fade exhibited by all of the cells was related to electrolyte interactions with the positive electrode.

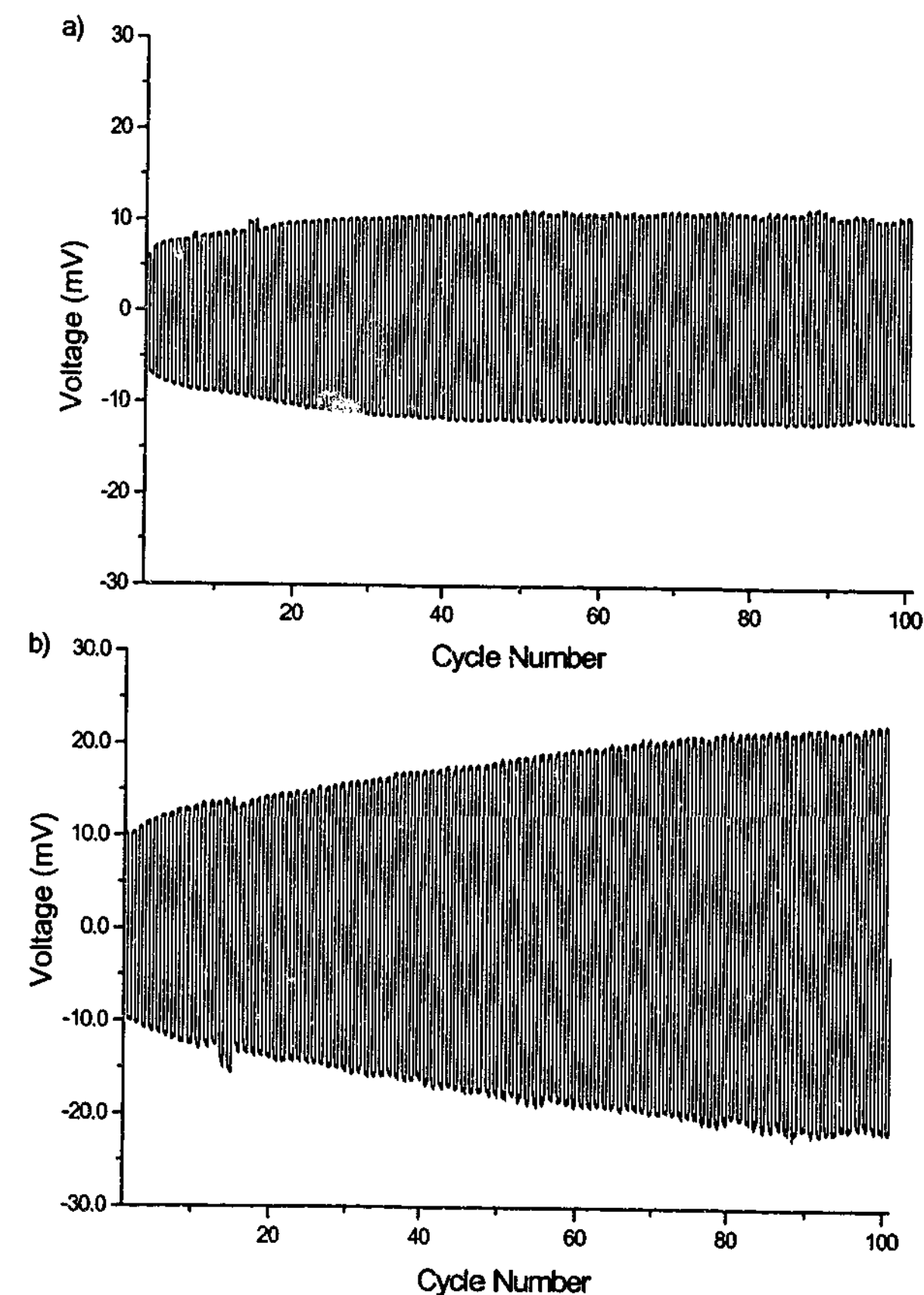


Fig. 3.6.7 Galvanostatic cycling of symmetrical lithium cells at the 'C/10' rate (0.0625 mAcm⁻², 2.25 Cm²) at 80 °C. a) Li / 0.5 molkg⁻¹ $\text{P}_{13}(\text{Tf})_2\text{N}$ - GFFP / Li, b) Li / 0.5 molkg⁻¹ $\text{PP}_{13}(\text{Tf})_2\text{N}$ - GFFP / Li.

3.6.4 Conclusions:

Under 'battery-like' conditions lithium cells incorporating the $P_{1X}(Tf)_2N$ electrolytes used in this study (i.e., $0.5 \text{ mol kg}^{-1} \text{ Li}(Tf)_2N$ solutions) were demonstrated to be limited to less than $\sim 0.25 \text{ mA cm}^{-2}$ at 50°C for continual cycling to be possible. Higher rates were possible but could not be sustained for lengthy periods. At lower rates the cycling was demonstrated to be highly reversible and very long cycle lives could be expected. The cells were able to operate at elevated temperatures (e.g., 80°C), apparently without any detriment to their cycling behaviour.

When 'battery' cells incorporating a positive electrode were cycled, all of the cells tested exhibited pronounced and rapid capacity fade, the best cells stabilised at $\sim 30\%$ of their theoretical capacity, where they were able to cycle for extended periods.

A comparison of $P_{13}(Tf)_2N$ with a recently reported system, $PP_{13}(Tf)_2N$,¹² was made. Contrary to the report, no significant superiority of the $PP_{13}(Tf)_2N$ system over the $P_{13}(Tf)_2N$ system was determined. However, there were enough differences between the conditions of the experiments reported here and those reported by Sakaebe and Matsumoto,¹² with respect to temperature, rate, lithium salt concentration and cell configuration, to allow for an explanation of the difference in observed behaviour. The cells used by Sakaebe and Matsumoto were apparently optimised for the $PP_{13}(Tf)_2N$ system. The work reported here indicated that the ability of the $PP_{13}(Tf)_2N$ system to cycle lithium was significantly inferior to that of $P_{13}(Tf)_2N$, and this was ascribed to the difference in their conductivities.

Most significantly, it was demonstrated that the capacity fade exhibited by the battery cells was wholly associated with the presence of the positive electrode. Thus, the work of Sakaebe and Matsumoto¹² indicates that, when the cycling rates were low enough to allow the $PP_{13}(Tf)_2N$ system to cycle lithium reversibly, then the $PP_{13}(Tf)_2N$ system demonstrated slightly better stability versus the positive electrode than the $P_{13}(Tf)_2N$ system. The work presented here demonstrated that, at higher rates, the difference was not significant and that the $PP_{13}(Tf)_2N$ electrolytes' (relatively poor) ability to cycle lithium was likely to become significant with prolonged cycling.

No attempt has been made here to determine the specific mechanism contributing to the capacity fade in the battery cells, other than to determine that it was related to the positive electrode. There are a number of possible mechanisms by which the positive electrode could exhibit capacity fade in a LMIL battery, and some possible mechanisms are listed below:

- Solvation of a component of the positive electrode active material matrix (due to the strong solvating power of the RTIL) causing its disintegration or delamination.
- Poorly reversible co-intercalation of the P_{1X}^+ cation within the positive electrode active material.
- Oxidation of the $(Tf)_2N^-$ anion at the positive electrode surface.

Teardown analysis of the cycled cells indicated that, at least superficially, the positive electrode material was intact and had maintained good contact with the current collector. Based on reports of oxidative instability demonstrated by the $(Tf)_2N^-$ anion,⁶⁻⁸ it seems that the oxidation of the anion could be the principal cause of the capacity fade. If electrolyte oxidation is the cause of the capacity fade, low voltage cells (i.e., $<3 \text{ V}$) might not exhibit the same behaviour. Alternatively, based on the evidence presented by Sakaebe and Matsumoto,¹² better capacity retention was exhibited by cells in which the RTIL incorporated a larger cation, suggesting that co-intercalation of the cation could be responsible for the capacity fade.

References

1. T. Hirai, I. Yoshimatsu and J. Yamaki, *J. Electrochem. Soc.*, **141**, 2300 (1994).
2. T. Hirai, I. Yoshimatsu and J. Yamaki, *J. Electrochem. Soc.*, **141**, 611 (1994).
3. E. Eweka, J. R. Owen and A. Ritchie, *J. Power Sources*, **65**, 247 (1997).
4. D. Aurbach (Ed.), *Nonaqueous Electrochemistry*, Marcel Dekker, New York (1999).
5. J. O. Besenhard (Ed.), *Handbook of Battery Materials*, Wiley-VCH, Weinheim (1999).
6. L. J. Krause, W. Lamanna, J. Summerfield, M. Engle, G. Korba, R. Loch and R. Atanasoski, *J. Power Sources*, **68**, 320 (1997).
7. H. Yang, K. Kwon, T. M. Devine and J. W. Evans, *J. Electrochem. Soc.*, **147**, 4399 (2000).
8. M. Morita, T. Shibata, N. Yoshimoto and M. Ishikawa, *J. Power Sources*, **119-121**, 784 (2003).
9. Y. Xia, Y. Zhou and M. Yoshio, *J. Electrochem. Soc.*, **144**, 2593 (1997).
10. M. M. Thackeray, *J. Am. Ceram. Soc.*, **82**, 3347 (1999).
11. X. Sun, H. S. Lee, X. Q. Yang, and J. Mcbreen, *Electrochemical and Solid State Letters*, **4**, A184-A186 (2001).
12. H. Sakaebe and H. Matsumoto, *Electrochemistry Communications*, **5**, 594 (2003).

Conclusions & Future Work

The work presented here endeavoured to find an approach that would allow the application of the lithium metal electrode in a rechargeable cell. Room temperature ionic liquid electrolytes were perceived to offer a possible solution to the problems associated with cycling lithium metal because of their unique properties, particularly because of their inherently inert nature (thermal, chemical and electrochemical) and because of their design flexibility. The idea that RTILs might impart unique properties to the SEI and, hence, the lithium deposit morphology, became a principal hypothesis associated with this work. The possibility that the design flexibility of RTILs can be harnessed to dictate the properties of the SEI is now an enticing prospect.

The investigation of ionic liquids as electrolytes for alkali metal electrodes is not a new concept (refer to section 1.4.5). Recently, however, the range of materials available for investigation has expanded rapidly, making their investigation increasingly topical. Undoubtedly, studies focussing on electrolytes incorporating these materials will continue to become more prevalent in the literature. Presently, particularly in the light of the work presented here and recent reports in the literature,¹⁻³ it seems that this type of electrolyte research offers some of the most exciting prospects for significant advances in the field of rechargeable batteries.

The development of an optical cell allowed the RTILs to be assessed in terms of their ability to reversibly cycle lithium metal while monitoring the evolution of the lithium deposit morphology. The optical cell experiments allowed numerous observations and a number of firm conclusions were drawn;

- A survey of a matrix of RTILs indicated that the $P_{1X}(Tf)_2N$ system was superior for lithium electrochemistry.
- Comparison of the different RTILs indicated that the cation role was to be stable versus reduction, while the anion formed a SEI, the properties of which dictated the deposit morphology with repetitive cycling.
- As the anion hydrophobic character increased, so did the RTIL cycling efficiency.

- Lithium deposit morphology was more favourable (i.e., fine, non-dendritic particles) in the most conductive (electrochemically stable) RTILs, and was apparently linked to the diffusivity of the Li^+ cation in the RTIL.

Optical cell experiments comparing the behaviour of the $\text{P}_{1X}(\text{Tf})_2\text{N}$ system under varied conditions allowed the following observations to be made;

- The applied current density had a strong influence on the lithium deposit morphology and hence the cycling efficiency.
- Repeated cycling indicated a strong influence of the SEI properties on the deposit morphology and hence the cycling efficiency.
- The type of substrate exerted a strong influence on the deposit morphology.
- Cycling efficiencies of less than 100% were due (in part) to side reactions between Li and the electrolyte and impurities (chemical effects).
- Cycling efficiencies of less than 100% were also due to surface fouling (which often over-rode contributions from side reactions) resulting from the build-up of lithium reaction products, which effectively reduced the electrode active surface area, leading to increased applied current density and hence dendritic deposit morphology and the formation of dead lithium (physical effects).
- The formation of dead Li resulted in a significant reduction in cycling efficiency and represented the most significant contribution to 'cell failure'.
- A marked difference in behaviour between the native Li surface and the Li on Cu deposit was noted. The Li surface exhibited a significantly reduced tendency to form dendritic growths.

Following the optical cell experiments, 3-electrode cell measurements were conducted on Pt and Cu substrates in $\text{P}_{1X}(\text{Tf})_2\text{N}$ electrolytes. The experiments confirmed a marked difference in behaviour depending on the type of substrate. This, in part, was attributed to the occurrence of under potential deposition on the platinum substrate. As a function of applied current density the cycling efficiency was found to be higher and more consistent on the Pt substrate. For both substrates the cycling efficiency exhibited a sharp decline above a certain maximum current density, this was attributed to the onset of dendritic deposit morphology. For the Pt substrate the decline commenced above 1.75 mAcm^{-2} (at

50°C) and above 1 mAcm^{-2} for the Cu substrate (at 50°C). The $\text{P}_{12}(\text{Tf})_2\text{N}$ system was not sufficiently conductive to cycle lithium reversibly under the conditions of the experiments. However, the $\text{P}_{12}(\text{Tf})_2\text{N}$ system becomes more conductive at higher lithium concentrations⁴⁻⁶, reaching a maximum at $\sim 0.9 \text{ mol/kg}$ ($\text{Li}(\text{Tf})_2\text{N}/\text{P}_{12}(\text{Tf})_2\text{N}$). Further investigation at these concentrations is warranted before the $\text{P}_{12}(\text{Tf})_2\text{N}$ system could be dismissed as a potential candidate. The $\text{P}_{13}(\text{Tf})_2\text{N}$ and $\text{P}_{14}(\text{Tf})_2\text{N}$ systems behaved similarly, the $\text{P}_{13}(\text{Tf})_2\text{N}$ system giving more consistently high cycling efficiencies on the Cu substrate.

Mass transport in the $\text{P}_{1X}(\text{Tf})_2\text{N}$ system was investigated using EIS and NMR spectroscopy. Transport in the solid $\text{P}_{12}(\text{Tf})_2\text{N}$ system was found to be dominated by the cation (P_{12}^+) diffusion. At higher Li^+ concentrations, Li^+ and $(\text{Tf})_2\text{N}^-$ diffusion became more significant. Transport was found to obey the Nernst-Einstein relation but required knowledge of the number of mobile species (for each ion) in the sample before the relationship could be quantified. The liquid systems, $\text{P}_{13}(\text{Tf})_2\text{N}$ and $\text{P}_{14}(\text{Tf})_2\text{N}$, were found to depart significantly from the Nernst-Einstein relation, the difference becoming increasingly significant at higher temperatures. This indicated that 'currentless' modes of diffusion became more prominent as the temperature was increased. This was rationalised in terms of the hole theory of the liquid state, where the proportion of 'paired vacancies' (a mode that allows currentless diffusion) is thought to increase as the amount of free volume in the liquid increases. The conductivity of $\text{P}_{13}(\text{Tf})_2\text{N}$ was found to be slightly higher than that of $\text{P}_{14}(\text{Tf})_2\text{N}$. The diffusivity of all three species (i.e., P_{13}^+ , $(\text{Tf})_2\text{N}^-$ and Li^+) was found to be similar (in general) over the temperature range studied. Transport numbers were calculated by the application of a cross-coefficient (to account for the departure from Nernst-Einstein behaviour), the transport number for lithium was found to be low (0.05 – 0.2 for a 0.5 mol/kg sample) for all of the samples, but tended to increase at higher temperatures. The $\text{P}_{14}(\text{Tf})_2\text{N}$ system exhibited slightly higher lithium transport numbers, and this was attributed to the presence of the larger P_{14}^+ cation.

The surface of lithium and lithium deposited on copper samples cycled in $\text{P}_{1X}(\text{Tf})_2\text{N}$ electrolytes were characterised using XPS, GAXRD, Raman, DRFTIR and EIS techniques. The measurements indicated a multilayer, multicomponent SEI dominated by reduction products of the $(\text{Tf})_2\text{N}^-$ anion, chiefly LiF and Li_2O . A distinct difference between the

native 'glovebox' lithium surface and the electrochemically deposited surface was evidenced. The native surface retained significant components of Li_2O and Li_2CO_3 . The SEI was estimated to be 200-300 nm thick. For the deposited surface, components related to the P_{1X}^+ cation were present; their nature was not clear from the analysis. A general model for the surface films was presented.

A range of additives were investigated in the $\text{P}_{13}(\text{Tf})_2\text{N}$ electrolyte, including polymers, inorganic fillers and inorganic salts. This approach was not successful in producing a significant improvement in the lithium cycling efficiency on a copper substrate. The addition of lithium salts other than $\text{Li}(\text{Tf})_2\text{N}$, specifically LiAsF_6 , produced an improvement in the cycling efficiency of the electrolyte. This offers a promising avenue for further investigation and supports the assertion that the anion dominates the SEI composition and hence the lithium cycling behaviour.

Cells incorporating a LiMn_2O_4 or a LiCoO_2 cathode were investigated. The cells exhibited rapid capacity fade from initial values that were close to theoretical. A role for the deterioration of the Al current collector was indicated by the superior behaviour of cells incorporating a Pt current collector. The LiCoO_2 cathode material appeared to give better capacity retention. Capacity fade (under the conditions of the experiment) resulted from a process at the cathode, as was evidenced by the reversible cycling behaviour of lithium symmetrical cells. The mechanism for the capacity fade produced by the presence of the cathode was not determined.

Based on the observations and conclusions made in this work, some basic requirements for a RTIL lithium battery electrolyte can be made:

- The cation should be electrochemically stable versus lithium and able to impart high conductivity and low melting point to the electrolyte; at present the quaternary ammonium cations are the best examples of cations for this role. The cyclic pyrrolidinium cations appear to provide additional stability.
- The anion should provide reduction products that produce a favourable SEI and should be small to impart high conductivity - perfluorinated anions appear to produce the most favourable film.

- The concentration and nature of the added lithium salt should be adjusted to optimise the RTIL electrolyte ability to cycle lithium, the properties (i.e., conductivity and electrochemical stability) of the RTIL plus salt are more important, with respect to electrolyte design, than are the properties of the neat RTIL.

The application of RTILs to lithium batteries, particularly those incorporating lithium metal electrodes holds significant potential. Their eventual application in electrochemical devices, including batteries, seems certain. The $\text{P}_{1X}(\text{Tf})_2\text{N}$ system investigated in this work, while not being ideal in terms of its lithium transport properties and electrochemical stability, approaches the requirements for a long life, high power, high energy density device that would be relatively safe, environmentally benign and easy to manufacture. The work presented here indicates a clear avenue of further investigation to discover and develop improved RTIL electrolytes for lithium metal rechargeable batteries.

Future work:

Plainly, the chief problem associated with the electrolytes presented here is the rapid capacity fade exhibited by a cell incorporating a transition metal cathode. Numerous avenues of investigation exist to attempt to remedy the problem, including the use of additives, variation of cation-anion combinations and the use of alternate cathode materials (e.g., inherently conducting polymers (ICPs)). In order to decide on the appropriate avenue to pursue, the mechanism by which the cathode produces the capacity fade must be determined. The most obvious approach would involve analysis of the components of the cycled cells, specifically XRD analysis of the cycled cathode material (as well as elemental analysis). Chemical analysis of the cycled electrolyte might also provide useful information.

The rate capability of the RTIL electrolytes represents another area where the electrolyte properties require improvement. The work presented in this thesis demonstrates that this is a complex issue, related to lithium transport in the electrolyte as well as the SEI, which in turn is related to the electrolyte stability and the chemistry of formation of the SEI. The work presented in section 3.3 indicated that the lithium transport number was low and that transport in the RTIL appeared to be diffusion limited. In addition, the RTIL appeared to be highly associated, thus reducing the measured conductivity. A method, by which the

transport properties of the RTIL could be improved, other than through the variation of cation and/or anion structure, would be through the addition of a molecular solvent, which may increase the contribution of the migration current in the electrolyte (as well as a possible reduction in viscosity). However, the presence of the molecular solvent is likely to compromise the beneficial properties of the RTIL (i.e., favourable SEI properties, non-volatility etc.). An alternative additive might be a zwitterion (e.g., 1-butylimidazolium-3-(n-butanedisulphonate). Some zwitterions that are liquid at room temperature have been synthesised.⁷⁻¹⁰ Zwitterions have been shown to enhance dissociation in polyelectrolyte gels¹¹ and may not compromise the physical, chemical and electrochemical properties of the RTIL electrolyte.^{8,10} Because the zwitterions have no net electrostatic charge, they may also allow for a substantial migration component of the current. A zwitterion that was liquid at room temperature, and thus would not result in a significant increase in viscosity when added to the RTIL, and was also electrochemically stable, may prove to be an excellent solvent or co-solvent for a lithium battery electrolyte.

The most obvious method to manipulate the properties of the RTIL is through the variation of the cation and/or anion structure. Slight variations in structure would most likely result in a drastic alteration in the behaviour of the lithium electrochemistry. As has already been mentioned, the range of possible variations is vast; the difficulty at present lies in the choice of the type of variations that are preferable.

An investigation of the lithium cycling behaviour of phosphate onium salts may clarify the role of the pyrrolidinium cation during lithium cycling. The phosphonium salts have been reported to possess greater electrochemical stability (versus reduction) than their ammonium analogues (as have the arsonium salts).¹² A logical progression would be to investigate the properties of phosphate analogues of pyrrolidinium and piperidinium, phospholanium and phosphorinanium respectively. A comparison of 3D energy minimised representations of these cations is shown in Fig. 4.1. RTILs comprising these cations have not been reported, however the synthesis and some properties of a variety of phospholanium and phosphorinanium salts have been reported.¹³⁻¹⁷ The synthesis of these cations is more difficult than their nitrogen analogues, primarily because the parent phospholanes and phosphorinanes are highly reactive, in some cases pyrophoric. It is difficult to predict the properties of the new salts, however, based on first principles comparisons of the ionic radius, formula weight and structural asymmetry, properties such

as melting point and viscosity might be expected to be similar to their nitrogen based counterparts. In their own right, the comparison of the physical and electrochemical properties of these materials would represent an important contribution to the literature. With respect to lithium battery applications the phosphate analogues could prove to possess greater electrochemical stability than their nitrogen analogues, in addition they could potentially be used to investigate the role of the cation in the capacity fade associated with the cathode.

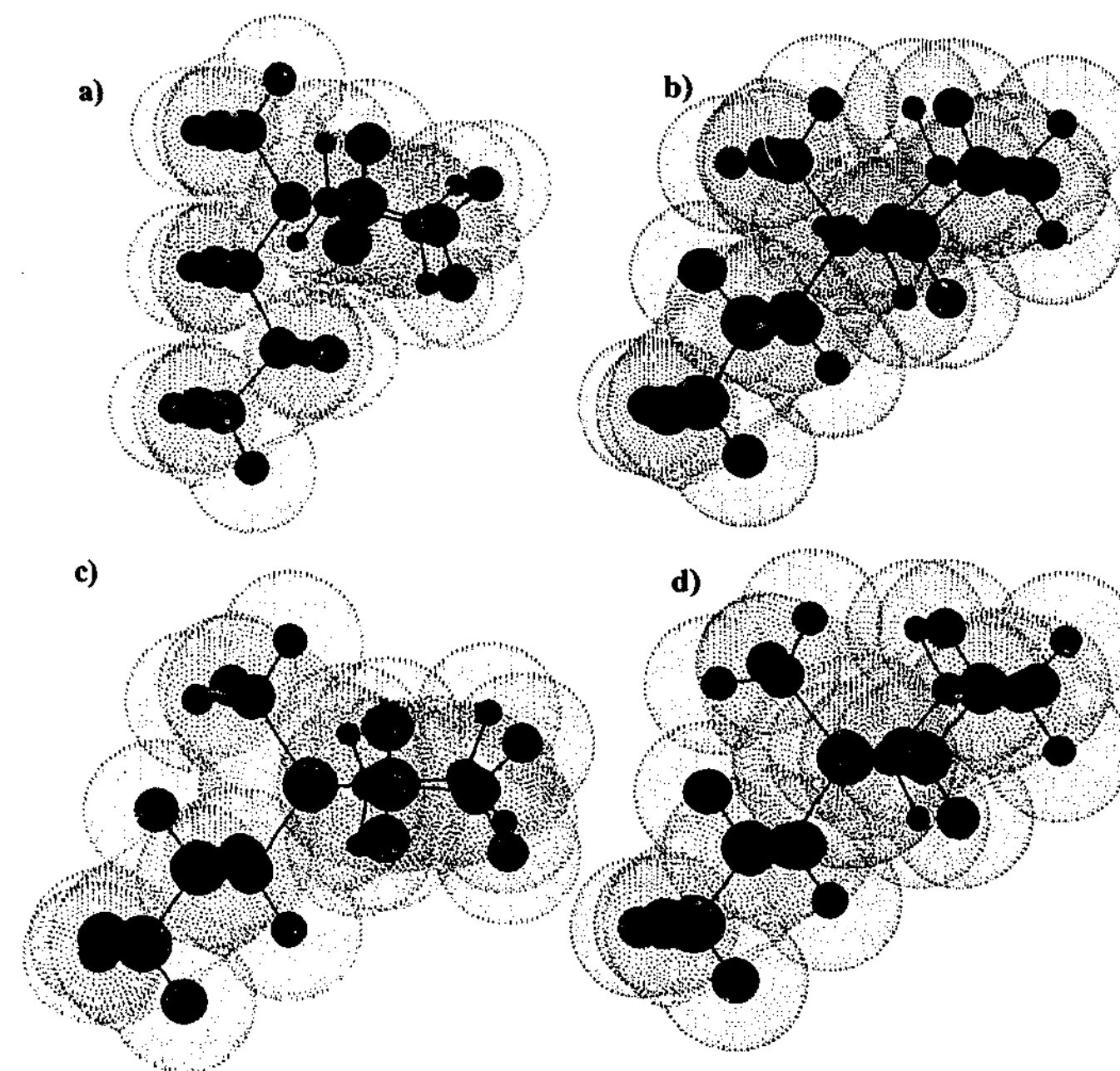


Fig. 4.1 Energy minimised 3D structures for a) methyl propyl pyrrolidinium b) methyl propyl piperidinium c) methyl propyl phospholanium d) methyl propyl phosphorinanium.

As has already been discussed (section 1.4.1 & 1.4.5) the range of anions available for application in lithium cells is expanding. Many of the new anions are likely to form RTILs. However, at present, an ideal anion that is small (i.e., like DCA), electrochemically stable and a 'good SEI former' has not been identified. The perfluoroalkyl phosphates (e.g., LiFAP) represent an interesting avenue of investigation; the anion has demonstrated electrochemical stability and is able to cycle lithium at high efficiency. RTILs incorporating the FAP anion having low melting points have been reported.¹⁸ However, the large ionic radius of the anion is likely to generate a viscous RTIL, resulting in ion transport limitations. Plainly, this is an important area of research and a significant amount of work geared towards generating new lithium salts for Li-ion batteries (with the goal of replacing LiPF₆ due to its tendency to hydrolyse) is occurring in the battery research community. In addition, new 'plasticising' salts for polymer electrolytes are being sought. The RTIL research community is also continually adding to the range of anions known to form RTILs. Fortunately, the requirements for anions for lithium battery electrolytes tend to coincide with those that are likely to form RTILs. In this respect, potential anions, worthy of investigation with cations such as pyrrolidinium, are likely to continue to appear in the literature.

One of the principle themes of the work presented here was the demonstration of the influence of the native SEI on the lithium deposit morphology and the way in which the native SEI persisted on the electrode surface in the RTIL after cycling. This observation indicates a possible avenue of future research investigating the influence of surface treatments prior to cycling in the RTIL. The influence of surface treatments on the cycling behaviour of lithium electrodes has been demonstrated on numerous occasions and was discussed in the introduction (section 1.5.3). A simple method for the formation of a Li₂CO₃ surface film, which produced favourable cycling behaviour, was reported recently.¹⁹ The work presented here indicates that films of this nature should be stable in the RTIL and are likely to result in favourable deposit morphology and cycling behaviour. The additives investigated in this work were shown to not have a significant effect on the cycling efficiency of the RTIL. However, a large range of additives remains to be assessed and factors such as the influence of their concentration in the RTIL need to be determined. The choice, and concentration, of the additive must also take into account its compatibility with the RTIL and its influence on the lithium transport properties of the RTIL. In

addition, the effect of additives on the cycling behaviour of the native lithium surface (as opposed to the electrochemical deposit surface) was not assessed.

Finally, there is significant work to be done to optimise the lithium cycling efficiency of the P_{1X}(Tf)₂N electrolytes presented here. The principle variables are the type and concentration of lithium salt to be added. As has been shown (section 3.5), the addition of LiAsF₆ improves the lithium cycling efficiency. However, there is an increase in viscosity (compared to the same concentration of Li(Tf)₂N) which reduces the rate capability of the electrolyte. Whether or not LiAsF₆ can be used as a low concentration additive has not been assessed. The influence of temperature also needs to be assessed. It was demonstrated that higher lithium salt concentrations were beneficial for higher temperature operation (section 3.5). For devices where the application temperature is high (e.g., ~150 °C), this could prove to be an important method for improving the electrolyte stability.

The application of RTILs in electrochemical devices is still in its infancy and the range of possible applications is vast. Presently, the majority of research is directed towards discovering new RTILs and in characterising their physical properties. The amount of research directed towards assessing RTILs as electrolytes (or as components of electrolytes) has been increasing steadily. Given their advantageous properties, it is reasonable to expect that the level of interest in these materials will continue to grow.

References

1. A. Webber and G. E. Blomgren, in *Advances in Lithium-ion batteries Ionic Liquids for Lithium Ion and Related Batteries*, W.A. van Schalkwijk and B. Scrosati p. 185, Kluwer Academic/Plenum Publishers, New York (2002).
2. H. Sakaebe and H. Matsumoto, *Electrochemistry Communications*, **5**, 594 (2003).
3. J. H. Shin, W. A. Henderson and S. Passerini, *Electrochemistry Communications*, **5**, 1016 (2003).
4. D. R. MacFarlane, P. Meakin, J. Sun, N. Amini and M. Forsyth, *J. Phys. Chem. B*, **103**, 4164 (1999).
5. D. R. MacFarlane, J. H. Huang and M. Forsyth, *Nature*, **402**, 792 (1999).
6. J. Huang, M. Forsyth and D. R. MacFarlane, *Solid State Ionics*, **136**, 447 (2000).
7. M. Yoshizawa, M. Hirao, K. Ito-Akita and H. Ohno, *J. Mater. Chem.*, **11**, 1057 (2001).
8. H. Ohno, M. Yoshizawa and W. Ogihara, *Electrochim. Acta*, **48**, 2079 (2003).
9. M. Yoshizawa, W. Ogihara and H. Ohno, *Polymers for Advanced Technologies*, **13**, 589 (2002).
10. M. Yoshizawa, Ph.D. Thesis, Tokyo University of Agriculture & Technology, 2002.
11. C. Tiyaipiboonchaiya, J. M. Pringle, J. Sun, N. Byrne, P. C. Howlett, D. R. MacFarlane and M. Forsyth, *Nature Materials*, **3**, 29 (2004).
12. A. I. Bhatt, I. May, V. A. Volkovich, M. E. Hetherington, B. Lewin, R. C. Thied and N. Ertok, *Journal of the Chemical Society. Dalton Transactions* 4532 (2002).
13. K. L. Marsi, *J. Am. Chem. Soc.*, **91**, 4724 (1969).
14. L. D. Quin, J. P. Gratz and T. P. Barket, *J. Org. Chem.*, **33**, 1034 (1968).
15. K. L. Marsi and J. E. Oberlander, *J. Am. Chem. Soc.*, **95**, 200 (1973).
16. N. J. Lawrence and H. Beynek, *Synlett*, **1998**, 497 (1998).
17. G. Baccolini, C. Boga and U. Negri, *Synlett*, **2000**, 1685 (2000).
18. Web Page, *Ionic Liquids* (Available: <http://www.ionicliquids-merck.de/servlet/PB/menu/1014040/index.html>, May 2003) Accessed 23 June 2003.
19. K. Chung, J.-D. Lee, E.-J. Kim, W.-S. Kim, J.-H. Cho and Y.-K. Choi, *Microchem. J.*, **75**, 71 (2003).

Publications

1. P.C. Howlett, D.R. MacFarlane and A.F. Hollenkamp, A sealed optical cell for the study of the lithium electrode | electrolyte interface, *J. Power Sources*, **114**(2), 177 (2003).
2. D.R. MacFarlane, P.C. Howlett and A.F. Hollenkamp and S.A. Forsyth, Room temperature ionic liquid electrolytes for lithium secondary batteries, Australian Pat. App. 2003901144 (2003).
3. P.C. Howlett, D.R. MacFarlane and A.F. Hollenkamp, High lithium metal cycling efficiency in a room temperature ionic liquid, *Electrochemical and Solid-State Letters*, In Press.
4. C. Tiyaipiboonchaiya, J. M. Pringle, J. Sun, N. Byrne, P. C. Howlett, D. R. MacFarlane and M. Forsyth, The Zwitterion Effect in High Conductivity Polyelectrolyte Materials, *Nature Materials*, **3**, 29 (2004).
5. J. M. Pringle, John Efthimiadis, P. C. Howlett, Jim Efthimiadis, D. R. MacFarlane, A. B. Chaplin, S. B. Hall, D. L. Officer, G. G. Wallace and M. Forsyth, Electrochemical Synthesis of Polypyrrole in Ionic Liquids, *Polymer*, **45**, 1447 (2004).
6. S.A. Forsyth, P.C. Howlett and D.R. MacFarlane, *N*-methyl-*N*-alkylpyrrolidinium nonafluoro-1-butanesulfonate salts: Physical properties and plastic crystal behaviour, *J. Mater. Chem.*, Submitted.
7. Qing Dai, D.R. MacFarlane, P.C. Howlett and M. Forsyth, Rapid I^-/I_3^- diffusion in a molecular plastic crystal: A novel electrolyte for solid-state photoelectrochemical cells, *J. Am. Chem. Soc. Comm.*, Submitted.

Papers are currently being prepared from sections 3.3 and 3.4.

ERRATA

- p 144: Fig. 3.1.17 Y-axis should contain the units, Volts (V).
 p 209 line 11: "dependent" for "dependant"

ADDENDUM

- p 39 line 1: The reference electrode referred to is Al/Al^{3+} (1.5:1 melt).¹
 p 42 line 9: The water insoluble product is the RTIL, *N*-methyl-*N*-propylpyrrolidinium bis(trifluoromethanesulfonyl)amide.
 p 115 end: The application of the Randles-Sevcik equation requires that the diffusion geometry at the electrode surface be linear (as in the case of a planar disk electrode) and requires a large interface. In addition, redox processes occurring at the electrode surface must exhibit Nernstian behaviour i.e., the process must be electrochemically reversible. Nernstian behaviour can be determined by the appearance of the cyclic voltammogram (CV) as follows;
 1. The peak separation exhibited by the CV (ΔE) must equal $0.059/n$ Volts (where n is the number of electrons involved in the redox process).
 2. The ratio of the peak heights must be one (i.e., the anodic and cathodic peaks, $I_{p,a}$ and $I_{p,c}$ respectively), thus $I_{p,a}/I_{p,c} = 1$.
 3. The peak height and the scan rate must increase proportionately (i.e., $I_p \propto v^{1/2}$), thus for a variety of scan rates, $I_{p,a}/v^{1/2}$ & $I_{p,c}/v^{1/2}$ should be constant.
 If these requirements are met, then mass transport to the electrode surface can be assumed to be diffusional with no migration component. An electrochemically irreversible process will not result in the generation of concentrations at the electrode surface as predicted by the Nernst equation because equilibria are not established rapidly. Electrochemically irreversible processes are brought about by slow electron transfer at the interface or from the presence of coupled chemical reactions (additional chemical processes occurring as a result of the electrochemically generated species). A non-zero intercept in the plot of I_p vs. $v^{1/2}$ indicates an ohmic limitation to charge propagation (i.e., slow electron transfer). If coupled chemical reactions are present at the electrode then $I_{p,a}/I_{p,c} \neq 1$.²
 p 126 end: The difference in appearance exhibited at the lithium surface when comparing the $\text{EMI}(\text{Tf})_2\text{N}$ and the PC/LiPF_6 cells could be attributed to a lower cycling current and a higher temperature combining to relieve the diffusion limitations that cause dendrite growth. In this respect the experiments are not directly comparable and it could be expected that the conventional system might exhibit a similar compact interphase at reduced rates and elevated temperature. However, the RTIL electrolyte exhibits similar conductivity to the conventional system at room temperature (i.e., $\sim 5 \times 10^{-3} \text{ Scm}^{-1}$) and given that all of the species in the RTIL contribute to conduction, then it can be expected that the diffusion of Li^+ to the electrode in the RTIL system is significantly slower. Thus, an increase in temperature and/or decrease in the applied current density (for the RTIL cell) should serve to render the experiments comparable in terms of the ability of the electrolyte to transport Li^+ to the surface. The possibility that elevated temperature could affect the kinetics of the SEI formation reactions and thus affect the properties of the SEI must also be considered when comparing the two experiments. With this in mind, clear conclusions about the superiority of the RTIL system over that of the conventional system cannot be drawn. However, the compact nature of the interphase and the non-volatility of the RTIL system offer an attractive situation warranting further investigation.
 p 147 line 6: The cycling efficiency is calculated using the average cycling efficiency equation (Eq. 2.10, p116). In the case of Fig. 3.1.19, the experiment progressed for 0.4 of a dissolution cycle, as shown in the inset, before the deposit was exhausted and the potential shifted to more positive (oxidative) values, thus substituting 0.4 for N , and using the other parameters as outlined (Table 3.1.1, p 137), provides an average cycling efficiency of 9.1 % ($\sim 10\%$).
 p 148: Fig. 3.1.22 (and others) shows dissolution potentials that often end at negative potentials, which is unexpected because lithium dissolution should occur at slightly

positive potentials (vs. Li/Li^+). While this could reflect a situation where under potential deposition or alloying has occurred, resulting in shifted potentials, the most likely explanation results from the calibration of the CSIRO BCU potentials to match those of the potentiostat, which becomes difficult in the mV range; this results in a systematic error in the recorded potentials.

p 207 line 10: The minor features visible at ~ 0.5 V, 1.7 V and 5 V vs. Li/Li^+ , became apparent only after the voltage range had been extended beyond ~ 0 and 6 V vs. Li/Li^+ . The features were not visible in the CV when the voltage range was not extended beyond these limits and are assumed to result from the presence of products formed by the oxidation/reduction of the electrolyte at extreme voltages. The minor features are assumed to not participate in the electrochemistry when the voltage range is held within ~ 0 to 6 V vs. Li/Li^+ .

p 210, 211: Under potential deposition (UPD): UPD often occurs when one metal is deposited on a different metal substrate. UPD occurs when the adatom-substrate bonding is stronger than the adatom-adatom bonding so that the first one or two monolayers are deposited at potentials positive of the Nernst potential for bulk deposition, the strength of the bonding is reflected by the metals' work function, which is defined as the smallest energy needed to extract an electron at 0 K. The work function of an electrode at which UPD occurs must be more positive than the work function of the metallic form of the metal ion depositing at underpotential. As UPD coverage increases, the work function of the substrate electrode shifts to more negative values until the work function of the active metal is reached. Then, the UPD ceases and deposition of the bulk form of the active metal occurs.³

Alloying: Electrodeposition of a metal from solution onto a foreign substrate can result in the formation of an alloy, either as an intermetallic compound, an amorphous material or an interstitial compound. This process occurs after the ion has been deposited from solution and does not affect the electrochemical response.³

The electrode response when UPD occurs can be treated as a similar situation to that which occurs when an electroactive species is adsorbed on the surface of an electrode. In this case, $I_p \propto \nu$ in contrast to the $\nu^{1/2}$ dependence observed for Nernstian waves for diffusing species. Thus, peaks arising from UPD tend to exhibit a greater dependency on scan rate, and if it is possible to resolve the individual peaks from the CV, this dependence can be used to distinguish between UPD and diffusion limited processes.⁴

p 214 line 9: The dominance of the lithium electrochemistry in $\text{P}_{13}(\text{Tf})_2\text{N}$ and $\text{P}_{14}(\text{Tf})_2\text{N}$ compared to $\text{P}_{12}(\text{Tf})_2\text{N}$ is evidenced by the much larger deposition and dissolution currents present in the CVs (Figs. 3.2.7 & 3.2.8 vs. Fig. 3.2.6). The larger 'lithium derived' currents cause the CV coulombic efficiency to reflect the lithium electrochemistry more accurately than the lower currents present in the $\text{P}_{12}(\text{Tf})_2\text{N}$ CV, where processes associated with the electrolyte are more significant.

p 234: The CVs shown in Fig. 3.3.1 indicate a significant IR distortion of the Randles-Sevcik response. It is possible to account for the distortion by monitoring the change in peak height (I_p) with respect to the peak separation ($E_p - E^0$). A plot of the $\ln(I_p)$ vs. ($E_p - E^0$) should be a straight line (shown below Fig. 3.3.2a), with a slope

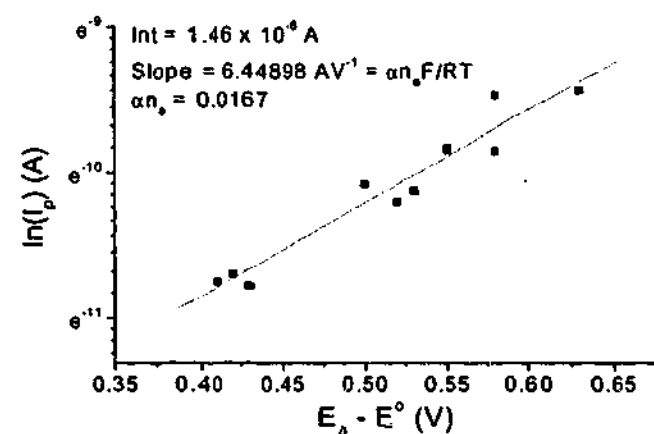


Fig. 3.3.2a Plot showing $\ln(I_p)$ versus ($E_p - E^0$) for 0.5 molkg⁻¹ $\text{P}_{14}(\text{Tf})_2\text{N}$ cyclic voltammograms.

proportional to $n(\alpha n_a)$ where α is the transfer coefficient.^{2,5} Using the equation describing the current response for a quasi-reversible process;

$$I_p = (2.99 \times 10^5) n(\alpha n_a)^{1/2} ACD^{1/2} \nu^{1/2}$$

allows the diffusion coefficient to be recalculated. The new value is $4.8 \times 10^{-7} \text{ cm}^2 \text{ s}^{-1}$ (cf. $1.0 \times 10^{-8} \text{ cm}^2 \text{ s}^{-1}$). The new value more accurately reflects the diffusion coefficient for Li^+ . However, it should be noted that this treatment does not account for the presence of an uncompensated IR drop at the electrode surface (which is likely in the RTIL). Thus, the true value of the diffusion coefficient is likely to lie between the two extremes, dependent upon the magnitude of the uncompensated IR drop present in the system.

References

1. M. A. M. Noel and R. A. Osteryoung, *J. Electroanal. Chem.*, **293**, 139 (1990).
2. J. Wang, *Analytical Electrochemistry*, VCH, New York (1994).
3. A. Wieckowski (Ed.), *Interfacial Electrochemistry: Theory, Experiment, and Applications*, Marcel Dekker, New York (1999).
4. A. J. Bard and L. R. Faulkner, *Electrochemical Methods, Fundamentals and Applications*, John Wiley and Sons, New York (1980).
5. R. S. Nicholson and I. Shain, *Anal. Chem.*, **36**, 706 (1964).